Institute of Experimental and Applied Physics

University of Kiel

Kinetic Physics with Solar Wind Heavy Ions Measured at 1 AU

Doctoral Thesis

Nils Peter Janitzek

First Investigator   Prof. Dr. Wimmer-Schweingruber
Second Investigator   Prof. Dr. Kersten

Abstract

ZUSAMMENFASSUNG

Contents

Chapter 1

Kinetic Physics of the Solar Wind

1.1 The Solar Wind

Based on observations of comet tail accelerations, that could not be explained by the solar photon radiation pressure, in 1951 L. Biermann developed the concept of a continuous plasma stream from the Sun that was first called *solar corpuscular radiation* [?] and which is today known as the solar wind. In 1958 E. Parker [?] presented a first model of the solar wind that could reproduce the high plasma outflow speeds of more than 500 km/s calculated by Biermann. This was achieved by assuming a stationary expansion of the solar corona instead of the previously common assumption that this outermost atmospheric layer of the Sun is in hydrostatic equilibrium. As depicted in Figure 1.1, the Parker model of the solar wind predicts outflow speeds between 200 and 800 km/s for coronal temperatures on the order of $T_e \approx 10^6$ K which is in good agreement with the coronal temperatures that were inferred already in the 1940ies from spectroscopic measurements of the solar corona [Aschwanden and references within]. In 1959 the existence of the solar wind could be proofed independently with in-situ particle measurements by the Russian Luna-1 and US-American Mariner-2 missions [? ?]. The plasma experiment on Mariner-2 measured almost the entire solar wind speed range that was predicted by the Parker model from speeds below 300 km/s to about 800 km/s [?]. This speed range is confirmed up to today by all following missions and thus can be considered as the regular solar wind speed range. Mariner-2 measurements also revealed the two major ion components of the solar wind as protons (H^+) and alpha particles (He^{2+}) that have relative abundances of 95% and 5% in the the average solar wind.

The Parker model based on the radial expansion of the plasma also has implications for
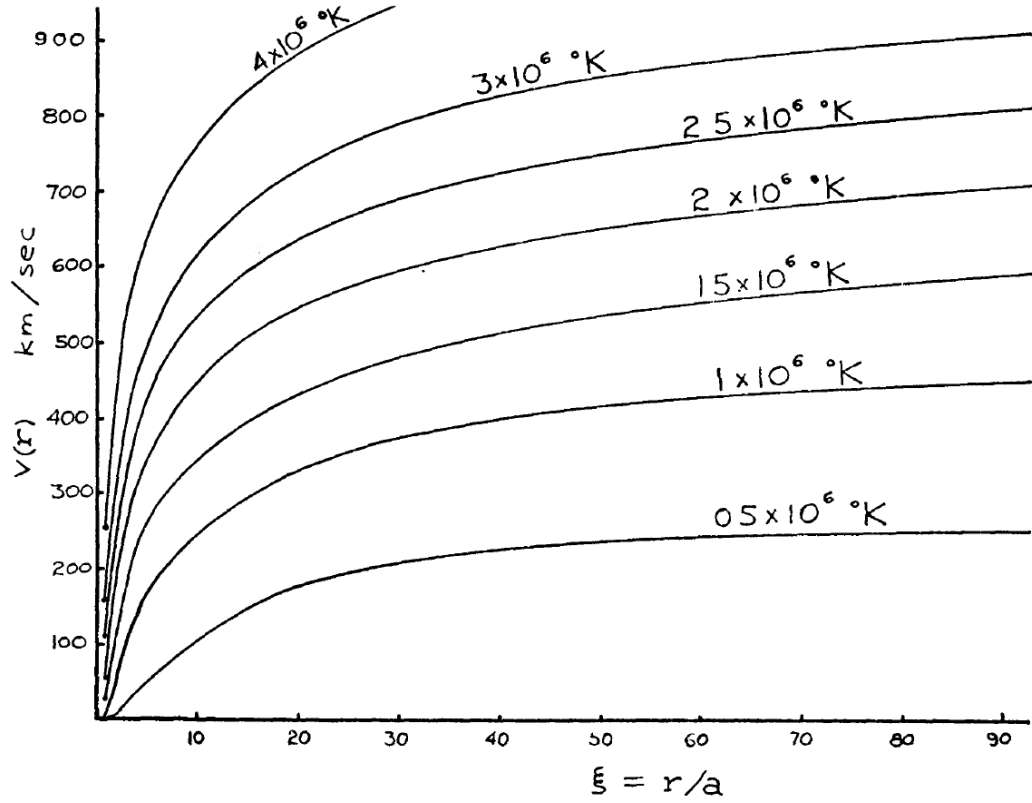
FIGURE 1.1: Predicted solar wind outflow speed v in dependence of of the distance to the solar center r for coronal temperatures $T = 0.5 \cdot 10^6$ K - $T = 4 \cdot 10^6$ K. The speeds are calculated as spherically symmetric hydrodynamic expansion velocity of an isothermal solar corona. The distance is given in units of the solar radius a, which has been approximated as $a = 10^6$ km. The Figure is taken from [?].

the topology of the magnetic field in the solar wind. This magnetic field is generated by processes within the Sun [?] and can be regarded in a first approximation (for the quiet Sun) as a dipole field perpendicular to the ecliptic plane of the heliosphere. The B-field expands from the solar surface, the photosphere, through the Sun's atmosphere out into interplanetary space. At a certain distance from the Sun, the local kinetic pressure in the surrounding plasma

$$p_{kin} = nk_B T \, , \tag{1.1}$$

depending on the plasma temperature T and particle number density n, overcomes the local magnetic pressure

$$p_{kin} = \frac{B^2}{\mu_0} \, , \tag{1.2}$$

where $B = |\underline{B}|$ is the magnitude of the ambient magnetic field and μ_0 is the vacuum permeability. At this point, where the so-called plasma beta parameter $\beta = p_{kin}/p_{mag}$ becomes larger than 1, the trajectories of the charged plasma particles are no longer confined to the solar magnetic field but instead the particles start to stream out radially

from the Sun and carry the magnetic field lines with them. The B-field is said to be *frozen* into the plasma from this point on and the surface that is defined by $\beta = 1$ is termed the *source surface* of the solar wind. It is estimated to be located at a distance of $R_0 \gtrsim 1 R_S$ above the Sun's surface where $R_s \approx 7 \cdot 10^5$ km is the solar radius (see Figure 1.2). The Parker model yields that the acceleration of the solar wind happens in a region close to the source surface that is narrow compared to heliospheric scales of at least several astronomical units (1 AU $\approx 1.5 \cdot 10^8$ km). From there on, the wind streams with nearly constant speed outwards in accordance with the speed profiles in Figure 1.1. Based on this approximation of constant speed one finds for the heliospheric steady state B-field that the field lines form an Archimedean spiral and their orientation (or winding angle) ϕ in the ecliptic plane at a radial distance $R \geq R_0$ relative to the center of the Sun is given by:

$$\tan(\phi) = \phi_0 - \frac{\omega}{v} R \tag{1.3}$$

where $\omega = 2\pi/25.38$ d is the (sidereal) angular speed corresponding to the solar rotation, v is the assumed constant flow speed of the solar wind and ϕ_0 is the azimuth angle at $R = R_0$ which is by definition of the particle outflow direction perpendicular to the source surface. The magnetic field $\underline{B}(R, \phi) = \underline{B}_r + \underline{B}_\phi$ at any location $\underline{r} = (R, \phi)$ in the ecliptic plane can then be calculated as

$$\underline{B}_r(R) = B_0 \left(\frac{R_0}{R} \right)^2 \underline{e}_r \tag{1.4}$$

and

$$\underline{B}_\phi(R, \phi) = B_0 \left(\frac{\omega}{v} \right) (R - R_0) \left(\frac{R}{R_0} \right)^2 \underline{e}_\phi \tag{1.5}$$

where $B_0 = |\underline{B}_0|$ is the magnitude of the magnetic field on the source surface and $\underline{e}_r$ and $\underline{e}_\phi$ are the radial and azimuthal unit vectors in polar coordinates, respectively. As we can see from 1.3 the mean magnetic field direction in the ecliptic plane varies with the distance to the Sun and also to some extent with the solar wind speed. For instance at the Lagrange-point L1 that is corotaing with the Earth at a solar distance of $R_{L1} \approx 1$ AU, we find for a solar wind speed of 400 km/s a mean B-field angle of $\phi = -45°$ with respect to the selected radial solar wind outflow direction $\phi_0 = 0$ if we substitute the sidereal angular speed by the synodical angular speed $\widetilde{\omega} = 2\pi/27.28$ d.

Since the establishment of the Parker model more than 60 years have passed and a number of missions dedicated to the Sun and the solar wind were launched, among
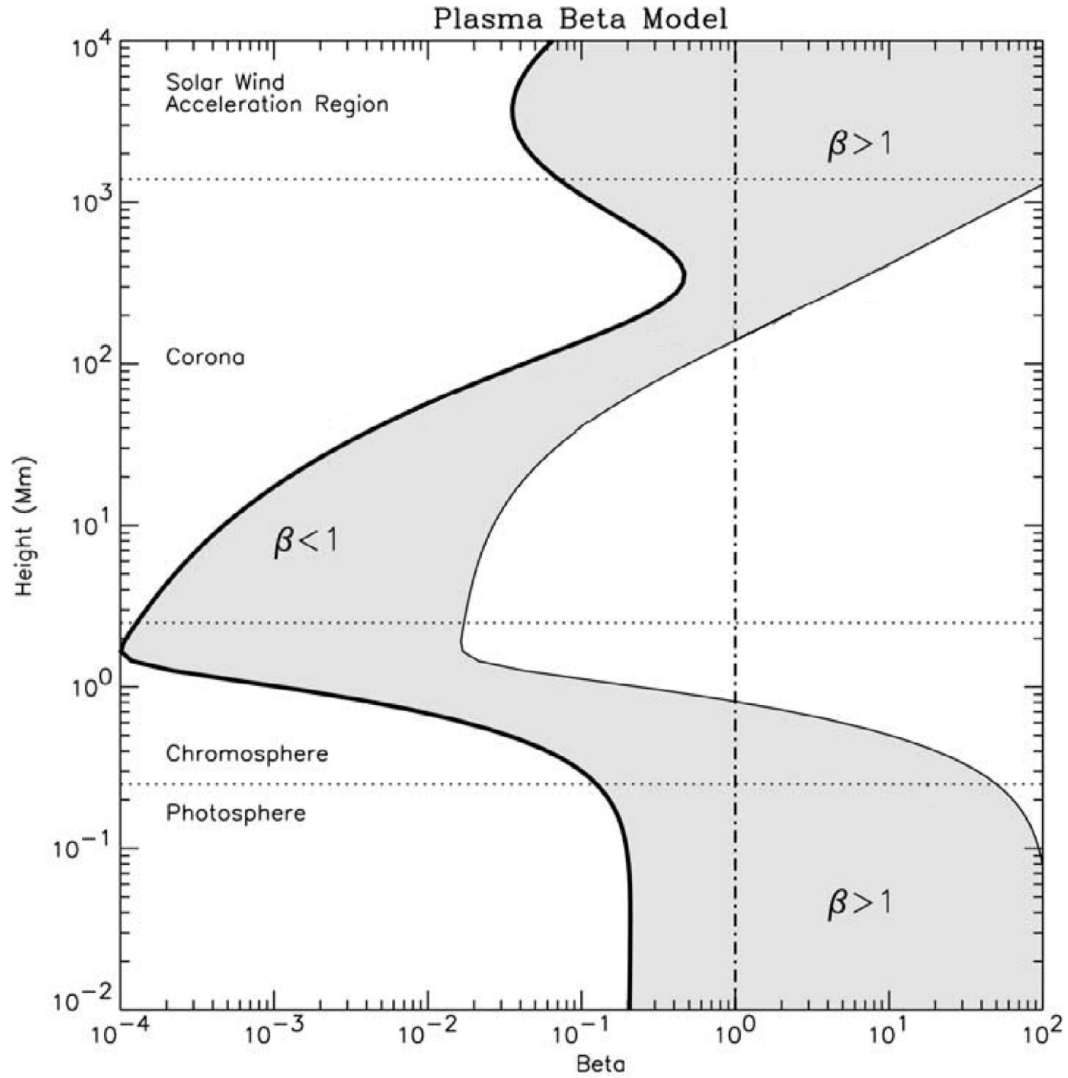
FIGURE 1.2: Modeled plasma beta parameter as a function of the height in the solar atmosphere. The figure is taken from [?].

them Helios, Ulysses, SOHO, ACE, Hinode, SDO, STEREO, and recently Parker(!) Solar Probe. These missions, together with particular experiments on planetary missions such as the famous Apollo11 [?] solar wind foil experiment, contributed to reveal a much more detailed picture of the solar wind i.e. by determining the kinetic properties of its main constituents at different distances from the Sun [?],[?],[?],[?], discovering and describing the heavy element component from helium to nickel [?], analyzing the wind's source regions [?] or unveiling the global 3-dimensional structure of the solar wind over the solar cycle [?],[?].

In the simplest scheme the solar wind is divided into two classes that are related historically to the typical observed speeds and are therefore called *fast wind* and *slow wind*. The slow wind is typically measured at velocities around 300 km/s up to velocities of

about 400 km/s while the fast wind is usually measured at speeds above 500 km/s and reaches up to about 800 km/s [2], [**?**]. Naturally, one also measures intermediate speeds for which the classical distinction can be ambiguous and there exist alternative scheme of classification schemes [**?**] that are currently also investigated with machine learning techniques [**?**]. Yet, for the purpose of this work it is sufficient to keep the two-class scheme that, besides its terminology, is nowadays based on more criteria than just the solar wind speed. Fast and Slow wind are also different in elemental and charge state composition of the so-called *heavy minor elements* with atomic number $Z > 2$ and relative abundances below 10^{-3} compared to solar wind hydrogen: While both wind types show an enhancement of so-called low-FIP elements (with a first ionization potential below $U_{FIP} \lesssim 10\,\mathrm{V}$ such as calcium, magnesium, silicon, and iron) compared to the photospheric composition, in the slow wind the over-representation of low-FIP elements is with a factor of about 3 much stronger pronounced than in the fast wind with a factor of about 1.5 [**?**]. Finally, the typical slow and fast wind streams also differ in the observed charge states of the heavy elements. One has to note that the (final) charge state of an ion that is measured in the solar wind is determined in the solar corona [e.g. [**?**], [**?**] (minor ion charge states etc)] where the higher particle densities yield short ionization and recombination times so that the mean charge state of a species can adapt to the plasma temperature, while the rapidly decreasing densities in the solar wind cause a so-called *freezing* of the charge states independent of the local plasma temperature. As one observes higher ion charge states in the slow wind compared to the fast wind [**?**], which links the slow wind to higher coronal temperatures, these observations pose a serious problem to the Parker model.

An alternative approach to understand the nature of the slow and fast wind is to look for its respective origin on the Sun by comparing in-situ kinetic and composition measurements with remote sensing observations of the solar corona. Within the ecliptic the back-mapping of small scale structures in the in-situ data back to the corona might be ambiguous but with Ulysses for the first time solar wind in-situ measurements out of the ecliptic were possible and as can be seen from Figure 1.3 one can recognize a simple large scale pattern of the solar wind outflow kinetics for the quiet Sun (in the left panel). It becomes clear that at quiet conditions the fast wind originates from extended regions at high latitudes while at low latitudes primarily slower wind is observed. By the comparison with EUV and soft X-ray images of the corona (e.g. SOHO/EIT, SDO/AIA) the source regions of the fast wind can be identified as the so-called *coronal holes*, which are extended regions of nearly radial magnetic fields in the corona which thus allow an efficient outflow of the plasma. As this causes low plasma density and temperatures in this regions they look darker at typical wavelengths of UV and soft Xray images of the corona [**?**].
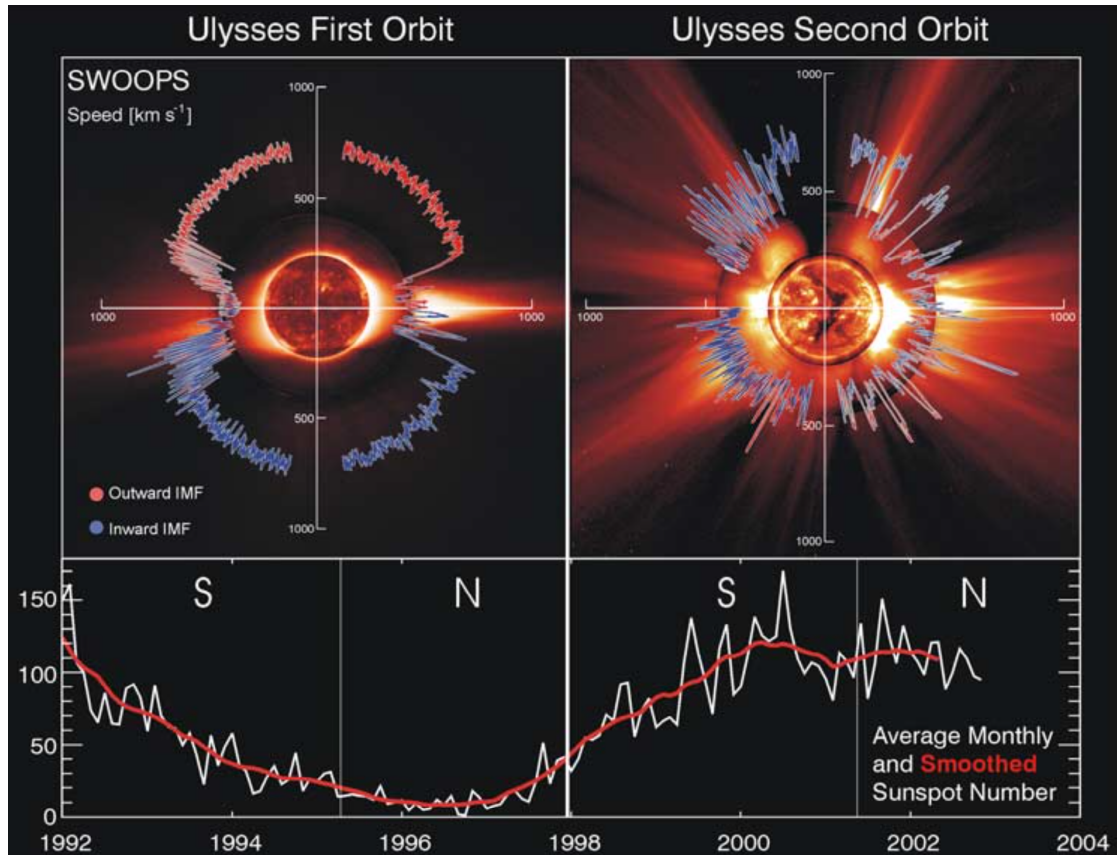
FIGURE 1.3: Upper panels: solar wind speed measured with the SWOOPS instrument onboard the Ulysses spacecraft on its first (left) and second (right) orbit plotted as a function of the Ulysses orbit latitude (in blue and red for the different magnetic polarity). As can be seen from the time-line of the sunspot number in the two lower panels, Ulysses' first orbit occurred mostly during solar minimum where the solar magnetic field can be well-approximated by a dipole field. In this situation the measured solar wind speed shows a clear latitudinal pattern: At higher latitudes above $30°$ a relatively constant fast wind with $700\,\text{km/s} < v < 800\,\text{km/s}$ is measured while at lower latitudes primarily slow wind $v \lesssim 400\,\text{km/s}$ is measured interrupted by occasional faster wind streams with speeds up to about $600\,\text{km/s}$. In the second orbit that coincided with solar maximum, the measured solar wind speed does not show any clear large scale pattern as the result of the ongoing change of magnetic field polarity that leads to a complex magnetic field structure all over the corona and in the heliosphere. Furthermore, at high solar activity the Sun frequently emits spontaneously large plasma structures into interplanetary space. These are termed *interplanetary coronal mass ejections* (ICMEs) and add additional complexity to the situation. The Ulysses speed observations are plotted over images characteristic of the corona at solar minimum on 17 August 1996 and solar maximum on 7 December 2000. From the center out, the images are composed of the recorded images by the Extreme Ultraviolet Imaging Telescope (EIT) on SOHO (spectral line: Fe XII at 195 A°), the Mauna Loa K-coronameter (spectral range: 700–950 nm), and the SOHO C2 Large Angle Spectrometric Coronagraph (white light). The Figure is taken from [**?**].

We note, that the established link between the fast wind and low coronal temperature is consistent with the trend in the coronal freeze-in temperatures obtained from heavy ion in-situ composition measurements, but it is in contradiction with the Parker model[1], and therefore illustrates the need for a better theoretical model. Besides the mean outflow speeds also the in-situ measured kinetic temperatures of the fast solar wind ions are not well-understood as one measures about mass-proportional (or even over mass-proportional) temperatures [?],[?], [1], [?] kinetic properties, [?] for the heavy ions with increasing particle mass while one expects equal temperatures for a thermal equilibrium. As these high heavy ion temperatures are already observed in the corona, they might also provide a key-observation for the still unsolved *coronal heating problem* that expresses the fact that the corona is up to three orders of magnitude hotter than the photosphere and chromosphere, although the energy that is created inside the Sun has to pass through these colder lower atmospheric layers to reach and heat the corona. Finally, the origin of the slow wind is another problem as the theoretical confinement of the plasma due to the strong magnetic field should prohibit the efficient release of plasma at low magnitudes where the slow wind is measured in-situ.

All described problems occur already for the simpler case of low solar activity, but the situation becomes even more complex for the active Sun (see right panel in Figure 1.3) where the solar magnetic field is in the middle of its polarity change that occurs approximately every 11 years [?]. At high solar activity the magnetic field structure is more complex allowing for different solar wind speed regimes at all latitudes. Furthermore, the Sun frequently emits spontaneously large plasma structures into interplanetary space, called ICMEs, that can be accompanied by the release of high energetic particles via flares or can create these particle populations through shock acceleration of the ambient plasma on their way out through the heliosphere [?]. ICMEs rarely happen during solar minimum which coincides with the period of the SOHO/CELIAS observations and they are most probably related to completely different initial acceleration processes than the classical continuous solar wind [A Model for Solar Coronal Mass Ejections [?]. Therefore they are not part of this work, although they are sometimes considered as its own solar wind class *transients* [?].

To solve the problem of solar wind acceleration and heating in the fast wind, over the last five decades more elaborated models of solar wind evolution have been developed, that proposed a variety of processes to accelerate the plasma in accordance with the existing observations [?]. A promising class of mechanisms involves wave-particle interaction such as turbulent heating by Alfvén waves [?],[?], or resonant wave particle interaction with ion-cyclotron waves [?], [?],[?], [?]. The latter might evolve through

---

[1]The Parker model, however, still explains successfully the large scale heliospheric magnetic field by Eq. 1.3 - 1.5.

a turbulence cascade from low-frequency Alfvén waves originating from the photospheric convection motion [**?**], [**?**]. Alternatively, the high-frequency ion-cyclotron waves could be created directly through reconnection of the flaring network in the lower transition region [**?**], [**?**].

In order to test and restrict these acceleration and heating models as well as further models of solar wind transport and thermalization, precise measurements of the of solar wind kinetic properties are needed. In particular the systematic measurements of solar wind minor ion species might yield additional information just by the fact that the heavy ions span a wide range in mass and charge and therefore couple differently to electromagnetic fields in the plasma. Furthermore, as these particles are in most cases negligible in terms of their number and mass density in the solar wind, their implementation into current models as test-particles might be realized relatively easy. Before we come to the measurement of these heavy minor ions with SOHO/CELIAS, in the following we give a short introduction into the theoretical framework of kinetic solar wind description and discuss possible mechanism of solar wind acceleration, heating, transport and thermalization.

1.2   Kinetic Description of the Solar Wind

As a plasma the solar wind is a many-body system and therefore its adequate description requires a statistical treatment. In the following we will rely mainly on the so-called *kinetic* plasma description[2] that is based on probability distribution functions $f(\underline{r}, \underline{v})$ that are defined in general in the 6-dimensional phase space composed of the 3 dimensions $\underline{r} = (x, y, z)$ and $\underline{v} = (x, y, z)$ in position and velocity space, respectively. The state of the plasma particle ensemble is fully described when we know the evolution of $f(\underline{r}, \underline{v})$ over time. As the particle measurements that we discuss are all obtained at one point in (position) space, the phase space distribution becomes a velocity distribution function (VDF): f($\underline{v}$). In theory f is often treated as a continuous function assuming large particle counting statistics ($N_p \rightarrow \infty$). In this limit a one-species plasma in thermal equilibrium is described by a Maxwellian VDF:

$$f(\underline{v}) = f(v_x, v_y, v_z) = \left(\frac{m}{2k_B T}\right)^{3/2} \exp\left[-\frac{m((v_x - v_{x0})^2 + (v_y - v_{y0})^2 + (v_z - v_{z0})^2)}{2k_B T}\right],$$

(1.6)

where $\langle\underline{v}\rangle = (v_{x0}, v_{y0}, v_{z0})$ is the species' mean velocity, m is the mass of the plasma species, k_B is the Boltzmann constant and and T is the kinetic temperature of the plasma

---

[2]The kinetic description has to be distinguished from the Magneto-Hydrodynamic (MHD) description that treats the plasma as a magnetized fluid.

which is given for the three dimensional distribution by

$$T = \frac{3mv_{th}^2}{2k_B} \tag{1.7}$$

with the thermal speed v_{th}. When the situation reduces to one dimension as it is approximately the case when one measures along a well-defined given axis (x) in velocity space, the Maxwellian distribution reduces to

$$f(v_x) = \left(\frac{m}{2k_B T_x} \right)^{1/2} \exp \left[-\frac{m(v_x - v_{x0})^2}{2k_B T} \right] \tag{1.8}$$

and the temperature along the given axis is is then given by

$$T_x = \frac{mv_{th,x}^2}{2k_B} \tag{1.9}$$

with the corresponding thermal speed $v_{th,x}$. We note that Eq. 1.8 has the mathematical form of a Gaussian [3] distribution with most probable speed v_x and standard deviation $v_{th,x}$. If we have several particle species in the plasma, than the thermal equilibrium is only reached when each species on its own obeys a Maxwell distribution and in addition all species have the same mean velocity $\langle \underline{v} \rangle$ and the same kinetic temperature T, which is *not* equal to the same thermal speed due to the mass-dependence of T.

In contrast to theory, in the measured particle data we have finite (and often very limited) particle count statistics. Also in many cases the space borne instrumentation is not capable of measuring full 3-dimensional velocity distribution functions (simultaneously at all directions) so that our information is limited to certain measurement directions and certain model assumptions have to be made to infer the full picture from the measurements. In particular, most heavy ion measurements are restricted to 1-dimensional measurements along a certain instrument axis that then result in the reduced 1D-VDFs that we obtain e.g. with SOHO/CELIAS/CTOF and which can be described approximately with Eq. 1.8 and Eq. 1.9.

One of the few experiments that measure 3-dimensional particle VDFs that can be well-resolved for protons and alpha-particles is the E1 plasma experiment onboard the Helios twin-spacecraft [?]. In Figure 1.4 we depict solar wind 2D-VDFs measured with Helios in the ecliptic plane at approximately 1 AU in the slow (left panel, $v_p = 360$ km/s) and intermediate speed regime (right panel, $v_p = 360$ km/s). In both panels we overlaid schematically the typically center of mass for the simultaneously measured

---

[3]Note that Eq. 1.8 should not be confused with the Maxwell distribution for the speed magnitude $v = |\underline{v}|$, that is just Eq. 1.6 transformed to spherical coordinates with the shift in coordinate-system origin $v_{x0} = v_{y0} = v_{z0} := 0$ that leads to an asymmetrical distribution in v due to the additional factor v^2 that arises from the transformation.

FIGURE 1.4: Measurements of 2-dimensional VDFs of the solar wind protons (black contour lines with orange to blue contour filling) recorded with the HELIOS E1 Plasma Experiment for two measurement periods at approximately 1 AU in the slow (left panel) and (somewhat) faster wind (right panel) with proton mean speeds of $\langle v_p \rangle = 360$ km/s and $\langle v_p \rangle = 474$ km/s, respectively. The 2D-cuts are done along the zenith angle of the magnetic field vector. Orange fillings mark the highest phase space densities and the contour lines correspond to a factor of 0.8, 0.6, 0.4 and 0.2 times the maximum phase space density (solid lines) and logarithmically spaced to 0.1, 0.032, 0.001, 0.0032 and 0.001 times the maximum phase space density (dashed lines). The integration period of the VDFs is $\Delta t \leq 20$ s. To illustrate the differential streaming between protons and heavy ions we overlaid schematically the center of mass of a typical alpha particle VDF observed by Helios for both cases as red circles. We see that the the proton VDF shows clear nonthermal features in the faster wind case compared to the approximately Maxwellian VDF shape in the slow wind, which can be recognized best by the pronounced asymmetry along the local magnetic field direction $\underline{B}$ which is primarily caused by the so-called proton beam. The alpha particles show a differential velocity that is also directed along the magnetic field but its magnitude Δv is smaller than the proton beam differential speed. The figure is adapted after [**?**].

alpha particle with a red circle. While the measured VDF in the slow wind is nearly isotropic, the VDF measured at intermediate speeds shows a pronounced elongation along the in-situ magnetic field that is measured simultaneously with the particles by the Helios fluxgate magnetometer. This nonthermal feature is primarily (but not entirely) the result of a second minor proton component, the so-called proton beam, that streams ahead of the core proton distribution if one follows the field line outwards in the solar wind center of mass frame. The alpha particle center of mass also streams ahead of the proton core distribution with a differential speed $\Delta v \lesssim v_A$ [**?**] measured along the B-field which is typically a bit less than the core beam differential speed. In general it is not surprising that the differential velocity of the nonthermal ion populations are aligned with the magnetic field as any perpendicular velocity component
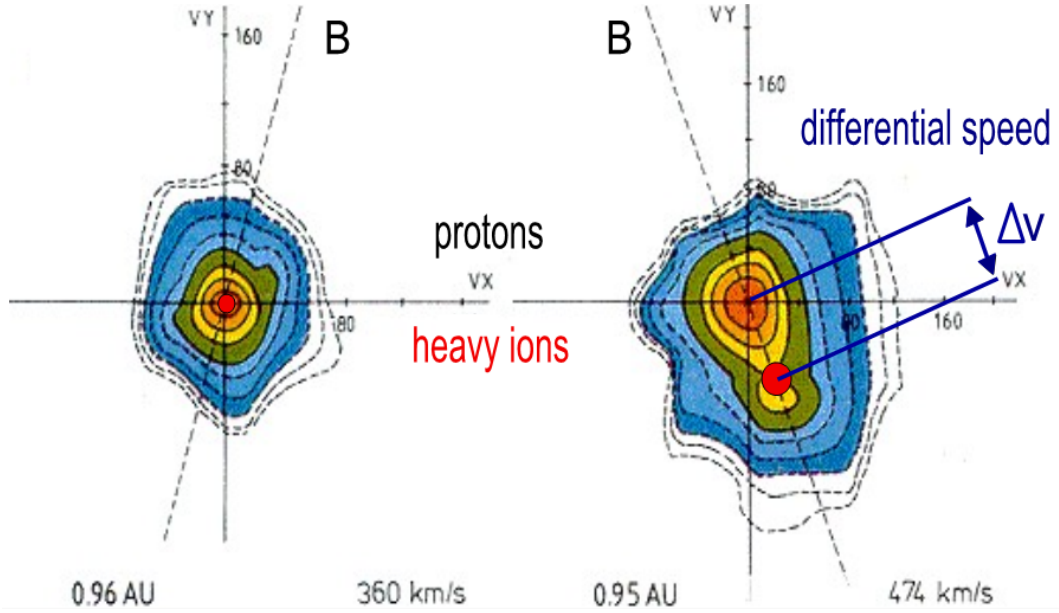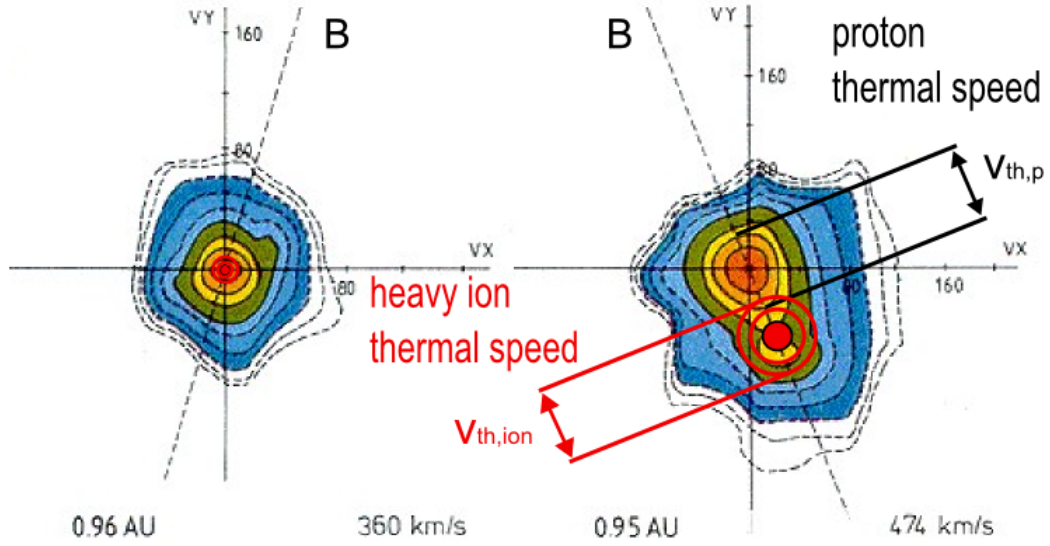
FIGURE 1.5: Same measurements of 2-dimensional VDFs of the solar wind protons (black contour lines with orange to blue contour filling) as in Figure 1.4. The sketched alpha species VDFs are again overlaid schematically (red concentric circles) only to illustrate approximately thermal (left) and nonthermal (right) ratios between heavy ion and proton thermal speeds. In the faster wind case in the right panel the thermal speed of the sketched alpha (core) VDF has approximately equal thermal speed as the proton (core) VDF which translates into the *nonthermal* feature of about mass-proportional temperatures while in the slow wind in the left panel the thermal speed of the heavy ion VDF is sketched about a factor of 2 lower than the proton thermal speed indicating a temperature ratio that are close to thermal equilibrium. The Figure is adapted after [**?**].

leads to a gyro-motion of the population that cannot be resolved in time with our measurements and thus contributes to the apparent perpendicular temperature.

In this work we aim to determine the differential speed Δv between protons and heavy minor ions ($Z > 2$) at 1 AU with the SOHO/CELIAS experiment. Depending on the expected underlying processes it is yet under debate whether the relevant differential speed should be measured from the proton core mean speed to the minor ion species mean speed as illustrated in Figure 1.4 or from the overall center of mass speed (including the alphas and the proton beam) to the minor species mean speed. As the CELIAS Proton Monitor only provides moment measurements of the protons, in any case we have to calculate Δv in this study as the latter one (see section 2.4 and the discussion in section **??**). In Figure 1.5 we show the same 2-dimensional solar wind proton VDFs as in Figure 1.4 but this time we overlaid typical thermal speeds for alpha particles by sketching the highest two contour lines of the alphas both for the slow wind case (left panel) and the faster wind case (right panel). In the right panel the thermal speeds for the proton (core) VDF and ion (core) VDF are approximately equal which translates into the *nonthermal* feature of about mass-proportional temperatures while in the slow wind in the left panel the thermal speed of the heavy ion VDF is about a factor of 2

lower than the proton thermal speed indicating a temperature ratio that are close to thermal equilibrium. Note, that for the comparison of the slow and faster wind case the, the proton thermal speed should be calculated ideally from the core only, as the beam is a separate nonthermal feature by itself. This assumes a very good separation between proton core and the beam population, which is not achieved with most proton experiments and neither by the CELIAS Proton Monitor (see discussion in section **??**). Despite the measurements of 3-dimensional VDFs, a second outstanding feature of the Helios mission was its highly elliptical orbit in the ecliptic plane that allowed measurements of the solar wind as close as 0.3 AU. We know now from these measurements [**?**] that the in-situ observed differential speed between alpha particles and proton shows a systematical behavior in dependence of both the solar wind speed regime and the distance to the Sun. While for the slow wind at proton speeds between $v_p \approx 300$ km/s and 400 km/s no differential speed was observed, for faster wind above $v_p \approx 400$ km/s an increasing differential speed with decreasing distance to the Sun was found. In the fastest wind between $v_p \approx 600$ km/s and $v_p \approx 800$ km/s differential speeds of $v_{\alpha,p} \approx 150$ km/s were measured at 0.3 AU which decreased to values of $v_{\alpha,p} \approx 40$ km/s close to 1 AU. Comparable values of $\Delta v_{\alpha,p}$ in the vicinity of 1 AU were found from observations by several spacecraft, eg from ISEE-1 [**?**], WIND [**? ? ?**] and ACE [**?**]. Concerning the preferential heating of alpha particles both mass-proportional and even over-mass proportional alpha particle temperatures were found between 0.3 and 1 AU e.g. from Helios [**?**], WIND [**?**],[**?**] [**?**], ACE [**?**]. Besides differential streaming and temperatures, there is the third typical nonthermal VDF feature of temperature anisotropy with respect to the magnetic field that are commonly observed for solar wind protons and alpha particles[[**?**],[**?**], [**?**], [**?**]. Unfortunately, these cannot be observed at all with SOHO/CELIAS due to the lack of a magnetometer onboard SOHO and the impossibility to extrapolate the B-field direction from other spacecraft on short timescales comparable to the frequency of directional change.

We finally emphasize that the discussed nonthermal features that shall be investigated with the SOHO/CELIAS data are not only of interest by themselves in terms of fundamental collisionless plasma physics but instead as pointed out by [**?**] they might play a keyrole to better understand the "solar wind acceleration itself" and to gain deeper insights into "interplanetary processes such as instabilities and wave-particle interaction". These links between the measured particle VDFs and such fundamental processes in the solar wind are discussed in the following two sections. We start with the discussion of ion-cyclotron resonance as a possible candidate process for solar wind acceleration close to the sun which can simultaneously create the observed nonthermal VDF features throughout the inner heliosphere.

1.3 Ion-Cyclotron Resonance as Candidate Mechanism for Solar Wind Acceleration and Heating

From a theoretical perspective one of the most investigated processes among the wave-particle interaction based mechanism is ion-cyclotron resonance. This is justified by the fact the process can simultaneously create all three observed nonthermal VDF features that we discussed in the previous subsection: Differential speeds between solar wind heavy ion species and the bulk protons, preferential heating of the heavy ions VDF as well as temperature anisotropies for all ion species so that $T_\perp > T_\parallel$. As the occurrence of the resonance itself depends on the gyrofrequency of the involved ions, one might further expect a distinct behavior of the ion species depending on their mass-per-charge values. Therefore, ion-cyclotron resonance is a natural candidate process to be investigated with a solar wind time-of-flight mass spectrometer such as CTOF that is able to measure a wider range of heavy ion species both in mass and mass and charge. In the following we describe shortly the basic concept of ion-cyclotron resonance and discuss some theoretical model predictions. In this whole section 1.3 we follow closely an early paper on resonant wave acceleration of minor ions by [**?**] and the review article on fast solar wind acceleration by [**?**].

The Single Particle-Wave Scenario of Resonant Ion-Cyclotron Interaction

The motion of charged particles in a magnetic field can be decomposed into a a translational motion along the magnetic field lines and a circular gyro-motion perpendicular to the field lines. The gyrofrequency of the particle is linked to its mass m and charge q as well as to the local B-field magnitude $B = |\vec{B}|$ as

$$\Omega = \frac{qB}{m} \ .$$ (1.10)

Due to their gyro-motion the ions in the solar wind can interact (exchange momentum and energy) with circularly polarized left-handed so-called ion-cyclotron waves in the plasma (check!) if the resonance condition is fulfilled (see e.g. [Hollweg and Isenberg2002):

$$\omega(k_\parallel) - k_\parallel v_\parallel = n\Omega$$ (1.11)

The term on the left side of Eq. 1.11 describes the Doppler-shifted wave frequency that is seen by the ion that moves with the speed $v_\parallel$ parallel to the magnetic field and which can be expressed as a function of the parallel wave number $k_\parallel$.
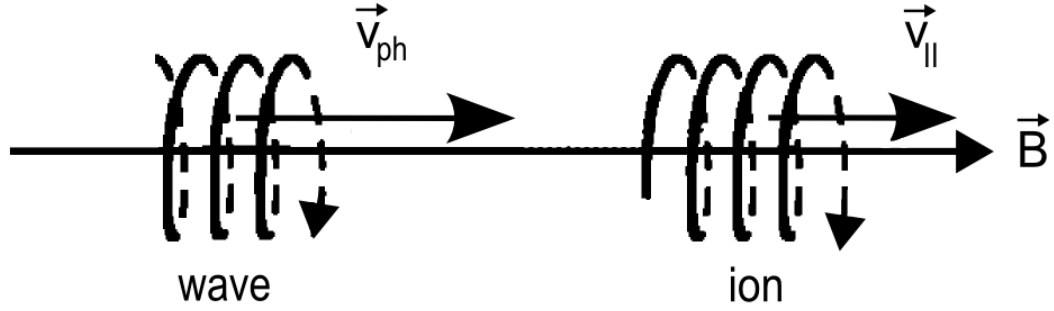
FIGURE 1.6: Schematic illustration of resonant wave-particle interaction between an ion with parallel velocity $\underline{v}_\parallel$ to the background magnetic field $\underline{B}$ and an over-taking ion-cyclotron wave that is propagating parallel to the magnetic field with an outward phase speed $v_{ph} > v_\parallel$. The Figure is adapted after [?].

While the integer n on the right side of the equation indicates that higher orders of resonance can occur at higher wave frequencies we concentrate in the following on the first order resonance $n = 1$ and for additional simplicity we only discuss waves that move parallel to the magnetic field so that we abbreviate $k := k_\parallel$.

If a gyrating ion encounters a wave with matching frequency ω as shown in Figure 1.6 the ion is accelerated in a direction perpendicular to $\underline{B}$ as it sees the corotating electric field $\underline{\delta E}(t)$ of the wave as a DC electric field in its own rest frame. The particle can thus increase or decrease secularly its perpendicular speed $v_\perp$ over its gyro orbit depending on the phase difference ϕ between the rotating wave E-field vector and its own perpendicular speed component at the moment of encounter. The rate of the ion's energy gain/loss over the time Δt while it is traveling a distance ΔL on its gyro-orbit can be written as:

$$\frac{\delta E_{kin}}{\Delta t} = \frac{q \delta E_\perp \Delta L}{\Delta t} \cos \phi = \frac{q \delta E_\perp v_\perp}{\Delta t} \cos(\phi) \tag{1.12}$$

where E_{perp} is the transverse electric field component (see above) and $v_\perp$ is the initial transverse ion speed along its gyro orbit. From Faraday's law we can relate the magnitudes of the electric and magnetic field vectors of the wave to each other

$$\delta E = \frac{\Omega}{k} \delta B \tag{1.13}$$

and thus express the change in the particle's squared perpendicular speed over the time Δt as a function of the wave's magnetic field δB:

$$v_\perp \delta v_\perp = \frac{q\Omega \delta B_\perp v_\perp}{mk} \cos(\phi)\Delta t \; . \tag{1.14}$$

We can now make use of the ion gyro-frequency definition in Eq. 1.10 to obtain the final expression

$$v_\perp \delta v_\perp = v_\perp \frac{\Omega^2}{k} \frac{\delta B_\perp}{B_0} \cos(\phi)\Delta t \; . \tag{1.15}$$

Due to the waves perpendicular magnetic field component there is in general also a Lorentz force acting on the gyrating particles with magnitude

$$F_L = q v_\perp \delta B_\perp \tag{1.16}$$

which accelerates them parallel to the background magnetic field $\underline{B}_0$. Using again Eq. 1.10 we can write this change in the parallel speed over the same time Δt as

$$\delta v_\| = \frac{F_L}{m} \cdot \Delta t = v_\perp \Omega \frac{\delta B}{B} \cos(\phi)\Delta t \tag{1.17}$$

With Eq. 1.15 and 1.17 the particle motion is completely described for all times as long as the ions remain in the adequate speed range to stay in resonance with the ion cyclotron wave(s). As the magnetic field is stationary in the frame moving with the wave, there should not be any work performed on the ions in this frame We show that the overall kinetic energy of the particles is conserved in this frame by calculating the total change of E_{kin} after any given time Δt:

$$\Delta E_{kin} = m(v_\perp \delta v_\| + v_\| \delta v_\perp) = m v_\perp \Omega \frac{\delta B_\perp}{B_0} \cos(\phi)\Delta t \left(\frac{\Omega}{k} + v_\| \right) = 0 \tag{1.18}$$

where we made use of the fact that in the wave frame the wave frequency ω is zero, so that we find from Eq. 1.11 for the parallel speed component of the particle

$$v_\| = -\frac{\Omega}{k} \; . \tag{1.19}$$

Model Predictions for Resonant Ion Acceleration and Heating

In the following we want to find a quantitative description/prediction of how strong the nonthermal VDF features can develop when we assume ion-cyclotron resonance as the dominant process. In particular we will see that certain limitations on the differential speed are already given by the resonance condition itself.

When we transform into the solar wind proton bulk rest frame so that $\langle \underline{v_p} \rangle := 0$ and restrict the situation again to parallel propagating waves ($|\underline{k}| = k_{\|}$) and to first-order resonance Eq. ($n = 1$) becomes

$$\omega'(k) - k\Delta v = \Omega \tag{1.20}$$

where

$$\Delta v = |\Delta \underline{v}| = |\underline{v} - \langle \underline{v_p} \rangle| \tag{1.21}$$

is the differential speed that equals the magnitude of the differential velocity between the velocity of the interacting ion and the solar wind proton bulk velocity. Note that we can directly omit the parallel index for Δv as any differential speed component perpendicular to $\underline{B}$ would immediately start to gyrate around $\underline{B}$ as already mentioned in subsection 1.2. In analogy we make the same transformation for the wave frequency so that we find in Eq. 1.20 for the Doppler-shifted wave frequency in the solar wind proton frame

$$\omega'(k) = \omega - k\langle v_{p,\|} \rangle . \tag{1.22}$$

When we now assume in a first approximation that the ion-cyclotron waves are entirely carried by the solar wind bulk protons and thus are unaffected by the heavy ion species we find in the SW frame for the dispersion relation [Marscha and McKenzie 1982]

$$k = \frac{\omega'}{V_A \sqrt{1 - \omega'/\Omega_p}} \tag{1.23}$$

where Ω_p is the proton gyro-frequency and v_A is the Alfvén speed

$$v_A = \frac{B}{\mu_0 \rho} \tag{1.24}$$

that can be calculated from the vacuum permeability μ_0, the magnitude of the background magnetic field B and the solar wind mass density ρ. Eq 1.23 is known as the cold plasma dispersion relation for ion-cyclotron waves and fully describes these waves in the plasma as it links the wave-number to the wave frequency and thus also determines the wave phase speed (in the SW frame) for any given frequency by

$$v'_{ph} = \frac{\omega'}{k} . \tag{1.25}$$

If we solve Eq. 1.23 for ω' and plot it as a function of k as it is done in Figure 1.7 we see that the ion-cyclotron waves have higher phase speed the higher their frequency is and
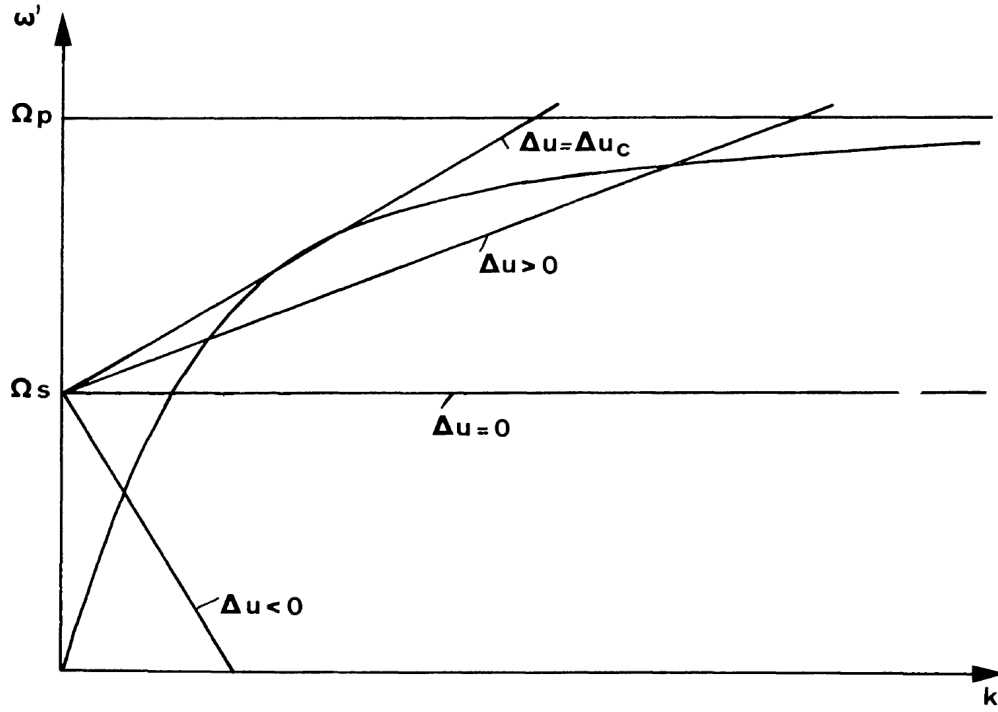
FIGURE 1.7: Visualization of the ion-cyclotron resonance condition in the solar wind plasma. The curved line marks the cold plasma dispersion relation $\omega'_w(k)$ of ion-cyclotron waves in the solar wind under the assumption that the waves are carried entirely by the solar wind bulk protons. Note that in this representation all frequencies $\omega'(k)$ are plotted in the solar wind (or proton bulk) rest frame, so that the doppler-shifted resonance frequency $\Omega' = \Omega + k\Delta v$ of ions that move with a relative speed Δv to the proton bulk in this frame is given by a straight line with gradient Δv and frequency offset Ω. As the resonance condition 1.11 is only fulfilled at the intersection between Ω' and the dispersion relation $\omega'_w(k)$, we see that there is for each species a characteristic maximum differential speed given by the slope of the tangent where we only find exactly one intersection. Therefore the particles can only be accelerated to a certain maximum differential speed. For protons at arbitrary speeds this is the bulk speed as Ω_p is an asymptotic limit of $\omega'_w(k)$. For heavy ions with higher mass-per-charge their gyrofrequency Ω is lower and therefore they can be accelerated to characteristic m/q-dependent maximum positive differential speeds, before the resonance limits itself. Adpated after [?], Mark $\omega'_w(k)$. change the u for v and Ω_s for Ω!.

eventually cannot exist anymore at the proton gyro frequency which is consistent with the complete dissipation of the wave energy to the thermal motion of the bulk protons that thus cannot longer carry the wave. When we also solve Eq. 1.21 for $\omega'(k)$ we obtain a linear function of the wave number with the gradient of the differential speed v and offset of the ion gyro-frequency Ω of the ion. In Figure 1.7, we sketched different linear functions $\omega'_{\Delta v}(k)$ for an alpha particle in dependence of its differential speed Δv with respect to the mean bulk proton speed. Thus for a given differential speed the resonance condition in Eq. 1.11 is fulfilled only at the intersections $(k, \omega)_{res}$ which represent waves with matching frequency and wave number. We see that for He^{2+} we

find two intersections for all differential speeds below a certain differential speed Δv_{max} and one intersection in the limiting case $\Delta v = \Delta v_{max}$, while for $\Delta v > \Delta v_{max}$ no resonant interaction can occur. Thus the particle cannot be accelerated to higher differential speeds by any resonant interaction with the existing ion-cyclotron waves and thus the resonant acceleration is self-limiting regardless of the available wave power. We also see that proton can only interact resonantly with the waves as long as it is slower than $\langle v_p \rangle$ as its gyro-frequency cannot be reached by any ion-cyclotron wave carried by the proton bulk as discussed above. On the other hand, all minor ion species have a higher mass-per-charge ratio and therefore lower gyro-frequencies as He^{2+}. As the dispersion relation is assumed to be independent of the solar wind heavy ions the differential speed cut-off of the minor ions due to the resonance condition occurs at even higher values $\Delta v_{max} > \Delta v_{max,\alpha}$. By taking the partial derivative of Eq. 1.23 with respect to k and setting

$$\frac{\partial \omega(k)}{\partial k} \overset{!}{=} \Omega + k \cdot \Delta v_{max} \tag{1.26}$$

we can obtain the differential cut-off speed for each heavy ion species in dependence of its gyro-frequency which can be then expressed in dependence of the ions charge-per-mass:

$$\Delta v_{max}(m, q) = \left[\frac{8 + 20 \cdot q/m - (q/m)^2 - (q/m)^{1/2} \cdot (8 + q/m)^{3/2}}{8} \right]^{1/2} v_A . \tag{1.27}$$

In Figure 4.30 we show the dependency of the predicted differential cutoff-speed on the ion's charge-per-mass for a number of typical solar wind ion species where the discussed case of wave propagation parallel to the magnetic background field is the lower branch. The upper branch shows the analog dependency for wave-propagation perpendicular to the magnetic field. The differential cutoff-speeds are given relative to the Alfvén speed. We see the same qualitative behavior for parallel and perpendicular wave propagation with maximum differences of about $0.1\ v_A$ between the branches. For the shown ion species the calculation yields maximum differential speeds of a bit more than $0.53\ v_A$ for Fe^{12+} in the perpendicular case. The lowest clearly observable iron charge state Fe^{7+} (not shown here, but see chapters 5-7) one expects a maximum differential speed of about $0.65\ v_A$ for perpendicular wave propagation. So far we could derive a quantitative prediction/expectation for the differential speeds based on a relatively simple analytic model of resonant ion-cyclotron interaction. However, when we go to a more realistic modeling of the solar wind plasma we have to include a number of effects that can change the obtained predictions significantly. One aspect to take into account is that the alpha particles represent on average about 5% of the number density
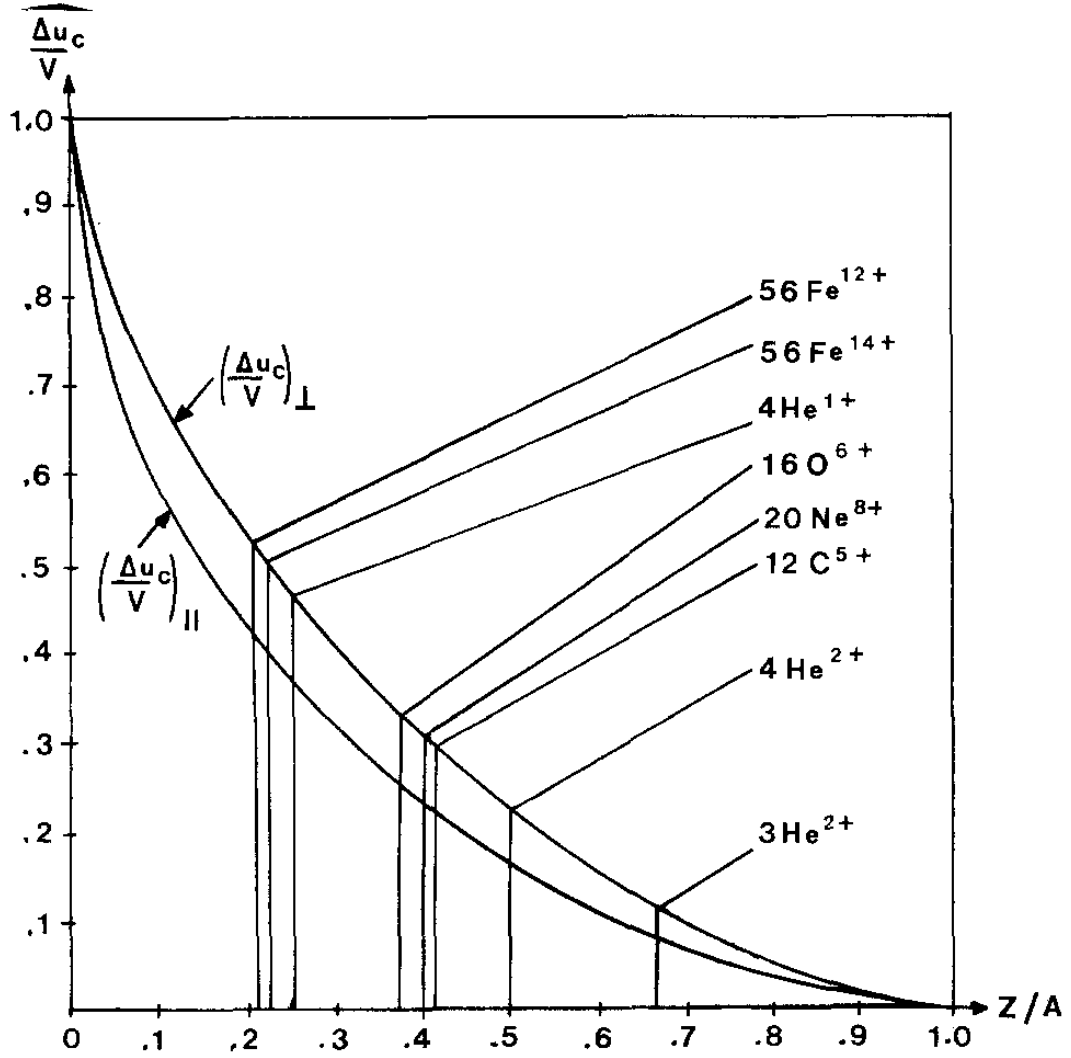
FIGURE 1.8: Characteristic differential speed cut-offs of heavy ion species due to ion-cyclotron resonance for the scenario of the waves propagating parallel to the background magnetic field $\underline{B}$ (lower branch, as calculated after Eq. 1.27) and perpendicular to $\underline{B}$ (not discussed here, but see [? ?]). Adapted after [?], change the u for v!

and 20% of the mass-density of the solar wind and thus in general it is hard to justify treating them as test-particles. When one therefore assumes that the alphas are part of the solar wind background plasma in which the waves propagate, one has to modify the dispersion relation of the ion cyclotron waves which then is written as [?], [?]:

$$(kv_A)^2 = \Omega_p \left[\frac{\omega^2}{\Omega_p - \omega} + \frac{2n_\alpha}{n_p} \frac{(\omega - kv_\alpha)^2}{\Omega_\alpha - (\omega - kv_\alpha)} \right] \tag{1.28}$$

where n_p and n_α are the proton and alpha number densities, Ω_α is the alpha gyro-frequency and v_α is the mean differential speed of the alpha population compared to the mean proton bulk speed v_p. As it is now clear that we do all calculations in the
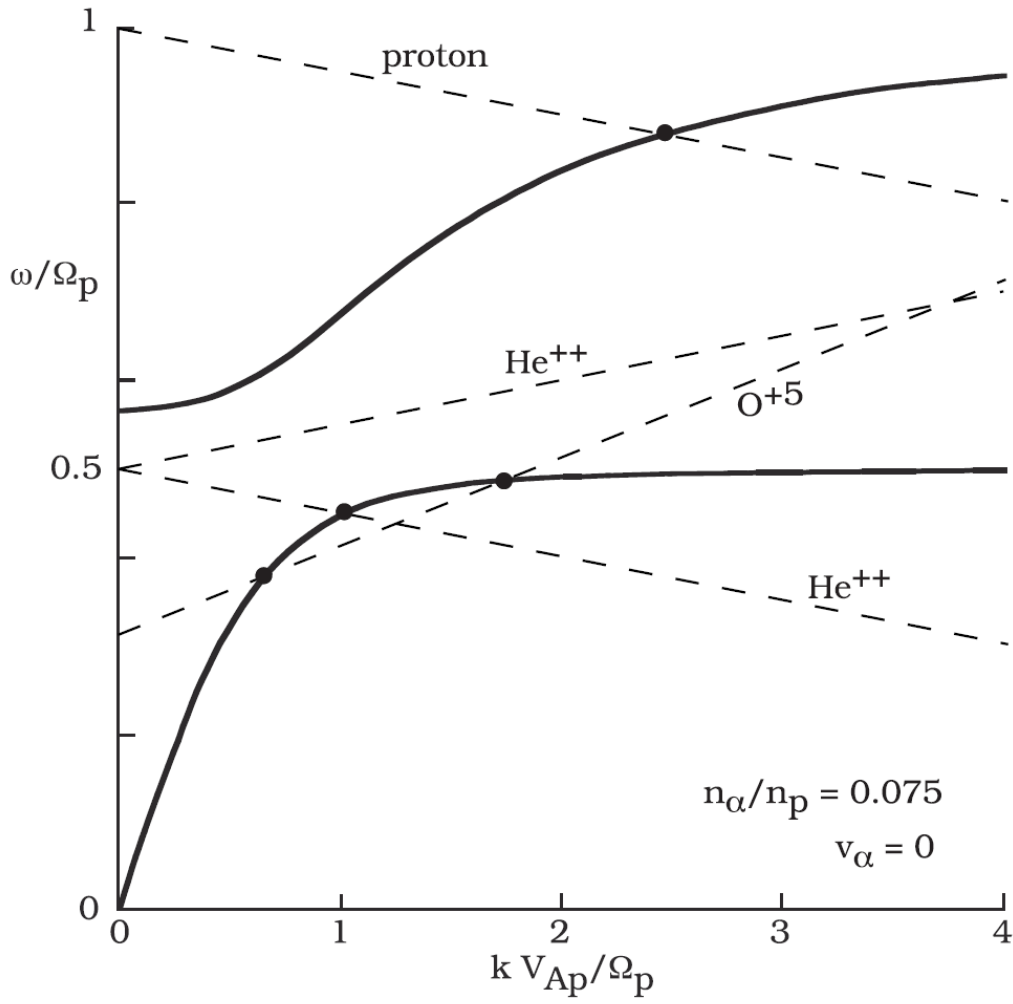
FIGURE 1.9: Visualization of the ion-cyclotron resonance condition in the solar wind plasma for the assumption that the ion-cyclotron waves are carried by both the solar wind bulk protons and alpha particles. The relative alpha-particle number density is taken as 0.075 relative to the protons and no differential speed between these bulk species is assumed. The determination of a differential speed limit for heavy ions is more complex in this case as the different ion species can resonate in principal with two branches. However, one has to note that the acceleration at resonances with large values of k is low as one has to assume a decreasing wave power spectrum $P(k)$ with increasing k. The Figure is taken from [**?**].

solar wind proton frame, we already denoted in Eq. 1.28 the wave frequency in this frame as $\omega' = \omega$. When one assumes zero (initial) differential speed between the protons and the alphas and a number density ratio of $n_\alpha / n_p = 0.075$ one obtains for the ion-cyclotron waves the dispersion relation depicted in Figure 1.9.

In the new situation we now have two branches indicating ion-cyclotron waves in two frequency bands. While a proton still can only interact resonantly with the waves when its speed is lower than v_p the depicted heavy minor ion O^{5+} can still be accelerated to positive differential speeds. In contrast to Figure 4.30 we note that, there is now even

no upper limit of the O^{5+} differential speed as the ion can in principal switch from the lower to the higher resonance branch by resonating there with waves at high wave numbers $kv_A/\Omega_p > 4$ (not depicted here) after leaving the lower branch and then returning to infinitely low wave numbers on the upper branch with further increasing differential speed. In this context it becomes obvious that so far we did not consider how much wave power is available at a given wave number (and branch). As the wave power $P(k)$ spectrum in a first approximation should decrease monotonically with increasing wave number one can estimate that the strongest acceleration occurs at the lowest frequencies while at sufficiently high wave numbers no effective acceleration takes place anymore, which then can provide the differential speed cut-off. Any reasonable quantitative model therefore has to take into account the local wave spectrum in the solar wind at the acceleration site. Interestingly, in the given situation, He^{2+} cannot be accelerated from zero differential speed on, but those helium particles that gained by some other mechanism already enough speed to resonate with the upper branch, can then be further accelerated by ion-cyclotron resonance. This, observation underlines the potential importance of other processes that can act together or subsequently with ion-cyclotron resonance on providing efficient acceleration (and heating) for some ion species more than others.

After understanding the cause and basic characteristics of the differential speed cut-off, we can now fully understand the trajectory of a resonantly interacting heavy ion in velocity phase space that is depicted as an example for O^{5+} in Figure 1.10 together with the trajectory of a proton (H^+). The origin of the depicted velocity space is centered in the solar wind bulk proton frame and the situation obeys rotation symmetry with respect to the parallel speed axis, so that we can reduce the following discussion to $v_\perp \geq 0$. When the O^{5+} ion interacts with the ion-cyclotron wave it can gain or lose momentum and kinetic energy in the solar wind frame that is associated with a change in $v_\perp$ and $v_\parallel$. However, as discussed in subsection 1.3, its kinetic energy in the frame moving with the wave is conserved so that during the resonant interaction its phase space trajectory is given by a semicircle centered around the phase speed v'_{ph} of the wave. The radius of the semicircle is given by the magnitude of the relative velocity between the initial particle velocity at the moment when the wave encounters the particle and the wave phase velocity (here always directed along the magnetic field, so that $v_{ph,\perp} = 0$). Due to the discussed differential speed cut-off the ions cannot access all velocities on the semicircles. When we assume the simple scenario of the waves being carried entirely by the solar wind bulk protons, we find from the Eq. 1.27 that O^{5+} can reach a differential speed of $v_\parallel = 0.3\,v_A$, while we still have for proton $v_\parallel \leq 0$. A second main difference between H^+ and O^{5+} is that in the discussed scenarios in Figure 1.7 and 1.9 ion species with higher mass-per-charge tend to resonate with faster waves

compared to those with lower mass-per-charge at least at moderate differential speeds. This is because their typical resonance wave numbers k_{res} are low compared to their respective resonance frequencies ω_{res} as a result of the rapid increase of the lower-branch dispersion relation at low values of k. This leads to larger semicircles for O^{5+} compared to H^+ which comes with the possibility to reach higher perpendicular speeds that in the shown case reaches up to almost $0.7\, v_A$ for O^{5+} compared to about $0.3\, v_A$ for H^+. In the wave frame the depicted situation is also known as the so-called pitch-angle scattering as the change between different states $(v_\parallel, v_\perp)$ under the condition of kinetic energy conservation has only one degree of freedom and can alternatively be fully described by the change of the pitch-angle θ which is the angle between the magnetic field direction and the ion velocity vector. It can be expressed in terms of the particle's perpendicular and parallel speed component by

$$\tan(\theta) = \frac{v_\perp}{v_\parallel} \ . \tag{1.29}$$

This last observation can be utilized to generalize the single-particle description of ion-cyclotron resonance to a statistical model that allows the derivation of (average) acceleration and heating rates for a given heavy ion test-particle population in the solar wind. As discussed in subsection 1.3 , from Eq. 1.15 and 1.17 we can derive the evolution of the parallel and perpendicular speed component due to resonant ion-cyclotron interaction for a single test-particle in a coherent wave field. However, waves in the solar wind plasma are generally incoherent. Therefore, in the following the wave field is modeled by assuming each wave to be coherent for a length L but then it undergoes a random phase shift $\Delta\phi$ and this procedure is repeated N times. In this way, one can still use Eq. 1.15 and 1.17 to describe the change in the speed components during the coherent periods but in the end $\delta v_\parallel(N)$ and $\delta v_\perp(N)$ undergo a random walk which is equivalent to diffusion in velocity phase space. As in the wave frame this diffusion can be described as diffusion in pitch-angle only, the temporal evolution of an ion test-particle population can be described with the common differential equation for pitch-angle diffusion:

$$\frac{\partial f(v,\mu)}{\partial t} = \frac{\partial}{\partial \mu}\left(D_{\mu\mu}\frac{\partial f(v,\mu)}{\partial \mu}\right) \tag{1.30}$$

where $v = \sqrt{v_\perp^2 + v_\parallel^2}$ is the magnitude of the heavy ion velocity in the solar wind frame, $\mu = \cos(\theta)$ is the cosine of the pitch-angle and $f(v,\mu)$ is the velocity distribution function (VDF) of the test-particle population parametrized by v and μ. From the described random walk scenario and Eq. 1.15 and 1.17 one derives after a few steps of

straightforward calculation the pitch-angle diffusion coefficient $D_{\mu\mu}$

$$D_{\mu\mu} = \frac{(1 - \mu^2)}{4|\mu|v} \left(\frac{q}{m}\right)^2 \delta B^2 L \tag{1.31}$$

with $L = t\Omega/(Nk)$ and the remaining quantities t, δB^2, Ω and k defined as in subsection 1.3. Assuming a scenario of weak plasma turbulence **??** one can link the diffusion coefficient to the ambient ion-cyclotron wave spectrum by just substituting δBL by a term $2\pi P_B(k_{res})$ that is proportional to the magnetic field wave power at the resonant wave number so that the explicitly wave-power dependent diffusion coefficient reads

$$D_{\mu\mu} = \frac{\pi}{2} \frac{(1 - \mu^2)}{|\mu|v} \left(\frac{q}{m}\right)^2 P(k_{res}) \,, \tag{1.32}$$

with $k_{res} = -\Omega/(\mu v)$.

When we now start for instance with a well-localized population in velocity space

$$f(v, \mu) = \frac{1}{2\pi v_{ph}^2} \delta(v - |v_{ph}|)\delta(\mu + 1) \tag{1.33}$$

that is described by a mono-energetic beam of particles that travels parallel to the background magnetic field at the same speed as the wave, we can calculate e.g. the perpendicular heating rate of $f(v, \mu)$ in analogy to an ordinary VDF moment calculation as

$$\frac{k_B dT_\perp}{dt} = \int \frac{mv_\perp^2}{2} \frac{\partial f(v, \mu)}{\partial t} d^3v = \frac{\pi|v_{ph}|q^2 P_B(k_{res})}{m} \tag{1.34}$$

where the actual calculation of the partial derivative $\partial f/\partial t$ is substituted by the calculation of the right term in Eq. 1.30. When we now assume as often observed a power-law for the wave spectrum in the relevant frequency range $P_B \propto k^{-\gamma}$ and use again Eq. 1.10 and Eq. 1.19, we find from Eq. 1.34 the relation:

$$k_B \frac{dT_\perp}{dt} \propto m \left(\frac{m}{q}\right)^{\gamma-2} |v_{ph}|^{\gamma+1} \,. \tag{1.35}$$

Thus, the heating rates depends both on mass and charge of the ion species as well as on the wave phase speed and the exponent of the wave power spectrum. We see that mass-proportional heating and over-mass-proportional hating are possible even if $\gamma < 2$ which is typically the case in the solar wind [?]. For the resonant acceleration of the same initial VDF $f(v, \mu)$ we obtain with the identical mathematical approach

$$a_{res} = \frac{dv_\parallel}{dt} \int v_\parallel \frac{\partial f(v, \mu)}{\partial t} d^3v = \pi\Omega^2 B^{-2} P_B(k_{res}) \,. \tag{1.36}$$
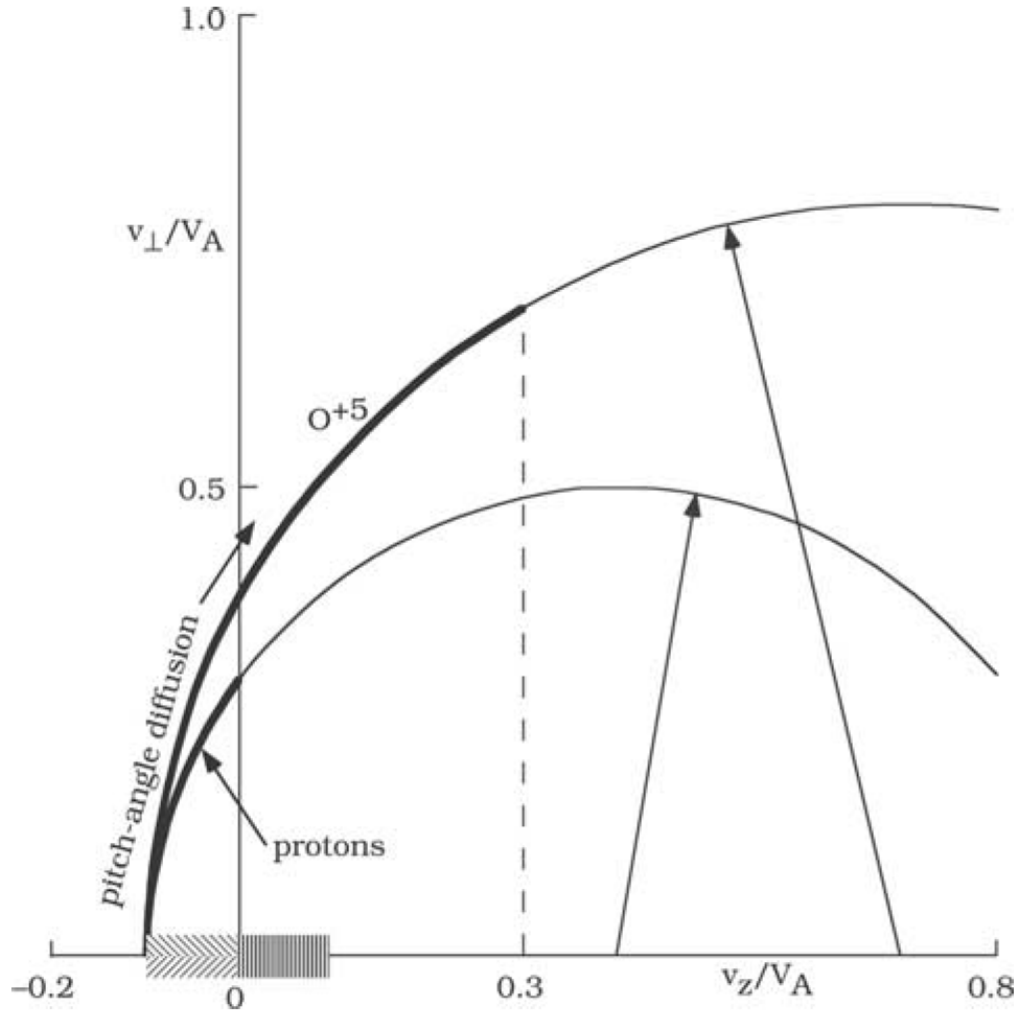
FIGURE 1.10: Visualization of acceleration and heating of solar wind ions (H^+ and O^{5+}) due to resonant wave-particle interaction depicted in velocity space parallel ($v_\parallel$) and perpendicular ($v_\perp$) to the ambient background magnetic field $\underline{B}$. Because the resonant ions conserve their kinetic energy in the frame moving with the ion-cyclotron wave after Eq. 1.18 they are restricted to semi-circles centered at the (parallel) wave velocity that is on average higher than the solar wind bulk parallel velocity. This trajectory in velocity space can be alternatively described by the change of particles' pitch-angle with respect to $\underline{B}$. As heavy ion species tend to resonate with faster waves than protons the two species are situated at different circles. Due to the differential speed cut-off, only a limited part of the respective semi-circles is accessible to the different species, that is marked fat here. The Figure is adapted after [**?**]. Assuming an initial beam-like distribution of particles which are located approximately at the same point in velocity space, one can generate a spread of this distribution when one assumes an incoherent ion-cyclotron wave field with random wave phases ϕ as explained in the text. This process can be interpreted as pitch-angle diffusion or heating of the particle distribution that happens simultaneously with the acceleration process of the ions. Substitute v_z by v_{ph}!.

Assuming the same power-law $P_B(k) \propto k^{-\gamma}$ this expression gives the relation:

$$a_{res} \propto \left(\frac{m}{q}\right)^{\gamma-2} |v_{ph}|^\gamma \tag{1.37}$$

that shows a similar mass-per-charge depending as the over-mass-proportional term of the heating rate. Both effects result from the strong dependency on the resonant wave numbers k_{res} that are linked to the ions' gyrofrequency. To finally obtain a parallel heating rate we have to assume an initial thermal spread of $f(v,\mu)$. If one assumes in the simplest case a Bi-Maxwellian distribution ($T_\parallel \neq T_\perp$) that initially rests in the SW frame, one obtains in a first approximation

$$k_B \frac{dT_\parallel}{dt} = \frac{2k_B^2 T_\perp}{mv_{ph}^2}\left(\frac{dT_\perp}{dt}\right)\left[1 + \frac{T_\parallel}{T_\perp}k_0\left(\frac{d\log(P_B(k))}{dk}\right)_{k_0}\right] \tag{1.38}$$

with $k_0 = \Omega/|v_{ph}|$. Thus, the parallel and perpendicular heating (or cooling) are coupled to each other.

The derived Eq. 1.35 - 1.37 that rely in principal still on the well-known [**?**] model are a relatively simple description of resonant ion-cyclotron as it they do not take into account the subtilities of the dispersion relation in a multi-species plasma as shown in Figure 1.9 and a crucial point is also that the the absorption of wave-energy by the particle species is not taken into account in a self-consistent manner, that would couple back to the wave power spectrum. Therefore, over the years more elaborated models [**?** **?**] have been developed subsequent later stages of (non-resonant) acceleration but they all rely on the described initial resonance mechanism that we illustrated.

In principal the models of resonant ion-cyclotron interaction give quantitative predictions of upper limits on differential speeds and temperatures as well as acceleration and heating rates that depend only on the magnetic field fluctuations and the ions mass and charge. Therefore, one can in principal test the proposed models with combined measurements of the B-field and the particle velocity distributions and even when one just has the particle measurements (as in the case of SOHO, where no magnetometer is onboard) a restriction of the models can be made from the simultaneous measurement of different ion species as they all feel the same B-field. However, we should not forget that the largest part of e.g the acceleration happens close to the Sun and for instance the differential speed decreases at least from 0.3 AU out to 1 AU [**?**] so that even if we find remnants from solar acceleration at 1 AU or local acceleration, these signatures are generally overlaid/regulated by other transport and thermalization processes that happen on the way out to 1 AU. Two known processes competing with ion acceleration and heating in the solar wind are 1) Coulomb collisions and 2) plasma instabilities that we briefly discuss in the next section.

1.4 Competing Processes in the Solar Wind

1.4.1 Coulomb Collisions

?? In their solar wind in-stu studies, [?] and [?] have shown that Coulomb collisions can play an important role in the shaping of ion VDFs in the slow wind. On the basis of proton and alpha particle data measured onboard the WIND spacecraft, [?] suggest that the observed relaxation of differential temperatures between alpha particles and protons in the solar wind could be explained purely/mainly by Coulomb interaction and [?] argue that Coulomb collisions might be the fundamental process to regulate speed and temperature differences as well as proton temperature anisotropy beyond a few tens of solar radii away from the Sun, disregarding the solar wind speed. In this picture both fast and slow wind possibly exhibit nonthermal features close to the Sun, but by the time the plasma reaches 1 AU these signatures have vanished in the slow wind because its plasma has a lower typical Coulomb interaction rate ν and also needs a longer traveling time $\tau = R/v_{sw}$ to arrive at the observation side R. Assuming an approximately Gaussian proton VDF with density n and temperature T the characteristic Coulomb collision rate ν_{pp} can be calculated analytically from the application of Rutherford scattering to proton-proton collisions as described in [? ? ?]:

$$\nu_{pp} = \left(8.77 \cdot 10^{-7} \cdot \frac{\text{m}^3 \text{K}^{3/2}}{\text{s}} \right) \left(\frac{n\lambda_{pp}}{T^{3/2}} \right) \tag{1.39}$$

where λ_{pp} is the Coulomb logarithm:

$$\lambda_{pp} = 2.51 + \ln\left[\left(\frac{1}{\text{m}^{3/2}\text{K}^{3/2}} \right) \left(\frac{T^{3/2}}{n^{1/2}} \right) \right] . \tag{1.40}$$

This Coulomb collision rate can be extended for collisions between heavy ions and protons to [? ?]:

$$\nu_{ip} = \left(0.35 \cdot \frac{\text{m}^6}{\text{s}^4} \right) \left(\frac{z_i^2 n \lambda_{ip}}{A_i (v_{th,i}^2 + v_{th}^2)^{3/2}} \cdot \frac{\phi(x)}{x} \right) \tag{1.41}$$

where

$$\lambda_{ip} = 23.0 - \ln\left[\left(\frac{1}{\text{m}^{3/2}\text{K}^{3/2}} \right) \left(\frac{A_i T + T_i}{z_i(1 + A_i)} \right) \left(\frac{T}{n} \right)^{1/2} \right] \tag{1.42}$$

is the ion-proton generalization of λ_{pp} and z_i, A_i T_i, and $v_{th,i}$ are the heavy charge in units of e, their mass number, kinetic temperature, and thermal speed, respectively, ϕ is the standard error function and x is the normalized differential speed between the

heavy ions and the protons:

$$x = \frac{|v_{i,p}|}{(v_{th,i}^2 + v_{th}^2)^{1/2}} \ .$$

(1.43)

By multiplying the collision rate with the solar wind expansion time τ to the measurement site, we obtain the collisional age[4] $A_C = \nu R / v_{sw}$ [?]. As one can see from equations (1.39) to (1.43) we can deduce both the proton-proton and ion-proton collisional age, $A_{C,pp}$ and $A_{C,ip}$, from the moments of the proton and heavy ion VDFs measured with CELIAS and therefore are capable to relate the observed differential speeds to these quantities.

Still rely only on measurements on one point which is probably enough to roughly distinguish different solar wind types, but an integration approach (as e.g. formulated by Kasper is more appropriate, but this needs than an (emprical) model for the evolution of the plasma parameters in a given solar stream). Remaining things to explain:
-With the given plasma parameters one can calculate: -differential speed deceleration rate and temperature equalization rate for Maxwellian VDFs (scenario: proton-minor ions with the latter as test particles) after [?]
-emphasize that in principal one could now assume a wave field and solar wind plasma parameters from the inner heliosphere to 1 AU and calculate the resulting nonthermal features as a the integration of wave and heating rates over the outflow time. But an additional class of processes is still missing: plasma instabilities.

---

[4]In ?] this quantity is named Coulomb number N_C, to distinguish it from an introduced more elaborated calculation of collisional age A_C, taking into account the variation of in-situ parameters $x_i(r)$ over the solar wind traveling distance R.
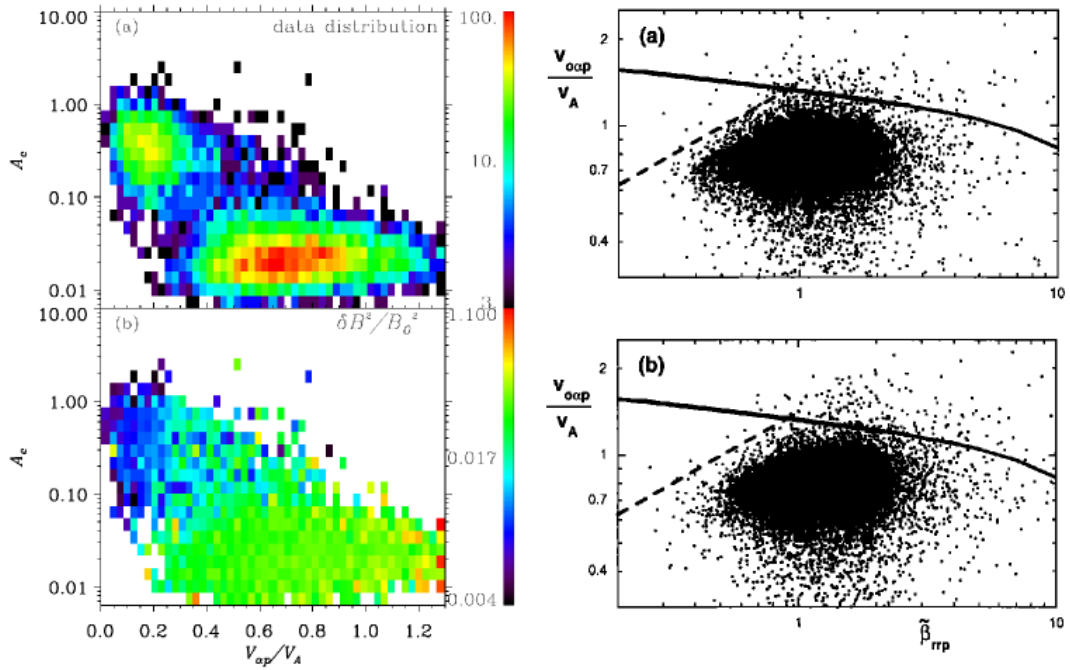
FIGURE 1.11: [?](left), [?](right): The subscript 'rr' refers to the fact that only time intervals were utilized for the analysis in which the magnetic field is co-aligned with the radial direction from the Sun. This is due to the fact that the (parallel) ion temperatures can be determined most accurately along the instrument axis, pointing radially to the Sun. The right panel is taken from [?].

1.4.2   Kinetic Plasma Instabilities

All kinetic plasma states that deviate from thermal equilibrium, (i. e. Maxwellian VDFs with equal temperature and flow speed for a multiple species plasma) are not in its minimum energy state. If the deviations from the thermal state exceed a certain characteristic threshold the plasma state becomes unstable and part of the excessive kinetic particle energy in the system is released by the emission of plasma waves that grow exponentially and can then again interact with the particles. These (kinetic) plasma instabilities therefore are thought to play an important role in the regulation of the discussed nonthermal features such as differential speeds or temperature anisotropies [?]. The investigation of plasma instabilities in space plasma physics is a complex topic in itself and the number of classified instabilities is large (see e.g. [?], [?]] and references within) so that we restrict ourselves to one example: [?] have shown that the so-called alpha-proton magnetosonic instability could play a key-role in the regulation of the differential speed between protons and alpha particles even beyond earth orbit by a comparison of Kinetic-MHD hybrid-simulations and in-situ observations of protons and alpha particles in the polar fast wind with Ulysses SWOOPS [?]

at $1.6\,\text{AU} \leq R \leq 1.8\,\text{AU}$ (upper panel) and $1.45\,\text{AU} \leq R \leq 1.6\,\text{AU}$ (lower panel), respectively. In Figure 1.11 the calculated differential speed threshold for the instability growth rate exponent $\gamma_m/\Omega = 0.001$ from the simulations is shown as the thick black line that obeys the relation

$$\frac{\Delta v_{\alpha,p}}{v_A} = \frac{1.38}{\beta_{\parallel,p}^{0.17}} \tag{1.44}$$

in dependence of the local solar wind plasma β-parameter parallel to the in-situ magnetic field that is calculated from protons only. As we can see the calculated threshold confines reasonably well the observed differential speeds shown as a scatter plot over a wider range of values for $\beta_{\parallel,p}$ which shows its applicability to a range of fast wind plasma conditions. However, at low $\beta_{\parallel,p}$ an additional empirical relation is needed to explain the confinement of the data in $(\Delta v, \beta_{\parallel,p})$-space, which is given as

$$\frac{\Delta v_{\alpha,p}}{v_A} = 1.4 \cdot \sqrt{\beta_{\parallel,p}} \,. \tag{1.45}$$

and marked as the dashed line in Figure 1.11. When now the Alfvén speed decreases with increasing radial distance as observed in the Helios measurements, the calculated differential speed threshold reduces the absolute differential streaming of the alpha particles and therefore due to the instability a part of the streaming energy is redistributed and the simulations suggest that it goes into the heating of the alpha particles while the solar wind is propagating outward [?]. [?] conclude in their study that a similar (ion-proton) magnetic instability should be able to equally reduce the differential speed of heavy minor ions and simultaneously heat them when they have similar gyro-frequencies as He^{2+} and investigate in their simulation the case of O^{6+}. Precise differential speed and temperature measurements of heavy minor ions, could be therefore useful to further restrict these models. However, up to date there exist no sufficiently accurate more-dimensional VDF measurements of minor heavy ions from which one can get reliable estimates of a temperature anisotropy $v_{th,i,\parallel}/v_{th,i,\perp} > 1$ that is commonly used as an additional indicator of the ion-proton magnetosonic instability [?] [?].

To summarize the theoretical situation in the inner heliosphere and in particular at 1 AU, we can have simultaneously acting

1. acceleration and heating mechanisms such as resonant ion-cyclotron interaction that are able to provide momentum and energy to the solar wind particles from the solar corona on and simultaneously create nonthermal features in the ion VDFs,

2. Coulomb collisions that constantly aim to thermalize the wind plasma,

3. plasma instabilities that are likely to regulate the observed nonthermal features while the wind is propagating outward,

To disentangle all these processes in order to finally determine the mechanisms that actually dominate the acceleration, heating and transport/thermalization of the solar wind (in certain regions) we need precise systematic in-situ measurements of the particle VDFs and electromagnetic fields at selected sites and solar distances throughout the heliosphere (and ideally in the corona). In particular, we showed that certain promising acceleration and heating processes such as ion-cyclotron resonance are sensitive to the mass and charge of the solar wind ion species and the same applies to Coulomb collisions and certain ion instabilities such as the described ion-proton magnetosonic instability. Therefore, the systematic measurements of a wide range of minor heavy ion VDFs can provide crucial additional information to restrict and eventually distinguish between different proposed models, provided that the measurement inaccuracies are sufficiently small to resolve the expected features. In the following last section we give a short overview over the measurements of minor heavy ions in the solar wind up to date and formulate on this basis the scientific objectives for the systematic measurements of heavy ion kinetic properties with SOHO/CELIAS in this work.

1.5 Systematic Measurements of Heavy Ion Kinetic Properties

Differential streaming of heavy minor ions:
While the differential streaming between alpha particles and protons has been studied for several decades [**? ? ? ? ?**], there exist only a few independent speed measurements of heavy minor ions. This is mainly because elements with atomic number Z¿2 are several orders of magnitude less abundant than helium, and therefore require very specific measurement instrumentation [**?**] [**?**]. However, due to their low number density and their wide range in mass and charge, the minor ion species can be considered as perfectly suited test particles to study possible mass- and charge-dependent acceleration and thermalization mechanisms in the solar wind.
From the early eighties on, case studies of the differential streaming of several relatively abundant minor ions such as O^{6+}, Si^{7+}, Fe^{9+} and Fe^{10+} [1**? ?**] were conducted in fast streams in the vicinity of 1 AU and even in the inner heliosphere [**?**], but until today the only systematic measurements of heavy ion differential speeds based on a wide set of solar wind ion species are available from the SWICS instruments on Ulysses [**? ?**] and from its twin instrument on the Advanced Composition Explorer [**?**] (mention that STEREO/Plastic is bad)!. As mentioned before, Ulysses orbited the Sun in

a highly elliptic polar Orbit between 1.4 and 5.4 AU. During four extended time periods of the mission, corresponding to northern coronal hole wind, southern coronal hole wind and ecliptic wind at solar minimum and solar maximum, respectively, [**?**] analyzed the speeds of 35 heavy ion species spanning a range in mass-per-charge of $2.0 \leq m/q \leq 9.3$. The study is based on 1-dimensional heavy ion VDFs, derived from measurements of the absolute ion speed v_i with an integration time of two hours. While the authors do observe preferential heating of the heavy ions, they do not observe any signature of differential streaming, so that all ions were observed to flow at proton speed during all observation periods. However, [**?**] state that this result is expected for most of the Ulysses orbit far beyond 1 AU, simply because the mean interplanetary B-field angle is almost perpendicular to the SWICS measurement axis and the differential streaming is supposed to act along the local B-field (compare subsection **??** for details). Nevertheless, there might be time periods where the B-field angle at the Ulysses orbit is sufficiently far off the nominal Parker angle and also when Ulysses is above the solar poles the magnetic field could align reasonably well with the instrument measurement axis. Therefore, one could argue, that the absence of differential speed during all four observation periods would point to truly vanishing differential speed between the heavy ions and protons beyond 1.4 AU (which is in contrast to the helium observations by Gary2000!). In contrast to Ulysses, the ACE spacecraft is located at 1 AU on a Halo orbit around L1. [**?**] used ACE/SWICS data to measure the differential speed between 44 heavy ions in the mass-per-charge range $2.0 \leq m/q \leq 8.0$ species and the solar wind protons. By analyzing the ion data in the intrinsic instrument resolution of 12 minutes and by correcting for the ambient magnetic field direction, the authors observed differential speeds for all analyzed ion species which were comparable, but significantly lower than the local Alfvén speed and were found to lie between 0.2 and 0.8 v_A for all investigated ions (with 35 out of 44 ions between 0.4 and 0.7 v_A). A comparison of the heavy ion differential speeds showed no clear m/q dependence.

While the differing results between the studies of [**?**] and [**?**] could be explained by the different measurement location and time resolution used in the analysis, the observations situation of differential streaming at 1 AU are not completely consistent either. In particular, there exist apparent differences between the ACE/SWICS results and the observations by [1] who analyzed the differential streaming of several ion species measured with the the CELIAS experiment onboard the SOHO spacecraft, which is also located in a Halo orbit around L1. [1] investigated heavy ion data from the CELIAS Charge-Time-of-Flight (CTOF) sensor with a time resolution of 10 minutes. Although CTOF is a time-of-flight mass spectrometer similar to the SWICS instruments and therefore capable to measure ions in a wide mass and mass-per-charge range, in the CELIAS
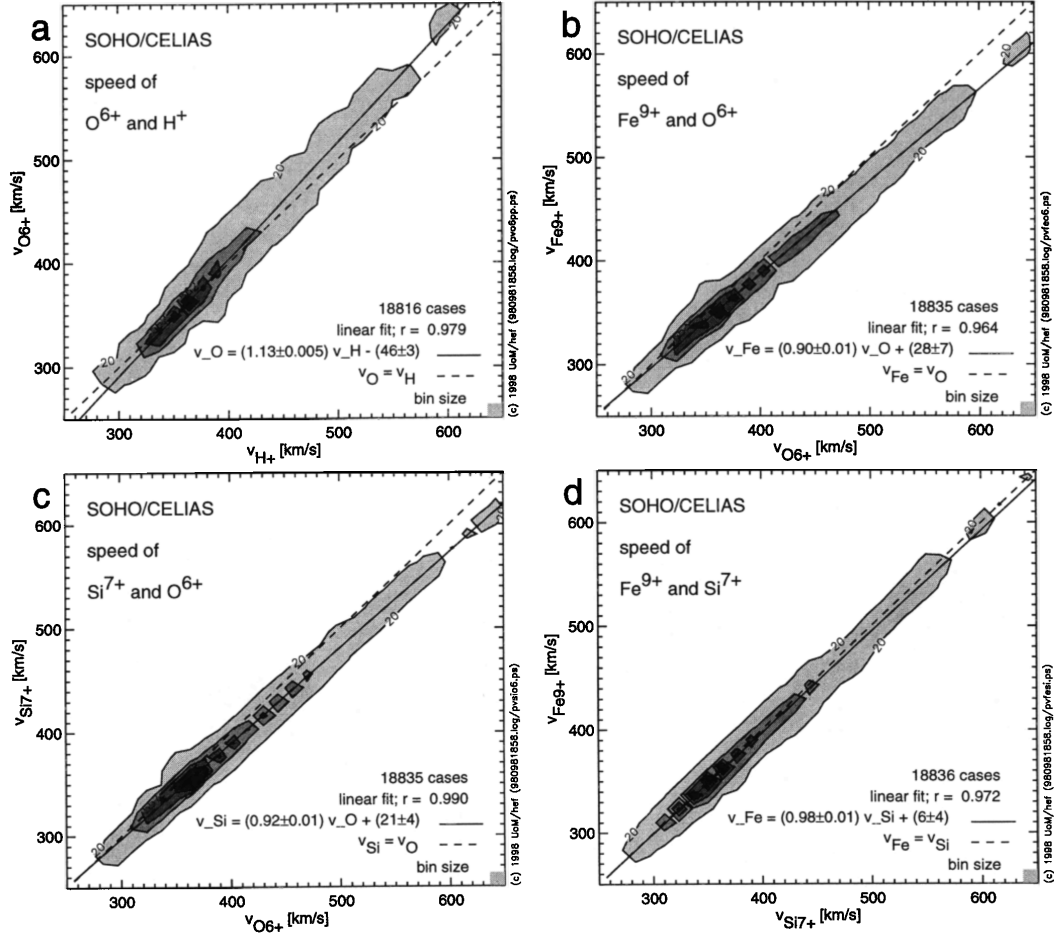
FIGURE 1.12: Hefti1998

study only three ion species O^{6+}, Si^{7+}, and Fe^{9+} were analyzed with the result that only O^{6+} showed systematic differential streaming compared to the solar wind bulk protons on the order of 20 km/s in the fast wind, while Si^{7+} and Fe^{9+} stream at the same speed as the protons or even slightly lower speed. Unfortunately the CELIAS/CTOF sensor was only in operation for a few months in 1996 due to a severe instrument failure on DOY 230 in 1996, so that the study by [1] is the only one conducted so far on kinetic properties of heavy ions measured with this instrument. However, The sensor's measurement principle provides very good charge-state separation facilitating precise identification of the heavy ion species while the unique combination of high measurement cadence with very high collection power enables the measurement of heavy minor ions with unprecedented high statistics. In particular the high time resolution allows a scan of the complete VDF for any given ion species within one minute and therefore under very similar in-situ plasma conditions. A typical minor ion VDF measured by CTOF consists of about 100 counts (see example of Fe^{10+} in the middle panel of Figure **??** which is roughly a factor of 10 more than ACE/SWICS at a similar distance to the Sun.
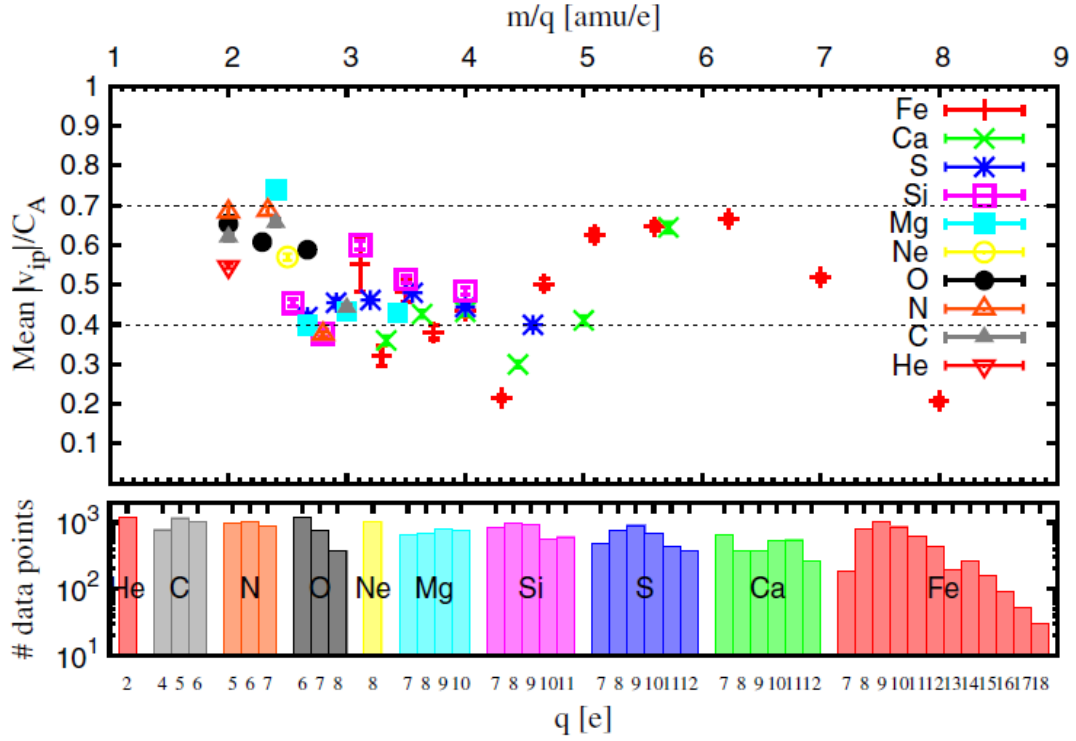
FIGURE 1.13: Berger.2011

These features allow the determination of heavy ion speed spectra and moments with high precision which makes the CELIAS/CTOF heavy ion data highly valuable despite the instrument's short measurement period. By conducting a systematic analysis of solar wind heavy ion differential streaming including 9 ion species in the energy-per-charge range between $2.7 \leq m/q \leq 6.2$ measured by the SOHO/CELIAS experiment we aim to gain a better understanding of the differential streaming at 1 AU. The presented analysis of the CELIAS/CTOF data takes into account both the onboard processed matrix rate (MR) data, originally utilized in [1], and the raw pulse height analysis (PHA) count data which has a higher mass and mass-per-charge resolution and is independent of the CTOF preflight calibration. We also compare our results for the ion species O^{6+}, Si^{7+}, and Fe^{9+}, with the earlier results by [1].

Goals of this work

To clarify the observational situation at 1 AU and provide restrictions for theoretical models of solar wind ion acceleration, heating, and transport/thermalization with this work we aim to answer the following questions:

1. Do we observe differential streaming between the solar wind heavy ions and protons in the SOHO data?

    If so,

    (a) do we observe significant differential speeds for all ion species or only for particular species?

    (b) what is the sign and magnitude of the observed differential speeds?

    (c) do we observe a general trend depending on mass and charge of the ion species?

    (d) how does the differential speed depend on the ambient solar wind plasma conditions/parameters, in particular solar wind speed/type and collisional age?

2. Do we observe preferential heating of solar wind heavy ions compared to the solar wind protons in the SOHO data?

    If so,

    (a) are the heavy ions heated strictly mass-proportional or do we observe signatures of over- or under-mass-proportional heating?

    (b) how do the observed heavy ion temperatures depend on the ambient solar wind plasma conditions, in particular on solar wind speed/type and collisional age?

Chapter 2

Measurement Instrumentation and Data Products

2.1   The CELIAS Experiment aboard SOHO

The Solar and Heliospheric Observatory (SOHO) was built to resolve several long-standing problems in solar physics, such as the coronal heating problem and the acceleration of the solar wind. Both topics are of special interest for the in-situ community which provided three particle instruments among them the CELIAS instrument (see figure (2.1)). Furthermore the spacecraft is suited with helioseismological and remote sensing instruments instruments which add up to a complete scientific payload of 12 instruments.

SOHO was launched in December 1995 and is still in operation. It is situated on an orbit close to L1 and is a 3-axis stabilized spacecraft, which means that all particle instruments point in the same direction all the time which is contrast to e.g. the Advanced Composition Explorer (ACE) or the Helios spacecraft which are/were all spinning around their axis.

2.1.1   The CELIAS Experiment: A short Overview of the Relevant Sensors

The *Charge, Element, and Isotope Analysis System* (CELIAS) aboard SOHO was built by the University of Bern in cooperation with the Max-Planck-Institute for Solar System Science at Katlenburg-Lindau (former Institute for Aeronomy) and consists of four different sensors which all investigate ions within or slightly above the solar wind energy
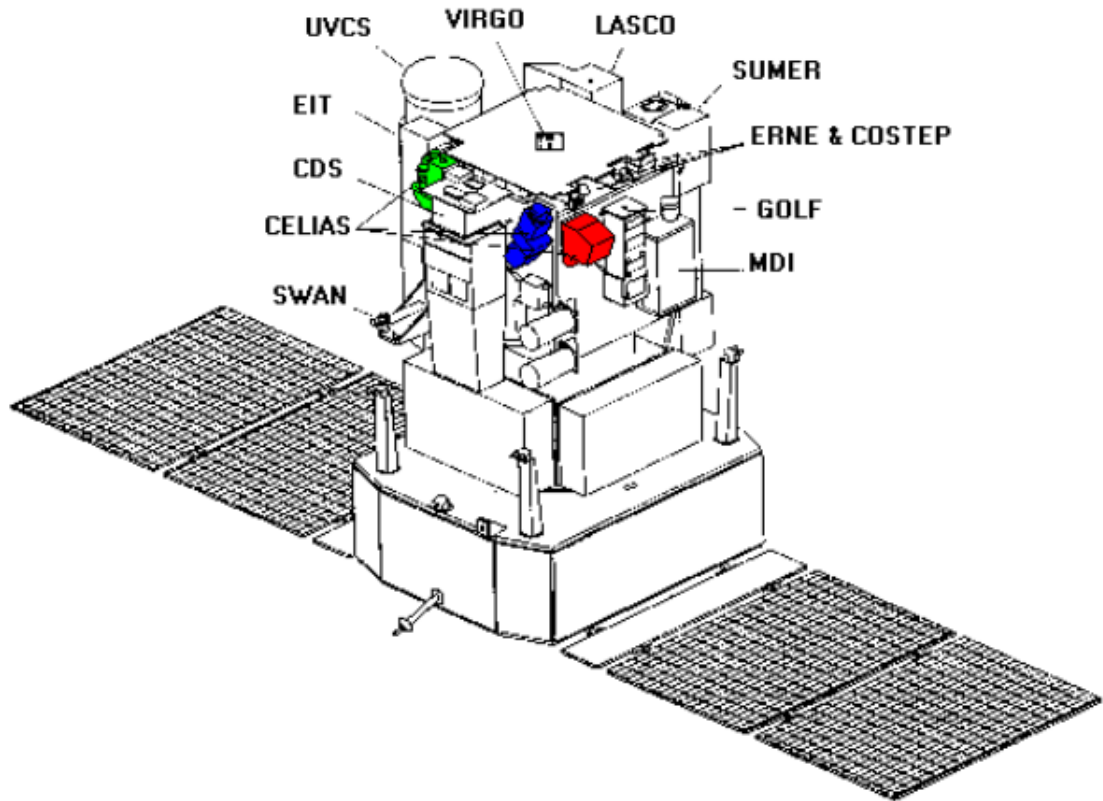
FIGURE 2.1: Overview of the SOHO spacecraft with its scientific payload. The picture
is adapted after [Domingo1995].

range. These sensors are the Charge-Time-OF-Flight Sensor (CTOF), the Mass Charge-
Time-OF-Flight Sensor (MTOF), the Suprathermal Charge-Time-OF-Flight (STOF) and
the Proton Monitor (PM). Explain the ovarall scientific goal of the experiment. Here we
concentrate on the CTOF sensor and the Proton Monitor:

CTOF   CTOF is a linear time-of-flight mass spectrometer with remarkable time-of-
flight resolution which allows for a very good separation of heavy ions in mass-per-
charge. Furthermore it has a large geometry factor by blending out the solar wind
protons. Unfortunately the instrument suffered a serious failure already on DOY 230
1996. so that it delivered only data of several months around solar minimum in 1996.
For a more detailed description of the CTOF sensor see the following section.

PM   The Proton Monitor is integrated in the MTOF housing and measures the proton
mean speed, temperature and particle density with an accuracy of at time resolution
of about one minute. Since the proton parameters of the solar wind at L1 are well-
known today, the PM data is not of great interest itself, but serves as solar wind plasma
parameter reference for the other three sensors. Especially the analysis of the Heavy

Ion Differential Streaming is done by comparison of the CTOF data with the PM data. For our analysis which is described in we used five-minute averaged PM data which we synchronized with the CTOF data.

2.2 The CELIAS/Charge-Time-Of-Flight Sensor

2.2.1 Principle of Operation

The CELIAS/Charge-Time-Of-Flight (CTOF) sensor is a linear time-of-flight mass spectrometer based on the carbon-foil technique which is designed to detect heavy ions with $Z \geq 2$ in the energy-per-charge range between 0.3 and 34.8 keV/e. The sensor measures the ions' mass m, charge q and speed v. To derive these three quantities, three measurements are performed subsequently on an incident ion: In the CTOF entrance system the ion's energy-per-charge (Epq) value is determined by the Electrostatic Analyzer (ESA), which is a semispherical capacitor, that the ion can only pass if its energy-per-charge is within a narrow passband around the selected energy-per-charge-step that corresponds to the applied voltage between the capacitor electrodes. Second, after being accelerated by a post-acceleration voltage the ion undergoes a time-of-flight (TOF) measurement. To trigger a start pulse for the TOF measurement the particle penetrates a thin carbon foil at the beginning of the TOF section from which secondary electrons are emitted that are then guided to a micro channel plate (MCP) detector. In a similar way a stop pulse is provided when the ion reaches a solid state detector (SSD) at the end of the TOF section by releasing secondary electrons from the SSD surface that are again detected by an MCP. Finally, the residual kinetic energy of the ion (ESSD) is measured in the solid state detector, which consists of a thin SiO_2 dead-layer on-top of a sensitive silicon layer, where the ions fully stop.

Within one CTOF instrument cycle, which has a duration of about 5 minutes, the electrostatic analyzer steps through a sequence of 117 energy-per-charge values by changing the applied ESA voltage U_j after:

$$\frac{1}{2} \cdot \frac{m}{q} \cdot v^2 = \left(\frac{E}{q} \right)_j = U_j = U_0 r^{s_{max}-j} \tag{2.1}$$

where j is the ESA step number obtaining values from $s_{min} = 0$ to $s_{max} = 116$ while U_0 and r are constants given in in the appendix B in Table B.1 that allow the exponential stepping of the E/q-value. For a given ion species with fix mass and charge the E/q-

CELIAS SYSTEM FOR SOHO
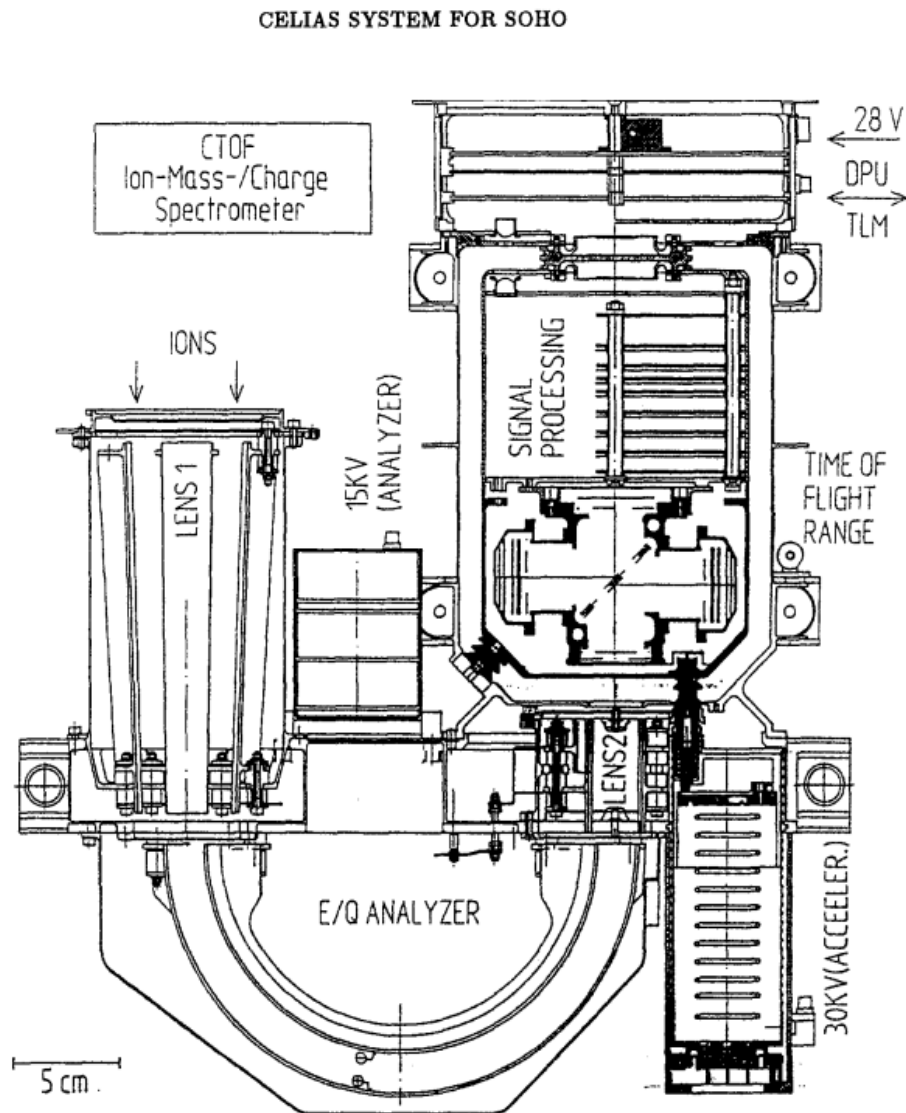
FIGURE 2.2: Cross-section of the CELIAS/CTOF sensor after [Hovestadt(1995)]. First the ions are focused by the quadrupole lens and pass through the electrostatic E/q-analyzer (ESA) in the entrance system if their energy-per-charge is appropriate. They are then further accelerated by a post-acceleration voltage and pass a thin carbon foil where the start pulse for the time-of-flight (TOF) measurement is triggered. Finally, the ions reach the solid state detector (SSD) at the end of the TOF section where they first trigger the stop pulse for the TOF measurement at the SSD surface and then deposit their residual kinetic energy within the SSD so that they fully stop.

stepping is equivalent to a scan in speed v, so that in principal[1] we obtain directly the reduced velocity distribution functions (VDFs) from the ion count rate $N_{ij} = N_i(v_j)$ for any given ion species i measured over the 117 Epq-steps.

Yet, as CTOF measures different ion species simultaneously we need to derive the ions' mass and charge from their measured TOF and ESSD signals at each E/q-step in order to apply Eq. 2.1 . For any ion with mass m_i and charge q_i its residual energy after the post-acceleration is well-defined for any given Epq-step j as

$$E_{acc}^{ij} := E_{acc}(q_i, j) = \left[\left(\frac{E}{q} \right)_j + U_{acc} \right] \cdot q_i \tag{2.2}$$

with the post-acceleration voltage U_{acc}, so that its speed after the post-acceleration reads

$$v_{acc}^{ij} := v(m_i, q_i, j) = \sqrt{\frac{2E_{acc}^{ij}}{m_i}} \ . \tag{2.3}$$

Now, in an ideal instrument the solid state detector would measure the exact residual energy of the particle

$$\epsilon_{ij} = E_{acc}^{ij} \tag{2.4}$$

and its time-of-flight would be determined as

$$\tau_{ij} = \frac{L_\tau}{v_{ij}} \tag{2.5}$$

where L_τ is the fix length of the TOF section between carbon foil and SSD surface. Thus, from the measured combined signals (τ, ϵ) one could unambiguously determine the ion's mass-per-charge by

$$\left(\frac{m}{q} \right)_i = \frac{2\tau_{ij}^2}{L_\tau^2} \left[\left(\frac{E}{q} \right)_j + U_{acc} \right] \tag{2.6}$$

and its mass by

$$m_i = \frac{2\tau_{ij}^2 \epsilon_{ij}}{L_\tau^2} \ . \tag{2.7}$$

with the known values L_τ and U_{acc} kV given in B.1 .

In Figure 2.3 we show show for E/q-step ? a two-dimensional histogram of the detected TOF and ESSD signals that were measured with CTOF over the whole DOY 150?

---

[1]These VDFs still have to be corrected for the difference in phase space coverage between the Epq-steps as it is explained in subsection **??**.
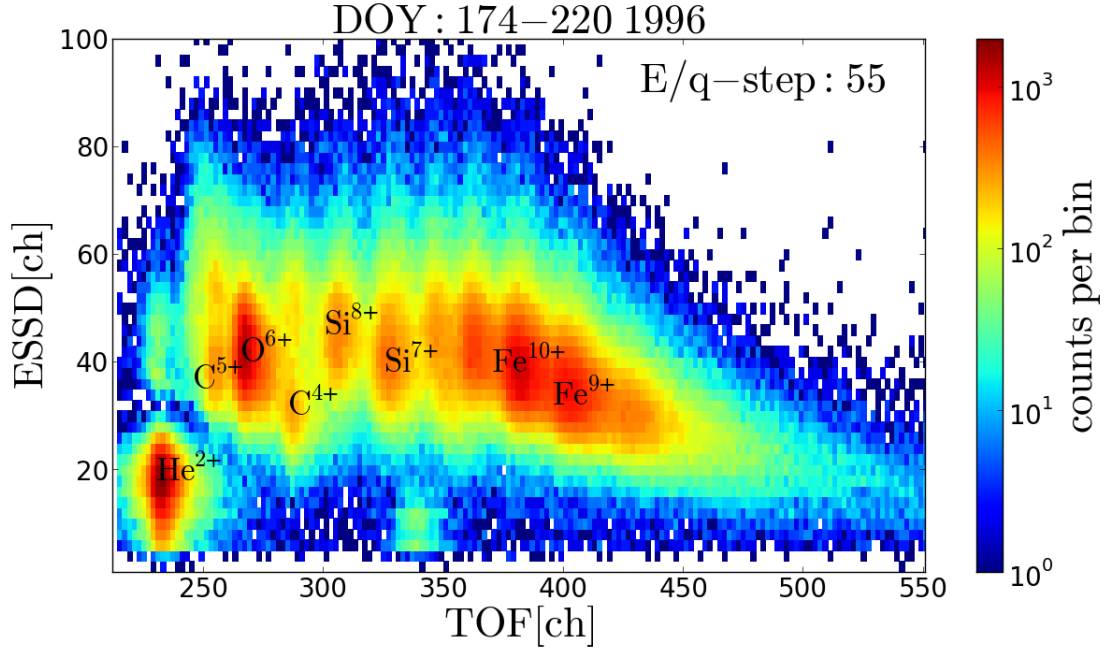
FIGURE 2.3: ET-matrix of the accumulated PHA data long-term counts for the whole measurement period DOY 174-220 at Epq-step 55. Note that these are only the transmitted counts due to the CTOF telemetry scheme as explained in subsection ?. The peaks of several more abundant ion species are well-recognizable by eye. For a fully calibrated ET-matrix with all ion species labeled compare Figure 4.4 in chapter 4).

1996. In the following we call these histograms ET-matrices for a given Epq-step accumulated over a given time-period which relates to a certain number of instrument cycles ($\approx$ 288 cycles per day). The TOF measurement is nominally resolved with 1024 channels while the ESSD measurement is resolved with 512 channels but the relevant solar wind events lie actually in a fraction of this total range ($150 < \tau < 600$, $\epsilon < 150$) and due to a clearly artificial bit-pattern we have to bin two channels together both in TOF and ESSD. One can clearly recognize sevaral peaks in the data that correspond to the positions of certain ion species as described in Eq. 2.6 and 2.7. But we can also see that the widths of these peaks are large and thus overlap, so that in reality one cannot separate the different ion species deterministically as Eq. 2.6 and 2.7 suggests. The observed peak widths are mainly caused by the straggling of the ion species both in the carbon foil and the SSD which causes a broadening of both the TOF and ESSD signal and which we did not consider in the ideal measurement case so far.

Due to the straggling the ion identification has to be considered in a statistical way now. Thus, Eq 2.6 and Eq. 2.7 only hold when we regard the calculated values (τ, ϵ) as the most probable channels to be measured for an ion of a certain species i at a given Epq-step j or equivalently as the respective (central) ion peak position in the ET-matrix at the given Epq-step. The remaining channels that form the peak in the close ET-environment of $(\tau_{ij}, \epsilon_{ij})$ must be taken into account to calculate the total count rate N_{ij}

of a given ion species at a certain Epq-step. Also, due to the peak overlaps the measured count rate in a certain ET-channel can contribute partially to different ion count rates N_{ij} which we assess in detail in the CTOF response model description in chapter 4.

In addition to the statistical ion straggling, we have to take into account two other phenomena that alter systematically the measured TOF and ESSD signals[SRIM/TRIM 2008]. The first effect is the energy loss of the ions in the carbon foil due to the ion's interaction with the foil electrons and nuclei. This causes in a first instance a shift of the TOF signal to higher values, and in a second instance a shift of the ESSD signal to lower values as the ESSD measurement is not independent of the TOF measurement. The second effect is the so-called *pulse height defect* (PHD) in the SSD, which actually subsumes two phenomena [references, (at least Oetliker and references within)]: The energy loss of the ions in the SSD dead-layer which is analog to the energy loss in the foil and the effect that part of the residual ion energy is lost to elastic interactions with the silicon nuclei in the sensitive SSD area and therefore is lost for the electron-hole pair creation. Thus, not the full residual energy of the ion is converted to an electronic energy signal which causes an additional shift of the observed ESSD signal to lower values. Both effects can be taken into account by transforming, Eq. (2.6) to:

$$\left(\frac{m}{q}\right)_i = \frac{2\tau_{ij}^2\alpha_\tau}{L_\tau^2}\left[\left(\frac{E}{q}\right)_j + U_{acc}\right] \tag{2.8}$$

and Eq. (2.7) to:

$$m_i = \frac{2\tau_{ij}^2\epsilon_{ij}}{\alpha_\epsilon L_\tau^2} \tag{2.9}$$

where the introduced factor α_τ is the ions' *residual kinetic energy fraction* (REF) after the carbon foil and the factor α_ϵ is the fraction of the ions' residual kinetic energy that is converted to an electronic signal in the SSD and which we denote as its *pulse height fraction* (PHF). Both factors can be only defined for a sample of measured ions in a statistical manner and depend on several quantities such as the atomic number Z of the ions, the speed v (or equivalently kinetic energy E_{kin}) of the ions prior to the carbon foil and SSD, the foil and SSD material, and the foil and SSD geometry, respectively. Therefore, α_τ and α_ϵ have to be determined in the instrument calibration for each relevant element[2] over the whole relevant energy range of the incident ions. As this is the starting point for the characterization of the CTOF response model in 4 we only mention

---

[2]Note, that at least in theory both quantities do not depend on the charge q of the ions as the particles lose their initial charge state information already within the first few layers of the carbon foil [SRIM/TRIM 2008].

here that further effects that could potentially infuence the observed ion peak signals such as the finite energy acceptance of the ESA condenser (Janitzek 2014) or the read-out electronics (Hovestadt1995) could be shown to have negligible impact compared to the aforementioned effects.

CTOF Data Products Overview

The CTOF sensor data, as processed in the CELIAS DPU, is sent down to Earth in four principal data products: the pulse height analysis (PHA) data, the matrix rates (MR) data, the matrix elements (ME) data and the sensor rates (SR) data.

CTOF Pulse Height Analysis Data

The most fundamental CTOF data product is the **pulse height analysis** (PHA) data which consists of the detected ion events for each CTOF 5-minute cycle time stamp with the events being represented by their Epq-step, TOF and ESSD channel. Note that not every ion reaches the SSD (with sufficient energy) to generate an electronic signal so that in these cases $E_{SSD} = 0$ ch and these events are classified as double coincidence events in contrast to the triple coincidence events for which ESSD ≥ 1 ch. Due to the limited telemetry budget the CELIAS DPU does not send the full PHA count data to Earth, but performs an onboard pre-processing of all measured PHA events to the compressed matrix rates and matrix elements data products. However, in order to be able to check the fine onboard classification algorithm of the PHA events to ion-specific matrix rate boxes, for each E/q step of each time stamp a number of PHA events, containing the full Epq, TOF, and ESSD information for these events, is transmitted as well. The transmitted events are selected according to a priority scheme which is based on a very rough onboard mass classification of the events using their TOF and ESSD information: double coincidence events are classified as priority range 0, while all triple coincidences are classified within the priority ranges 1 (anticipated iron mass range) to 5 (anticipated helium mass range). A different number of PHA events is selected for each priority range with the aim to have sufficient statistics to reconstruct the full composition and kinetic information of all major solar wind ion species, despite their substantial relative differences in abundance. Furthermore, these numbers are not constant over time but also vary at each time stamp with the ambient solar wind proton

conditions to make sure, to sample for each species in the whole solar wind bulk. Nevertheless, within each priority range the selection of the events is completely independent of their Epq, TOF and ESSD to assure a statistical sample of the measured ions for unbiased reconstruction of the ion species properties.

CTOF Matrix Rate Data

The **matrix rates** data product is derived by the DPU from the PHA data in the following way: During a given CTOF instrument cycle the onboard algorithm, (documented in detail in the appendix of this paper), which is based on the pre-flight calibration of the CTOF sensor [**? ? ?**] assigns each measured PHA event to a so-called matrix rate within a certain mass-mass-per-charge (m-m/q) box depending on the event's E/q, τ and E_{SSD} value. The solar wind heavy ion speed during each CTOF cycle is estimated from the solar wind iron speed measured in the previous CTOF cycle, which is derived from a numerical moment calculation of all events within certain pre-assigned iron boxes in the PHA ET-matrix over all E/q steps. Subsequently, for each m-m/q box an E/q center step is calculated which corresponds to the estimated mean solar wind heavy ion speed for the m/q value of this box, so that the estimated solar wind bulk center of the respective ion species is supposed to be measured exactly at this step[3].

In the end, for each m-m/q box a new count rate histogram is created of which the central bin contains the count rate of the center E/q step. Consequently, the two lower (higher) neighboring bins contain the count rates of the two higher (lower) E/q steps. In the following, the count rates of steps that lay further away from the estimated solar wind bulk center are summed up together in fewer bins than steps after a fixed scheme, so that the original 117 step E/q resolution is compressed to 21 meta count rates, the so-called matrix rates. The compression scheme from E/q step count rates to matrix rates can be found in table ?
In Figure ? the CTOF matrix rate box scheme is shown, containing in each box the accumulated counts for DOY 174-220 1996 for matrix rate 10 which for each ion species and each CTOF cycle is supposed to be the count rate measured at the ambient solar wind (heavy ion) speed. -explain plot: boxes are sorted from left to right with increasing m/q and from bottom to top with increasing mass, so that every ion species is centered at a certain predefined box (i.e. O6+ at box 235, or Si7+ at box 201). -Note that the scaling along both axis is not exactly linear, since the box position is derived from a preflight

---

[3]Note that this algorithm definition assumes already to some degree that all heavy ions stream roughly at iron speed(!).Thanks to the moderate data compression within the algorithm this assumption turns out to be not too critical to derive meaningful heavy ion VDFs.
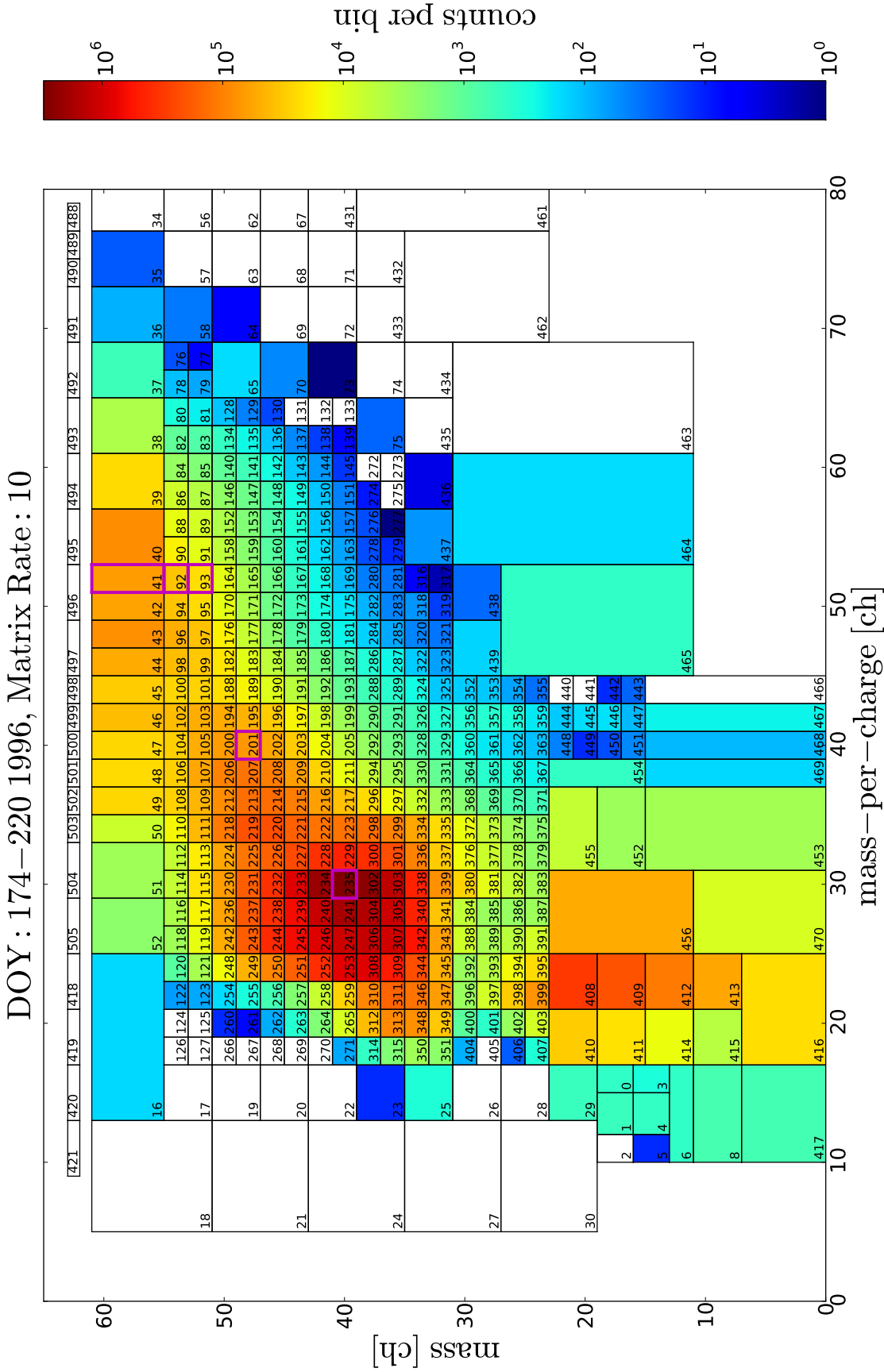
FIGURE 2.4: The accumulated CTOF Matrix Rate (MR) data for the whole measurement period DOY 174-220 for matrix rate MR10. Note, that the assigned mass (m) and mass-per-charge (m/q) are still given in the nominal instrumental channels. The dominant O^{6+} peak centered around $m/q \approx 30$ and $m \approx 40$ can be well-recognized, while other ion species peaks are harder to determine by eye. Also note, that the He^{2+} peak, which nominally should have orders of magnitude higher count rates than O^{6+} (compare Aschwanden? for rough factor), is not prominent in the data, due to the frequent interruption of the ESA-stepping in the high-speed He^{2+} flank and the additional onboard suppression with the PID. The boxes 235, 201, and (41,92,93), that are framed magenta, are used for the derivation of the O^{6+}, Si^{7+} and Fe^{9+} velocity distribution functions from the Matrix Rate data in chapter 3.Shorten this caption if necessary and put part in the text.

simulation that already takes into account a certain ion specific energy loss in the carbon foil as well as element specific pulse height defect. boxes have different widths in mass and mass-per-charge in order to resolve the anticipated set of ion species which are supposed to lie in the respective parts of the matrix scheme.

The m-m/q classification scheme, which can be seen in Figure 2.4, contains 508 boxes of different sizes which all together span a mass range sufficiently wide to measure all elements from 4 to 56 amu and their charge states from 2 to 10 amu/e. In addition to the 508 × 21 matrix rates, for each CTOF cycle the MR data also contains an estimated value for the solar wind iron speed. This value is calculated from the previous CTOF cycle from an onboard moment calculation of the count rates within the predefined iron boxes.

2.2.1.1 Matrix Elements

The **matrix elements** data is very similar to the matrix rate data, except for the fact that the all events within a certain m-m/q box are integrated during a given CTOF cycle over all E/q steps, so that the spectral velocity information is lost. Instead the resolution m and m/q resolution is doubled in both dimensions. Therefore the ME data is suitable for evaluating absolute abundances of specific ions or to derive the charge state distributions from which the freeze-in temperatures can be derived as done by **?**], but cannot be utilized to deduce kinetic properties of the heavy ions.

2.2.1.2 Sensor Rates

Finally, the **sensor rates** data is not intended for concrete scientific utilization, but contains the raw output values of the different subsensors inside the CTOF instrument at each E/q step during a given CTOF cycle. In particular the data includes the E/q analyzer voltage and operation status, the total number of triggered start and stop pulses in the TOF section, the number of SSD surface hits and the overall number of double and triple coincidence events. We used this data to follow in detail the configuration of the electrostatic analyzer and to cross-check the obtained PHA and Matrix Rates with the overall obtained number of events in the different instrument sections during each instrument cycle.

2.2.2 Base-Rate Correction of the CTOF PHA Data
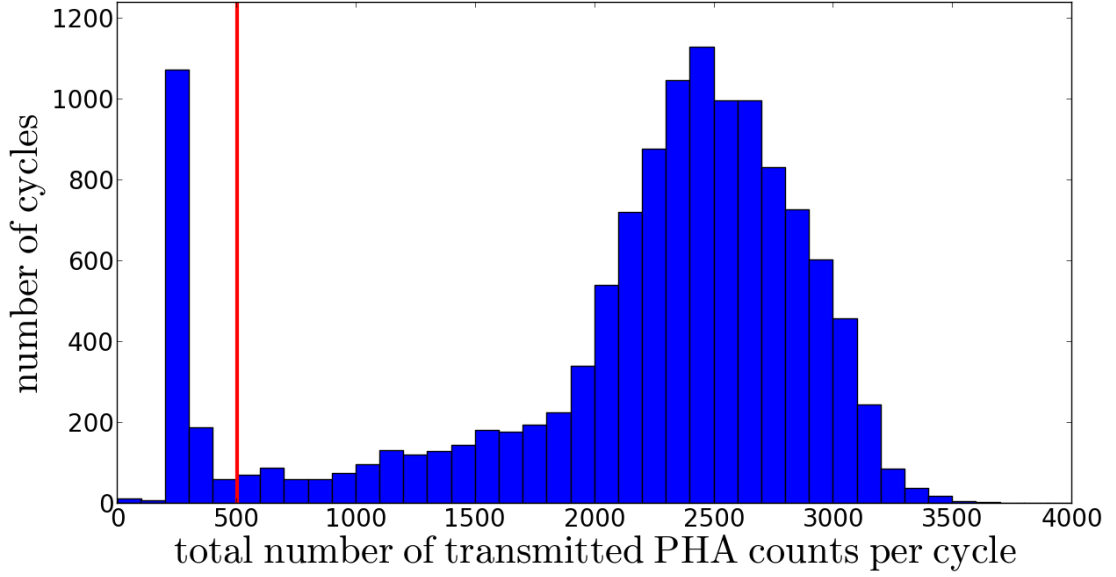
FIGURE 2.5: Histogram of the total number of transmitted PHA words per CTOF 5-minute cycle (for the whole ET-range and over all 117 Epq-steps). In most cases the telemetry limit of PHA words is between 2000 and about 3000, but also cycles with lower limits occur. The very low transmission numbers that form the peak between 200 and 400 PHA words are from cycles with strongly reduced CTOF telemetry budget due to internal budget changes between the CELIAS sensors. We excluded all cycles with less than 500 transmitted PHA counts from the analysis as it is not possible to reconstruct the base rate factors reliably for these cycles.

FIGURE 2.6: The left panel shows the definition of the Priority Ranges 1-5 (from top to bottom) in the ET-matrix as we obtain it from the *Range* data pro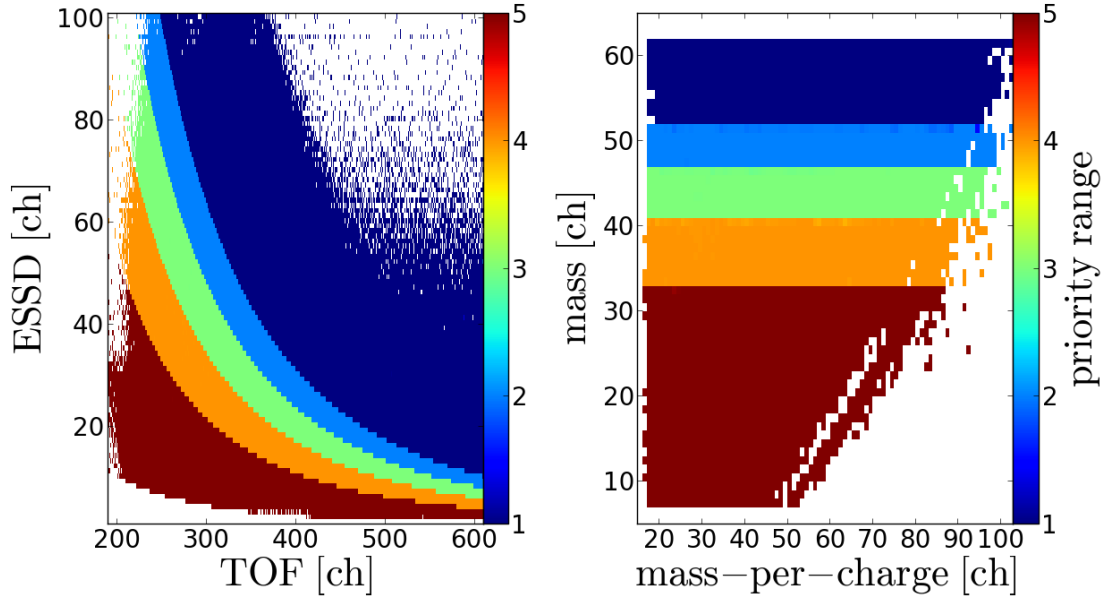duct in the CTOF PHA data. The assignment of the priority range for each PHA count depends only on its detected TOF and ESSD channel but not on the Epq-step, indicating that the ranges are defined in mass only. This can be confirmed by the right panel which shows the range of the PHA counts after their TOF and ESSD channels have been translated into mass and mass-per-charge after Eq. ? and ?. In both panels the counts of all Epq-steps $0 \leq j \leq 116$ are included. As can be seen the borders in mass in the right panel are very sharp, so that the nominal conversion algorithm from E/q, TOF, ESSD to m, mpq, MR (after Hefti/Aellig) can be proofed valid. The only exceptions are a few bins in PR2 and PR4 at the border to PR1 and PR3 respectively, which are probably due to unreconstructable rounding/truncation errors (explain how the plots are created (with weighted histograms) in the text.)
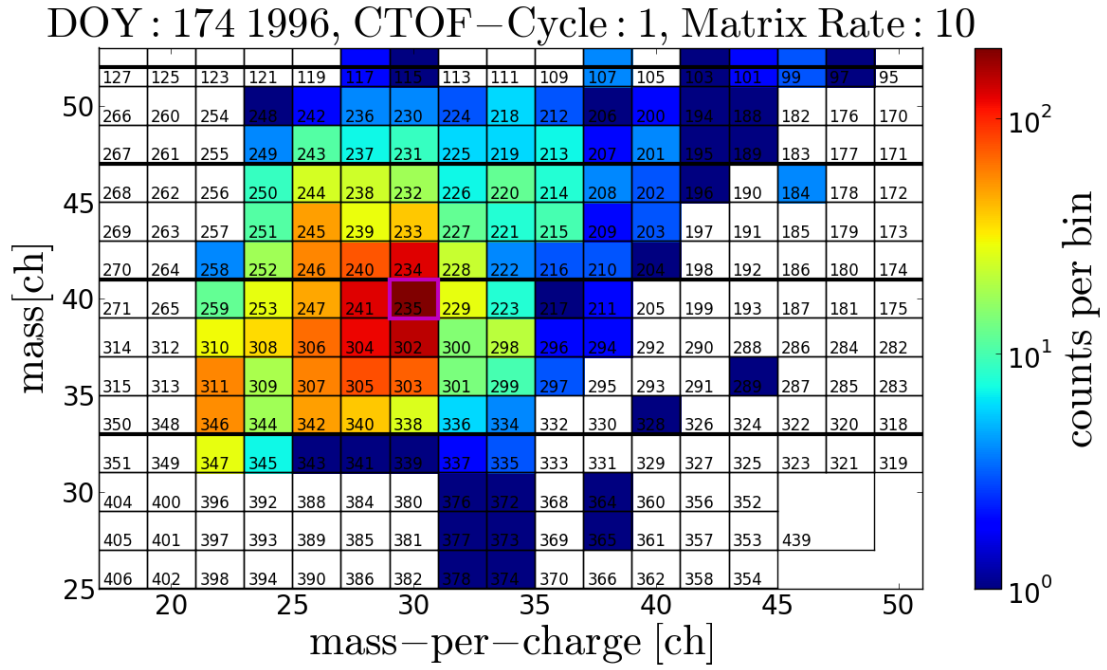
FIGURE 2.7: Close-up of the matrix rate box scheme filled with the measured (and onboard assigned) counts during the first 5-minute CTOF cycle measured on DOY 174 1996 for matrix rate MR10. The magenta framed box is the nominal box for O^{6+} after [Hefti1998].
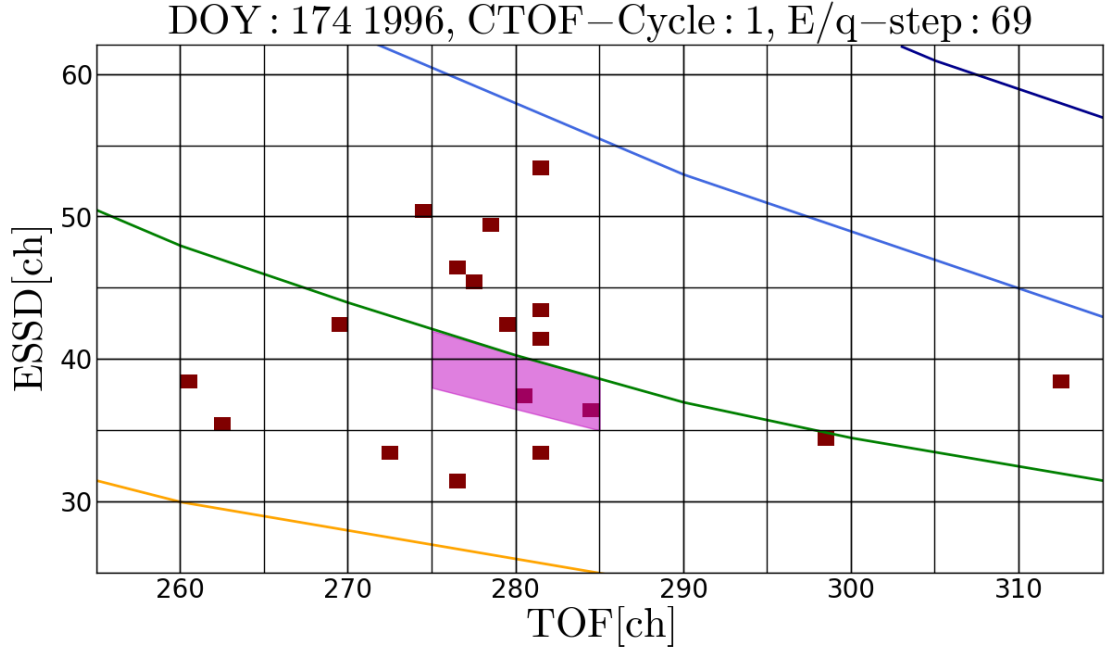
FIGURE 2.8: Close-up of the ET-matrix filled with the transmitted PHA counts during the first 5-minute CTOF cycle measured on DOY 174 1996 for Epq-step 69. This step corresponds to matrix rate MR10 for MR-box 235 at the onboard estimated heavy ion speed of 395.4 km/s at the given cycle, which is the same as in Figure 2.7. The MR-box 235 corresponds to the magenta-shaded area in the ET-matrix which at the Epq-step 69 only contains two transmitted PHA words while e.g. for the whole priority range PR4 (limited by the orange and green lines) 9 PHA counts were transmitted. In this case the same number of 9 PHA counts is also transmitted for PR3 (limited by the green and light blue lines) at the given Epq-step.
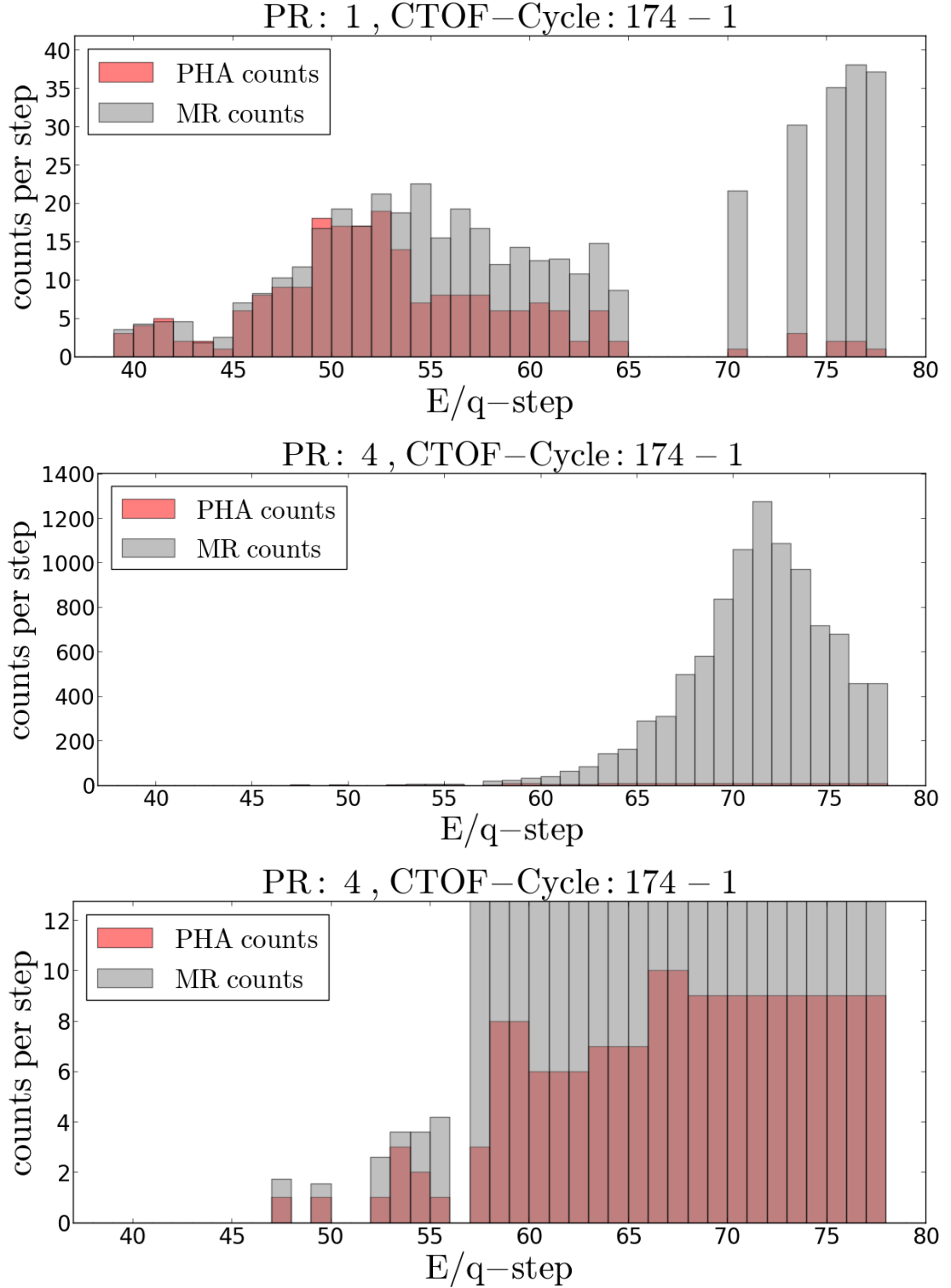
FIGURE 2.9: Comparison of the measured MR counts (gray) and the transmitted PHA counts (red) in priority ranges PR1 (upper panel) and PR4 (middle and lower panel) for the first cycle on DOY 174 for all relevant Epq-steps with at least one detected count. The ratio of the two quantities at each cycle and each step yields the base rate weights with which the PHA counts have to be multiplied to represent the true number of measured counts. While for PR1 the measured MR and transmitted PHA counts are of comparable order, the difference between the two quantities reaches up to two orders of magnitude in PR4 so that the lower panel is a close-up of the middle panel that allows a better recognition of the transmitted PHA words. At Epq-step 69 we find $N_{PHA} = 9$ and $N_{MR} = 845$ yielding a base-rate weight of $w_{br}^{PR4} = N_{MR}/N_{PHA} \approx 93.89$ for priority range PR4 at the given cycle and Epq-step.

FIGURE 2.10: Comparison of the uncorrected (upper panel) and corrected (lower panel) count rates for the accumulated long-term PHA data (DOY 174-220) for Epq-step 70. We note for instance that the O^{6+} peak at ($\tau \approx 280, \epsilon \approx 40$) is strongly enhanced in count rate by al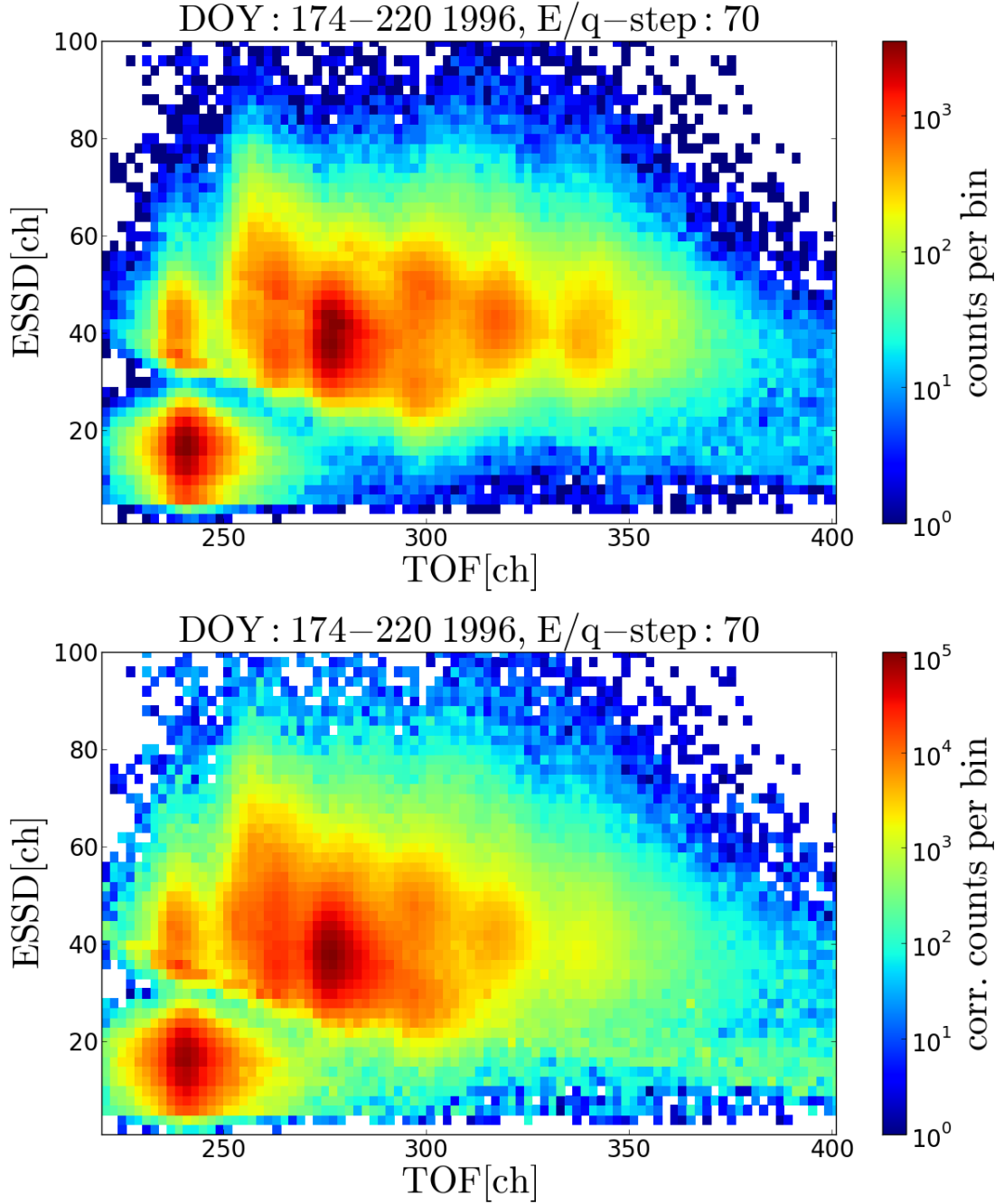most 2 orders of magnitude while the Si^{7+} peak at ($\tau \approx 340, \epsilon \approx 40$) increased by a less than 1 order of magnitude. We also note that the artificial diagonal steps in count rate in the upper panel at the priority range borders between PR2 and PR3 and PR4 and PR5, respectively, have vanished in the lower panel, so that e.g. the O^{6+} peak has a more continuous shape now. Unfortunately, the counts in priority range 5 cannot be reconstructed properly due to the additional PID suppression of He^{2+} that is not documented in detail in the available instrument descriptions. In fact, the base-rate reconstruction causes an over-representation of the unsuppressed transmitted PHA counts in PR5 that lie at the border to PR4 causing an artificial step in this area of the ET-matrix that can be seen best in the C^{6+} peak at ($\tau \approx 240, \epsilon \approx 40$). In appendix ? we show in addition the base rate corrected long-term count rates for the ET-matrices at Epq-steps 40, 50, 60 and 80 to give a representative overview of the reconstruction results.

2.3 The CELIAS Proton Monitor

The CELIAS Proton Monitor measures routinely with a resolution of half a minute the solar wind proton radial mean speed, thermal speed and density as well as the the solar wind flow direction in the plane perpendicular to the ecliptic plane. The instrument is a subsensor of the CELIAS/MTOF sensor which was developed at the University of Maryland. A detailed description of the instrument, its data products and the utilized analysis method can be found in the original publication by **?**]. Since the PM was originally designed to assist in the interpretation of MTOF data, it uses a relatively wide energy bandwidth and angular acceptance electrostatic analyzer which limits the accuracy of the derived solar wind proton bulk parameters. However, because the original SOHO Plasma Instrument [**?**] was not incorporated in the final spacecraft payload configuration [**?**], the CELIAS PM is the only SOHO sensor which measures the in-situ (proton) plasma parameters. The sensor consists of an electrostatic E/q analyzer similar to the one of MTOF and CTOF and a microchannel plate (MCP) with a two-dimensional cylindrically symmetric position sensing anode. The PM E/q analyzer is stepped through six E/q steps corresponding to a logarithmically (60% step size) increased deflection plate voltage between 0.3 and 3 kV within a total cycle time of 30 seconds. The proton speed information is derived from the radial position distribution of the incident protons on the sensing anode at each of the six E/q steps while the zenithal inflow direction is derived from the angular position. Unfortunately, the measurement principle leads to an ambiguity between incident angle and incident energy/charge which however, was intentionally designed into the PM to match as closely as possible the behavior of the deflection system for the main MTOF sensor. In order to improve the accuracy of the PM data to reach to the performance of regular plasma instruments, [**?**] applied a sophisticated analysis scheme to the raw data detected by the sensing anode: In a first step two independent methods, a simple numerical moment calculation and a fit approach based on a sensor response model are used to determine the density, mean and thermal speed. In a second step to obtain a corrected proton speed (less dependent of the azimuthal inflow angle), the ratio of the proton speeds of both methods is correlated with the ratio of the proton speed of the moment method and the proton speed measured by the SWE instrument on WIND, which was extrapolated to the SOHO site. In a similar way the corrected proton thermal speed is obtained from the correlation of the ratio of the thermal speeds, obtained from both determination methods, and the ratio of the thermal speed calculated from the moment method and the measured WIND/SWE thermal speed. Finally, the density is derived from the correlation of the ratio of the proton density, obtained from both determination methods, and the ratio of the density derived from the fit method and the measured WIND/SWE
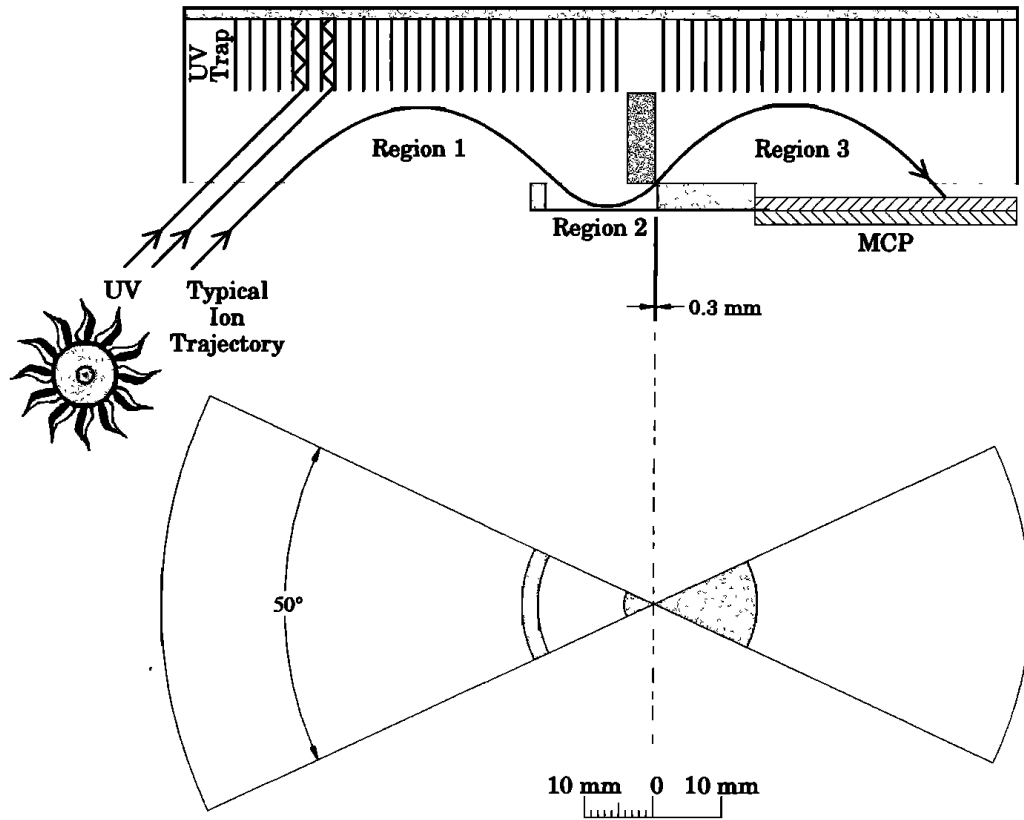
FIGURE 2.11: Schematic side view (upper panel) and front view (lower panel) of the SOHO CELIAS Proton Monitor (PM) after [Ipavich1998?]. The PM E/q analyzer consists of three 50° wedge-shaped parallel plate deflection regions, which are arranged such as to provide a high suppression of UV-photons given the relatively high PM geometry factor. The three regions are cylindrically symmetrical about a 0.3 mm diameter hole in the beryllium-copper sheet between region 2 and region 3. If a particle has the appropriate E/q-value at a given analyzer Epq-step it follows the typical ion trajectory as a result of the applied electric fields in regions 1 to 3 and finally triggers a signal in the MCP. The secondary electrons that are then released from the MCP create a localized signal in the cylindrically symmetrical anode that is situated 1 cm behind the MCP output. From the radial and angular position (R, θ) of the electron signal on the anode the speed and zenith incident angle information (in the plane perpendicular to the ecliptic) of the detected primary particle can be obtained simultaneously (see text for details).

density.

For the derived proton mean speeds **?**] estimated the PM measurement accuracy by comparison with the speeds measured by the SWE instrument onboard the WIND spacecraft. For the time period DOY 20 in 1996 to DOY 31 1997, the authors mapped the SOHO speed back to the WIND location which was on average 104 Earth radii closer to Earth in the X_{GSE} coordinate, corresponding to an average time delay of 26 minutes. For two hour averaged data periods they found a very good agreement of PM and SWE measurements with no significant systematic deviations and statistical deviations of $((\sigma v_p)_{rel} \approx 2\%)$. Due to the different measurement location of the two spacecraft one can assume that part of this deviation is real and therefore consider this value as upper

limit of the measurement uncertainty.

Despite the former work, in a sanity check of the proton data for the time interval DOY 150-220 we observe that the proton thermal speeds never decrease to values below 20 km/s, but they remain at the same or slightly higher values over extensive periods. This effect leads to an accumulation of thermal proton speeds at values in the positive vicinity of 20 km/s which coincides with an accumulation of proton speed values below 325 km/s. Since we consider these highly increased occurrences for certain combinations of mean and thermal speed at the edge of the PM parameter range as potentially unphysical we systematically exclude all time stamps where we measure a thermal speed below 22 km/s, which automatically also excludes all speed values with very low proton speeds below 325 km/s. This accounts for about 5% of the measurement cycles. Besides these minor irregularities the PM is operated successfully to the current date and the instrument data can be downloaded from the University of Maryland website [4].

2.4 Measurement Geometry

In the right panel of Figure **??** we show a schematic of the CELIAS measurement geometry for heavy ions and protons. The protons stream nearly radial outward from the Sun with velocity $\vec{v}_p$[5], while the heavy ion velocity $\vec{v}_i$ is composed of a radial component and the differential velocity $\vec{v}_{ip}$ which points along the local interplanetary magnetic field. The last assumption holds on timescales comparable to and larger than the ion gyration periods because a differential velocity can only be maintained parallel to the B-field. The true differential streaming magnitude is $|\vec{v}_{ip}| = v_{ip}$, but with the described time-of-flight spectrometers such as SWICS and CTOF we cannot measure v_{ip} directly. Instead we only measure the absolute value of the proton velocity which we denote as v_p and the absolute value v_i of the ion velocity which in the case of CTOF is transformed into a vector of same absolute value pointing along the instruments measurement axis by the focusing quadrupole lens in the sensor's entrance system. As can be seen in the schematic, the difference between the measured proton and ion speed $u_{i,p} = v_i - v_p$ in general does not equal the true differential speed $v_{i,p}$, but always underestimates this $v_{i,p}$ with the two exceptional cases where the magnetic field is pointing radial outward from or inward to the Sun. In principal, this bias could be corrected with the formula

---

[4]SOHO/CELIAS/MTOF/PM data and documentation can be found at $http : //umtof.umd.edu/pm/$.

[5]In this measurement scheme we neglect for simplicity, that in the presence of waves the protons rotate around the heavy ions with the differential velocity vector, as it can be observed in the HELIOS data.
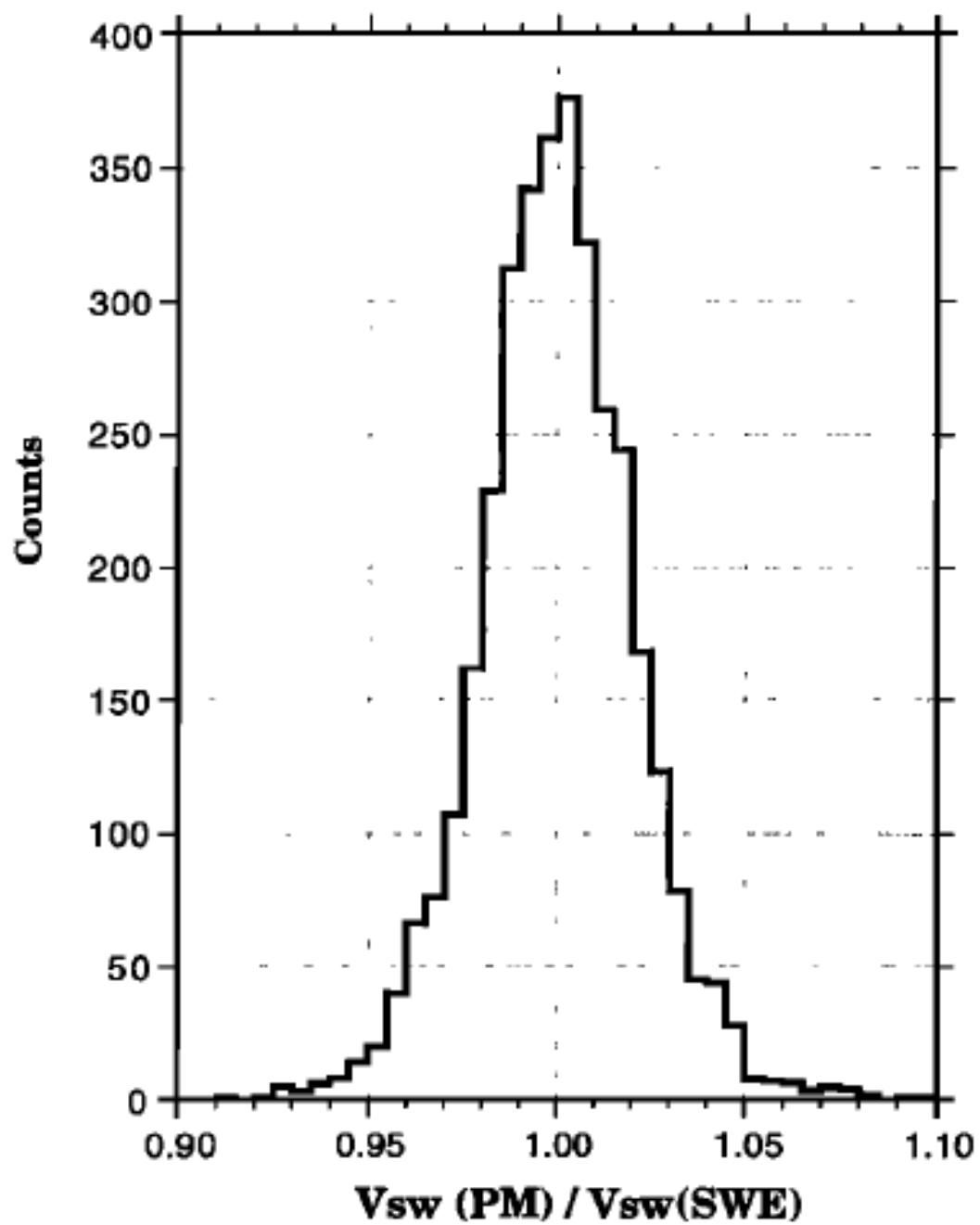
FIGURE 2.12

given in the bottom of the left panel of Figure **??**, if one had a simultaneous measurement of the in-situ magnetic field at the SOHO site, which would give us the angle θ. Unfortunately there is no magnetometer onboard SOHO, so that we cannot make this correction but have to have in mind that the absolute magnitude of the differential speeds measured with CELIAS are always a lower limit of the actual differential speeds. As a rough estimation of the systematic bias that this geometrical effect has, one calculates that for an average Parker angle of $\theta = 45°$, the true differential speed v_{ip} would be a factor of $f_{geo} \approx 1/\cos(\theta)$ larger than the measured differential speed u_{ip}. Regardless of the nomenclature in this geometry description, for convenience, in the following we denote the *measured* differential speeds as v_{ip}. Also explain correction factors in velocity and real space.
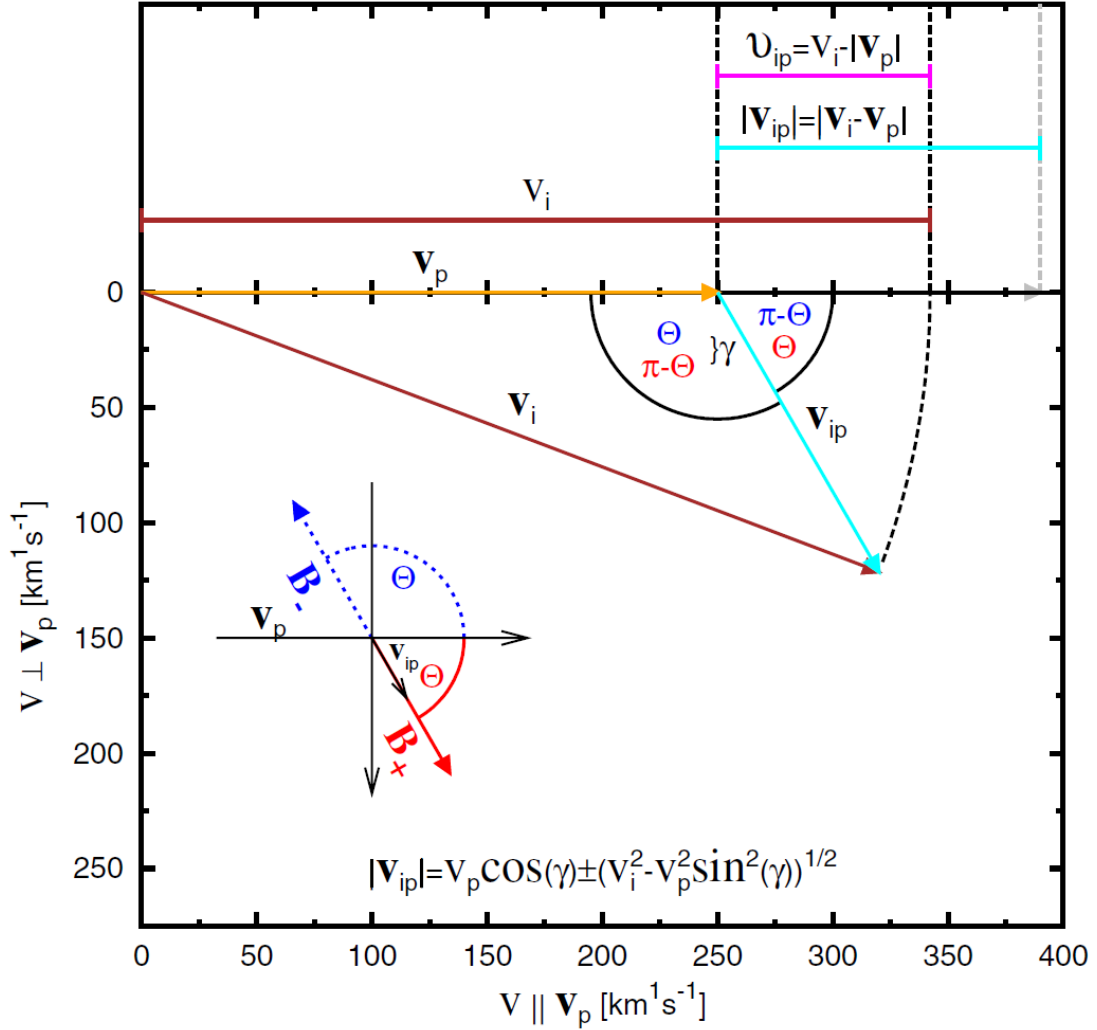
FIGURE 2.13: Measurement geometry for solar wind heavy ions (brown vector $\underline{v}_i$) and protons (yellow vector $\underline{v}_p$) in two-dimensional velocity space ($v_\parallel$, $v_\perp$) in the ecliptic plane. Both PM and CTOF measure the absolute value of the ion speed and not the full velocity vector. Therefore, the magnitude of the differential velocity $\underline{v}_{ip}$ (also called differential speed $\Delta v = v_{ip}$) which is oriented along the in-situ magnetic field, is systematically underestimated as $v_{ip} = |\underline{v}_i| - |\underline{v}_p|$ (pink length bar) instead of $v_{ip} = |\underline{v}_i - \underline{v}_p|$ (cyan length bar). If the in-situ B-field angle θ is measured simultaneously with the particles the true differential speed v_{ip} can be reconstructed from the combination of both measurements after Eq. ?. Unfortunately, in the case of SOHO there are no magnetic field measurements conducted on the spacecraft, so that we can only apply a mean correction to the differential speed assuming a mean magnetic field angle of $45°$ in the ecliptic plane corresponding to the Parker angle. The Figure is taken from [?] illustrating the measurements of solar wind ions at L1 with ACE/SWICS but is equivalently valid for our SOHO measurements. Also note, that the same geometrical relations between the shown ion velocities apply when we assume that the heavy ions flow approximately radially outwards from the Sun and instead the proton velocity shows a small deviation from the radial direction, as it is often observed for the case of alfvénic waves that are carried by the protons while the heavy ions surf these waves (see subsection 1.?)

.

Chapter 3

A Critical Revision of Heavy Ion Speeds Derived from CTOF Matrix Rate Data

In this section we utilize the CTOF matrix rates to check whether we can reproduce the results of the earlier CELIAS study by [1]. This shall not only provide a consistency check for the CTOF MR data and the transformation from matrix rates to E/q steps as described in **?**] but we also aim to revise the differential speeds derived from the MR data in greater detail. As explained in section **??** we only can reconstruct the heavy ion speeds with the documented MR classification algorithm for the subperiod DOY 174-220 compared to the full analysis period in [1] between DOY 84 and 230 in 1996. However, statistically this subsample is large enough that a systematic differential streaming of a given ion species should be visible also in this data set, if it is a permanent feature in the covered solar wind (speed) regime. We concentrate on the three heavy ion species analyzed by Hefti: O6+, Si7+, Fe9+.

change this in a way that we want to derive the ion speeds as it was originally planned for the CTOF data with the matrix rates

3.1 Derivation of Heavy Ion Velocity Distribution Functions from CTOF Matrix Rates

In Figure 2.7 of chapter2 we showed as an example the measured counts for matrix rate MR10 for the first measurement cycle on DOY 174 1996. To illustrate the matrix rate data processing we take now all counts measured during this cycle in the defined

box 235 for all 21 matrix rates MR0 - MR20 and convert them to a short-term reduced 1D-VDF for O^{6+} as it is anticipated by the design of the CTOF instrument and onboard-algorithmus. In contrast to the Epq-steps the matrix rates do not correspond to a fix speed for a fix ion species but are kept flexible as described in section **??**, so that the central matrix rates, contain the core of the VDF in any solar wind speed regime. For this reason the solar wind ion speed for every cycle i is approximated from the calculated mean speed of the major iron species measured in the previous cycle $(i-1)$[1]. With this speed a certain central Epq-step is predicted for the current cycle for every matrix box and the counts measured in the corresponding area in ET-space at this Epq-step are assigned to the central matrix rate 10. The remaining 20 matrix rates are then filled with the counts of the remaning 116 Epq-steps after the scheme given in Table ?, which naturally comes with certain compression factors for all matrix rates except for MR8 - MR12. Concretely, in each of the matrix rates MR5-MR7? and MR13-MR15 the counts of two Epq-steps are summed up, and in MR3-MR4 as well as in MR16-MR17 the counts of 4 Epq-steps are summed up in each matrix rate, respectively. This assignment continues with increasing compression factors, so that we have lower Epq-step resolution in the matrix rates with larger distance to the central matrix rate which finally corresponds to lower speed resolution in the flanks of the VDFs.

The central Epq-step j_c is calculated for each cycle onboard by the function:

$$ j_c = 116 - \ln(\widetilde{v}_{swi}) \cdot V_1 + V_2 - (S+1)/2 \,, \tag{3.1} $$

where $V_1 = 49.8516$ and $V_2 = -164$ are fix algorithm values during the whole analyzed time period. The value $\widetilde{v}_{swi}$ (in km/s) is stored as data product in the matrix rate data together with the 20 matrix count rates for each of the 503 matrix boxes[2]. The remaining number S is a shift that corresponds to the the given matrix box number of the selected species. This shift is defined for each box in the *Look-up Table for the CTOF Matrix rates Center Step* in Figure A.1. It has the same format as the *Matrix Box Definition* table in Figure A.2 so that box number and shift can be mapped to each other by position. All float values that appear in Eq. 3.1 by the application of the logarithm or by division are truncated to the next-lowest integer value.

Once we have the central Epq-step, we reconstruct the Epq-spectrum by inverting the scheme in Table 4.30 which can only be done in a unique way for the 5 Epq-steps that are equal to the 5 central matrix rates. For the remaining Epq-steps we assume in a first

---

[1]Note, that $v_{swi,est}$ is calculated onboard from the full Epq-ET-resolution, but it is not documented which areas in ET-space are actually considered for the calculation, so that this calculation cannot be reconstructed anymore.

[2]Note that $\widetilde{v}_{swi}$ is stored in the same cycle (i) in which it is used for the calculation of the central Epq-step j_c and not in the cycle in which it was calculated (i-1).
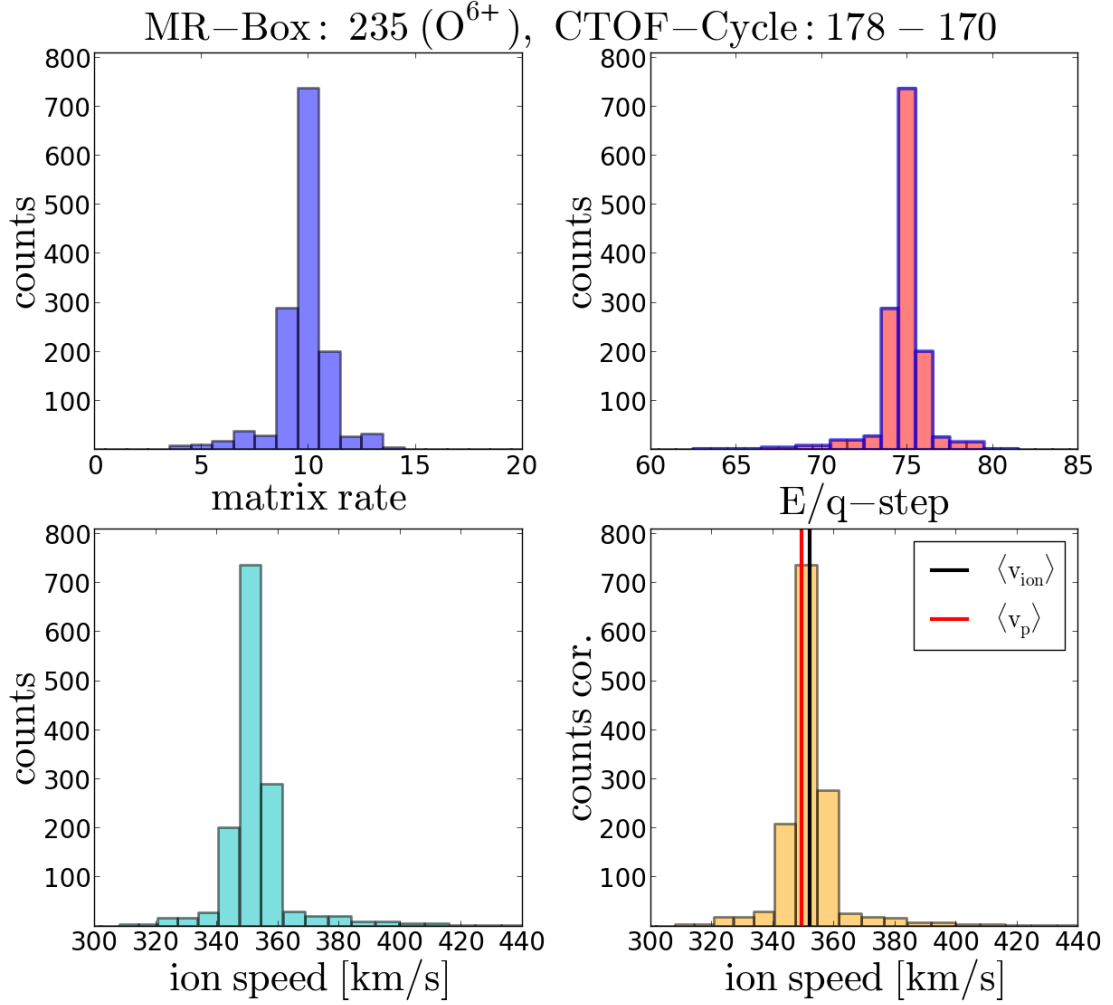
FIGURE 3.1: In the upper left panel we show the CTOF matrix rate spectrum for MR-box 235 at cycle 170 on DOY 178 1996 as an example of the obtained matrix (count) rates that are measured in the slow solar wind. The selected MR-box is the same that was selected by [Hefti1998] for the determination of the mean O^{6+} speed. As explained in the text one can convert this matrix rate spectrum to an Epq-step spectrum which is shown in the upper right panel. We see that the spectrum is centered around the central Epq-step 75 for which the count rate corresponds to the MR-box matrix rate MR10. In the lower left panel we use Eq ? to convert the Epq-spectrum into a speed spectrum of the identified ion species, given the known mass and charge of O^{6+}. Finally, the measured spectrum has to be corrected for the systematic over-representation of fast particles both in position and velocity space after Eq. ? and ? to obtain the actual speed spectrum. In the terms of kinetic plasma description this spectrum can now be interpreted as a reduced one-dimensional velocity distribution function (VDF). From this reduced VDF, we obtain the mean ion speed in a first approximation by simply calculating the first moment. We compare it to the mean proton speed that is simultaneously measured with the CELIAS PM to obtain the differential speed. In the depicted cycle the proton speed is $\langle v_p \rangle = 349\,\text{km/s}$ (marked as red vertical bar in the lower right panel) and the calculated ion speed is $\langle v_{O^{6+}} \rangle = 352\,\text{km/s}$ (marked as black vertical bar). (vsi7=342,vFe9=343)

approximation equal count rates for all Epq-steps that contribute to the same matrix rate. In the core of the VDF this approximation should not be critical as the count rates of two adjacent speed bins should not be too different on average. Very far away from the central steps this approximation is potentially more problematic, but for the relatively narrow solar wind VDFs there are hardly any counts in these steps[3]. The translation from the matrix count rate? spectra to Epq-step spectra is shown for O^{6+} in the upper two panels of Figure 3.1 for cycle 170 on DOY 178 1996, which is a representative example of a cycle measured under slow wind conditions. We see that the matrix rate spectrum is centered properly around MR10 in the upper left panel which corresponds to Epq-step 75 after Eq. 3.1 with the estimated speed for this cycle $\tilde{v}_{swi} = 345\,\mathrm{km/s}$ as can be seen in the upper right panel. The Epq-spectrum can then be translated into a 1D speed spectrum using Eq. 2.1 which is shown in the lower left panel of Figure 3.1. As this spectrum still corresponds to the raw count rates measured by CTOF disregarding instrumental efficiencies, it has to be corrected for the different phase space coverage at different speeds. This is done simply by multiplying the obtained count rates $N(v)$ with a relative factor $1/v^2$ that is derived in section **??**. This finally results in the reduced 1D velocity distribution function that is shown in the lower right panel and thus can be interpreted as a phase space density in 1D velocity (or more specific *reduced speed*?) space. From these VDFs we calculate the ion mean speed as the first and second moment of the distributions as

$$\langle v_{ion} \rangle = \frac{1}{C} \cdot \sum_{i=0}^{116} c_i \cdot v_i \tag{3.2}$$

respectively, where $N_i = N(v_i)$ are the measured (phase-space corrected) counts at the given speed v_i that correspond to the 117 Epq-steps and $C = \sum_{i=0}^{116} c_i$ is the appropriate normalization. The mean ion ($v_{ion} = 352$) speed for the analyzed cycle is shown in the lower right panel as red vertical bar that can be then compared to the mean proton speed that is measured simultaneously with the CELIAS/PM and also calculated as the first moment of the proton distribution as explained in section **??**.
In an analog way the thermal speed is calculated as the second moment of the VDF:

$$v_{ion,th} = \sqrt{\frac{1}{C-1} \cdot \sum_{i=0}^{116} (\langle v_{ion} \rangle - c_i \cdot v_i)^2} \tag{3.3}$$

with the same normalization C (check!) as in Eq. 3.2.

In Figure 3.2 we derive the reduced O^{6+} 1D-VDF in the same way as in Figure 3.2, but for cycle 120 on DOY 214 1996 which is a representative example of a VDF measured

---

[3]This observations in fact changes if the measured VDFs were not properly centralized in the matrix rates, as we discuss below

under fast wind conditions. We can see that the matrix rate spectrum is considerably wider as for the slow wind case, which agrees well with the expectation of higher kinetic temperatures in the fast solar wind as described in section 4.30 ?. However, we also recognize in the upper left panel that the central matrix rate 10 is not even close to meet the matrix rate with the highest count rate. This mismatch indicates that the onboard estimation of the solar wind heavy ion speed does not work correctly in the fast wind. As a result, the calculated central Epq-step does not match well with the center of the VDF, but it is shifted to the low-speed flank as can be seen in the upper right panel. Although we can still obtain meaningful VDFs due to the moderate resolution loss in the VDF flanks, the miscalculation leads to differences in the count rate resolution between the low- and high-speed flanks of the VDFs. This effect already introduces a systematic bias in the calculation of the ion mean speed, depending on the concrete form of the Epq-step reconstruction that is chosen. As can be seen from the lower right panel in Figure 3.2 we find for the given cycle a mean ion speed of $\langle v_{O^{6+}} \rangle = 561$ km/s while the simultaneously measured mean proton speed is $\langle v_p \rangle = 525$ km/s. Thus for this fast wind cycle we measure a differential speed of $\Delta v_{ip} = 36$ km/s, while in the slow case the differential speed was $\Delta v_{ip} = 3$ km/s which is on the order of the statistical measurement uncertainties.

In Figure 3.3 we show the VDF derivation for the same fast wind cycle DOY 214 120 for Si^{7+} that is associated with MR box number 201 after the preflight calibration [?] (see Figure 2.4). In comparison with Figure 3.2 we see that the count rates for Si^{7+} are about a factor of 50 lower than for O^{6+} which is roughly in agreement with the expected relative abundances (compare subsection 4.2 and 5.4, (calculate concrete expectation for Si^{7+}, maybe as example in subsection 5.4)). Similar to the O^{6+} case we also observe that the central matrix rate 10 does not match the matrix rates with the highest count rates but the measured core of the matrix rate spectrum is shifted to lower matrix rates to an extend that at the nominal central matrix rate 10 no counts are measured at all. Thus, the calculated energy-per-charge center step 47 lies in a gap between the core of the VDF and a subpopulation at higher Epq-steps as can be seen in the upper right panel. The calculated mean speed for Si^{7+} in the given cycle is $\langle v_{Si^{7+}} \rangle = 543$ km/s which has to be compared to the same proton speed $\langle v_p \rangle = 525$ km/s as in Figure 3.2

In Figure 3.4 we show the VDF derivation for the same fast wind cycle DOY 214 120 for the counts in matrix box 92. This MR-box is one of the three boxes that were selected by [Hefti1998] for the determination of the mean Fe^{9+} speed. In comparison with Figure 3.3 we find comparable count rates for Fe^{9+} and Si^{7+} as one would expect from a rough estimation of the relative coronal abundances as done in subsection 4.2
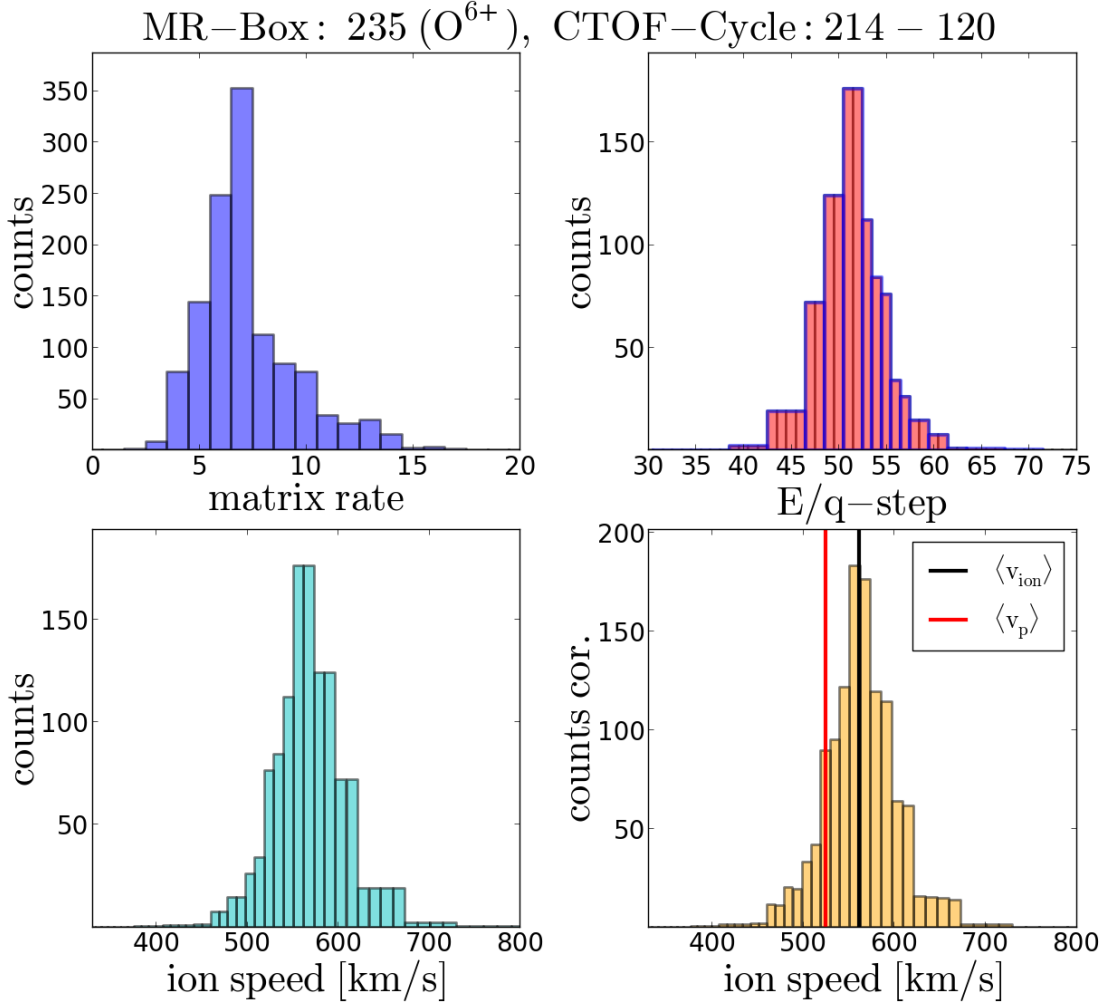
FIGURE 3.2: Translation from the matrix count rate spectrum (upper left panel) to the reduced 1D VDF (lower right panel) for MR-box 235 in the same way as in Figure 3.1 but for cycle 120 on DOY 214 1996 which is measured in the fast solar wind. We find for the given cycle a mean ion speed of $\langle v_{O^{6+}} \rangle = 561\,\mathrm{km/s}$ while the simultaneously measured mean proton speed is $\langle v_p \rangle = 525\,\mathrm{km/s}$.

(calculate concrete expectation for Fe^{9+}, maybe as example in subsection 5.4). Also for this MR-box we find that the measured VDF is shifted to lower matrix rates compared to the nominal central matrix rate 10, so that no count rates are measured at MR10. We further observe a similar subpopulation of counts at lower Epq-steps as in the Si^{7+} case. However, for Fe^{9+} this apparent subpopulation is much clearer separated from the core of the distribution, which means that these particles are measured at much lower speeds than the majority of Fe^{9+} counts. This raises the question whether these counts could be actually Fe^{9+} counts as they are statistically in contrast with approximately Maxwellian speed distributions. We also note that due to the relatively large speed difference of these low-speed counts to the VDF core, these counts are subject to a substantial phase space correction up to a factor of 3 as can be seen in the lower
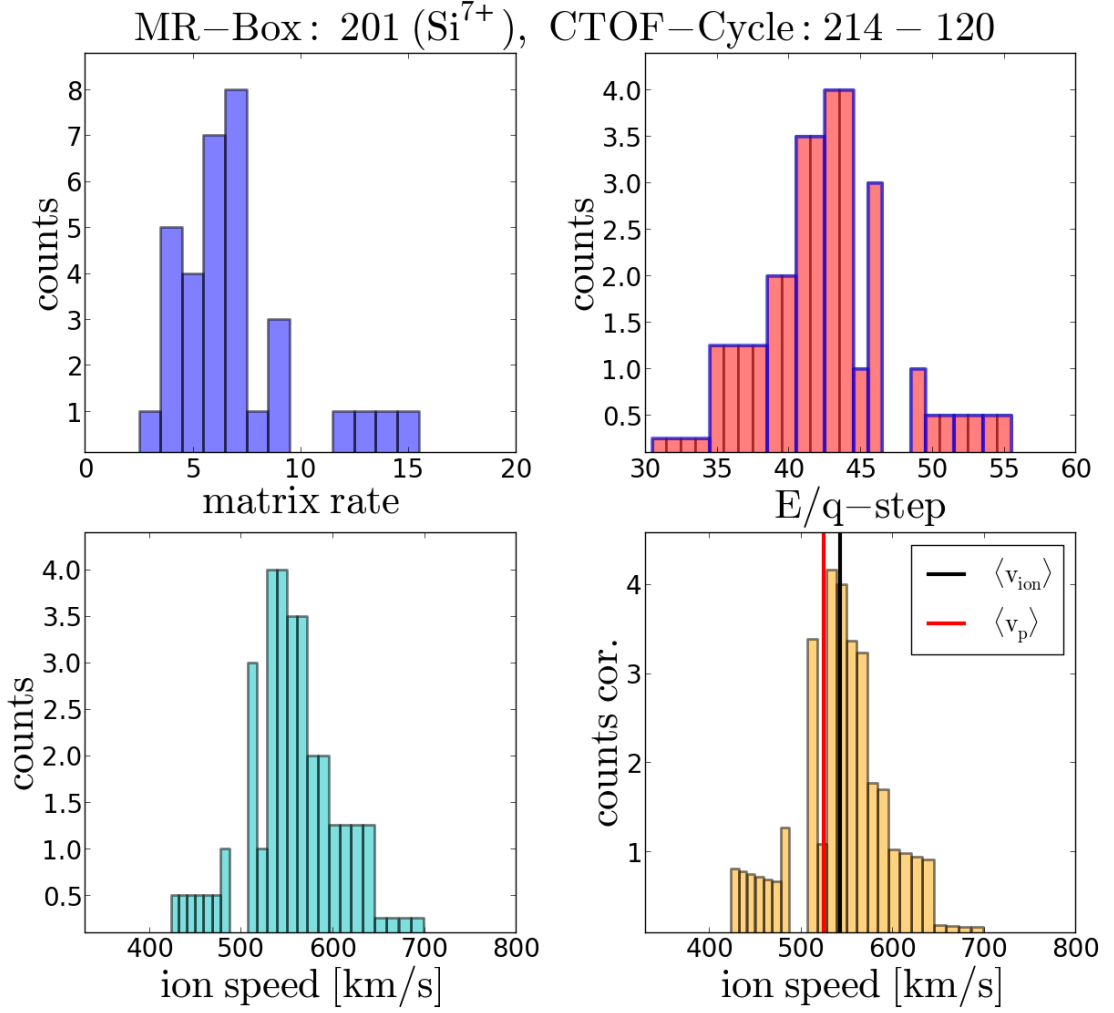
FIGURE 3.3: Translation from the matrix count rate spectrum (upper left panel) to the reduced 1D VDF (lower right panel) for the same fast wind cycle 120 on DOY 214 1996 as in Figure 3.2 but for MR-box 201. The selected MR-box is the same that was selected by [Hefti1998] for the determination of the mean Si^{7+} speed. The calculated mean speed for Si^{7+} in the given cycle is $\langle v_{Si^{7+}} \rangle = 543 \, \text{km/s}$ which has to be compared to the same proton speed $\langle v_p \rangle = 525 \, \text{km/s}$ as in Figure 3.2.

right panel of Figure 3.4 As an overall result we would obtain a very low ion mean speed of $\langle v_{Fe^{9+}} \rangle = 468 \, \text{km/s}$ if we just calculated the mean speed routinely as the first moment of the whole count sample, which is obviously not a good statistical measure for the observed distribution. On the other hand, as such apparent low-speed subpopulations are seen in most measured Fe^{9+} (and many Si^{7+}) VDFs one cannot offhand exclude these particles without clearly identifying an instrumental effect that explains their occurrence in the respective ion MR-boxes.
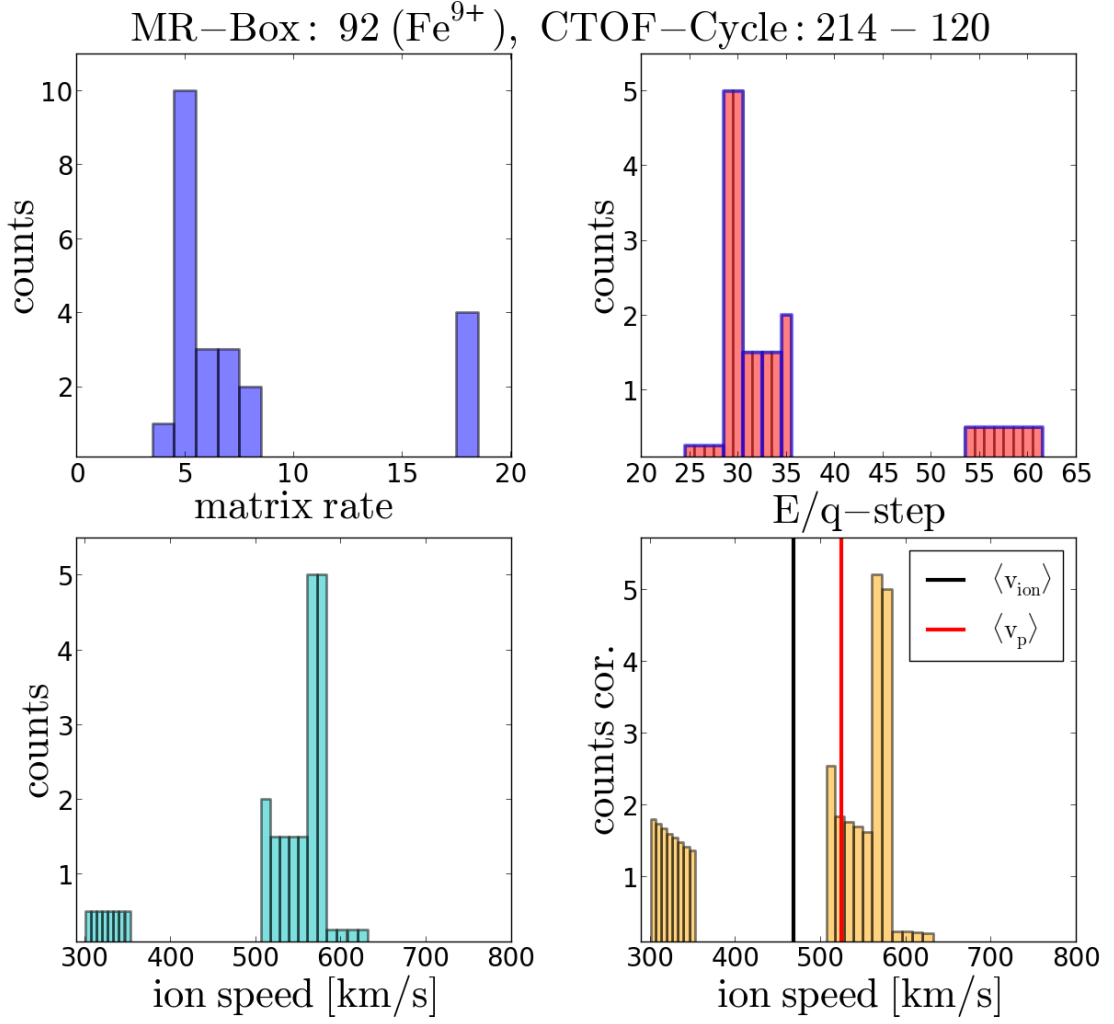
FIGURE 3.4: Translation from the matrix count rate spectrum (upper left panel) to the reduced 1D VDF (lower right panel) for the same fast wind cycle 120 on DOY 214 1996 as in Figure 3.2 and 3.3 but for MR-box 92.

3.2 Statistical Analysis of Heavy Ion Mean Speeds

-We want to make a statistical study with the differential speeds calculated as described above from 5-minute cycle, derived from the CTOF PHA data over the period DOY 174-220 in 1996. In Figure 3.5 we show 2-dimensional histograms of the ion-proton differential speeds Δv_{ip} of O^{6+} (upper panels), Si^{7+} (middle panels), and Fe^{9+} (lower panels) versus the simultaneously measured proton mean speed for the full time period DOY 174-220 in 1996. The left three panels show the absolute measured number of occurrences for a combination $(v_p, \Delta v_{ip})$ within a given (proton speed, differential speed)-bin, while in the right panels the number of occurrence is normalized to the maximum at each proton speed bin. On the first glance the obtained statistical differential speed pattern depending on the proton speed is quite different for the three ion species. The

calculated mean differential speeds at each proton speed bin are given by the black dots, that are connected by the solid black line to guide the eye. In the very slow wind below proton speeds of 380 km/s we find that O^{6+} streams at the same speed as the protons. Between 480 and 540 km/s we find a plateau of the highest observed differential speeds with values of around 35 km/s. At the highest two proton speed bins the differential speed drops to values of about 25 km/s. Considering the underlying occurrence statistics, we see that the center of mass of the distribution lies between 320 and 400 km/s, so that we measure most of the time in the slow wind and only occasionally in the fast wind above $v_p \approx 500$ km/s. As discussed in section 1.1, this is the natural outcome of the SOHO measurement site in the ecliptic around solar minimum in 1996, where no speeds comparable to the polar wind speeds of about 800 km/s can be detected. However, the total measurement statistics of more than 12000 cycles are sufficiently high to ensure the significance of the observed trend also in the fast wind where we have several 100 VDFs measured. This is also confirmed by the (1σ-) standard errors of the calculated mean differential speeds that are given by the black error bars for each calculated mean differential speed $\langle \Delta v_{ip} \rangle$. For every proton speed bin this standard error is calculated as

$$\Delta(\langle \Delta v_{ip} \rangle) = \sqrt{\frac{1}{(N-1)N} \cdot \sum_{k=1}^{K} \left(\langle \Delta v_{ip} \rangle - n_k \cdot \Delta v_{ip,k} \right)^2} \qquad (3.4)$$

where K is the number of $(v_p, \Delta v_{ip})$-bins in each proton speed bin that contain at least $n_k \geq 10$ occurrences and $N = \sum_k^K n_k$. The condition $n_k \geq 10$ is applied in order to exclude outliers of differential speed measurements that can be caused by an ion mean speed calculation from a VDF that contains an extremely low number of counts which is sometimes the case. For Si^{7+} we find that in the slow wind below 400 km/s we observe small negative differential speeds between -5 and -10 km/s. Also at intermediate proton speeds between 400 km/s and 480 km/s the differential speed obtains mainly small negative values between -5 and -10 km/s. In the fast wind above 480 km/s we find a plateau similar to the one observed for O^{6+} but at lower maximum differential speeds of about 15 km/s before also a similar decrease to differential speeds values of around 0 km/s at the highest proton speeds above 540 km/s. For Fe^{9+} we only find negative differential speeds between -10 and -35 km/s, so that this species seem to lack significantly behind the protons: In the slow wind below 400 km/s the differential speeds are about -20 km/s, while at intermediate speeds between 400 and 480 km/s this differential speed decreases even further to the observed minimum values of -35 km/s. In the fast wind at proton speeds between 480 km/s and 540 km/s we find on average a small increase of differential speeds compared to the intermediate speed range so that we observe values of $\Delta v_{ip} \approx -20$ km/s.
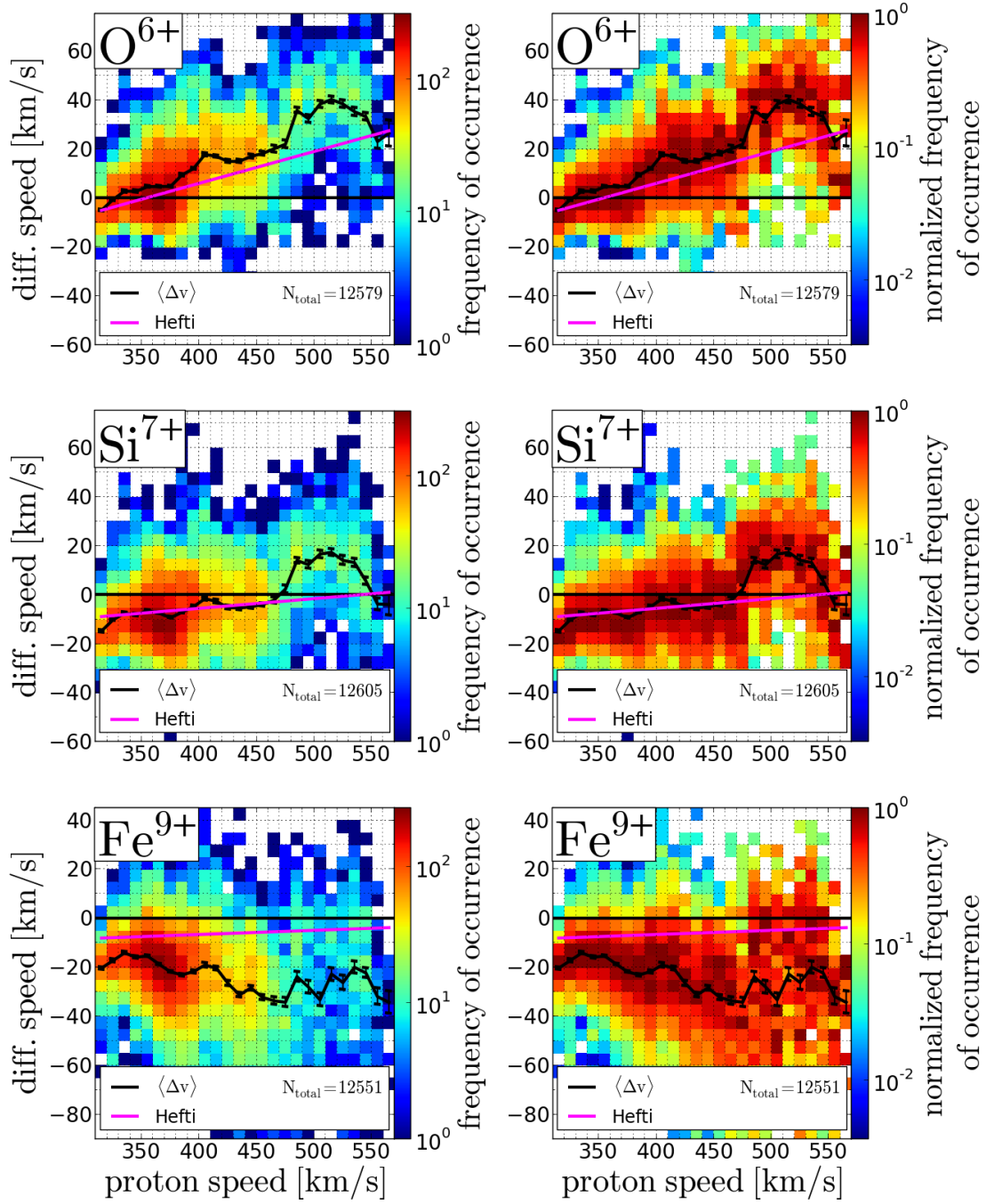
FIGURE 3.5: Two-dimensional histograms of the observed differential speeds between O^{6+}, Si^{7+}, Fe^{9+} and the solar wind protons, respectively, derived from the CTOF matrix rate data for the measurement period DOY 174-220 in 1996. The left three panels show the absolute measured number of occurrences for a combination $(v_p, \Delta v_{ip})$ within a given (proton speed, differential speed)-bin. The black line represents the mean differential speed $\langle \Delta v_{ip} \rangle$ at a given proton speed bin, the error bars mark the 1σ standard error of $\langle \Delta v_{ip} \rangle$. The magenta lines show the linear best fit obtained by **?**], for the time period DOY 80-230 in 1996. The three right panels show the number of occurrence for a for a combination $(v_p, \Delta v_{ip})$ normalized to the maximum within each proton speed, so that the maximum and spread of the differential speed distribution is better visible for all solar wind proton speeds.

Finally, we compare our findings with the results by S. Hefti **??** that were obtained from the CTOF matrix rate data over the time period DOY 80-230 1996, that we shortly discussed in section 1.5 in the context of Figure **??**. Their resulting linear relations for the differential speed of O^{6+}, Si^{7+} and O^{Fe9+} with respect to the proton speed are plotted as magenta line into the panels of Figure 3.5 and although the time period of the earlier study is about a factor of 3 larger, we aim to compare the findings. We can see that for the case of O^{6+} we find a good agreement between the observed trend in particular for the slow and intermediate speed range where, where both studies studies find a similar gradient for increase of differential speed with increasing proton speed and only a small absolute speed difference of about 5 km/s, which could be easily explained by the additional data in the earlier study but also by the different calculation method for the mean speed as **??** applied a fit to the short term VDFs to derive the mean speed. At high proton speeds above 480 km/s our differential speeds for O^{6+} deviate already by a somewhat larger amount of 10-15 km/s which corresponds which however could also be possible as the solar wind streams in our smaller data set could be over-represented in wave activity since the difference between the two observations is on the typical order of $0.1\,v_A$ at 1 AU. In principal

-Finish comparison with hefti by also mentioning how in particular Fe9 it would look, when we have no sub population (in particular for iron). - give possible explanation for negative speeds at the highest speeds: magnetic field direction for the last fast stream in (almost) perpendiclar configuration?

3.3   Discussion

To summarize, the differential speed analysis of the MR data reveals significant differences in the magnitude of differential speeds among the three ion species which includes for Si^{7+} and Fe^{9+} even a change of the sign in Δv_{ip}. On the other hand, the three ions species show a similar increase pattern of the differential speed with increasing proton speed: In particular for O^{6+} and Si^{7+} we find two transitions between differential speed regimes around the same proton speeds of 420 and 480 km/s. These transition are also visible, but less pronounced in the Fe^{9+} data. The comparison with the [**?**] results give a qualitative agreement for the O6+ data, but show also clear quantitative deviations in the fast wind in a way that we find higher differential speeds for O6+ and positive differential speeds for Si7+ while for Fe9+ negative differential speeds are observed (with a magnitude that depends on the calculation method) which is in qualitative agreement with **??**Hefti].

These observations leave us with an inconclusive picture of the CTOF matrix rate data:

On one hand the similar increase pattern for all three ions suggests that the observed differential streaming is not an isolated feature for O^{6+} as suggested by **?**], but that the speed of all observed heavy ions is regulated by the same processe(s). On the other hand, while it seems possible that differences in differential speed magnitude can be produced by the same candidate process, the change in sign of the differential speeds is very hard to explain in a consistent manner. To solve this contradicting situation, in the following we conduct a revised data analysis of the CTOF heavy ion data including an instrument calibration which is based on Pulse Height Analysis (PHA) data. This data product does not only have higher resolution in mass, mass-per-charge and ion speed but is also independent from the CTOF preflight-calibration on which the MR data analysis is based.

Chapter 4

Characterization of the CTOF Sensor Response

In order to derive velocity distribution functions from the (base-rate corrected) CTOF PHA data we need to determine for all relevant ion species $1 \leq i \leq N_{ion}$ at all Epq-steps $0 \leq j \leq 116$ the measured count rates N_{ij} from the measured accumulated count rates $C, (\tau, \epsilon)$ in the ET data.

To achieve this goal, we develop in this chapter a model of the CTOF instrumental response which predicts the individual peak positions and shapes in ET space for each ion species for elements $2 \leq Z \lesssim 59$ at any given energy-per-charge step. On the basis of this sensor response model the measured particle counts $C, (\tau, \epsilon)$ at any time resolution down to the nominal cadence of 5 minutes can be probabilistically assigned to certain ion species, depending on the particles' signal in energy-per-charge, time-of-flight and residual energy.

In the end we also discuss the treatment of the so-called instrumental background, which are contributions to the measured count rate data that originate either from irregular ion measurements such as random-coincidences or energy pile-ups or are signals from other particle populations than solar wind (or pick-up) ions.

4.1   Probabilistic Ion Count Assignment

The simplest way of identifying measured PHA counts as certain ion species is to form two dimensional boxes in ET space that contain a fixed range of TOF and ESSD channels for each Epq-step and all counts measured in these channels are assigned to the same ion species. It is possible to follow such an approach, but the only improvement to the box scheme in chapter 2 would be that one defines the boxes on the basis of

in-flight long-term data. However, these ET-boxes (or m-m/q-boxes) are a massive over-simplification of the actual problem because in the PHA data we can see the substantial overlap between the ion peaks in the ET matrices. Thus, the majority of counts cannot be assigned deterministically to a certain species but instead, we have to assign them in a probabilistic manner:

For every Epq-step the total count rate at each channel (bin) in ET space can be modeled as the sum of the count rate for all detectable ion species $1 \leq i \leq N_{ion}$:

$$\widetilde{C}(\tau, \epsilon) = \sum_{i=1}^{N_{ion}} \widetilde{C}_i(\tau, \epsilon) \tag{4.1}$$

with the (unknown) step-dependent individual species count rate contributions $\widetilde{C}_i(\tau, \epsilon)$ for each ET-bin. For a sufficiently large number of measured counts the contributions $\widetilde{C}_i$ can be regarded as quasi-continuous distributions in ET space and the shape of these distributions i.e. the relative count rate at each channel compared to all other channel count rates does not change anymore with even increasing measured count rates, assuming that the detector itself does not change over time. One can then separate the distributions into a constant normalized part $R_i(\tau, \epsilon)$ that describes the shape of the species distribution and a variable scaling parameter N_i:

$$\widetilde{C}_i(\tau, \epsilon) = R_i(\tau, \epsilon) \cdot N_i =: \widetilde{C}(N_i, \tau, \epsilon) \, . \tag{4.2}$$

with the normalization of R_i:

$$\forall \, i : \; \sum_{\tau} \sum_{\epsilon} R_i(\tau, \epsilon) = \sum_{\tau, \epsilon} R_i(\tau, \epsilon) = 1 \, . \tag{4.3}$$

The function R_i can be considered as a probability density function that we call the sensor response for the respective ion species at the given Epq-step. The complimentary scaling parameter N_i is then the (total) count rate for the given ion species at this Epq-step, which is the quantity that we are ultimately interested in.

As the species responses are independent of the count rate it is clear, that once they are known from the instrument calibration measurements with high counting statistics, they are constant at any given measurement time as long as no physical changes of the instrument occur. Instead, for any finite ion count rate N_i the distribution of the actually measured count rates $C_i(T, E)$ in the ET-matrix can be considered as sampled from the model distribution $\widetilde{C}(N_i, \tau, \epsilon)$ and the deviations that occur are purely due to the statistical nature of the ion interaction in the carbon foil and the SSD. Thus, as each detected ion event is statistically independent from all others, the probability that a certain ion species is measured with the count rate C_i at a certain ET-bin is given by a

Poisson distribution with the expectation value $\lambda_i = \widetilde{C}(N_i, \tau, \epsilon)$:

$$P_{\tau,\epsilon}(\lambda_i, C_i) = \frac{\lambda_i^{C_i}}{C_i!}e^{-\lambda_i}, \quad C_i \in \mathbb{N}, \quad \lambda_i \in \mathbb{R}_{>0}. \tag{4.4}$$

Consequently, the probability that the overall measured count rate in a certain ET-bin obtains a value C is given as

$$P_{\tau,\epsilon}(\lambda, C) = \frac{\lambda^C}{C!}e^{-\lambda}, \quad C \in \mathbb{N}, \quad \lambda \in \mathbb{R}_{>0}. \tag{4.5}$$

with the expectation value

$$\lambda = \sum_{i=1}^{N_{ion}} \widetilde{C}_i(\tau, \epsilon) =: \widetilde{C}(\underline{N}, \tau, \epsilon), \tag{4.6}$$

where $\underline{N}$ denotes the vector containing all total ion count rates $1 \leq N_i \leq N_{ions}$. The vector-form is motivated by the fact that the count rate model is linear in the ion count rates and therefore can be expressed in a more compact way as

$$\widetilde{C}(\underline{N}, \tau, \epsilon) = \underline{N} \cdot \underline{R}(\tau, \epsilon) \tag{4.7}$$

where the response model of all ion species is expressed as the vector $\underline{R}(\tau, \epsilon) = (R_1(\tau, \epsilon), ..., R_i(\tau, \epsilon), ..., R_{N_{ions}}(\tau, \epsilon))^T$.

In the given situation, where the probability to measure certain count rates $C(\tau, \epsilon)$ depends on the underlying ion count rate vector $\underline{N}$ we can apply a maximum-likelihood estimation [Numerical Recipes] and derive the most probable values of $\underline{N}$ as the ones which maximize simultaneously the probability of obtaining the *actually* measured count rates $C(\tau, \epsilon)$ at the given ET-bins. By multiplying the probabilities of the measured count rates $C(\tau, \epsilon)$ of all ET-bins we find the total probability of the measured count rate sample which has to be maximized as

$$P = \prod_{\tau,\epsilon} P_{\tau,\epsilon}(\widetilde{C}(\underline{N}), C) = \prod_{\tau,\epsilon} \left(\frac{\widetilde{C}(\underline{N})^C}{C!}e^{-\widetilde{C}(\underline{N})} \right) \tag{4.8}$$

Instead of maximizing Eq. it is mathematically equivalent and numerically favorable to minimize the negative logarithm of the probability product:

$$
\begin{aligned}
-\ln(P) &= -\ln\left[\prod_{\tau,\epsilon}\left(\frac{\widetilde{C}(\underline{N})^C}{C!}e^{-\widetilde{C}(\underline{N})}\right)\right]\\
&= \sum_{\tau,\epsilon}\left[-\ln\left(\frac{\widetilde{C}(\underline{N})^C}{C!}\right)+\widetilde{C}(\underline{N})\right]\\
&= \sum_{\tau,\epsilon}\left[-C\ln(\widetilde{C}(\underline{N}))+\ln(C!)+\widetilde{C}(\underline{N})\right]
\end{aligned}
\tag{4.9}
$$

Since the term $\ln(C!)$ is independent of the model $\widetilde{C}$ we can neglect it in the minimization so that we find the following merit function:

$$
M(C,\widetilde{C}(\underline{N})) = \sum_{\tau,\epsilon}\left[\widetilde{C}(\underline{N})-C\ln(\widetilde{C}(\underline{N}))\right]
\tag{4.10}
$$

which can be numerically minimized. As the count rate model $\widetilde{C}(\underline{N},\tau,\epsilon)$ is essentially a parametrization of the response model with the free parameter vector $\underline{N}$, we call this numerical minimization a fit of the response model $\underline{R}(\tau,\epsilon)$ to the measured data $C(\tau,\epsilon)$. As fit- or minimization-algorithm we utilize the Levenberg-Marquardt algorithm [ref] and the BFGS algorithm [ref] as they are implemented in the 'optimize' module as part of the numarical python ('numpy') library [webref,version]. Further details about the concrete usage of these algorithms are given in the context of concrete fit results in the following sections and chapters.

Finally, we note that for the case of sufficiently high counting statistics within each relevant ET bin the measured count rates follow approximately a normal distribution

$$
P_{\tau,\epsilon}(\mu,\sigma,C) = \frac{1}{\sqrt{2\pi}\sigma}\cdot\exp\left(-\frac{(C-\mu)^2}{2\sigma^2}\right)\quad C\in\mathbb{N},\quad\lambda\in\mathbb{R}_{>0}.
\tag{4.11}
$$

with the same expectation value as the Poisson distributon $\mu := \lambda = \widetilde{C}(\underline{N})$ and standard deviation $\sigma := \sqrt{\lambda} = \sqrt{\widetilde{C}(\underline{N})}$. In analogy to Eq. 4.8 - 4.9 we can then derive a merit function for the normally distributed count rate approximation by calculating the total sample probability:

$$
\begin{aligned}
-\ln(P) &= -\ln\left[\prod_{\tau,\epsilon}\left(\frac{1}{\sqrt{2\pi}\sigma}\cdot\exp\left(-\frac{(C-\mu)^2}{2\sigma^2}\right)\right)\right]\\
&= \sum_{\tau,\epsilon}\left[-\ln\left(\frac{1}{\sqrt{2\pi}\sigma}\right)+\frac{(C-\mu)^2}{2\sigma^2}\right]
\end{aligned}
\tag{4.12}
$$

Yet, if we used directly this expression as the merit function M, the σ-values would depend on $\underline{N}$ and thus would vary during the minimization. This turns out to be problematic for the numerical convergence of the fit as large deviations between modeled count rate $\widetilde{C}$ and measured count rate C are scaled down for large model values $\widetilde{C}$. To avoid this problem, we calculate the σ-values from the measured count rates in each ET-bin instead, so that they are constant during the minimization[1]. So when we approximate $\sigma = \sqrt{C}$ and then omit in Eq. 4.12 all terms and factors that are independent of $\underline{N}$ we obtain as merit function

$$M(C, \widetilde{C}(\underline{N})) = \sum_{\tau, \epsilon} \left[\frac{(C - \widetilde{C}(\underline{N}))^2}{C} \right] = \sum_{\tau, \epsilon} \left[\frac{(C - \mu(\underline{N}, \underline{R}))^2}{\sigma^2} \right] = \chi^2(\underline{N}, \underline{R}) \qquad (4.13)$$

the regular χ^2-distribution that is used in the standard 'weighted least-square fitting' procedure with the weights $w = 1/\sigma^2$ and normally distributed statistical errors σ around the model value μ. The advantage of Eq. 4.13 over Eq. 5.2 is that Eq. 4.13 directly provides a standard goodness estimation of the fit which we can use to compare the goodness of different proposed response models $\underline{R}$ (see sections 4.4 and 4.5).

4.2 Systematic Ion Selection for the CTOF Response Model

To derive the response model for the CTOF sensor we first need to select a physically meaningful set of ion species that we expect to be detectable in the CTOF data. In principal, the design of the CTOF entrance system as well as the TOF and ESSD measurement range allow a large number of different ion species to be measured with a valid signal in the CTOF TCR data at reasonable solar wind and suprathermal speeds. However, as every measurement has limited counting statistics it is not meaningful to include all these ion species in the response model as we have reliable upper estimates from other experiments and theoretical considerations that many of these species have very low abundances so that they cannot be resolved in the data. To allow for a systematic selection of physically meaningful solar wind ion species we use a comprehensive overview of elemental abundances in the solar corona [Aschwanden. page 31 and references within Table 1.2], as this is the source region of the solar wind, in combination with model calculations of ion charge state abundances [Arnaud and Rothenflug 1985, Table IV] in dependence of the coronal electron temperature.

---

[1]This way of defining the weights $w = 1/\sigma^2 = 1/C$ in the minimization function is known as Neymann's (weighted) χ^2 [Baker and Cousins 1984] which is justified by the fact that as the fit convergences, both σ-values become similar $\sigma_{\widetilde{C}} \to \sigma_C$. Furthermore, as our model is linear in the count rates $\underline{N}$, Neymann's χ^2 approach is (in the convergence limit) even algebraically equivalent to the ordinary (Pearson's) χ^2 approach[Read and Cressie (1988)] in Eq. 4.12 ???. Source: Goodness-of-Fit Statistics for Discrete Multivariate Data, Timothy R. C. Read, Noel A. C. Cressie, 1988, Springer New York, page 31, check properly!

Considering first the elemental abundances we include all elements that have a relative coronal abundance larger than 10^{-6} times the coronal hydrogen abundance which yields the elements helium, carbon, nitrogen, oxygen, neon, sodium, magnesium, aluminum, silicon, sulfur, argon, calcium, iron and nickel. Among the elements with low and intermediate masses ($m \leq 20$ amu) the most abundant elements are helium, carbon, oxygen and neon which compared to hydrogen have relative coronal abundances of 8.5%, 0.032%, 0.063% and 0.012%, respectively. Among those with high mass numbers ($m \geq 28$ amu), which can be well-separated in the CTOF measurements from the former elements, the most abundant elements are silicon and iron both with relative coronal abundances of 0.0040% compared to hydrogen. As nitrogen, magnesium and sulfur show relative coronal abundances of 0.0079%, 0.0040% and 0.0016% with respect to hydrogen, their abundances are lower, but still comparable in order of magnitude with respect to some of their neighbor elements. We thus include them in the response model not only because they potentially influence the speed spectra of their adjacent more abundant ion species but also their own most abundant charge states can be resolved at least in the CTOF long-term data matrices for the slow wind case. In contrast the elements sodium, aluminum, argon, calcium and nickel have relative coronal abundances between 0.0002% and 0.00025% with respect to hydrogen which makes them even one order of magnitude less abundant than magnesium and sulfur. Yet, as the charge state distribution is quite different for each element and can even vary considerably with the solar wind type we include these elements as well, as they could still influence the count rates of certain other ion species. This is in particular true, as we have to take into account that in the ET-matrices we compare adjacent ion species at slightly different speeds which virtually enhances the measured count rate of the ion species that is just sampled at the maximum of its speed distribution at a given Epq-step. The next abundant elements are phosphorous, chlorine, and cobalt which have relative coronal abundances below 0.0001% with respect to hydrogen, and are more than one order of magnitude less abundant than their adjacent elements, so that we do not include these elements in the response model.

We assess now the relative charge state abundances utilizing the zero-density(?) model calculations by [Arnaud and Rothenflug] and the coronal freeze-in (electron) temperatures that were derived by [Aellig, JGR,1998] for the CTOF iron charge states Fe^{8+} - Fe^{12+} for the time interval DOY185-220 1996, that covers a large part of the analysis period in this work. The study yields freeze-in temperatures in the range between $T_{Ce} = 10^{5.9}$ K and $T_{Ce} = 10^{6.2}$ K which is in very good agreement with many other studies on the coronal electron temperature both based on remote-sensing and in-situ measurements [e.g. Gabriel 1976, Geiss1995, Landi2014]. At these typical coronal electron temperatures a large fraction ($\geq 80\%$) of the solar wind helium, oxygen and neon

particles is expected to occur as He^{2+}, O^{6+}, and Ne^{8+} as these charge states are strongly favored due to the complete vacancy of their respective outermost atomic electron shell. For carbon the situation is more complicated because the relative carbon charge state abundances, that result from the typical coronal temperature range, are highly sensitive to small deviations in T_{Ce} due to the comparable ionization potentials of C^{4+}, C^{5+} and C^{6+}. The same applies for silicon and iron for which a wide range of charge states is expected to occur that is centered around the species Si^{8+} - Si^{9+} and Fe^{9+} - Fe^{11+} for an average value of $T_{Ce} = 10^{6.1}$ K. In general, the expected abundances of the most abundant solar wind ions are in good agreement with the observed solar wind charge states over longer time periods [i.e. von Steiger2000, Landi2012, Landi2014].

For the CTOF response model we include for each of the selected elements all charge states with expected relative abundances larger than 10^{-3} at least for one of the listed electron temperature values $T_{Ce} \in \{10^{5.9}$ K$, 10^{6.0}$ K$, 10^{6.1}$ K$, 10^{6.2}$ K$\}$ in [Arnaud and Rothenflug]. Hence, even in the case of underestimated ion count rates due to inaccuracies in the charge state abundance modeling by a factor of 10 we include all relevant charge states down to a few percent relative count rate contribution. In this manner, the largest ion set that is currently included in the CTOF response model, i.e. for which we calculated individual ion response functions R_i contains 91 ion species of the 14 aforementioned elements helium - nickel.

Yet, in many case in which we deal with subsamples of the CTOF data, the response model ion set has to be systematically reduced due to low counting statistics. This is done in order to allow a numerically stable fit of the most relevant ion species over all relevant Epq-steps. In fact, the largest ion set which we apply in the heavy ion velocity distribution analysis consists of 71 ion species belonging to 11 elements: helium, carbon, nitrogen, oxygen, neon, magnesium, silicon, sulfur, calcium, iron, and nickel. In section 4.6.1 we explain the systematic reduction of the response model ion set for low counting statistics in detail.

4.3 Derivation of the CTOF Response Model

So far we described in section 4.1 how we can derive the ion count rates $\underline{N}$ from the measured count rates in the ET-matrix $C(\tau, \epsilon)$ based on an instrumental response model $\underline{R}(\tau, \epsilon)$ for a given set of ion species that we obtained in section 4.2. Once we know, which ion species to include in the response model, one could in principle determine the individual responses $R_{ij}(\tau, \epsilon)$ at each Epq-step $0 \leq j \leq 116$ for each of these species separately in a preflight calibration by exposing the CTOF sensor to the respective ion beam and adjusting the particle energy. However, in the available ion sources at the time of the CTOF preflight-calibration there were only a limited number of elements

available that are relatively easy to vaporize in pure form (mainly light ions and noble gases). Furthermore, these limited pre-flight calibration runs, were not even conducted for the assembled instrument but only for each of the three measurement sections (E/q, TOF, ESSD) separately [Hovestadt1995,Hefti1997, Aellig1998, Oetliker1993]. As much as this information is helpful for plausibility checks, on the whole it is not enough to derive a systematic response model from it. Instead, it could be shown for similar time-of-flight mass spectrometers such as Ulysses/SWICS and ACE/SWICS, that given the in-flight measured PHA data acumulated over longer time periods one can derive a sophisticated response model of these sensors [vonSteiger?, Berger, Koeten, Wimmer-Schweingruber? to name a few] that is even superior to preflight-data based models in the aspect that some instrument components are subject to small changes during the launch and cruise phase (i.e. due to outgasing in space and mechanical stress from launch vibrations and temperature changes).

In the following we describe the derivation of the response model on the basis of such an in-flight calibration. As mentioned before, we can assume that the response model $\underline{R}(\tau,\epsilon)$ is independent of the measured plasma samples for all times and so we can use at each given Epq-step j the total accumuluated count rate $C_j(\tau,\epsilon)$ to determine $\underline{R}_j(\tau,\epsilon)$. But still, in the in-flight calibration $C(\tau,\epsilon)$ is in general the sum of the count rate of several ion species within each ET-bin and thus the individual ion responses have to be obtained from a similar minimization as described in section 4.1. As the measurement principle is universal for all ion species, we can assume that all species responses can be represented by a general peak model R so that the individual ion peak at each Epq-step is a parametrization of this universal model:

$$R_{ij}(\tau,\epsilon) := R(\underline{P}_{ij},\tau,\epsilon) \tag{4.14}$$

with the individual parameter vector $\underline{P}_{ij}$ that fully describes the observed ion peak. Mathematically, the minimization function can still be exactly expressed as in Eq. 5.2 and as we deal with high counting statisics we approximate this function as in 4.13:

$$M(C,\widetilde{C}(N_{ij},\{\underline{P}_{ij}\})) = \sum_{\tau,\epsilon} \left[\frac{(C - \widetilde{C}(N_{ij},\underline{P}_{ij}))^2}{C} \right] \tag{4.15}$$

Compared to Eq 4.13 we now have in addition to the (physically meaningless) accumulated long-term count rates N_{ij} an additional number of free parameters in the fit given by the set of parameter vectors $\{\underline{P}_{ij}\}$ fo all ion species at all Epq-steps. This set has the dimension $N_{steps} \times N_{ions} \times N_{params}$ where $N_{params} = dim(\underline{P}_i)$ depends on how many parameters we need to parametrize each of the ion response functions R_i at a given Epq-step. When we just assume a 2-dimensional Gaussian as the simplest realization

of the general peak model:

$$
\begin{aligned}
R(\underline{P}_{i,j}, \tau, \epsilon) &= R_\tau(\underline{P}_\tau^{ij}, \tau) \cdot R_\epsilon(\underline{P}_\epsilon^{ij}, \epsilon) \\
&= G(\tau_0^{ij}, \sigma_\tau^{ij}, \tau) \cdot G(\epsilon_0^{ij}, \sigma_\epsilon^{ij}, \epsilon) \\
&= \frac{1}{\sqrt{2\pi}\sigma_\tau^{ij}} \cdot \exp\left(-\frac{1}{2} \cdot \left(\frac{(\tau - \tau_0^{ij})}{\sigma_\tau^{ij}}\right)^2\right) \cdot \frac{1}{\sqrt{2\pi}\sigma_\epsilon^{ij}} \cdot \exp\left(-\frac{1}{2} \cdot \left(\frac{(\epsilon - \epsilon_0^{ij})}{\sigma_\epsilon^{ij}}\right)^2\right) \\
&=: G_{2D}(\underline{P}_{G,ij}, \tau, \epsilon)
\end{aligned}
\tag{4.16}
$$

the individual parameter vector for each species is given as $\underline{P}_{i,j} = (\tau_0^{ij}, \epsilon_0^{ij}, \sigma_\tau^{ij}, \sigma_\epsilon^{ij})^T$ and thus contains four parameters per Epq-step. Thus, we would have to deal with about 450(!) free parameters at a given E/q step if we tried to fit the responses of all ion species simultaneously. As theoretically required, this number is still lower than the number of information-containing data points which is given by about 10^3-10^4 filled ET-bins for the approximately 50 most relevant-Epq-steps for the solar wind energy range. Yet, due to the large overlap of the ion peaks in the ET-matrices it is in practice impossible to obtain a stable and physically meaningful fit with such a large set of free parameters.

Yet, the parameters $\underline{P}_{i,j}$ are not random, but follow measurement systematic, depending on the ion species properties mass m, charge q and atomic number Z as well as their speed v_{pacc} with which they enter the TOF section and which can be calculated from Eq. 2.9 for every Epq-step. Therefore, the $\underline{P}_{i,j}$ are related to each other both between the ion species and among all Epq-steps, so that we can massively reduce the number of free parameters in the response model fit if we can describe their relations in a proper physical way based on the known instrument characteristics described in chapter 2. In order to understand and finally predict the behavior of the parameters $\underline{P}_{i,j}$ we build-up the full CTOF response model subsequently/consecutively? as it is described in the following sections of this chapter: First, we determine the ion positions in the ET-matrices for all ion peaks at each Epq-step (section 4.4). Second, we determine the peak shapes of all ion species with their already fixed positions (section 4.5). Third, we assess the overall goodness and consistency of the response model by checking its sensitivity to small deviations in peak position and shape (section **??**).

4.4 Characterization of Ion Peak Positions

As the starting point of the CTOF in-flight calibration we show in Figure 4.1 as an example the long-term data ET matrix for Epq-step 55. By combining our knowledge of the CTOF measurement principle from section 2.2.1 with our expectation of elemental
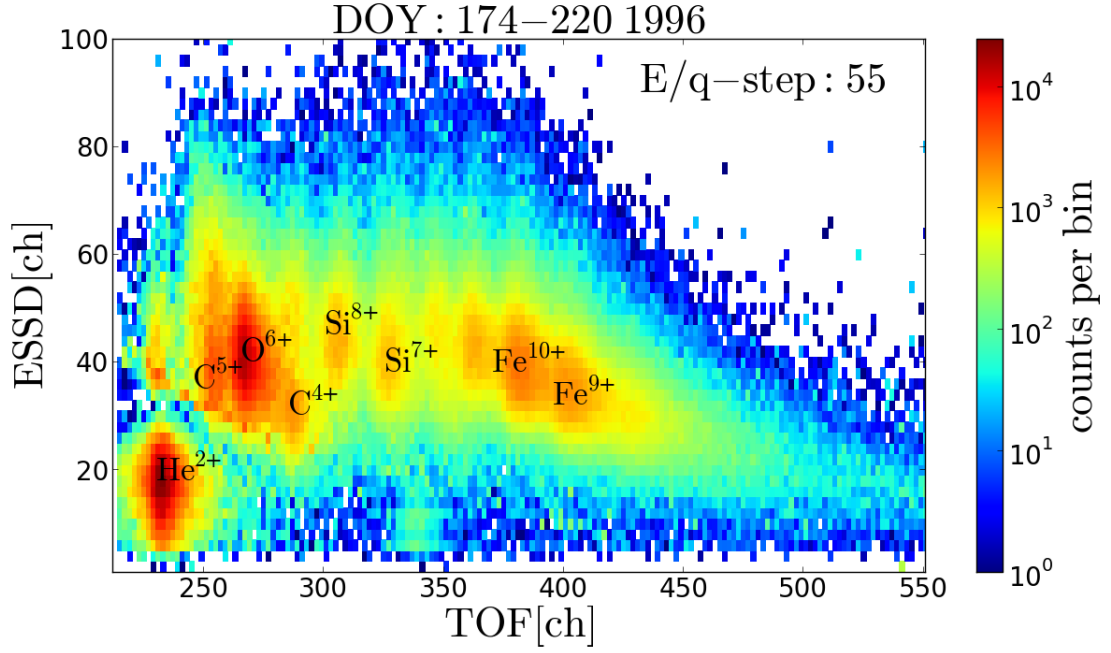
FIGURE 4.1: CTOF ET-matrix at Epq-step 55 for the base-rate corrected long-term PHA data with the accumulated count rate for DOY 174-220 1996. We can clearly identify the peaks of several more abundant ion species such as He^{2+}, C^{4+}, C^{5+}, O^{6+}, Si^{7+}, Si^{8+}, Fe^{8+} - Fe^{11+}, of which are used in the inflight-calibration of the CTOF sensor.

and charge state abundances from section 4.2 we can identify several ion species of the most abundant solar wind elements such as He^{2+}, C^{5+}, Si^{7+} - Si^{9+}, Fe^{8+} - Fe^{11+} which have clear peak signals at this Epq-step. We can also identify the He^+ peak which is the only dominant pick-up ion peak in the triple coincidence data. On a large scale the identified ions seem to be well-ordered with increasing mass-per-charge from low to high TOF channels, following the simplified relation $\tau \propto \sqrt{m/q}$, that we derived in Eq. 2.6. Yet, we already see from the comparison of He^+ and Si^{7+} that the peaks of ion species with the same m/q-value but larger difference in mass are not centered at the same TOF channel. Similarly, when we compare C^{4+} and Si^{9+} we find that the ESSD signal is not proportional to the incident energy at the SSD. Instead the central Si^{9+} ESSD channel is only about 1.6 times higher than the respective ESSD channel of C^{4+}, while one would expect an energy ratio of $m_{Si}/m_C = 2.3$ as both peaks are located at about the same TOF channel. Both observations show the non-negligible presence of the ions' speed- and element-specific energy loss in the carbon foil (α_1) and their pulse height defect in the SSD (α_2), which we discussed theoretically in Eq. 2.8 and 2.9

For a limited range of Epq-steps we can directly determine the position of several predominant ion species by applying 2-dimensional Gaussians as given by Eq. 4.16 as fit-function to these ion peaks. However, due to the unknown dependence of α_1 and α_2 on v and Z it is difficult to extrapolate all ion species positions from the few identified

species at a relatively small number of E/q steps in a consistent way to a much wider set of ion species over the whole Epq-step range. Therefore, we simulated the passage of the ions through the foil and their stopping in the SSD with the TRIM (Transport of Ions in Matter) Monte-Carlo simulation code [Ziegler, Ziegler, Biersack, (1985), (2008)] to obtain a consistent set of ion peak position predictions of the most relevant species for all E/q steps.

Using the TRIM simulation tool a first CTOF ET-matrix position calibration was conducted already by [Janitzek, 2014] for a small set of solar wind ions, following a similar approach by [Taut2014] that was developed for the CTOF double coincidence data in the pick-up ion energy range. In the initial attempt we used seven so-called reference ion species He^{2+}, O^{6+}, Si^{7+}, Si^{8+}, Fe^{8+}, Fe^{9+}, and Fe^{10+} to derive a limited response model that allowed first estimates for the differential speeds of O^{6+}, Si^{7+} and Fe^{8+} - Fe^{10+} which could be then compared to the derived values by [Hefti1998]. The following position calibration builds-up on the former calibration by generalizing the approach to the more comprehensive ion set described in the previous section 4.2 and taking into account the devations in the ET-matrices due to the base-rate correction of the PHA data, that was not considered in the former calibration. For completeness, we first briefly summarize in the next subsection **??** the conducted simulations to derive the ET-positions for the solar wind reference ions, before in subsection 4.4.2 we apply a correction to the obtained positions that follows from the base rate correction and then describe the generalization to the full response model. For further details concerning the conducted TRIM simulations we refer the reader to the original work [Janitzek2014].

4.4.1 Simulated Ion Peak Positions

For the TRIM simulation we took as incident particles the seven aforementioned reference ions He^{2+} - Fe^{10+} at incident energies that correspond to the nominal kinetic energies of the ions at Epq-steps $27 \leq j \leq 73$ after the post-acceleration

$$E_{acc}(q_i, j) = \left[\left(\frac{E}{q} \right)_j + U_{acc} \right] \cdot q_i \qquad (4.17)$$

where we used $U_{acc} = 23.85$ kV as the post-acceleration voltage [Taut 2014]. As the detector geometry is limited in the TRIM simulation package, the carbon foil was represented by a 24 nm thick carbon layer [Taut2014] while the SSD consisted of a 75 nm thick $SiO2$ dead-layer [Oetliker1993, Janitzek2014] stacked on a several micrometer thick sensitive silicon layer in which the ions fully stop. In the latter, only the energy deposit that is transferred to the target electrons and thus can excite them to the conduction band is

taken into account as electronic energy loss that can be measured by the SSD.

It turns out, that when we consider the simulated relative energy loss in the carbon foil α_τ in dependence of the incident energy E_{acc}, that it can be approximated for all elements[2] with the empirical relation

$$\alpha_1^{ij} = \alpha_\tau(E_{acc}(q_i, j)) = \frac{A_i}{B_i \cdot E_{acc}(q_i, j)} + C_i \tag{4.18}$$

where A_i, B_i and C_i are element-specific constants that we obtain from a fit to the simulated values α^{ij} and which are given in Table B.3 in appendix B. The simulated TOF values are then given by

$$\tau_{ij}[\text{ns}] = \sqrt{\frac{m_i \cdot L_\tau^2}{2 \cdot \alpha_\tau^{ij} \cdot E_{acc}(q_i, j)}} \tag{4.19}$$

where $L_\tau = 70.5$ mm is the length of the TOF section as described in section 2.2.1. From the comparison of the simulated TOF values $\tau[\text{ns}]$ with the observed ET-matrix TOF positions $\tau[\text{ch}]$ of the reference ion species we could confirm with a good accuracy of $\Delta\tau = \pm 1$ ch the linear conversion from instrumental channel to the physical time-of-flight that was found by Taut[2014] for the pick-up ion energy range as:

$$\tau[\text{ns}] = A_\tau \cdot \tau[\text{ch}] + B_\tau \tag{4.20}$$

with universal conversion constants $A_\tau = 0.200723$ ns/ch and $B_\tau = -1.46909$ ns that are valid for all reference ion species over all their simulated Epq-steps, respectively. When we now assume that the instrumental dependencies in Eq. 4.18 and Eq. 4.20 hold for all ion species i and all Epq-steps $0 \leq j \leq 116$, we can predict the ion positions in all 117 ET-matrices with the general expression:

$$\tau_{i,j}[\text{ch}] = a_\tau^{-1} \cdot \left(\sqrt{\frac{m_i \cdot L^2}{2 \cdot \alpha_{i,j} \cdot \left[(E/q)_j + U_{acc} \right] \cdot q_i}} - b_\tau \right) \tag{4.21}$$

where m_i and q_i are the ion species' mass and charge.

For the full ion set we simulated the relative relative energy loss for the remaining more abundant elements carbon, nitrogen, neon, magnesium and sulfur so that their constants A_i, B_i, and C_i can also be found in Table B.3. For carbon, neon and magnesium we also compared the observed position of their most abundant charge states C^{4+} - C^{6+} and Ne^{8+}, Mg^{10+} at several Epq-steps in ET with the simulated ion positions and found

---

[2]Note that the charge state of the ion species is only relevant for calculating the incident energy of the particles but does not influence the energy loss in the carbon foil as the ions lose their initial charge state information already within the first layers of the foil [SRIM/TRIM 2008].
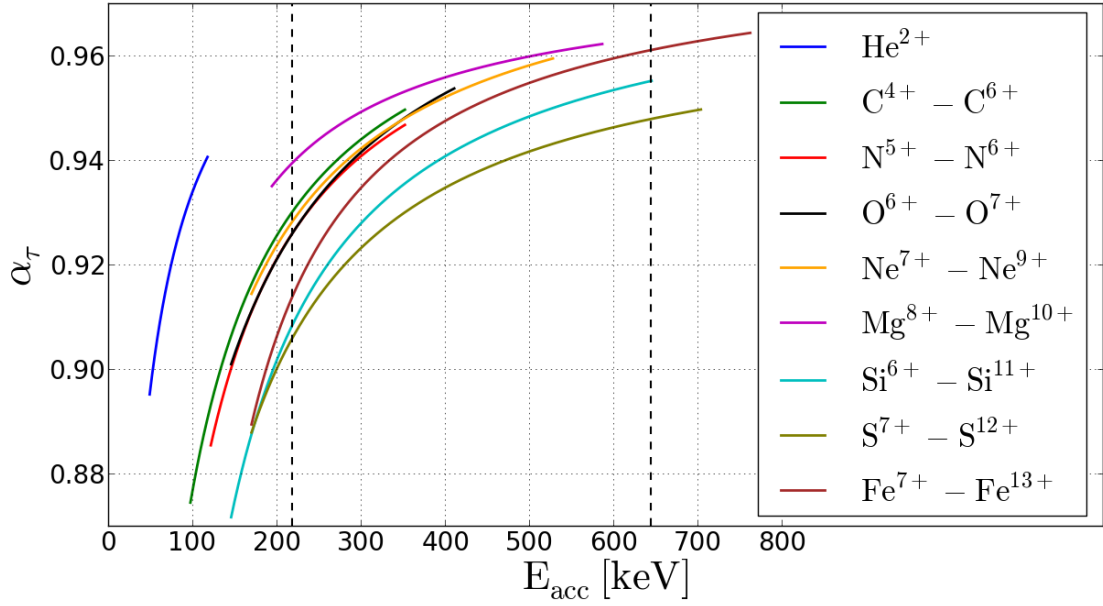
FIGURE 4.2: Simulated remaining energy fraction α_τ for the most abundant solar wind elements helim - iron as a function of their kinetic energy after the post-acceleration E_{acc}. The lower (higher) energy range limit correspond to Epq-step 116 (0) of the lowest (highest) clearly observed charge state in the CTOF data within this work which e.g. for iron is Fe^{7+} (Fe^{13+}). As an example, we also overlaid the energy range for the most abundant calcium species Ca^{9+} - Ca^{11+} for Epq-steps 0-116, as calcium is one of the low-abundance elements for which we approximated α_τ with the iron value $\alpha_{\tau,Fe}$. Note that, the energy ranges are already quite a conservative estimation as the Epq-steps in which the bulk of the solar wind species is measured lies between Epq-step 15 and 90 depending on the m/q-value of the ion species and the solar wind speeds (compare also the long-term ET-matrices in appendix C).

only small deviations of $|\Delta\tau| \leq 2$ ch. Finally, for the remaining least abundant elements sodium, aluminum, argon, calcium, and nickel we just interpolate their TOF positions.

From Figure 4.3 we find that there is no clear systematic in the relative energy loss in the carbon foil α_τ with the element atomic number and the maximum difference between the minor elements ($Z > 2$) at equal energies is about $\Delta\alpha_\tau = 2\%$. Therefore, we approximate the value α_τ for the remaining elements with the energy loss that we obtained from the simulation of iron which is over the whole range of incident energies close to the mean relative loss of all calibrated elements. Consequently we calculate the TOF position of sodium - nickel for all Epq-steps with Eq. 4.21.

Similar to the derivation of the TOF positions we obtained from the comparison of the simulated electronic energy deposit ϵ[eV] in the SSD and the measured residual energy positions ϵ[ch] the pulse height fractions α_ϵ of the reference ion species, together with the linear conversion from ESSD channel to the physical electronic energy loss in the

SSD[Janitzek2014]:

$$\epsilon[\text{keV}] = A_\epsilon \cdot \epsilon[\text{ch}] \qquad (4.22)$$

with the universal conversion constant $A_\epsilon = 0.5098$ keV/ch. By including the additional species C^{5+} in the comparison we found that for all elements heavier than helium the obtained PHF is speed/energy-independent and thus scales only with the atomic number Z, which is in agreement with the SSD pre-flight calibration by [HeftiPHD]. We then interpolated the PHF values of neon and magnesium linearly in Z and found good agreement ($|\Delta\epsilon| \leq 2$ ch) with the observed positions for Ne^{8+} and Mg^{10+}, so that we interpolated the pulse height fractions of the remaining elements (with $2 < Z < 26$) nitrogen, oxygen, sodium, aluminum, sulfur, argon, and calcium in the same way. For nickel ($Z = 28$) we ran an additional simulation that confirmed the extrapolated value of its pulse height fraction which leads to slightly lower predicted ESSD peak positions than iron. All obtained pulse height fractions $\alpha_\epsilon(Z_i)$ for the minor ions are given in Table B.5 in appendix B. With the given pulse height fractions $\alpha_\epsilon^i = \alpha_\epsilon(Z_i)$ and by combining Eq. 2.8 , Eq. 4.20, and Eq. 4.22 we can finally express the ESSD peak position for each ion species i at each Epq-step j in dependence of the previously calculated TOF peak position:

$$\epsilon(\tau_{ij}) = A_\epsilon \cdot \alpha_\epsilon^i \frac{m_i \cdot L_\tau^2}{(A_\tau \cdot \tau_{ij} + B_\tau)^2} \cdot \qquad (4.23)$$

4.4.2 Ion Position Corrections

So far, the calculated values for the TOF and ESSD positions were derived from the PHA data before the base rate correction was conducted. This has the effect that in particular the ESSD position of most ion species is actually over-estimated due to the fact that nearly all species peaks are distributed over at least two priority ranges and thus the respective low-priority range part of the peaks (that lies at lower ESSD channels) is under-represented in count rate in the uncorrected data. We find that this effect is negligible for iron check as the base rate weights are relatively low in PR1 and PR2, but can be clearly observed for carbon, oxygen, neon, magnesium, silicon (i.e. compare Figure **??** in previous chapter **??**). As the deviations are still relatively small (~ 2 ch) compared to the overall measurement range in residual energy the base rate correction does not change fundamentally the observed measurement systematic in the ESSD positions. Thus, we do not conduct a new calibration from scratch, but apply systematic corrections to the calculated positions: For the aforementioned well-observable elements carbon - silicon we shift the former calculated peak ESSD positions to lower channels
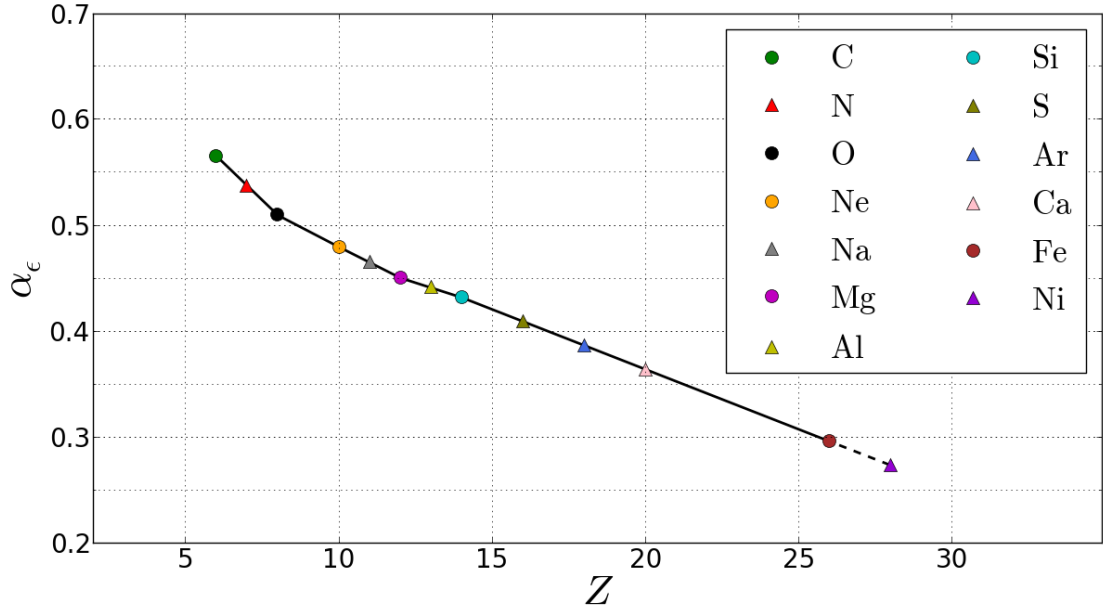
FIGURE 4.3: Calibrated pulse height fractions α_ϵ for all calibrated minor elements ($Z > 2$) in dependende of their atomic number Z. The ESSD position corrections are already included in the phf values so that these are calculated as $\alpha_\epsilon = \alpha_{\epsilon,uncor} \cdot \alpha_{\epsilon,relcor}$ with the derived values $\alpha_{\epsilon,uncor}$, $\alpha_{\epsilon,relcor}$ in Table B.5. For all elements with well-observable ion species peaks (marked with a circle) we find a TOF-independent pulse height defect over the observed TOF range. For all other elements (marked with a triangle), we assumed the same TOF-independence and interpolated α_ϵ as a linear function of its atomic number. For nickel, we extrapolated α_ϵ as its atomic number is still relatively close to iron. For helium we found a TOF-dependent pulse height defect. The corresponding values $\alpha_\epsilon(\tau)$ can be calculated from Eq. B.1 and Table B.4 in the appendix and yield $0.66 < \alpha_\epsilon < 0.91$ for He^{2+} for Epq-steps $0 \leq j \leq 116$.

until we reach a minimum in the χ^2-value that we derive from a fit of the now corrected response model to the count rate data after Eq. 4.15[3]. We apply this procedure consecutively for each element carbon - silicon in the order of decreasing elemental abundance. As the ESSD position after Eq. 4.23 is not explicitly depending on the ion charge q_i or the Epq-step j this correction is automatically applied to all charge states of a given element and at all Epq-steps simultaneously. For helium and iron no correction had to be applied, for all other elements for which the ESSD peak position cannot be observed well with the necessary accuracy (nitrogen, sodium, aluminum, sulfur, argon and nickel) we interpolated the corrections linearly. The correction for carbon might be biased, as the border region of PR5 to PR4 could not be reconstructed properly in the previous chapter. The obtained channel corrections are listed for all mentioned elements in the last column of Table B.5 in the appendix.

---

[3]For this fit we initially use a 2D-Gaussian peak shape as given in Eq. 4.16 with estimated peak widths as in Eq. 4.24 and 4.26 and later the improved peak shape model as in Eq. **??**, but it turns out that the optimal ESSD position calibration is little sensitive to the peak shape.

We also observed small shifts in the TOF position ($\sim$ 2 ch) towards lower TOF channels after the base rate correction which is due to the same former count rate underrepresentation of the low-priority range part of each peak that lies at lower TOF channels. We corrected this effect in the same way as for the ESSD channels, by shifting all ion charge states of a given element towards the new observed positions of its dominant charge states. However, further improvement could be achieved here, as each ion species could be adjusted individually after Eq. 4.21 as long as these shifts are still small compared to the distances among the charge states of each element so that the overall systematical approach is kept. All TOF channel corrections are given in the last column of Table B.3 in the appendix.

In Figure 4.4 we show an example of the calibrated ion positions for the full ion-set response for Epq-step 55 at which a large number of ion species peaks can be directly observed. A comprehensive overview of the calibrated ET-matrices at a wider range of Epq-steps is given in appendix C.

4.5 Characterization of Ion Peak Shapes

In order to assign the measured ion counts to certain ion species, we do not only need the most probable ion species peak position at any given Epq-step but we also need an estimation for the extension of the characteristic peaks in ET space. In a first step, we approximate the ion species peak shapes as 2-dimensional Gaussians $G_{2D}(\underline{P}_{G,ij}, \tau, \epsilon)$ after Eq. 4.16.

4.5.1 The Gaussian Peak (Shape) Model for CTOF

The Gaussian peak approximation has been used for most solar wind heavy ion studies with time-of-flight mass spectrometers, in particular for all studies that used the full Triple Coincidence information to conducted a systematic investigation of a larger solar wind heavy ion set [Berger, vonSteiger on Ulysses, Shearer/Lepri/Zurbuchen?], if not the even simpler box rate schemes were applied similar to [Hefti, etc].

To fully parametrize the Gaussian peak model, one needs to determine the standard standard deviations of the peaks in time-of-flight and residual energy σ_τ and σ_ϵ which for convenience we denote in the following also as the *peak widths*. For the CTOF response model, we obtained a first estimate of the peak widths from the fit of the reference ion species in the previous section 4.4, in which all ion peak parameters $\underline{P}_{G,ij} = (\tau_0^{ij}, \epsilon_0^{ij}, \sigma_\tau^{ij}, \sigma_\epsilon^{ij})$ were treated as free parameters for each ion and each Epq-step, so that we obtained σ_τ and σ_ϵ consistently with the ion positions for a number
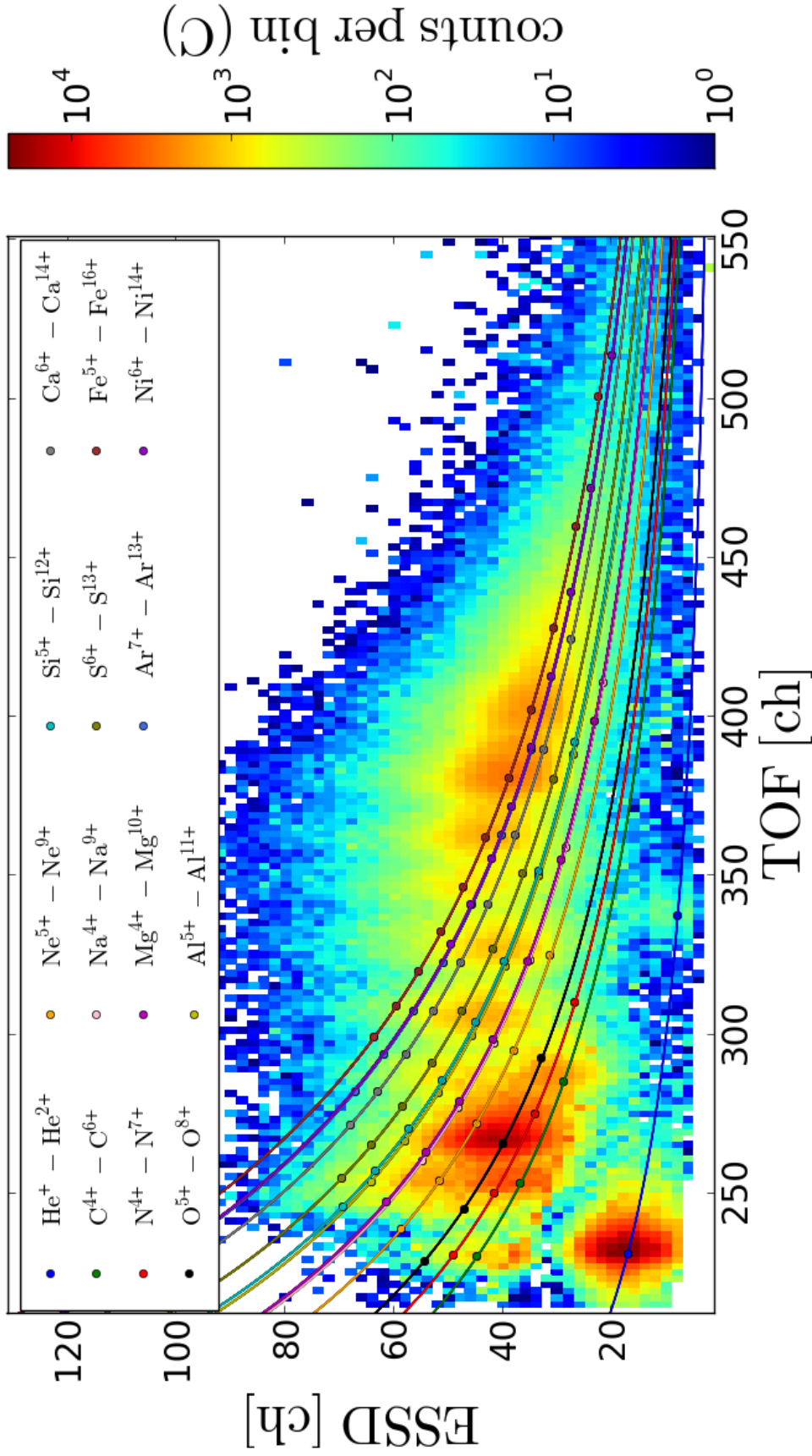
FIGURE 4.4: Calibrated peak positions at Epq-step 55 for the 91 ion species that are included in the CTOF response model after section 4.2. As we can see, the calibrated (step-independent) elemental hyperbola $\epsilon_i(\tau_i)$ yield very similar ESSD positions in particular for the ion peaks of sodium and aluminum in comparison with their more abundant adjacent elements with similar atomic number. Similarly the argon peak position are very close to nickel due to the increasing pulse height defect with increasing Z. Therefore, sodium, aluminum and argon had to be excluded in the speed spectra analysis to obtain stable fit results as it is explained in subsection 4.6.1.

of Epq-steps. As we investigated in [Janitzek,MsC], the determined TOF and ESSD signal widths unfortunately do not fit well the estimated widths by the TRIM simulation. Instead, the simulation rather underestimates the widths by relative values up to about 50% e.g. for iron ions, even if we took into account potential broadening effects such as the velocity acceptance of the CTOF entrance system. Therefore, we cannot make further use of the TRIM simulations for the quantitative description of the peak shapes. On the other hand, we know that the ion species lose their initial charge state information already in the first atomic layers of the carbon foil [SRIM/TRIM and references within] from where on they obtain a (low) equilibrium charge state which only depends on their initial energy E_{acc} and atomic number Z. Thus, in a first approximation all ion species of a given element do not only have the same most probable TOF and ESSD position when they enter with the same energy into the foil but also behave identical in their statistical scattering process, so that we can assume that for each element the widths σ_τ and σ_ϵ for all charge states can be expressed as a universal function of their entrance speed v_{acc} given in Eq. 2.3, or almost equivalently as a function of their measured TOF and ESSD position at any given Epq-step.

In fact, the conducted 2D-Gaussian fits yield that the TOF widths scale in good approximation linearly with the entrance speed of the ion species into the carbon foil at the respective Epq-step [Janitzek,Msc] even regardless of the atomic number Z:

$$\sigma_\tau^{ij} = A_{\sigma_\tau} \cdot v_{acc}^{ij} + B_{\sigma_\tau} \tag{4.24}$$

where $A_{\sigma_\tau} = (0.0040 \pm 0.0002)\,\mathrm{ch}/(\mathrm{km\,s^{-1}})$ and $B_{\sigma_\tau} = (10.3 \pm 0.2)\,\mathrm{ch}$ are in a good approximation universal parameters that are valid for all reference ion species. A similar relation was found by Berger[Phd?] for the Gaussian peak widths of the very similar SWICS instrument onboard the ACE spacecraft, who found a linear relation between the observed TOF positions and TOF widths of the measured ion species for all Epq-steps. The increasing TOF width with decreasing entrance speed (or increasing time-of-flight) can be understood qualitatively due to 1) the increasing TOF resolution with increasing TOF channel and 2) the increasing cross-section for elastic scattering due to collisons with the carbon nuclei in the foil for slower ions. For CTOF it turns out that Eq. 4.24 is also a reasonable approximation for the remaining well-observable ion peaks of carbon, neon, and magnesium so that we use it as the general TOF width parametrization for the Gaussian response model.

For the residual energy measurement, we found from the initial 2-dimensional Gaussian fits of He^{2+}, O^{6+} and Fe^{8+} - Fe^{10+} a similar linear relation between the ESSD ion peak position ϵ_{ij} and the ESSD peak width σ_ϵ^{ij} for each ion species over the respective

Epq-steps:

$$\sigma_\epsilon^{ij} = A_{\sigma_\epsilon} \cdot \epsilon_{i,j} + B_{\sigma_\epsilon} \tag{4.25}$$

where $A_{\sigma_\epsilon} = (0.102 \pm 0.003)$ and $B_{\sigma_\epsilon} = (0.102 \pm 0.003)$ ch are again universal parameters that are valid for most reference ion species simultaneously. Yet, for some ion species such as Si^{7+} and Si^{8+} we obtained from the Gaussian fits considerably larger values for the energy widths. This can be explained by the fact that these ions have a strong overlap in ESSD with the adjacent ion species of S^{8+} and S^{9+}, that have the same (or very similar) mass-per-charge ratios but slightly higher mass. In addition, the respective sulfur charge states are lower but comparable in order of magnitude to the fitted silicon charge states. Furthermore, also other elements such as magnesium and calcium can contribute with their non-negligible charge states such as Mg^{6+}, Mg^{7+} or Ca^{10+} to the appearant silicon peaks, that thus is hard to describe properly along the ESSD axis. In general, we have to state that although the absolute values of the TOF and ESSD standard deviations are comparable, the overall peak resolution is much higher in the TOF measurement as here all ion species are distributed over about 400 channels, while in the ESSD measurement these species are distributed over only 80 channels.

In fact, when we consider the full response model ion species set with, we find that such overlaps occur for many ion species with (potentially) comparable abundances as one can also see from Figure 4.4 so that the initially observed peaks turn out to be over-estimated in many cases. Furthermore, as one can see from Figure 4.30 in the previous chapter the base rate correction further reduces the width of some prominent peaks such as O^{6+}. Therefore, we refine the energy peak widths in a similar manner as the position correction in the previous section: By linearly varying all ion widths simultaneously for several Epq-steps we find that a scaling factor $\sigma_{\epsilon,rel} = 0.85$ multiplied with the initially found σ_ϵ values produces the lowest χ^2 so that the final energy width calibration valid for all ion species i at all Epq-steps j reads

$$\sigma_{\epsilon,cor}^{ij} = \sigma_{\epsilon,rel} \cdot \left(A_{\sigma_\epsilon} \cdot \epsilon_{i,j} + B_{\sigma_\epsilon} \right) . \tag{4.26}$$

4.5.2 A Critical Revision of the Gaussian Peak Shape Model

While the 2D Gaussian peak shape model is a convenient choice for its analytic simplicity, there is no physical reason that the time-of-flight or residual energy signal should follow this shape in detail. To assess the goodness of the model in detail we have a look at several dominant ion species peaks in order to compare the measured peak shape with the fitted 2D Gaussian model. For the comparison we choose He^{2+} and the
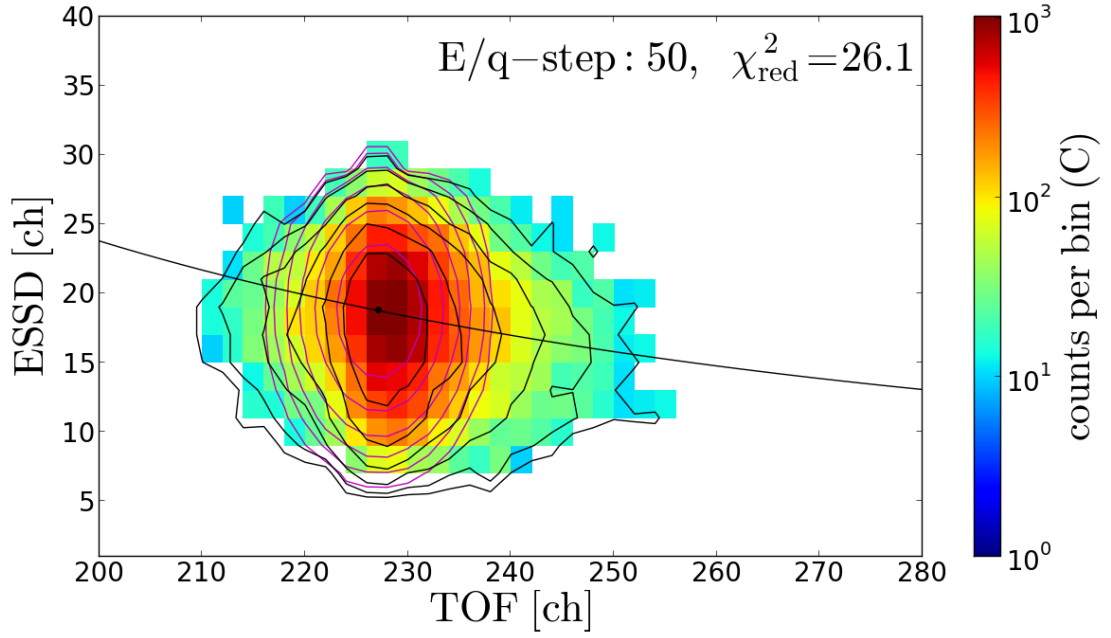
FIGURE 4.5: Fit of the 2D-Gaussian peak model to the measured He^{2+} long-term data peak. The position and width parameters are taken from the calibrated CTOF standard response model as described in the previous subsections 4.4.1 - 4.5.1 and only the count rate is fitted as described in Eq. 4.27. The black and magenta contour lines represent the 50%, 10%, 5%, 1%, 0.5%, 0.1% count rate levels with respect to the data or model maximum, respectively. Only ET-bins with at least 10 actually transmitted PHA counts are considered.
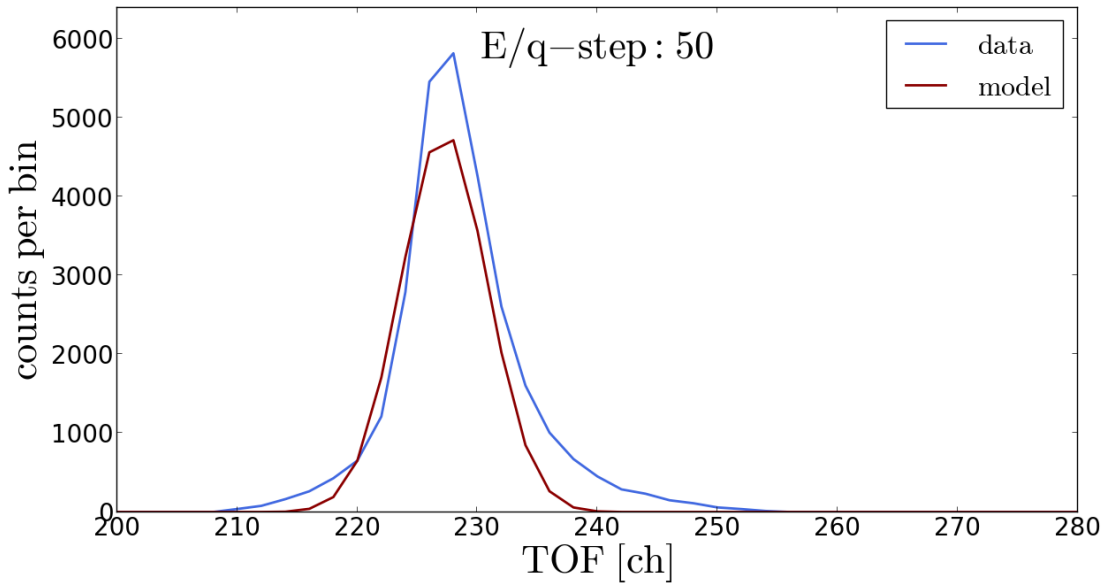
FIGURE 4.6: Comparison of the measured TOF histogram with the energy-channel integrated (= reduced) 2D-Gaussian peak model fit (green line) that is identical as in Figure 4.5.

iron sequence Fe^{7+} - Fe^{11+} which lie at the lower and upper boundary of the measurement range in mass and mass-per-charge. While He^{2+} is well separated from all other ions due to its low mass and mass-per-charge value, the selected iron species have by an order of magnitude higher abundances than the nearby elements calcium and nickel with comparable mass and mass-per-charge, so that the contamination of the main iron peaks due to the latter should be relatively small. Figures 4.5 - 4.8 show the fit of the Gaussian response model to the observed He^{2+} peak in the long-term data[4] accumulated over the full period DOY 174-220 1996 at Epq-step 50. In the fit, the position and widths of the peak are calculated from the response model after equations 4.21, 4.23, 4.24, and 4.26, and only the count rate N is fitted as a free parameter, which is bijectively related to the height of the modeled peak. In Figure 4.5 the measured long-term data counts are visualized in the ET-matrix cut-out by the black contour lines while the fit is represented by the magenta contour lines. Both sets of contour lines represent the 50%, 10%, 5%, 1%, 0.5%, 0.1% count rate levels with respect to the data or model maximum, respectively.

In Figure 4.6, the solid blue line is the measured reduced count rate histogram for the time-of-flight measurement which can be also considered as the count rate integral over all ESSD bins for each TOF bin. It can be compared to the reduced response model which is the integral over the fitted response model over all ESSD bins for each TOF bin. Note that the shown fit (green line) is *not* equal to a (reduced) fit of the TOF measurement alone, since the applied fit-model is the same as in Figure 4.5, defined on the full 2-dimensional ET space, and thus contains the full residual energy information.

In the fit we only include ET-bins $1 \leq k \leq n$ with sufficiently high measured count rate $C_k(\tau, \epsilon) \geq 10$ and each bin contains 2×2 channels in the ET-matrix as described in section 2.2.1. Due to the high counting statistics within the peak in general, the lower count rate limit is only a minor restriction for the determination of the peak shape, but it allows us to assume that the count rate uncertainty in each bin is approximately normally distributed around the measured value. Thus, the merit function to be minimized in the fit has the standard form of Eq. 4.13:

$$\chi^2 = \sum_{k=1}^{n} \left(\frac{(C_k - \widetilde{C_k}(N))^2}{\sigma_k^2} \right) \tag{4.27}$$

---

[4]In the case of He^{2+} the measured peak is almost entirely located in priority range PR5 so that no significant change of the peak shape due to the base rate correction occurs. Instead, due to the problematic reconstruction of the whole priority range PR5, the attempt to correct the count rate is more likely to introduce artificial bias. Therefore, we conduct the peak shape analysis for He^{2+} with the uncorrected count rate data as the accumulated count rate in the long-term PHA data is more than sufficient to assess the shape of the peak adequately.

where n is the number of bins with sufficient count statistics and $\sigma_k = \sqrt{C_k}$[5] is the statistical count rate uncertainty derived from the measured count rate. The goodness-of-fit is then given by the reduced χ^2 which includes the number of contributing ET-bins and free parameters:

$$\chi^2_{red} = \frac{\chi^2}{n - n_p} \, . \tag{4.28}$$

where n_p is in general equal to the number of fitted ion species and therefore in the isolated He^{2+} case we have $n_p = 1$ and $n \approx 200$.

From Figure 4.5 and 4.6 we can see that the measured peak shape shows major deviations compared to the modeled peak shape. To quantify the deviations, in Figure 4.7 we show the fit residuals $\Delta C = C - \widetilde{C}$ in units of the count rate standard deviation, which we call the relative deviation

$$\Delta C_\sigma := \Delta C / \sigma \tag{4.29}$$

and in Figure 4.8 we show the residuals scaled by the measured count rate which we denote as the relative count (rate) difference

$$\Delta C_{rel} := \Delta C / C \tag{4.30}$$

or shorter as the relative residuals. Both quantities ΔC_σ and ΔC_{rel} give us complimentary information and together with the absolute measured count rates C we can identify crucial systematic deviations between data and model that can lead to significant systematic errors in the resulting velocity distribution functions:

As ΔC_σ represents the contributions to the calculated χ^2-value per bin, it allows to estimate how likely it is that the actual measured count rates in a given area of the ET-matrix were sampled from the model. If the count rates are too unlikely to be statistical deviations, we can identify them as local systematic deviations from the model. On the other hand these systematic deviations do not need to cause large systematical errors in the resulting VDFs that we obtain from the total ion count rates N_{ij} over the whole E/q-range (see Eq. 4.30) as the count rates enter in the speed weights both in the enumerator and denominator: $w_{ij} = N_{ij} / \sum_j N_{ij}$. Thus, a large systematic error in the VDF can only occur if at a given Epq-step the measured absolute value N_{ij} is high but also the relative count rate error $\Delta N^{ij}_{rel} = \Delta N_{ij} / N_{ij}$ is large. For the latter the local sum

---

[5]Note, that when the fits are applied to the base-rate corrected PHA count rate, as it is the case for all minor heavy ions ($Z > 2$), the value σ_k has to be calculated as the square-root of the uncorrected count rate scaled with the base rate factor: $\sigma_k = \sqrt{C_{uncor}} \cdot w_{br} \geq \sqrt{C_{cor}}$ where w_{br} are the base rate weights calculated from Eq.? in **??**. This is because we do not actually have the statistics of the base rate corrected count rate in each ET-bin but a scaled uncorrected count rate.
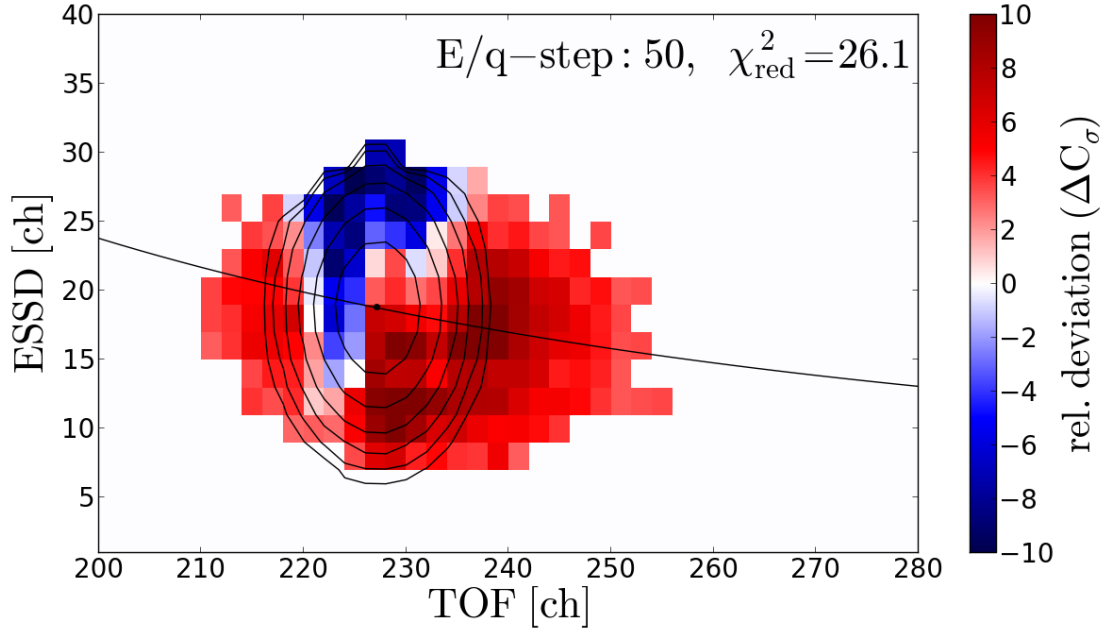
FIGURE 4.7: Relative deviation for the same 2D-Gaussian peak model fit as in Figure 4.5. The overlaid contour lines are the same model count rate levels as in Figure 4.5.
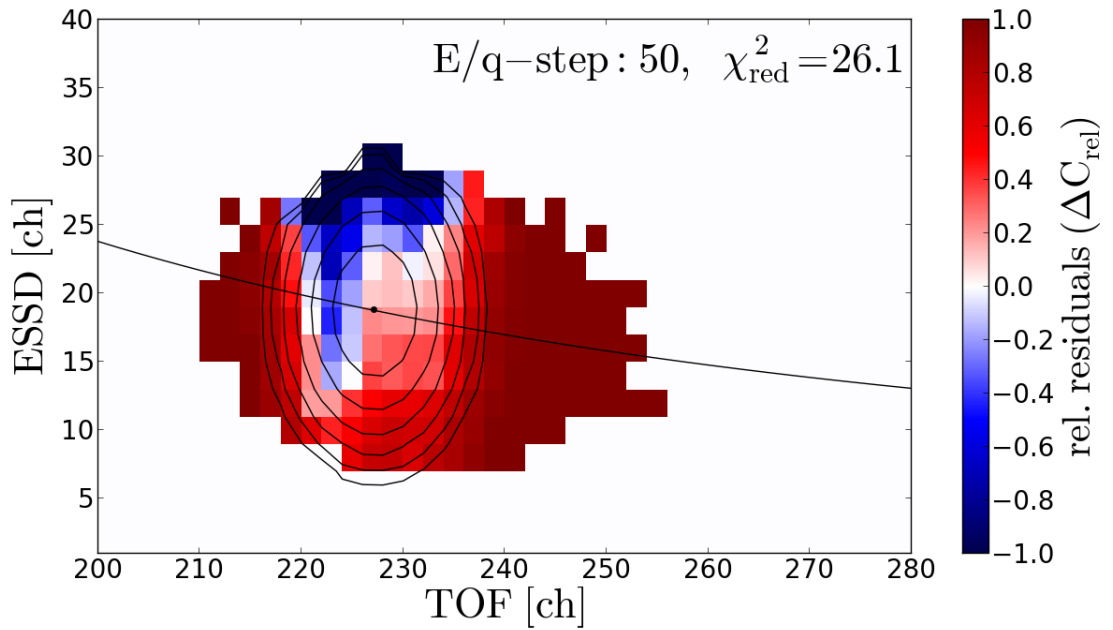

FIGURE 4.8: Relative residuals for the same 2D-Gaussian peak model fit as in Figure 4.5. The overlaid contour lines are the same same model count rate levels as in Figure 4.5.

of the relative deviations $\sum_k \Delta C_{k,rel}$ is an upper estimate[6] of ΔN_{rel}^{ij} for the dominant ion species in a given area of the ET-matrix.

Hence, the analysis of all three quantities C, ΔC_σ and ΔC_{rel} together as shown in Figures 4.5, 4.7 and 4.8 can be used to identify systematic errors in the ion speed determination that arise from systematic errors in the response model. This can be achieved by spotting systematic count rate deviations (large ΔC_σ) in the high-count rate areas of the ET-matrix (large C) that are also large compared to the measured count rate (large ΔC_{rel}) and therefore might eventually sum up to large deviations $\Delta N_{ij}/N_{ij}$ of the measured ion species of interest. Yet, we also note that given large count rates C neither ΔC_σ nor ΔC_{rel} alone is sufficient for a crucial error identification, since the observed deviations (ΔC) can be systematic but negligible for the VDF determination (happens frequently for high count rates per bin), or significant for the VDF determination but not systematic (happens frequently for low count rates per bin), so that they cannot be improved by a better response model.

Analyzing Figures 4.5 - 4.8 in the explained way, we find large systematic deviations between the data and the Gaussian model both in the core and at the flanks of the He^{2+} peak. From the residual plots we find relative deviations up to $\Delta C_\sigma = 10(!)$ σ even at the highest count rates within the 10% model count level. These differences between data and model yield also large relative residuals of the average order of $\Delta C_{rel} = 40\%$ and up to $\Delta C_{rel} = 80\%$ of the count rate in the core. In the flanks of the peak we find that the largest relative deviations occur along the time-of-flight axis where the data peak shows tails which cannot be modeled adequately with the Gaussian model. In particular the pronounced tail at the high-TOF flank is largely underestimated for all energy channels which contributes a to a large part to the overall underestimation of the count rate as we can see from Figure 4.6. On the whole, the assumed Gaussian peak shape model fails to reproduce the actual data resulting in a poor goodness-of-fit estimation of $\chi^2_{red} = 26(!)$ with an overall underestimation in count of about $\Delta N_{rel} \approx 25\%$ when we sum over the whole peak. As these differences are of comparable order in magnitude to the count rate itself, the observed systematic differences in the model can play a role in the calculation of the corresponding VDFs and the accurate determination of the VDF moments if they show a systematic pattern over the Epq-step range. This would be even more the case if the considered ion peak had an adjacent ion species in its high-TOF flank with lower abundance. For this minor species a small percentage of

---

[6]Note that there can be still systematic errors in the model without major deviations between C and $\widetilde{C}$, if one just mixes up the positions of species or add species to the model, that can a priori not occur in the solar wind. To avoid or at least minimize these miss-assignments it is important to apply a systematical calibration approach. Also for ion species that have small count rates N_{ij} compared to the dominant species at the given Epq-step j the relative error can be much larger if for example the whole count rate difference $\sum_k \Delta C_{k,rel}$ is assigned to the low-count rate species i. Therefore, naturally the dominant ion species with the highest abundances are the most reliable ones as only for these species major systematic deviations between model and data can be spotted reliably.
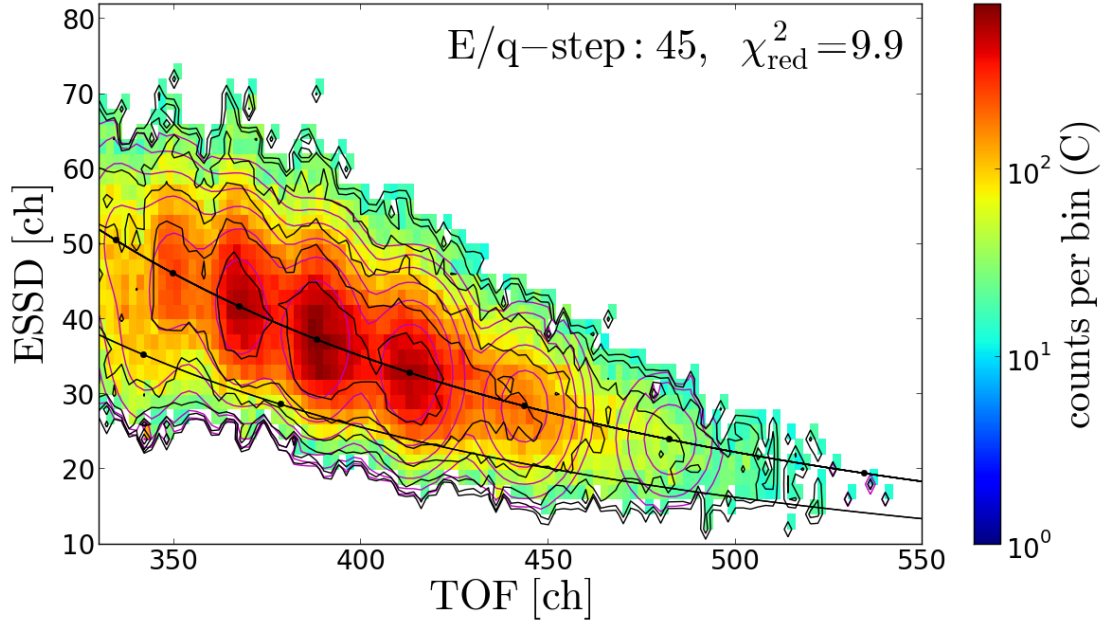
FIGURE 4.9: Fit of the 2D-Gaussian peak model to the measured main iron long-term data peaks Fe^{7+} - Fe^{11+}. In the fit we also include the adjacent species Si^{5+}, Si^{6+}, and Fe^{6+}, Fe^{12+}. The position and width parameters are taken from the calibrated CTOF standard response model as described in the previous subsections 4.4.1 - 4.5.1 and only the nine species count rates are fitted as described in Eq. 4.27. The black and magenta contour lines represent the 50%, 10%, 5%, 1%, 0.5%, 0.1% count rate levels with respect to the data or model maximum, respectively. Only ET-bins with at least actually transmitted PHA counts are considered.

non-assigend counts of the main peak could easily exceed its own absolute count rate and change completely the measured VDF in dependence as a pure effect of the model accuracy. So while the isolated He^{2+} is the best example to study the pure differences between model and data as no other ion species can compensate the observed deviations, it misses the essential point of overlapping peaks that we study in the following example of the iron ion sequence.

The peaks of the aforementioned iron species ions Fe^{7+} - Fe^{11+} have strong overlap among each other and partially also with a few non-negligible silicon charge states. In Figures 4.9 - 4.12 we analyze the applied fit of the Gaussian response model in the same way as for the He^{2+} case. We fit only ET-matrix excerpts which contain in their center the well-resolved ion species Fe^{7+} - Fe^{11+} and include in addition the adjacent species Si^{5+}, Si^{6+}, and Fe^{6+}, Fe^{12+}.

The Figures clearly show that the two-dimensional Gaussian model is over-simplified as the asymmetric data contours barely match the model count contours. From the relative deviations in Figure 4.11 we see that the model underestimates systematically
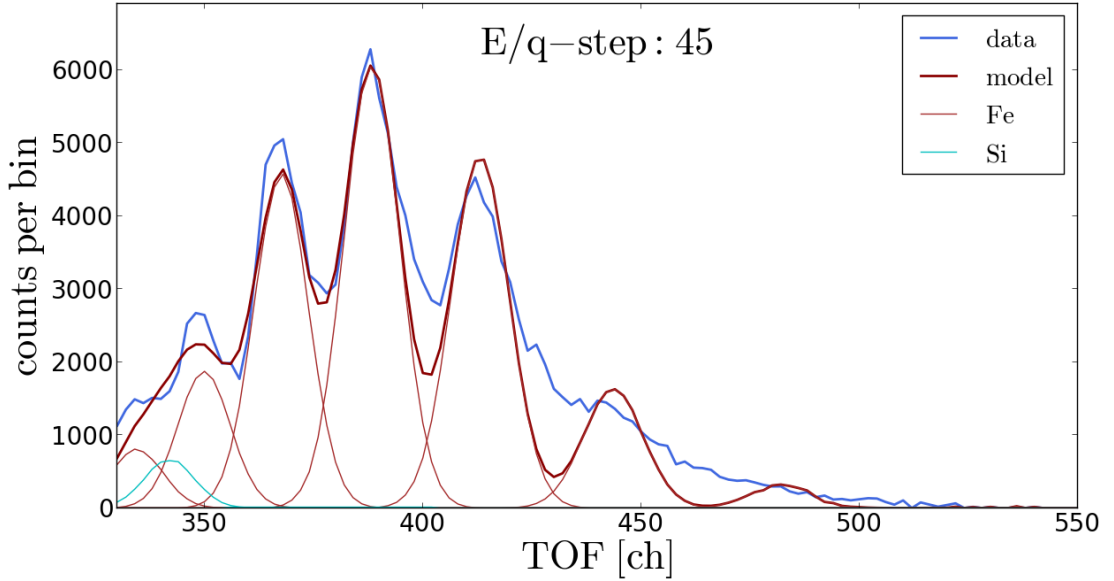
FIGURE 4.10: Comparison of the measured TOF histogram with the energy-channel integrated (= reduced) 2D-Gaussian peak model fit (green line) that is identical as in Figure 4.9. Also the individual species peaks are the energy-integrated peaks of their corresponding 2D-peaks which contribute to the overall model. Thus the area of each individual peak equals the overall count rate of the peak and can be used for count rate comparison between the species at the given Epq-step. The black peaks are Fe^{12+} - Fe^{6+}, and the red peaks are Si^{6+} and Si^{5+} (from left to right, respectively).

the count rate of the time-of-flight channels between the iron peaks while at the peaks center the fit tries to compensate this effect with an overshoot in count rate. These large deviations up to values of $\Delta C_{\sigma} = 9$ lead to a poor goodness-of-fit value $\chi^2_{red} \approx 13$. Figure 4.12 and 4.10 show that the observed systematic deviations are also large compared to the measured count rate and reach values up to $\Delta C_{rel} = 80\%$. Since the absolute measured count rates are high in the described areas of massive model under- and over-estimation the deviations in count rate can in principal cause substantial errors in the resulting velocity distribution functions.

In Figure 4.13 we see that the long-term data fit of the iron sequence cannot be improved substantially by including additional minor ion species from the response model. In fact, the extended model yields relative abundances for Ni^{8+} and Ni^{9+} compared to the most abundant iron charge states Fe^{9+} - Fe^{11+} that are about an order of magnitude larger than expected from remote-sensing studies[Aschwanden] of the photosphere and corona. The counts that are thus (most probably) falsely assigned to nickel and other species are missing in the iron VDFs.

From the detailed analysis of Figures 4.5 - 4.13, we could observe at least one major systematic deviation between model and data that occurred for all investigated ion peaks,
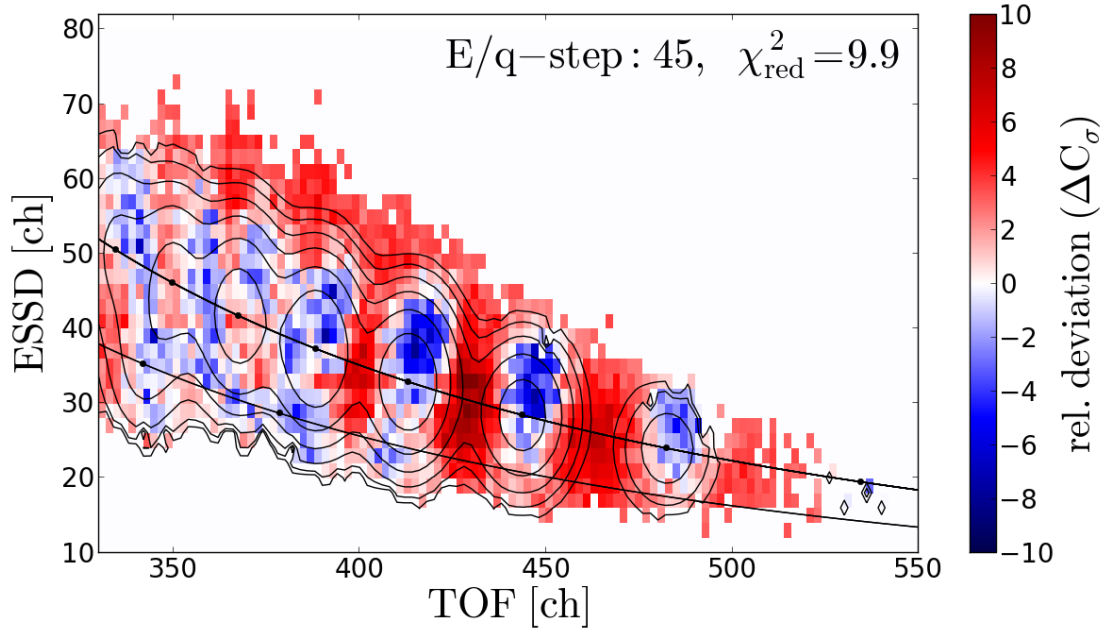
FIGURE 4.11: Relative deviation for the same 2D-Gaussian peak model fit as in Figure 4.9. The overlaid contour lines are the same model count rate levels as in Figure 4.9
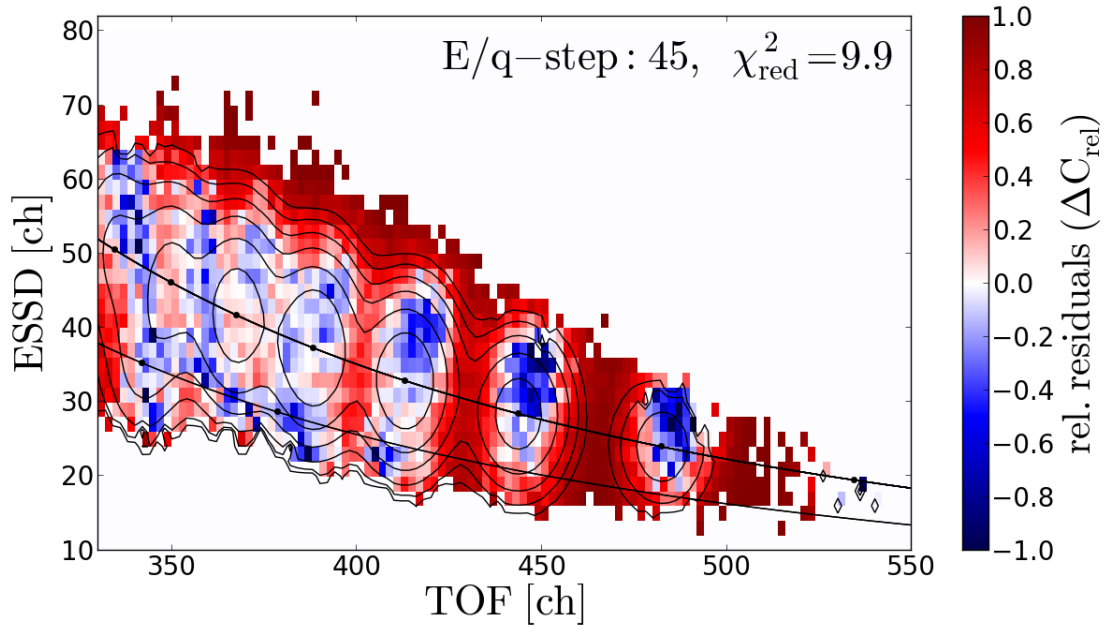

FIGURE 4.12: Relative residuals for the same 2D-Gaussian peak model fit as in Figure 4.9. The overlaid contour lines are the same model count rate levels as in Figure 4.9
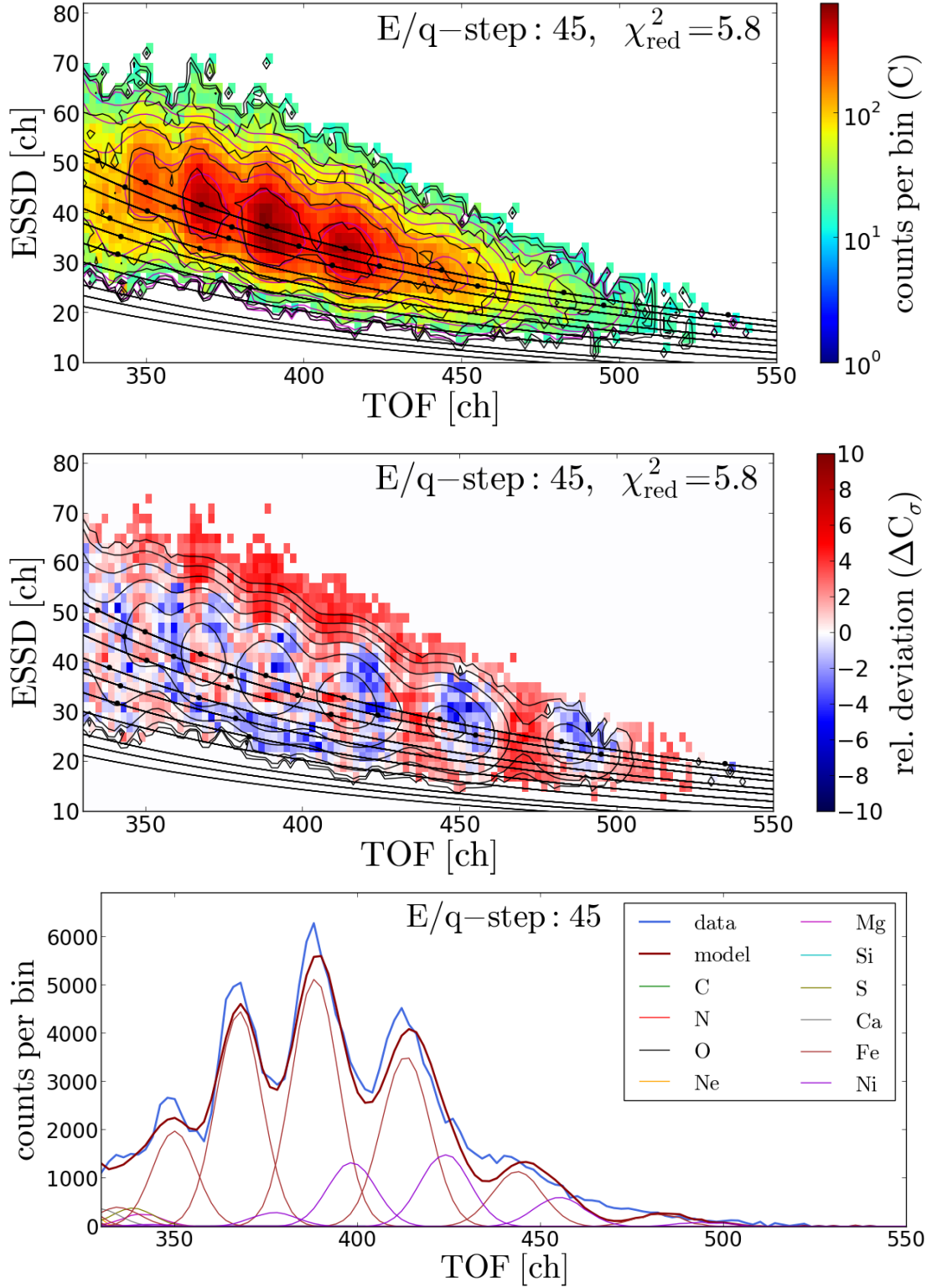
FIGURE 4.13: Fit of the 2D-Gaussian peak model to the measured main iron long-term data peaks Fe^{7+} - Fe^{11+}. In the fit we include all ion species of the listed elements carbon - nickel that lie in the wider vicinity of the iron peaks. The position and width parameters are taken from the calibrated CTOF standard response model as described in the previous subsections 4.4.1 - 4.5.1 and only the species count rates are fitted as described in Eq. 4.27. The three panels are analog to Figures 4.9, 4.11 and 4.10. We omitted the relaitive residuals here for brevity, but a similar comparison is given in Figure 4.30 for the whole ET-matrix at Epq-step 55.

which is the presence of pronounced tails at the high-TOF flank of the peaks. This feature can be seen already for He^{2+} but even more pronounced for all heavy minor ions (compare also O^{6+} in Figure 4.1) and in particular for the investigated iron ions. The formation of high-TOF (or equivalently low-energy) tails can be well-understood in qualitative manner as the result of multiple effects that are inherent to the measurement principle of time-of-flight mass spectrometers based on the carbon-foil technique:

1. The electronic energy loss of an ion event in a thin target such as the foil cannot be described by a Gaussian, but more accurately by a Landau-distribution[Landau1944] that already shows an asymmetrical tail towards low energies.

2. In addition to the electronic energy loss, the ions also lose energy to the target nuclei via elastic collisions. Since the nuclear interactions are more effective for heavier ions at lower energies [SRIM/TRIM] this effect is not negligible at solar wind energies (even after the post-acceleration) and leads to an increased low energy tail for many species.

3. The transformation from the energy loss distribution to time-of-flight is not symmetrical but leads to skewed distribution that appears to have tails at the high TOF-flank due to the increasing time-of-flight resolution per channel with increasing TOF channel.

4. In addition to the energy loss, even the pure scattering in the carbon foil leads to a asymmetrical time-of-flight distribution. This can be easily recognized by the fact that at each Epq-step there is a well-defined minimum time-of-flight for those ions that pass the foil without any scattering, but in principle no upper limit for the time-of-flight exists.

On a quantitative level the situation is complicated and therefore, simulations such as TRIM are commonly used to assess the first, second and fourth point simultaneously. Unfortunately for our of case very low ion speeds compared to most other applications, already the widths of the time-of-flight peaks could not be estimated accurately by TRIM[Janitzek2014] so we cannot assume that the simulation is an accurate quantitative prediction of the peak shape.

Yet, we need to include the observed tails into the response model as we showed that the fraction of potentially assigned counts is not negligible compared to the number of overall counts assigned to many species. In the past, a few empirical approaches were made to describe the observed peak shape of certain ion species more accurately. As an example [Köten,PHD] parametrized the He^{2+} peak shape very accurately with a larger set of empirical parameters in order to use this parametrization for the characterization of the much less abundant C_{13}^{4+} isotope signal. In the case of CTOF [Aellig,PHD]

analyzed the iron data for the period DOY 185-220 1996 by applying an asymmetric Gaussian fit to the TOF measurement with two different σ_τ-values for the low-TOF and high-TOF flank, respectively. While the approach by [Köten,PHD] is not feasible for a response model with a large number of ion species due to the high number of parameters per peak, the asymmetric Gaussian peak shape applied by [Aellig] still yields relatively large deviations from the actual observed peak shape, in particular when a larger part of the iron sequence is fitted simultaneously and the full 2-dimensional ET-information is used. Therefore, we develop in the following section an alternative analytical peak shape model which allows a more accurate description of the observed peak-tails based on a small set of parameters that can be scaled easily for all solar wind ion species.

4.5.3 An Improved Peak Shape Model for CTOF

As the starting point for our model we choose a parametrization of the Moyal function [Moyal1955] to model the high-TOF flank of the observed ion peaks:

$$R^{ij}_{\tau \geq \tau_0} = M^1(\tau_0^{ij}, \sigma_\tau^{ij}, c_\tau^{ij}, \tau) = N \cdot \exp\left[-\frac{1}{2}\left(\frac{(\tau - \tau_0^{ij})}{c^{ij} \cdot \sigma_\tau^{ij}} + \exp\left(-\frac{(\tau - \tau_0^{ij})}{c^{ij} \cdot \sigma_\tau^{ij}} \right) \right) \right] \quad (4.31)$$

where τ_0^{ij} are the TOF position and width-parameter for ion species i at Epq-step j obtained from Eq. 4.21 and 4.24, respectively. To adapt the high-TOF flank of the model to the observed peak tails, R^{ij} includes the additional scaling parameter σ_τ^{ij} that still has to be determined empirically. The normalization $N = e^{-1/2}$ is chosen so that that M^1 reaches its maximum at a value of 1.

For most heavy elements the low TOF-flanks of their well-observable ion peaks show no significant deviations from a Gaussian peak shape (and in fact were even better modeled than with a Moyal function) as we find from the fits of the reference ions O^{6+}, Si^{7+}, Si^{8+} and Fe^{8+} - Fe^{10+}. The only exceptions are the two lightest calibrated elements helium and carbon for which we find small low-TOF tails. These can be well-observed for He^{2+} (as seen in Figure 4.6) and C^{6+}, but not particularly well for He^{+}, C^{4+} and C^{5+} as the pick-up ion species has lower count rates and is disturbed by the SSD energy threshold and the carbon species have major adjacent ion peaks O^{6+} and O^{7+} at their low-TOF flank, respectively. Therefore, we model the low TOF-flank with

the general approach of a Kappa-function:

$$R^{ij}_{\tau \leq \tau_0} = K^1(\tau^{ij}_0, \sigma^{ij}_\tau, \kappa^{ij}_\tau, \tau) = \left[1 + \frac{1}{2\kappa^{ij}_\tau} \left(\frac{\tau^{ij}_0 - \tau}{\sigma^{ij}_\tau} \right)^2 \right]^{-\kappa^{ij}_\tau} \tag{4.32}$$

which becomes a regular Gaussian in the limit of infinitely high κ^{ij}_τ-values:

$$\forall \, \tau^{ij}_0, \sigma^{ij}_0, \tau \in \mathbb{R} : \lim_{\kappa^{ij}_\tau \to \infty} K^1((\tau^{ij}_0, \sigma^{ij}_\tau, \kappa^{ij}_\tau, \tau)) = G1(\tau^{ij}_0, \sigma^{ij}_\tau, \tau) \tag{4.33}$$

where the index 1 just denotes that both functions are already normalized to a maximum value of 1. We find that both for the helium peaks and C^{6+} the observed tails do not change systematically over the observed Epq-steps and can be therefore described with an element-specific constant

$$\kappa^{ij}_\tau = \kappa^i_\tau = \begin{cases} 1.5 & \text{if } Z = 2 \\ 1.8 & \text{if } Z = 6 \\ 10 & \text{if } Z > 6 \end{cases} \tag{4.34}$$

where the value $\kappa_\tau = 10$ is just chosen high enough so that we cannot find any difference between a Gaussian and a Kappa-flank within the given TOF measurement resolution. We admit that in contrast to the well-justified high-TOF flanks we have no secured theory of the instrumental origin of the small low-TOF (or high energy) tails, but one speculation is that these could be channeling effects[7] in the carbon foil, implicating that a small number of the helium and carbon ions can practically penetrate the foil without any interaction. Nevertheless, the low-TOF flank tails are much less pronounced than the high-TOF flanks and do not play a role for the vast majority of measured ion species, so that we do not investigate this point further and also approximated nitrogen with the Gaussian flank as no clear low-TOF flank observations are possible for this element.

With the described functions K^1 and M^1 the new peak shape function in time-of-flight

---

[7]This hypothesis is only based on the observation that the low-tof tails for He^{2+}, and C^{6+} reach down to the minimum possible TOF channels, that we obtain when we just convert their kinetic energies prior to the foil E^{ij}_{acc} into the corresponding TOF channels over the course of the Epq-steps j. Channeling effects are a well-known phenomenon in solid state detectors for which they are studied comprehensively [references]. As helium and carbon are the lightest elements and enter with relatively high entrance speeds they might have also the lowest overall interaction cross-sections in the foil, but the exact calculations are complicated [references] and beyond the scope of this work. Unfortunately, channeling effects are not included in TRIM.

can be written as

$$R_\tau(\tau_0^{ij}, \sigma_\tau^{ij}, \kappa_\tau^{ij}, c_\tau^{ij}, \tau) = \begin{cases} K^1(\tau_0^{ij}, \sigma_\tau^{ij}, \kappa_\tau^{ij}, \tau) & \text{if } \tau \leq \tau_0 \\ M^1(\tau_0^{ij}, \sigma_\tau^{ij}, c_\tau^{ij}, \tau) & \text{if } \tau \geq \tau_0 \end{cases} \quad (4.35)$$

As can be seen from Figures 4.5 and 4.9 the He^{2+} and iron peaks also show a small asymmetry along the residual energy axis but they are skewd in the opposite direction so that we neglect this point for the general model. What we see in both cases is that the tails are not exactly along the TOF axis but the counts seem to be smeared out along the elemental hyperbolae, causing part of the asymmetry along the ESSD axis. This effect can be explained by the fact that both TOF and ESSD measurement are not independent of each other but those particles which lose a larger amount of energy in the carbon foil are measured on average both at higher TOF channels and lower ESSD channels. We can take this effect into account by keeping in principal the Gaussian shape along the energy-axis

$$R_\epsilon(\epsilon_0^{ij}, \sigma_\epsilon^{ij}, \epsilon) = G^1(\epsilon_0^{ij}, \sigma_\epsilon^{ij}, \epsilon) , \quad (4.36)$$

where σ_ϵ^{ij} is given by Eq. 4.26, but substituting the fix energy position ϵ_0^{ij} at each TOF-bin τ with a τ-dependent value by generalizing Eq. 4.23 to[8]. :

$$\epsilon_0(\tau) = A_\epsilon \cdot \alpha_\epsilon^i \frac{m_i \cdot L_\tau^2}{(A_\tau \cdot \tau + B_\tau)^2} \quad (4.37)$$

By expressing the ESSD position as a function of the TOF-bin the energy signal is always normally distributed around the most probable ESSD bin for each TOF bin

$$R_\epsilon(\sigma_\epsilon, \tau, \epsilon) = G^1(\epsilon_0(\tau), \sigma_\epsilon, \epsilon) , \quad (4.38)$$

and the tails of the peak follow the curvature of the elemental hyperbolae given by Eq. 4.23 and shown in Figure 4.4. Thus, the new 2-dimensional *Kappa-Moyal* peak shape model reads:

$$R(\underline{P}_{ij}, \tau, \epsilon) = N \cdot R_\tau(\tau_0^{ij}, \sigma_\tau^{ij}, \kappa_\tau^{ij}, c_\tau^{ij}, \tau) \cdot R_\epsilon(\sigma_\epsilon^{ij}, \tau, \epsilon) =: R_{KM}(\underline{P}_{ij}, \tau, \epsilon) . \quad (4.39)$$

where $\underline{P}_{ij} = [\tau_0^{ij}, \sigma_\tau^{ij}, \kappa_\tau^{ij}, c_\tau^{ij}, \sigma_\epsilon^{ij}]$ is the individual parameter vector for each ion species i at a given Epq-step j that fully determines the individual response function R_{ij}, and N

---

[8]Note that this generalization is only possible because in Eq. 4.23 the ESSD position ϵ_{ij} does not depend explicitely on the Epq-step but is completely defined by the TOF position τ_{ij}.

is a normalization that has to be chosen adequately for each combination (i, j) so that it holds $\sum_{\tau, \epsilon} R_i(\tau, \epsilon) = 1$.

As κ_τ^{ij} is defined in Eq. 4.34 for all species and all other parameters of the new peak shape model are well determined from the standard Gaussian peak shape model, the only remaining problem is to find an adequate parametrization of the tail parameter c_τ. Similar to the peak width parametrization in subsection 4.5.1, we can assume that for a given element all charge states should show the same peak shape when their peak is measured at the same position in the ET matrix. So that we can express c_τ as a function of the TOF position and this function should increase monotonously with increasing TOF position because the tails become more pronounced with decreasing particle energies. As a simple ansatz we chose a linear parametrization over the whole TOF-range of interest:

$$c(\tau) = A_c \cdot \tau \qquad (4.40)$$

with a fixed constant $A_c > 0$ which can be different for each element.

To obtain the optimal tail parametrization for iron we scan the one-dimensional parameter space for A_c by fitting the iron peak sequence with a set the Kappa-Moyal response models $\underline{R}_{KM}(A_C)$ with increasing values A_C and select the A_C value that gives the lowest χ^2_{red} in the minimization after Eq. 4.13. As an additional condition we require that the selceted A_c value has to stay relatively constant over the whole range of Epq-step 39 to 60. In order to neglect contributions from most other ion species we only fitted at each Epq-step excerpts of the ET-matrices which contain in their center the well-resolved ion species Fe^{7+} - Fe^{11+} and include in addition the adjacent species Si^{5+}, Si^{6+}, and Fe^{6+}, Fe^{12+} in the same way as in Figure 4.9. For iron we find an optimal value of $A_c = (0.0040 \pm 0.0010)$ ch^{-1} where we consider the fluctuation of the value over the Epq-step range as the uncertainty. This uncertainty is sufficiently small as it translates into a difference in peak volume of less than 10%, if we consider the change of the iron TOF response function R_τ given in Eq. 4.35 with typical iron peak TOF parameters $\tau_0 = 380$ ch and $\sigma_\tau = 6$ ch. As a lower estimation for the lighter ion species we applied the same approach to the well-separated He^{2+} peak for the Epq-step 40-80 which yields the optimal value of $A_c = 0.0035 \pm 0.0005$ ch^{-1} with a deviation that is even lower than for iron because the flanks of the He^{2+} peak are not contaminated by other species. Unfortunately, the He^+ peak could not be used for a meaningful estimation of A_c because it shows major irregularities in its peak shape (in particular a double peak structure along the ESSD axis for many Epq-steps) as it lies very close to the energy threshold of the SSD. For most other elements such as neon, magnesium
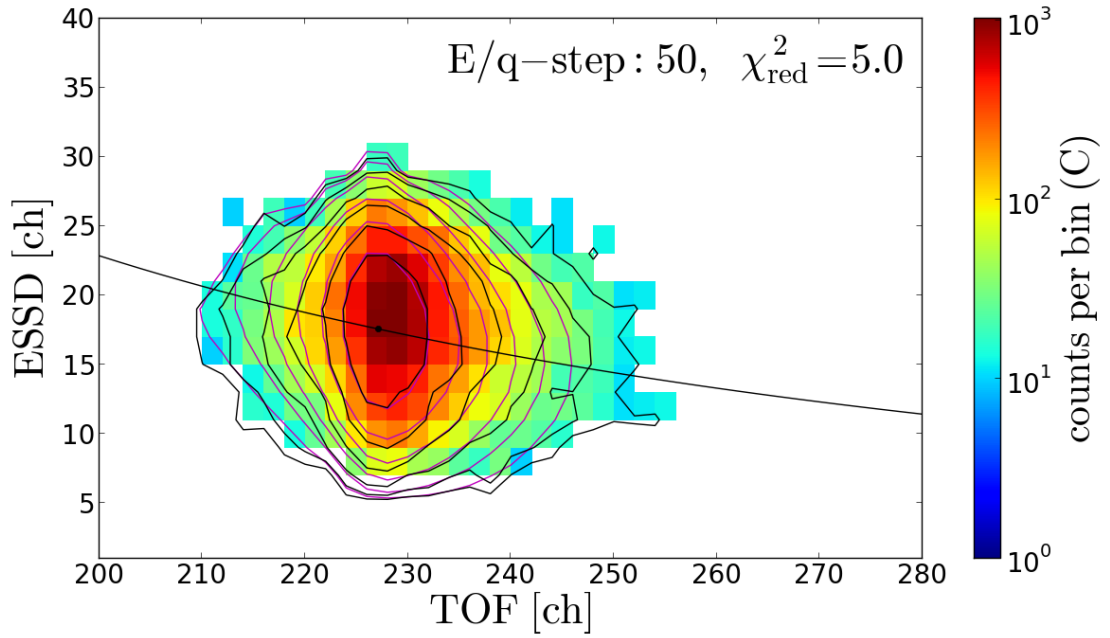
FIGURE 4.14: Fit of the Kappa-Moyal peak model to the measured He^{2+} long-term data peak. The black and magenta contour lines represent the 50%, 10%, 5%, 1%, 0.5%, 0.1% count rate levels with respect to the data or model maximum, respectively. Only ET-bins with at least 10 actually transmitted PHA counts are considered.
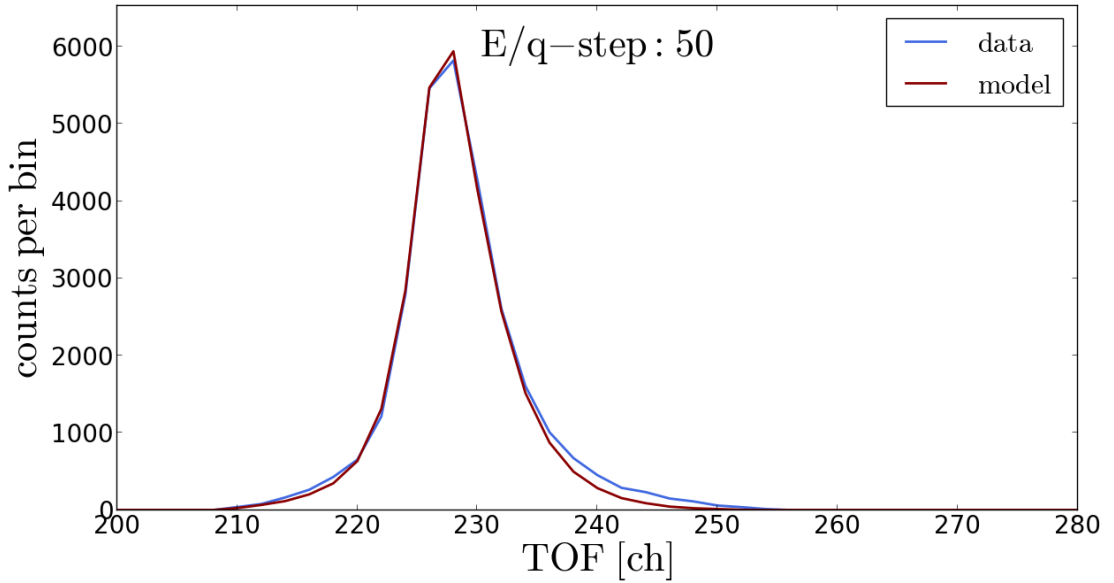

FIGURE 4.15: Comparison of the measured TOF histogram with the energy-channel integrated (= reduced) Kappa-Moyal peak model fit (green line) that is identical as in Figure 4.14.

or silicon a direct estimation of the peak parameter is also problematic as they have less visible tails than iron and significant overlap with their adjacent ion spcies. The only exception is the O^{6+} peak which due to its very high relative abundance allows at least an estimation of the upper limit of the scaling parameter as $A_c \leq 0.0035$, even if there is a contribution of N^{5+} in its high-TOF flank. From these estimations we find that the observed deviation between the A_c-values for different elements is within the uncertainty of the scaling parameter. Hence, we conclude that within the limitations of this strongly simplified model there is actually no significant evidence for an elemental dependence of the scaling parameter so that we obtain the universal value of $A_c = 0.0035 \, \text{ch}^{-1}$ for all elements and thus the high-TOF tails scale only with the TOF position of the peak. This observation is not obvious as one would rather expect an explicit mass dependence of the tails. However, it is phenomenologically similar to the observed behavior of the TOF widths in subsection 4.5.1 that do not show any major dependence on ion mass, either. One way to explain this finding is that the most abundant ion species that dominate the estimation of both parameters σ_τ and A_c are ordered approximately on a diagonal in the ET-matrices, so that it is hard to disentangle the dependencies on mass or atomic number (that scale with ESSD) and time-of-flight with our simple parametrizations. Deeper insides could give here a detailed analysis of the peak shapes of Mg^{10+} and (if the SSD threshold effects can be understood) He^+, as these species are relatively abundant and are the ones which lie most off of this diagonal. Yet, in this work we use the tail scaling parameter A_C for all ion species since He^{2+} and the analyzed iron ions mark the lower and upper limits of the measurement range both in TOF and ESSD and thus the generalization can be considered as interpolation. As the Kappa-Moyal peak shape model is now completely parametrized we can evaluate it in the same way as the Gaussian model. In Figures 4.14 - 4.17 we show the fit of the new peak shape model to the long-term data He^{2+} peak at the same Epq-step 50 as in Figure 4.5. We see from Figure 4.14 that over all the peak is modeled significantly better compared to the Gaussian model in Figure 4.9 as the contour lines match well for all flanks down to the 10% count rate level and partially beyond. We also find that the observed deviations are on average more than a factor of 2 lower for almost all parts of the peak so that we find a goodness-of-fit value $\chi^2_{red} = 4.7$ that is about five times lower than for the Gaussian model. On the other hand this value is still much larger than a value for a truly good model $\chi^2_{red} \gtrsim 1$ and we (still) observe in Figure 4.16 several areas of the data peak that show significant systematic deviations from the model, e.g. at the low-ESSD flank around channels ($\tau = 227 \, \text{ch}, \epsilon = 10 \, \text{ch}$), at the low-ESSD/high-TOF flank around ($\tau = 233 \, \text{ch}, \epsilon = 14 \, \text{ch}$), or further out at the high-TOF flank for all ET-bins with $\tau > 240 \, \text{ch}$. Hence, the measured count rate data on the whole is still very
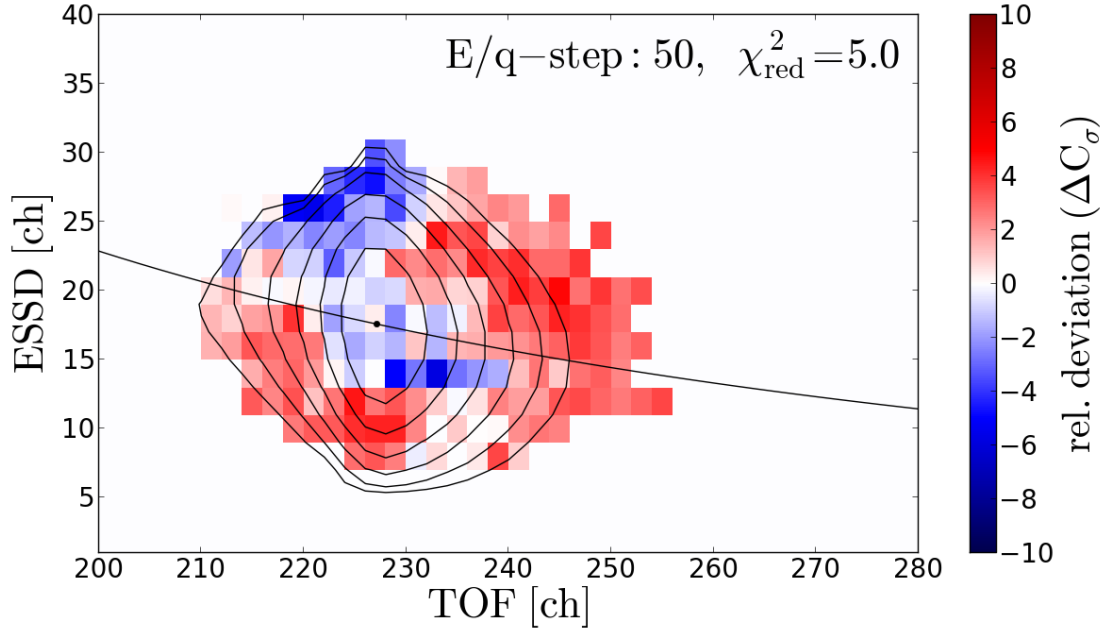
FIGURE 4.16: Relative deviation for the same Kappa-Moyal peak model fit as in Figure 4.5. The overlaid contour lines are the same model count rate levels as in Figure 4.14.
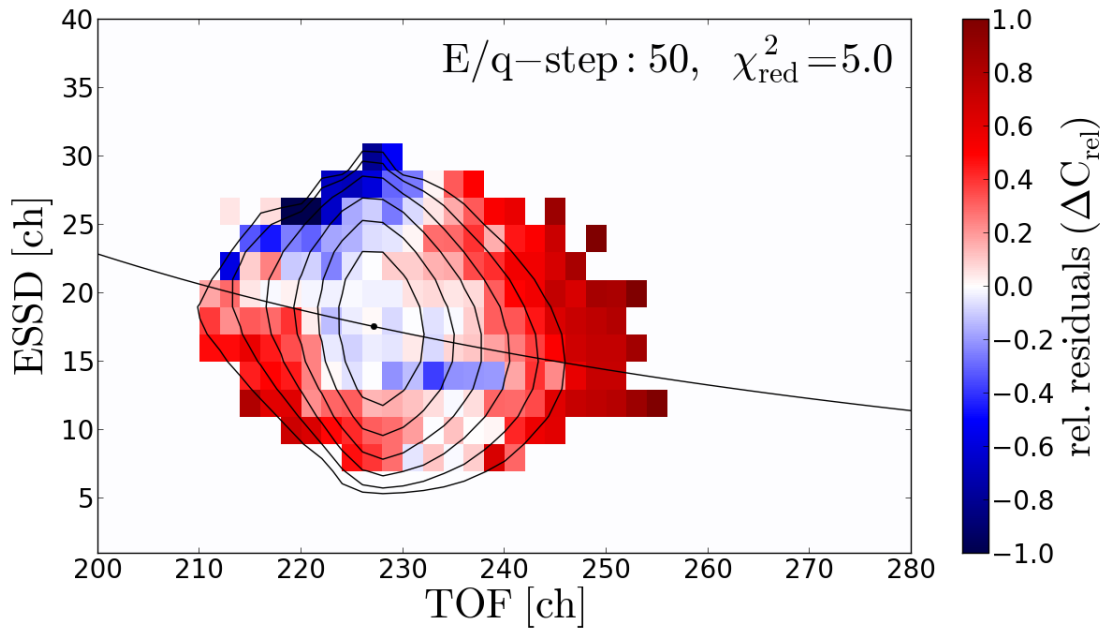

FIGURE 4.17: Relative residuals for the same Kappa-Moyal peak model fit as in Figure 4.5. The overlaid contour lines are the same same model count rate levels as in Figure 4.14.
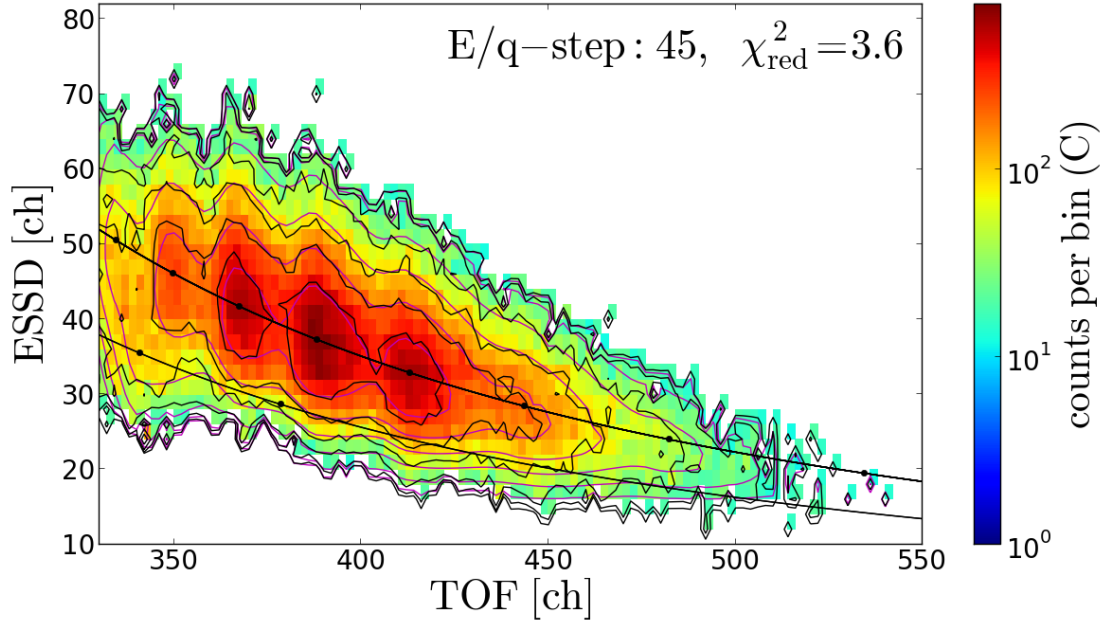
FIGURE 4.18: Fit of the Kappa-Moyal peak model to the measured main iron long-term data peaks Fe^{7+} - Fe^{11+}. In the fit we also include the adjacent species Si^{5+}, Si^{6+}, and Fe^{6+}, Fe^{12+}. The black and magenta contour lines represent the 50%, 10%, 5%, 1%, 0.5%, 0.1% count rate levels with respect to the data or model maximum, respectively. Only ET-bins with at least 10 actually transmitted PHA counts are considered.

unlikely to be sampled from the exact model peak shape. This is not so surprising as we cannot really model the peak shape from first principles as discussed in the previous subsection, but rather made the approach of a simple and scalable model that should just catch the main systematic deviations. Therefore, following our analysis in the previous subsection 4.5.2 we now have a look at the relative count rate differences in Figure 4.17 in order to estimate how strongly the observed systematic deviations can affect the overall count rate. We find that in the area within the 10% count rate contour level which contains about 90% of the total peak count rate, there is only one ET-bin that is more than 30% off the model value and the average deviation is now about 10% of the count rate for all of these ET-bins. Large deviations on the order of the count rate $\gtrsim$ 50% can be found only around and beyond the 1% model count rate contour level. This yields that the possible count rate deviations are on the order of a 10% effect. If these deviations show a systematic increase or decrease with the Epq-step (which is the worst case scenario) their impact is comparable to the (small) effect that speed dependent detection efficiencies can have on the measured VDFs and their moments (see subsection 4.6.4.

We continue the Kappa-Moyal peak model evaluation with the iron sequence Fe^{7+} - Fe^{11+}. In Figures 4.18 - 4.22 the individual ion response functions have the form of the
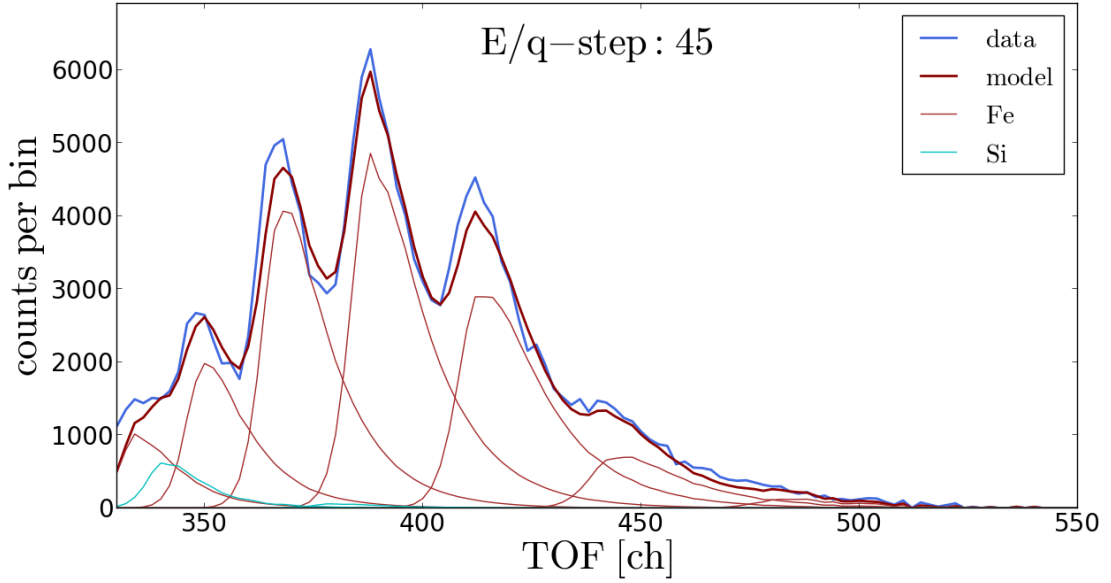
FIGURE 4.19: Comparison of the measured TOF histogram with the energy-channel integrated (= reduced) Kappa-Moyal peak model fit (green line) that is identical as in Figure 4.18. Also the individual species peaks are the energy-integrated peaks of their corresponding 2D-peaks which contribute to the overall model. Thus the area of each individual peak equals the overall count rate of the peak and can be used for count rate comparison between the species at the given Epq-step. The black peaks are Fe^{12+} - Fe^{6+}, and the red peaks are Si^{6+} and Si^{5+} (from left to right, respectively).

new peak shape model with the only exception that along the energy axis we used a Gaussian with two different width parameters $\sigma_{\epsilon,up}$, $\sigma_{\epsilon,low}$[9] for R_ϵ instead of the regular Gaussian G_ϵ to model better the high energy flank of iron. The exact modeling of the upper energy flank is possible since there are no elements of comparable abundance expected that lie at higher energy channels than iron. For R_τ we use the exact expression as in Eq. 4.35 with the universal tail scaling parameter $A_c = 0.035$ ch^{-1}. In the fit we included the same ET matrix excerpt as for the Gaussian peak model with the same ion species Si^{5+}, Si^{6+} and Fe^{5+} - Fe^{12+}.

Similar to the He^{2+} case, we find that the Kappa-Moyal peak model reflects better the observed shape of the iron ion peaks, so that the observed gaps and overshoots of the model along the TOF axis are not present anymore and the vast majority of ET-bins within the 10% count-level area shows a relative deviation of less than 3σ. As can be seen from Figure 4.21 also the relative count rate difference within this area shows little fluctuation so that it rarely exceeds a value of 0.2 and has an average value even below 0.1. This is a good indicator that also the count contributions among the iron ion species are modeled consistently. The only part of the fitted ET-matrix excerpt where

---

[9]The ESSD-position dependent scaling for $\sigma_{\epsilon,up}$, $\sigma_{\epsilon,low}$ is given in Eq. B.3 - B.5 in the appendix.
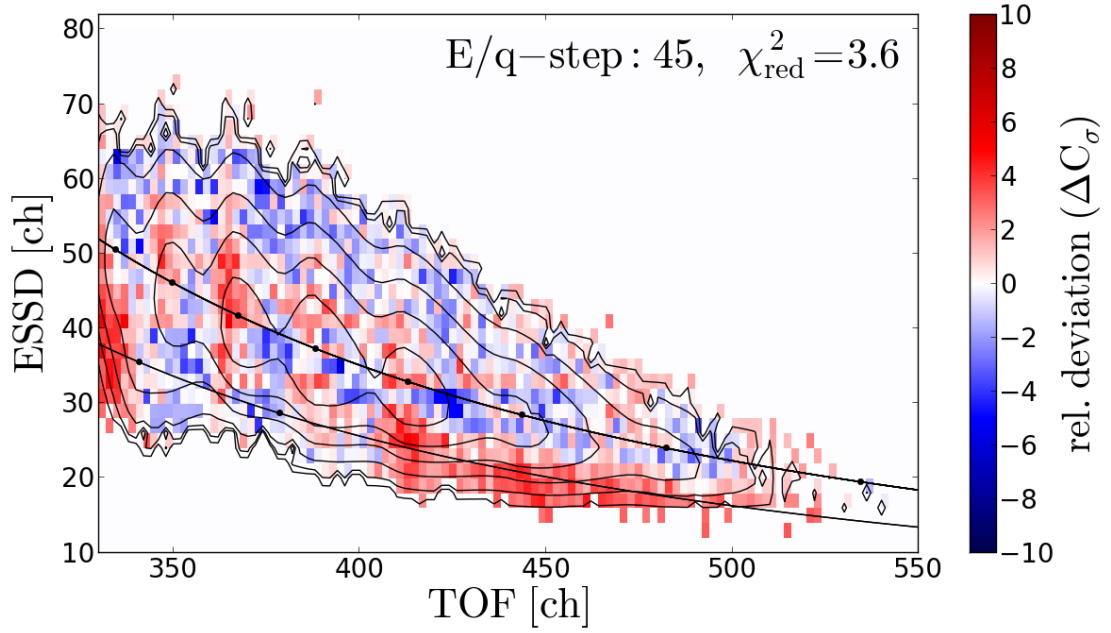
FIGURE 4.20: Relative deviation for the same Kappa-Moyal peak model fit as in Figure 4.18. The overlaid contour lines are the same model count rate levels as in Figure 4.18.
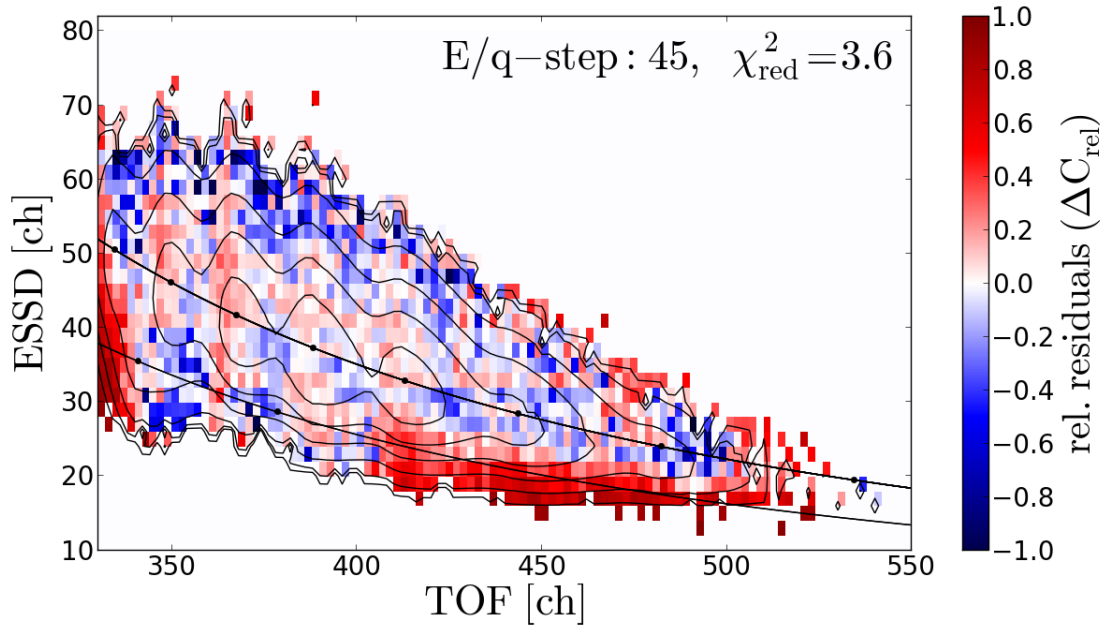

FIGURE 4.21: Relative residuals for the same Kappa-Moyal peak model fit as in Figure 4.18. The overlaid contour lines are the same model count rate levels as in Figure 4.18.

the model deviates stronger from the data is in the area $\tau \geq 410\,\text{ch}$ and $\epsilon \approx 20\,\text{ch}$ where the model underestimates the lower energy flanks of Fe^{7+} and Fe^{8+}. However, this part of the ET matrix is also contaminated by helium random coincidences that we discuss in subsection 4.6.3, so that this is not necessarily a problem of the peak shape model itself. The overall goodness-of-fit value is calculated as $\chi^2 = 2.9$ and is therefore more than four times lower as for the Gaussian peak shape model.

When we compare Figure 4.19 with Figure 4.10 we find that the iron ions' count rate contributions to each of the observed peaks are modified due to the asymmetric tails. Each ion peak gives a substantial contribution to the peak at its high-TOF flank, so that the formerly observed gaps between the peaks are closed and a smooth tail at very high-TOF channels is formed with contributions from several ion species. This also means that the count rate of the ion species that are on the high-TOF flank of a larger peak tend to lose systematically in count rate while those at the low-TOF flank tend to gain counts in comparison to the Gaussian fit. In the demonstrated case in the given Epq-step this is seen best for Fe^{12+} which was most under-estimated by the Gaussian model while Fe^{7+} was most over-estimated. Furthermore, we can see from Figure 4.22 where we included the same additional ion species as in Figure 4.13 that the count rates of Ni^{8+} and Ni^{9+} have decreased dramatically compared to the Gaussian model fit and all nickel charge states are now on the order of 1-10% compared to the most abundant iron charge states. This is in good agreement with the coronal abundance ratio of 5%[Aschwanden] between iron and nickel that is found from remote-sensing data. However, we also would expect the calcium peaks at a comparable count rate level with nickel, but Ca^{6+} still shows a higher count rate even if it is considerably lower than those of nickel in Figure 4.13. This shows that also the improved peak model has its limitations, but we recall that nickel and calcium are among the elements with the lowest relative abundances in the model so that naturally we have to regard their count rates with caution. Before we present the measured speed distributions in the next chapters we give a short summary of the full improved response model, discuss the overall model sensitivity to small deviations in the calibration and have a look at the instrumental background that mainly consists of random coincidences of the most abundant ion species.
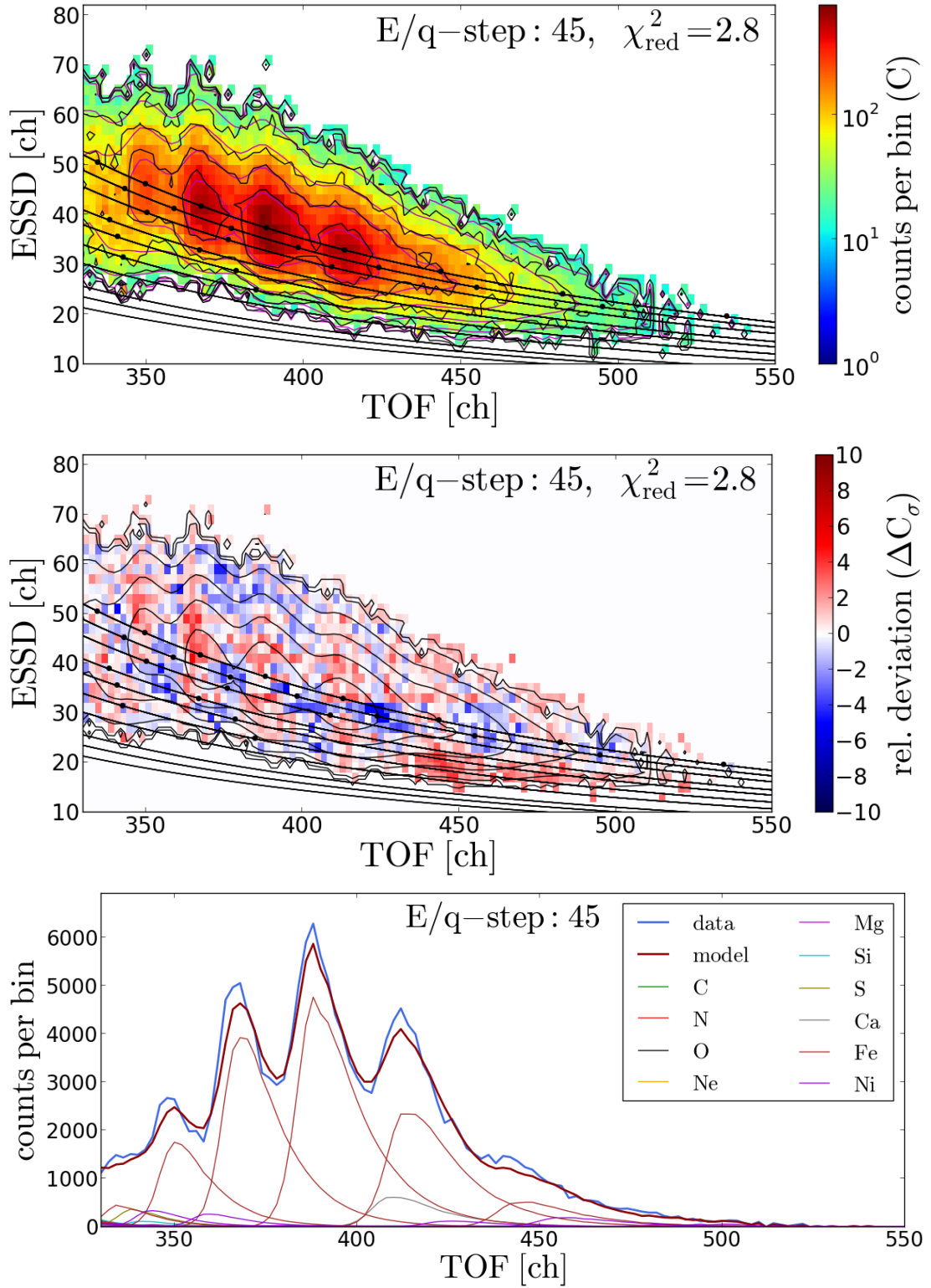
FIGURE 4.22: Fit of the Kappa-Moyal peak model to the measured main iron long-term data peaks Fe^{7+} - Fe^{11+}. In the fit we include all ion species of the listed elements carbon - nickel that lie in the wider vicinity of the iron peaks. The three panels are analog to Figures 4.18, 4.20 and 4.19. We omitted the relaitive residuals here for brevity, but a similar comparison is given in Figure 4.30 for the whole ET-matrix at Epq-step 55.

4.6 The Full CTOF Response Model

Summarizing the previous sections of this chapter, the full CTOF response model contains the individual ion responses of 91 ion species of the 14 most abundant heavy solar wind elements helium, carbon, nitrogen, oxygen, neon, sodium, magnesium, aluminum, silicon, sulfur, argon, calcium, iron and nickel. All included ion species are given in the second? column of Table 4.1. For the individual response functions $R_{i,j}(\tau,\epsilon)$, that model the observed ion peaks in the ET-matrices for every calibrated species $i \in \{1,2,...,91\}$ at every Epq-step $0 \leq j \leq 116$, two general models R are available: The standard 2D-Gaussian peak model R_G and the improved Kappa-Moyal peak model R_{KM}. The 2D-Gaussian peak model is defined in analogy to the existing response models of ACE/SWICS (BergerPHD) and Ulysses/SWICS(KötenPhD) in Eq. 4.16 with the individual peak model parameter vector for each species $\underline{P}_G^{i,j} = (\tau_0^{ij}, \epsilon_0^{ij}, \sigma_\tau^{ij}, \sigma_\epsilon^{ij})^T$ where the peak TOF τ_0^{ij} and ESSD positions ϵ_0^{ij} can be obtained from Eq. 4.21 and Eq. 4.23, respectively, and the width parameters σ_τ^{ij} and σ_ϵ^{ij} are given by Eq. 4.24 and Eq. 4.26, respectively. The new Kappa-Moyal peak model is defined in Eq. 4.39 with the peak model parameter vector for each species $\underline{P}_{KM}^{i,j} = (\tau_0^{ij}, \epsilon_0^{ij}, \sigma_\tau^{ij}, \kappa_\tau^{ij}, c_\tau^{ij}, \sigma_\epsilon^{ij})^T$ where the additional peak parameters κ_τ^{ij} and c_τ^{ij} can be obtained from Eq. 4.34 and Eq. 4.40, respectively. For iron an even more accurate parametrization of the ESSD peak shape could be obtained and is included in the Kappa-Moyal model that contains separate parametrizations of the lower and upper ESSD peak flank as given in Eq. B.3 with two width parameters $\sigma_{\epsilon,up}$ and $\sigma_{\epsilon,low}$ that can be calculated from Eq. B.4 and Eq. B.5 in the appendix.

4.6.1 The Full and Reduced Response Model

In order to derive the most consistent Velocity Distribution Functions from the data it would be ideal to fit the full calibrated response model $\underline{R}_{ij}(\tau,\epsilon)$ to the respective ET-matrix count rates $C_j(\tau,\epsilon)$ after Eq. 5.2. However, when including all calibrated ion species it turns out that frequently the fit does not converge (numerically / to the desired accuracy) with any of the applied minimization algorithms. The reason is that some ion species have very similar positions in the ET-matrices due their very similar mass and mass-per-charge values as can be seen from Figure 4.4. This causes in combination with the limited counting statistics of the investigated data subsamples (i.e. restricted solar wind proton speed or restricted time periods) that the fit is underdetermined in parts of the ET-matrix due to the large overlap of such peaks. This problem even occurs in the long-term data speed spectra analysis, where we investigate the accumulated counts over the whole measurement period DOY 150-220 1996 but filtered

Included Element:	Full Calibrated Model	Full Stable Model	Red. Stable Model
Criterion: $A_{Z,rel} > 10^{-6} \cdot A_H$	Criterion: $A_{q,rel} > 10^{-3}$	Crit: Overall Fit Convergence	Crit: Elem. Overlap & $A_{q,rel} > 10^{-2}$
Helium*	He^+, He^{2+}	-	-
Carbon	C^{4+} - C^{6+}	C^{4+} - C^{6+}	C^{4+} - C^{6+}
Nitrogen	N^{4+} - N^{7+}	N^{4+} - N^{7+}	-
Oxygen	O^{5+} - O^{8+}	O^{5+} - O^{8+}	O^{6+}, O^{7+}
Neon	Ne^{5+} - Ne^{9+}	Ne^{5+} - Ne^{9+}	Ne^{6+} - Ne^{8+}
Sodium	Na^{4+} - Na^{9+}	-	-
Magnesium	Mg^{4+} - Mg^{10+}	Mg^{4+} - Mg^{10+}	-
Aluminum	Al^{5+} - Al^{11+}	-	-
Silicon	Si^{5+} - Si^{12+}	Si^{5+} - Si^{12+}	Si^{5+} - Si^{12+}
Sulfur	S^{6+} - S^{13+}	S^{6+} - S^{13+}	-
Argon	Ar^{7+} - Ar^{13+}	-	-
Calcium	Ca^{6+} - Ca^{14+}	Ca^{6+} - Ca^{14+}	-
Iron	Fe^{5+} - Fe^{16+}	Fe^{5+} - Fe^{16+}	Fe^{5+} - Fe^{16+}
Nickel	Ni^{6+} - Ni^{14+}	Ni^{6+} - Ni^{14+}	-

TABLE 4.1: *: Helium is not in the applied models because we have to exclude priority range PR5 because of the onboard PID suppresion that does not allow a base rate reconstruction for PR5. check number of included ions in the applied models!

for a very narrow proton speed interval (see section **??**). Therefore, we systematically exclude those elements from the fitted response model that have the lowest abundances and their ion species have very similar ion positions to their adjacent more abundant ion species. We thus exclude for the systematic speed measurements all ion species of the elements sodium, aluminum, and argon, for which it would be anyways hard to resolve their speed distributions due to their expected low count rates[10]. It is clear that this artificial change of the response model might influence the count rates of adjacent ion species that have higher but still comparable abundances as the excluded species. Yet, for the most relevant species that have at least an order of magnitude higher count rates this effect is negligible because the resulting local count rate deviations are below the typical response model accuracy (see section 4.5).

Finally, we also have to exclude the priority range PR5 from our analysis as we cannot reconstruct properly the count rates in this area of the ET-matrix as explaind in section ?. This is necessary as we can see from Figure ? that the border region of PR5 to PR4 is systematically over-estimated in count rate after the base-rate correction and this could cause systematic bias of certain ion species such as the carbon species that partly lie in this area. On the other hand, when we exclude PR5 completely we only lose a fraction of a few percent in count rate for C^{4+} and C^{5+} as can be seen from Figures ? - ? in the appendix. Since He^{2+} cannot be included in the analysis anayways

---

[10]Compare the speed spectra for calcium and nickel in section 6.?.

due to the PID onboard suppression and practically all He$^+$ counts can be considered as pick-up ions [Arnaud and Rothenflug] the exclusion of PR5 is not a major restriction for the overall systematic speed analyisis. After the response model reduction, the largest set of ion species that allows a numerically stable fit for all Epq-steps in the long-term data contains 69 ion species which are given in the third colum of Table 4.1. Thus the corresponding response model that we call in the following the *Full Stable Model* (FSM) for CTOF includes the ten remaining elements carbon, nitrogen, oxygen, neon, magnesium, silicon, sulfur, calcium, iron and nickel with all their charge states that we selected in section 4.2.

While the FSM leads to an overall fit convergence for the analysis of the long-term CTOF data both in the slow and in the fast wind, it turns out that for the fast wind case where we have a much lower number of measurement cycles available, many ion species even among the most abundant ones show large count rate fluctuations in their count rate spectra over all Epq-steps due to the (already) low counting statistics and their (still) large peak overlap with adjacent ion species (see section 6.?). Therefore, we conduct complimentary fits with a Reduced Stable Model (RSM) to further analyze the count rate spectra of the most abundant ion species under the assumption that their less abundant neighbor species can be neglected (see section ?). In the RSM we only include the five best-resolved elements (except for helium): carbon, oxygen, neon, silicon and iron with their most abundant ion species that have an expected relative charge states abundance of at least 10^{-2}. In this way we obtain 28 ion species for the RSM which are given in the last column of Table 4.1. We also use the RSM for the CTOF short term-data analysis in chapter 6 both in the slow wind and fast wind case as for the short term data analysis we naturally have to deal with very low counting statistics for all kind of solar wind regimes. In the following we assess the goodness of both the FSM and RSM response models over the whole ET-matrix both for the Kappa-Moyal peak model and the 2D-Gaussian peak model.

4.6.2 Goodness and Sensitivity of the Response Model

In Figure 4.23 we analize the FSM response model for Epq-step 55 in the same way as we did with He2+ and the iron species Fe7+ - Fe11+ in section 4.5 with the only difference that we omit the the reduced TOF histograms for brevity. As before, we only include ET-bins with more than ten counts per bin to allow a meaningful approximation of the χ^2_{red} value and we also exlude priority range PR5 as explained above as the failed base rate reconstruction in this area would strongly bias the overall χ^2_{red} value. Thus the shown fit of the response model to the data includes 69 free count rate parameters N_i that are bijectively related to the modeled peak heights of each ion species,

respectively, while all other parameters of the model are fixed as explained in sections 4.4 and 4.5. The same conditions apply for the shown cases of the FSM Gaussian response model in Figure 4.24. In an analog manner we have 28 free parameters for the cases of reduced response model (RSM) fits in Figures 4.25 and 4.25 for the Kappa-Moyal peak shape and Guassian peak shape, respectively.

From the contour plot in the upper panel of Figure 4.23 we see that the model and the data contour levels match well at almost all parts of the ET matrix with a few deviations for the Si9+ and C4+ peaks at ET-channels () and () where we can see that the model is able to catch the presence of these peaks in the vicinity of the much larger O6+ peak, but it does not reflect their shape very accurately. On the other hand some other features are modeled quite precisely such as the C5+ and Ne8+ peak at ET-channels () and (), respectively or even the Fe12+ peak at ET channel ?. Also the iron peak shapes are modeled accurately as one would expect from subsetion ? with the only exception that the Fe8+ peak is slightly over-estimated, although the count rate maximum close to the position of Fe8+ can be modeled precisely.

In the middle panel of Figure 4.23 we can see that the vast majority of ET bins the measured count rates show moderate deviations from modeled count rate below 3σ although we find several small areas where the deviation is larger and reaches up to 6σ (mention 2 examples!) in the vicinity of O6+, C4+ and Fe10+. On the other hand when we consider the relative residuals in the lower panel of Figure 4.23, we find small values $\Delta C_{rel} < 0.2$ for the whole relevant ET-matrix where we find high count rates, so that the observed systematic deviations in the middle panel are not crucial for count rate determination of the major ion species. While this the case for the whole central matrix from C^{5+} at the lowest TOF and ESSD channels to the iron ions Fe7/8+? - Fe14/16?+ at the high TOF and ESSD cahnnels, the relative residuals are below 0.2, we find large deviations for the boundaries, where the count rate is negligibly low, except for the C6+ peak, where we can see the influence of He2+ pile-up counts (see subsection ?). When we compare the Kappa-Moyal model fit with the Guassian model fit in Figure 4.24, we see that several features are modeled worse, such as the C4+ and Si9+ peaks that are not caught well by the Gaussian model besides the clear deviations in the iron tails. Consequently, we observe on average higher relative deviations that reach up to $\Delta C_{\sigma} = 10$ in the vicinity of the O6+ peak and the overall goodness of fit is significantly almost factor of 3 worse than for the Kappa-Moyal response model fit. We also see that the some areas with large relative deviations relative residuals in particular between C5+, O6+, C4+ and Si9+ result in larger relative residuals that are with about
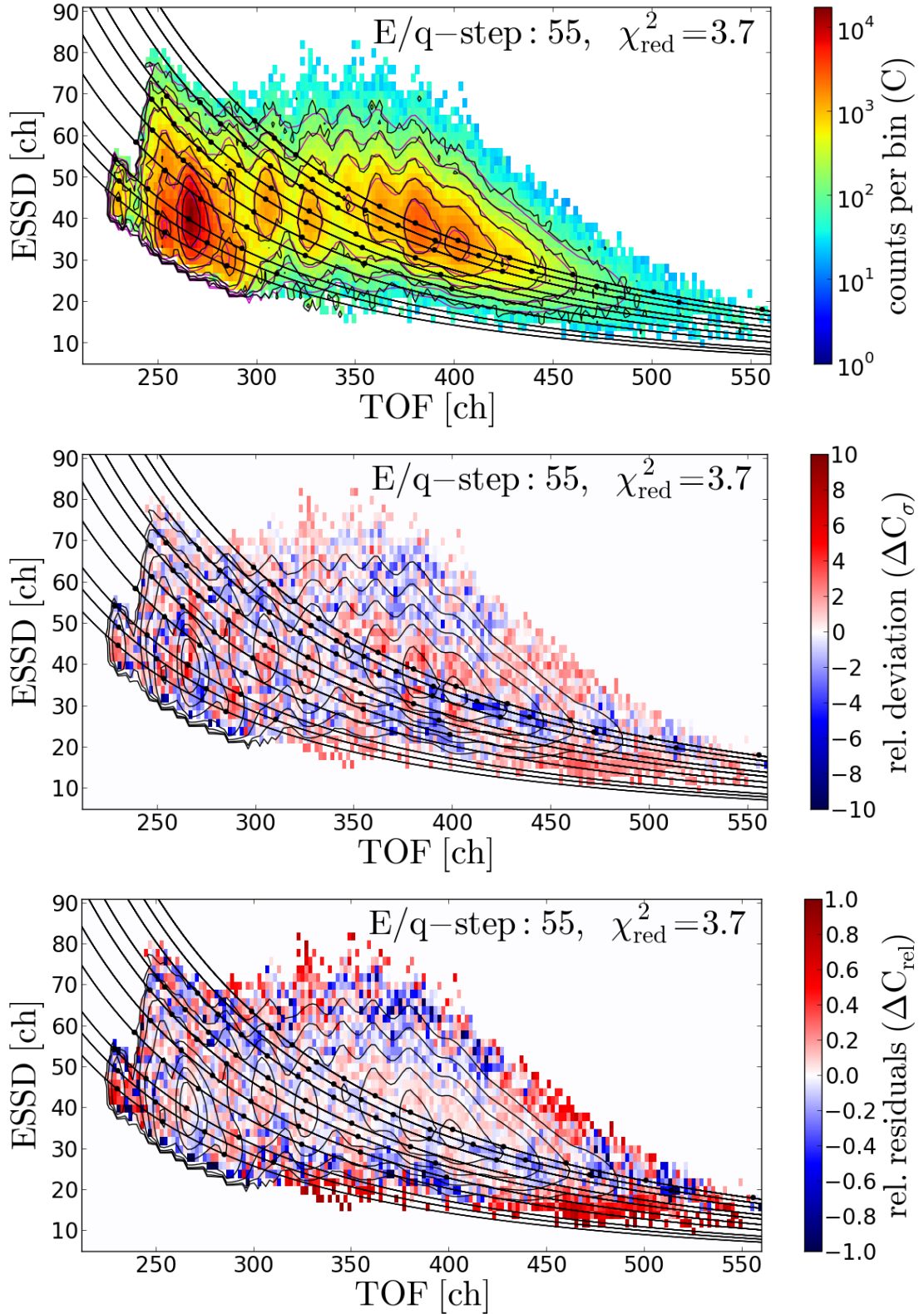
FIGURE 4.23: 2-dimensional contour plot of the full model fitted to the full ET-histogram at Epq-step 55.
In all plots the black data contour lines correspond to $10^{-1/3}$, $10^{-2/3}$, 10^{-1}, $10^{-4/3}$, $10^{-5/3}$, 10^{-2} times the maximum data count rate C_{max}, which is located within the O6+ peak. The magenta contour lines show the count rate levels of the fitted count rate model $\widetilde{C}(\underline{N}, \underline{R})$ also scaled by the maximum data count rate C_{max}
. as in he previous figures the black lines represent the 50%, 10%, 5%, 1%, 0.5% and 0.5% count levels with respect to the maximum count rate in the histogram and the magenta lines represent the corresponding levels of the model fit.
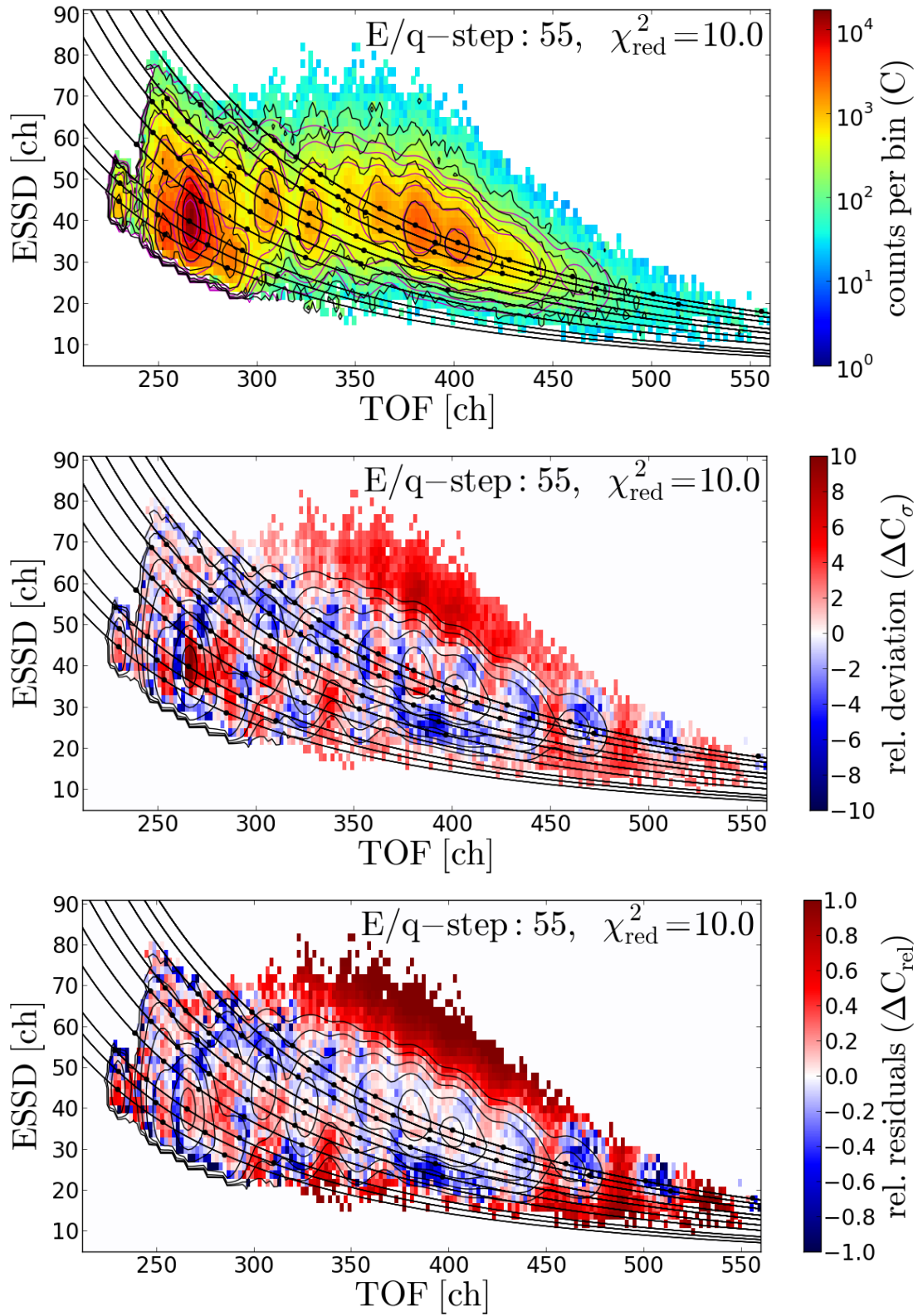
FIGURE 4.24
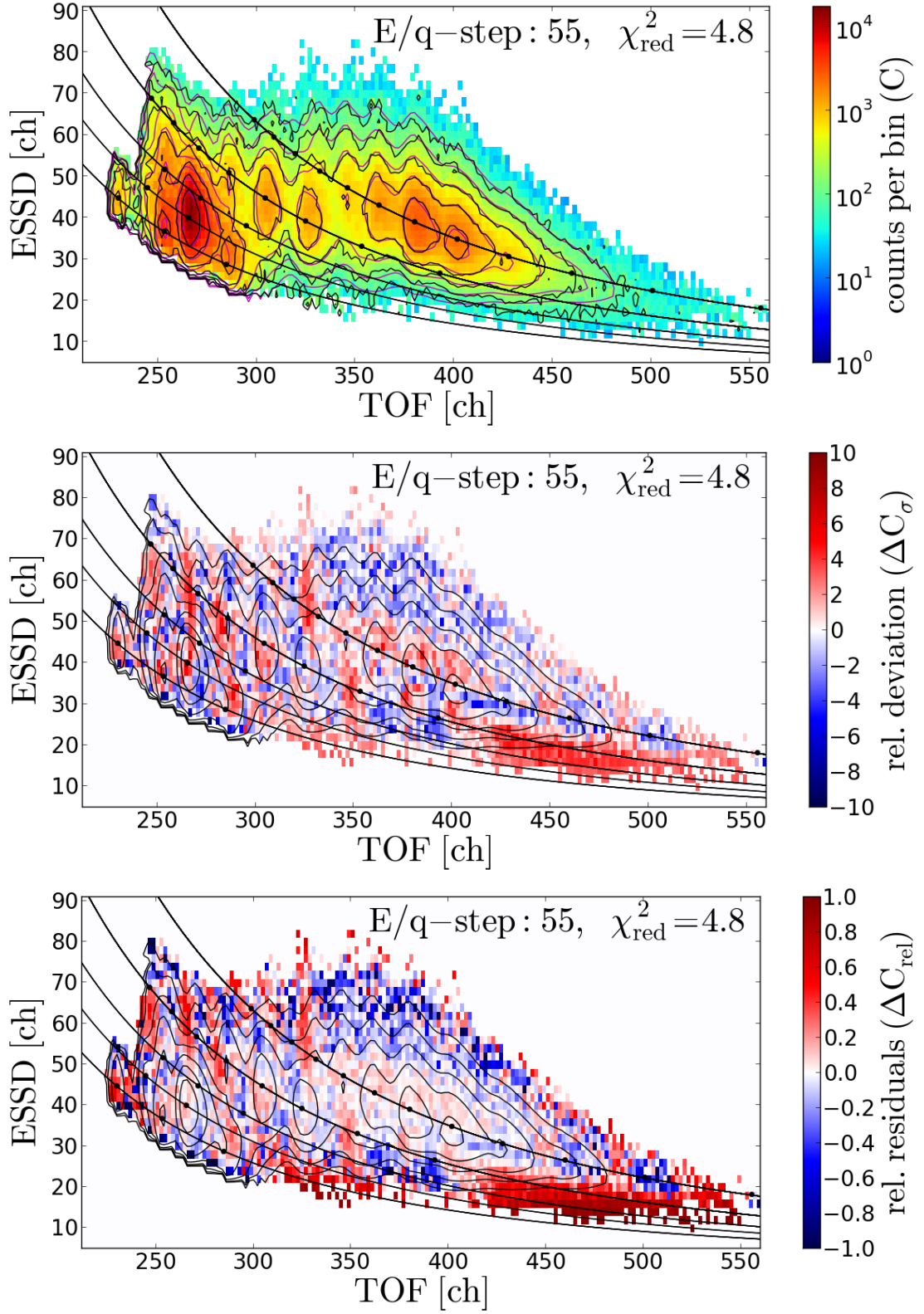
FIGURE 4.25
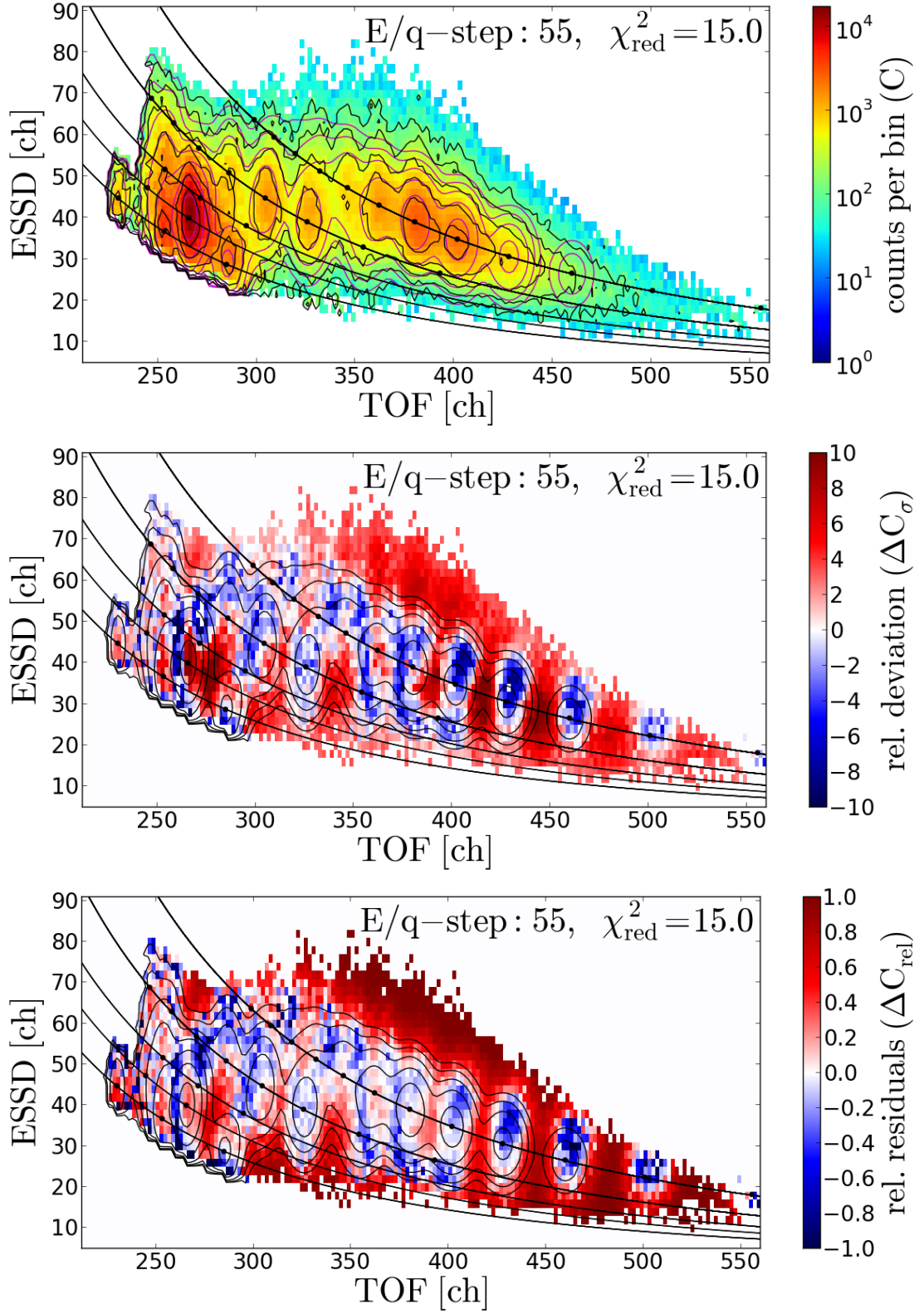
FIGURE 4.26
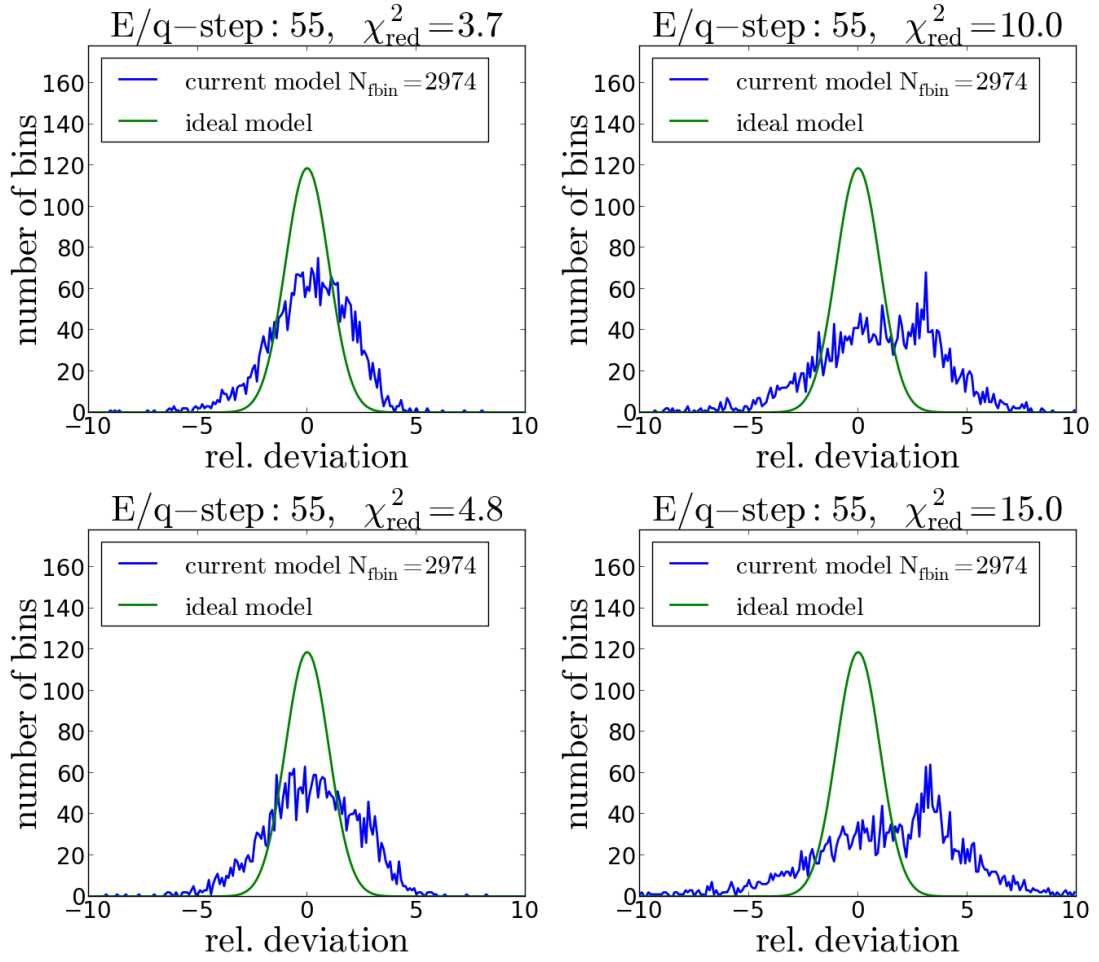
FIGURE 4.27

$\Delta C_{rel} = 0.4$ comparable to the count rate and one has to be cautious with the count rate evaluation. The same applies for the high-TOF flank of Fe8+ and Fe7+ in general.

As we discussed in Figure ?, we have to have in mind that due to the large number of ion species in the fit part of the model deviations can be compensated by unphsyically high count rates for certain minor species which we did not take into account in the evaluation yet. To avoid such effects, the analysis of the count rates with the reduced model is an important complimentary approach (both here and in the speed spectra analysis itself in section?), so that we also compare the RSM model fits for the Kappa-moyal and Gaussian peak shapes. In Figure ? (Kappa-moyal) we can see that the reduction does not have dramatic effects neither on the relative deviations nor on the relative residuals for most parts of the ET-matrix and also the model goodness is only moderately worse (as it is still by a factor of 2 better than the model goodness for the full Gaussian model). give some exmples and then conclude fast with the dramatically worse Gaussian model, for whcih however in some areas the fit is ok (?) or at least it could be ok, if the ystematic deviations do not change much over the Epq-step range,

nbut it is obviously better to have lower deviations as these are the upper boundary of the expectable systematic changes.

with the only exceptions at the boundaries. Thus we do not expect that the observed systematic deviations cause dramatic errors in the count rates at least for the ion species that dominate the count rates in the respective areas. In appendix B? we show this comparison between CTOF PHA long-term data and fitted response model for a representative set of Epq-steps: $j \in \{39, 50, 60, 70, 80, 86\}$ where Epq-step is the lowest step for which we had enough statistics to fit the full model in a numerically stable way in the normal count rate approximation and Epq-step 86 is the highest step where the statistics allowed this fit.

In Figures ? - ? we show the comparison between the PHA long-term data and the Reduced Response Model at the same Epq-step 55?. As one would expect from the lower number of ion species (29) we see in Figure ? that in some parts of the ET-matrix the RRM fit does not model the data as good as the FRM fit in Figure ? and it also has a worse goodness-of-fit χ^2_{red} than the full ion model. On the other hand the contour models match still better than for the Gaussian response model that we show for comparison in Figures ? - ? with the full (69!) ion set included and for which we find a very poor goodness-of-fit value of $\chi^2_{red} = ?$. When we consider the relative deviations for the RRM case in Figure ?, we find a few areas with somewhat larger deviations between the data and the fitted response model, but the relative residuals in Figure ? show again that these deviations are of comparable order to the FRM case for all areas that are relevant for the evaluation of the most abundant count rates. Also for the reduced ion set RRM and for the Full Gaussian Response Model we show the full comparison between data and fitted model in appendix B? for Epq-steps $j \in \{39, 50, 60, 70, 80, 86\}$.

When we compare the goodness of fit for the reduced and full model over all Epq-steps given in the appendix, we find that both show decreasing χ^2_{red} values with decreasing Epq-step, down to identical?/very similar values of $\chi^2_{red} = 1.9, 2?$ for E/q step 39/40?. This however, does not automatically mean that the model gets actually better for low Epq-steps but this is mainly explained with the decreasing number of total counts with decreasing Epq-step as most ions with low and intermediate m/q values are not occurring at these steps yet. With lower statistics it becomes just less visible how good (or bad) the peak shape is determined in detail. This can be seen from the comparison of relative count rate difference and rel. deviation for the low Epq-steps, where the relative residuals increase with lower Epq-steps but the rel. deviation decreases just because the σ increases relative to the lower number of counts in each bin. On the other hand, we find for both models increasing χ^2_{red} values with increasing Epq-step, since the total count rate is increasing and now the count rate σ in each bin becomes small compared to the deviation, even when the relative count rate is small at these

steps. for both (all?) models The reduced χ^2_{red} values reaches its maximum around step 70 simultaneously with the maximum observed total count rates. For all Epq-steps the calculated χ^2_{red} values are significantly lower than the corresponding values for the Gaussian model. When the total count rate drops again strongly around Epq-step 80 where only the ions with the lowest m/q values remain in the ET-matrix we can see for that for the full model also the χ^2_{red} value drops again. This also happens for the reduced ion set (check!) but at at higher steps. [11].

We finally investigate the sensitivity of the response model to small systematic deviations to check whether the calibrated configuration of peak parameters yields actually a significant minimum in parameter space and the observed low deviations are not just a random result due to the superposition of many ion species. In order to check in particular the ET environment of the best resolved and therefore presumably most reliable ion species we change in Figures? -? artificially the optimized position of O^{6+}, Si^{7+} and Fe^{9+} for (only) +2 channels in TOF in order to observe the corresponding change in the the rel. deviations and relative count rate differences as well as in χ^2_{red}. As we can see from Figure ? the biggest change is observed for the change of O^{6+}, as one would expect due its high relative count rate. We can easily see that now the model significantly underestimates the data at the low-TOF flank of the O^{6+} peak while it over-estimates the high TOF flank. The corresponding chi2 value doubles due to the arranged change. A smaller but still clearly visible effect can be seen if we shift the TOF position of $Fe^{9/10+}$ analogously by a of +2 channels which causes pronounced deviations along the TOF axis among the iron sequence while the global χ^2_{red} value is only increased by about ?. Finally for $Si^{7/8+}$ we do not see any significant change at all neither in the rel. deviation or count rate nor in the χ^2_{red}. This means that the TOF position of $Si^{7/8+}$ is not that well defined and could be easily shifted by a few channels in TOF. This illustrates well the kind of under-determination of the peak parameters within parts of the ET-matrix with many adjacent ions where as a consequence also the resulting speed spectra are subject to higher systematic uncertainties. On the other hand, a similar shift of the ESSD position of ± 2 channels (not shown here) yields similar results for O^{6+}, Si^{7+} and Fe^{9+} of $\Delta\chi^2_{red} \approx$? , so that for all corresponding elements an optimum in ESSD position is found.

We thus conclude that, for all heavy ion species for which the the relative systematic count rate error is on the same order of about 10%, our model is sufficiently good to

---

[11]The main reason is that in the reduced ion model the ion Mg^{10+} is missing which is highly abundant in the slow wind, but less important in the slow wind and thus also the reduced χ^2_{red} is substantially higher for Epq-step 80 for the RRM. As the RRM set is mainly designed for application in the fast wind scenarios, Mg^{10+} is not included in it for elemental consistency reasons, but it can be easily included for future studies, as well as any other species of the FRM set ions if the physical problem requires it.
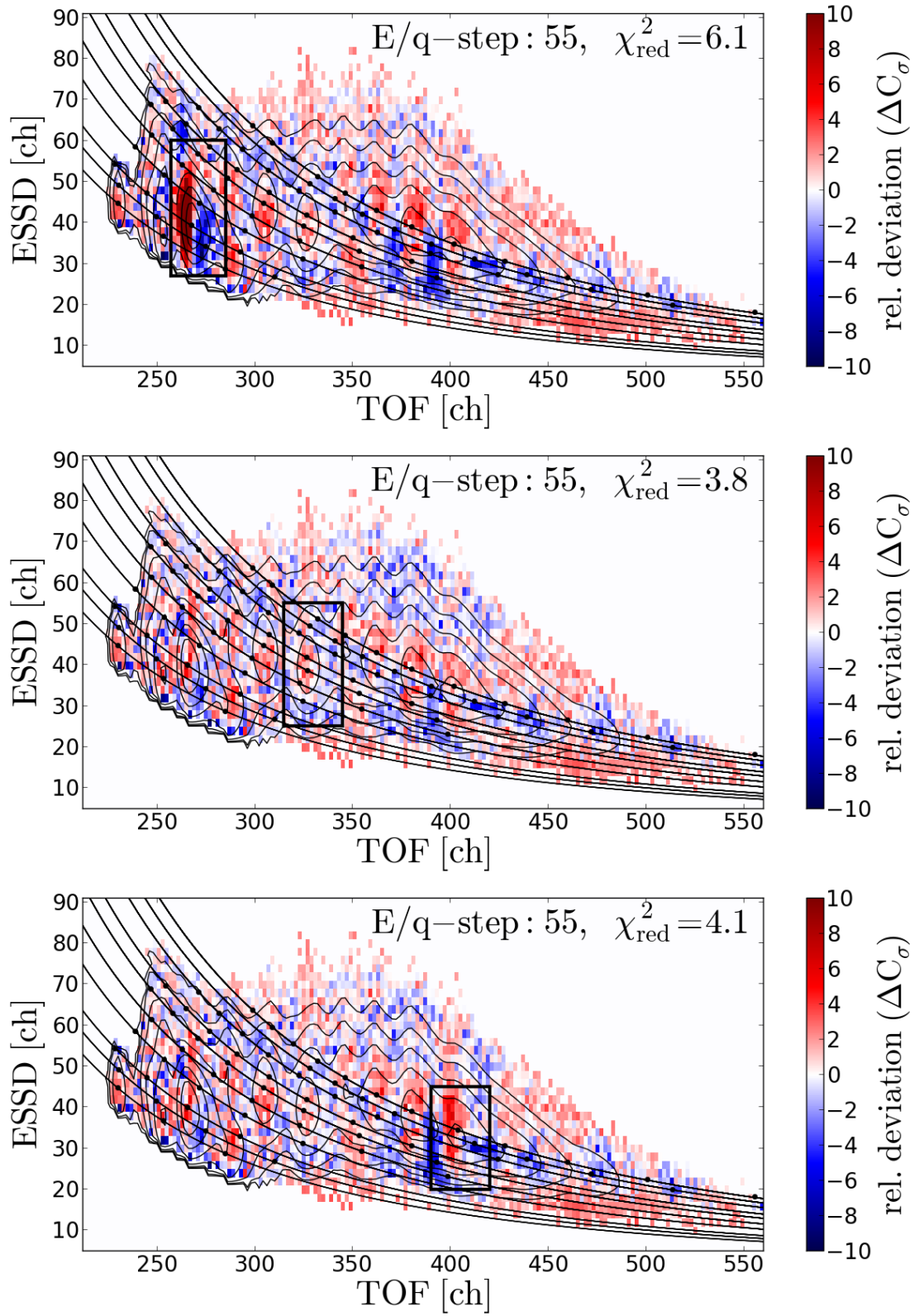
FIGURE 4.28

measure their VDFs with high precision and thus should be able to resolve differential streaming on the order of a few tens of km/s.

4.6.3   Instrumental Background

As a last point we discuss the instrumental back-ground which can be defined for the CTOF experiment as all count signals that do not represent a valid measurement of a heavy solar wind or pick-up ion, so either the measurement of other particles (solar wind protons, high energy particles/cosmic rays, photons) or the measurement of solar wind or pick-up ions at clearly unphysical TOF or ESSD channels.

High Energy Particles / Cosmic Rays: During the whole measurement period DOY 174-229 we found only a few (< 100) counts that we would identify we would identify as higher energetic/cosmic ray particle as these were measured at clearly higher energy channels in the SSD probably while a regular solar wind ion triggered a start condition at the carbon foil. Therefore, it seems that the anti-coincidence worked reliably during the whole measurement time and any back-ground from high energetic particles is negligible.

Secondary UV Photons: We also find that the suppression of UV photo electrons in the CTOF entrance system [Hovestadt], works well as otherwise these electrons would constantly trigger start pulses in the carbon foil and thus the energy signal of many ions would not be related to its TOF measurement any more and the ion peaks would be much less visible in a uniform back ground. In other words, we would observe a much lower signal-to-noise ratio.

Solar Wind Ion Energy Pile-Ups: In Figure ? we recognize that the energy shape of the C^{6+} peak is actually a double-peak structure. As this Figure still shows the base-rate uncorrected data and the lower peak is situated at about twice the ESSD position of the He^{2+} peak., we conclude that this peak is caused by He^{2+} pile-up events where in the case of high particle high fluxes two of He^{2+} ions are measured simultaneously at the SSD surface and are assigned to only one time-of-flight measurement, virtually doubling the energy of the detected particle. Anyway, the C^{6+} measurement cannot be analyzed properly in many cases as it has the same m/q value as He^{2+} and is therefore also cut-off in its speed distribution due to the interrupted Epq-stepping and thus we do not make any efforts to correct the pile-ups. For other species no pile ups could b observed. *Solar Wind Protons*: In the CTOF TCR data we do not observe any proton signal at the nominal peak position due to the suppression by the onboard fast analog identification system (PID) which during the CTOF pre-fligth tests was found to suppress 100% of the proton counts and 90% of the helium counts [Hovestadt] due to the control of the E/q stop-step and further filtering of the transmitted PHA data (see
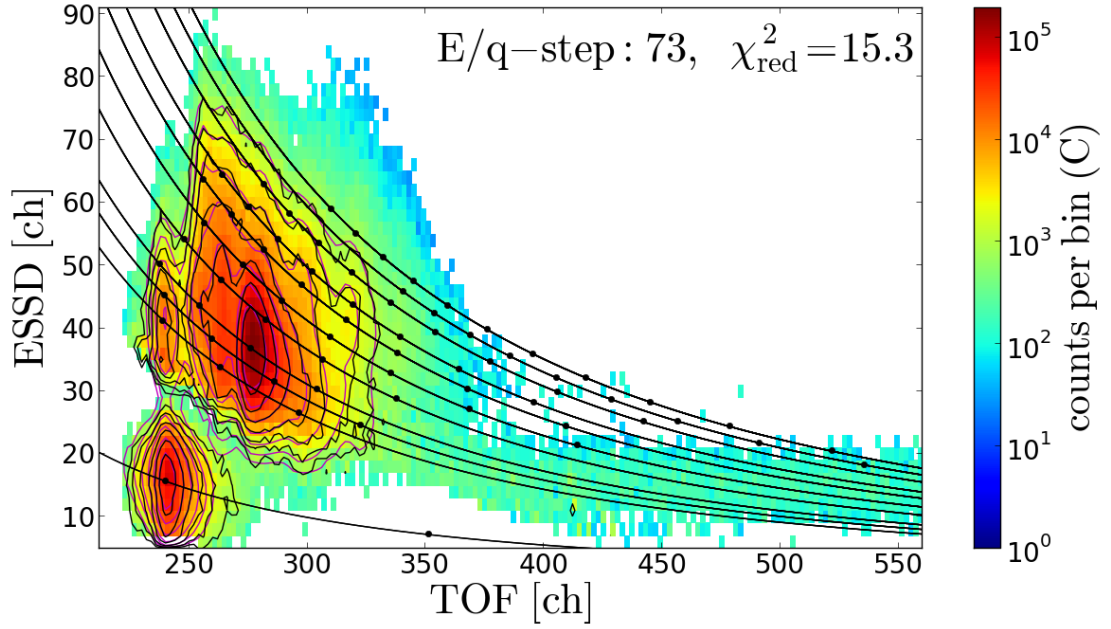
FIGURE 4.29

chapter 2?). Still, it is possible that a smaller fraction of the random coincidences that we discuss below is due to solar wind protons that could not be identified by the PID logic. (This last one is the major point!)

We finally turn to the most significant background contribution that results from random coincidences of the most abundant solar wind ions, in particular He^{2+}. In Figure ? we show the long-term PHA data for Epq-step 80 for DOY 174-220. At this step He^{2+} is measured at a speed of ? km/s which is close to the most frequent proton speed over the respective measurement period and thus the He^{2+} random coincidences (RC) are extremely pronounced in the ET matrix. As one would expect, the RC counts can be found at the same energies as the He^{2+} (include He^{2+} in the plot!) peak and they reach out with nearly constant intensity to very high TOF channels. But even if the RC count rates are high, due to their well defined location only ions at low energies are contaminated and due to the dependence in Eq? these ions are measured at high TOF channels and have relatively high m/q-values such as Mg^{5+}, Si^{6+}, Fe^{7+} and Fe^{8+}. On he other hand, He^{2+} has a very low m/q value which causes that the critical ion species are measured at much lower speeds than He2+ for the same Epq-step and thus their speed distribution is already completely scanned before the the Epq-steps are reached in which the He^{2+} random coincidences start to appear. Therefore, we do not observe any regular count rate distributions for these ions at the shown Epq-step 80 as even
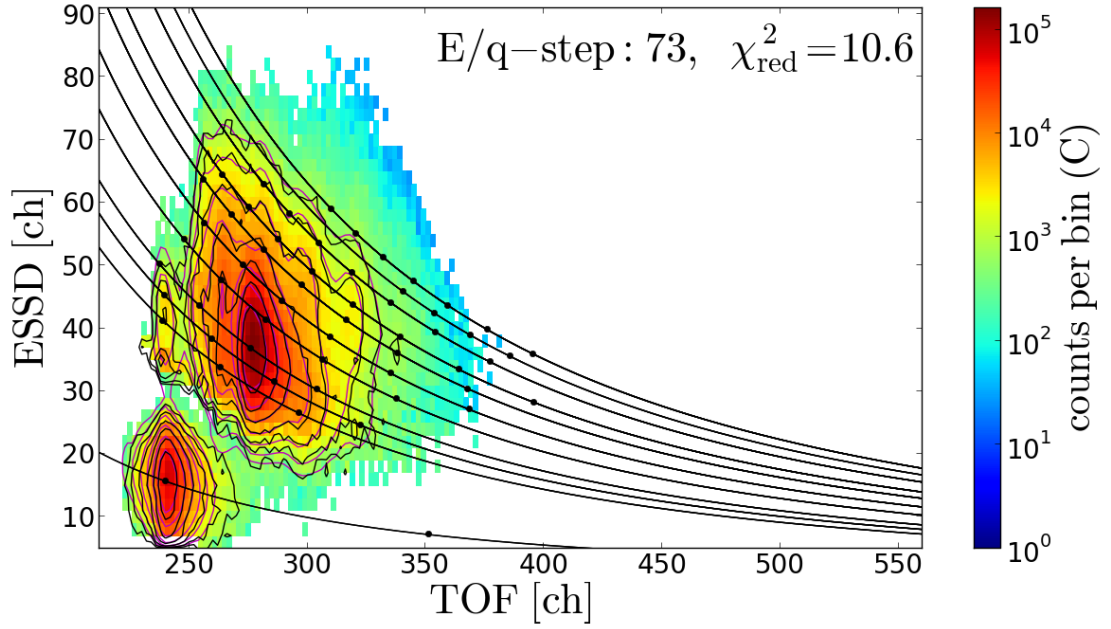
FIGURE 4.30

Mg^{5+}/Si^{6+} is measured at a very low speed of ? km/s for Epq-step 80. To illustrate how narrow the speed band is in which the random coincidences appear, we make use of the fact that in any case the ion speeds are still relatively close to the proton speed, and filter the PHA data for time intervals in which the proton speed is below 345? km/s which is about 2?3? thermal speeds lower than the He2+ speed in Epq-step 80 (even if we assume some reasonable amount of differential speed). As a result, it can be seen in Figure? that the RC background has vanished completely.

The relation that the He^{2+} random coincidences never appear at the same step in which the actual distribution of the relevant high m/q is measured is valid both for the slow and the fast wind as can be seen from the long-term spectra in the next chapter, even if the speed distributions in the fast wind are considerably wider. Thus, we do not need to cut-out the background counts in the ET data, but can separate this background in the obtained speed spectra as it is shown in the next chapter.

As the last point, we note that we can also have a small fraction of proton random coincidences as these could probably not be filtered out by the PID when they appear at higher TOF channels, but they can be sorted out in the same way as He^{2+} since they appear at even higher E/q -steps as He^{2+}. A bit more problematic are RC counts from O6+ as these lie both at higher energies so that they can also contaminate Si^{7+}, Fe^{9+} or Fe^{10+} for instance and appear also at lower Epq-steps, so that they have some overlap with these ions in particular in the fast wind. However, as O^{6+} is much less abundant compared to He^{2+} (as can be seen from the much less pronounced tails around Epq-step 75, that corresponds for O6+ to the most frequently measured proton speed in the

CTOF long-term data), these events occur much less frequent and thus have a very limited statistical impact on the calculated mean speeds of the most abundant silicon and iron ions.

He1+ random coincidences and other background e.g. heavy pick ups

4.6.4 Instrumental Detection Efficiences and Model-Related Speed Uncertainties

- speed dependent instrumental detection efficiencies that exist besides the different phase space coverage (discussed in section 2?) which are caused by the detection principle.

To cause a double coincidence particles must - to pass through the carbon foil and release enough secondary electrons from the carbon foil that trigger a start signal in the first MCP (including efficiency of MCP itself) - to reach the SSD (after being scattered in the carbon foil) and release again enough secondary electrons from the SSD surface that trigger a start signal in the first MCP (including efficiency of MCP itself) To cause a triple coincidence particles must in addition penetrate the SSD dead-layer and create enough electron-hole pairs to create an electronic signal that exceeds the SSD energy threshold

(All these processes are not only element specific but depend also on the energy of the incident particles). Given a certain species of incident particles all mentioned effects favour the detection of fast particles over slow particles as -the mean number of secondary electrons both in the foil and SSD surface increases with higher kinetic energies of the projectile -the mean scattering angle of the particles after the foil decreases due to lower cross-sections for scattering with the carbon foil nuclei -the mean number of created energy-hole pairs increases with higher kinetic energy of the incident particle

This means that in the measured VDF for any given ion species we over-estimate the faster particles compared to the slower ones and we have to estimate this systematic effect in order to quantify for instance its influence on the calculated mean speed.

With precise simulations of each contributing sensor component also inclusing the focusing of the incident ion populations in the CTOF entrance system as well as the respone of the MCPs one could in principle derive the detection efficiencies for all relevant ion species as it was accomplished by [Köten] for the Ulysses/SWICS sensor, although these models can have large uncertainties if several of the instrument parameters are not well-known so that a large set of possible parameter combinations arises.

This in particular the case for CTOF where after 20 years we only have limited documentation of the sensor so that for instance we have no detailed information of the quadrupole lens in the entrance system or of the MCP response.

Therefore, we relie for our estimations on an efficiency model for iron ions that was developed by [Aellig Phd] on the basis of calibratiton measurements with the CTOF flight spare model and the ACE/SWICS solid stae detector which is similar to the CTOF SSD. In Table ? in the appendix we list the estimated DC efficiencies η_{DC} that we extracted from Figure 4.10 in [Aellig Phd]. These values are extrapolated from oxygen and argon measurements with the TOF section of the CTOF sensor by H. Grünwaldt at the Max-Planck-Institute for Aeronomy in Katlenburg-Lindau in (pc Aellig - Gruenwaldt,1998). The measurements were performed over the energy-per-nucleon range 1-20 keV/nuc which fully covers the energy range of all relevant solar wind ion species after the post-acceleration. The obtained DC efficiency dependence on the partciles energy after the post-acceleration is shown as the blue curve in Figure ?. The SSD efficiencies η_{SSD} are modeled by [Aellig] on the basis of measurements of the ACE/SWICS solid stae detector which is similar to the CTOF SSD, which were performed by teh University of Bern at the ion beam facility of the University of Giessen. The SSD efficiency values are given in Table ? and are extracted from Figure 4.14 in [Aellig PhD]. They are represented by the red curve in Figure ? which we scaled by factor of 0.33 so that the small speed gradient of the DC efficiency is still visible. As a particle has to trigger both a double coincidence and a valid SSD signal to contribute to the triple coincidence count rate, we obtain the speed dependent TC efficiency for iron by a simple multiplication

$$\eta_{TC} = \eta_{DC} \cdot \eta_{TC} . \tag{4.41}$$

We TC efficiency is shown as the black curve in Figure ? where we also overlaid the E_{acc}-range that corresponds to the relevant solar wind speed range between 300 and 700 km/s for the iron species Fe8+ and Fe12+. In contrast to other studies that focus on elemental or charge state abundances, we are not interested in the absolute efficiencies at of a certain ion species compared to a differnt one, but we only need an estimation of the detection efficiency gradient over the solar wind speed range. From Figure ? we can directly see that this gradient is very flat for both iron species as it only changes of about ? and ? over their whole relevant range and we have to keep in mind that the core of a typical solar wind VDF is measured over a much smaller fraction of this speed range. In the upper left panel of Figure ?, we therefore show the effect that the estimated iron detection efficiency has on an ideal Maxwellian VDF that has a mean speed of 500 km/s and a thermal speed of 50 km/s which are typical values for the fastest wind (check vth again!) that we measure with CTOF in the time preiod DOY 174-220 1996. We see that
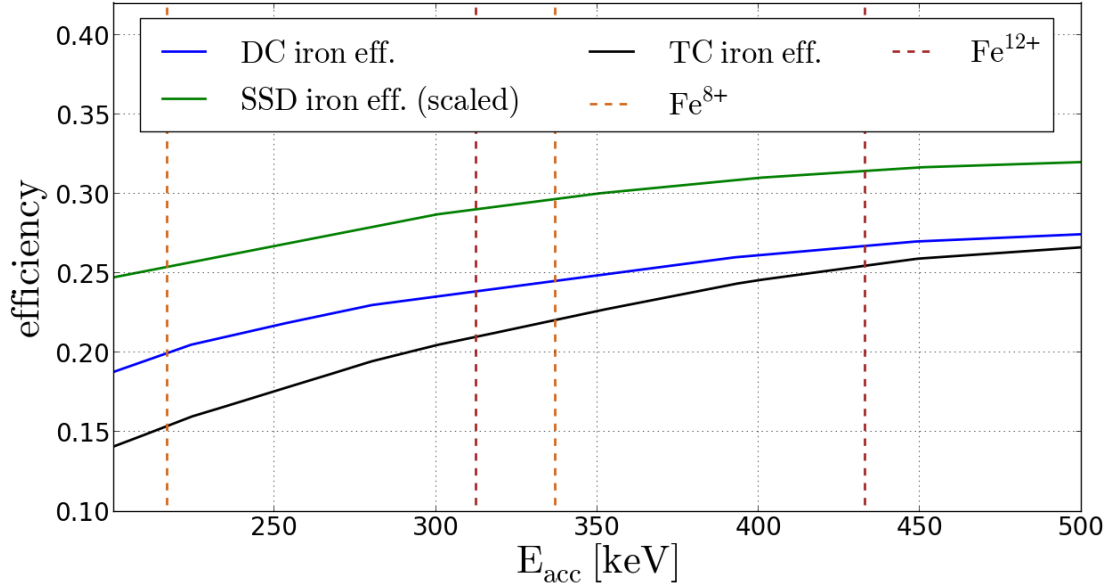
FIGURE 4.31: Estimated Triple Coincidence (TC) efficiency for iron ions (red) together with the Double Coincidence efficiency (blue) and the the SSD efficiency (black) which we scaled with a factor of 0.33 to allow a better recognition of the weak effciency gradient with the total ion energy E_{acc} after post-acceleration. The DC efficiency was modeled by Aellig(PHD) after measurements by H. Grünwaldt with the CTOF flight spare model and has an uncertainty of less than 10%. The SSD efficiency is modeled by Aellig(PhD) after measurements of the ACE/SWICS SSD, which is similar to the CTOF SSD. for the SSD efficiency no uncertainty was given here. Overlaid are the E_{acc}-ranges for Fe^{8+} and Fe^{12+} that correspond to measured speeds (before post-acceleration) between 300 and 700 km/s. The DC and SSD efficiency values are given in Table ? and Table ? in the appendix.

the shape of the measured VDF N_{meas} including the modification of count rates due to the destimated etection efficiency

$$N_{meas}(v) = \eta(v) \cdot N_{true}(v) \qquad (4.42)$$

compared to the assumed true VDF count rates N_{true} are small which results in a very small difference in the obtained mean speed of $\Delta_\eta \langle v \rangle = 2 \, km/s$. This is well below the differential speeds $\Delta v \gtrsim 10 \, km/s$ that we aim to resolve. We can see from Figure ? that the efficiency gradient is larger for Fe8+ as for Fe12+ which is a typical behaviour of the detection efficiency with the given detection principle where the overall detection probability is very sensitive close to the detection energy threshold and than saturates to a an almost constant value for larger kinetic energies/speeds. Unfortunately, from the limited laboratory calibration measurements we can only estimate the TC efficiency for iron ions as the SSD efficiency is given for iron only by [Aellig]. However, we discussed in section ?, the low charge states of iron have the lowest speeds (E_{acc}/nuc) of all ion species after passing the post-acceleration and are therefore also expected to have

the largest efficiency gradients of all ion species and thus Fe8+, as the lowest charge of the well-resolvable iron species, can serve as an upper estimate of the efficiency gradient for all ion species. This means that the instrumental efficiencies can be completely neglected for our studies mainly due to the fact that the solar wind speed distributions are relatively narrow (even in the fast wind) compared to e.g. pick-up ion distributions where the instrumental detection efficiencies can play a crucial role (i.e. Drews/Taut Anne fragen).

To conclude the discussion of the CTOF response model, we relate the observed systematic deviations between the CTOF response model(s) shown in Figures ? - ? (full model pictures) to the possible effect that these deviations cause in the measured velocity distribution functions. In the upper right Figure ? we assume a worst case scenario for the (Full Stable) Kappa-Moyal response model in which the occuring relative count rate deviations $|\Delta C_{rel}(\tau, epsilon)| \leq 0.2$ translate into comparable relative ion count rate differences $\Delta N_{ij}/N_{ij} = \Delta|N_i(v_j)/N_{ij}(v_j)| \leq 0.2$ and these deviations are increasing systematically from -0.2 to $+0.2$ over the Epq-steps j that correspond to the respective ion speeds $v_j \in [\langle v \rangle - v_{th}, \langle v \rangle + v_{th}]$ within the core of the VDF. Mathematically, the relative deviation can be treated as an efficiency that is given by the concrete response model and thus we obtain the measured VDF from the multiplication of an assumed true VDF with the relative ΔN_{rel}. As the VDF modifications are most critical for wide VDFs with high thermal speeds we assumed (again, mention already above) a typical VDF in the fastest wind measured by CTOF $\langle v \rangle = 500$ km/s with a thermal speed of $v_{th} = 50$ km/s. As, the gradient of ΔN_{rel} is considerably larger than the instrumental efficiency gradient we find a difference between the observed and true speed of about $7\,\text{km/s}$[12]. We note that this speed difference is not completely negligible anymore in comparison to the expected differential speeds that we aim to quantify in the fast wind, which is exactly the demonstrated scenario. On the other hand $\Delta_\eta \langle v \rangle$ is still less than 10 km/s (or corresponds to about 15% of the expected Alfven speed at 1 AU) and we emphasize that the demonstrated estimation is clearly a worst case scenario and not very probable to occur in suc a pure form although we constructed it in a way that the change ΔN_{rel} only occurs over a limited speed range in the core of the distribution which corresponds to less than 10 Epq-steps which might not be completely unrealistic [13]. In the lower left panel of Figure ? we increased the gardient of $\Delta N_{rel}(v)$ so that $\Delta N_{rel,min}$ and $\Delta N_{rel,max}$ correspond roughly to the mean observed

---

[12]Note that this difference is independent of the assumed mean speed, but it only depends on $v_t h$ and ΔN_{rel}, and we just chose $\langle v \rangle = 500$ to have a realistic ratio between $\langle v \rangle$ and v_{th}. This also emphasize that the most critical cases appear in the fast wind, where we actually aim to resolve the differential streaming which we do not have to confuse with these systematic response model effects.

[13]Note that the obtained mean speed difference is little sensitive on the exact linear increase of ΔN_{rel} as one obtains similar values if one assumes for instance a step-function of the ΔN_{rel} that changes its value from 0.8 to 1.2 at $v = \langle v \rangle$ as long as we do not alter the thermal speed.
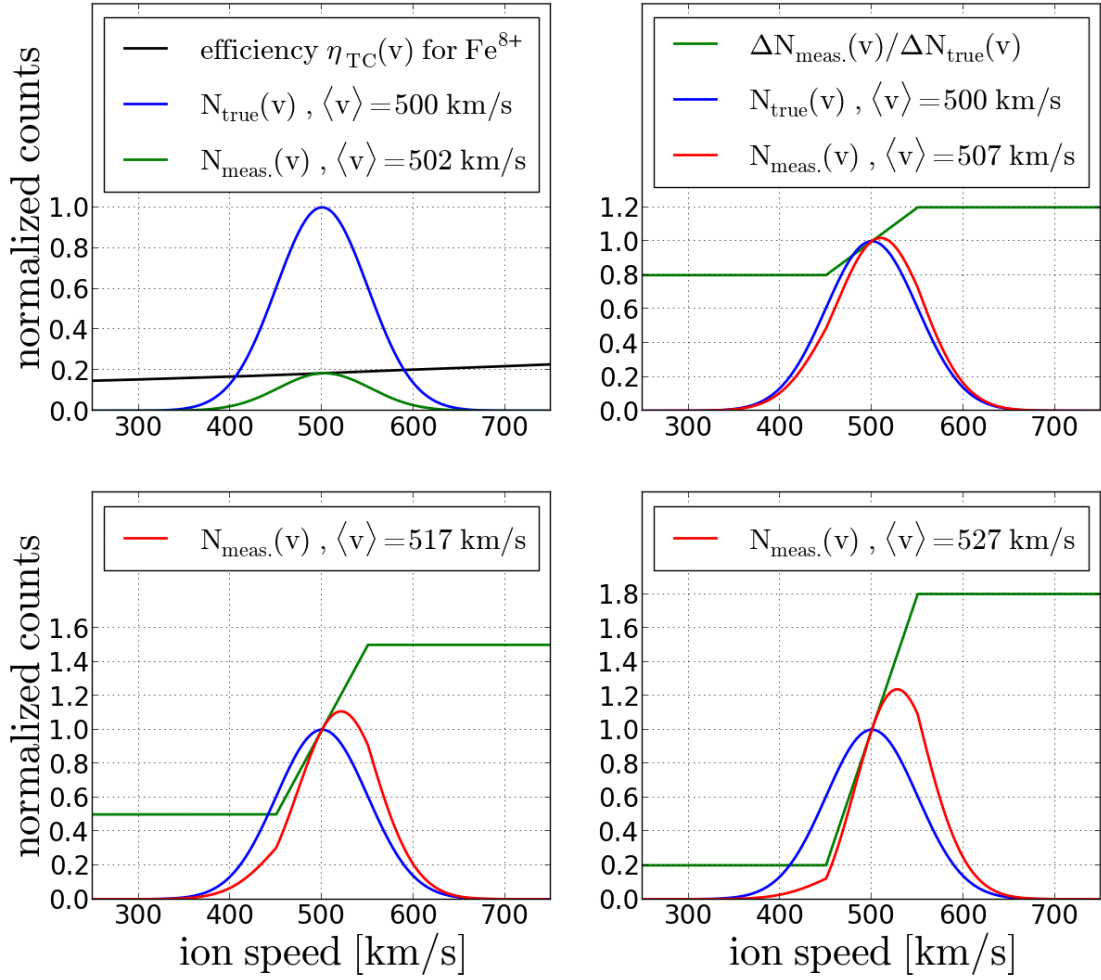
FIGURE 4.32

relative count rate changes in the critical ET-matrix areas of Figure ? or ? that show the full and reduced response model for the Gaussian peak model. We can see that for these values of ΔN_{rel} the difference between measured and assumed true VDF mean speed is already 17 km/s which is definitively comparable to the expected differential speeds after section 1? (ACE/SWICS plot by Lars). While this is a very conservative estimation for the possible deviations, it is important to have these maximum systematic measurement uncertainties at all as the systematic errors can be much larger than the statistical ones and cannot be estimated at all from the obtained VDFs that show no major deviations from the expected approximately Gaussian shape. In this context, the reduction of these upper limits for the systematic errors by more than 50% as we can see from the comparison of panel ?, and ? is a very important component for the reliable resolution of such subtle features as differential speeds at 1 AU. In the lower right panel of Figure ?, we show that we increase the gradient of ΔN_{rel} even further one can in principal observe very high values of $\Delta\langle v \rangle$ although they are completely

artificial. While the demonstrated case is very unlikely for the dominant ion species in the ET-matrix neither for the Kappa-Moyal nor the Gaussian peak shape (or simple box rates) it can be easily realized for ion species with relatively low abundance in the flank of the dominant species, in the case that we do not resolve the peak properly over all Epq-steps and instead measure the dominant ion species flank instead of the minor ion species itself for a part of the speed range. We come back to this point in the systematic error estimation of the long-term-speed spectra in section ? of the next chapter. [**?**]

Chapter 5

Heavy Ion Long-Term Speed Spectra at 1 AU

In this chapter we present the first results of our CTOF studies in the form of long-term integrated velocity distribution functions that we call *long-term speed spectra*. To derive these distributions functions, in a first step we integrate the base-rate corrected PHA short term count rates $C_k(\tau, \epsilon)$ over all valid[1] CTOF cycles $0 \leq k \lesssim 10^4$ in the measurement period DOY 174-220 in which the simultaneously measured proton speed, obtained from the CELIAS Proton Monitor, lies within a narrow well-defined speed range $v_p \in [v_{p,min}, v_{p,max}]$. This is equivalent to filtering the long-term data count rates $C(\tau, \epsilon)$ that we used for the response model characterization in the previous chapter 4 for the respective time periods with $v_p \in [v_{p,min}, v_{p,max}]$. In a second step we then fit the CTOF response model to these filtered long-term count rates $C_{v_p}(\tau, \epsilon)$ as described in Eq. 5.2 for each Epq-step $0 \leq j \leq 116$. From these fits we obtain directly the long-term ion count rates $N_{ij}^{v_p} = N_i^{v_p}(v_j)$ for all included ion species i of a given CTOF response model. These count rates represent the resulting long-term speed spectra hat are measured in a well-defined proton speed regime.

The relatively high integrated ion count rates $N_i^{v_p}(v_j)$ allow in a first instance for systematic reasonabilty checks of the derived speed spectra by a systematic comparison of the measured relative ion species abundances and spectral shapes. However, In the main instance we aim to analyze the long-term speed spectra for signatures of differential streaming which we identify by calculating the mean speeds of the obtained long-term speed distributions and see whether they deviate significantly from the well-defined mean proton speeds $\langle v_p \rangle \in [v_{p,min}, v_{p,max}]$.

---

[1]See section 5.1 for details of the cycle selection.

In this long-term spectra analysis one has to be aware of the fact that besides the restricted proton speed the other solar wind plasma parameters such as the proton density and kinetic temperature vary in general over the extended time period and might thus influence the occurrence and size of non-thermal plasma features. Furthermore, as described in section 2.4 also the in-situ magnetic field can influence present differential speeds in two ways: First in the case of an actual dependence of the ion (differential) speed magnitude on the local Alfvén speed and second by the in-situ field direction that determines the projection of the present differential speed on the instrument measurement axis and thus determines the measurable amount of occurring differential speeds. From these considerations it is clear that one has to be a bit careful with the interpretation of the derived long-term speed spectra, as they represent a long-time average over different solar wind plasma and magnetic field conditions that are present in the given solar wind speed range. For this reason we chose to call the long-term integrated speed distributions presented in this chapter long-term *speed spectra* in contrast to the short-term *velocity distribution functions* that we derive in the next chapter 6 from the CTOF short-term PHA data, as the latter are only integrated over the intrinsic CTOF 5-minute cycle duration and thus can provide a direct link to the local plasma and magnetic field conditions at each given measurement cycle.

On the other hand, the overall measurement period DOY 174 - 220 1996 is short compared to a solar cycle and as we measure at solar minimum conditions the solar wind outflow is relatively well-structured by the large-scale magnetic dipole field of the Sun which reduces the variability of the measured solar wind regimes. In fact as the full investigated period only includes about 1.7 Carrington rotations, it is comparable to typical time scales of larger changes in the coronal hole structure. Therefore, as already stated in chapter 3 it is likely that we observe fast wind from the same coronal hole that extends down to low latitudes in the two periods after DOY 188 and DOY 215, so that the primary acceleration conditions of this wind might be comparable. From this perspective the long-term averaging could be less problematic, although we still have the super-imposed effects of the varying local magnetic field.

Finally, the precise evaluation of the thermal speeds from the long-term spectra is more complicated as even small changes of the mean speed on the order of 10 km/s which corresponds to the proton speed filter intervals that we use for our analysis are comparable to the thermal speeds of the VDFs in the slow and intermediate wind regimes. We therefore can only get a rough estimation of the thermal speeds from the long-term measurements and consequently we investigate the thermal speeds almost exclusively in the short-term data in chapter 6.

5.1 Data Selection and Sample Sizes

In the following we analyze the derived speed spectra integrated over all CTOF measurement cycles within the full measurement period DOY 174-220 1996 under the condition that the simultaneously measured proton bulk speed falls within a well-defined narrow speed range. To give an overview of the number of cycles that we can include for the long-term analysis, we show in Figure 5.1 the histogram of the maximum reached Epq-steps[2] for all measurement cycles in which a 5-minute average proton speed was measured within the intervals [330 km/s, 340 km/s], [490 km/s, 500 km/s], [500 km/s, 510 km/s], and [510 km/s, 520 km/s] and where the condition of more than 500 transmitted PHA words is met. We find that we have about a factor 10 more available cycles in the slow wind interval than in each of the fast wind intervals. This is mainly due to the low number of fast wind streams that could be measured at the SOHO site during solar minimum in 1996 and partly due to the unfortunate CTOF telemetry scheme that yields an over-proportional number of cycles with an extremely low number of transmitted PHA counts in the fast wind periods (as discussed in section **??**). We further see that the distributions of the ESA stop-steps consist of two different populations for solar wind (proton) speed intervals. This is because the ESA stops either in the rising high-speed flank of He^{2+} (lower Epq-steps) or in the high-speed flank of H^+ (higher Epq-steps) depending on the solar wind density and temperature. In general, for any given solar wind speed the ESA is stopped already in the He^{2+} flank when the wind is dense and/or cold as then the threshold in the SSR rate is more easily reached at a given Epq-step (see section **??**).

For the goal of a comparative analysis of long-term integrated speed spectra over the same cycles and a relatively large speed range it is crucial to only take into account those cycles that cover a sufficiently large span in Epq-steps in order not to artificially cut-off the low-speed flank of the spectra for certain ion species. In order to find a compromise between the highest possible number of included cycles and a reasonably wide speed range for a high number of ion species it is a natural choice to set the minimum stop-step filter in the gap of the bimodal stop-step distribution. In this way, we lose a fraction of the cycles and might also introduce a small bias as we implicitly select low density/high temperature cycles. Yet, this is not a major problem as in this first analysis, we only aim to evaluate whether there can be found any signature of differential speeds in the long-term data at all, even when this is only the case under certain solar wind conditions. On the other hand, the selected ESA stop-step filter allows for a speed scan of ion species with mass-per-charge values as low as m/q =2.3 down to about 2

---

[2]We call the maximum reached Epq-step for each cycle in the following the *ESA stop-step*, corresponding to the lowest measured energy-per-charge value in the electrostatic analyzer for the given cycle.
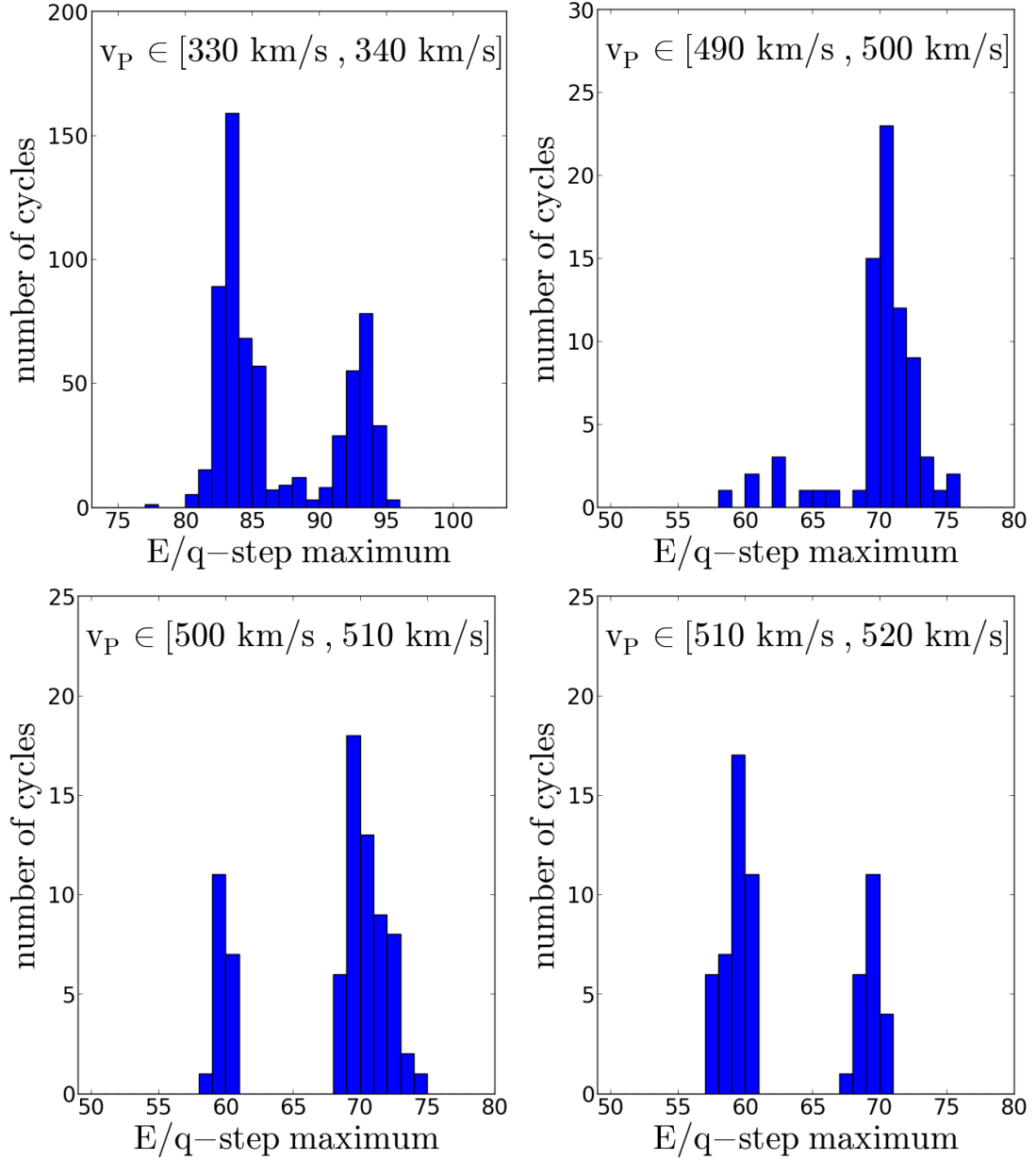
FIGURE 5.1: Histogram of the maximum reached Epq-step (*stop-step*) by the CTOF electrostatic analyzer (ESA) for measurement cycles in the slow solar wind with simultaneously measured proton speed $v_p \in [330\,\text{km/s}, 340\,\text{km/s}]$ (upper left panel) and in the fast wind with proton speed $v_p \in [490\,\text{km/s}, 500\,\text{km/s}]$, $v_p \in [500\,\text{km/s}, 510\,\text{km/s}]$, and $v_p \in [510\,\text{km/s}, 520\,\text{km/s}]$ (upper right panel and both lower panels, respectively). Mark selected minimum stop-step filter with red vertical line!!!

thermal speeds below their speed distribution maximum as we show below.

For the following comparison of speed spectra in the slow and fast wind, we choose the proton speed ranges of [330 km/s, 340 km/s] and [500 km/s, 510 km/s], respectively. While for the slow wind case the choice of the proton speed bin is not critical in terms of cycle statistics and we just choose a bin close to the minimum speed that can be reliably measured by the CELIAS proton monitor, for the fast wind case we see from Figure 5.1 that when we switch from the [490 km/s, 500 km/s] to the [500 km/s, 510 km/s] proton speed interval, we find a relatively large drop in cycle numbers in particular in the population of high stop-steps (57 compared to 22 valid cycles). We therefore use for this first analysis the proton speed interval [500 km/s, 510 km/s] and set the minimum ESA stop-step filter condition inclusively on Epq-step 68 to utilize the full cycle statistics of the higher stop-step population. Analogously, we set this condition inclusively at Epq-step 90 for the slow wind case. This leaves us with a sample size of about 190 cycles in the slow wind bin [330 km/, 340 km/s] and 55 cycles in the fast wind bin [500 km/s, 510 km/s] which corresponds to a total measurement period of aprroximately 16 hours in the slow wind and about five hours, respectively. While the slow wind sample is measured over several periods over the whole measurement period, the fast wind is measured on 5 days only: DOY 185, 186, and 213, 214, 215 containing measurement periods of a few minutes to hours. Due to the time difference of about 27 days between the two observed fast periods it is likely that both originate from the same recurrent coronal hole that extended to low latitudes over the consecutive Carrington rotations 1911 and 1912 [1].

5.2 Derivation of Speed Spectra from CTOF PHA data

In order to derive speed spectra for individual ion species we finally apply the CTOF response model to the PHA count data to conduct the probabilistic ion count assignment as described in section 4.1. Note that for these fits we have to use the Poisson χ^2-minimization function in Eq. as even in the long-term data for the lowest Epq-steps (corresponding to highest Epq-values) the low count rates cannot be approximated with normal statistics anymore. However, this is not a problem as we already estimated the goodness of the response model in the previous section and as discussed there the instrument response itself can be assumed as constant for all times and does not depend on the count statistics nor on the solar wind conditions. To conduct the fits we use the Broyden-Fletcher-Goldman-Shanno (BFGS) minimization algorithm [? ? ?] which is also a conjugate-gradient method similar to the Levenberg-Marquardt (LM)

algorithm [**? ?**][3]

As a last check we also compared the overall estimated count rates by the fit with the overall number of actually measured counts in the ET-matrix at any relevant Epq-step j and find differences up to the order of a few percent for the fits with the Kappa-Moyal response model in the long-term term data. As in total we have to assign the exact number of counts to the ion species that are actually measured we renormalize the fitted count rate contribution at each ET-bin within any given ET-matrix j by assuming after the fit conduction that

$$\forall \tau, \epsilon : \widetilde{C}(\tau, \epsilon) \stackrel{!}{=} C(\tau, \epsilon) \tag{5.1}$$

so that for each ion species its $\widetilde{C}_i$ contribution that adds up to the model total count rate $\widetilde{C}$ is normalized as

$$\widetilde{C}_{i,norm}(\tau, \epsilon) = \frac{\widetilde{C}(\tau, \epsilon)}{C(\tau, \epsilon)} \cdot \widetilde{C}_i(\tau, \epsilon) \tag{5.2}$$

so that the final ion count rate for a given ion species at a given Epq-step $0 \leq j \leq 116$ reads

$$N(v_{ij}) = N_{ij,norm} = \sum_{\tau, \epsilon} \widetilde{C}_{i,norm}(\tau, \epsilon) \tag{5.3}$$

where v_{ij} is again the nominal ion speed that corresponds to the given Epq-step after Equation 2.1. The explained normalization procedure follows exactly the applied procedure in [Berger, PhD]. One can argue that one could include condition 5.1 already as a boundary condition/restriction in the fit itself, but in the applied way we have an additional check how stable the obtained VDF moments are as we can calculate them before and after the correction. For a sufficiently good fit the difference in mean speed $\Delta \langle vv_{norm} \rangle v = |\langle v \rangle v - \langle vv_{norm} \rangle v|$ should be negligible in comparison to the expected differential speeds. For all ion species that could be measured with a reasonable peed spectrum and are analyzed below in this chapter we find $\Delta v | v_{after} - v_{after} | \leq 1 \, \text{km/s}$ in the slow wind and $\Delta v | v_{after} - v_{after} | \leq 3 \, \text{km/s}$ in the fast wind.

---

[3]The reason for the application of the BFGS algorithm instead of the LM algorithm is purely a practical one, as the BFGS algortihm is implemented in the *fmin* method of the *python scipy optimize* library that can be used with a user-defined minimization function, while the standard *scipy optimze leastsq* routine that works with the Levenberg-Marquardt algorithm expects the standard χ^2-minimization function given in Eq. 4.13. For the model calibration fits we used the latter method as it calculates automatically the covariance matrix from which one can directly calculate the estimated errors of the fitted ET positions and widths in section 4.4 and 4.5. We compared the obtained ion count rates for both minimization algorithms and found differences far below the deviations between data and response model regardless of the count statistics.

5.3   Spectra Analysis

We illustrate the long-term spectra analysis with the measured spectra of O^{6+} and O^{7+} that are shown in Figure 5.2 for the described slow wind case ($v_p \in [330\,\text{km/s}, 340\,\text{km/s}]$). When fitting a 1D-Gaussian as a 1D-Maxwellian approximation to the measured reduced speed spectra we can see that both ion spectra consist of a thermal core which is well-described by the fit and a supra- (and sub-) thermal tail at very low and high speeds that follows a power-law. One can now either obtain the (core) mean speed $\langle v_i \rangle$ of a given ion species from the applied fit or derive it from a moment calculation that we define in analogy to chapter 3:

$$\langle v_i \rangle = \frac{1}{\sum_{j=s_{min}}^{s_{max}} N_{ij}} \cdot \sum_{j=s_{min}}^{s_{max}} N_{ij} \cdot v_{ij} \tag{5.4}$$

where $N_{ij} = N(v_{ij})$ is the (phase space corrected) count rate measured at the speed v_j that is calculated for the given ion species from the respective Epq-step j after Eq. ?. As discussed in the previous section we cannot simply calculate the mean speed over the full Epq-step range $0 \leq j \leq 116$ as we have to take into account the interruption of Epq-stepping, but on the other hand we have to ensure that the selected speed range is symmetrical with respect to the core of the distribution in order not to bias the calculated mean speeds. Making again use of the Gaussian approximation for the distribution, we determine 1σ-, 1.5σ-, and 2σ- intervals for the calculation of the mean speed that are centered around the most frequently measured speed v_{max} with count rate N_{max}. These intervals are illustrated in Figure 5.2 as vertical blue lines for O^{6+}. The most narrow 1σ interval is limited by the speed values on both flanks of the spectrum where a running average of the count rate drops (the first time) below a value which is 0.61 times lower than N_{max}. Accordingly, we limit the 1.5σ and 2σ environments at the speed bins where the distribution drops below values of $0.32 \cdot N_{max}$ and $0.14 \cdot N_{max}$, respectively. The 2σ-environment is also marked for O^{7+} as red vertical line in Figure 5.2. We use the running average to ensure a higher stability in the presence of non-monotonic flanks of the spectra. In the slow wind the running average is calculated over 3 adjacent speed values only, to be applicable for the relatively cold ion distributions, while in the fast wind we use a running average of 5 adjacent speed values.
The three different intervals used for the calculation of the mean speed are needed in order to ensure the independence of the mean speed on the selected calculation interval. When we compare the mean speeds obtained from the moment calculation in Figure 5.2 among each other, we find a very good agreement with differences below $1\,\text{km/s}$ for O^{6+} and $1\,\text{km/s}$ for O^{7+}. Also the comparison of the fitted mean values with the calculated moments yields a very good agreement for both species with a maximum
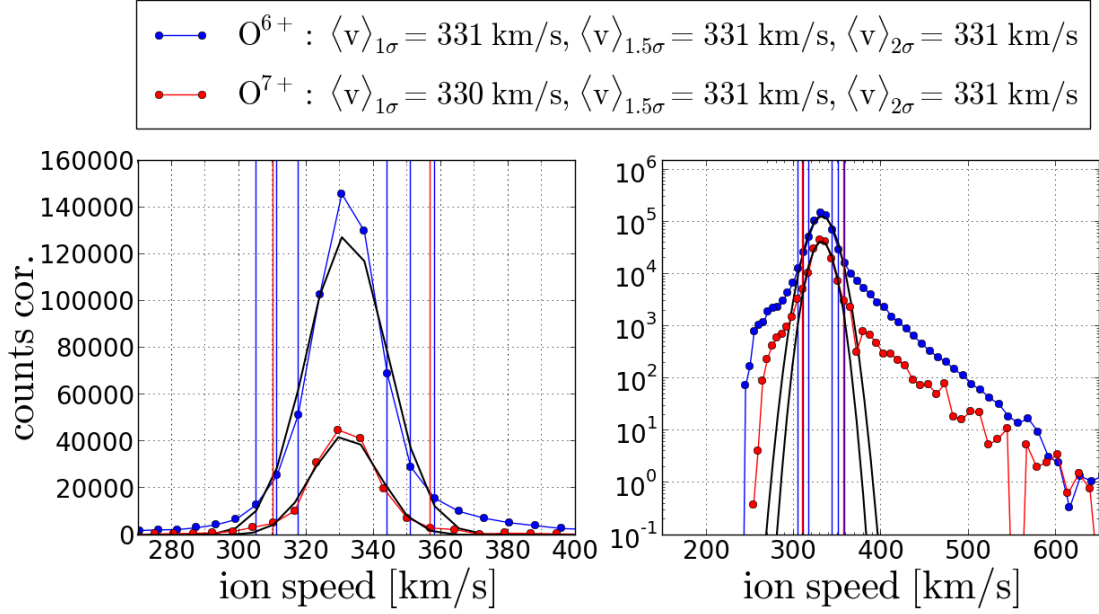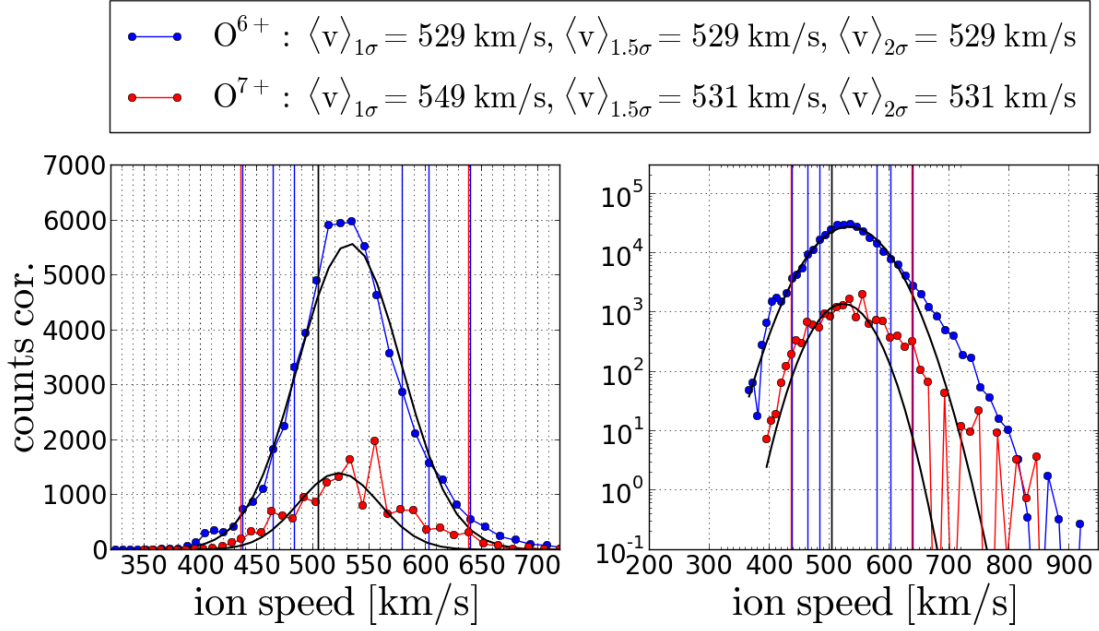
FIGURE 5.2: Long-term accumulated speed spectra for O^{6+} and O^{7+} under the condition $v_p \in [330\,\text{km/s}, 340\,\text{km/s}]$ for DOY 174-220 1996. The spectra are shown in linear (left) and logarithmic (right) count rate scale. Estimated mean speeds from the Gaussian fit: O6+: 332 km/s, O7+: 332 km/s

speed difference of 2 km/s, which is about one order of magnitude lower than the differential speeds we aim to resolve.

The main advantage of the moment calculation method compared to the fit is the higher stability in the presence of larger count rate fluctuations in the spectrum. This can be illustrated with a comparison of the two methods for the same ion species O^{6+} and O^{7+} in the fast wind case ($v_p \in [500\,\text{km/s}, 510\,\text{km/s}]$) that is shown in Figure 5.3. For the case of O^{6+} we find a similar picture as in the slow wind, with zero difference between the mean speeds obtained from the moment calculation and a slightly higher maximum difference of 3 km/s compared to the fitted mean speed. However, for O^{7+} where we have much lower count rates the fit yields a much lower speed value of 522 km/s because it most likely underestimates the high speed flank while the presumed 1σ-interval moment yields a very high speed value of 549 km/s because it is centered around the most frequent speed which is probably just the effect of a large statistical fluctuation in this case[4]. Finally, when we increase the intervals used for the moment calculation, we find identical values of 331 km/s for the 1.5σ- and 2σ-intervals which thus give a robust estimate for the mean speed in this case.

---

[4]These large count rate variations are the result of relatively large peak overlaps in ET-space and the (still) limited count statistics for less abundant ions. Note that the presented spectra show the base-rate corrected count rates that are often a factor of 20-50? higher than the truly transmitted PHA counts for ion species in the priority ranges 3 and 4. A reduction of the fluctuations can be achieved by including less ions into the fit as it is discussed in section ?.
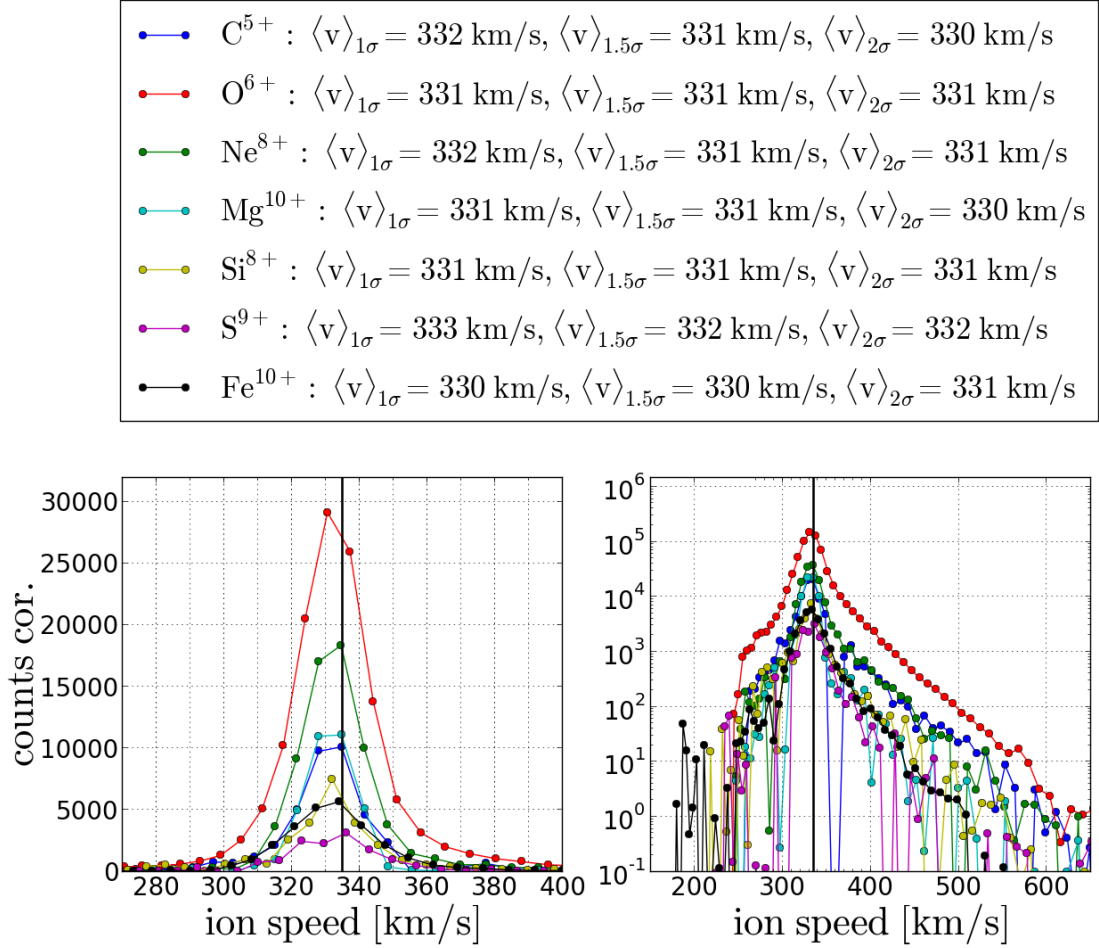
FIGURE 5.3: Long-term accumulated speed spectra for O^{6+} and O^{7+} under the condition $v_p \in [500\,\text{km/s}, 510\,\text{km/s}]$ for DOY 174-220 1996. The spectra are shown in linear (left) and logarithmic (right) count rate scale. In the linear scaling the count rates of O^{6+} are scaled down by a factor of 0.2. Estimated mean speeds from the Gaussian fit: O6+: 532 km/s, O7+: 522 km/s.

As higher count rate fluctuations appear frequently in the measured speed spectra of the minor ions in particular in the slow wind, we apply in the following the moment calculation technique for the calculation of the ion mean speeds. The standard error of the mean speed for the analyzed speed spectra is on the order of a few km/s, while the differential speeds that we aim to resolve start realistically (including systematic uncertainties of the PM and CTOF[5]) at about 15? km/s. We therefore consider two mean speed values calculated from two different σ-intervals as compatible if their difference is less than 12? km/s. On the other hand, one can consider the difference between the calculated mean speeds within the different environments as an indicator of statistical stability of the derived mean speed. This is of additional interest because the true statistical uncertainty is otherwise hard to determine since one would have to ultimately propagate it from the non-normally distributed count rate uncertainty for each bin within the ET matrix where the count statistics are even superimposed with the telemetry priority scheme.

We finally check that the artificial cut-off of the ion spectra at the ESA stop-step does not influence the calculation of the mean speeds from the given σ-intervals. As can be seen in Figures 5.2 and 5.3 the spectra reach different minimum speeds as a result of

---

[5]see section 5.?

the ions' different m/q values with the O^{7+} scan finishing at a higher minimum speed. However, we note that the observed minimum speed corresponds to the absolute maximum Epq-step reached within all valid cycles which belongs to Epq-step 95 in the selected slow wind range and to step 74 in the fast wind range as can be seen in Figure 5.1. The important speed for O^{7+} in the slow wind is $v_{stop,slow} = 281$ km/s which belongs to our selected minimum stop-step 90, and $v_{stop,fast} = 436$ belonging to stop-step 68 in the fast wind. While in the slow wind due to the cold plasma the lower boundary of the 2σ-environment ($v_{2\sigma} \approx 310$ km/s) is far away from $v_{stop,slow}$, the boundary in the hotter fast wind ($v_{2\sigma,fast} = 436$) just equals the critical value $v_{stop,fast}$. Finally, we find a drop of the count rate starting for both ions shortly after the respective stop-speed is reached, which is not physical but just the end of the Epq-scan for a rapidly increasing number of cycles between Epq-step 90 and 95 in the slow wind and 68 and 74 in the fast wind. For O^{6+} the same thing happens at lower speeds and is thus less critical. In fact O^{7+} is the ion with the lowest mass-per-charge ($m/q = 2.29$ amu/e) that we include in the analysis and is therefore supposed to be the most crucial case, but we also applied the same check to all analyzed physically meaningful ion spectra to exclude that ion species with slightly higher mass-per-charge values are affected in case they show considerably hotter distributions than O^{7+}.

5.4 Slow Wind Speed Spectra

high count rates allow in a first instance for systematic reasonability checks of the derived speed spectra for all included ion species by analyzing the following points for each species such as - the measured relative abundance compared to the most abundant solar wind ion species - the measured relative abundance compared to the other charge states of the same element - the observed shape of the speed distribution in particular the level of count rate fluctuations between the speed bins v_j that correspond to the scanned Epq-steps

In Figure 5.4 we show the accumulated long-term spectra for the best-resolved[6] charge states of the elements carbon, oxygen, neon, magnesium, silicon, sulfur, and iron in linear (left) and logarithmic (right) count rate scale. Note that in the linear representation we scaled for better comparison of the spectral shape the count rate of O^{6+} with a factor of 0.2 and the count rates of C^{5+}, Ne^{8+} and Mg^{10+} with a factor of 0.5. We find for

---

[6]In most cases the best-resolved charge state of a given element is the one with the highest relative abundance in the given solar wind speed regime (such as O^{6+}, Ne^{8+}, Mg^{10+}, or Fe^{10+}), but in some cases a slightly less abundant charge state is even better resolved due to its dominant count rate compared to the ion species in its close environment in the ET-matrices while the more abundant species is located close to an even more abundant species (as it is the case for Si^{8+} and Si^{9+}).

FIGURE 5.4: Long-term accumulated speed spectra for C^{5+} - Fe^{10+} under the condition $v_p \in [330\,\text{km/s}, 340\,\text{km/s}]$ for DOY 174-220 1996. The spectra are shown in linear (left) and logarithmic (right) count rate scale. In the linear scaling the count rates of C^{5+}, O^{6+}, Ne^{8+}, and Mg^{10+} are scaled down by a factor of 0.5, 0.2, 0.5, and 0.5, respectively.

all depicted ions a very similar spectral shape as they all consist of an approximately Maxwellian core and an extended suprathermal tail as described in the previous section 5.3. For most ions we can also find the signature of a subthermal tail, although one has to be careful with the spectral comparison at low speeds as the different species are cut-off at different speeds due to the interruption of the Epq-stepping as explained above, as well as due to the occurrence of He^{2+} random coincidences in particular for several silicon and iron charge states (see section **??** and the more detailed description of the iron results in this section).

We note that the suprathermal tail can be measured to about 500-600 km/s for the presented ion species and follows a power law which has a slightly steeper slope for the very heavy ions Mg^{10+} - Fe^{10+} compared to the lighter heavy ions C^{5+} - Ne^{8+}. In general the observed power law tails are a signature of stochastic acceleration (refs?, refs?)

that is happening most likely at shocks in the inner heliosphere, which during periods of low solar activity are formed mainly at Corotating interactions (CIRs). Due to this difference in the underlying acceleration mechanism that can energize a small fraction of the ions up to several tens of MeV/nuc [?], these tails are not further analyzed in this work but will be investigated in the future within the context of particle shock acceleration from solar wind energies to suprathermal energies and beyond e.g. in a combined study with the SOHO/STOF sensor.

In the spectral cores, the calculated mean speeds from the 1σ-, 1.5σ- and 2σ-intervals centered around the most frequently measured speeds show very little variation for each of the selected ion species with a maximum difference of $2\,\mathrm{km/s}$. Thus, we find fairly symmetrical cores for all of these ion species which yields a well-defined mean speed calculated with the given method over these extended core intervals which ensures a meaningful comparison between the different ion species. For all shown ion species in Figure 5.4 we calculate mean speeds between 330 and $333\,\mathrm{km/s}$ which is clearly comparable to the mentioned differences in mean speed calculated from the different σ-intervals and we can thus conclude that within the measurement accuracy the measurements are consistent with the hypothesis that all these species stream at the same speed in the analyzed slow wind case $v_p \in [330\,\mathrm{km/s},\ 340\,\mathrm{km/s}]$. On the other hand, when we calculate the mean speed of the protons for all cycles in this given speed range (both density-weighted and not density-weighted) we find a mean speed of $335\,\mathrm{km/s}$ as one would expect for a large number of cycles. The proton mean speed is marked by the black vertical line in Figure 5.4. Thus, if one only considers the small statistical spread between the calculated ion species mean speeds[7] one could conclude that the heavy ion species are streaming even a bit slower than the protons in the slow solar wind, but in fact the observed difference of maximum $5\,\mathrm{km/s}$ between the mean heavy ion and proton speeds is on the order of the estimated systematic measurement accuracies both in the CTOF and PM measurements as we discuss below.

Before continuing with the comparison of the individual charge states of each element, we conduct a plausibility check of the observed relative abundances, not only to ensure one last time the correct assignment also of the less abundant elements in the ET-matrix, but also to proof that the base-rate correction yields reasonable ratios between the strongly corrected low-mass ions and only weakly corrected high-mass ions and thus works properly. In the last column of Table 5.1 we show the long-term slow-wind abundances measured with CTOF for the ion species C^{5+} - Ni^{9+} relative to O^{6+} over the period DOY 174-220 in 1996. As before, these charge states are selected as a sample of the best resolved ion charge states for each of the 9 analyzed elements other

---

[7]The 1-sigma standard error of the mean speed for all shown speed spectra is even below the spread between the calculated ion species on the order of $\leq 1\,\mathrm{km/s}$ for all shown species due to the high counting statistics.

than oxygen. We compare these measured relative abundances with the predictions that we derive from the semi-empirical approach of observed elemental abundances in the corona [?] and theoretically calculated charge state abundances for an estimated coronal temperature [?], that we already used in section **??**. Thus, the predicted relative ion abundances in the second and third column of Table 5.1 are calculated as

$$\left(\frac{N_{ion}}{N_{O^{6+}}} \right)_{pred} = \frac{N_{el,ion} \cdot N_{q,ion}(T_{el})}{N_O \cdot N_{q=6}(T_{el})} \tag{5.5}$$

where $N_{el,ion}$ and N_O are typical elemental abundances obtained from remote sensing measurements in the corona after **??** while $T_{el} = 10^{6.1}\,\text{K}$ and $T_{el} = 10^{6.2}\,\text{K}$ represent approximately the lower and upper limit of observed coronal (electron) temperatures range during subperiods of slow solar wind at the time of our measurements. These are calculated as the iron freeze-in temperatures derived from the in-situ iron charge state abundances by [?] who used for their study the identical SOHO/CELIAS/CTOF iron PHA count data that we use in this work during the time period ? - ?. We see that

Ratio:	Prediction		CTOF
N_{O6+} /	$\log(T_{el}/K) = 6.1$	$\log(T_{el}/K) = 6.2$	
$N_{C^{5+}}$	4	7	7
$N_{N^{6+}}$	18	12	17
$N_{Ne^{8+}}$	5	4	4
$N_{Mg^{10+}}$	7-22*	5-14*	7
$N_{Si^{8+}}$	14-41*	40-120*	21
$N_{S^{9+}}$	76	78	60
$N_{Ca^{10+}}$	124-372*	171-513*	250
$N_{Fe^{10+}}$	17-52*	28-85*	30
$N_{Ni^{9+}}$	210-631*	349-1047*	500

TABLE 5.1: Ion species abundances relative to O^{6+}: predicted vs. measured with CTOF in this work. The predictions are derived from the combination of the observed elemental abundances in the solar corona **??** and the Arnaud and Rothenflug model **??** for ionization and recombination rates at a given plasma electron temperature T_{el}. The predictions denoted with * have a large uncertainty range due to the observed discrepancies between coronal and solar wind abundances which are commonly explained with the FIP effect which might enrich the listed low-FIP elements up to a factor of 3 in the solar wind **??**. The estimates of the electron temperature T_{el} in the coronal source region of the slow solar wind are the calculated freeze-in temperatures obtained from an earlier CTOF study during the same time interval as our measurement by [Aellig.1998]?. The relative CTOF abundances are measured without any correction for the elemental instrumental efficiency and have an accuracy of about 10 %. For further details see text.

except for the sulfur charge state S^{8+} all selected ion species are observed with a relative abundance compared to O^{6+} that is within the expected range determined by the obtained coronal temperatures during the same? measurement period. When strictly

following the predictions we should observe about 20 % less S^{8+} and thus we might overestimate sulfur compared to its adjacent elements silicon and magnesium. Yet, we consider the overall relative charge state abundance comparison as acceptable because 1) the CTOF abundances are derived without elemental efficiency corrections due to the scarce preflight-calibration data (see section **??**), 2) the observed differences are comparable to the deviations and uncertainties of typical heavy minor measurements both in the corona and solar wind [**? ?**] and 3) the shown deviations are unlikely to cause fundamental changes in the mean speed of the ion species (see again section **??**). We restrict the comparison here to the slow wind as we have much higher integrated counting statistics in the slow wind so that here we can also determine more reliably the count rates of the less abundant ion species. However, as both the calibration and the base-rate correction are in principal independent of the solar wind conditions there is no reason to expect strongly biased count assignment only in the fast wind and we can also use the observed shift in the mean charge states of the different elements between slow and fast wind to check the fast wind abundances for consistency (maybe later in the fast wind?!).

In the following, we compare for a given analyzed element the measured speed spectra of its best-resolved charge states among each other. We discuss explicitly the charge states of carbon, oxygen, silicon and iron that alone cover a wide range in mass and mass per charge. A larger, representative sample of measured long-term speed spectra of ion species belonging to all ten analyzed elements carbon - nickel are shown in appendix D.

As expected, we can see for the case of *carbon* in Figure 5.5 that C^{4+} is much less abundant in the measured slow wind than C^{5+}. Despite the small asymmetry in the core, we find for C^{4+} very similar mean speeds between 330 km/s and 334 km/s calculated from all three different σ-intervals. As we can see, these speeds are also very close to the calculated mean speeds of C^{5+} that lie between 330 and 332 km/s. When we have a look in the logarithmic representation, we find that the spectra of C^{4+} and C^{5+} also resemble each other over a wider speed range. The spectrum of C^{6+} is not analyzed here, due to the strong influence of the Epq-stepping interruption on it as well as due to the contamination with He^{2+} pile-up counts (see section**??**).

As discussed already in the method description for *oxygen* we find very similar mean speeds for O^{6+} and O^{7+} The spectrum of O^{8+} is not analyzed here as it has again the same mass-per-charge as He^{2+} and thus is biased by the ESA cut-off as well, while O^{5+} has a relatively low abundance and cannot be separated well from the more abundant C^{4+} peak.

For *silicon* we show in Figure 5.6 the best-resolved charge states Si^{7+} - Si^{11+}. Si^{6+} has a
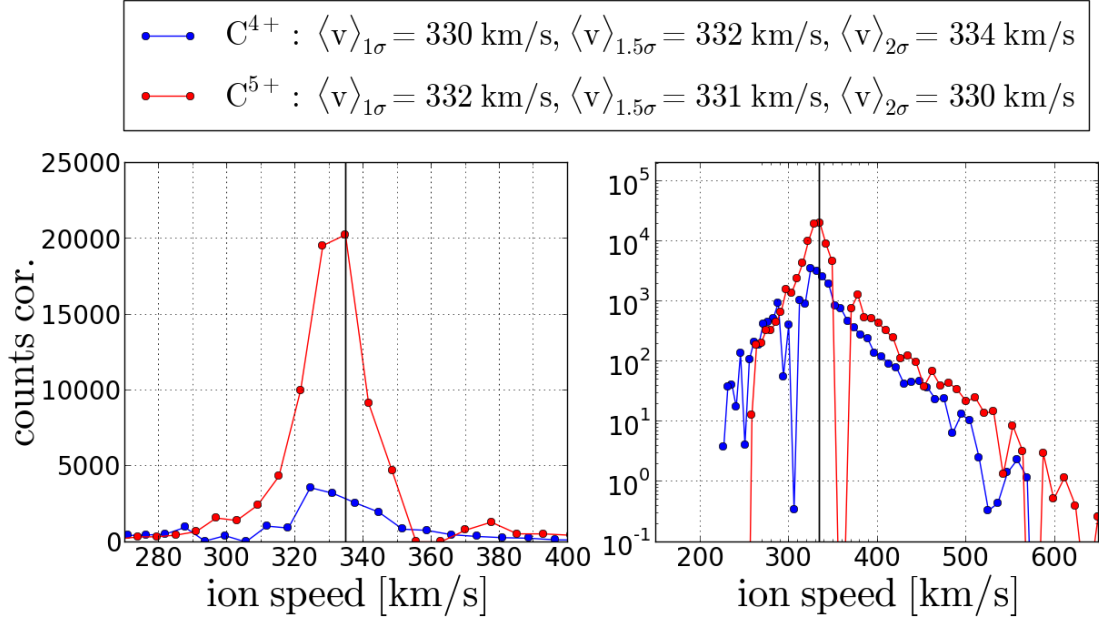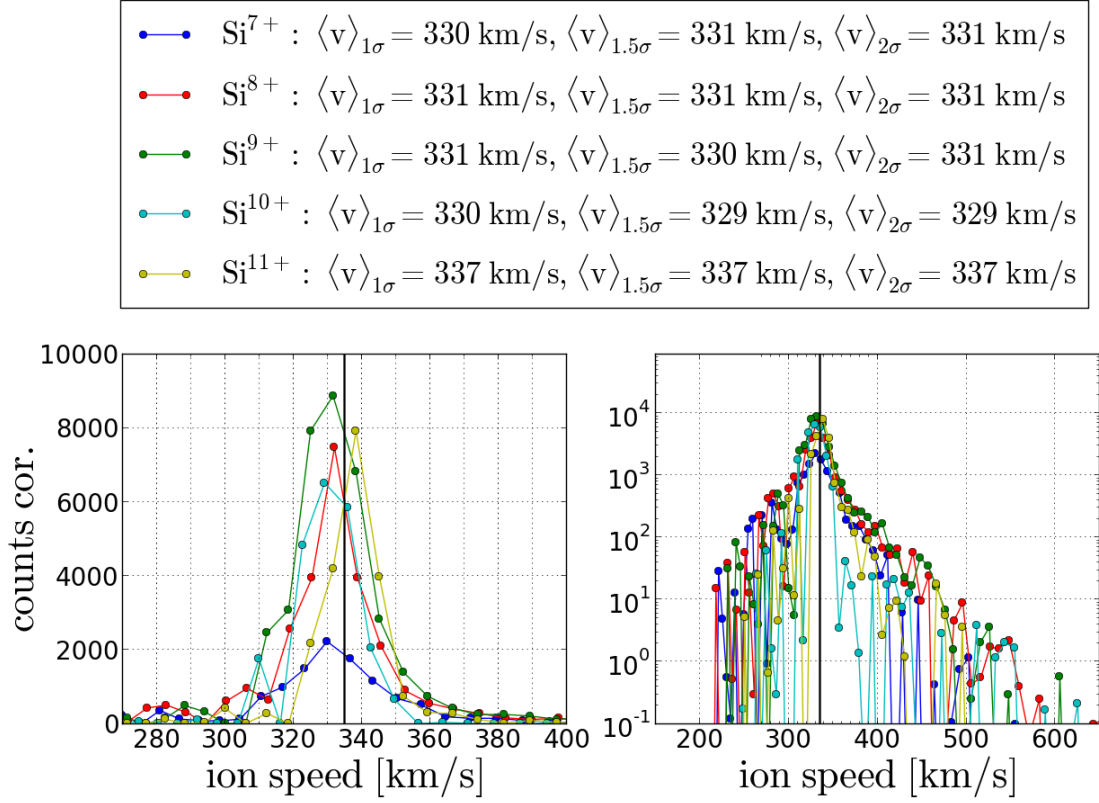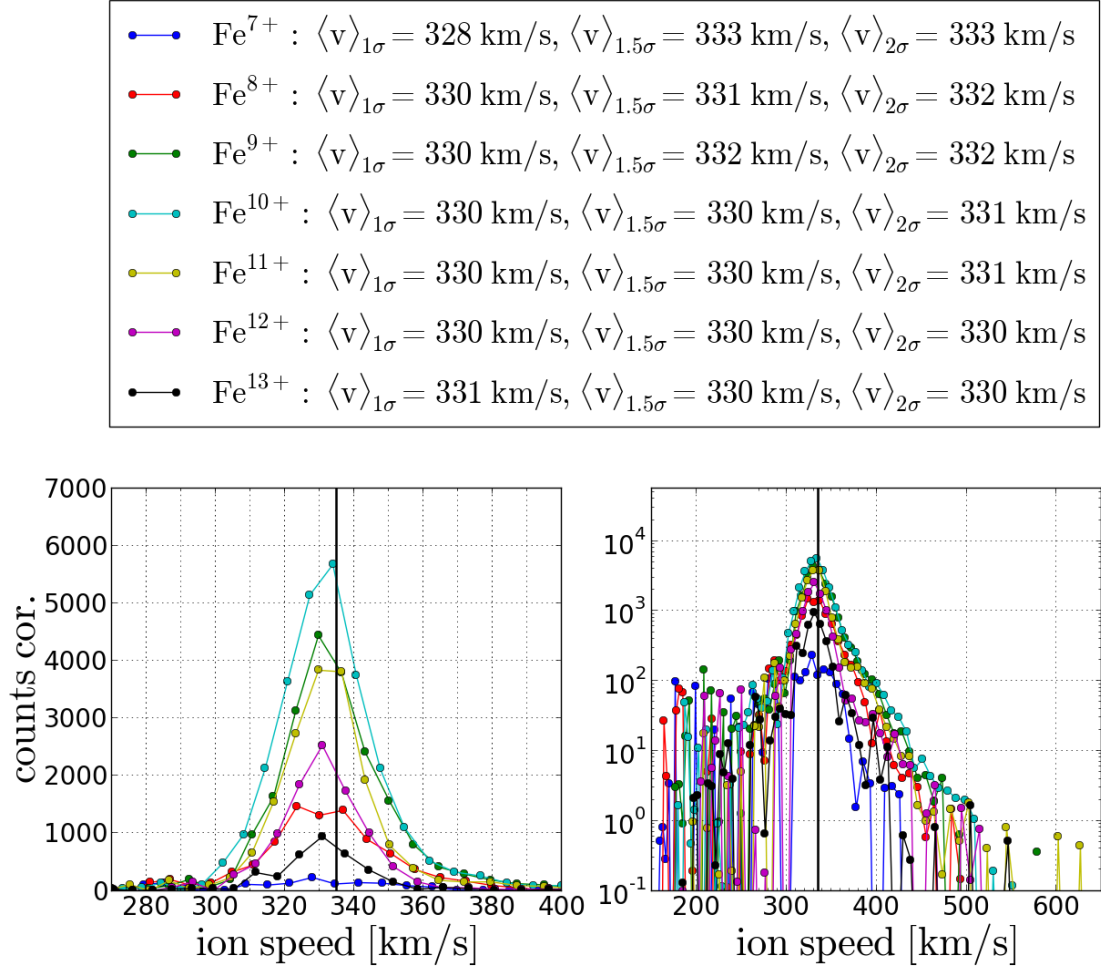
FIGURE 5.5: Long-term accumulated speed spectra for C^{4+} - C^{5+} under the condition $v_p \in [330\,\text{km/s}, 340\,\text{km/s}]$ for DOY 174-220 1996. The spectra are shown in linear (left) and logarithmic (right) count rate scale.

low abundance in the slow wind while the spectrum of Si^{12+} shows large fluctuations in its core so that there is a clear interference with other adjacent more abundant ion species such as Mg^{10+}. We see that the the depicted silicon species show a reasonable charge state distribution centered around the most abundant species Si^{9+}, except for Si^{11+}, that is slightly over-represented compared to Si^{10+}. Interestingly, this ion species is also the only one that shows a significantly higher mean speed of 337 km/s compared to the other silicon charge states that are all measured at 330 ± 1 km/s, which fits well into the mean speeds of most other major charge states of the other discussed elements. As the Si^{11+} spectrum does not show any major signatures of irregularities or interference with other adjacent species it should be investigated closer in the future. In the case of *iron*, we show in Figure 5.7 the spectra of the most abundant charge states Fe^{7+} - Fe^{13+}. In the left panel we can see a very similar spectral core shape for Fe^{7+} - Fe^{12+}. For Fe^{13+} we find a wider distribution, which however might be influenced by to adjacent species at the flanks as the respective Fe^{13+} count rates are relatively low. Nonetheless, all spectra show very similar mean speeds both considering the different calculation intervals for each of the species as as well as the mean speeds among the different charge states which very between 328 and 333 km/s.

FIGURE 5.6: Long-term accumulated speed spectra for Si^{7+} - Si^{11+} under the condition $v_p \in [330\,\text{km/s}, 340\,\text{km/s}]$ for DOY 174-220 1996. The spectra are shown in linear (left) and logarithmic (right) count rate scale.

Comment shortly on other elements (2 sentences) and on criteria imposed on the ion species spectra (2 sentences , after fast wind is evaluated)

In Figure 5.8 we show the mean speeds that we calculated just as the arithmetic mean[8] of the derived 1σ-, 1.5σ-, and 2σ-interval mean speeds for all species that fulfilled the above criteria, which results in the shown 29 species for the elements carbon - iron. We can see that out of the resulting 28 ion species only Ne^{7+} is outside a $5\,\text{km/s}$ tolerance interval, that also represents the range of filtered proton speeds. We find for the whole sample that the most frequently measured mean speed is $331\,\text{km/s}$ and the mean speed is $332\,\text{km/s}$. As already observed for the more abundant ion species, this might statistically indicate that the heavy minor ions stream on average a few km/s slower than the solar wind protons, but this effect can easily be created by a small mismatch of the inter-calibration between the SOHO/CELIAS CTOF sensor and the Proton Monitor as a difference of less than $5\,\text{km/s}$ in the slow wind is well within the 1σ-standard deviation of the SOHO/CELIAS/PM speed compared to the WIND/SWE proton speeds shown in Figure 2.12. As explained in section **??** there are also other uncertainties in

---

[8]With exception, when one of the 3 mean speed values is off more than $10\,\text{km/s}$? from both of the others. In this case, the mean speed is calculated from the remaining two values.

FIGURE 5.7: Long-term accumulated speed spectra for Fe^{7+} - Fe^{13+} under the condition $v_p \in [330\,\mathrm{km/s}, 340\,\mathrm{km/s}]$ for DOY 174-220 1996. The spectra are shown in linear (left) and logarithmic (right) count rate scale.

the proton and heavy ion measurements that are on the order of a few km/s such as the ion-specific instrumental detection efficiencies and small geometry effects that we cannot take into account so that differential speeds.

The largest source of systematic uncertainty within the CTOF instrument is the utilized response model. In a first instance we investigate to which extent the measured speeds of the analyzed charge states of carbon, oxygen, neon, silicon and iron vary when we conduct the exact same analysis as described above with the (Kappa-Moyal) reduced stable response model that we introduced in section **??** and which contains 28 ion species in the applied fits belonging to the five aforementioned elements only. In section 4.30**?** in the appendix we show a representative sample of the derived long-term speed spectra for the reduced stable response model (RSRM)**?** model under the same slow-wind filter condition $v_p \in [330\mathrm{km/s}, 340\mathrm{km/s}]$ integrated over the same measurement period DOY 174-220. When we apply the same criteria to these speed
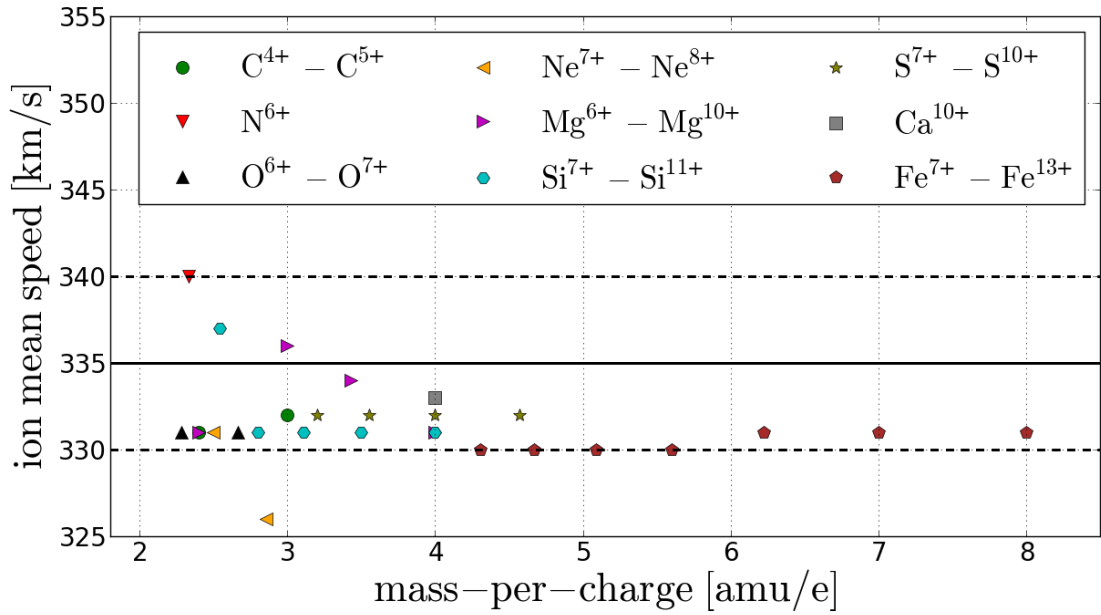
FIGURE 5.8: Long-term heavy Ion mean speeds as a function of the ions' mass-per-charge derived from the CTOF Full Stable Response Model for DOY 174-220 1996 under the condition $v_p \in [330\,\text{km/s}, 340\,\text{km/s}]$, Mg9+ is not included because of count rate criterion (compare Mg9+)
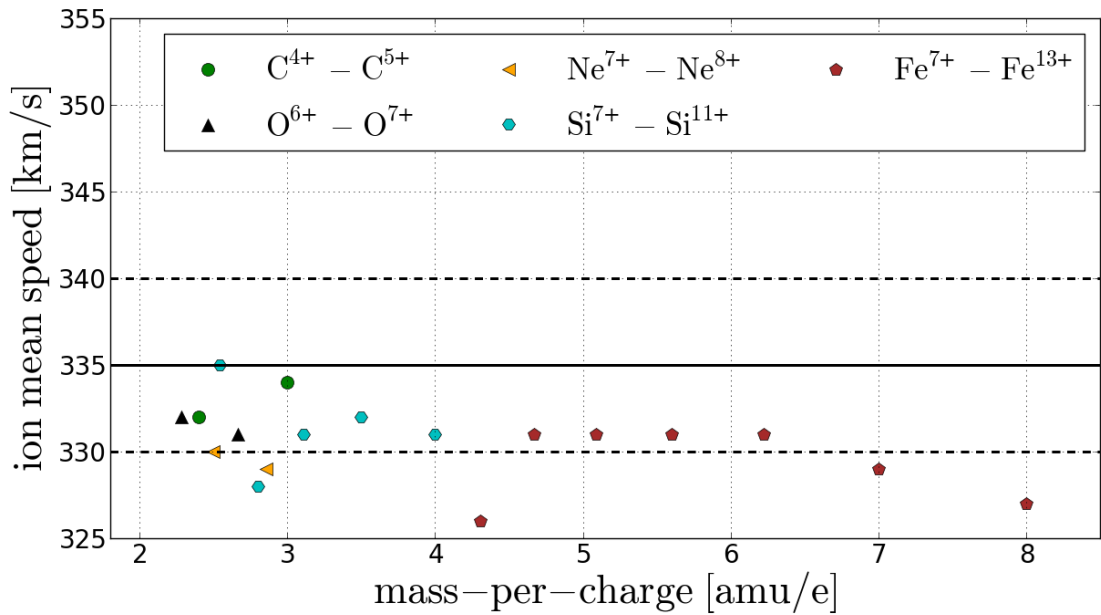
FIGURE 5.9: Long-term heavy Ion mean speeds as a function of the ions' mass-per-charge derived from the CTOF Reduced Stable Response Model for DOY 174-220 1996 under the condition $v_p \in [330\,\text{km/s}, 340\,\text{km/s}]$

spectra as above for the full model, and again calculate the mean ion speed as the arithmetic mean of the 1σ-, 1.5σ- and 2σ-interval mean speeds we obtain the following ? minor ion mean speeds depicted in Figure 5.9.

On the whole we find very similar speeds compared to Figure 5.9 so that the most frequently measured mean speed is still 331 km/s, the overall measured mean minor ion speed of the sample has only changed by about 1 km/s to 331 km/s and for all shown ion species the change in their individual mean speeds is below 5 km/s. This means that no significant systematic bias (on the order of the anticipated differential speed magnitude) can be introduced (in the slow wind case) by a (systematic) reduction of the ion set. This observation will be used in the next chapter for the analysis of the short-term data samples that often do not contain enough count statistics to evaluate them with the full response model (maybe better after the fast wind!). However, for certain ion species the shift in the measured ion mean speed due to the response model change is larger than for others. The biggest shifts can be observed for Fe^{7+} (-4 km/s), Fe^{13+} (-4 km/s), Ne^{7+} (+3km/s) and Si^{10+} (-3 km/s). As expected, these ion species have relatively low abundances compared to at least one of their adjacent ion species which can be a charge state of the same element such as for Fe^{7+} (Fe^{8+}) and/or a prominent ion species such as for Fe^{13+} (Si^{7+},Fe^{12+}), Ne^{7+} (primarily O^{6+}), and Si^{10+} (primarily O6+). On the other hand, for the dominant ion species such as O^{6+}, C^{5+}, or Fe^{10+} the magnitude of the observed change in ion speed due to the response model reduction is below 2 km/s in the analyzed slow wind case, so that as expected, they yield the most reliable speed measurements.

5.5 Fast Wind Speed Spectra

In an analog manner to the slow wind measurements we present in the following the long-term speed spectra for the fast wind case that is given by the filter condition $v_p \in [500 km/s, 510 km/s]$ as explained in section **??**. In Figure 5.10 we show the fast-wind long-term speed spectra for the same charge states as in Figure 5.4. The spectra are shown in linear (left) and logarithmic (right) count rate scale and again in the linear representation the count rates of C^{5+}, O^{6+}, Ne^{8+}, and Mg^{10+} are scaled down by a factor of 0.5, 0.2, 0.5, and 0.5, respectively. As can be seen the measured count rates are up to one order of magnitude lower in the fast wind spectra compared to Figure 5.4 which is mainly to the fact that we have a much lower number of measurement cycles in the fast wind during the whole measurement period, but also due to lower particle densities in the fast wind. The lower count rates, (that are already the base-rate corrected count rates and thus in reality are derived from even fewer statistically independent

C^{5+} : $\langle v \rangle_{1\sigma} = 531$ km/s, $\langle v \rangle_{1.5\sigma} = 529$ km/s, $\langle v \rangle_{2\sigma} = 529$ km/s

O^{6+} : $\langle v \rangle_{1\sigma} = 529$ km/s, $\langle v \rangle_{1.5\sigma} = 529$ km/s, $\langle v \rangle_{2\sigma} = 529$ km/s

Ne^{8+} : $\langle v \rangle_{1\sigma} = 531$ km/s, $\langle v \rangle_{1.5\sigma} = 536$ km/s, $\langle v \rangle_{2\sigma} = 537$ km/s

Mg^{10+} : $\langle v \rangle_{1\sigma} = 513$ km/s, $\langle v \rangle_{1.5\sigma} = 519$ km/s, $\langle v \rangle_{2\sigma} = 531$ km/s

Si^{8+} : $\langle v \rangle_{1\sigma} = 540$ km/s, $\langle v \rangle_{1.5\sigma} = 539$ km/s, $\langle v \rangle_{2\sigma} = 532$ km/s

S^{9+} : $\langle v \rangle_{1\sigma} = 508$ km/s, $\langle v \rangle_{1.5\sigma} = 508$ km/s, $\langle v \rangle_{2\sigma} = 498$ km/s

Fe^{10+} : $\langle v \rangle_{1\sigma} = 524$ km/s, $\langle v \rangle_{1.5\sigma} = 526$ km/s, $\langle v \rangle_{2\sigma} = 528$ km/s
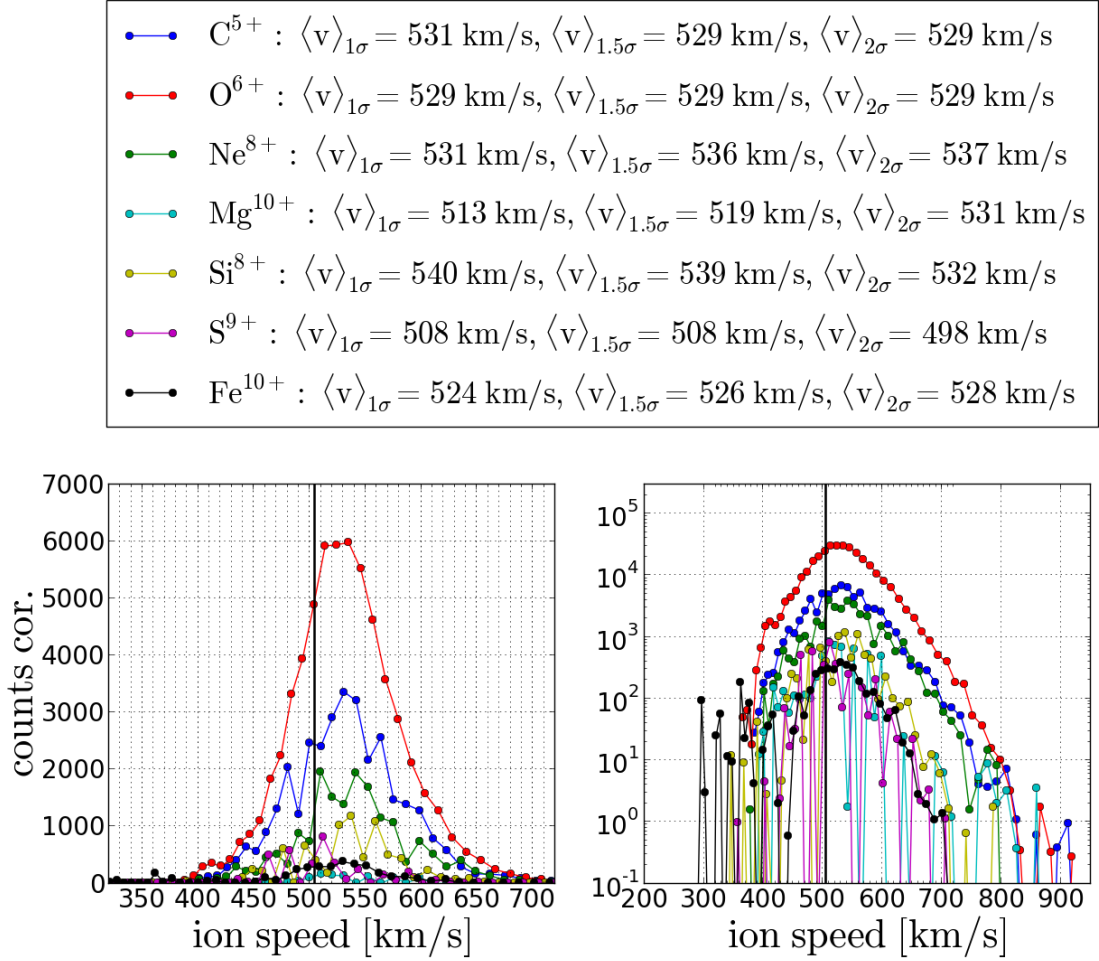
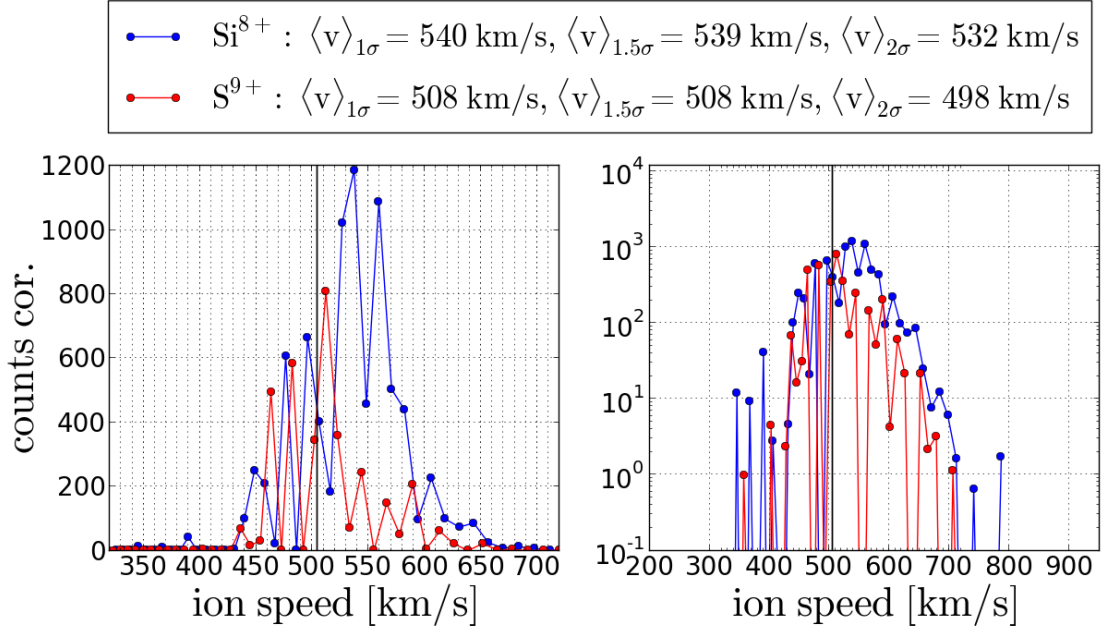FIGURE 5.10: Long-term accumulated speed spectra for C^{5+} - Fe^{10+} under the condition $v_p \in [500\,\text{km/s}, 510\,\text{km/s}]$ for DOY 174-220 1996. The spectra are shown in linear (left) and logarithmic (right) count rate scale.In the linear scaling the count rates of C^{5+}, O^{6+}, Ne^{8+}, and Mg^{10+} are scaled down by a factor of 0.5, 0.2, 0.5, and 0.5, respectively.

transmitted PHA counts) lead to stronger fluctuations in the spectra even among the more prominent ion species as can be recognized in Figure 5.10. For the less abundant elements such as sulfur, calcium or nickel these count rate fluctuations reach the magnitude of the actual count rate even in the core of their distribution[9].

In principal, we find two main differences for the measured fast wind heavy ion speed spectra compared to the slow wind case, which are 1) the larger widths of the distributions that correspond to higher kinetic temperatures and 2) the higher mean speeds for the minor ion species compared to the mean proton speed ($\langle v_p \rangle = 505\,\text{km/s}$) marked again as the black vertical line. In the following the mean speeds are again calculated as the first moment of the 1σ, 1.5σ and 2σ- intervals as explained in section 5.3.

---

[9], so that it is not possible to resolve these least abundant elements with the necessary accuracy and we restrict therefore the analysis to the elements carbon, oxygen, neon, magnesium, silicon and iron?.
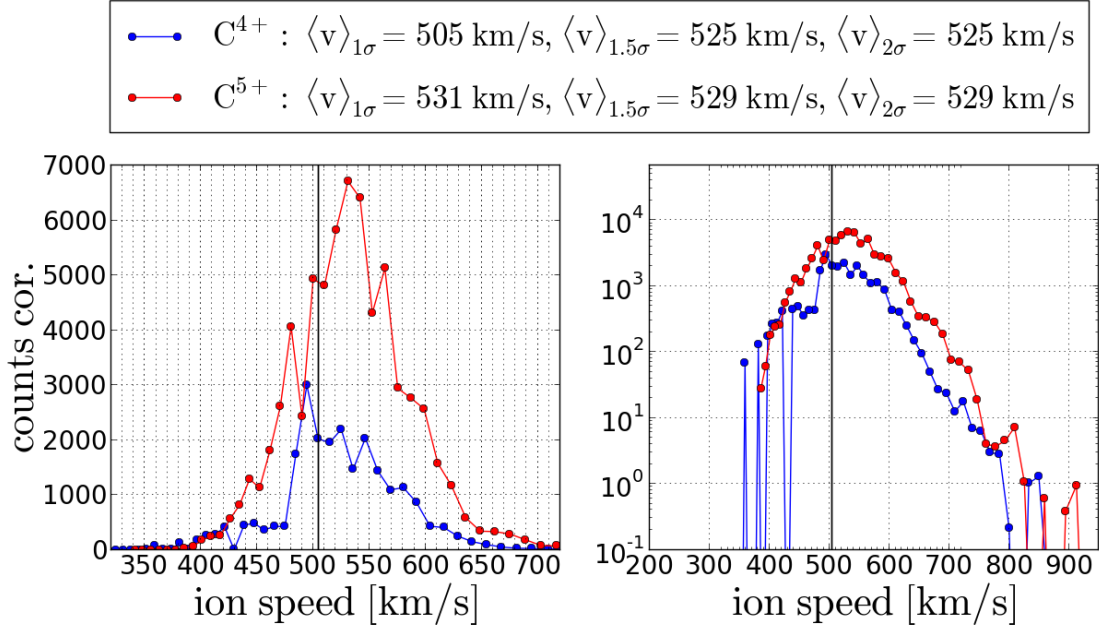
FIGURE 5.11: Long-term accumulated speed spectra for C^{4+} - C^{5+} under the condition $v_p \in [500\,\mathrm{km/s}, 510\,\mathrm{km/s}]$ for DOY 174-220 1996. The spectra are shown in linear (left) and logarithmic (right) count rate scale.

In general, we observe that the differences between the derived mean speeds of the three different σ-intervals are higher in the fast wind which can be explained by the lower count rates in combination with the wider speed distributions. However, in detail we can see from Figure 5.10 that the calculated speeds deviate less for certain ion species such as for C^{5+}, O^{6+}, and Fe^{10+} ($< 5\,\mathrm{km/s}$) than for others such as Ne^{8+}, Mg^{10+}, Si^{8+}, S^{8+} (5-10 km/s) with the largest differences calculated for S^{8+} which coincides with the highest relative fluctuations in the core of the S^{8+}. When we have a look at the differential speeds in Figure 5.10 we find that the species with the most stable/robust mean speeds show differential speeds of about 20 to 25 km/s, while the group with less stable speeds show a wider spread of -7 to 35 km /s with only S^{8+} showing negative differential speeds. To study these differential speeds in the fast wind case in greater detail we analyze in the following the long-term speed spectra of of the most abundant carbon, oxygen, silicon and iron charge states in greater detail in analogy to the slow wind case. Again, an even wider sample of ion speed spectra is shown in section ? in appendix D also including the spectra of less abundant elements such as sulfur and calcium.

In Figure 5.11 we show the long-term integrated speed spectra of the *carbon* charge states C4+ and C5+ for the time period 174-220 1996. We see that C5+ is still more abundant in the given fast wind $v_p \in [500\,\mathrm{km/s}, 510\,\mathrm{km/s}]$ than C4+ which indicates after ?? a kinetic temperature of around $T_{el} \approx 10^{6.0}\,\mathrm{K}$, that is in reasonable agreement with
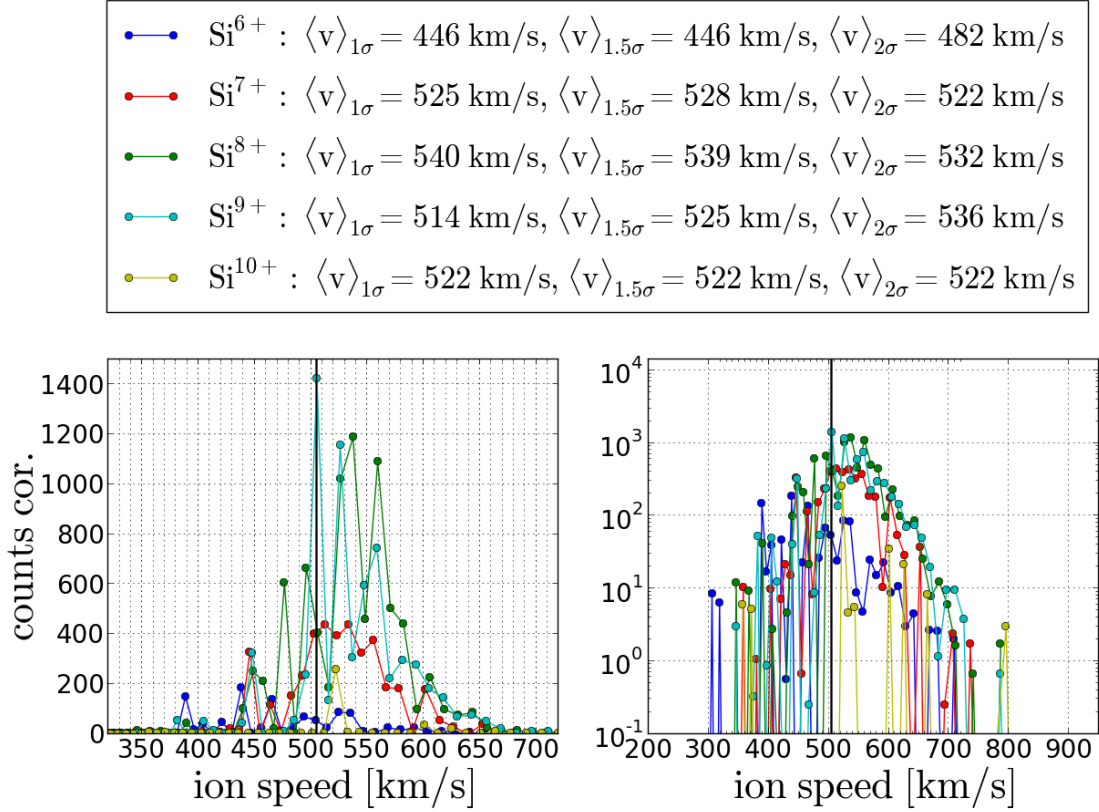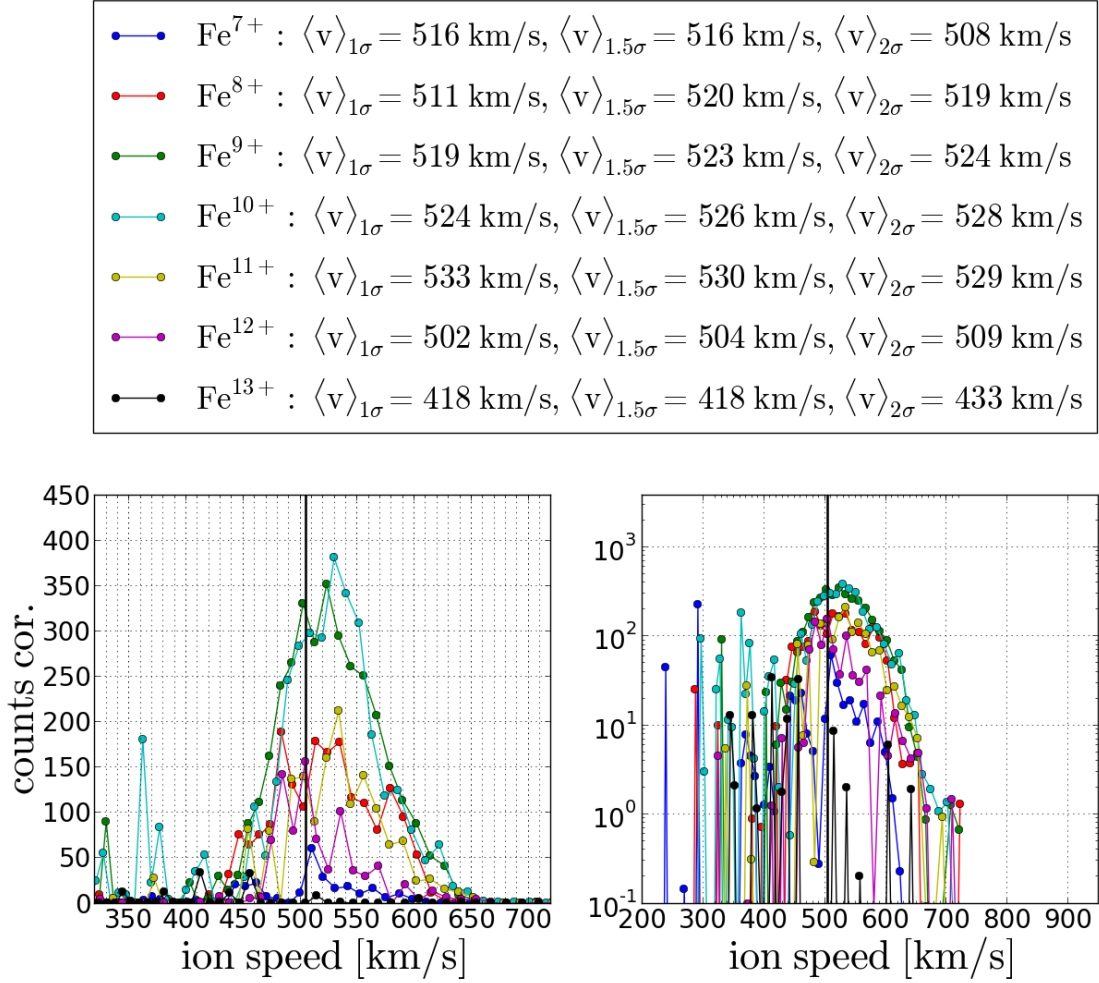
FIGURE 5.12: Long-term accumulated speed spectra for Si^{6+} - Si^{10+} under the condition $v_p \in [500\,\text{km/s}, 510\,\text{km/s}]$ for DOY 174-220 1996. The spectra are shown in linear (left) and logarithmic (right) count rate scale.

most other observed elemental charge state distributions in this fast wind case. Also in the fast wind the spectrum for C4+ and C5+ consist of approximately Maxwellian distributions in the core of the VDF, but from 650 km/s (which corresponds to about 2.5σ) on the suprathermal tail is clearly observed. In the core C4+ looks more asymmetric than C5+ with the maximum count rate at 490 km/s. Yet, the observed asymmetry is mainly due to an exceptionally high count rate at this single speed bin, which causes also the (apparent) low mean speed for the 1σ-interval, as by definition the reference speed for the calculation is the most frequently measured speed. As the number of included speed bins increases for the 1.5σ- and 2σ-interval respectively, we see that the calculated mean speeds for C4+ of 525 km/s are much closer to the average calculated mean speed of C5+ of about 530 km/s. This is very similar to the measurement of the *oxygen* ions O6+ and O7+ in Figure 5.3 with the only difference that in the case of C4+ the most frequently measured speed that dominates the calculation within the 1σ-interval lies at the low-speed flank of the distribution.

In the case of *silicon* we see that for the given proton speed interval only Si7+, Si8+ and Si9+ are measured with sufficient count statistics to calculate the mean speeds from the

FIGURE 5.13: Long-term accumulated speed spectra for Si^{6+} and S^{9+} under the condition $v_p \in [500\,km/s, 510\,km/s]$ for DOY 174-220 1996. The spectra are shown in linear (left) and logarithmic (right) count rate scale.

Maxwellian approximation of their distribution cores. We further recognize that as expected the relative abundances of the lower charge states are higher compared to solar wind case, so that e.g. Si8+ and Si9+ are now measured with comparable count rates. While Si7+ shows relatively small count rate fluctuations in the core and we therefore measure relatively consistent mean speeds for the 1σ-, 1.5σ- and 2σ-interval, the spectra of Si8+ and Si9+ show larger fluctuations and thus we also find a larger spread in their mean speeds between 514 and 540 km/s.

The origin of the fluctuations can be better understood from the comparison of adjacent ion species with comparable abundance and large overlap such as Si8+ and S9+ that are depicted in Figure 5.13 and show pronounced fluctuations. We can see in particular from the linear plot in the left panel that the count rates of Si8 and S9 alternate in an anti-correlated pattern from one speed-bin to the next which can be observed best at their lower speed flank. As both species have very similar mass-per-charge, the same speed bin relates to the same Epq-step so that the overall existing counts in the ET-matrix environment of both species are assigned (almost) entirely to one species in one Epq-step and then (almost) entirely in the subsequent Epq-step to the other species, which is not likely to be a true physical feature of the distributions. Thus, in this Epq-step range the two species cannot be resolved well enough under the given count statistics in the fast wind, despite the systematic calibration approach. While on

Fe^{7+} : $\langle v \rangle_{1\sigma} = 516$ km/s, $\langle v \rangle_{1.5\sigma} = 516$ km/s, $\langle v \rangle_{2\sigma} = 508$ km/s

Fe^{8+} : $\langle v \rangle_{1\sigma} = 511$ km/s, $\langle v \rangle_{1.5\sigma} = 520$ km/s, $\langle v \rangle_{2\sigma} = 519$ km/s

Fe^{9+} : $\langle v \rangle_{1\sigma} = 519$ km/s, $\langle v \rangle_{1.5\sigma} = 523$ km/s, $\langle v \rangle_{2\sigma} = 524$ km/s

Fe^{10+} : $\langle v \rangle_{1\sigma} = 524$ km/s, $\langle v \rangle_{1.5\sigma} = 526$ km/s, $\langle v \rangle_{2\sigma} = 528$ km/s

Fe^{11+} : $\langle v \rangle_{1\sigma} = 533$ km/s, $\langle v \rangle_{1.5\sigma} = 530$ km/s, $\langle v \rangle_{2\sigma} = 529$ km/s

Fe^{12+} : $\langle v \rangle_{1\sigma} = 502$ km/s, $\langle v \rangle_{1.5\sigma} = 504$ km/s, $\langle v \rangle_{2\sigma} = 509$ km/s

Fe^{13+} : $\langle v \rangle_{1\sigma} = 418$ km/s, $\langle v \rangle_{1.5\sigma} = 418$ km/s, $\langle v \rangle_{2\sigma} = 433$ km/s

FIGURE 5.14: Long-term accumulated speed spectra for Fe^{7+} - Fe^{13+} under the condition $v_p \in [500\,\text{km/s}, 510\,\text{km/s}]$ for DOY 174-220 1996. The spectra are shown in linear (left) and logarithmic (right) count rate scale.

the low-speed flank it is likely that the nominally less abundant S9+ ion is assigned with a too high count rate due to the described pattern, on the high speed flank it is possible that Si8+ is over-represented in count rate which would explain the asymmetry of both observed distributions simultaneously. In general, the observation of the bad separation between silicon and sulfur charge states might explain the finding in the previous section 5.4 that sulfur is probably over-estimated by a small factor in the CTOF data. A small refinement of the model in this range might lead to less asymmetric spectra for silicon and sulfur in the fast wind and simultaneously to even more similar speeds among the ion species. Ion species with lower counting statistics in the vicinity of more or equally abundant species are naturally more affected by this effect than the dominant ion species and therefore show a wider spread in the observed mean speeds.

Finally, we have a look on the *iron* ions in the fast wind. These cover a wide span in the higher mass-per-charge range and are therefore crucial for the understanding of the heavy ion speeds on the whole. From Figure 5.14 we can see that the most abundant iron charge states in the measured fast wind are Fe9+ and Fe10+ with almost the same relative abundance and which show only little fluctuations so that they are calculated with relatively consistent mean speeds between 519 and 524 km/s and 524 and 528 km/s, respectively for their 1σ - 2σ environments. For Fe8+ we calculate somewhat lower mean speeds between 511 and 520 km/s, where the 1σ-interval measurement of 511 km/s can be again denoted to an exceptionally high count rate in the low speed of the distribution while the two larger intervals give a consistent value of 520 km/s. For Fe11+ we find the highest iron mean speeds between 529 and 533 km/s. On the other hand, Fe7+ and Fe12 yield quite asymmetrical spectral shapes with higher count rates at the low-speed flank, which lead to low but consistent mean speeds between 508 and 516 km/s and 502 and 509 km/s, respectively. The count rates assigned to Fe13+ in this fast wind case are for most speed bins extremely low, so that no meaningful distribution can be recognized and the nominal mean speed is falsely calculated from the He2+ random coincidences (see above and section ?). Similar to the other elements the observed iron charge state distribution yields a lower mean charge state than for the fast wind, where the highest count rates were clearly observed for Fe10+.

In order to gain an overview over the heavy ion mean speeds measured by CTOF under the fast wind condition $v_p \in []$ we finally calculate from the derived mean speeds of the three σ-intervals a most consistent mean speed for a given species by calculating the arithmetic mean speed for the case of the three ion species, except for the case that the 1-σ speed is is measured with a difference of more than 15 km/s away from the other two species. This speed is then considered as an outlier due to a miss-assignment of counts in a certain Epq-step as described above and the mean speed is calculated from the remaining two mean speed calculations (see e.g. C4+ and O7+). In the comparison we only include ion species that 1) have sufficient counting statistics to identify an approximately Maxwellian core (e.g. not Fe13+), 2) do not have fluctuations of their own count rate magnitude in the distribution core (e.g. not S8+) and 3) have a reasonable relative abundance compared to the discussed dominant ion species (compare with slow wind conditions!). From this procedure, we obtain for the given fast wind case the mean speeds of 21 ion species (out of the 69 species included in the applied ET-matrix fits with the full stable response model) that are depicted in Figure 5.15. We can see that most ion species that fulfill the above criteria are measured at speeds
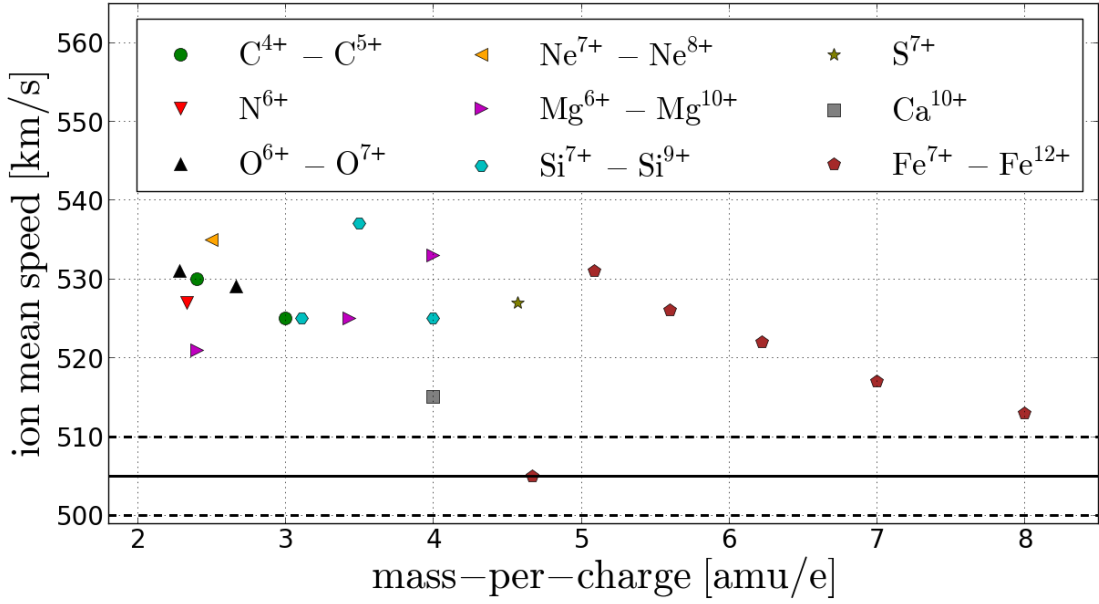
FIGURE 5.15: Long-term heavy Ion mean speeds as a function of the ions' mass-per-charge derived from the CTOF Full Stable Response Model for DOY 174-220 1996 under the condition $v_p \in [500\,\text{km/s}, 510\,\text{km/s}]$, Mg8,Mg9 are not included because of count rate criterion, Ne7 is not shown as it is at 560 km/s? (compare appendix). The black solid line marks the mean proton speed and the dashed black line mark the filtered proton speed interval.

between 520 and 535 km/s and no species measured at speeds below the mean proton speed. Thus, when taking the measured differences between the different sigma-interval speeds as an estimation of the statistical uncertainties[10] of the derived mean speeds, we see a statistically highly significant signature of differential streaming in the investigated fast wind speed interval with the majority of differential speeds observed between 15 and 30 km/s. This corresponds to spectral mean speeds that are measured at Epq-steps that are more than 1 and up to 3 Epq-steps away from the Epq-step corresponding to the nominal proton speed for the given species, respectively.

In general, we cannot identify any significant trend in the measured differential speeds in dependence of the ion species up to a mass-per-charge value of $m/q \approx 5\,\text{amu/e}$. In the mass-per-charge range above $m/q \approx 5\,\text{amu/e}$, we find a decreasing trend of differential speeds with increasing mass-per-charge [on the order of $\Delta(\langle\Delta v\rangle)/(m/q) \approx 5\,(\text{km/s e})/(\text{amu})$]. However, before we make any further attempts to quantify any observed trend, we compare again the differential speeds obtained from the full stable response model with the differential speeds that we derive from the reduced response model, to get an estimation of the stability of the measured speed values. In Figure

---

[10]As already mentioned before, the 1σ standard errors of the spectral mean speeds for the presented ion species are even lower than the observed deviations between the σ-interval mean speeds, even if we use for the error calculation the rue underlying count statistics of the meaured PHA counts.
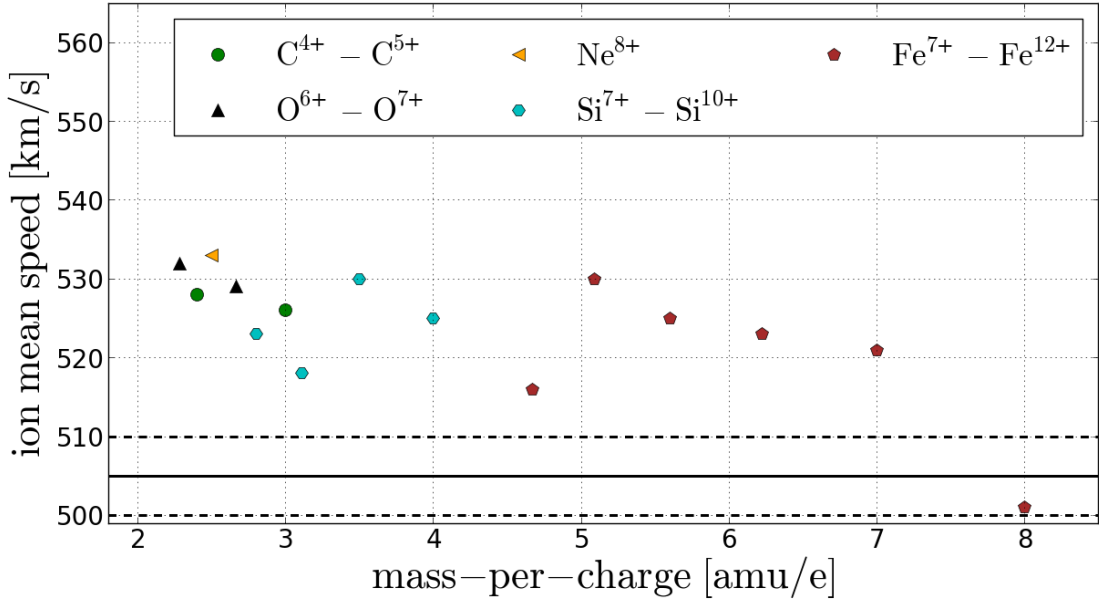
FIGURE 5.16: Long-term heavy ion mean speeds as a function of the ions' mass-per-charge derived from the CTOF Reduced Stable Response Model for DOY 174-220 1996 under the condition $v_p \in [500\,\mathrm{km/s}, 510\,\mathrm{km/s}]$

5.16 we depict the 15 ion mean speeds that we obtain from the CTOF RRM? with the same calculation procedure and under the same spectral criteria as for the CTOF FRM?. We see that the main result is the same i.e. that the vast majority of ion species are measured at positive differential speeds betwen 15 and 30 km/s compared to the main proton speed. Yet, we do observe for few ion species major shifts in differential speed when comparing Figure 5.15 and 5.16 that are (almost) comparable in magnitude with the observed differential speeds compared to the protons. The largest changes are observed for Fe12+ (-14 km/s), Fe7 (-11 km/s), Si8+ (-7 km/s), Si9+ (-7 km/s), while all other observed shifts are below 5 km/s. These relatively large changes can be again explained by the relatively low abundances of Fe12+ and Fe7+ compared to their adjacent dominant charge states (Si7+, Fe11+ and Fe8+,respectively) while for Si8+ and Si9+, probably the pure number of adjacent ion species (in particular sulfur and magnesium ion species) makes it hard for the fit to assign a more consistent count rate to the silicon species in the fast wind case. As we could see before, with the higher counting statistics in the slow wind the speed of the silicon species could be determined more reliably. When comparing 5.15 and 5.16 we also see that the trend observed for the iron ions in 5.15 has to be be questioned now as in Figure 5.16 Fe8+ and Fe7+ do not line up anymore to an approximately linear decrease and in particular Fe7+ could be identified as one of the most unreliable measurements. In order to investigate this last question to which extend such a possible decreasing trend with increasing mass-per-charge can be produced purely by an instrumental effect or whether it has to be caused

by an independent (true) physical effect, in the next section we conduct a systematic error estimation which concludes this chapter.

maybe useful: - some relatively abundant ion species do not show credible spectra at all: Si7+-Si9+, reason: fit not stable over all steps where other ions with comparable abundance are included (S, and Mg in case of Si), problem could not be solved with small systematic variation of positions, therefore we conclude that the fit cannot resolve these ions with the given statistics. Similar effects can be expected for other ion species: mainly Mg and Ne charge states, C and N, but also Ca and Ni with less abundant charge state of Fe: Fe7+ Fe12+, Fe13+). Therefore we reduce the number of ions, knowing that the results in particular for silicon are combined results for Si and S and for Si7 (and 8+?) also with Mg6? and Ca10+?.
However in case of Si7+, S8+, Mg6+ and Ca10+ these ions lie all at he same mass-per-charge, so that these have to be treated similar in a theoretical analysis, for Si8+,S9+ and Si9+, Mg10+ the difference in mass-per-charge is ?, this small deviations are possible, but silicon is by far expected to be the dominant component, so that we list all these ions as Si in the following Figures, but denote the included non -resolvable species in the caption.

explain: the summary plot: criteria for the ion species plot:

5.6 Systematic Error Estimation

- we have seen in Figure ? that iron ions behave different/might show a physical trend with increasing mass-per-charge, on the other hand we have seen in chapter **???** that these iron species (high m/q-species) are also the ones that show the largest deviations from the Gaussian peak shape and the Kappa-Moyal model was mainly created to take into account their different shape due to the massive straggling in the carbon foil.

-Therefore, in the following we want to investigate how the measured mean speeds of both the low-m/q and high-m/q ion species behave when we apply a systematical transition of the peak shape from a Gaussian peak model to the Kappamoyal model (with the optimal tail parameter) to even more extreme tail parameters.

As the observed changes are better visible, when we include less ions in the fit, this systematic uncertainty analysis is illustrated for the Reduced response model but is also valid for the full model. In Figure 5.17 we show in blue the calculated reduced chi2-values for the CTOF RRM at Epq-steps 40 (dotted line), 60 (solid line) and 80 (dashed line) which represent the typical Epq-step range of nearly all minor ion species
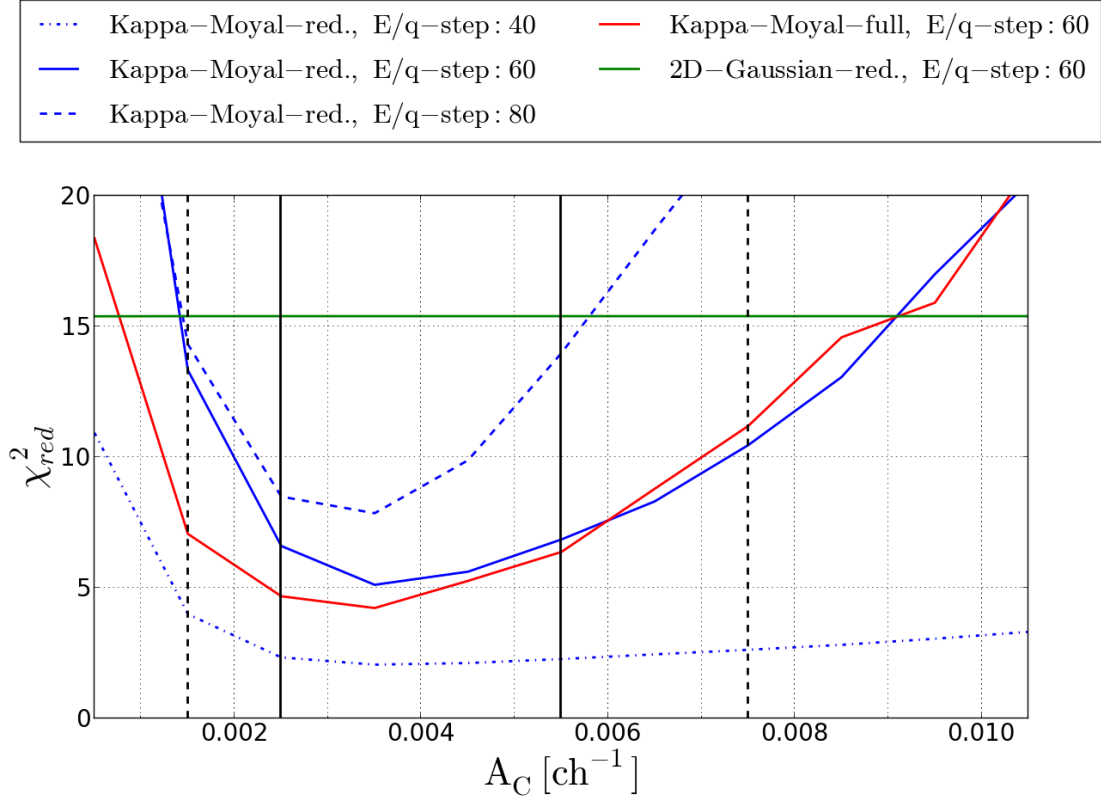
FIGURE 5.17: Response model goodness (χ^2_{red}) as a function of the universal tail-scaling parameter A_C for the CTOF Kappa-Moyal Reduced Response Model (KM-RRM) in blue for Epq-step 40 (dotted line), 60 (solid line) and 80 (dashed) line. The systematic 1σ-uncertainty interval is calculated from the KM-RRM model for Epq-step 60 as dexcribed in the text and marked by the vertical black solid lines. To investigate the systematic change of the heavy ion mean speeds in dependence of the adjusted tail parameter in the applied KM-RRM response model, we evaluated the mean speeds for a sample of ion species in the interval $[A_C = 0.0005\,\text{ch}^{-1}, A_C = 0.0075\,\text{ch}^{-1}]$ (see the following Figures 5.18 - 5.20). The case $A_C = 0.0005\,\text{ch}$ describes the case of an approximately Gaussian peak shape as can be also seen from the comparison with the Gaussian Reduced Response Model (G-RRM) at Epq-step 60 shown by the red solid line.

(see section ? and appendix C?)as a function of the tail parameter A_C that we introduced in section 4.? to parametrize the peak tail as a function of the peak TOF position. The chi2 values are calculated for (relatively coarse) discrete values of $A_C \in \{0.5 \cdot 10^{-3}\,\text{ch}^{-1},\ 1.5 \cdot 10^{-3}\,\text{ch}^{-1},\ 2.5 \cdot 10^{-3}\,\text{ch}^{-1},\ ...\ ,\ 9.5 \cdot 10^{-3}\,\text{ch}^{-1},\ 10.5 \cdot 10^{-3}\,\text{ch}^{-1}\}$. By the red solid line we also show the calculated chi2 values in dependence of A_C for the full CTOF response model, that shows naturally smaller values for chi2 as more ions are included, but it also has its minimum at $A_C = 0.0035\,\text{ch}^{-1}$. Finally, we plotted the chi2 of the reduced response Model with the Gaussian peak model for comparison as the green solid line, which is by definition independent of any tail scaling parameter. As we can see, for all three Epq-steps the selected optimal peak scaling parameter A_C yields

the lowest chi2 as it is supposed to be for a response model that should be valid for all Epq-steps[11]. Note that Kappa-Moyal RRM curve for step 40 shows naturally a small dependency on the tail parameter as the low counting statistics in this step does not allow a very good distinction between the different models, while the curve at step 80 would in principle allow for the best distinction between the models due to the high count rates, if not at this Epq-step only ions species with low m/q (at low TOF positions) and thus with relatively small tails would be measured. Therefore, probably the best model distinction can be done at an intermediate Epq-step 60, where still several iron and silicon ion species are present in the data and the count rates are sufficient to observe the goodness of the model in dependence on the tail scaling parameter A_C. Thus, following [Numerical recepies] we obtain the boundaries of the 1σ confidence interval for the tail-parameter at those values A_C where the solid blue line $\chi^2_{red,KMR-60}(A_C)$ exceeds the minimum value $\chi^2_{red,KMR-60}(A_C = 0.0035\,\text{ch}^{-1})$ by an absolute difference of $\Delta\chi^2_{red} = 1$. This is the case approximately at $A_C = 0.0025\,\text{ch}^{-1})$ and $A_C = 0.0055\,\text{ch}^{-1})$ and these values are marked by the black solid vertical lines in Figure 5.17. As we now managed to calculate a systematic uncertainty in dependence of the tail-scaling parameter, We can now evaluate the mean speeds for different tail-scaling parameters by fitting the long-term data with response models of different tail parameters A_C[12] and relate them to the calculated (systematic) uncertainty range that depends on the same parameter. We show this evaluation here for the discussed fast wind case [vp] and examine first the case of a very low tail-scaling parameter $A_C = 0.0025\,\text{ch}^{-1})$ that virtually equals the Gaussian case under as can be also seen from Figure 5.17 where the chi2 values of the reduced Gaussian and Kappa-Moyal response model intersect approximately at this value. In Figure 5.18 we show the derived mean speeds for the ion species C4+, O6+, Ne8+, Si8+ and Fe8+ - Fe11+, which are just shown as a minimum example of relatively reliable ion species that cover a wide range in mass-per-charge. The calculated uncertainty range at each ion's m/q-value that we obtain from the mean speed values of the ions derived from the model with tail-scaling parameter $A_C = 0.0025\,\text{ch}^{-1})$ (lower speed uncertainty boundary) and $A_C = 0.0055\,\text{ch}^{-1})$ is given as the gray shaded area. We see that the systematic uncertainty due to the peak tail scaling is small for ions with low mas-per-charge as these lie on average at lower TOF values and have naturally small tails that do not alter much when the tail-scaling parameter changes. On the other hand for the iron ions the uncertainty is much larger and reaches up to almost 20 km/s for Fe8+ which is comparable to the observed differential speeds. We see now that for the Quasi-Gaussian model ($A_C = 0.0005\,\text{ch}^{-1})$), marked in Figure 4.30 by the left vertical dashed black line the calculated mean speeds are even below

---

[11]The shown chi2 values for the optimal value $A_C = 0.0035\,\text{ch}^{-1}$ can be directly read out from the response model plots for a wide range of Epq-steps in appendix C?, both for the reduced and full CTOF response model.

[12]The corresponding spectra are shown in section ? of appendix C?.
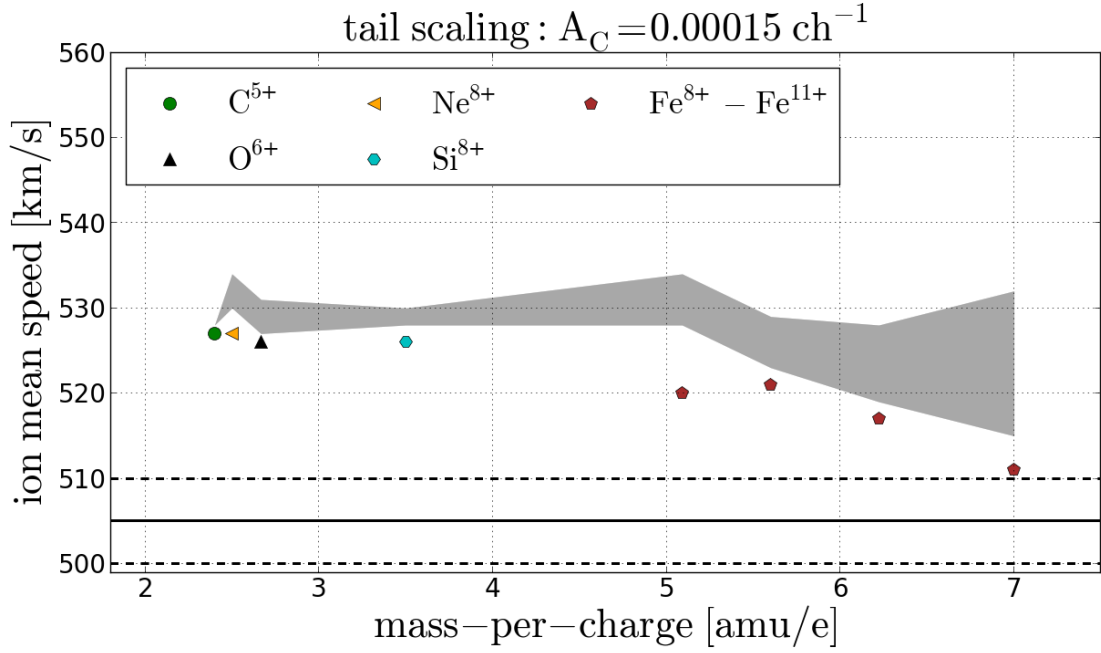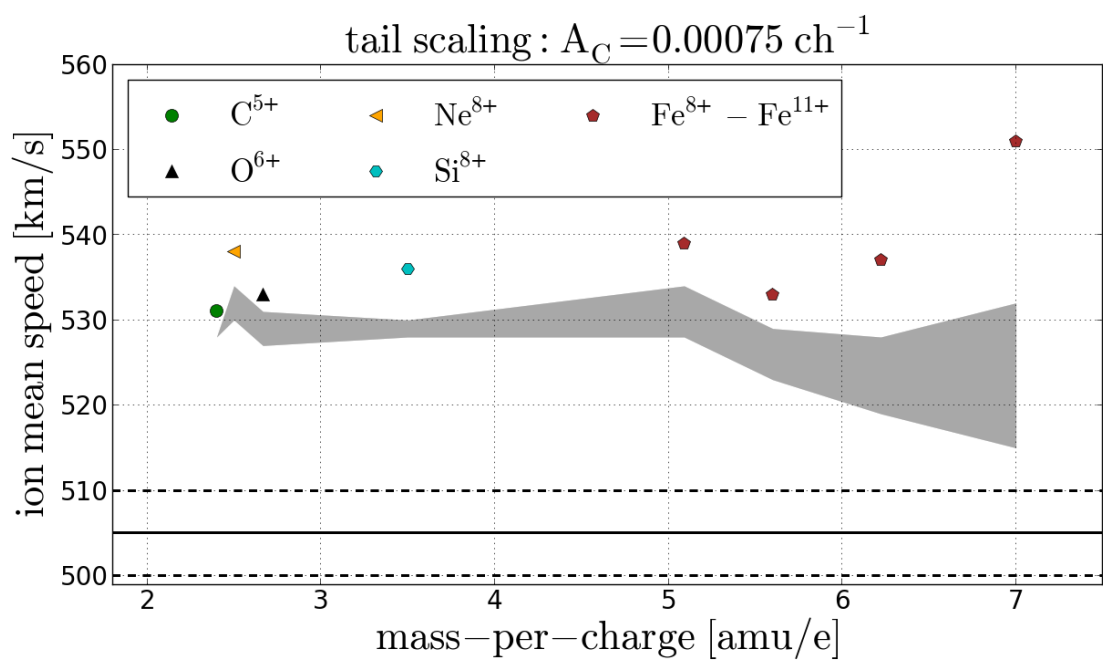
FIGURE 5.18: Mean speeds for the heavy ion species C^{4+} - Fe^{11+} derived from the Kappa-Moyal Reduced Response Model with tail scaling parameter $A_C = 0.0035\,\text{ch}^{-1}$ that represents approximately the case of a Gaussian peak shape. The 1σ-uncertainty interval that is represented by the shaded gray area is given by the differential speeds derived for the shown ion species with the KM-RRM model with $A_C = 0.0025\,\text{ch}^{-1}$ (lower speed boundary) and $A_C = 0.0055\,\text{ch}^{-1}$ (upper speed boundary) as can be seen in Figure 5.17.

the lower boundary of the uncertainty interval. For the case of the optimal tail-scaling parameter($A_C = 0.0035\,\text{ch}^{-1}$)) shown in Figure the calculated mean speeds are approximately in the center of the uncertainty interval which is the result of Figure 4.30 in the previous section, which. Consequently, for very large tail scaling parameters that are beyond the upper uncertainty limit such as ($A_C = 0.0075\,\text{ch}^{-1}$)) and that is marked as the right vertical dashed black line in Figure 4.30, we find mean speeds that are above those speeds that are calculated from the upper speed uncertainty limit. In this way it becomes clear that the observed mean speeds (and thus differential speeds) for the high-m/q ion species (in particular the major iron charge states) are a sensitive quantity that depend crucially on the applied peak shape model, while for the low and intermediate m/q-values this effect is small. When we now consequently apply the 1-sigma uncertainty estimation to the measured long-term differential speeds, we conclude that within these systematic uncertainty both a trend of decreasing mass-per-charge on the order of Delta v per e/amu is possible, as well as now significant trend at all (all minor
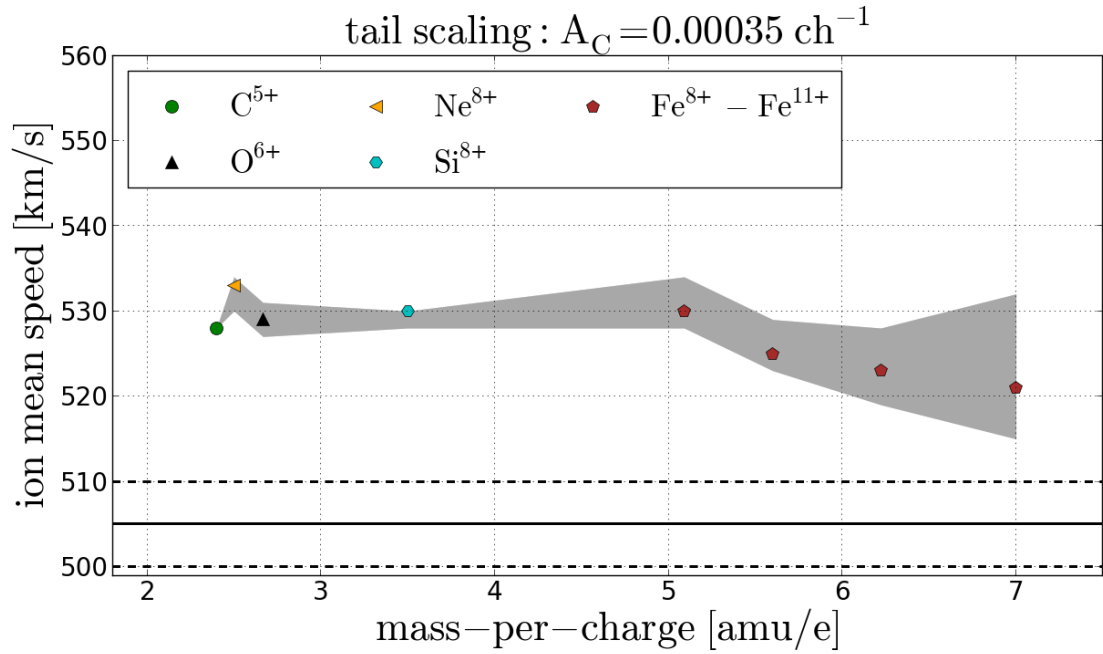
FIGURE 5.19: Mean speeds for the heavy ion species C^{4+} - Fe^{11+} derived from the Kappa-Moyal Reduced Response Model with tail scaling parameter $A_C = 0.0035 \, ch^{-1}$ that represents the optimal tail scaling parameter that was also used in the evaluation of the whole ion set above. The 1σ-uncertainty interval that is represented by the shaded gray area is given by the differential speeds derived for the shown ion species with the KM-RRM model with $A_C = 0.0025 \, ch^{-1}$ (lower speed boundary) and $A_C = 0.0055 \, ch^{-1}$ (upper speed boundary) as can be seen in Figure 5.17.

species stream with the same speed). The most likely scenario is a small trend of ? that corresponds to the optimal tail parameter ($A_C = 0.0035 \, ch^{-1}$)).

FIGURE 5.20: Mean speeds for the heavy ion species C^{4+} - Fe^{11+} derived from the Kappa-Moyal Reduced Response Model with tail scaling parameter $A_C = 0.0075 \, \text{ch}^{-1}$ that represents a very large tail scaling parameter that is beyond the 1σ-uncertainty interval as can be seen from Figure 5.17.

Chapter 6

Heavy Ion Kinetic Properties Derived from Short-Term Velocity Distribution Functions at 1 AU

introduction/motivation for short term data measurements:

1. long term data is in general problematic due to possible integration over a wide range of plasma conditions:

2. naturally periods with higher particle densities are over-represented

3. even if a certain plasma parameters is well-defined (such as proton speed) other parameters and in particular the in-situ magnetic field can vary massively over the integration time and the wind type is different

4. short term data is a clear improvement in the above aspects (cadence 5 minutes, integration time about 1 minute for any given ion species)

5. Despite the fact that the solar wind conditions are better defined during the measurement, a second major advantage of the short term

6. data analysis is that one can relate the different observations to each other in time, i.e. by creating a time series of the differential speed and comparing it with other parameters.

7. the natural downside of short-term data is the very low counting statistics for heavy minor ions, but CTOF is strong in this aspect as it allows for a relatively high geometry factor due to the Epq-stepping interruption if the proton/helium

fluxes become too high (higher counting statistics as ACE/SWICS within shorter cadence of 5 minutes compared to 12 minutes)

6.1 Derivation of Short-Term Velocity Distribution Functions

1. we fit the PHA data for each valid CTOF cycle (same cycle criteria ($N_{PHA} > 500$) as in chapter 5) with RSM (Reduced Stable Response Model), example for the ET-excerpt of iron ions in Figure 6.1

2. Mention explicitly that so far fits conducted only with Gaussian peak model

3. Poissonian Minimization Function is used with BFGS algorithm as solver (both as in chapter 6)

4. fit is conducted before the PHA base rate correction is applied, because the high correction factors in combination with very low counting statistics lead to a highly unphysical count rate that is not compatible with the physical response model and therefore the fit of the base-rate corrected PHA data leads to unphysical fit results

5. base rate is multiplied with the counts at each bin in ET-matrix (for each Epq-step)

6. normalization of the counts as in chapter 5

7. apply phase space correction (proportional to $1/v^2$) as in chapter 3 and 5.

8. Final VDF example (that belongs to the above fit at Epq-step 43 in Figure 6.1) is shown in Figure 6.2

To point 7. :
Once we obtained the base-rate corrected short-Epq-step spectra as explained in the previous subsection, the derivation of the short-term VDFs follows the same procedure as explained in section 3.? with the only difference that this time the spectra have naturally the full resolution of 117 Epq-steps. We therefore only have to convert for each ion species the Epq-steps to the corresponding ion speeds after Eq ? and then multiply the count rates with a factor of $c_{ps,cor} = 1/v^2$ to correct for the instrumental phase space coverage as explained in subsection 2/3.?. Finally, we obtain the reduced 1D velocity distribution functions from which we can calculate the first and second moment to derive the mean and thermal ion speeds for each 5-minute CTOF/measurement cycle.
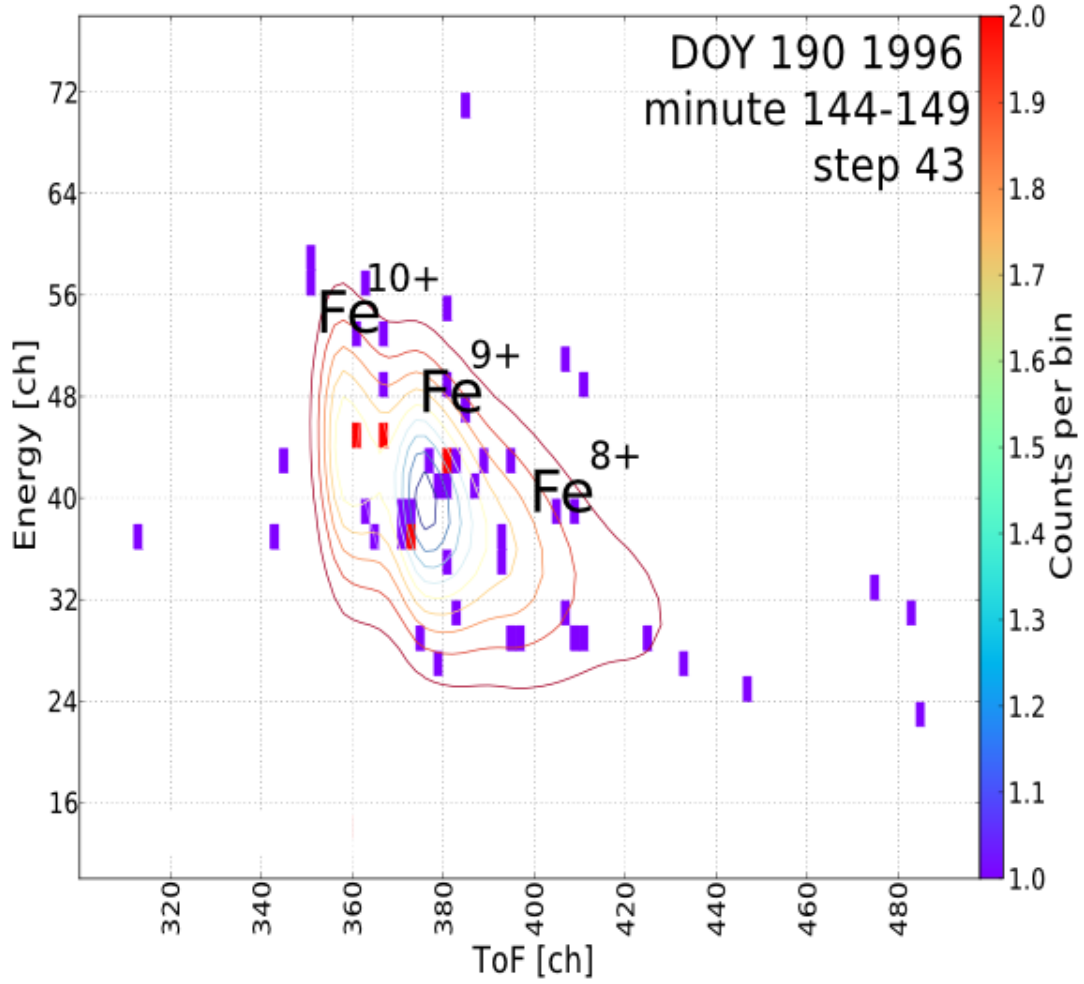
FIGURE 6.1: <mark>Substitute Energy by ESSD!, Adapted after Janitzek. Solar Wind 14, Proceedings, Wehai, (2016)</mark>

6.1.1 Derivation of Mean and Thermal Speeds from the Short-Term Velocity Distribution Function

Similar to the analysis in the previous chapter, we only include cycles with a sufficient number of PHA words ($N_{PHA,min} \geq 500$) and we have to ensure that these moments are not biased by the instrumental cut-off due to the interruption of the ESA stepping. In contrast to the long-term analysis we have to ensure now for each cycle individually that the moments that we derive from the VDF are not influenced due to this artificial cut-off. This is done by looking up the maximum reached Epq-step corresponding to the lowest measured speed at each cycle and then mirroring this speed to the upper flank of the VDF to obtain the maximum included speed for a symmetrical moment
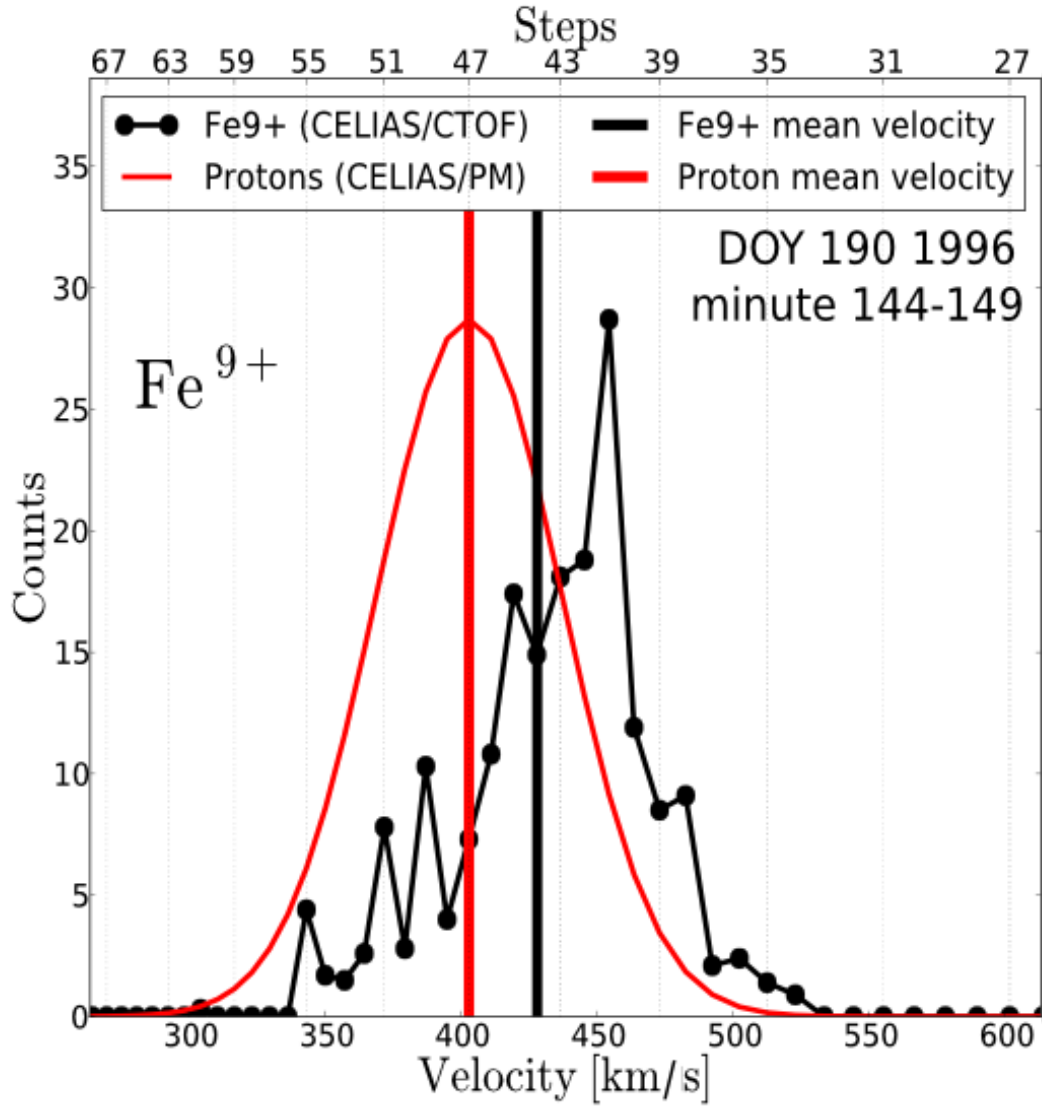
FIGURE 6.2: Substitute velocity by speed!, Adapted after Janitzek. Solar Wind 14, Proceedings, Wehai, (2016)

calculation. Thus, we calculate the mean speed as

$$\langle v \rangle = \frac{1}{C} \cdot \sum_{i=s_{min}}^{s_{max}} c_i \cdot v_i \tag{6.1}$$

where the lowest speed is the ESA cut-off speed $v_{s,low} := v_{s,cut} \leq v_{s,max}$ and the highest included speed $v_{s,up}$ is the highest speed v_s that fulfills

$$v_s \leq v_{s,cmax} + (v_{s,cmax} - v_{s,cut}) \, , \tag{6.2}$$

so that we obtain a symmetric speed range around the most frequently measured speed $v_{s,max}$ with the highest observed count rate C_{max}. Naturally, this approach only ensures

an unbiased calculation of the mean speed, when a sufficiently large part of the VDF is scanned to ensure that the actual most probable speed (that one would calculate if the VDF was not cut) is not even below the cut-off speed. For all (major) ions with mass-per-charge equal or larger than the mass per-charge of O^{6+} ($m/q \gtrsim 2.7$) we find that the average speed difference $\Delta v = v_{s,cmax} - v_{s,cut}$ observed in the roughly 10^4 short term data VDFs is at least $\Delta v \gtrsim \sigma_v$ for all proton speed regimes[1], where σ_v is the standard deviation of the measured long-term speed spectra which is about $15\,\text{km/s}$ in the slow wind and $50\,\text{km/s}$ in the fast wind. This corresponds to a difference of 2 and 5 Epq-steps, respectively. Assuming again approximately 1D-Maxwellian/Gaussian distributions, we can conclude with the given counting statistics (mention at the beginning in chap2!) that the mean speeds of these ion species calculated with the described symmetrized speed-range method are statistically very unlikely to be biased, as the probability that the actual most probable speed lies below the ESA cut-off speed for a significant number of VDFs is very low.

-explain how to deal with He2+ random coincidences

-describe also calculation of the thermal speeds

6.2 Heavy Ion Differential Speeds Derived from Short-Term PHA Data

6.2.1 Differential Speed Time-Series

All (≈ 10000) calculated mean ion speeds for DOY 174-220 in 1996, that are obtained for the major ion species from the CTOF PHA data as described in the previous section can be visualized as a time series that is shown in Figures 6.3 and 6.4. In the Figures we present the mean ion speeds of O^{6+} (black), Si^{8+} (cyan) and Fe^{10+} (brown), together with the solar wind proton speed (green), measured by the CELIAS PM. In the upper panel of Figure 6.3 we show an overview over the whole measurement period, that consists of only two subperiods DOY 185 - 186 and DOY 213 - 216 1996 where we measure speeds that are typically classified as fast wind ($v_p \gtrsim 500\,\text{km/s}$). We further observe several subperiods of intermediate speeds between $400\,\text{km/s}$ and $500\,\text{km/s}$ and two longer periods of slow wind below $400\,\text{km/s}$ at DOY 714 - 184 and DOY 206 - 209 1996. Several time intervals with very low proton speeds are excluded from the study as these occur together with low proton thermal speeds that show an artificial distribution pattern below $v_{th} = 21\,\text{km/s}$ as described in section 2.3. The excluded time are

---

[1]Compare Figure 6.? for the minimum cut-off steps in the slow and fast wind.

marked by the gray shaded areas in the upper panel of Figure 6.3.

In the middle panel of Figure 6.3 we show with a higher time and speed resolution the subperiod between DOY 174 and 179 in the slow solar wind while in the lower panel the subperiod 195 - 200 is shown, where we measure slow and intermediate wind speeds. Note that this distinction between slow, fast and intermediate speeds corresponds roughly to the identified speed regimes in Figure 3.5 of chapter 3 and we will further justify it in the next subsection 6.2.2. For the slow solar wind period we see that there are no continuous periods of clear positive differential speeds $\Delta v_{ip} \gg 10\,\mathrm{km/s}$ between the heavy ions and the protons recognizable, but only one shorter period of small negative differential speeds during a few hours at the end of DOY 177 and the beginning of DOY 178. In the time interval DOY 195-200 we can observe for certain periods some speed differences between the protons and ions up to a maximum of $20\,\mathrm{km/s}$, but these differential speeds alternate in their sign, as sometimes the heavy ions are faster than the protons (e.g. beginning of DOY 195, end of DOY 199) and at other times it is the opposite (e.g. mid of DOY 196, end of DOY 198) and no clear correlation with the proton speed is observed. The only general feature that one might already recognize in the slow and intermediate wind is that among the heavy ions, the Fe^{10+} speed tends to be the lowest in most cases.

When we now focus on the fast wind streams in the upper two panels of Figure 6.4 (which for direct comparison are depicted with the same scaling on the y-axis as the two lower panels of Figure 6.4) we do observe clear signatures of differential speeds over extended time periods. In the upper panel one can recognize that all heavy ions stream faster than the protons with differential speeds between about $20\,\mathrm{km/s}$ (mainly for Fe^{10+}) and 30-40 $\mathrm{km/s}$ (mainly for Si^{8+} and O^{6+}) over a continuous period of about one day (end of DOY 185 - end of DOY 187). This period coincides with the highest proton speeds in the shown subperiod that contains the full first fast stream. At somewhat lower proton speeds of around $450\,\mathrm{km/s}$ or between the beginning of DOY 187 and the mid of DOY 188 the pattern is again more complex with O^{6+} and Si^{8+} streaming mostly faster than the protons while Fe^{10+} streams partly faster and partly slower than the protons.

In the middle panel of Figure 6.4 we see a rapid transition from a slow to a fast wind structure on DOY 213 1996. These pattern typically occurs when the fast wind runs into the slow wind at corotating interaction regions in the inner heliosphere [2]. Between midday on DOY 213 until the end of DOY 215 we find thus the second observed fast stream with proton speeds of more than $500\,\mathrm{km/s}$ almost over the entire period of 3 days. Yet, in detail we observe a finer structure of three short periods (substreams?) with the highest observed proton speeds of the whole sample up to about $550\,\mathrm{km/s}$. A
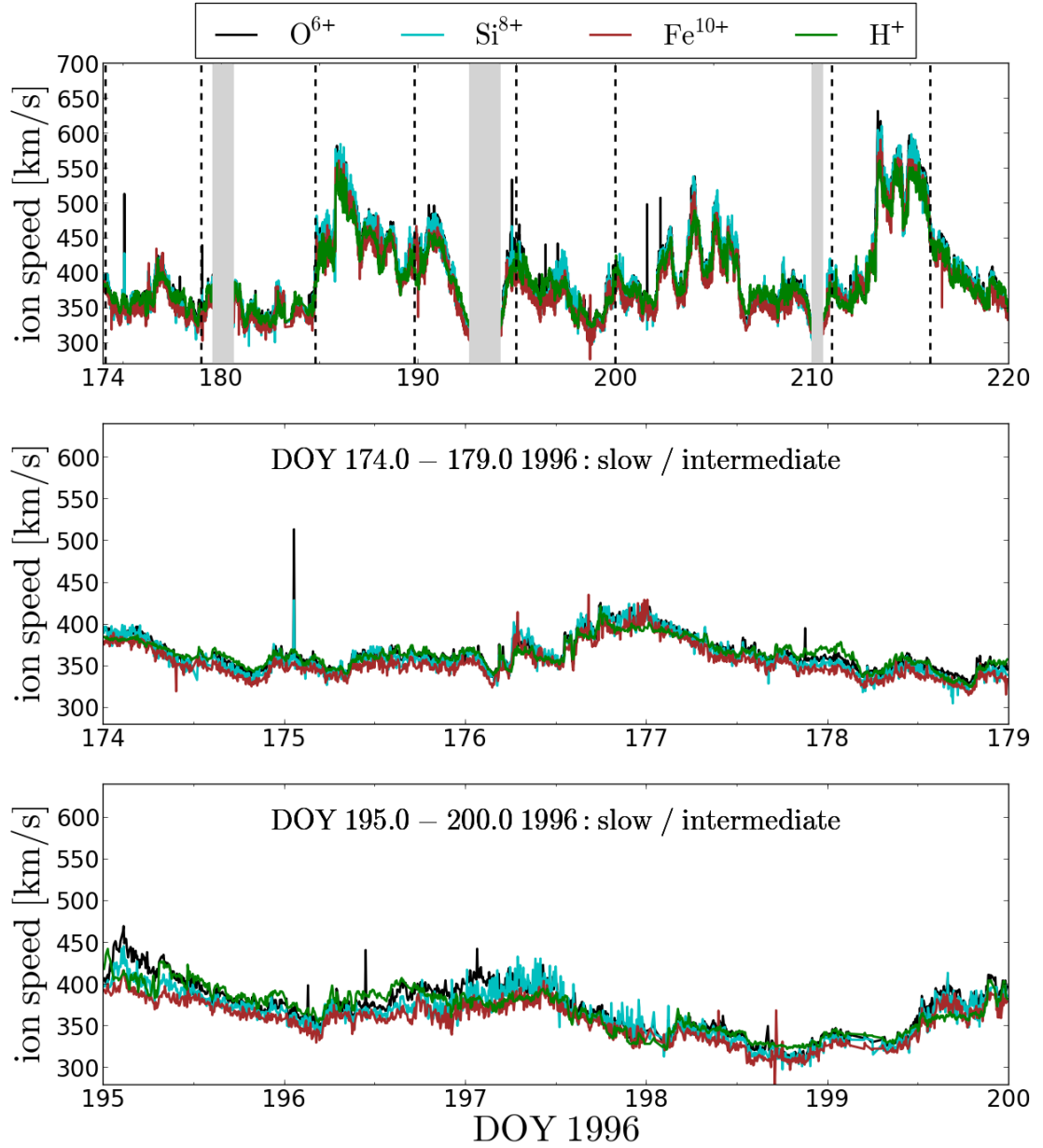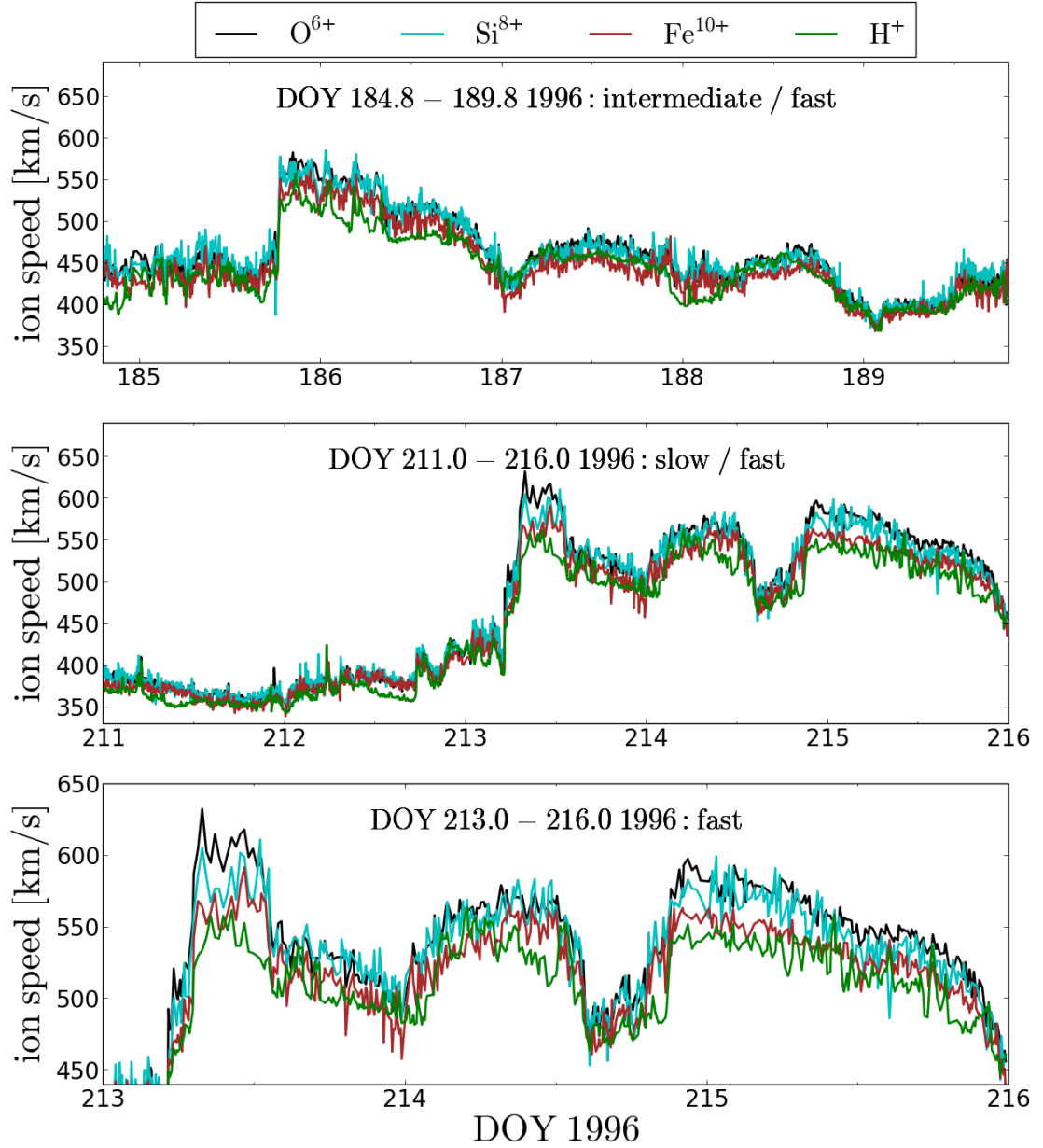
FIGURE 6.3: Time series of the mean ion speeds obtained from the CTOF short term data analysis for O^{6+} (black), Si^{8+} (cyan) and Fe^{10+} (brown), that can be compared to the mean proton speeds (green) which are measured simultaneously with the CELIAS Proton Monitor (PM). In the upper panel the full measurement period is shown for DOY 174-220, that contains almost 10^4 valid measurement cycles. The four time intervals between the vertical dashed lines (with the first interval starting on DOY 174) are described in greater details in the text. In the two lower panels we show two of these subperiods in the slow and slow/intermediate speed range between DOY 174 - 179 and DOY 195 - 200 in 1996, respectively, in larger resolution. The gray shaded areas are excluded from the analysis as the proton monitor measurements are not reliable for very cold and slow wind. Note that in the time series we rarely see extreme fluctuations in the derived mean speed which is a good indication for the quality of the applied fits which are conducted generally on very low counting statistics.

zoom of this fast wind period between DOY 213 and 216 is shown in the lower panel of Figure 6.4, from which we can see that in particular for O^{6+} differential speeds of about 50 km/s are reached within the first substream while in the second substream the differential speeds are (only) on the order of 20-30 km/s. In the third substream they increase again in the beginning where they again reach up to 40-50 km/s before they slowly reduce to about 20 km/s by the end of the stream. The observed differential speed difference between the three streams is interesting as the proton speed is about equal over large parts of the substreams, but the differential speed behaves differently. If we only had measurements of one heavy ion species one could explain this observation with an ambient magnetic field that is more co-aligned with the measurement axis in the first and the third case but more perpendicular aligned in the second case (see 2.4). However, we observe that both in the first and the third stream the heavy ion speeds are well-ordered by mass-per-charge (with the highest speed observed for O^{6+} as the ion species with the lowest m/q) while in the second substream all ion speeds are very similar with average differential speeds among each other of less then 10 km/s and in particular Fe^{10+} has even higher differential speeds in the second stream than in the third stream. Such subtle features could in general be a signature of different acceleration / speed regulation mechanism dominating in the different streams and should be investigated in detail in the future. As the discussed signatures are stable over a few hours, they are not only statistically significant but might also be investigated with extrapolated magnetic field measurements from the Wind spacecraft that is in the given time-period in the vicinity of L1. Yet, as the CTOF measurement period is limited such a study can only have the character of a case study, while a complimentary analysis with e.g. ACE/SWICS measurement data would allow a search of such features over long time periods (see the discussion in section **??** both for the B-field extrapolation and the comparison with ACE/SWICS measurements). In the following, we focus on a statistical analysis of the differential speeds observed over the full analyzed measurement period DOY 174-220 that can be compared to the results obtained from the CTOF matrix rate data in chapter 3.

6.2.2 Statistical Analysis of Differential Speeds

In the following we present a statistical study of the differential speeds calculated as described above from 5-minute cycle short term PHA data over the period DOY 174-220 in 1996. (actually we use the identical mean speeds as they were shown in the time series!) We analyze the measured differential speeds for their dependence on the simultaneously measured mean proton speeds as well as for their dependence on the simultaneously measured (proton-proton and ion-proton) collisional age.

FIGURE 6.4: Time series of the mean ion speeds obtained from the CTOF short term data analysis for O^{6+} (black), Si^{8+} (cyan) and Fe^{10+} (brown), that can be compared to the mean proton speeds (green) which are measured simultaneously with the CELIAS Proton Monitor (PM). In the two upper panels we show the two remaining subperiods marked by vertical dashed lines in the upper panel of Figure 6.3 between DOY 184.8 - 189.8 and DOY 211 - 216 in 1996, respectively. The upper panel shows the transitions between intermediate and fast wind speeds for the first observed fast stream. The middle panel shows the transition from slow to fast wind for the second observed fast wind stream. The speed scale on the y-axis in these two panels is the same as in the two lower panels of Figure 6.3, so that the speed differences can be compared by eye. The lowest panel is a zoom of the second fast stream between DOY 213 and 216 1996 with increased resolution both on the time and speed axis.

6.2.2.1   Differential Speed Dependence on the Solar Wind Proton Speed

In Figure 6.5 and 6.6 we present the 2-dimensional histograms of the ion-proton differential speeds Δv_{ip} of the ion species C^{4+}, O^{6+}, Si^{7+} - Si^{10+}, Fe^{8+} - Fe^{11+} versus the simultaneously measured proton mean speed for the full time period DOY 174-220 in 1996. In these Figures we show the absolute measured number of occurrences for a combination $(v_p, \Delta v_{ip})$ within a given (proton speed, differential speed)-bin, while in Figure 6.7 and 6.11 we depict the corresponding 2D-histograms for the same ion species with the respective frequency of occurrence for every $\Delta v_{ip} - v_p$ bin normalized to 1 within each proton speed bin, so that the maximum and spread of the differential speed distribution is better visible for all solar wind proton speeds. The shown results can be directly compared to the three ion species O^{6+}, Si^{7+}, Fe^{9+} that were analyzed with the matrix rate data in chapter 3[2]. Again, in all Figures the calculated mean differential speeds at each proton speed bin are given by the black dots, that are connected by the solid black line to guide the eye. In Figure 6.5 and 6.6 the (1σ) standard error of the mean differential speed $\langle \Delta v_{ip} \rangle$ for each proton speed bin is calculated in the exact same way as in Eq. 3.4. In addition we plot in Figures 6.7 and 6.11 as dashed lines the standard deviation of the distributions for every proton speed, which can be regarded as a measure for the variability of the measured differential speed under well-defined proton speed conditions.

In general we find for all analyzed ion species a step-like differential speed pattern that can be described within the aforementioned three different speed regimes of slow, intermediate and fast wind: In the slow wind below proton speeds of 380 km/s we observe differential ion speeds that are similar or lower than the proton speed yielding relatively constant differential speeds for any given ion species between about -15 km/s (for Fe^{8+}) and a bit less than 5 km/s (for O^{6+}) in this speed regime. After the transition to intermediate proton speeds between 380 and 400 km/s that leads to a small increase of the differential speeds, we find small between 400 and 480 km/s a positive differential speeds on the order of 10 km for O^{6+} and the analyzed silicon ions, while for C^{4+} we observe only a slight positive differential speed of maximum 5 km/s and for the iron ions we measure still mostly negative speeds. These differential iron speeds lie in the range between 0 and -5 km/s for Fe^{10+} while for Fe^{8+} they cover again a lower range between -10 km/s and -15 km/s, which is only slightly higher than in the slow wind regime. At a relatively sharp border of 480 km/s we find for all ion species a

---

[2]However, note that the overall number of occurrences in each panel are about 20% smaller than for the analyzed matrix rate data, which is due to the fact that we filter out all cycles with very low proton thermal speeds $v_{th} < 21$ km/s and in addition we had to exclude from the PHA data analysis all time intervals with too small counting statistics caused by the limited CTOF telemetry budget.
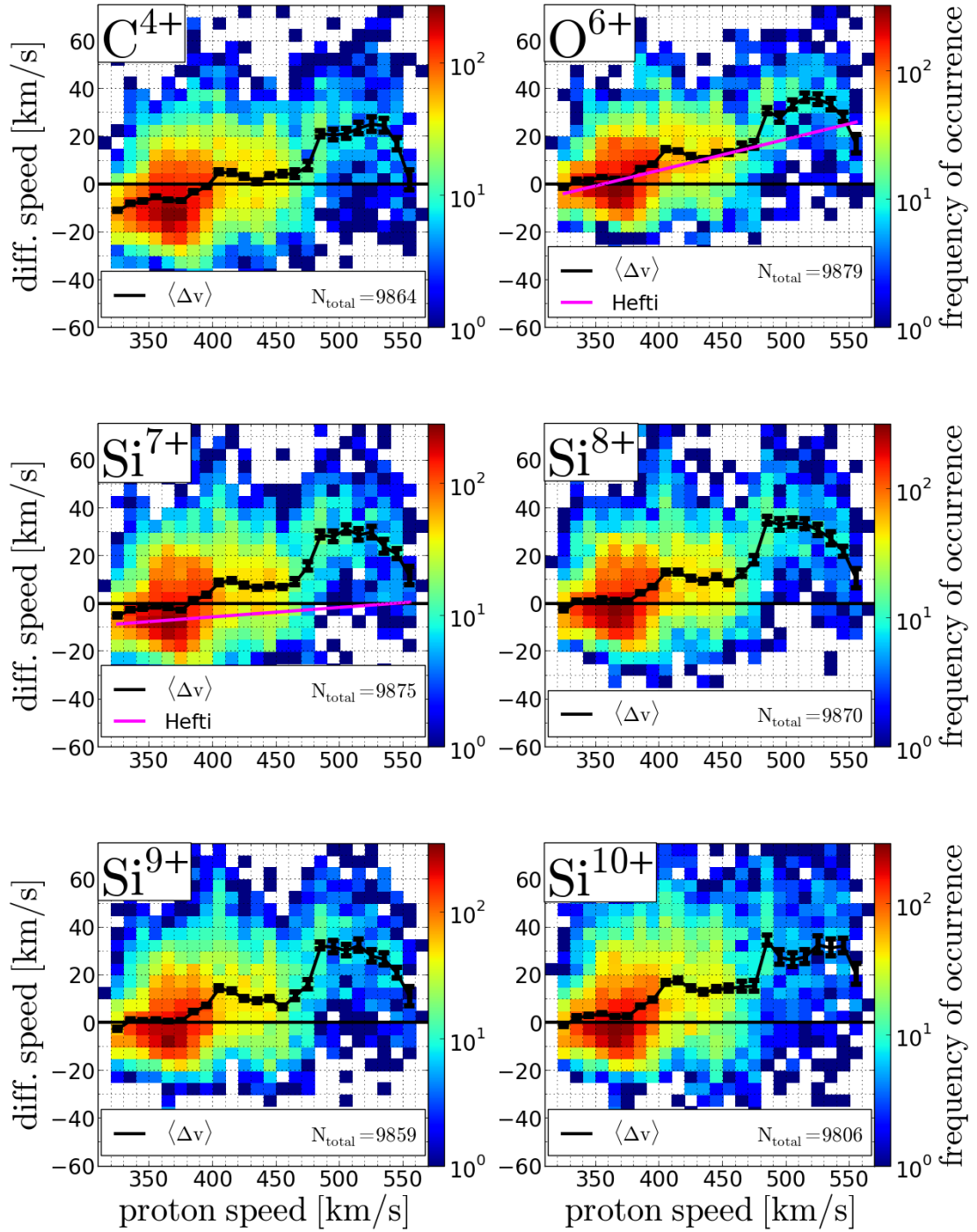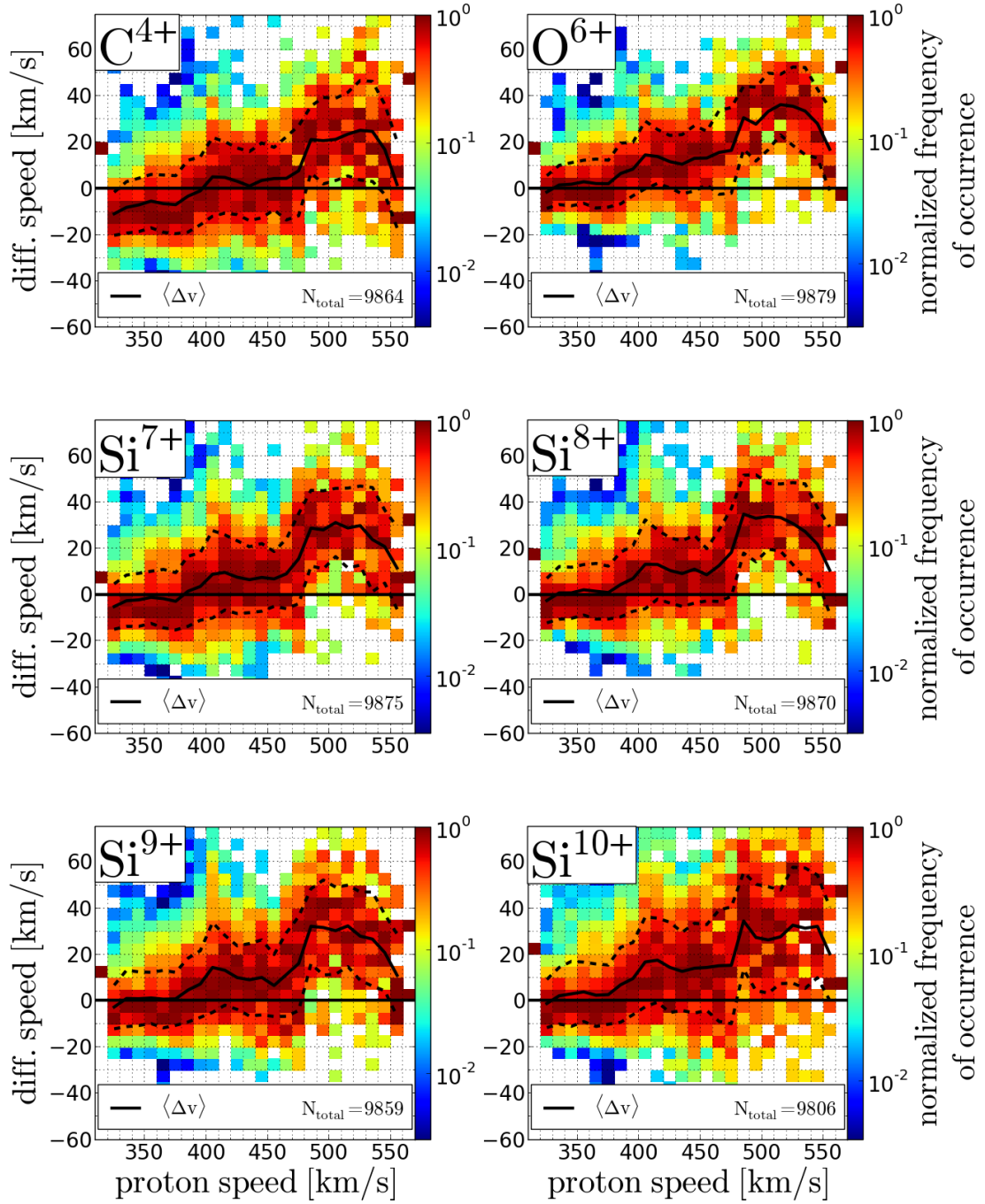
FIGURE 6.5: Two-dimensional histograms of the observed differential speeds between C^{4+}, O^{6+}, Si^{7+}, Si^{8+}, Si^{9+}, Si^{10+} and the solar wind protons, respectively, derived from the CTOF PHA data for the measurement period DOY 174-220 in 1996. The panels show the absolute measured number of occurrences for a combination $(v_p, \Delta v_{ip})$ within a given (proton speed, differential speed)-bin. The black line represents the mean differential speed $\langle \Delta v_{ip} \rangle$ at a given proton speed bin, the error bars mark the 1σ standard error of $\langle \Delta v_{ip} \rangle$. The magenta lines in the panels corresponding to O^{6+} and Si^{7+} show the linear best fit obtained for the mean differential speed by ?], for the time period DOY 80-230 in 1996.
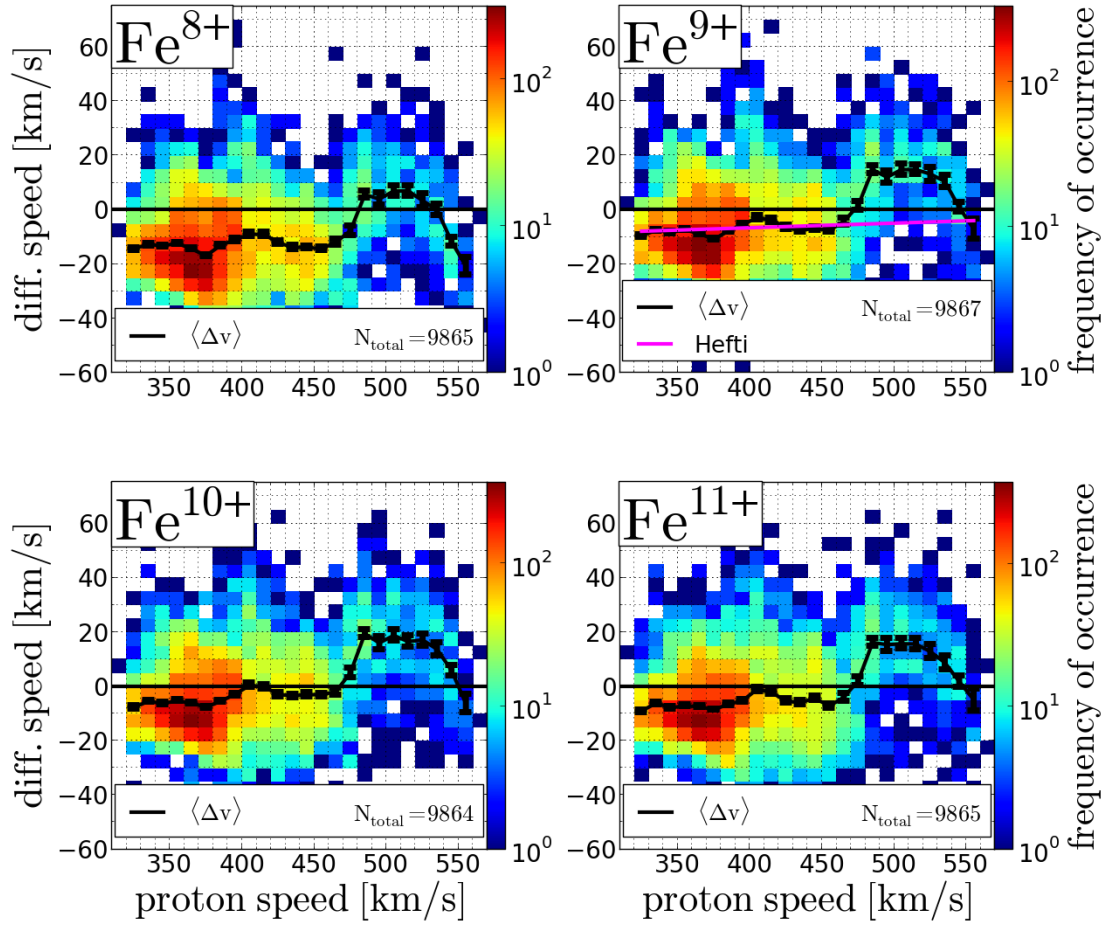
FIGURE 6.6: Two-dimensional histograms of the observed differential speeds between Fe^{8+}, Fe^{9+}, Fe^{10+}, Fe^{11+} and the solar wind protons, respectively, derived from the CTOF PHA data for the measurement period DOY 174-220 in 1996. The panels show the absolute measured number of occurrences for a combination $(v_p, \Delta v_{ip})$ within a given (proton speed, differential speed)-bin. The black line represents the mean differential speed $\langle \Delta v_{ip} \rangle$ at a given proton speed bin, the error bars mark the 1σ standard error of $\langle \Delta v_{ip} \rangle$. The magenta line in the panel corresponding to Fe^{10+} shows the linear best fit obtained for the mean differential speed by ?], for the time period DOY 80-230 in 1996.

significant increase in differential speed of about 20 km/s regardless of their differential speed magnitude at intermediate speeds which is followed for all ion species by a plateau of nearly constant speed in the fast wind at proton speeds above 480 km/s up to proton speeds of 540-550 km/s. Therefore, the differential speeds reached at these plateaus are different, so that we find for O^{6+} and the silicon ion species the highest speeds at around 30-35 km/s while for C^{4+}, we find a differential speed in the fast wind between 20 and 25 km/s. For iron the observed magnitude of high-speed differential speed is lower on average and depends once more on the charge state. While we measure between 15 and 20 km/s for Fe^{9+} - Fe^{11+}, we find for Fe^{8+} only about 5 km/s. The observed differences between the ion species in the fast wind are in their maximum

25-30 km/s (between O6+ and Fe8+), but we note that the ion species with smaller differential speeds in the fast wind have at the same time also larger negative differential speeds in the slow wind as can be seen from the comparison of the O^{6+} and Si^{6+} - Si^{6+} with C^{4+}, Fe^{9+}-Fe^{11+} and in particular Fe^{8+}, for which the absolute value of negative differential speeds in the slow wind is even larger than the observed differential speed in the fast wind.

We discuss this result in chapter **??** in the context of mass-and charge-dependence of the observed differential speeds (see next subsection 6.2.3) and in particular in the light of the systematic measurement uncertainties that we we derived from the long-term data systematical error analysis in the previous chapter.

On whole the observations from the statistical analysis of the short-term differential speeds yield a different picture than the results found by [1] for the (wider extended) time period DOY 80-230 1996. For comparison the earlier results that were derived from the CTOF matrix rate data for O^{6+}, Si^{7+} and Fe^{9+} as straight line fits to their mean speed distributions are again plotted as the magenta lines for the respective ion species in Figures 6.5 and 6.6. Although we observe a good agreement in the slow wind regime, the earlier results yield significantly lower mean ion speeds in the fast wind with differences between the two studies of 10-15 km/s for O^{6+}, about 30 km/s for Si^{7+} and about 20 km/s for Fe^{9+}. Thus, our result of both significant differential speeds in the fast wind for almost all analyzed ion species (both concerning the statistical and systematic uncertainties) is in clear contrast to the conclusions of the earlier SOHO/CELIAS study, that only found clear positive differential speeds for O^{6+} in the fast wind while Si^{7+} and Fe^{9+} were found to practically stream with the same mean speed as the solar wind protons.

discussion: thus it is possible that at these few cycles that are observed during a short time interval in the middle of DOY 213 the magnetic field points nearly perpendicular to the CTOF measurement axis and thus the decrease is due to this projection effect. The observed differential speed pattern?

6.2.2.2 Differential Speed Dependence on the Solar Wind Collisional Age

As discussed in section 1.4 the differential speed in the solar wind can be thermalized by Coulomb collisions between the solar wind ions and protons. At a given measurement location such as the SOHO site at L1 one can estimate the impact of Coulomb collisions on the measured plasma sample by the collisional age A_C. Therefore, despite

FIGURE 6.7: Two-dimensional histograms of the observed differential speeds between C^{4+}, O^{6+}, Si^{7+}, Si^{8+}, Si^{9+}, Si^{10+} and the solar wind protons, respectively, derived from the CTOF PHA data for the measurement period DOY 174-220 in 1996. The panels show the measured number of occurrences normalized to the maximum of a each proton speed bin, respectively. As in Figure 6.5 the black line represents the mean differential speed $\langle \Delta v_{ip} \rangle$ at a given proton speed bin, while the additional dashed lines represent the standard deviation of the differential speed distribution at each proton speed bin.

FIGURE 6.8: Two-dimensional histograms of the observed differential speeds between Fe^{8+}, Fe^{9+}, Fe^{10+}, Fe^{11+} and the solar wind protons, respectively, derived from the CTOF PHA data for the measurement period DOY 174-220 in 1996. The panels show the measured number of occurrences normalized to the maximum of a each proton speed bin, respectively. As in Figure 6.5 the black line represents the mean differential speed $\langle \Delta v_{ip} \rangle$ at a given proton speed bin, while the additional dashed lines represent the standard deviation of the differential speed distribution at each proton speed bin.

the proton speed the collisional age A_C is another possible parameter to order the differential speed of the measured solar wind. We note that with the measurements of the CELIAS CTOF sensor and Proton Monitor we can measure all parameters that are necessary to calculate both the proton-proton ($A_{C,pp}$) and proton-ion collisional age $A_{C,ip}$ of the measured plasma samples after Eq. 1.39 - Eq. 1.43. In Figure 6.9 we show the 2-dimensional histograms of the ion-proton differential speeds Δv_{ip} for the ion species O^{6+}, Si^{7+} and Fe^{10+} versus the simultaneously measured decadic logarithm of the proton-proton collisional age (left panels) and the ion-proton collisional age (right panels) for the analyzed time period DOY 174-220 in 1996. As we have already seen that the absolute frequencies of occurrence are much higher in the slow wind and thus at low collisional ages, just because of the SOHO measurement site, we take this information as given and only show the histograms of the normalized frequency of occurrence.

In analogy to Figures 6.7 and 6.7 these are obtained by normalizing the absolute occurrence frequencies to the respective in every given collisional age bin. The calculated mean differential speed for each collisional age bin with at least 10 occurrences is connected by the black solid line, while the dashed line mark the (1σ-) standard deviation calculated in each bin. The (1σ-) standard error is even smaller as for the protons for all statistically relevant bins and therefore not shown here. Here we only show in detail the analysis O^{6+}, Si^{7+} and Fe^{10+} as our measurements showed that the differences between the ion species are small compared to the overall observed trend.

As can be seen from all six panels, we find a clear trend of decreasing differential speeds with increasing collision age for all ion species as one would expect it for any real nonthermal signature. Naturally, the ion-proton collisional age is higher than the proton-proton collisional age as the age scales in a first approximation proportional to q^2/m. At the lowest collisional age we find for each ion species differential speeds that are comparable in magnitude not only between the $A_{C,pp}$ and $A_{C,ip}$ case but also compared to the maximum differential speeds reached at high proton speeds between 480 and 540 km/s. Interestingly, at the the highest collisional ages we find now for *all* ion species small negative differential speeds of less than -5 km/s for O^{6+} and about -10 km/s for Fe^{10+}. However, on the whole the difference in spanned $\langle \Delta v \rangle$ does not increase significantly for any analyzed order parameter v_p, $A_{C,pp}$ and $A_{C,ip}$ compared to the average standard deviation of the differential speed distributions of ≈ 20 km/s that given by the mean difference between the solid and dashed line over all x-axis bins. Thus, we cannot conclude from Figures 6.7 - 6.9 that any potentoal order parameter v_p, $A_{C,pp}$, $A_{C,ip}$ of the differential speed is superior to the other two. Therefore, a strong role of collisions in the regulation of the ion-proton differential speed in the analyzed solar wind plasma is compatible with the observed trends but cannot be proofed from the shown measurements alone.

6.2.3 Mass- and Charge-Dependency of Differential Speeds

We finally also analyze the differential speeds that we obtained from the short-term VDFs for their dependence on the ions species' mass and charge. In Figure **??** we show the differential speeds of the ion species C4+, O6+, Si7+ - Si9+ and Fe8+ - Fe11+ as a function of their mass-per-charge value since we have seen from section 1? that the magnitude of differential speed might be sensitive to the ions-mass-per charge if resonant ion-cyclotron resonance plays a crucial role in the determination of the differential speeds. The shown ion species are the same as in Figure? - ? with the exception of Si10+ that has larger fluctuations in the mean differential speed and a relatively wide spread of the differential speed distribution in the fast wind (compare Figure ?). Since it is also
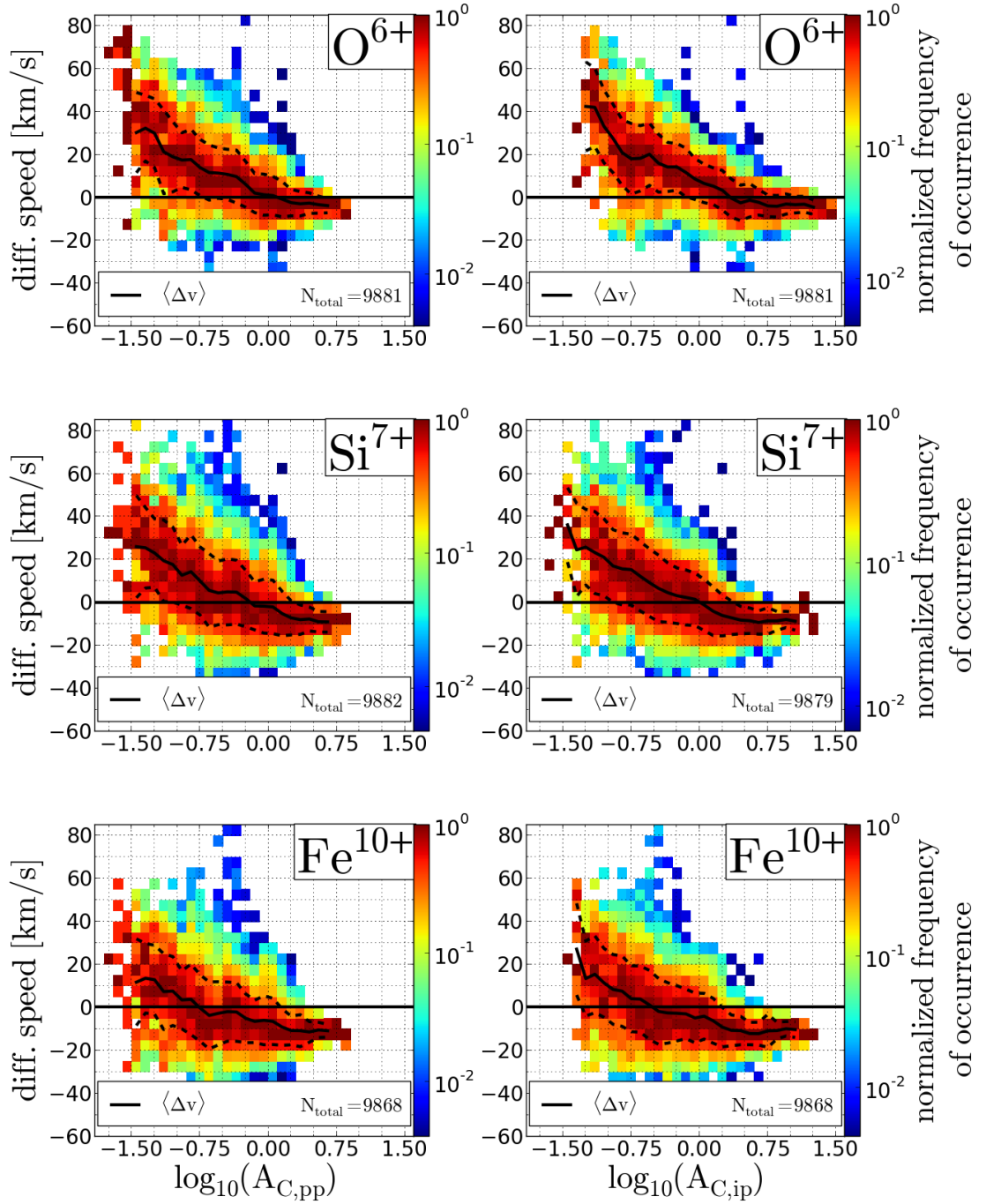
FIGURE 6.9: Two-dimensional histograms of the observed differential speeds between O^{6+}, Si^{7+}, Fe^{9+} and the solar wind protons versus the simultaneously measured decadic logarithm of the proton-proton collisional age (left panels) and the ion-proton collisional age (right panels) for the measurement period DOY 174-220 in 1996. The panels show the measured number of occurrences normalized to the maximum of a each collisional age bin, respectively. As in Figure 6.5 the black line represents the mean differential speed $\langle \Delta v_{ip} \rangle$ at a given collisional age bin, while the additional dashed lines represent the standard deviation of the differential speed distribution at each proton speed bin.
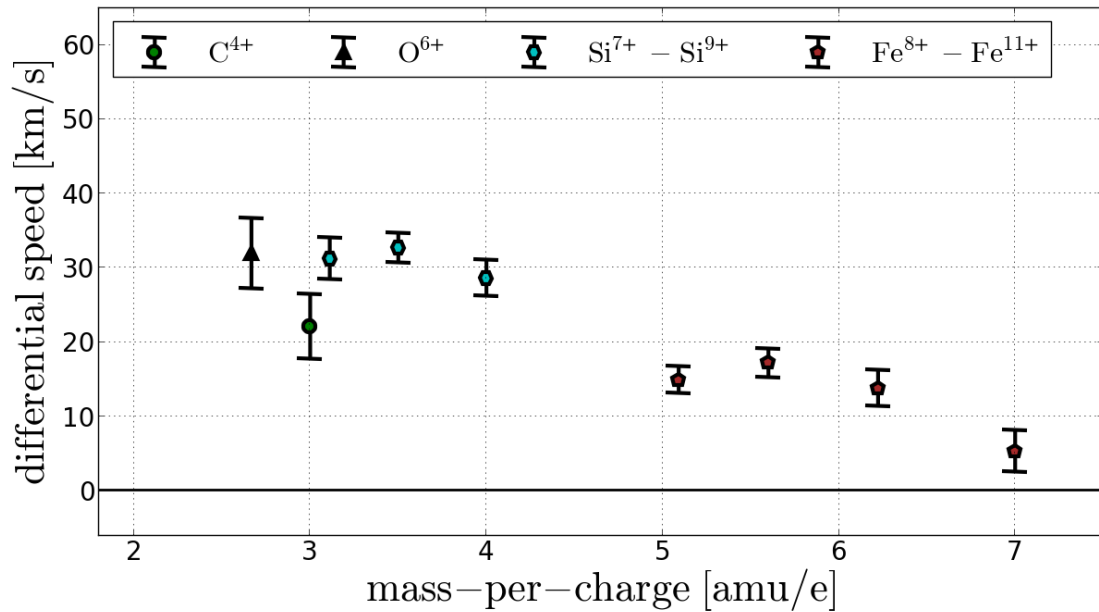
FIGURE 6.10

the least prominent among the selected ion species (see Figure ? all ion calibration), this might indicate some stronger influence of adjacent ion distributions in the Si10+ counts such as O6+.

-Explain calculation of mean speeds and the calculation of error bars, note that O6+ and C4+ have the largest error bar, which might be caused by the high base-rate factors.

We can see in Figure 6.10 that among the ion species with lower mass-per-charge $m/q \leq$ 4 amu/e O6+ and Si7+ -Si9 are measured with mean differential speeds of about 30 km/s without any statistically significant differences as can be seen from the overlapping error bars for this group. As already discussed in ? Within this group C4+ is measured at a somewhat lower mean differential speed of 22 ± 4 km/s with only very small overlap of the error bar with Si7+ and no overlap with the other species. The analyzed ion species group at higher mass-per-charge values consists (only) of the four best resolved/central iron charge states. The gap between the two groups is given by the fact that neither Si6+ nor any of the higher iron charge states yields very stable differential speeds in the long-term data. As already discussed in subsection 4.30?, the iron ion species on the whole show lower differential speeds in particular in the short-term data with mean values of less than 20 km/s, but in particular Fe8+ is measured with a very small speed difference of about 5 km/s. Thus, on the whole we find from the (current) analysis of the short-term VDFs a (seemingly clear) trend of decreasing differential speed with increasing mass-per-charge among the investigated heavy minor ion species. Assuming for simplicity an approximately
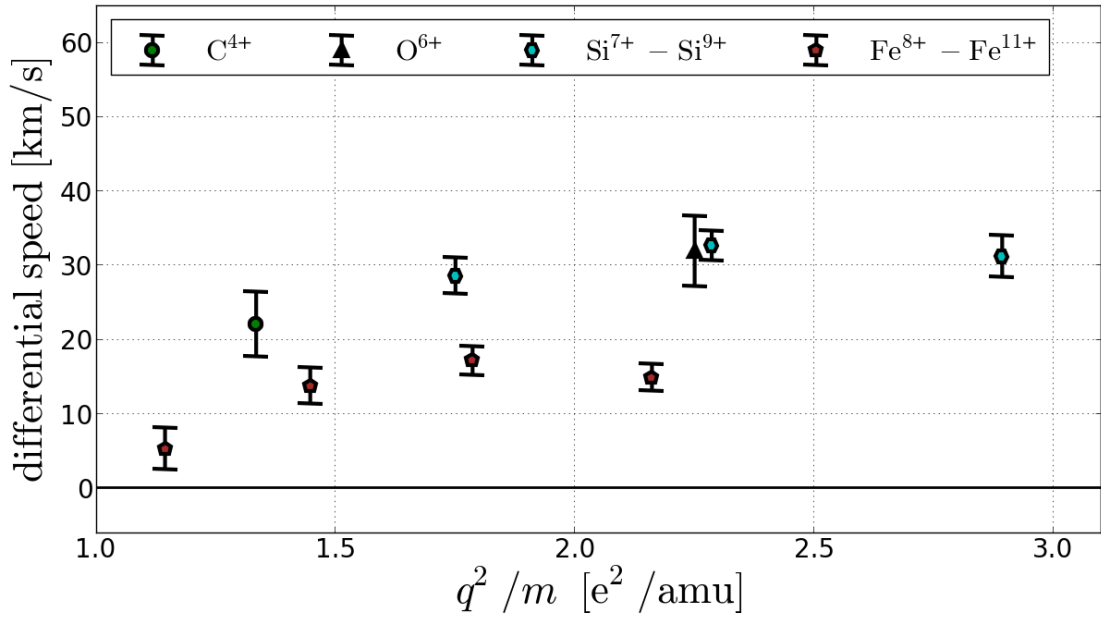
FIGURE 6.11

linear relation with mass-per-charge, the gradient of this trend can be calculated as $\Delta(\langle \Delta v_{ip} \rangle)/(\Delta m/q) \approx -5 \, (\mathrm{e\,km})/(\mathrm{amu\,s})$. (Note that this trend would predict no differential speed for ion species with $m/q \geq 8$ (Fe7+).) -we note that these differential speeds are derived from the Gaussian fit model, for which we showed that it systematically underestimates the differential speeds of the heavy ion and in particular for iron. Therefore, the found trend is quite likely to be modified to a certain extend when the more accurate Kappa-Moyal model is applied to the short-term data. We discuss the expected modification in the next subsection ??.

From section 4.30? we know that not only the potential acceleration processes in the solar wind can be mass- and charge-dependent but also thermalization processes such as Coulomb collisions are. Thus, if one assumes that any kind of acceleration process close to the Sun accelerated the different minor ion species to a certain level of differential speed with only small differences between the species or alternatively that after the initial acceleration up to a certain point the regulation of the differential speed is dominated by a given m/q-independent instability but from there on collisions are dominating and causing a thermalization of the differential speeds (even in the fast wind), one might expect a mean differential speed that is well ordered among the ion species by the ion-proton collisional age so that one expects after Eq. ? to first order a decreasing differential speed with increasing q^2/m. However, in Figure 6.11 we can see that the ordering of the ion species after q^2/m does not give any conclusive picture of the observed differential speeds in the fast wind. Explain pattern (wrong weak

thrend, only iron below, which can be attributed to the instrument response model)
One can argue that this is the expected result for the fast wind, where collisions play
only a minor role (Marsch1982 etc.), but compared to other studies the collisional ages
are not so low (in the faster wind ¿480 km/s of this study which is centered around a
collisional age of -1) as we never measure in the classical polar fast wind with mean
speeds of about 800 km/s and Kasper? claims that in this regime Coulomb collision
have already a measurable effect (are the dominant process), which cannot be deduced
from these results. On the other hand due to the mentioned competing processes in the
solar wind, the simple assumption that all heavy ion species are accelerated or regu-
lated to the same differential speed before Colulomb collisions start to influence their
speed might be just an appealing over-idealization. For completeness, we also looked
into the ordering of the differential speeds with increasing q^2/m in the intermediate
proton speed range $400 \leq v_p \leq 480$ km/s (not shown here), as one might expect some
clearer signature of Coulomb collisions here as the mean collisional age in this regime is
higher. Yet, the expected pattern could not be found in this data either and the situation
is even more complicated as the the differential speeds in this speed regime are hardly
significant in terms of systematical measurement uncertainties for most ion species.

6.3 Heavy Ion Thermal Speeds

6.3.1 Statistical Analysis of Thermal Speed Ratios
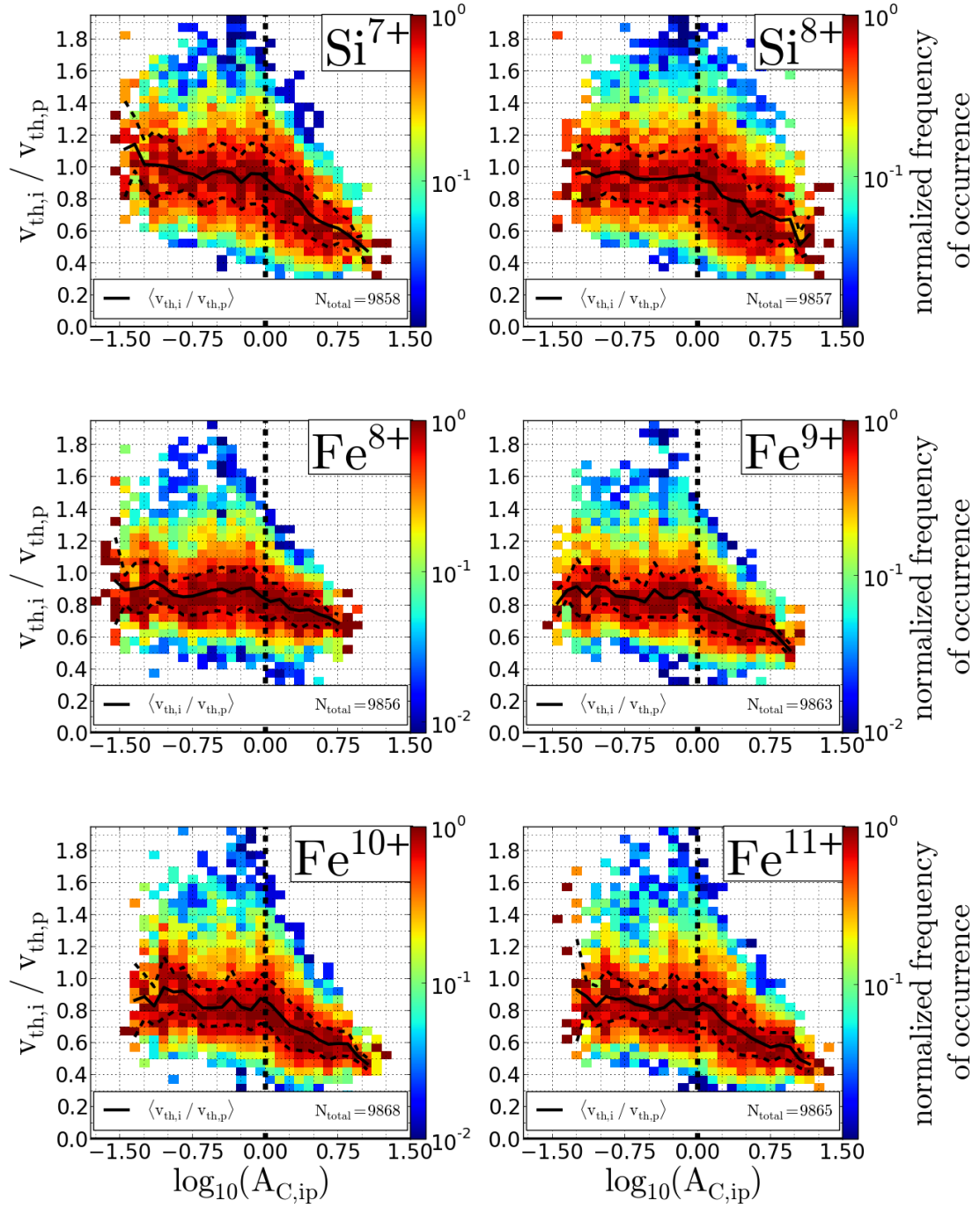
FIGURE 6.12

Chapter 7

Summary and Discussion

7.1 Summary: Kinetic Properties of Solar Wind Heavy Ions Measured with SOHO/CELIAS

In this work we measured the kinetic properties of solar wind heavy minor ions at 1 AU measured with SOHO/CELIAS/CTOF and compared them with the Proton proton properties that were simultaneously measured with the SOHO/CELIAS/PM.

-in long term data we were able to investigate 69 ion species (mass range: $2 < A <= 59$, mass-per-charge range: $2.3 \leq m/q \leq 8$?, elements: C-Ni) in the slow and fast wind by filtering the long-term data for a narrow proton speed of [330,340] km/s and [500,510] km/s interval as explained in section 5.?. The results were conducted from a probabilistic assignment method based on an inflight calibration that includes a systematic description of the ion species peak positions and shapes where the latter were modeled as asymmetric Kappa-Moyal functions in accordance with the measurement principle based on the carbon foil technique. -For ? of the investigated ion species their spectra showed acceptable count rate fluctuations in the core so that a consistent (bulk/core) mean speed determination was possible.

7.1.1 Long-Term Speed Spectra

We find in the slow wind - long term-speed spectra that consist of a Maxwellian core and sub/suprathermal tails on both the high speed and slow speed flanks for almost all investigated species. -of these ? the Maxwellian core showed an ion speed within +-5 km/s around the mean proton speed. In particular for all ion species with expected and observed high relative abundances the mean ion speed was within the given interval.

-So that within the systematic errors of our method, in particular the PM uncertainty, we conclude that the speed of the vast majority of measured ion species, among them the ones measured most reliably, is consistent with zero differential speed in the slow wind.

We find in the fast wind for the ? investigated ion species -also long term-speed spectra consisting of a Maxwellian core and sub/suprathermal tails similar to the slow case as far as they can be determined for the more abundant ion species within the reduced count statistics. - We find that due to the reduced counting statistics only ? of the 69? investigated ion species showed acceptable count rate fluctuations in the core so that a consistent (bulk/core) mean speed determination was possible. - among these ? ion species ? showed a differential streaming of more than ? km/s among them all of the most abundant ion species? -From this systematic analysis of all observed heavy ion species and including the systematic error analysis that takes into account the most important systematic uncertainties of the CTOF response model we conclude, that the all reliably measured heavy ion species show a significant differential streaming between 15 km/s and 30 km/s in the fast wind in the proton speed interval between 500 and 510 km/s. As can be seen from Figures ? and ? for the most prominent ion species of the most abundant investigated heavy elements, this result is also valid for other speed intervals with representative number of cycles in the fast wind between 480 and 540 km/s.
- we show only weak dependency on mass-per-charge, basically only iron ions show that trend to a statistically significant effect, but it is strongly response model dependent i.e. stronger gradient stronger for the full response model (grad) set also different quantitative results for Gauss and Kappamoyal model in particular for the very heavy iron ion species (lower heavy ion speeds for both speed regimes observed) - For all (these) investigated ion species the statistical errors are an order of a few km/s which means about a magnitude smaller than the obtained differential speeds and could consistently derived over different fractions of the (approximately) Maxwellian VDF (1sigma-2 sigma intervals around maximum).

our observations are back-up by generally meaningful/expected observations/behaviour in(of the data -The relative abundances of the most abundant ion species for each of the 10 investigated elements are in good agreement with the expected abundances as described in section ?. -compared to the slow wind case the we find for all investigated elements lower mean charge state in agreement with the expected coronal origin of the fast wind. - wider distributions 50 km/s in the fast wind observed than in the slow wind 15 km/s(no difference between ions observed?) - this finding does not change when we conduct the same analysis with a smaller set of ion species (give respective

numbers here) but shows slightly smaller mean ion speeds if the peak shape is substituted by the regular Gaussian peak shape in particlar for the very heavy ion species that show pronounced tails (down to -5km/s for certain iron species,check!)

7.1.2 Short-Term Velocity Distribution Functions

Short-term data, obtained for the 10 best resolved ion species (up o now only from Gaussian response model) with $2.7 \leq m/q \leq 7$ -identified from time series that the positive differential speeds appear over longer connected time intervals (¿1 day) during fast wind streams (almost exclusively) at speeds over 480 km/s, while in the slow wind the ions stream at the or slightly lower speed and in the intermediate wind the differential speed pattern alternates/is more variable but hardly resolvable with the current resolution (maybe this in discussion). - from 2d-histograms differential speed versus proton speed statistically confirm the time series measurements of positive differential streaming at fast speeds over 480 km/s for all analyzed species - magnitudes between 15 and 35 km/s (except for Fe8) comparable to long-term measurements, but a bit higher for low ($m/q \leq 4$)-ions - ordering by (proton-proton, or ion-proton) collisional age yields an equally good alternative to ordering by proton speed, so that both parameters can be regarded as potential ordering parameters (the proton speed probably more indirectly through the higher wave activity in the fast wind streams, that is in this small data set quite well-couled to the solar wind (proton) speed. - relatively strong dependence on mpq found (grad:) related to the upper point of differential speed magnitude.

- thermal speeds from short term data: all 6 analyzed major ion species (that are not biased by the Epq-stepper stop) of Si7, - Fe10 show approximately thermal speeds (ratios 0.9-1.0) at low collisional ages (fast wind), while a clear trend towards equal temperatures is observed for coll. age larger than O1 -therefore about mass-proportional heating observed and thermalization due to coulomb collisions consistent with the observations. In particular clearer breaking point signature in the collisional age than in the protons? (Maybe here the collisions kick in and not in already earlier by the regulation of the differential speed, which is already about zero at this collisional age).

7.2 Discussion: MpQ dependence / Systematic Error analysis

Both the long-term speed spectra and the short-term VDFs show significant differential speeds of the solar wind heavy ions compared to the protons in the fast wind. Comparing the magnitude of Δv_{ip} for different ion species, both measurements also show

higher differential speeds for ion species with lower mass-per-charge, but the difference between low-m/q and high m/q-ion species is less than $10\,\text{km/s}$ in the long-term data (see Figure 5.15 and 5.15 in chapter 5) while it is about $20\,\text{km}$ in the short term data as we see in Figure 6.10. This yields a much stronger dependence in differential speed on mass-per-charge in the short-term data because a difference of $10\,\text{km/s}$ is already a substantial fraction of the overall observed differential speeds at 1 AU. The observed quantitative trend difference between the two results are mainly because of the four reliably measured iron ions Fe^{8+} - Fe^{11+} (which alone span a relative large range of $\approx 40\%$ of the investigated m/q-range) that are measured with $5\,\text{km/s} \leq \Delta v_{ip} \leq 15\,\text{km/s}$ in the short term data while they are measured with $15\,\text{km/s} \leq \Delta v_{ip} \leq 30\,\text{km/s}$ in the long-term data as can be seen from the comparison of the same Figures 5.15 5.15 and 7.1. The difference between the two results can be explained mainly due to the fact that the short-term data is analyzed still with the Gaussian response model while the shown long-term data in chapter 5 is already analyzed with the more accurate Kappa-Moyal peak model. To illustrate this point we show in Figure 7.1 for several major heavy ion species the comparison between the observed mean short-term differential speeds (in the proton speed range between 480 km/s and 540 km/s, filled symbols) and the measured long-term differential speeds for the proton speed range $v_p \in [500, 510]$ (empty symbols) but this time derived with the Gaussian peak shape model for direct comparison. We see that in this case the long-term differential speeds match exactly with the short-term differential speeds for iron when they are derived with the same response model. The gray shaded area shows the estimated range of systematic uncertainty that we derived from the long-term mean speed error estimation in chapter 5 for the different peak tail parameters, with the best tail parameter $A_c = 0.0035\,\text{ch}^{-1}$ lying roughly in the middle of this area. Thus, one can anticipate the systematic correction that one has to apply to the obtained short-term differential speeds to correct them for the inaccurate peak shape model[1]. As can be seen from the extension of the gray area, that we already discussed in chapter **??**, this correction is larger for ions with high mass-per-charge such as the iron ions, so that the strong decreasing trend of differential speeds with increasing mass observed in the short-term data, is reduced.

In general, we also note that the improved peak shape model also reduces the negative differential speeds for iron in the slow wind that we recognized for instance in Figure 6.6. This can be seen from Figures 5.8 and 5.9, where we only observe small negative differential speeds for the iron ions of about -5 km/s which is comparable to the other ion species and can be easily explained by the inaccurcies of the CELIAS Proton Monitor.

A second minor reason for the stronger trend in the short term data is the difference

---

[1]Ideally, the short-term data should be also evaluated with the more accurate Kappa-Moyal peak model in the future to verify this explanation also with identically low short-term counting statistics.

in average differential speed that is observed for the low-m/q ions that are measured with differential speeds around 25 km/s in the long-term data while we find differential speeds around 30 km/s in the short-term data. As can be seen from Figure 7.1, this difference cannot be explained by the difference in the response model. Since it is in general plausible that nonthermal features in the short-term data are more pronounced as they are less likely to be averaged out over shorter integration periods, it is not clear why this should only apply to the heavy ion species with lower mass-per-charge, but not to iron as can be seen from Figure 7.1. Thus, it might be the case that we have an instrumental effect here that causes a small systematic bias e.g. due to the PHA count rate multiplication with higher base rate factors for the low-m/q species compared to iron. This idea is related to the fact that for small counting statistics in the applied fits (i.e. where many ET-bins are empty), the true count rates cannot be approximated that well with a much smaller subsample of PHA counts that are multiplied with a high correction factor.
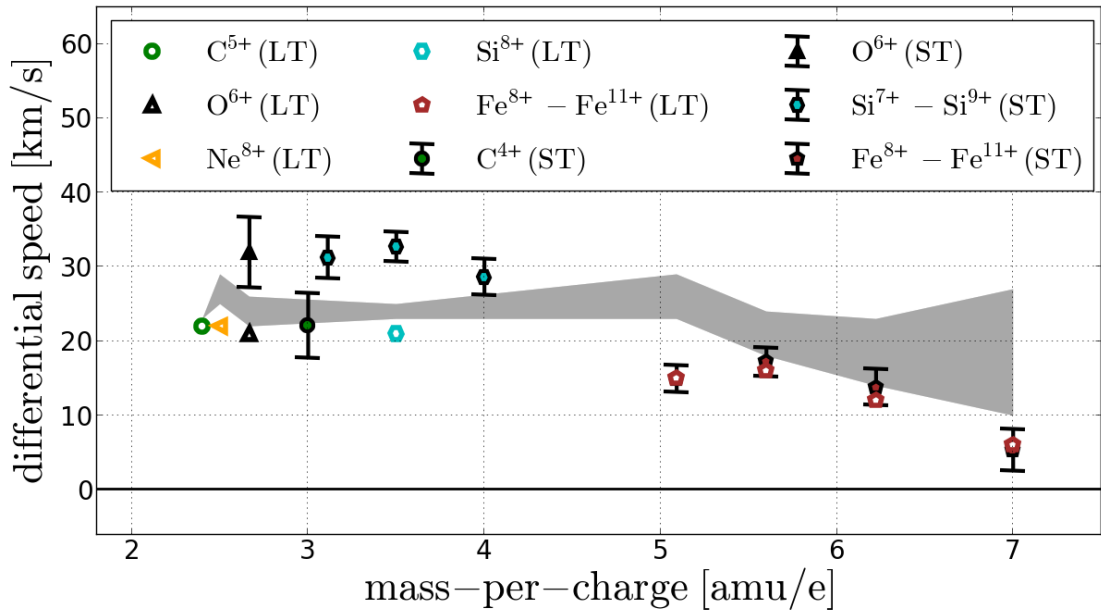
FIGURE 7.1: Long-term (LT) and short-term (ST) differential speeds obtained for several major ion species derived with the Gaussian Response model. The gray shaded area is the systematic uncertainty interval that we obtained from the long-term speed measurements in chapter 5.

Under the two discussed circumstances, the observed trend that looks at a first glance quite substantial in terms of relative differential speed, might vanish completely with a more elaborated response / peak shape model, so that we cannot exclude that all ion species flow at exactly the same differential speed of about 20-30 km/s compared to the solar wind bulk protons. Yet, what is statistically very unlikely from the measured long-term and short-term data and the systematic error analysis is that the ion species

follow the opposite trend of increasing differential speed with increasing mass-per-charge. This is particularly interesting as such a trend can be expected, if the ions were accelerated locally to their differential speed cut-off that results form the resonance condition in chapter 1.

7.3 Discussion: Kinetic Properties of Solar Wind Heavy Ions at 1 AU

Discuss the comparison between SOHO and ACE results with Figure 7.2 and 1.13 in chapter 1.
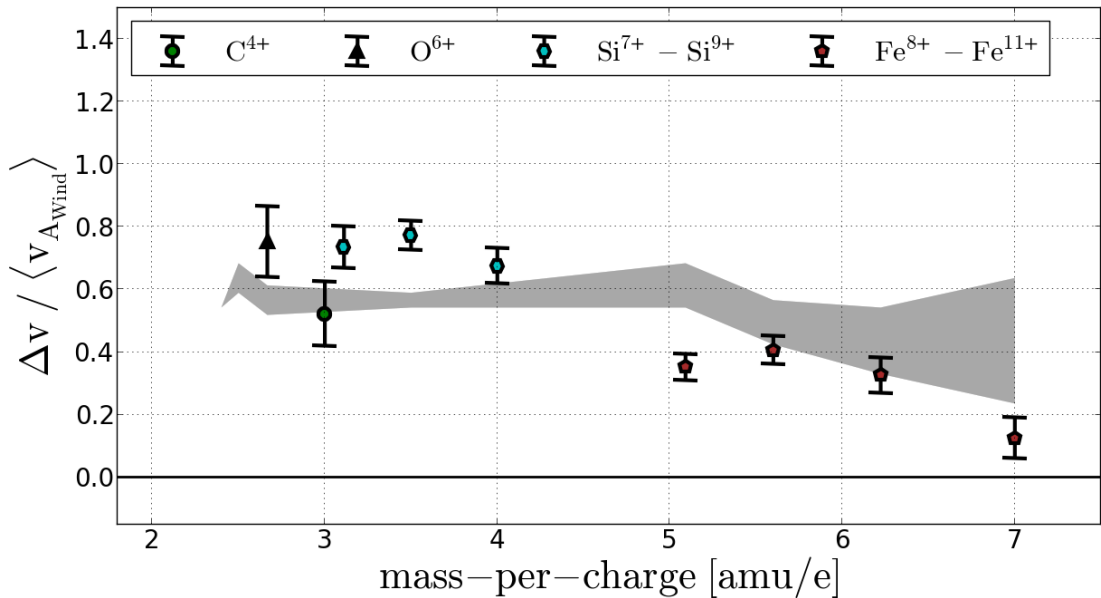
FIGURE 7.2: Differential Speeds obtained from the short term data for the major ion species O6+ - Fe11+, in units of the average extrapolated Alfén speed from wind for the fast wind stream between DOY 213 and 216 1996. The gray shaded area corresponds to the systematic uncertainty interval that we obtained from the long-term speed measurements in chapter 5

7.4 Discussion: Collisional Evolution of Nonthermal Heavy Ion Velocity Distribution Functions

If time left:

discuss the collisional evolution with the Hernandez-Marsch model.

7.5 Stop Reading

main results/findings (probably putting here a summary table similar to ESAC presentation would be a good idea here):

-1) all (major) ions show the same qualitative behavior both as a function of proton speed and collisional age (this is also the case for ions where the measurement uncertainties are large due to their low abundances or/and the measurement set-up. in particular by improvements in the data analysis (using MR and PHA data, improved response model for (very) heavy ion species, maximum-likelihood approach instead of box rates) that are also taken into account in the uncertainty analysis we could solve the issue seemingly contradictory differential speeds of the Hefti (1998) study.

2) all (with SOHO/CELIAS) investigated ions (minimum Si7+,Si8+,Fe12+,Fe11+,Fe10+,Fe9+) that can be resolved with the highest (and sufficient) accuracy show mean speeds that are equal to the simultaneously measured proton speeds in the slow wind and significant (1,2,3? sigma) positive differential speeds in the fast solar wind regime - both in long-term averages and in short-term resolution (compare also B-field extrapolation by Nemecek et al. o Taut el al for the short term data)

3) making use of the systematic analysis approach (although limited by instrumental effects: E/q-stepper, reconstructed PHA counts), when we compare all ion species we find that within the (overall) uncertainties all these species stream at the same differential speed at 1 AU at all (slow, fast, intermediate) observed solar wind regimes. In particular the best resolved ions (Si7+,Si8+,Fe12+,Fe11+,Fe10+,Fe9+) show no (clear/significant) trend with m/q in the fast or intermediate wind, neither we find a trend with m^2/q. The absence of such a trend in the fast (or more precisely in the collisionless wind) sets constraints on acceleration models including resonant wave-particle interaction with resonances of order $n > 0$ both in the case of local acceleration or acceleration close to the Sun, when we just consider this single (main) acceleration mechanism and only take into account Coulomb collisions as the (main) relaxation mechanism. Instead, in the fast solar wind the equal differential speeds could be well-explained by Landau-resonance/damping ($n = 0$) which would yield mass-per-charge independent speeds. Furthermore, since we see no trend with q^2/m (when we compare silicon and iron ions) in the intermediate wind (colage classification?), where collisions are expected to have some influence on the kinetic properties of the ions, this might point to a local acceleration as source of the differential streaming rather than interpreting it as remnant signature, but this last point should be seen carefully since there are only a few ions which could be measured with sufficient accuracy and also only for a very limited time period.

4) -remind: In ACE data we do not have (yet) such an elaborated response model

(should be ok for most abundant ions) and in particular no systematic error estimation yet, at SOHO we have no in-situ Bfield data, but we are now able to draw a relatively consistent picture of differential speeds (in the ecliptic at 1 AU): the observed differential speeds are in (very) good agreement with ACE observations. No differential streaming in slow (collisional) wind, few tens of kilometers per second in the fast (collisionless) wind (give numbers), mind that we only measure the reduced/projected speeds. When we take expected values of Alvfen speed, instruments (disregarding systematic uncertainties) show the common observation that the differential speed is about half the ambient alfven speed (not the full alfven speed as one wuld expect from simple considerations (why?). Recapitulate with Lars here our major points of our current understanding (see also picture that we send to Nemecek).

For temperatures: - keep in mind that with the time-of-flight mass spectrometers on SOHO and ACE we only measure "reduced" temperatures. With SOHO these cannot be related to onboard in-situ data, so that these are in general a mix of parallel temperatures with the mean B-field configuaration along the Parker angle.
1) we observe nonthermal temperatures in the collisionless (fast) wind and a clear trend towards thermal equlibrium. The transition occurs around a collisonal age of 1 (average scattering of 90 degrees (stddev) for each particle) as expected(?) by i.e. Narsch and livi (check!)
2) for all well-resolved ions (check in particular strongly telemetry corrected ions,such as O6+), we find (quite) exact mass-proportional heating ($vth_i on/vth_p = 1$) in the collisionless wind, which is different from the ACE results. This is either a true a true temporal difference (low statistics for ACE/SWICS? probably cannot reproduce this effect, or?), or one of the measurements is slightly off. (check for ACE measurement issues in ACE/SWICS or SOHO/ACE PM measurements), ask Lars for the ACE data and check definitions), also give systematic uncertainties for thermal speed measurement. The difference between mass-proportional or over-mass proportional heating is a crucial difference to test detailed model predictions of resonant ion cyclotron interaction (such as by Isenberg and Hollweg)
3) Reduced (asynchronous) perpendicular and parallel temperatures look different/have to be distinguished as can be seen with ACE/SWICS, but subject to a reliable extrapolation from WIND to SOHO.

Both differential streaming and temperatures seen together: -when plotting both differential speeds and temperatures as a function of collisional age we find that the equalization of differential speeds starts at least about one order of magnitude in collisional age earlier than the equalization of kinetic temperatures, which is in contradiction to the predictions of the relaxation process that one can would get analytically when only

assuming Coulomb collisions acting between a Maxwellian sample of solar wind heavy (minor) ion test particles and the solar wind protons (also Maxwellian VDF). The latter would predict an almost simultaneous decrease of both quantities (on a logarithmic scale). At a first glance the temperature (thermal ratio) curve looks more or less similar as in the analytical model, but the differential speeds start to decrease at much lower collisional ages than expected, which means (when we do not shift significantly in col. age) that it is not collisions that are the main driver of the relaxation process, but probably the build up and/or maintainance of differential speeds is regulated by a different process inherent to wave-particle interaction itself. the easiest explanation would be a coupling to the ambient alfven speed, which could be already much lower at intermediate coll. age than at low col. age values. Also check, whether in the analytical model, the temperature curve changes significantly, if we fix the differential speed evolution as measured. If yes, this means that an additional heating (energy transfer process from mono-directional kinetic energy to heating occurs (the heating might be also only just waves resolved with insufficient time resolution). If no, it means that in contrast to the differential speed the different heavy ion temperatures are indeed regulated mainly by Coulomb collisions with the solar wind bulk protons. In the easy picture of a strong coupling of the differential speeds to the ambient alfven speed, this could be (easily) explained consistently because the ion temperatures do not (explicitely) depend (check!) on the local alfven speed.

-the CTOF short-term and long-term data showed a very similar speed pattern for all analyzed solar wind ion species:

About equal speeds or even small negative speeds in the fast wind and positive differential speeds in the fast wind

statistically differential speeds

7.6 Possible Experimental Improvements and Future Measurements

Asymmetric peak shapes: The few exceptions [Mu, sulfur by Cohen?, Bob? others], concentrated on the isolated description of single ion species peaks in order to derive more accurate elemental and/or charge states abundances, but no systematic attempt was made to find a general substitution for the Gaussian peak shape for the complete set of solar wind heavy ions (maybe better emphasize this in the summary/discussion chapter).

Appendix A

Supplementary Documentation of the CTOF PHA-Data Base-Rate Reconstruction

CTOF Matrix Rate Data

Idea of this appendix is to allow complete reproducibility of the derived data products (from the physical point of view), even if there might appear only a brief/shortened description of the applied procedure in the respective chapters. Give here necessary additional functions, tables information in any form to achieve this goal.

FIGURE A.1

196

Lookup Table for the CTOF Matrix Rates Center Step

mass−per−charge [ch]

mass[ch]

FIGURE A.2

DOY : 174−220 1996, E/q−step : 40

DOY : 174−220 1996, E/q−step : 40

FIGURE A.3

FIGURE A.4

DOY : 174−220 1996, E/q−step : 60

FIGURE A.5

FIGURE A.6

DOY : 174−220 1996, E/q−step : 80

DOY : 174−220 1996, E/q−step : 80

Figure A.7

Appendix B

Supplementary Documentation of the CTOF Response Model

B.1 CTOF PHA Data Calibration

B.1.1 Fundamental CTOF Instrument Parameters

Instrument Parameter	Value	Unit	Reference
L_τ	70.5	mm	[Aellig/Hefti(PhD,1998,1997)]
U_0	0.331095	kV	[Aellig/Hefti(PhD,1998,1997)]
r	1.040926	1	[Aellig/Hefti(PhD,1998,1997)]
U_{acc}	23.85	kV	[Taut(Master,2014)]
d_{C-foil}	24	nm	[Taut(Master,2014)]
$d_{SSD-SiO2}$	75	nm	[Oetliker(1993), Janitzek(Master,2014)]
$\delta v_{E/q}$	0.0121	1	[Aellig(PhD,1998)]

TABLE B.1: Summary of fundamental CTOF instrument parameters for the In-flight calibration and derivation of the velocity distribution functions.

B.1.2 TRIM Simulation Input-Spectra

Ion	min. step	max. step	min. E_{acc} [keV]	max. E_{acc} [keV]
He^{2+}	30	73	**52**	**69**
O^{6+}	40	70	**156**	**185**
Si^{7+}	38	58	**191**	220
Si^{8+}	38	58	218	**251**
Fe^{8+}	27	57	**219**	285
Fe^{9+}	25	60	242	329
Fe^{10+}	27	60	270	**356**

TABLE B.2: Simulation input energies calculated as reference ion energy range after post-acceleration. The table is adapted from Janitzek(Master,2014).

B.1.3 TOF-Position Calibration

Element	A	B	C	TOFCOR [ch]
He	5.889321	17.70091	0.015628	0
C	13.08489	21.96882	0.015237	-2
N	13.19550	14.60739	0.017141	-1
O	17.35453	45.98613	0.008159	-2
Ne	13.62666	26.34092	0.015860	-3
Na*	12.28412	-35.53477	0.018663	-2
Mg	8.235615	6.927236	0.023816	-2
Al*	12.28412	-35.53477	0.018663	-2
Si	14.71547	-7.057364	0.021663	-1
S	13.89511	1.125358	0.030509	-1
Ar*	12.28412	-35.53477	0.018663	0
Ca*	12.28412	-35.53477	0.018663	0
Fe	12.28412	-35.53477	0.018663	0
Ni*	12.28412	-35.53477	0.018663	0

TABLE B.3: Look-up Table for the calculatation of the TOF positions in the CTOF baserate corrected PHA ET-matrices. The constants A,B,C are for the calculation of the relative energy loss in the carbon foil α_τ according to Eq. 4.18 in section 4.4. The asterisk * marks the elements, for which we did not obtain α_τ from a TRIM simulation but approximated it with the iron value $\alpha_{\tau,Fe}$ as an approximation of the mean relative energy loss (see section 4.4). The value TOFCOR is the correction of the TOF channels for all ion species of the given element and for all E/q-steps $0 \leq j \leq 116$.

B.1.4 ESSD-Position Calibration

Helium is the only element for which we observe a TOF-dependent pulse height defect (in agreement with [Hefti,1997,PhD]). The corresponding PHF-value is calculated from a polynomial fit $\alpha_\epsilon^{He}(\widetilde{E}_{nuc}(\tau_{ij}))$ to the TRIM simulation that is in good agreement with the measured ESSD position of He^{2+} (see section 4.4 and Janitzek(Master,2014)):

$$\alpha_\epsilon^{He}(\widetilde{E}_{nuc}) = C0_{\alpha_\epsilon,He} \cdot \widetilde{E}_{nuc}^3 + C1_{\alpha_\epsilon,He} \cdot \widetilde{E}_{nuc}^2 + C2_{\alpha_\epsilon,He} \cdot \widetilde{E}_{nuc} + C3_{\alpha_\epsilon,He} \tag{B.1}$$

with the constants $C0_{\alpha_\epsilon,He}$ - $C3_{\alpha_\epsilon,He}$ given in Table B.4 and the energy/nucleon-proportional term:

$$\widetilde{E}_{nuc} = \frac{L_\tau^2}{2} \cdot (A_\tau \cdot \tau_{ij} + B_\tau)^{-2} \cdot \frac{\text{amu}}{\text{keV}} \tag{B.2}$$

where τ_{ij} is the calibrated TOF peak position at Epq-step $0 \leq j \leq 116$ for He^{2+} or He^+, respectively, and the remaining constants L_τ^2 as given in Table B.1, A_τ, B_τ as given in Eq. 4.20 and amu$= 1.66 \cdot 10^{-27}$ kg and keV$= 1.602 \cdot 10^{-16}$ C.

For all other calibrated elements carbon - nickel for which we obtained a TOF-independent pulse height defect the constant PHF-value is given in Table B.5 and can be directly used in Eq. 4.23.

Element	$C0_{\alpha_\epsilon,He}$	$C1_{\alpha_\epsilon,He}$	$C2_{\alpha_\epsilon,He}$	$C3_{\alpha_\epsilon,He}$
He	5.117329e-05	-2.923190e-03	6.387425e-02	2.480608e-01

TABLE B.4: Look-up Table for the calculatation of the ESSD positions in the CTOF (base-rate corrected) PHA ET-matrices for helium (He^{2+}, He^+).

Element	PHF ($= \alpha_{\epsilon,uncor}$)	PHFCOR ($= \alpha_{\epsilon,relcor}$)
C	0.609	39.0/42
N*	0.575	39.2/42
O	0.542	39.5/42
Ne	0.510	39.5/42
Na*	0.495	39.5/42
Mg	0.479	39.5/42
Al*	0.464	40.0/42
Si	0.448	40.5/42
S*	0.423	40.7/42
Ar*	0.397	40.9/42
Ca*	0.372	41.1/42
Fe	0.296	42.0/42
Ni*	0.273	42.0/42

TABLE B.5: Look-up Table for the calculatation of the ESSD positions in the CTOF (base-rate corrected) PHA ET-matrices as described in section 4.4 for all calibrated elements with atomic number $Z > 2$ for which we obtain a pulse height defect that is independent of the ions TOF position. The PHF-value is derived for the uncorrected PHA count rate data. The PHF-value for the base-rate corrected PHA count rate data is calculated by $\alpha_\epsilon = \alpha_{\epsilon,uncor} \cdot \alpha_{\epsilon,relcor}$. The elements that are marked with a * are linearly interpolated as described in section 4.4.

B.1.5 ESSD-Width Calibration for Iron

As the dominant iron species Fe^{8+} - Fe^{11+} are well separated from other ion species of comparable abundance, their ESSD peak shape can be modeled more accurately from the CTOF long-term data. We use an asymmetrical Gaussian for this purpose:

$$R_{\epsilon,Fe}(\sigma_{\epsilon,up}, \sigma_{\epsilon,low}, \tau, \epsilon) = G^1_{asym}(\epsilon_0(\tau), \sigma_{\epsilon,up}, \sigma_{\epsilon,low}, \epsilon)$$

$$= \begin{cases} \exp\left(-\dfrac{(\epsilon_0 - \epsilon(\tau))^2}{2\sigma^2_{\epsilon,low}}\right) & \text{if } \epsilon \leq \epsilon_0(\tau) \\ \exp\left(-\dfrac{(\epsilon_0 - \epsilon(\tau))^2}{2\sigma^2_{\epsilon,up}}\right) & \text{if } \epsilon \geq \epsilon_0(\tau) \end{cases} \tag{B.3}$$

where $\sigma_{\epsilon,up}$ and $\sigma_{\epsilon,low}$ are the width parameters for the upper and lower ESSD flanks, respectively and $\epsilon_0(\tau)$ is the calibrated most probable ESSD channel at each given TOF channel after Eq. 4.23. Assuming a linear scaling of both width-parameters with $\epsilon_0(\tau)$:

$$\sigma_{\epsilon,up}(\epsilon_0(\tau)) = A_{\sigma_{\epsilon,up}} \cdot \epsilon_0(\tau) + B_{\sigma_{\epsilon,up}} \tag{B.4}$$

and

$$\sigma_{\epsilon,low}(\epsilon_0(\tau)) = A_{\sigma_{\epsilon,low}} \cdot \epsilon_0(\tau) + B_{\sigma_{\epsilon,low}} \tag{B.5}$$

we find from fits to the iron data peaks at Epq-steps 39 - 55 the optimal scaling parameters $A_{\sigma_{\epsilon,up}} = 0.167$, $B_{\sigma_{\epsilon,up}} = 0.5$ and $A_{\sigma_{\epsilon,low}} = 0.139$, $B_{\sigma_{\epsilon,low}} = -1.0$ ch. We recognize that the upper ESSD-flank in the data is more pronounced than the lower ESSD flank, which is in agreement with [Aellig,PHD], although one would expect it the other way around if the energy loss in the SiO_2 dead-layer was the main reason for the peak asymmetry along the ESSD axis (see the TRIM simulations in [Janitzek(2014)]). Clearly, a deeper understanding of the ESSD signal formation for very heavy ions i.e. from laboratory calibration measurements is necessary here to improve the peak shape models for time-of-flight mass spectrometers in current or future missions.

B.1.6 CTOF Detection Efficiencies

E_{acc}/nuc [keV/amu]	DC-Efficiency, Iron
1	0.035
1.5	0.080
2	0.110
2.5	0.140
3	0.165
3.5	0.185
4	0.205
4.5	0.218
5	0.230
6	0.245
7	0.260
8	0.270
9	0.275
10	0.280
12	0.290
14	0.295
16	0.298
18	0.300
20	0.300

TABLE B.6: Double Coincidence efficiencies for iron [after Aellig/Gruenwaldt 1998], modeled after measurements of oxygen and argon with CTOF flight spare model at MPAe Katlenburg-Lindau (oxygen could be also put here measered and modeled). The values are extracted manually from Figure 4.11 in [Aellig, PhD). The model uncertainties, which are 10% in the typical energy range for the main charge states of iron [estimated by Aellig, PhD, 1998).

E_{acc} [keV]	SSD-Efficiency, Iron
200	0.75
250	0.81
300	0.87
350	0.91
400	0.94
450	0.96
500	0.97

TABLE B.7: SSD efficiencies [estimated by Aellig, PhD, 1998]) after measurements of the ACE/SWICS SSD at the Ion Beam Facility at the Univeryity of Giessen. The values are obtained manually from Figure 4.14 in [Aellig, PhD, 1998].

Appendix C

CTOF Response Model Details/Information

Give short description of this appendix part.
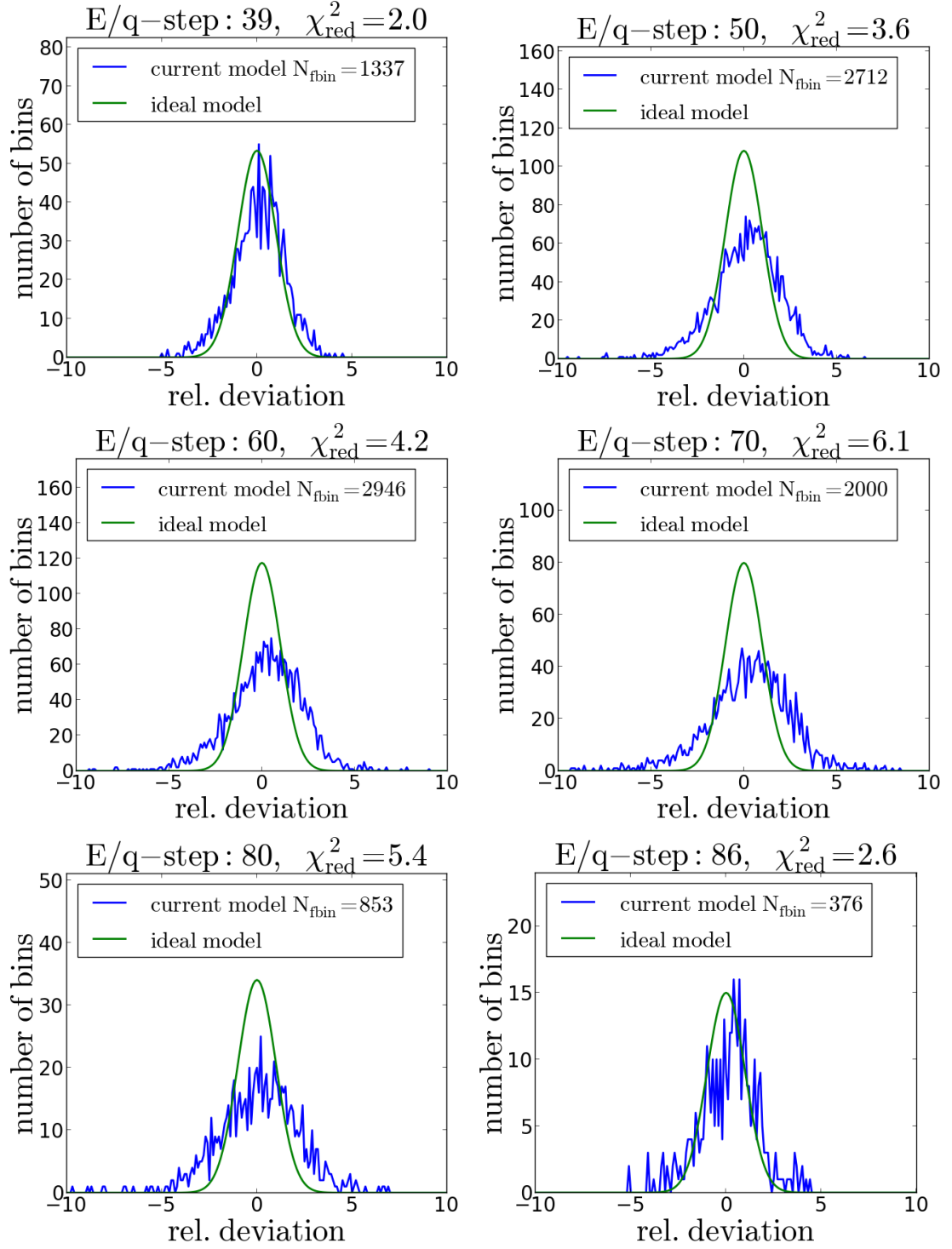
C.1 Full Stable Response Model

### C.1.1 2D-Gaussian Peak Model
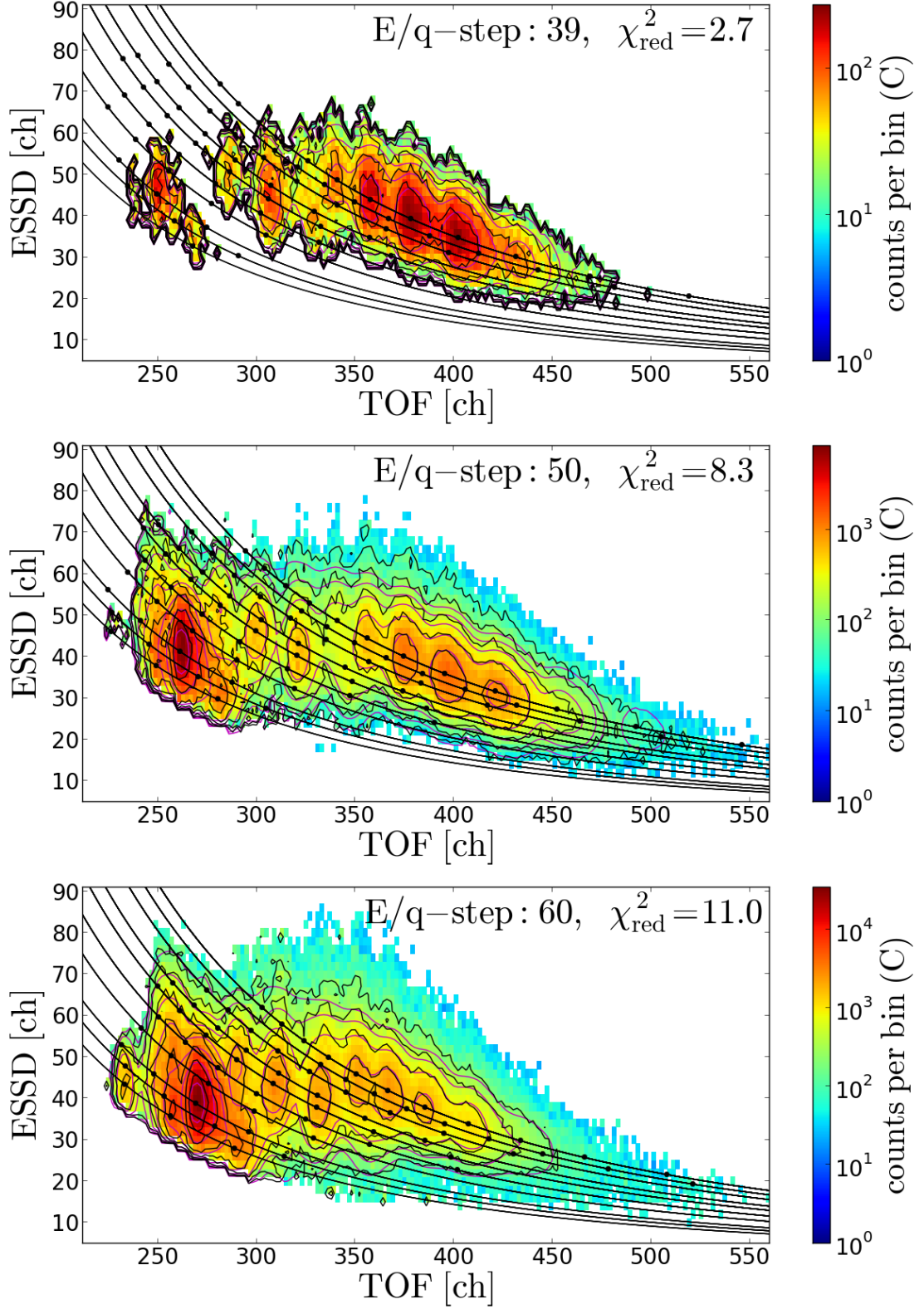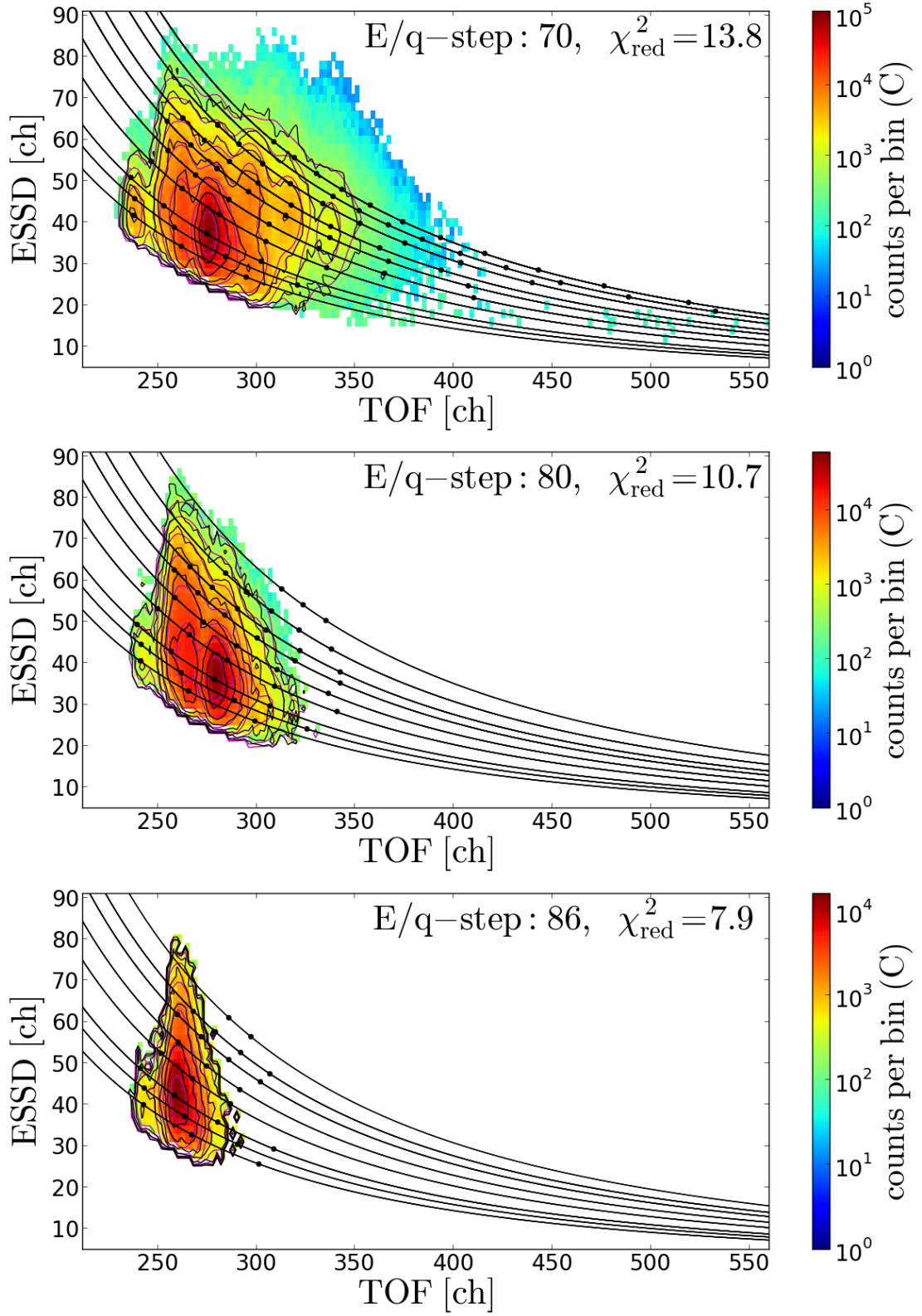
FIGURE C.1

FIGURE C.2
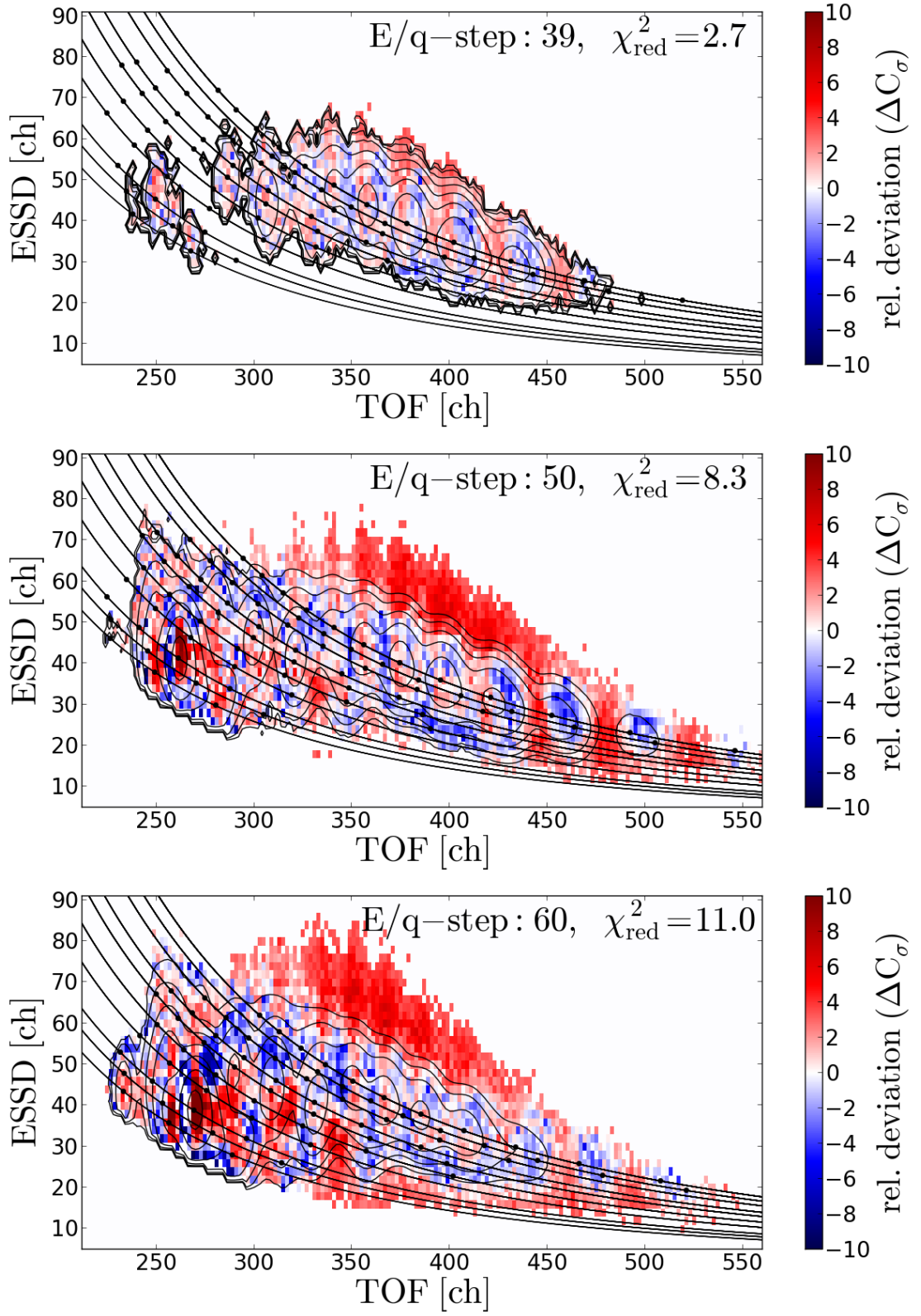
FIGURE C.3
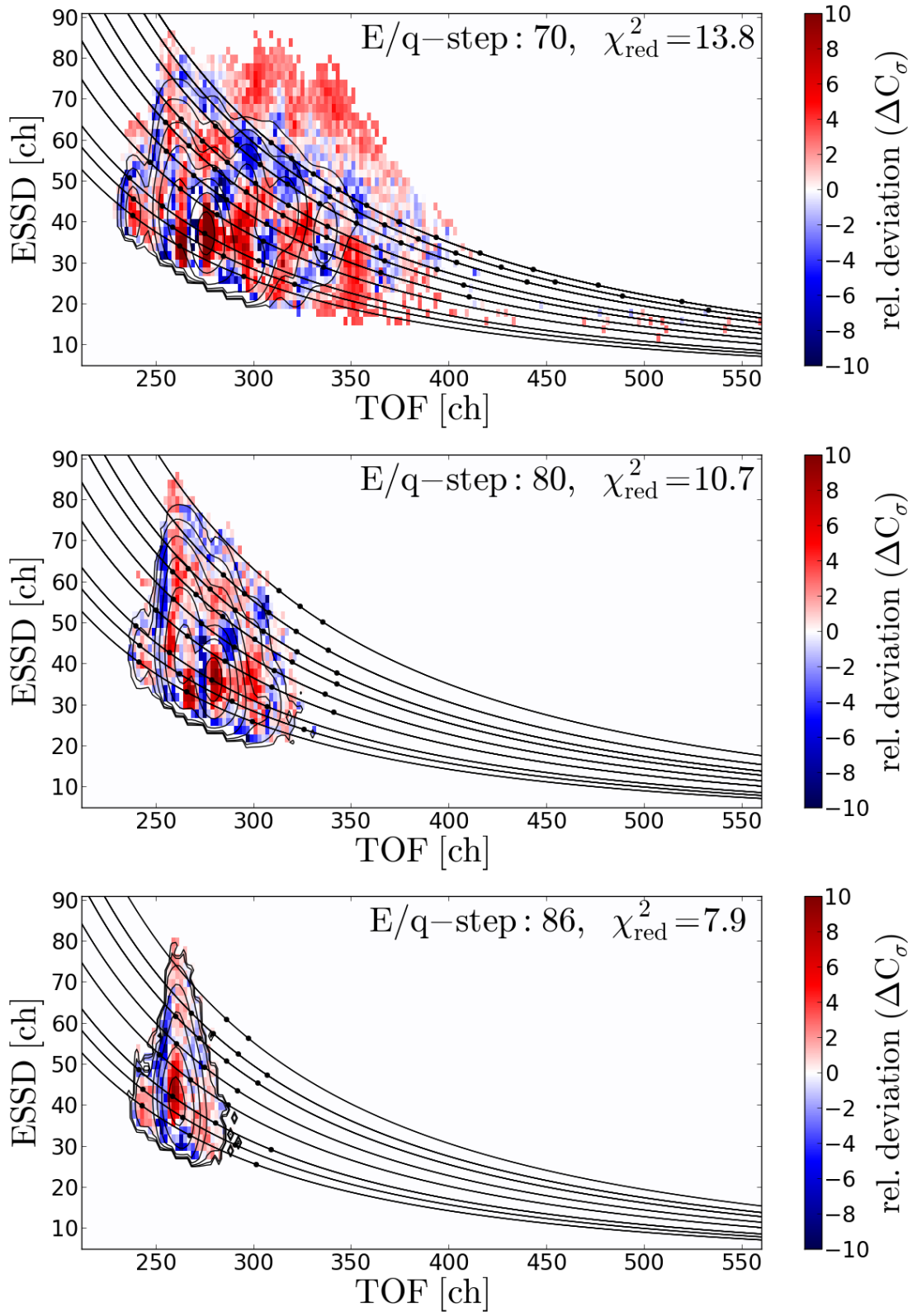
FIGURE C.4

FIGURE C.5

216
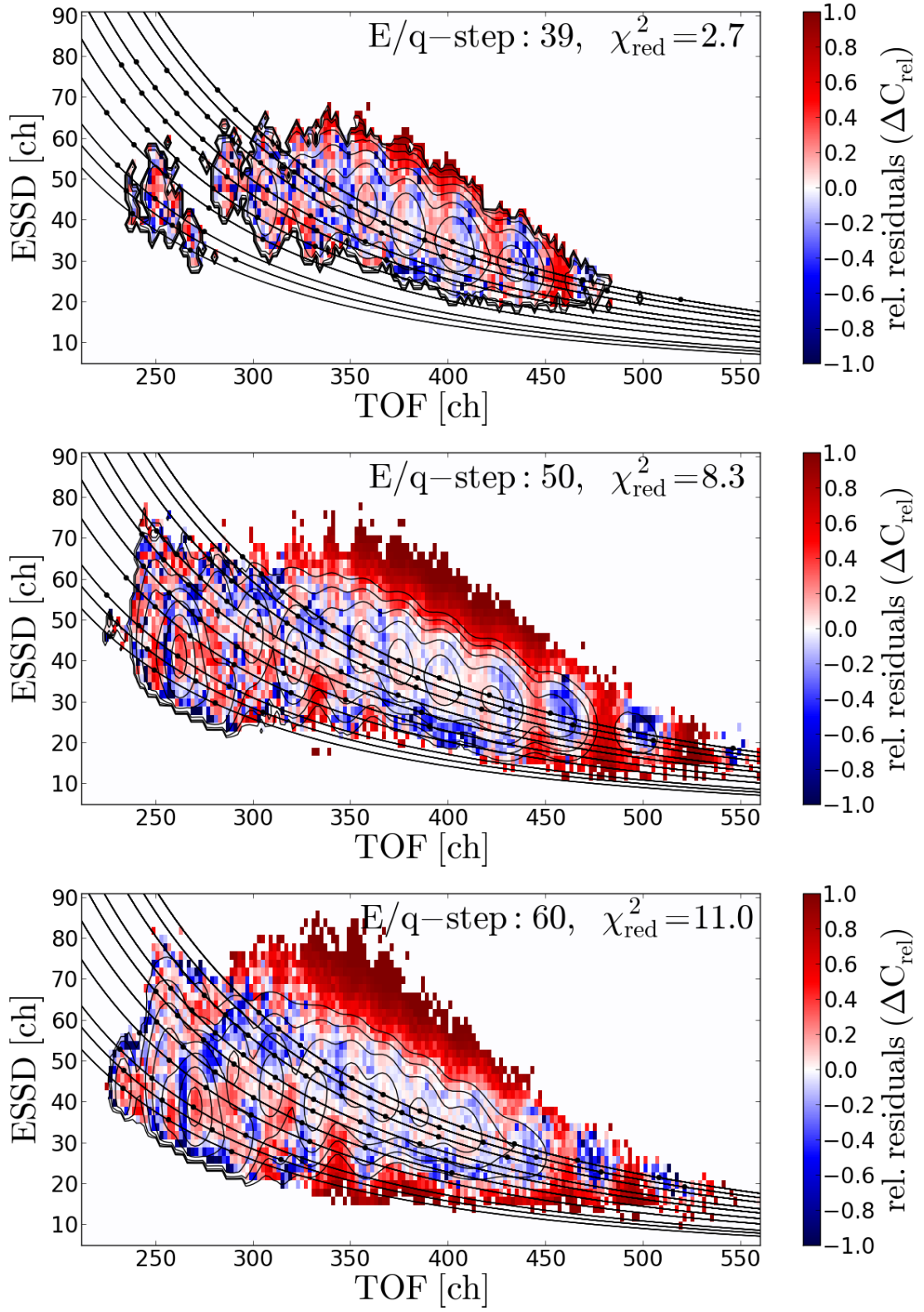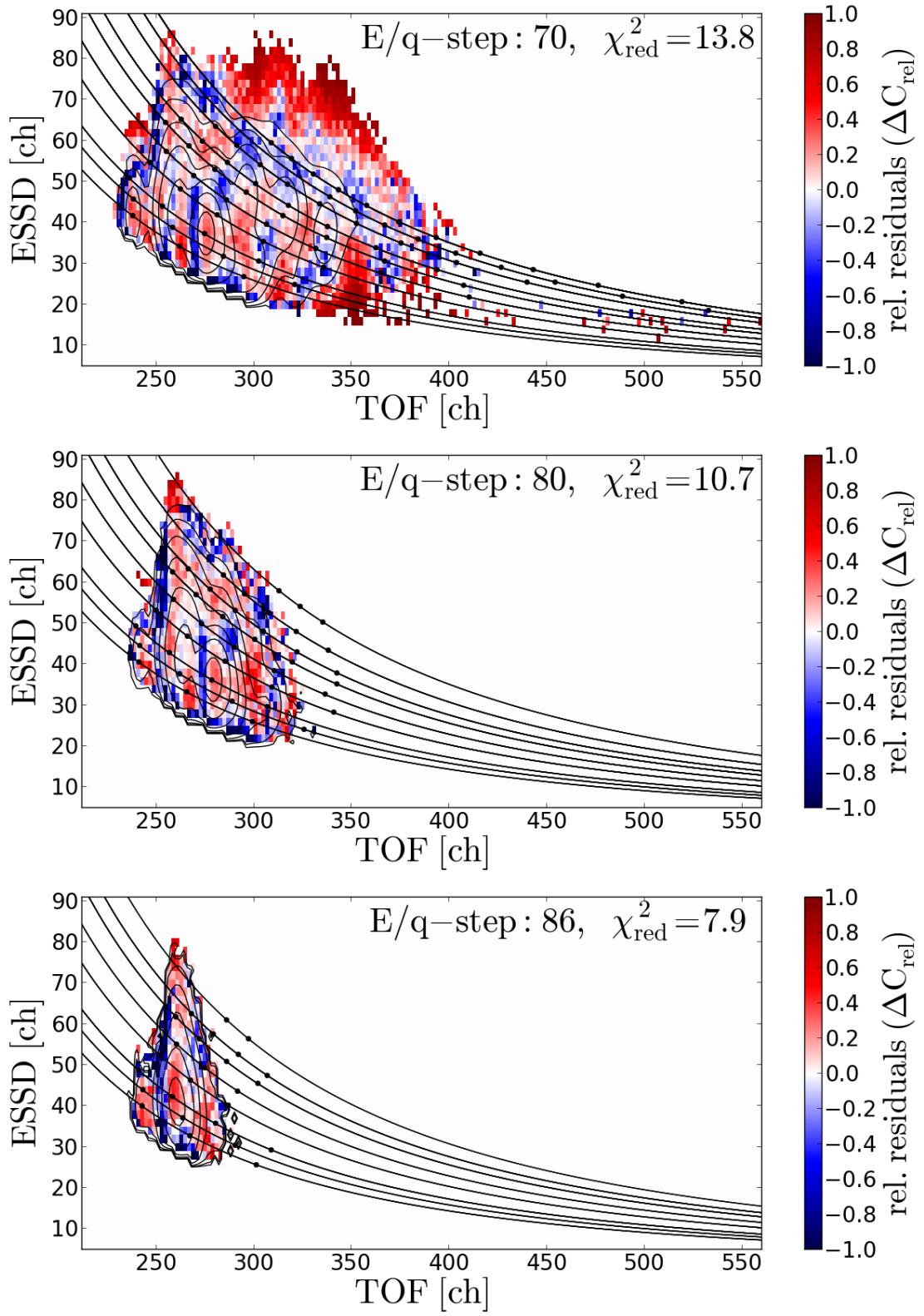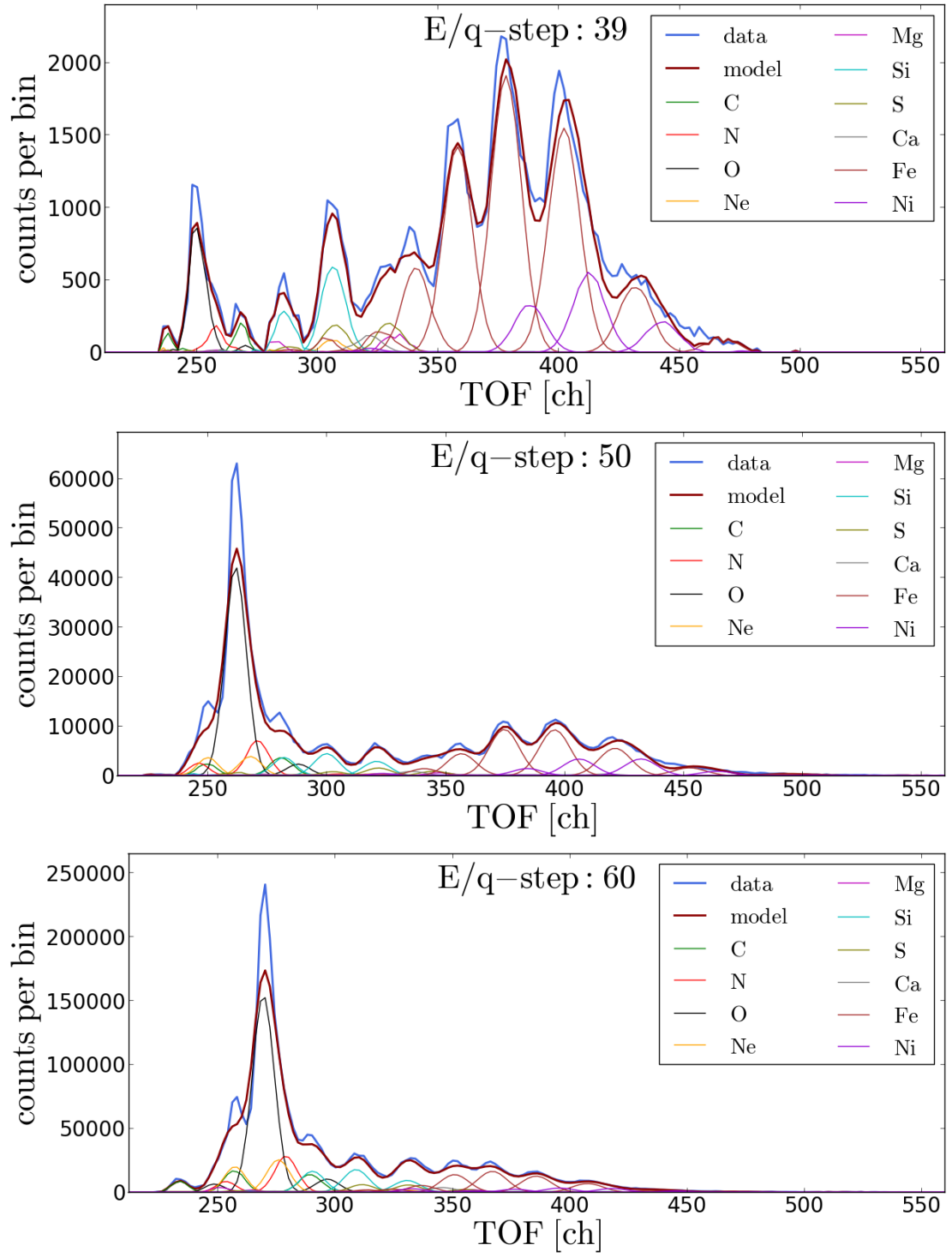
FIGURE C.6

FIGURE C.7
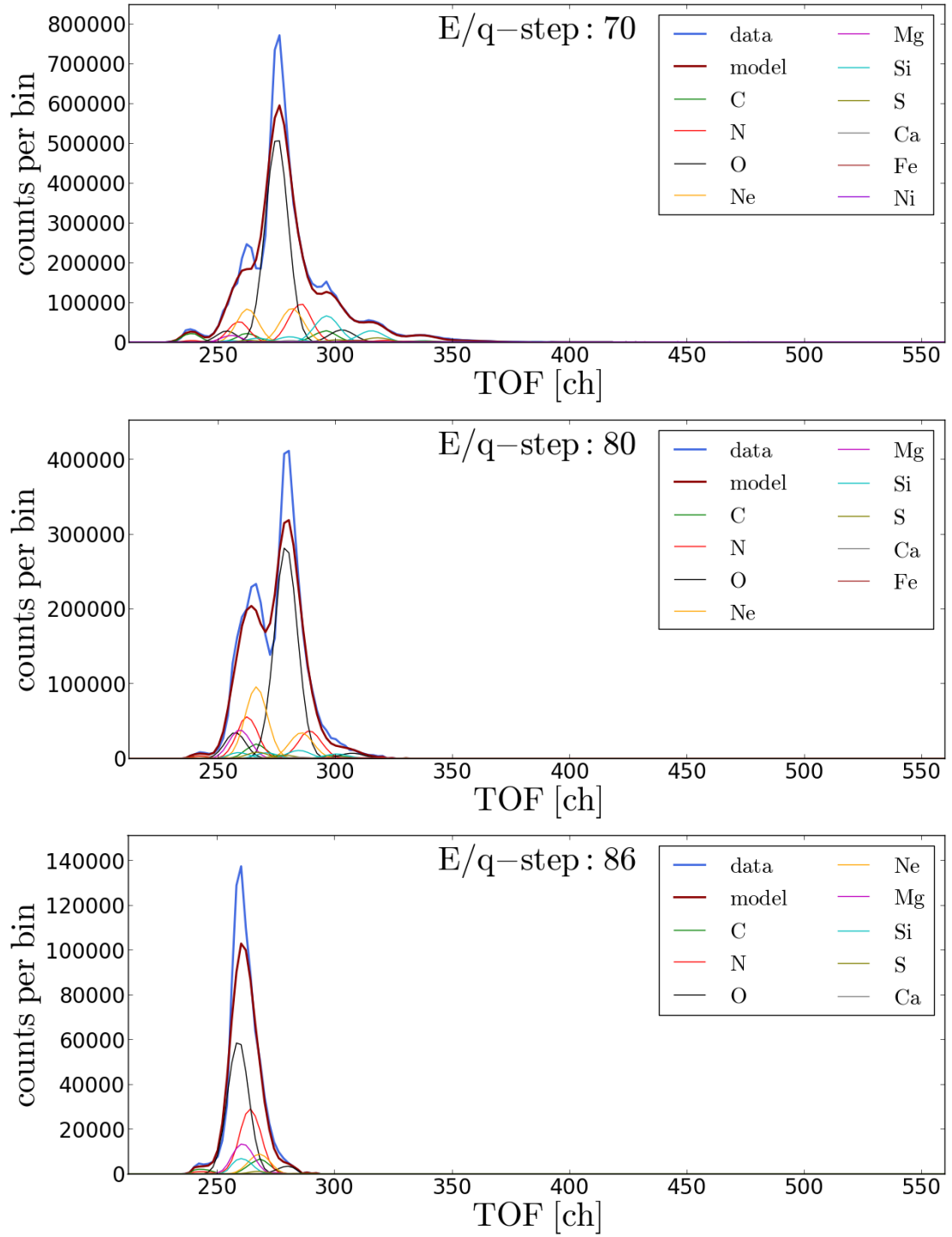
FIGURE C.8
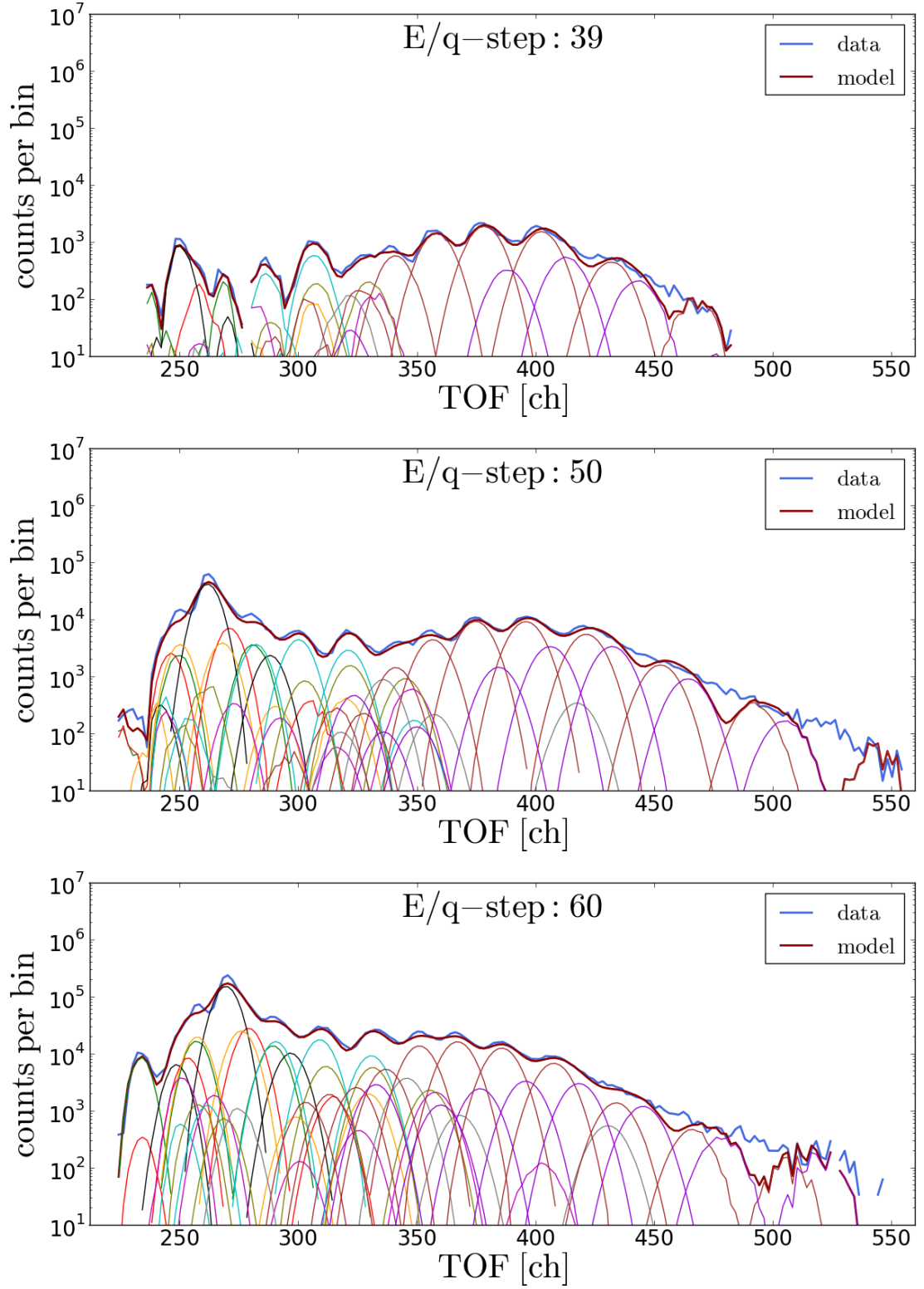
FIGURE C.9
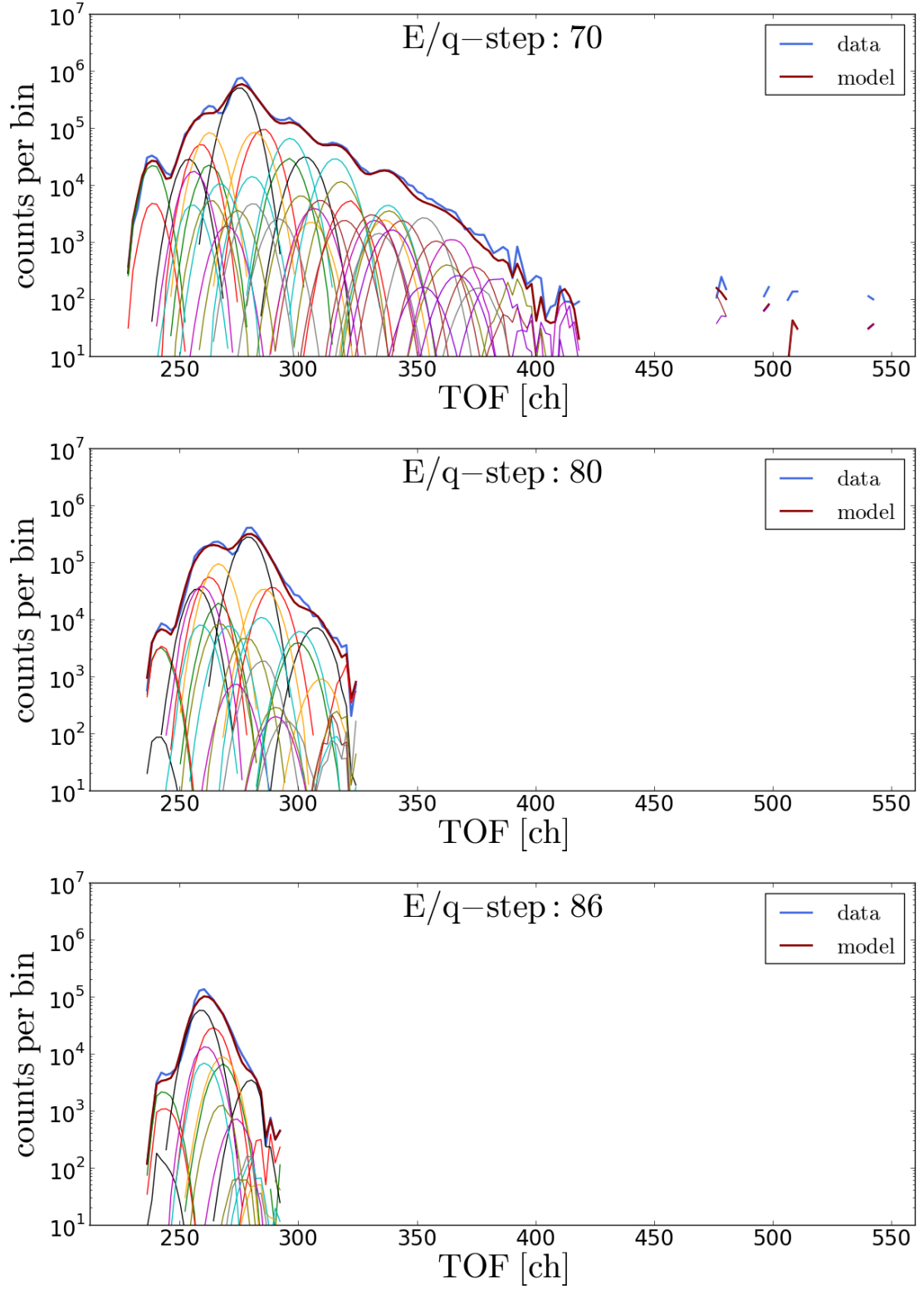
FIGURE C.10
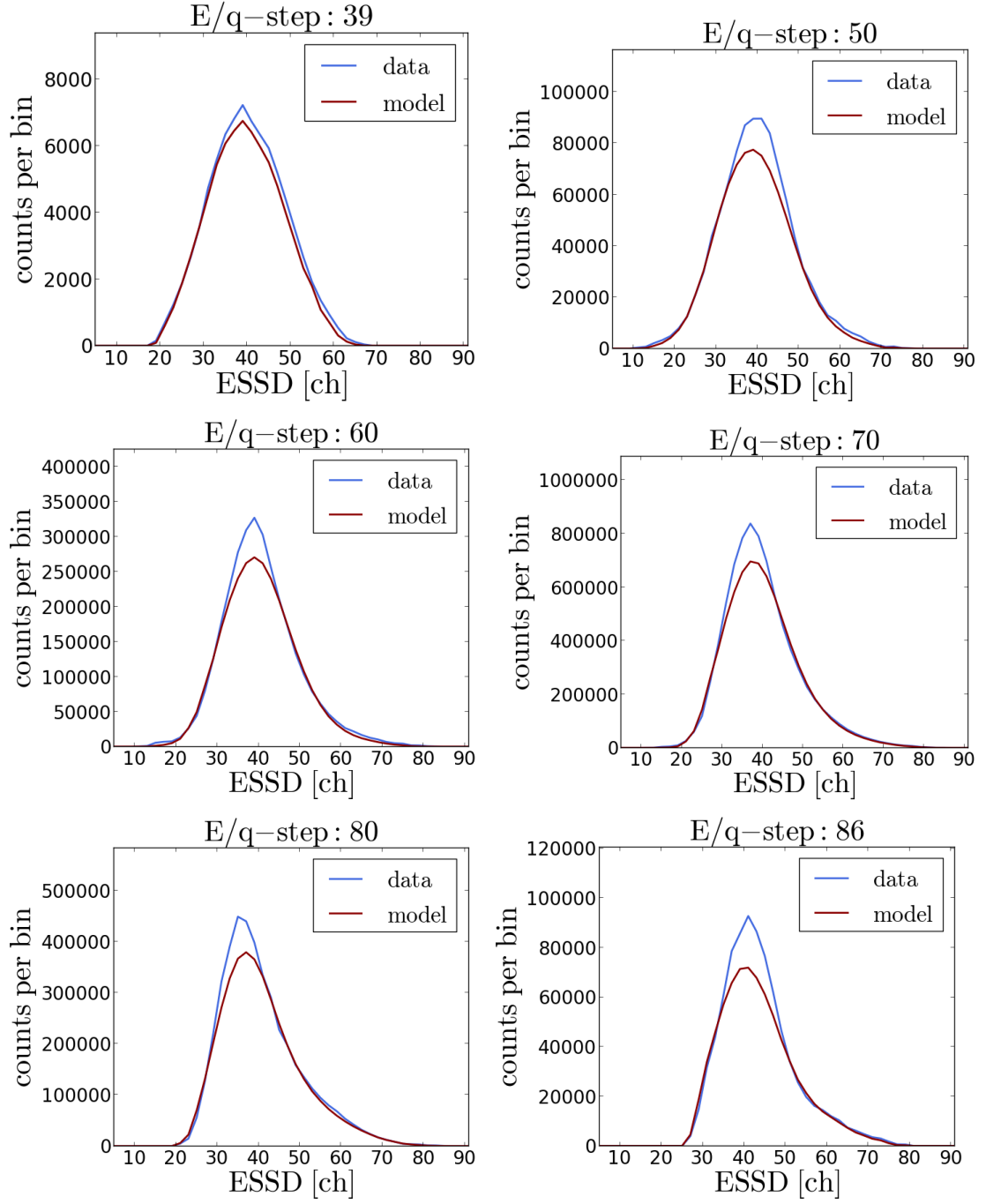
FIGURE C.11
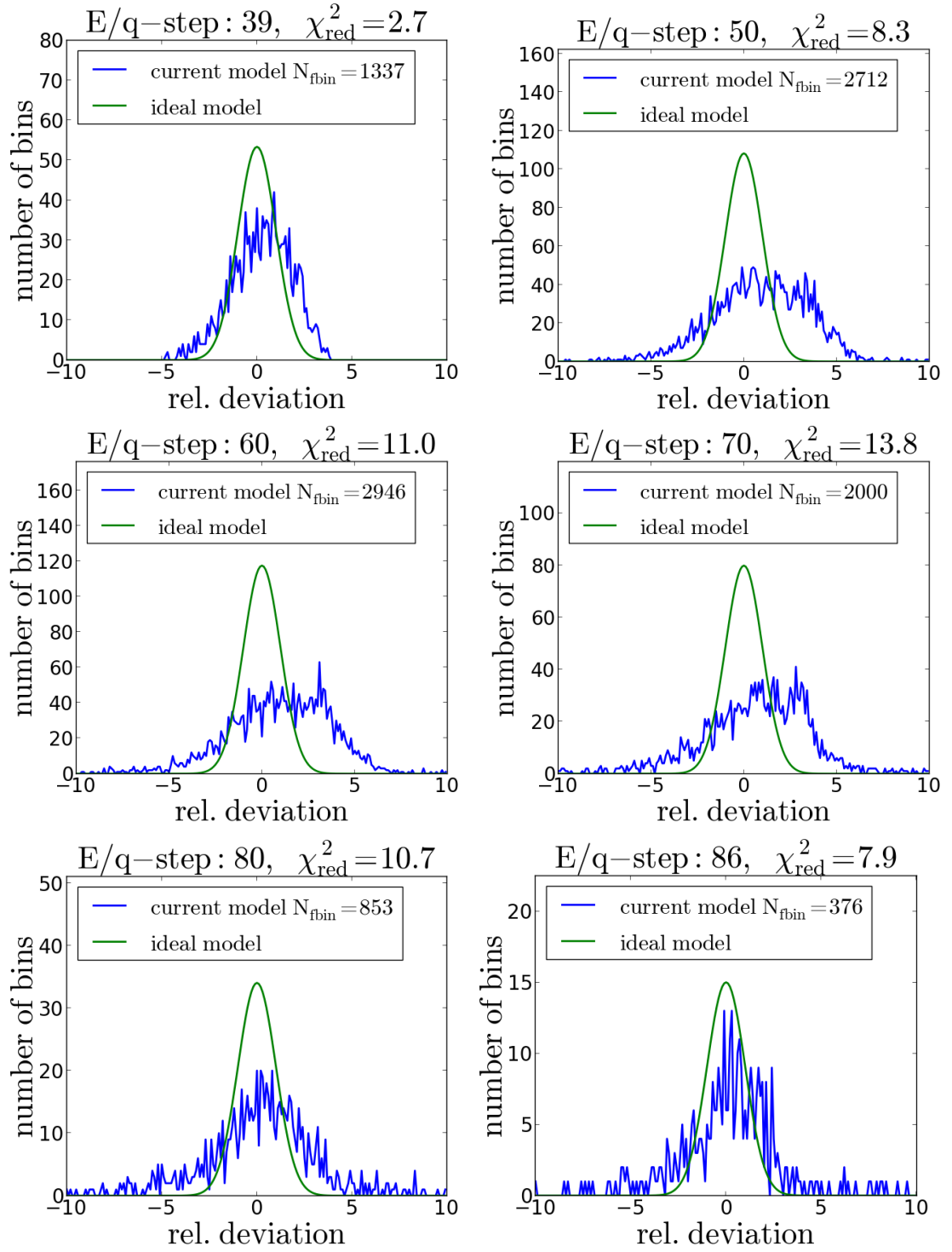
FIGURE C.12

C.1.2 Kappa-Moyal Peak Model
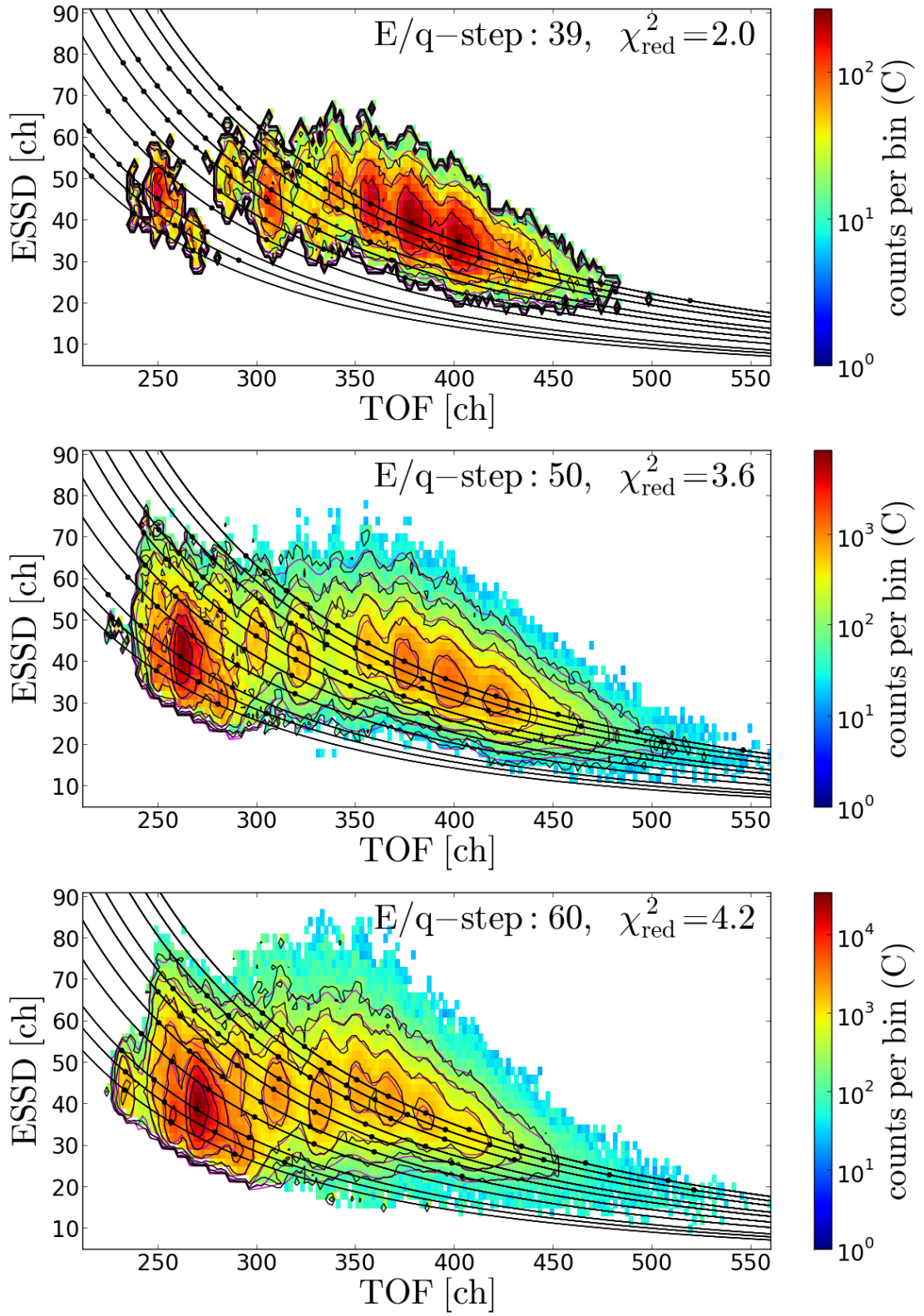
FIGURE C.13
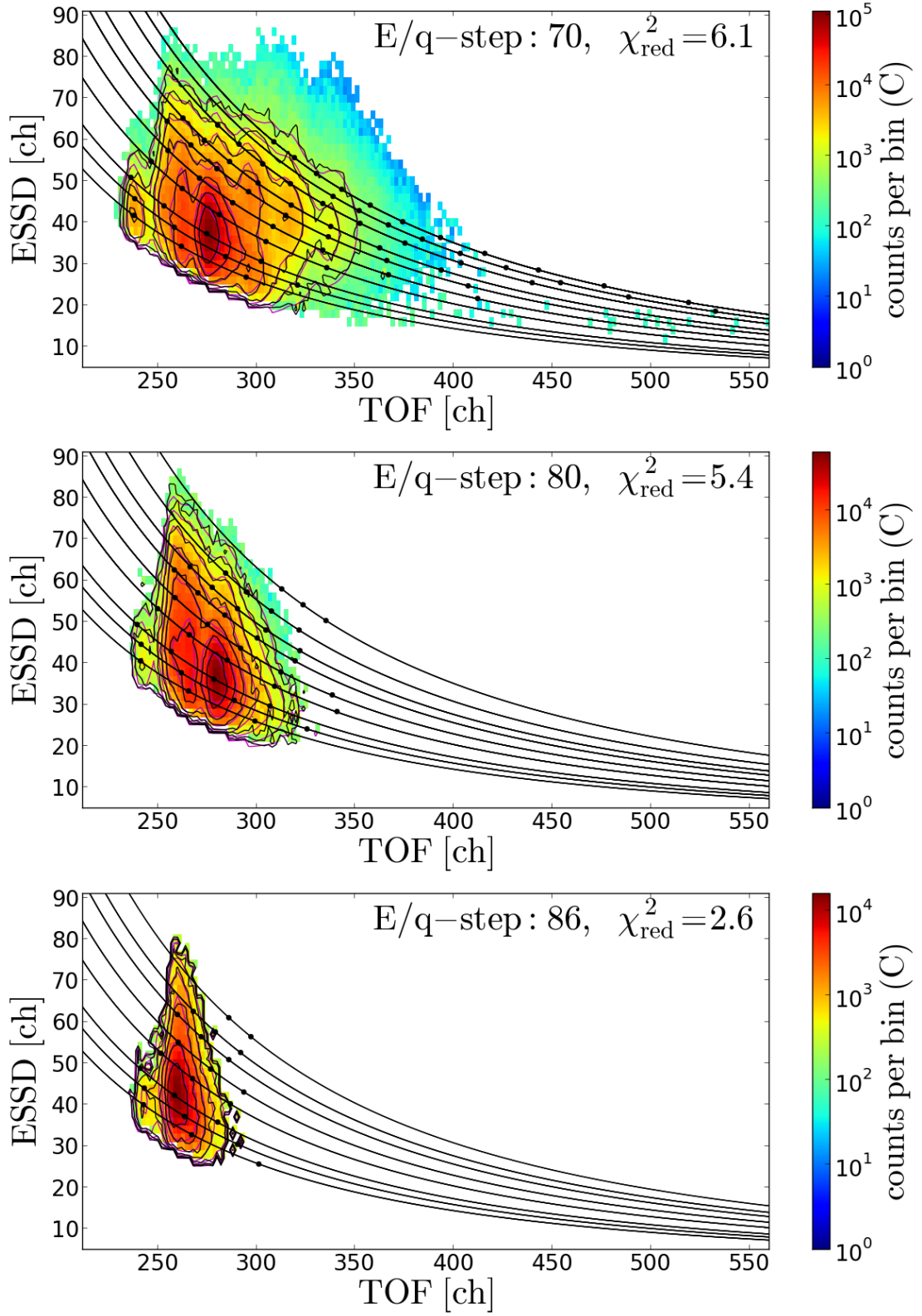
FIGURE C.14
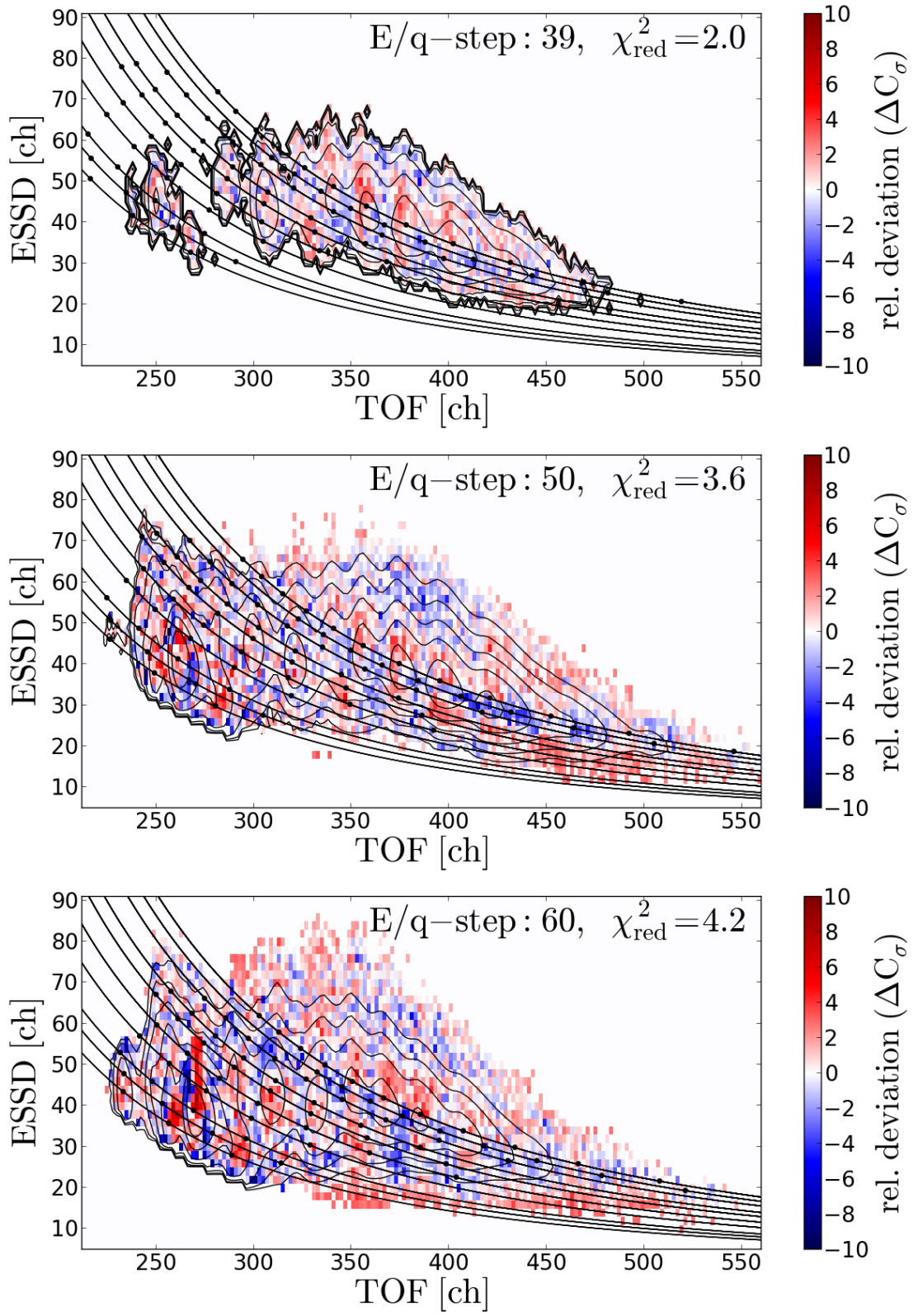
FIGURE C.15
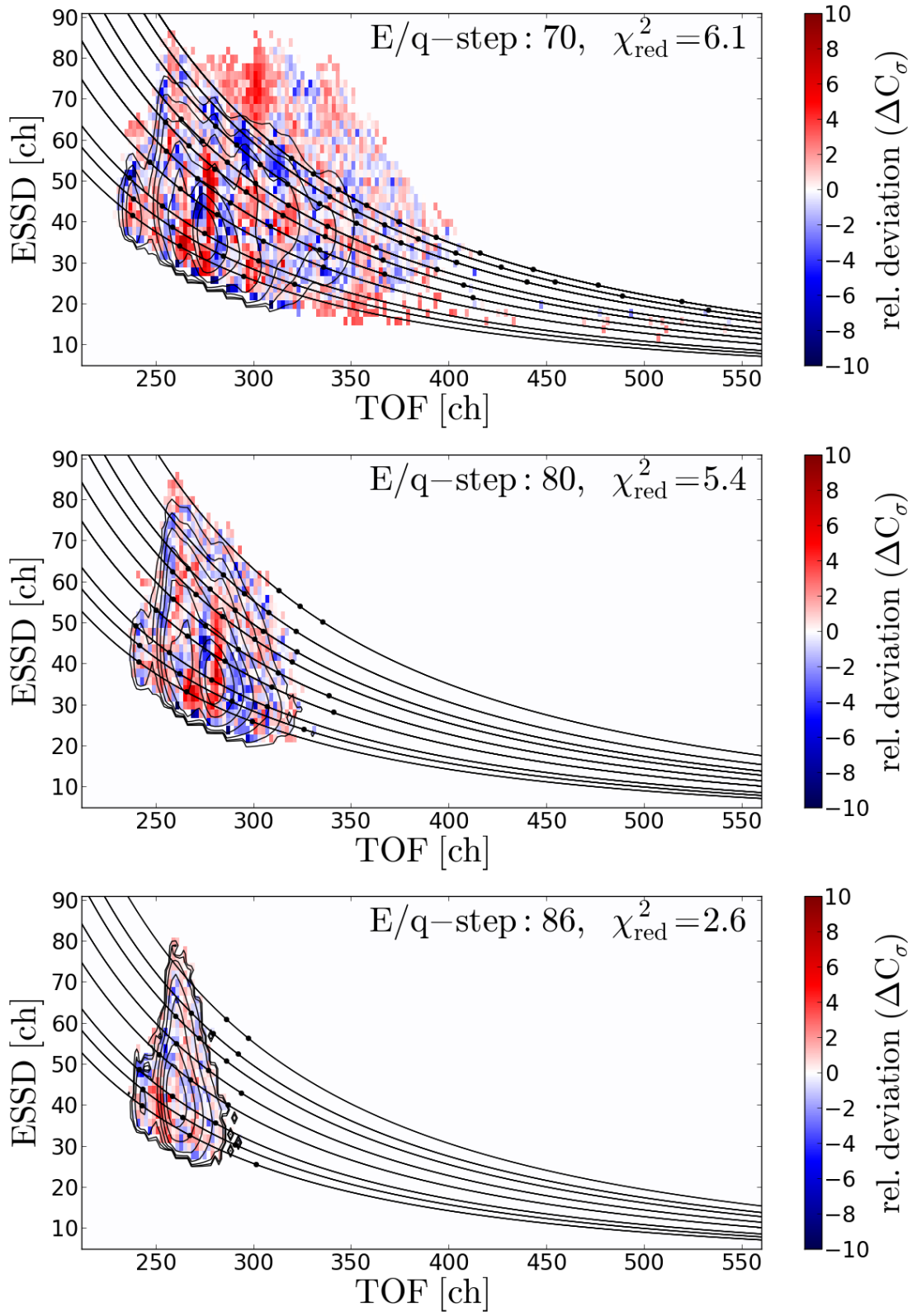
FIGURE C.16

FIGURE C.17

228
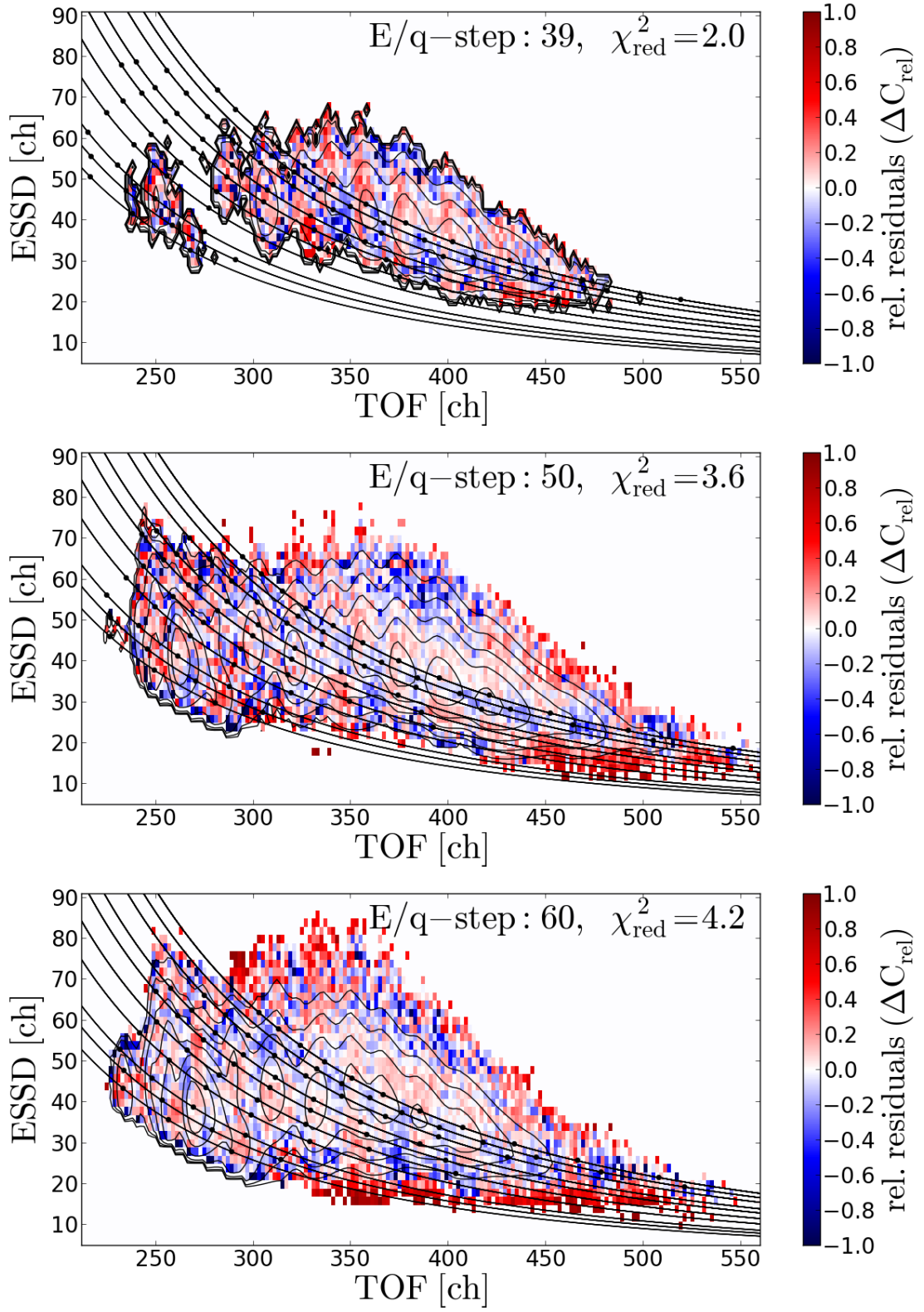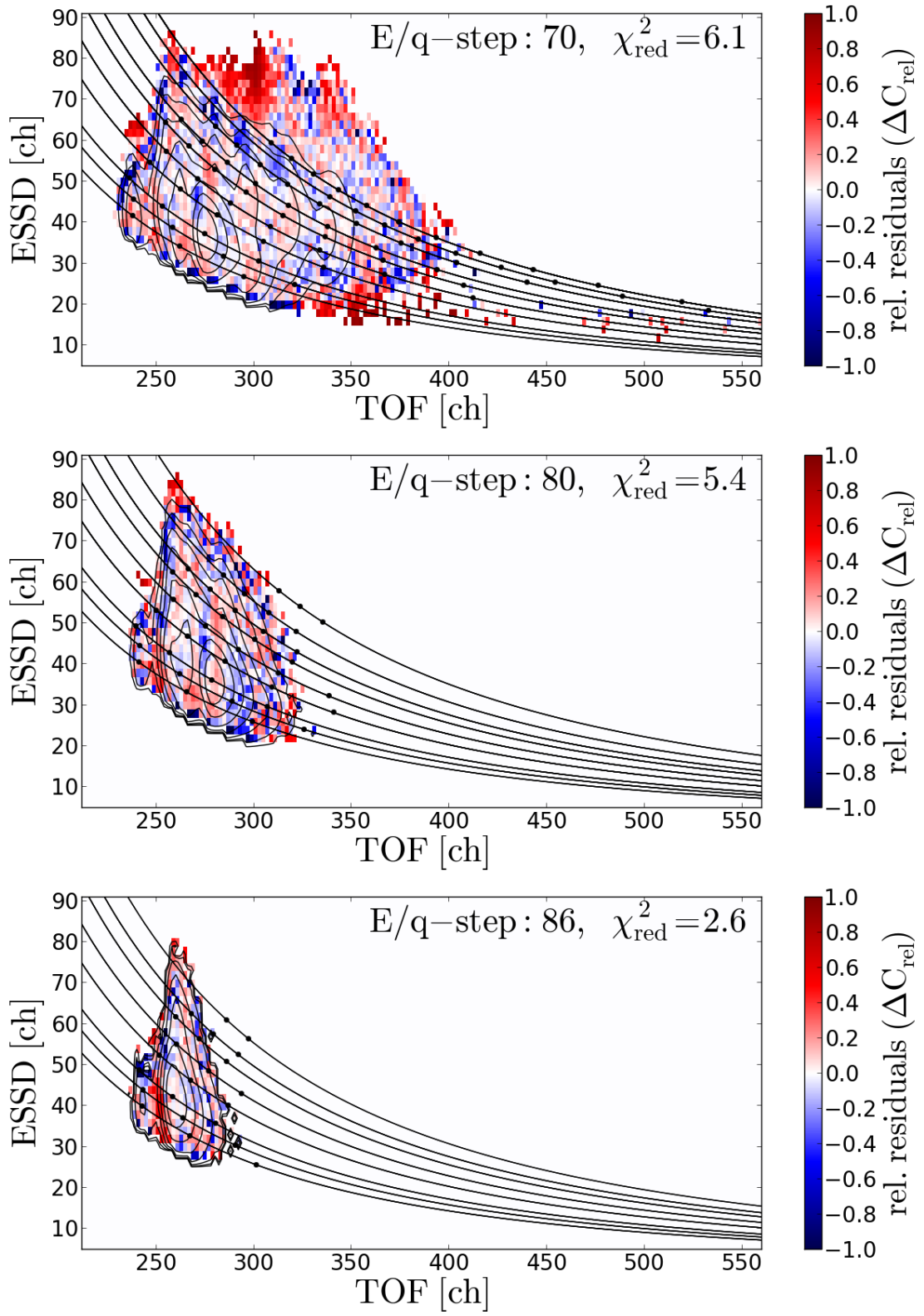
FIGURE C.18

FIGURE C.19

230
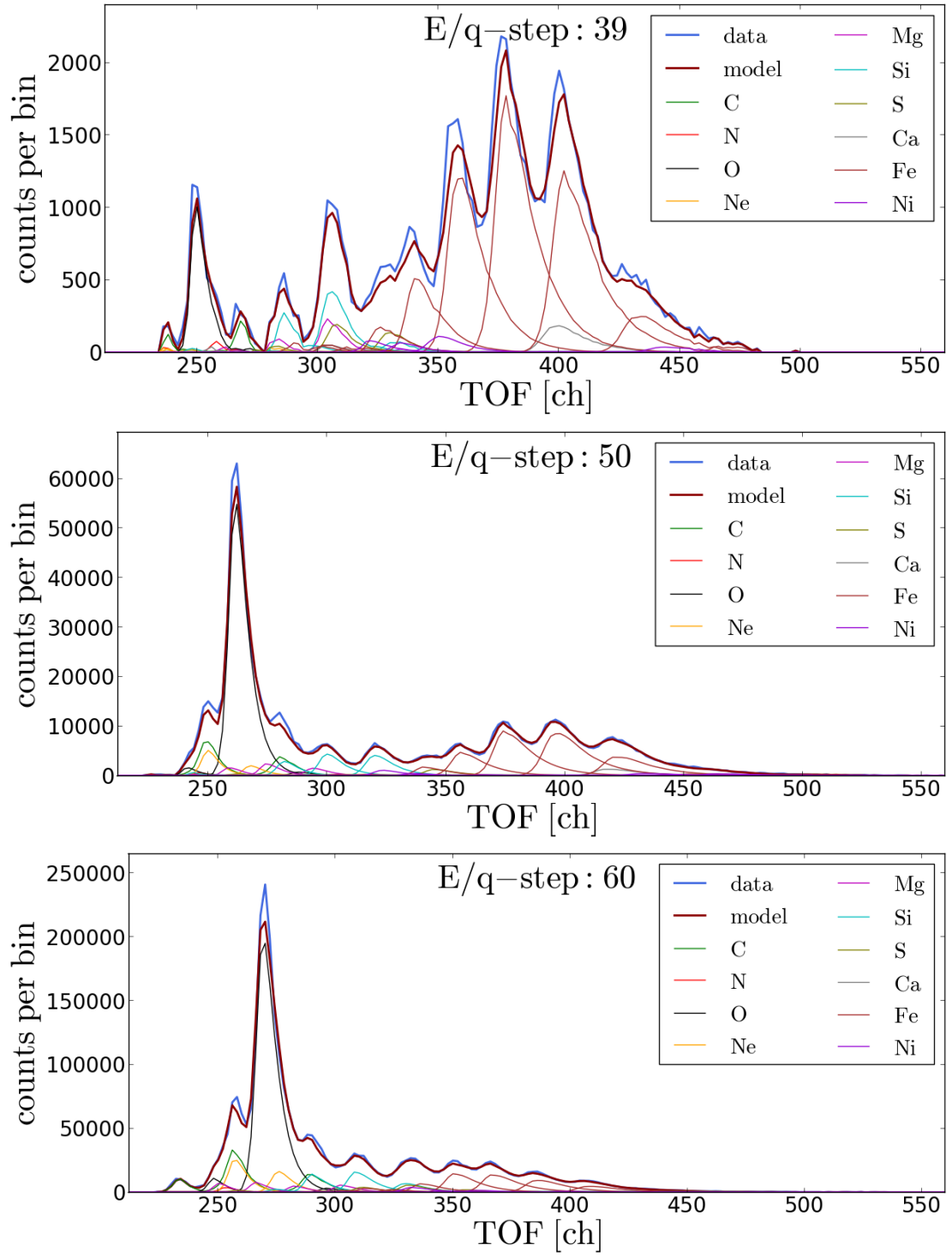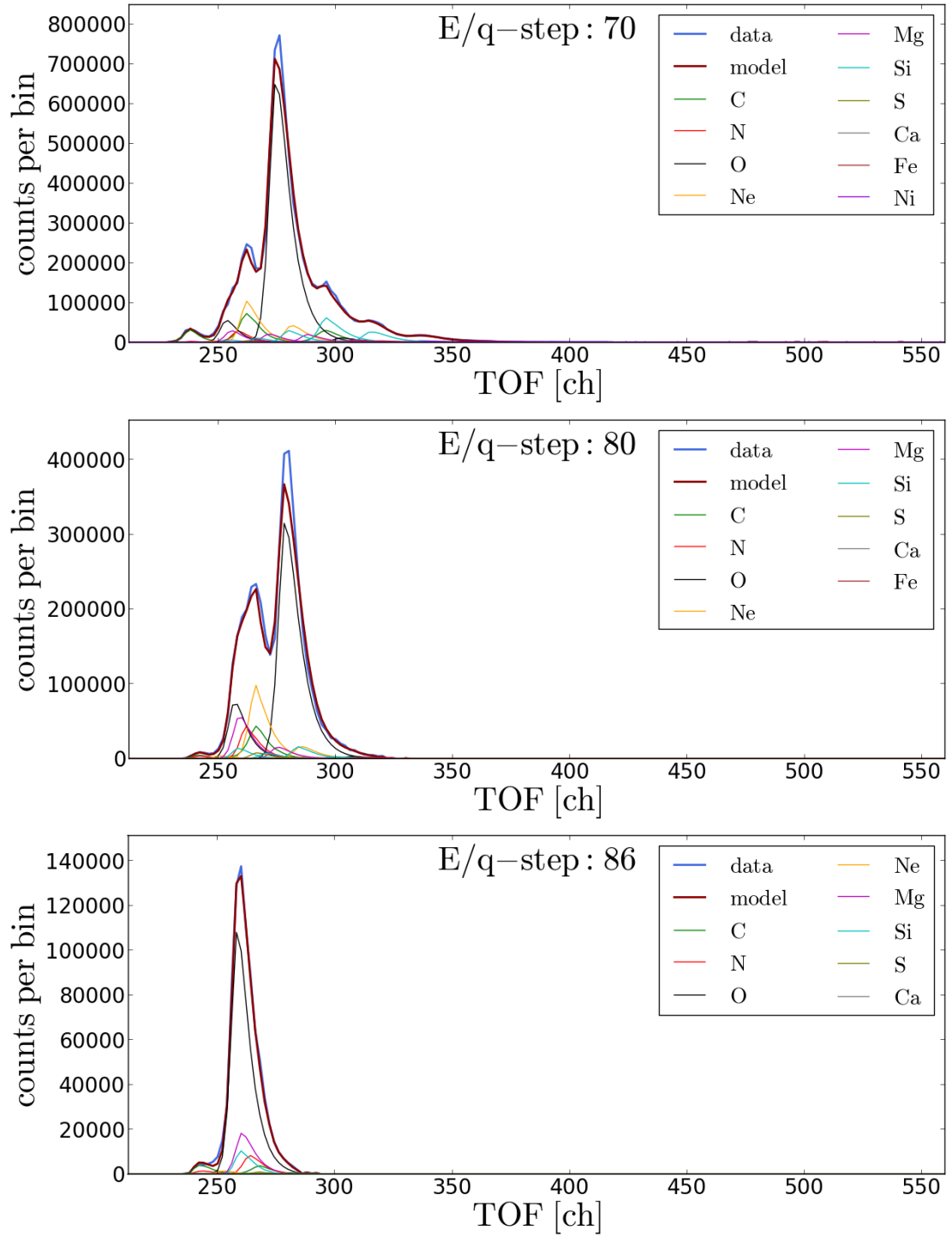
FIGURE C.20

FIGURE C.21

232
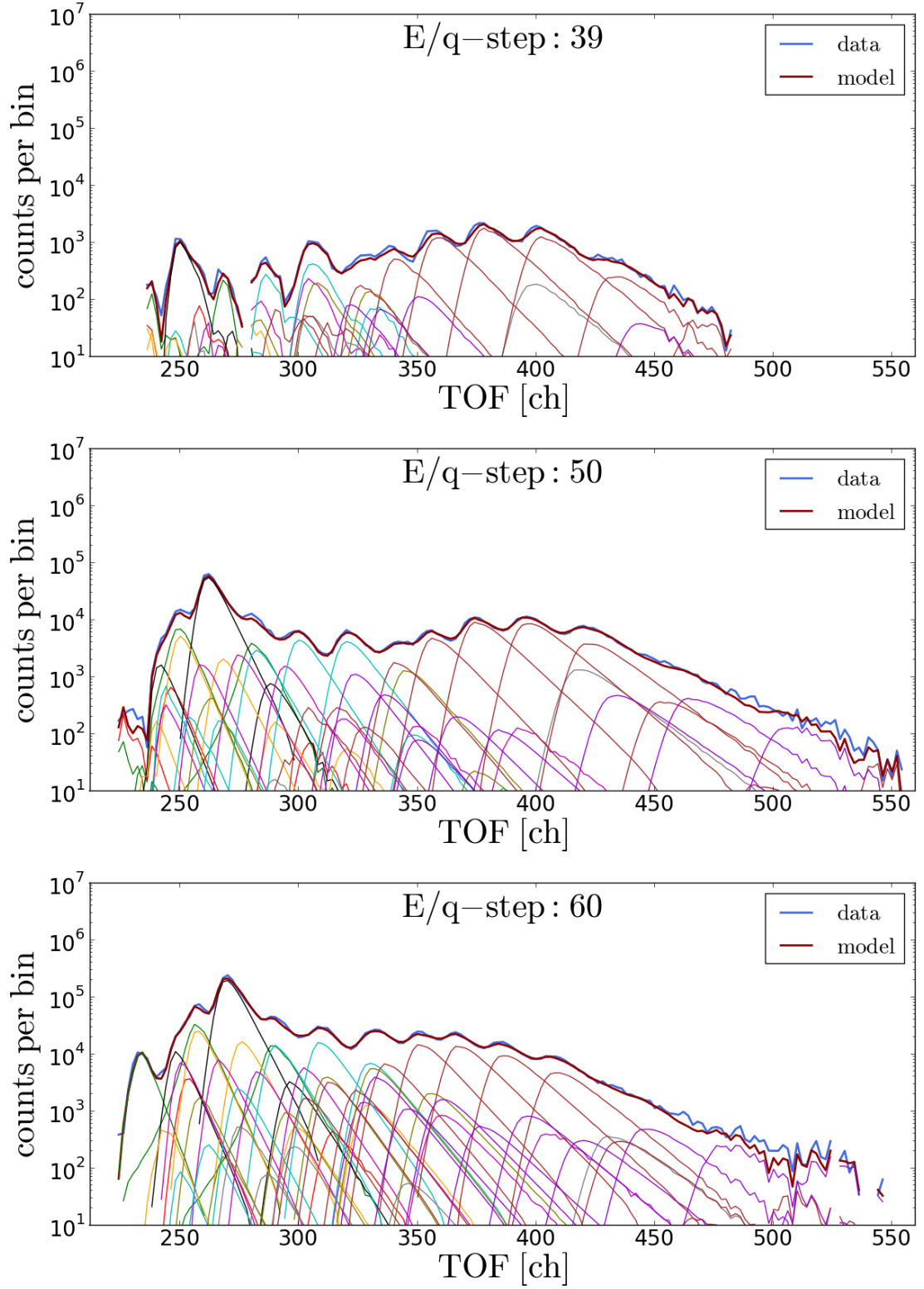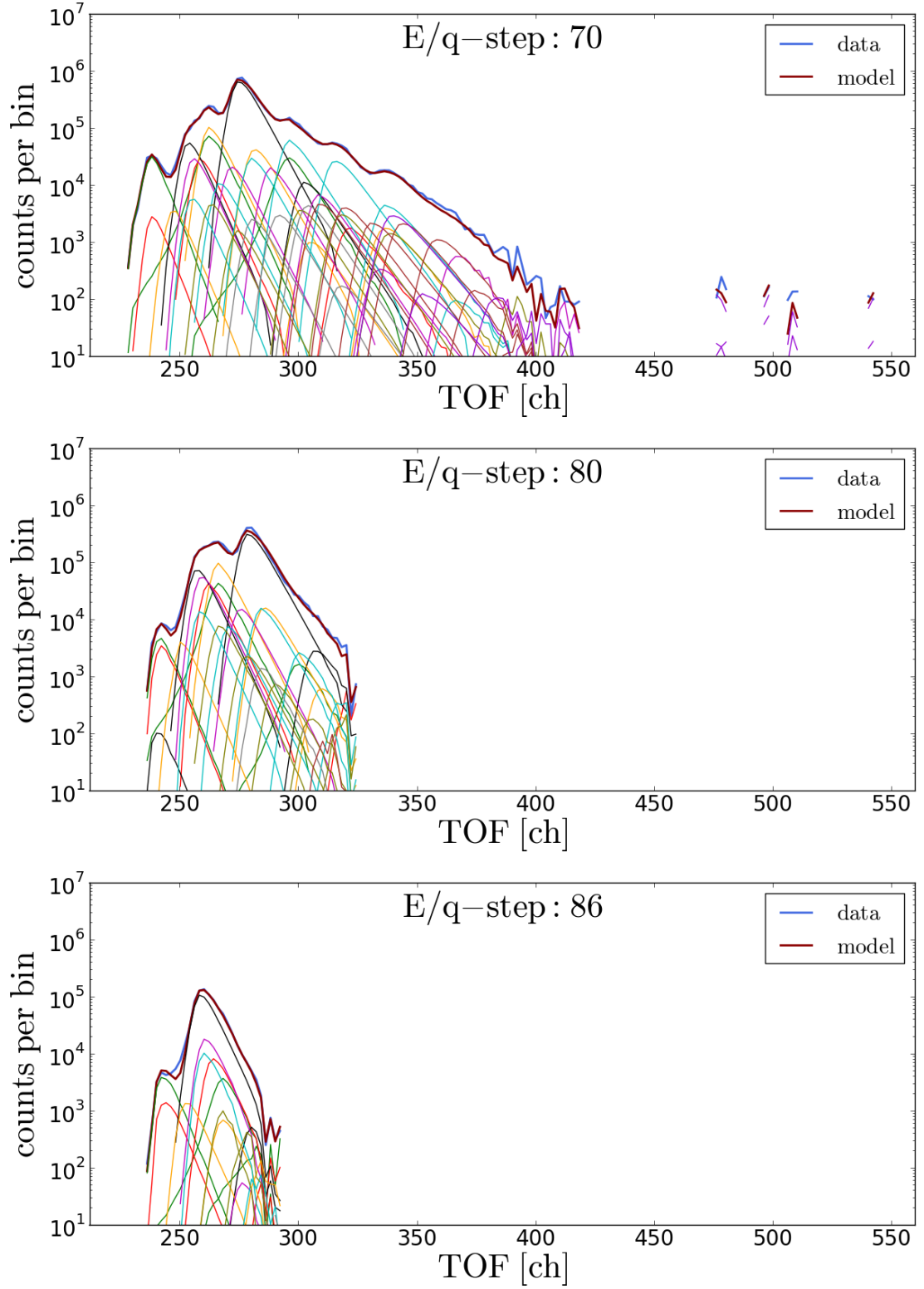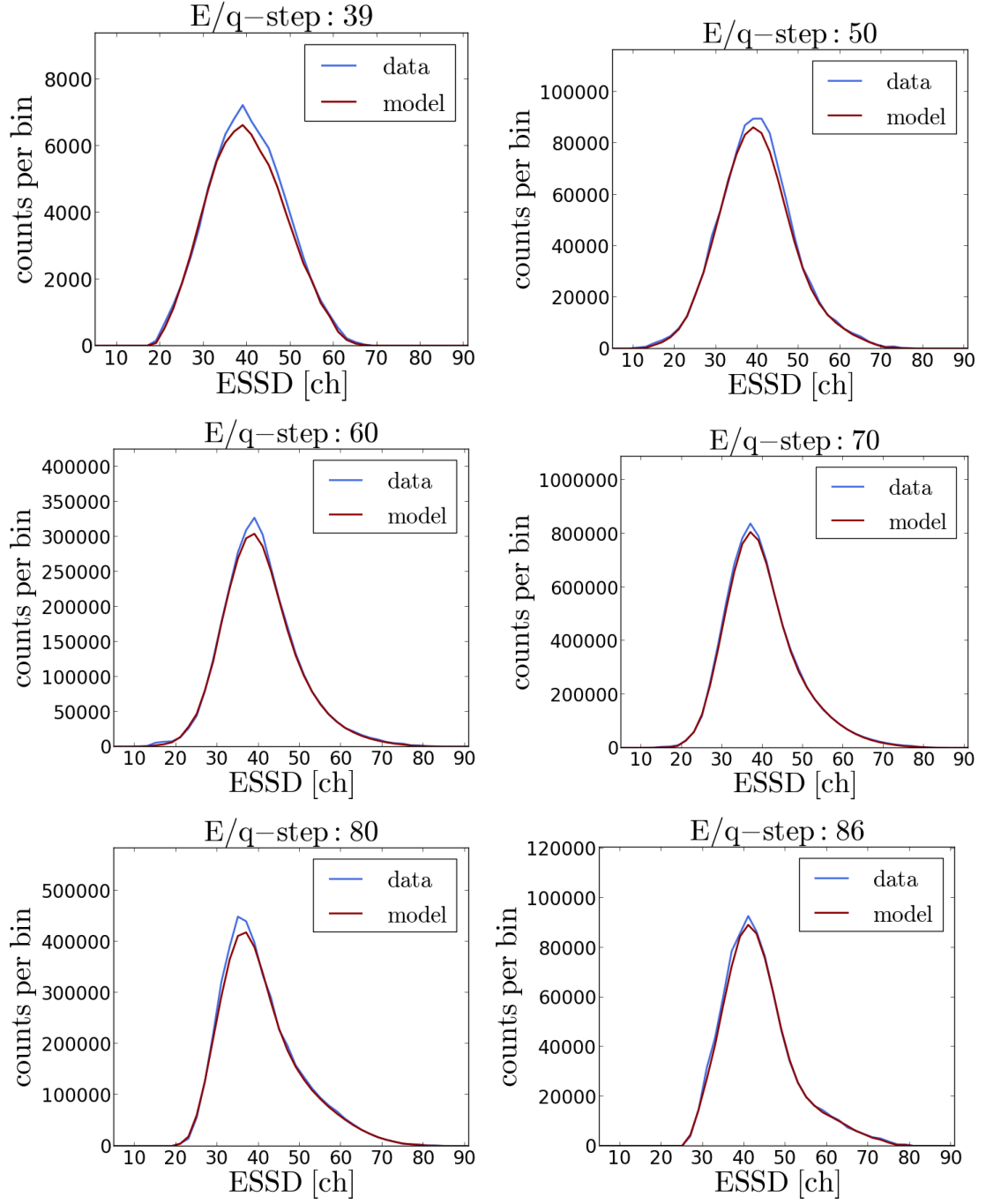
FIGURE C.22

FIGURE C.23

FIGURE C.24

C.2   Reduced Stable Response Model

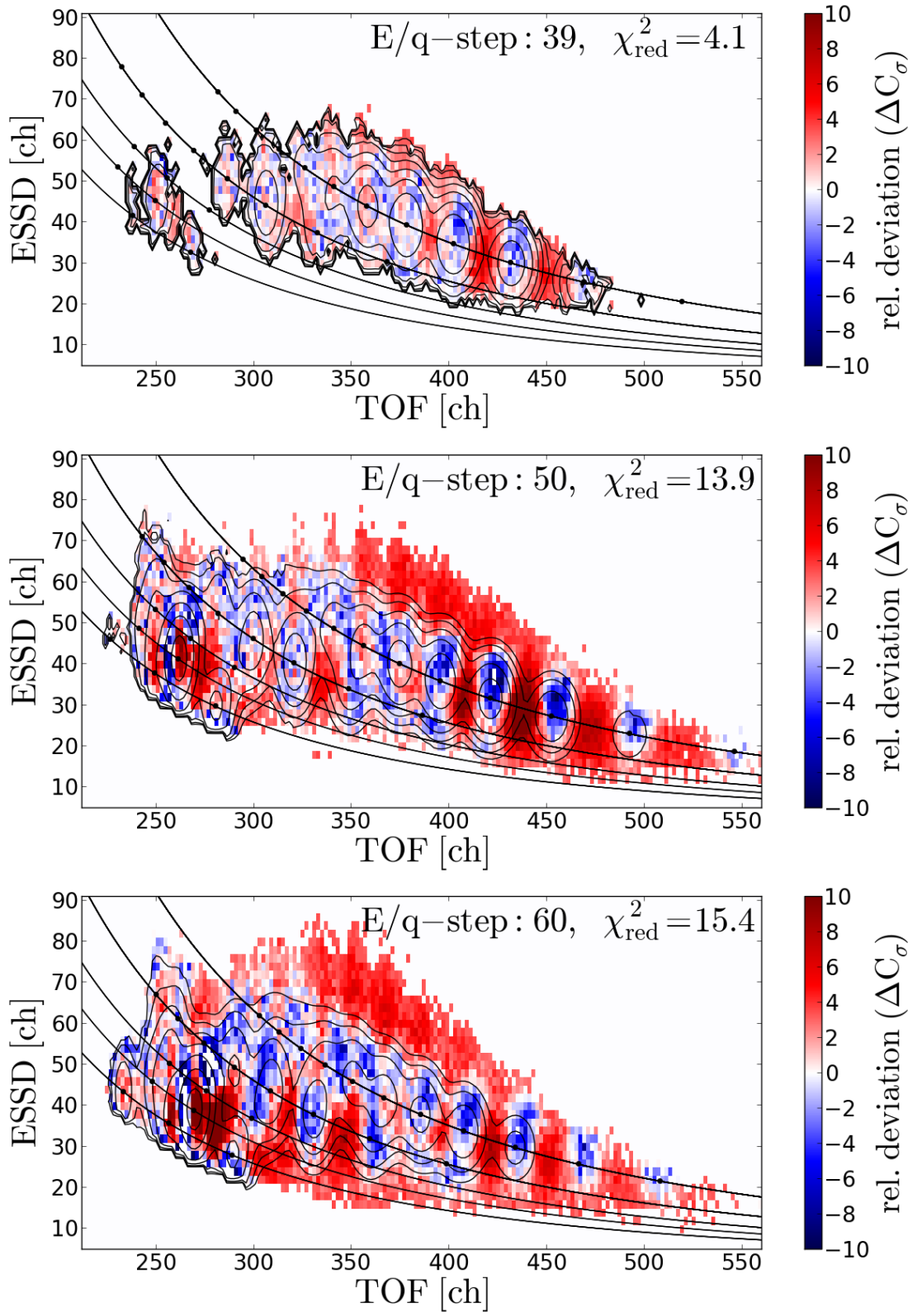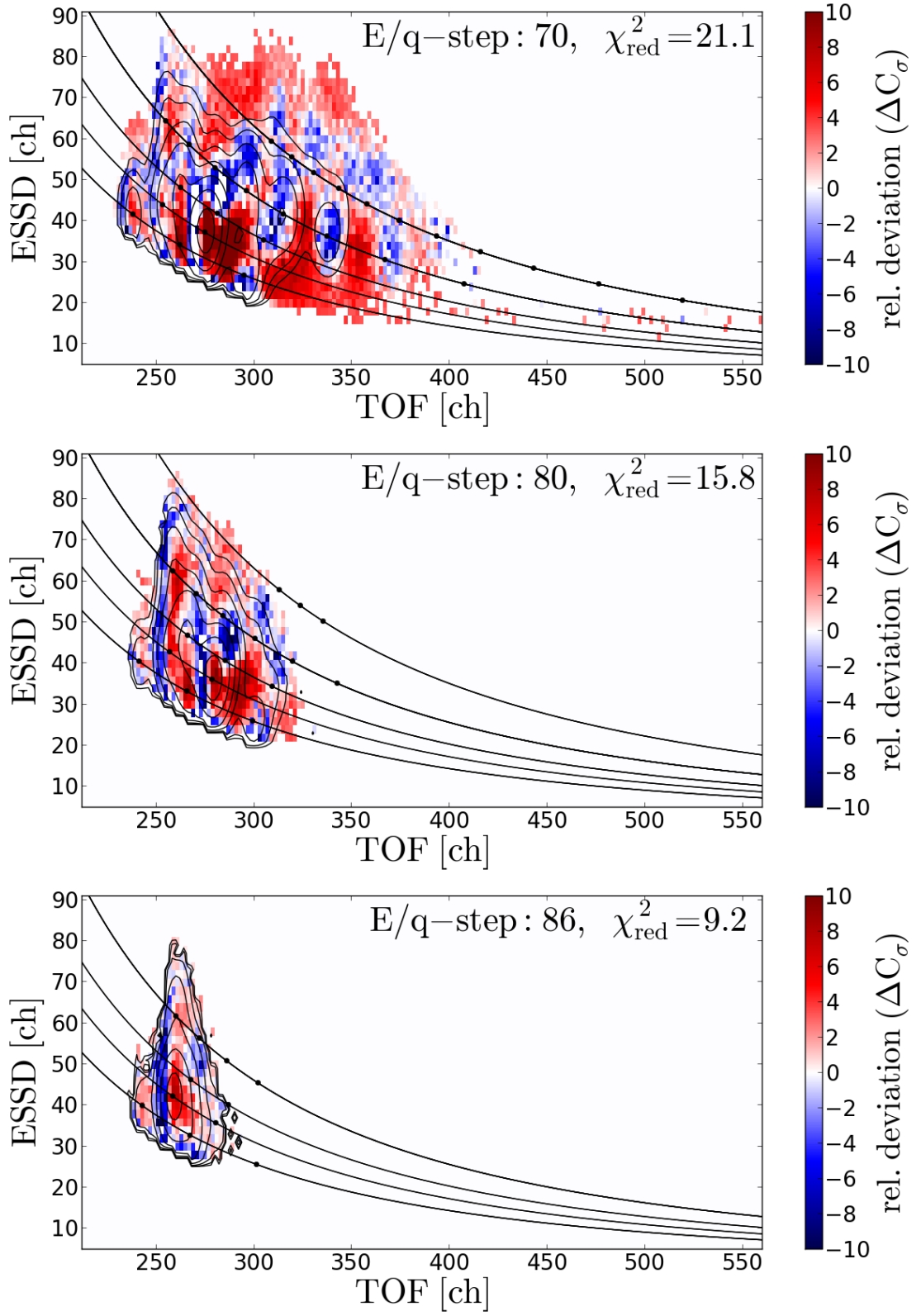### C.2.1   2D-Gaussian Peak Model
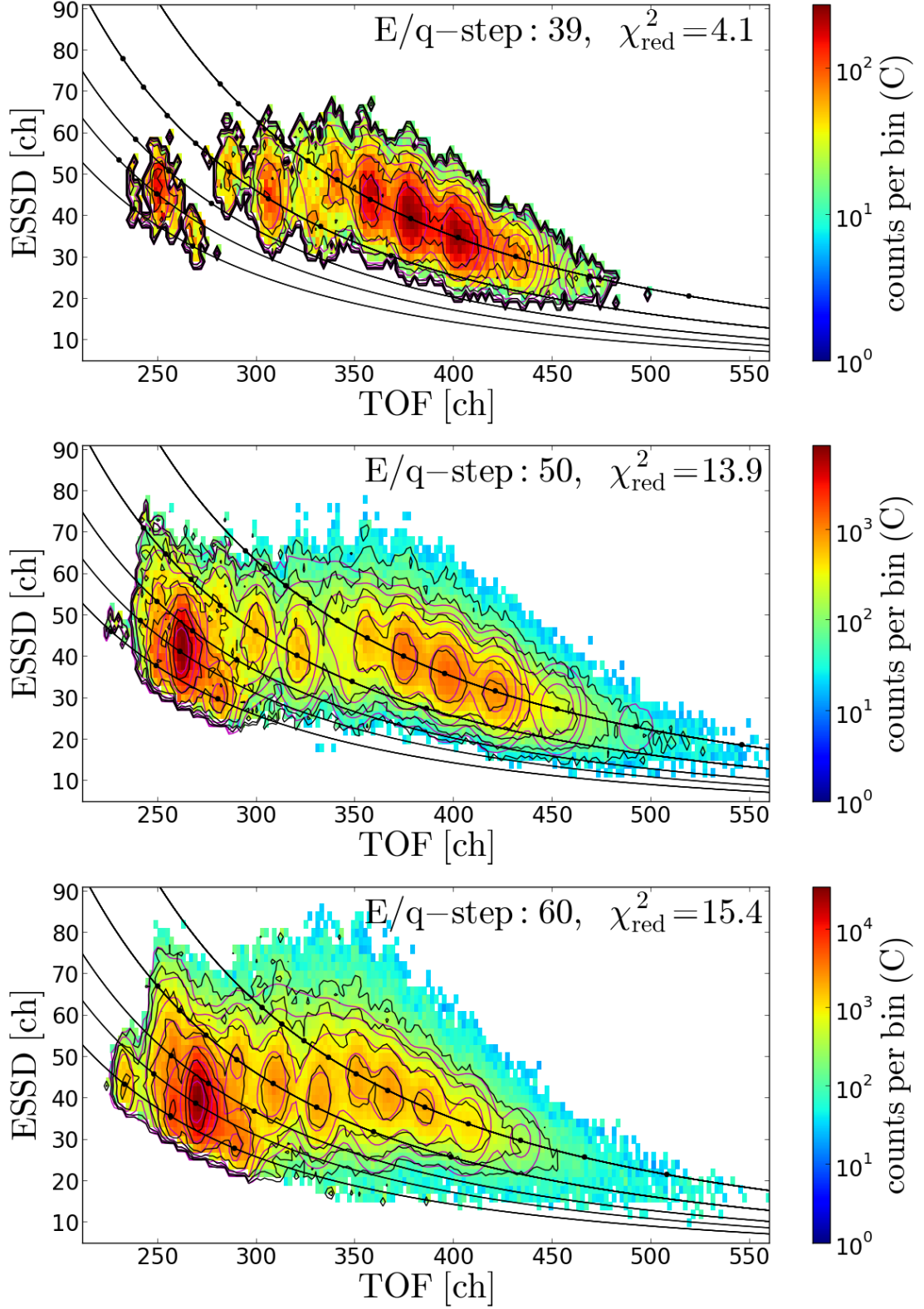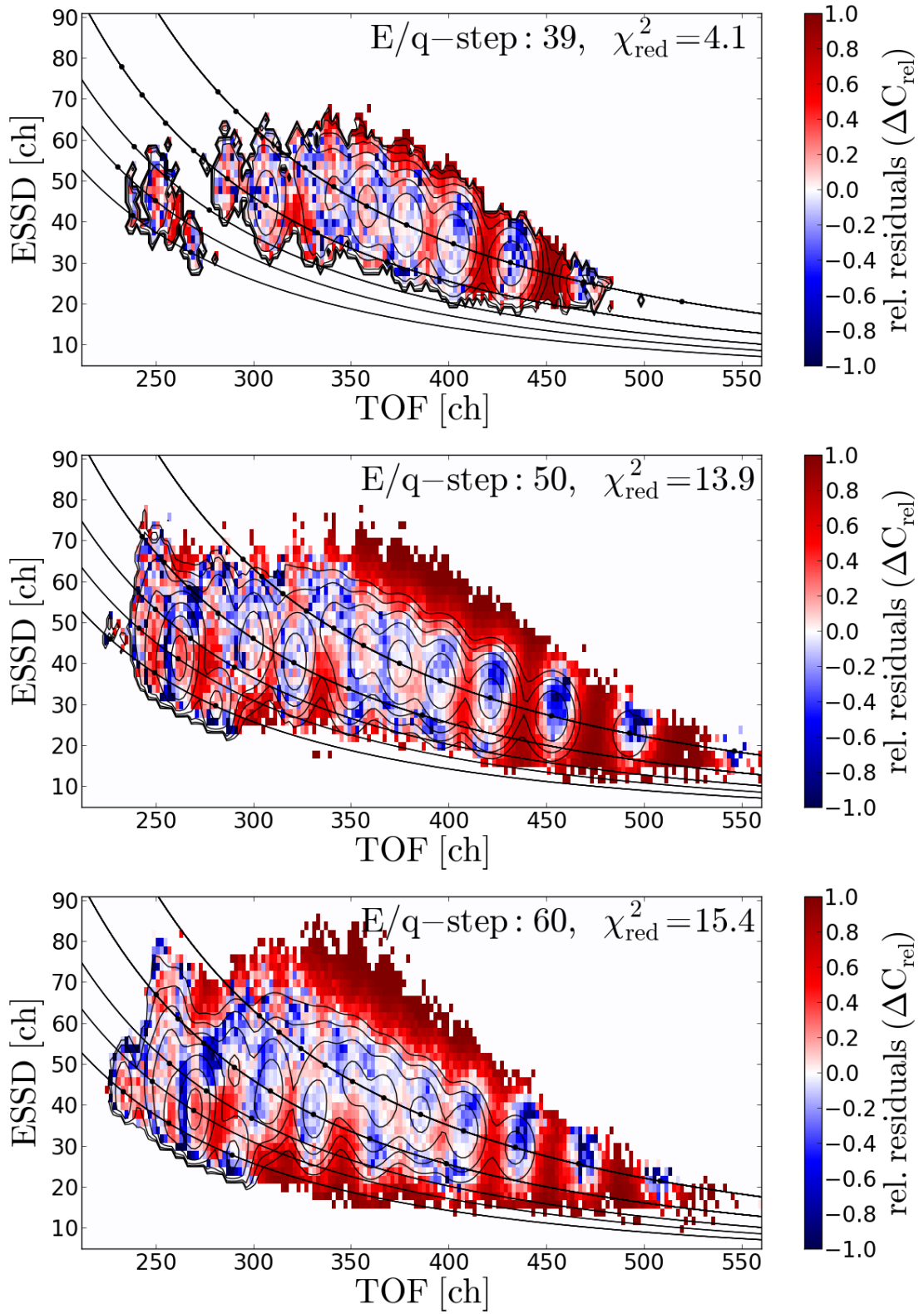

FIGURE C.25
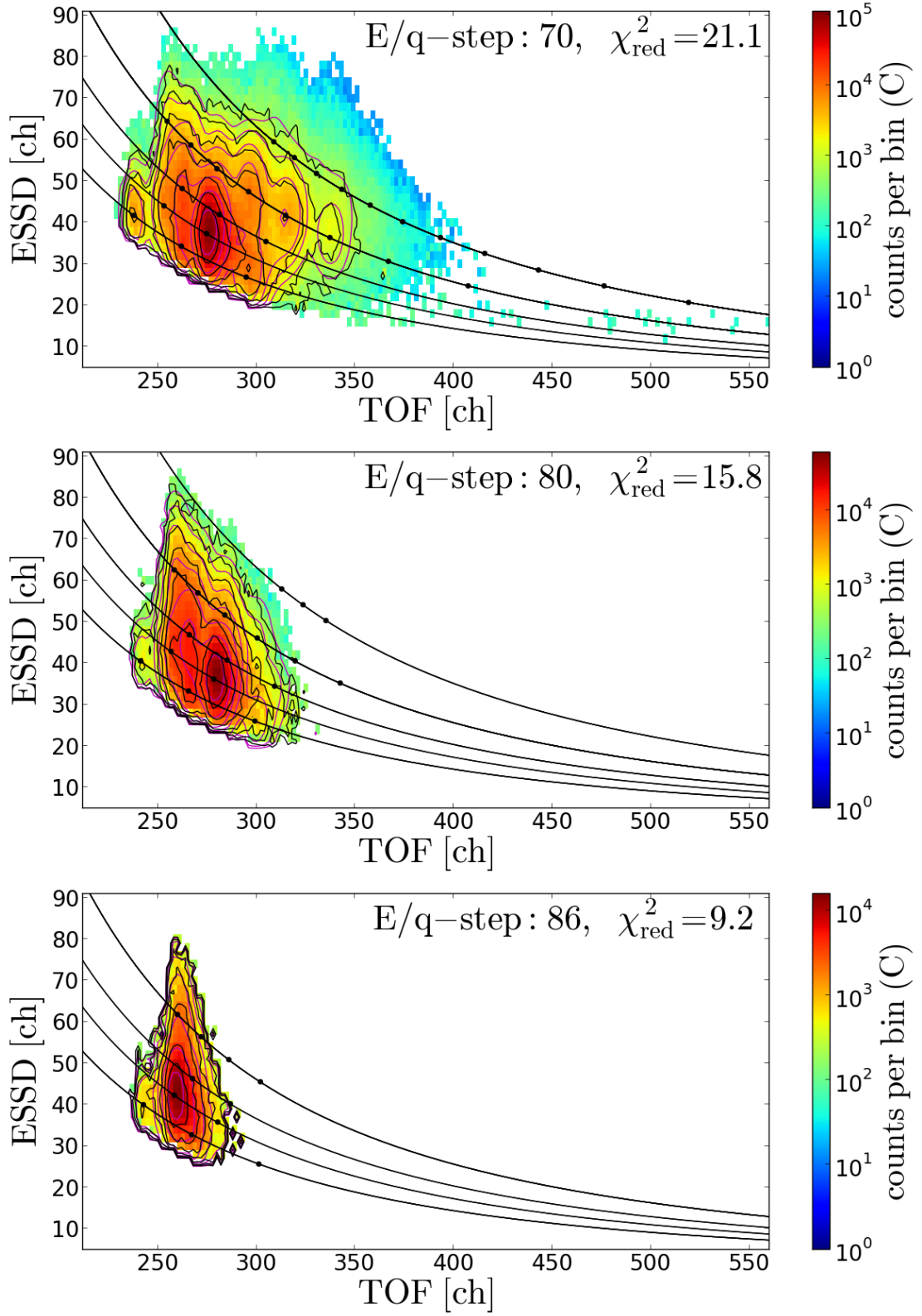
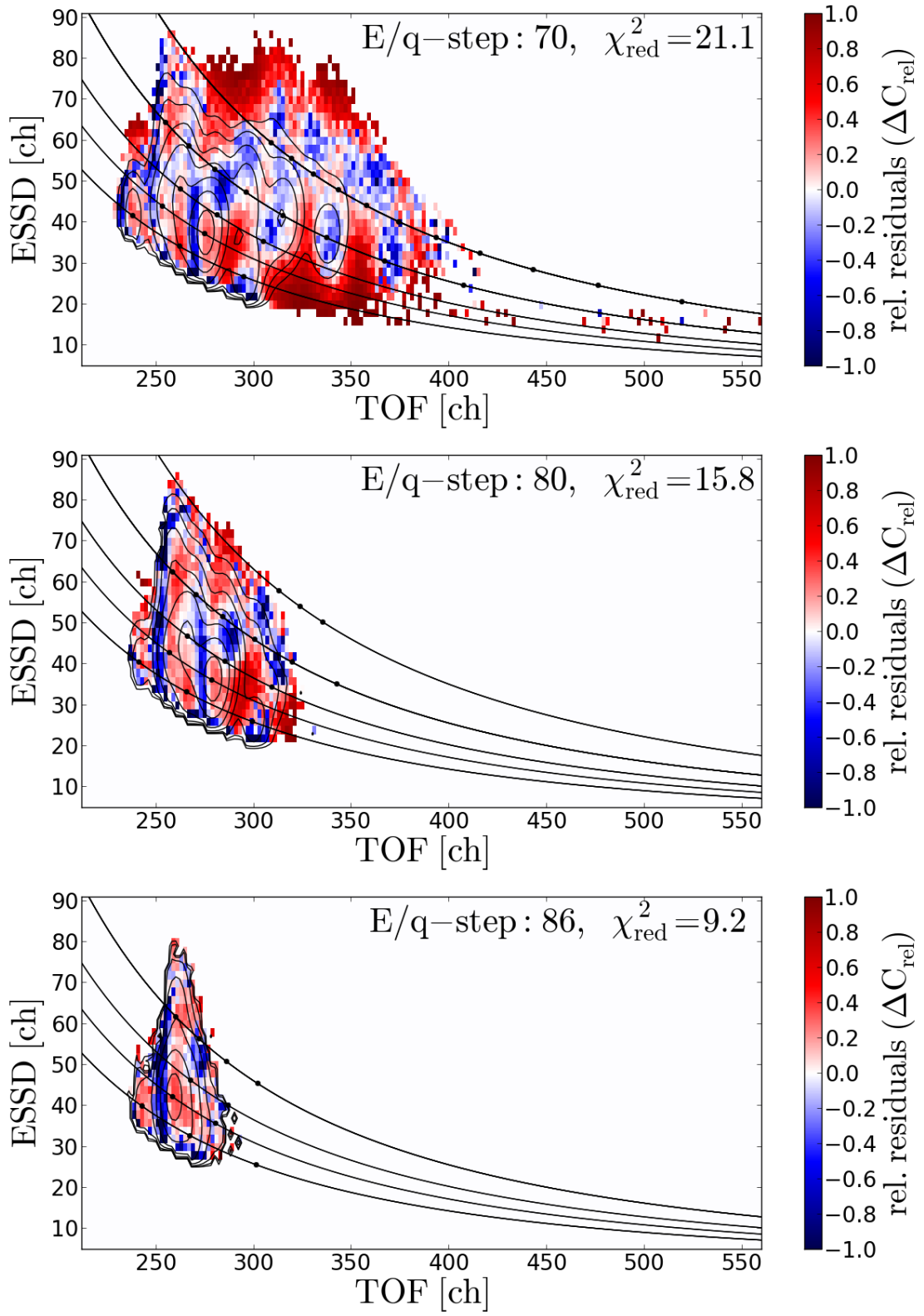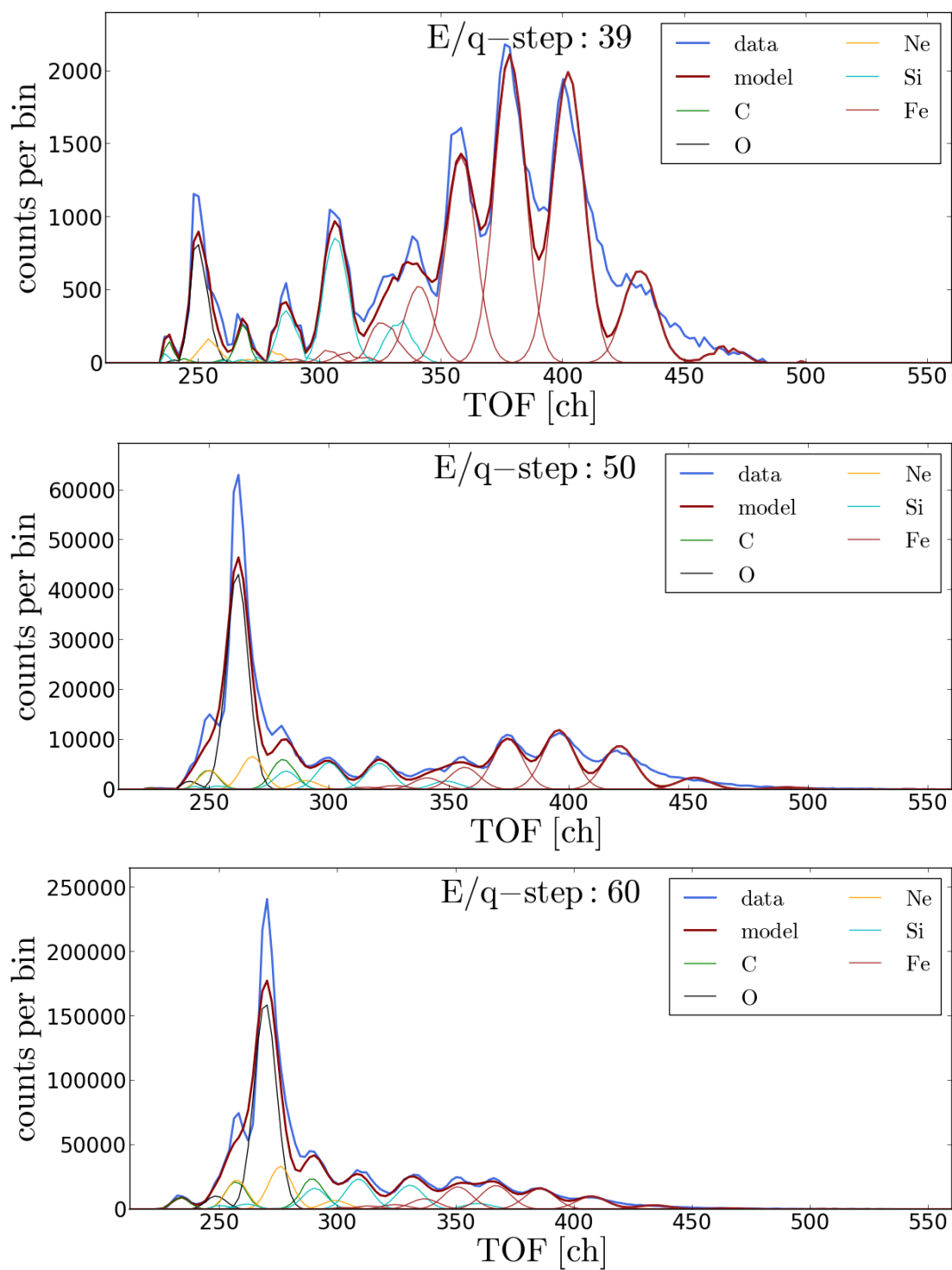FIGURE C.26
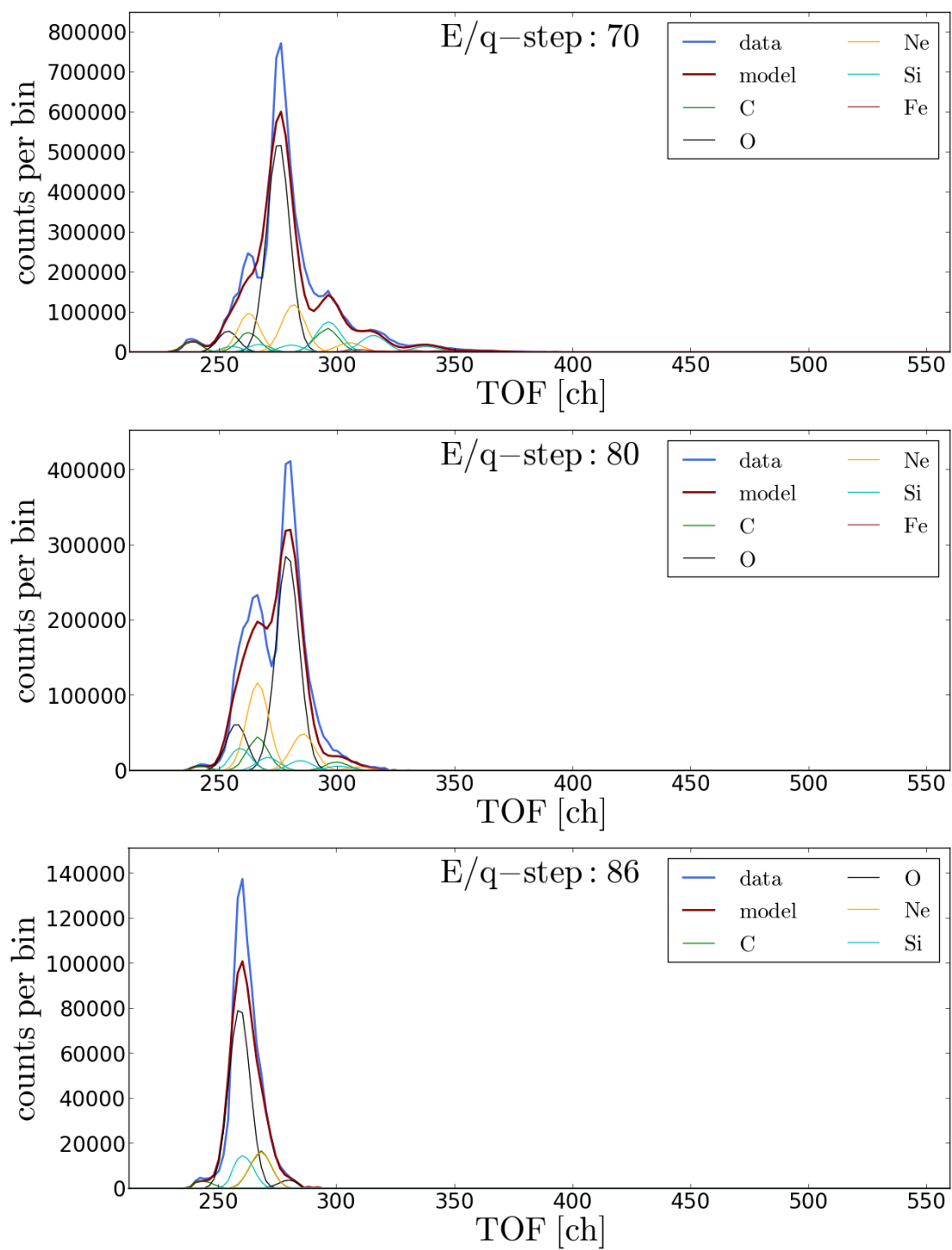
FIGURE C.27

239

FIGURE C.28

FIGURE C.29

FIGURE C.30

FIGURE C.31

F<small>IGURE</small> C.32
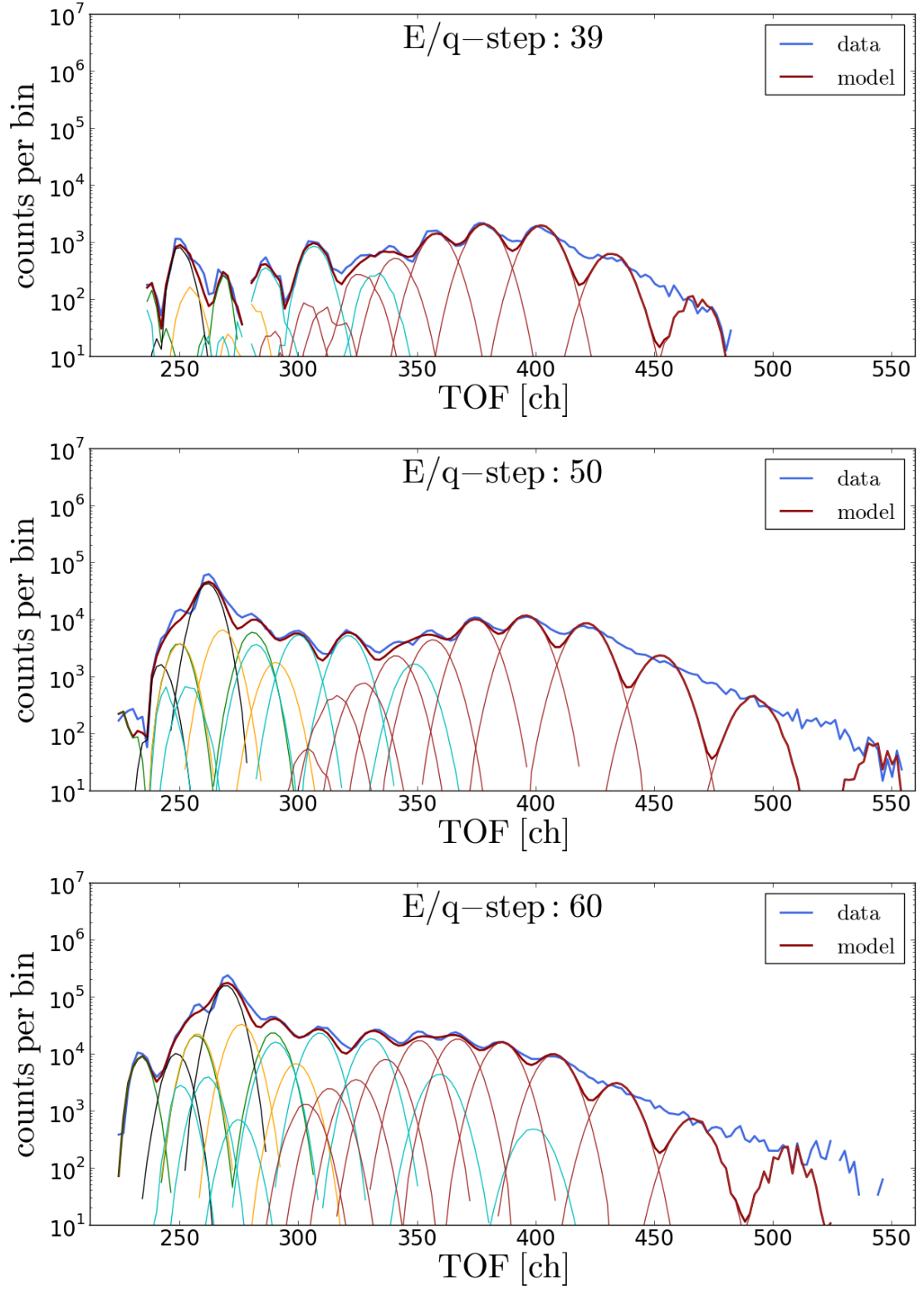
FIGURE C.33
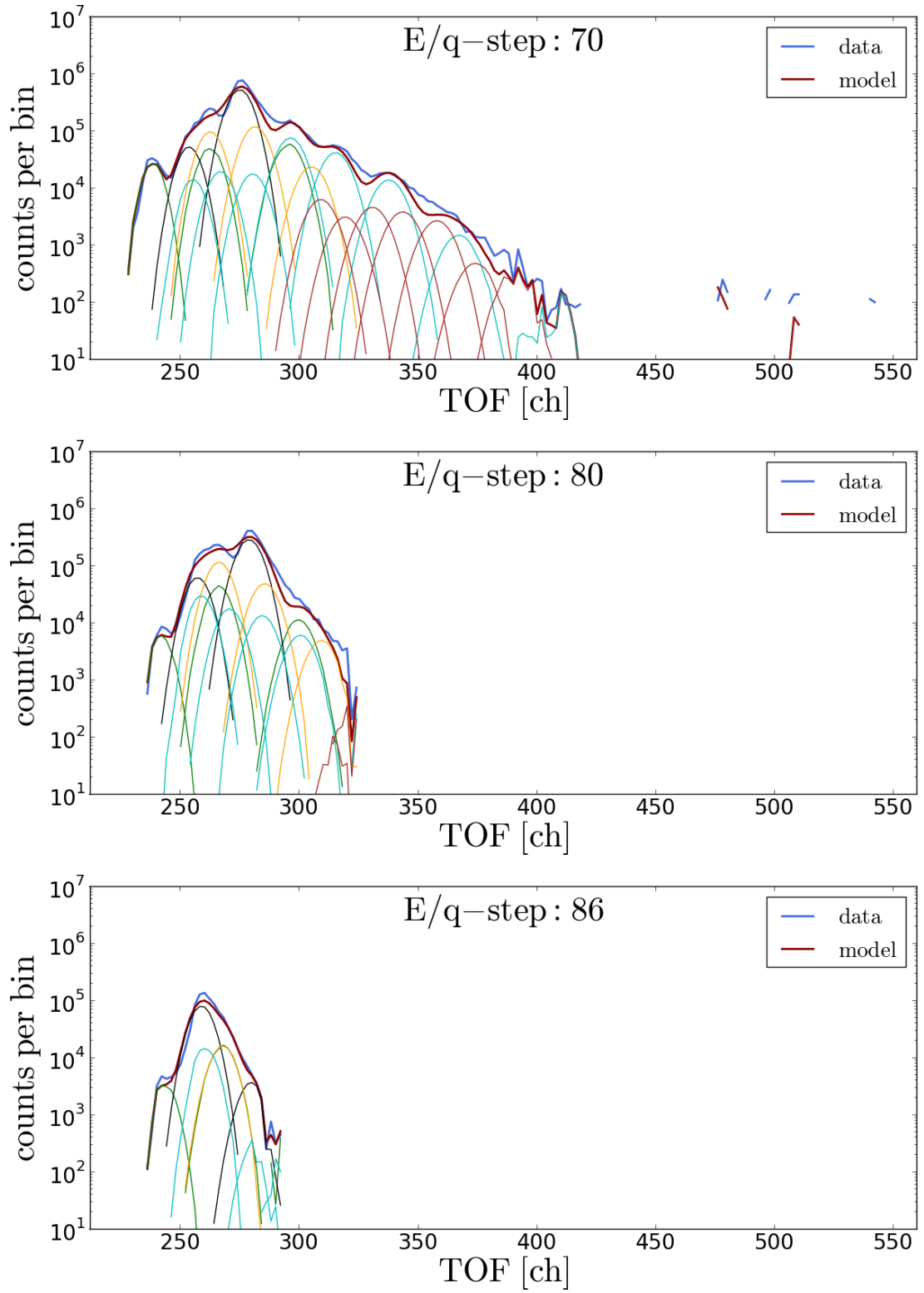
FIGURE C.34
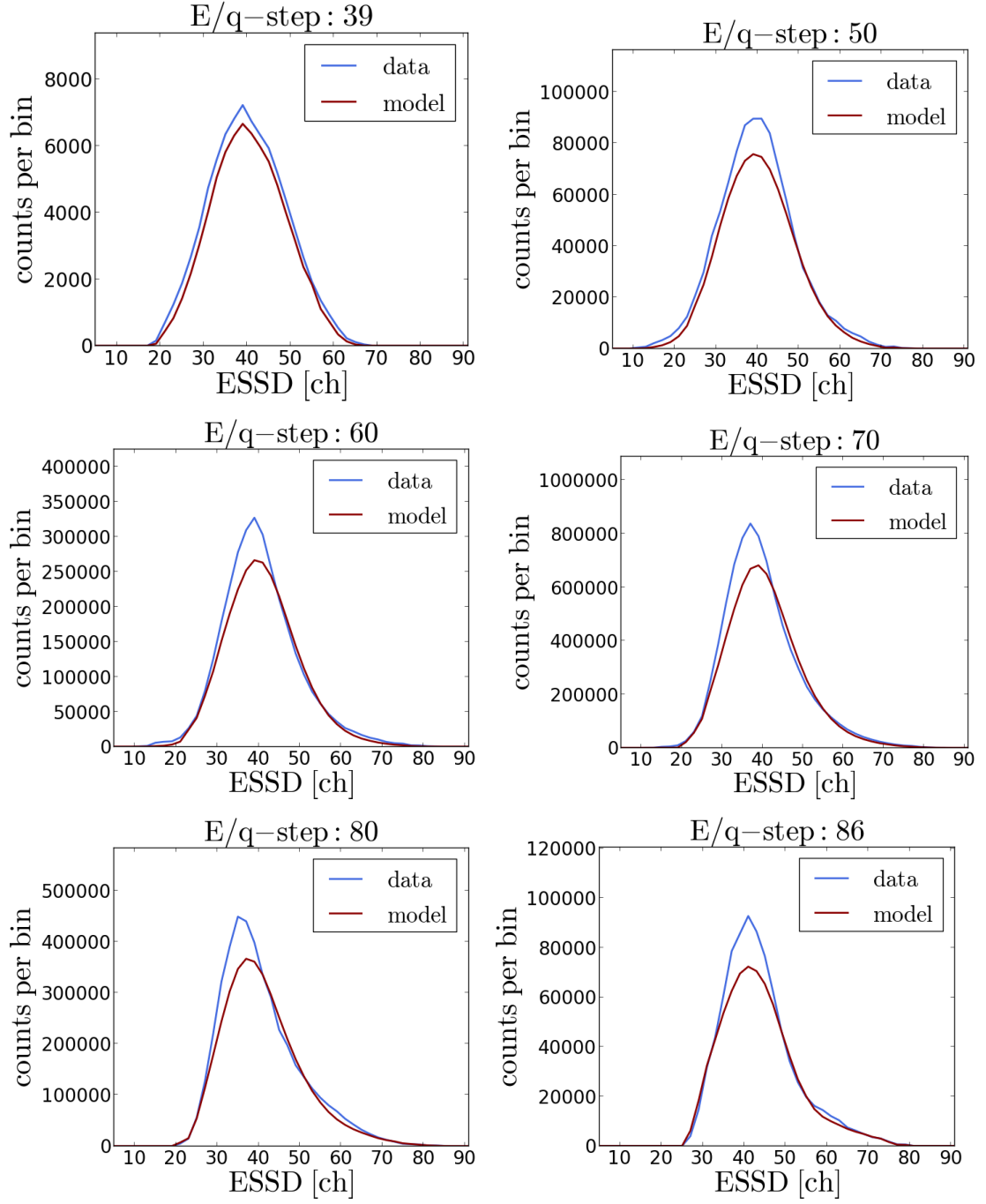
FIGURE C.35
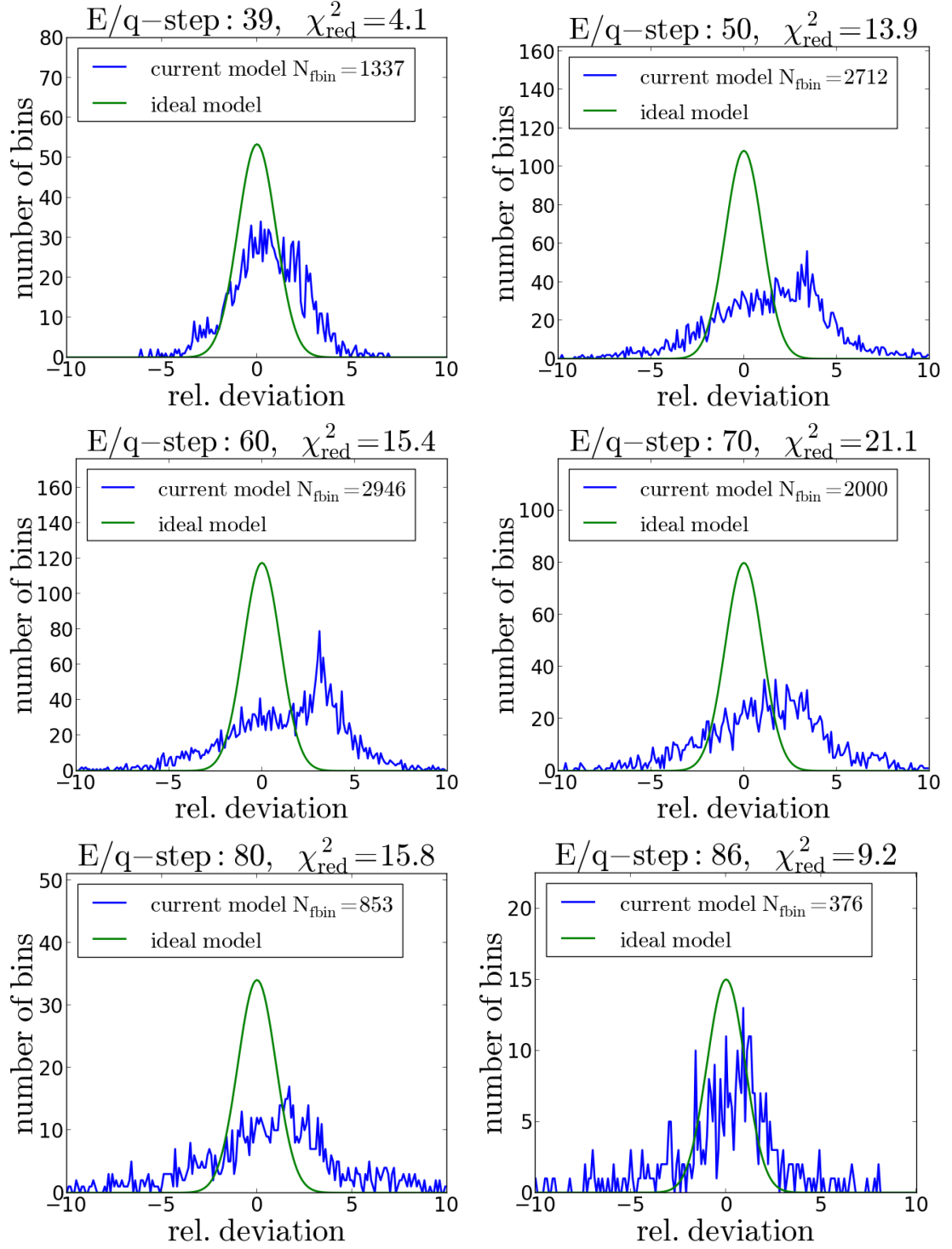
FIGURE C.36

C.2.2 Kappa-Moyal Peak Model
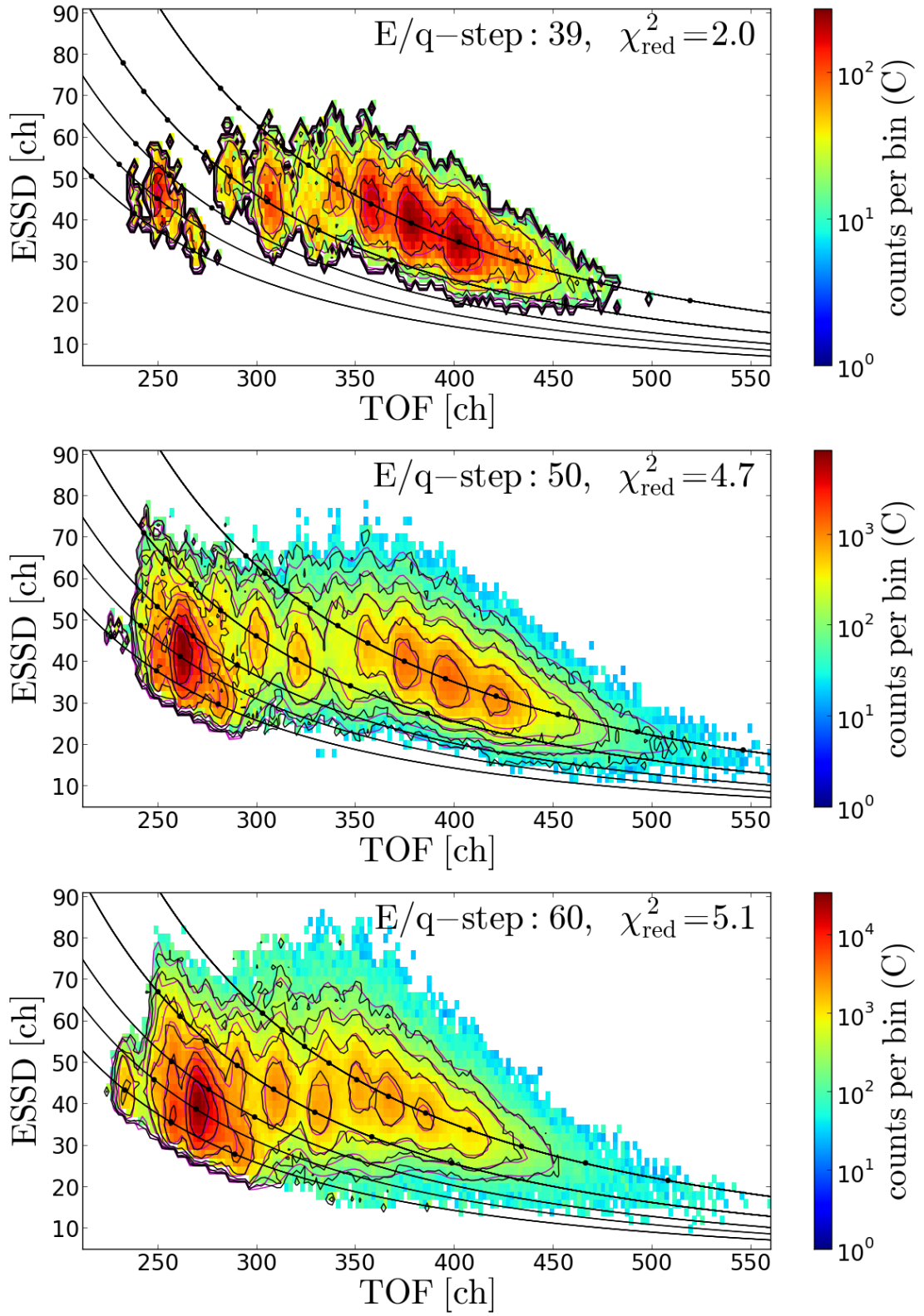
FIGURE C.37
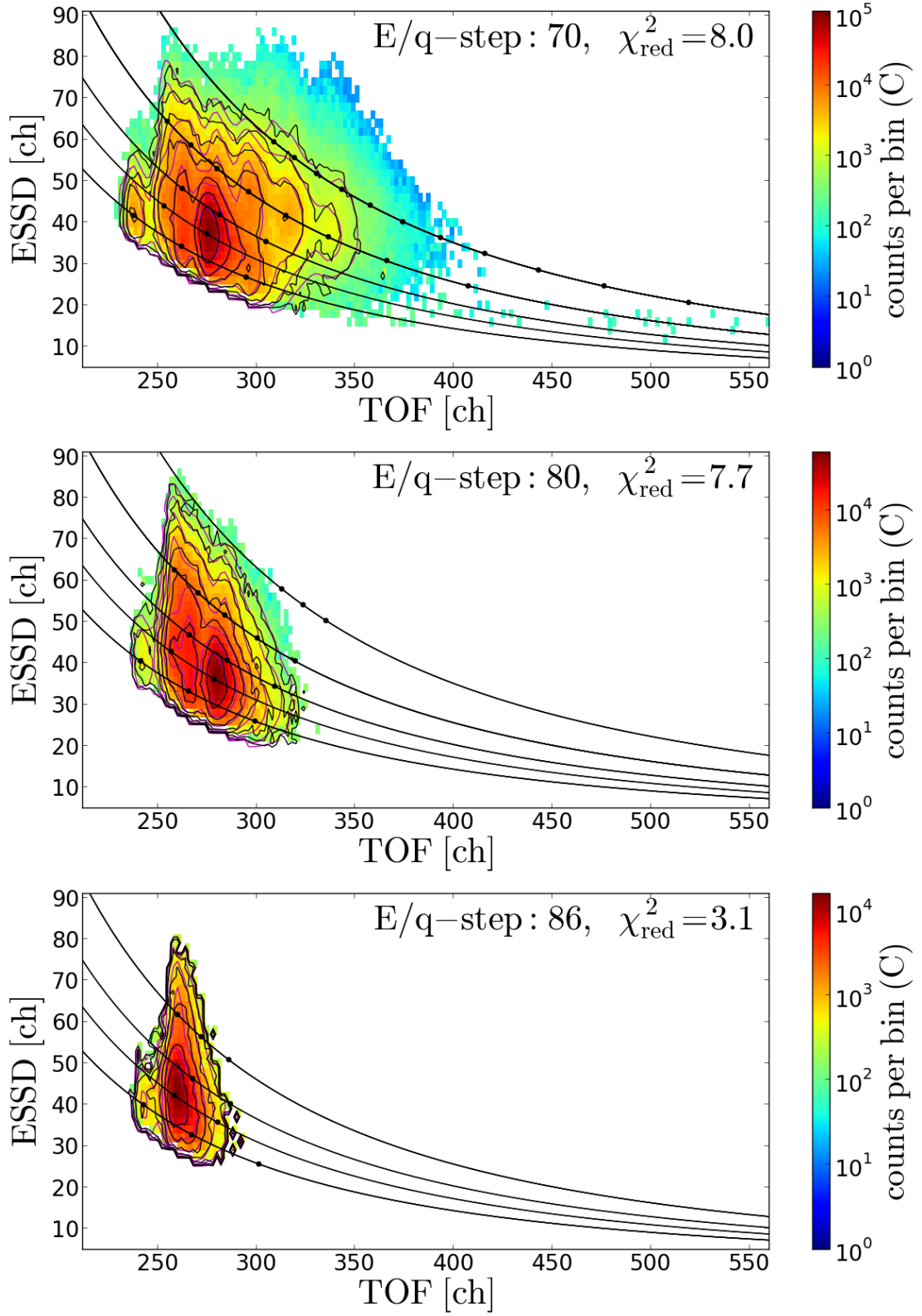
FIGURE C.38
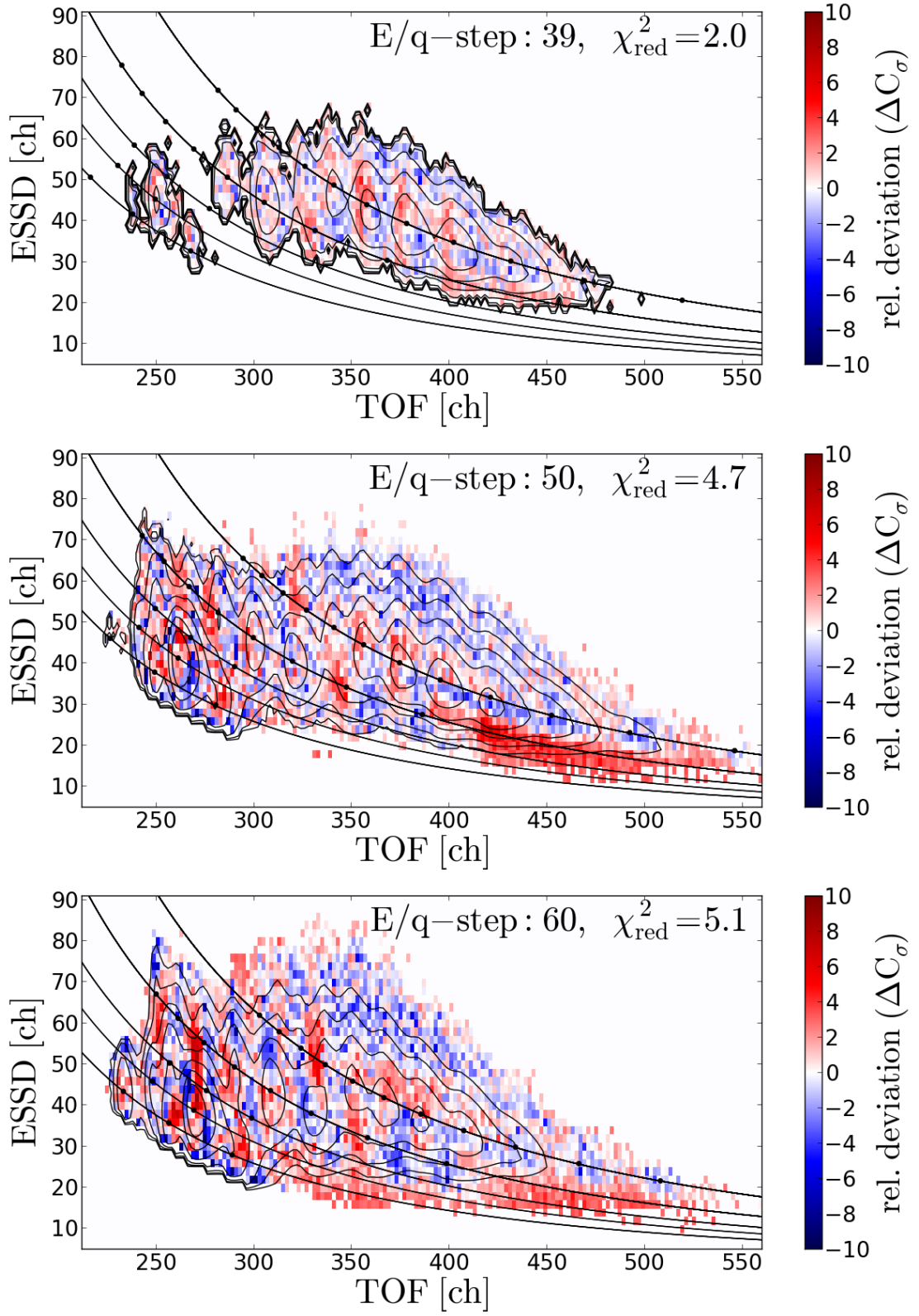
FIGURE C.39
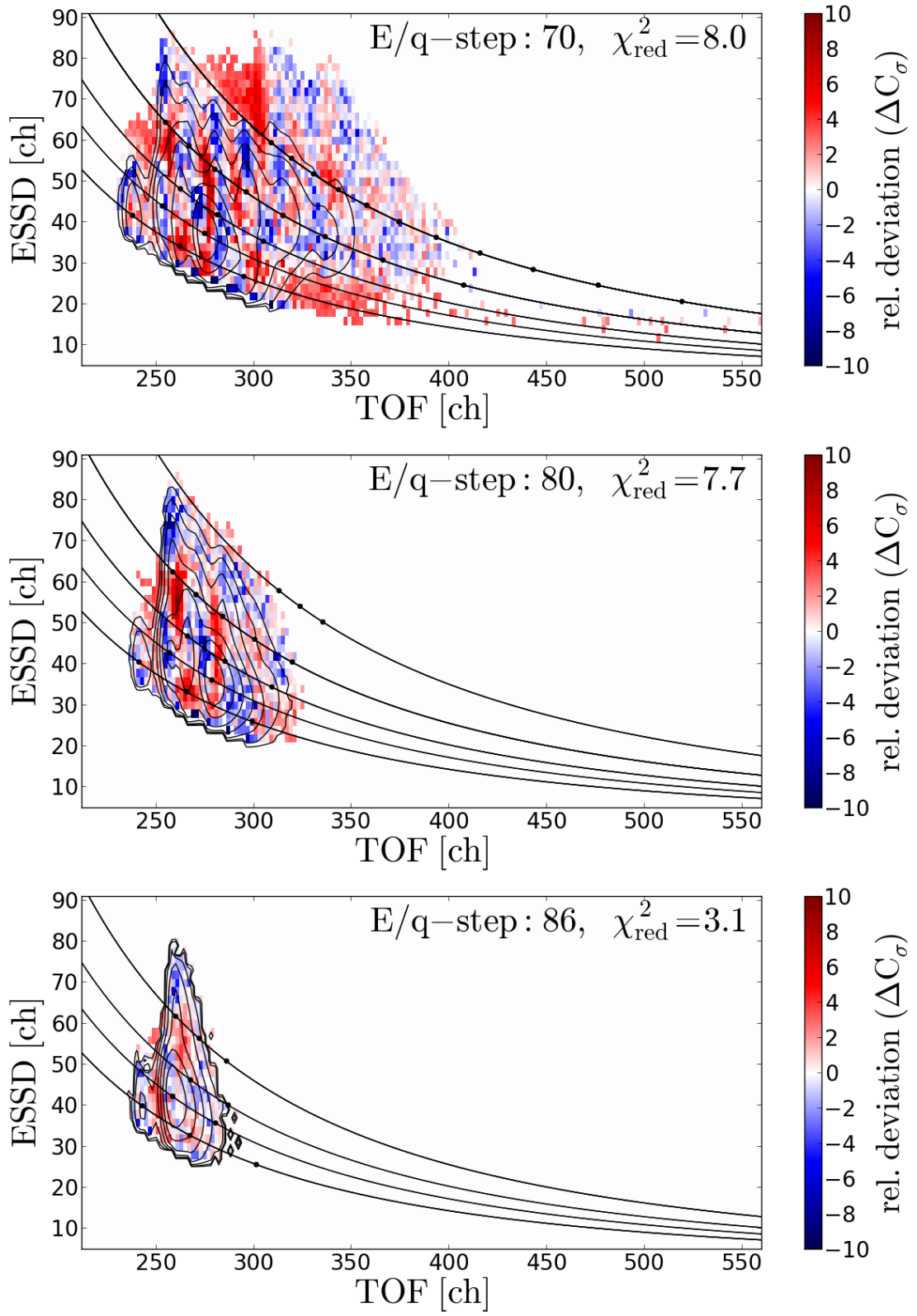
FIGURE C.40

FIGURE C.41

253

FIGURE C.42

254
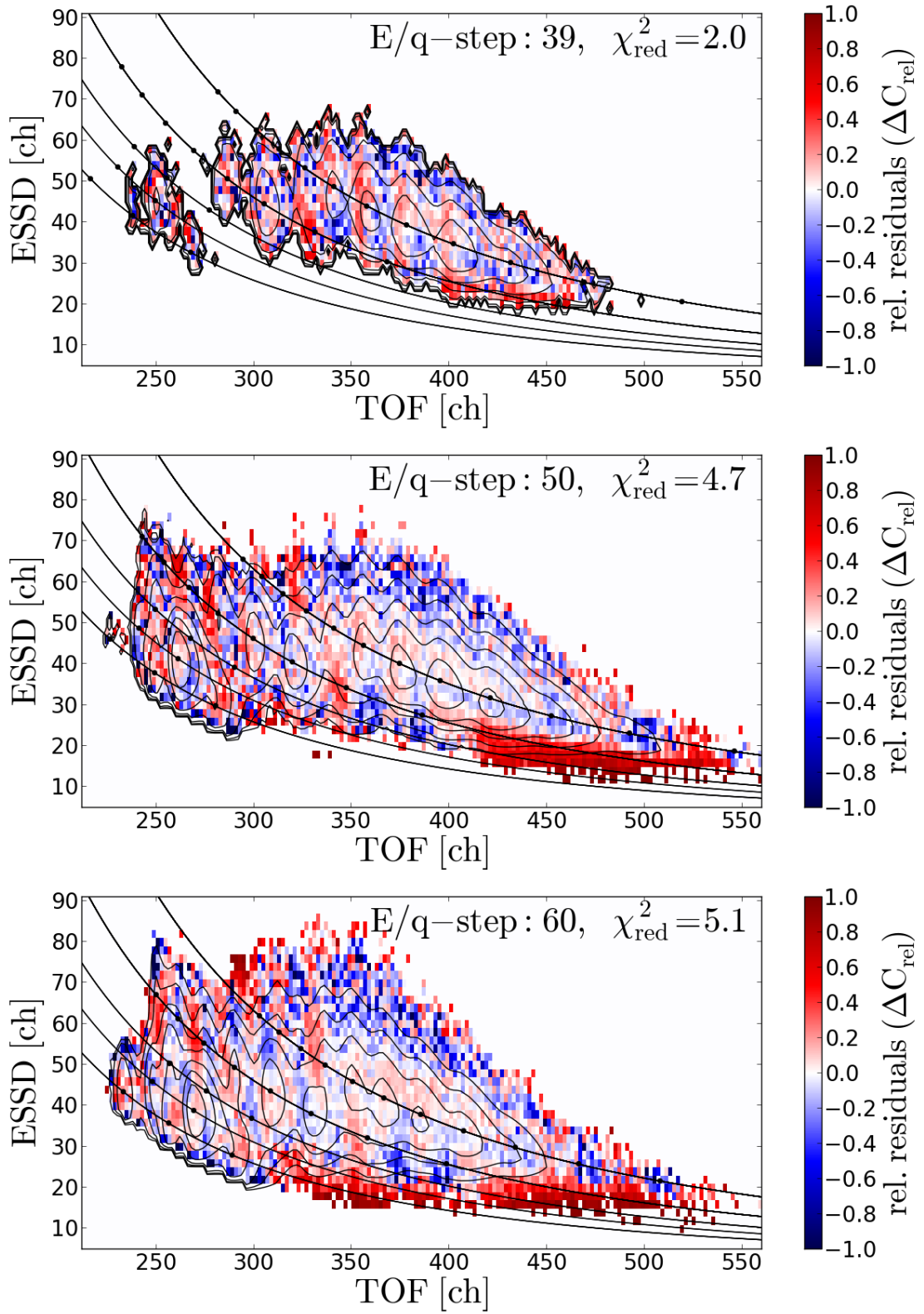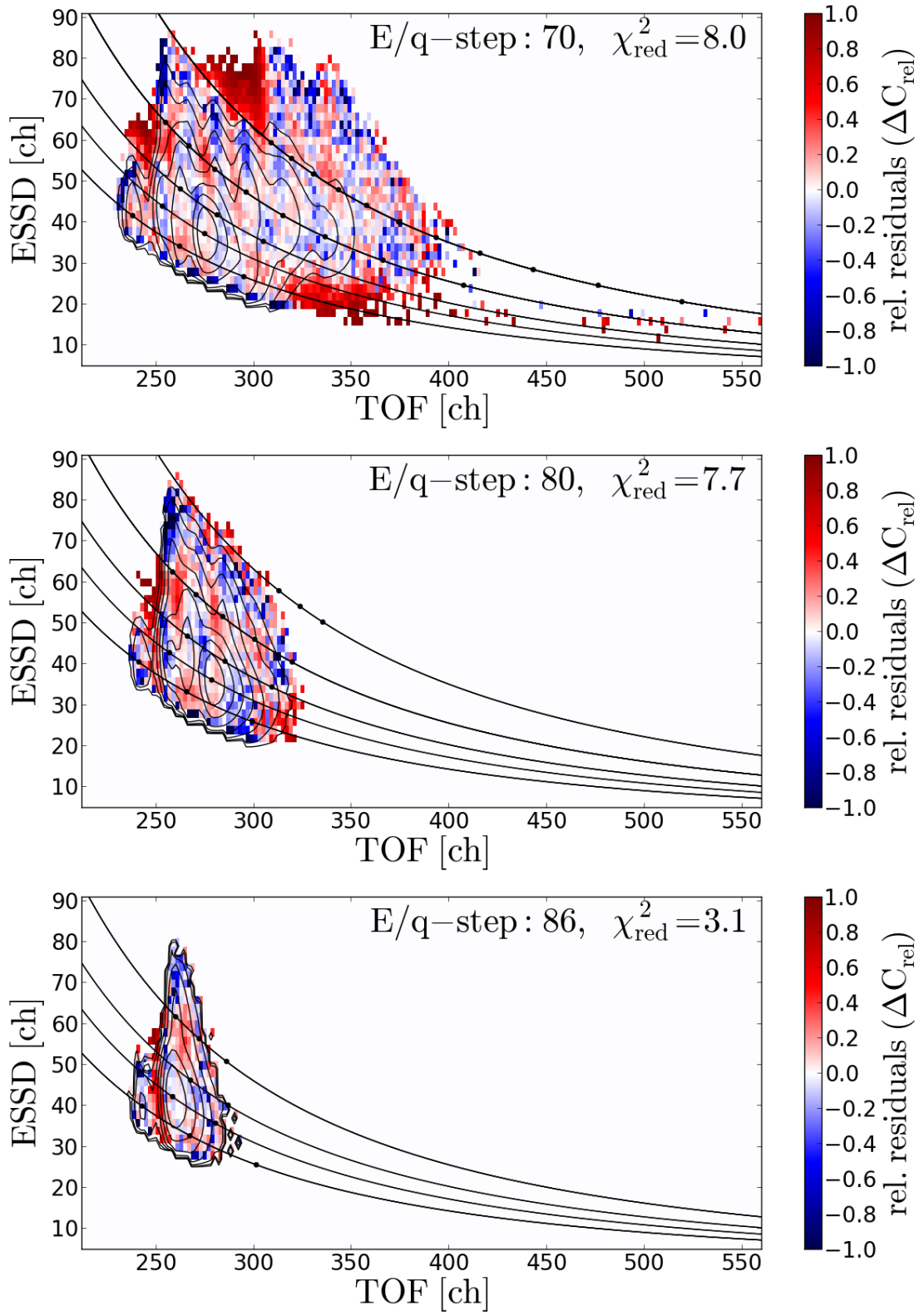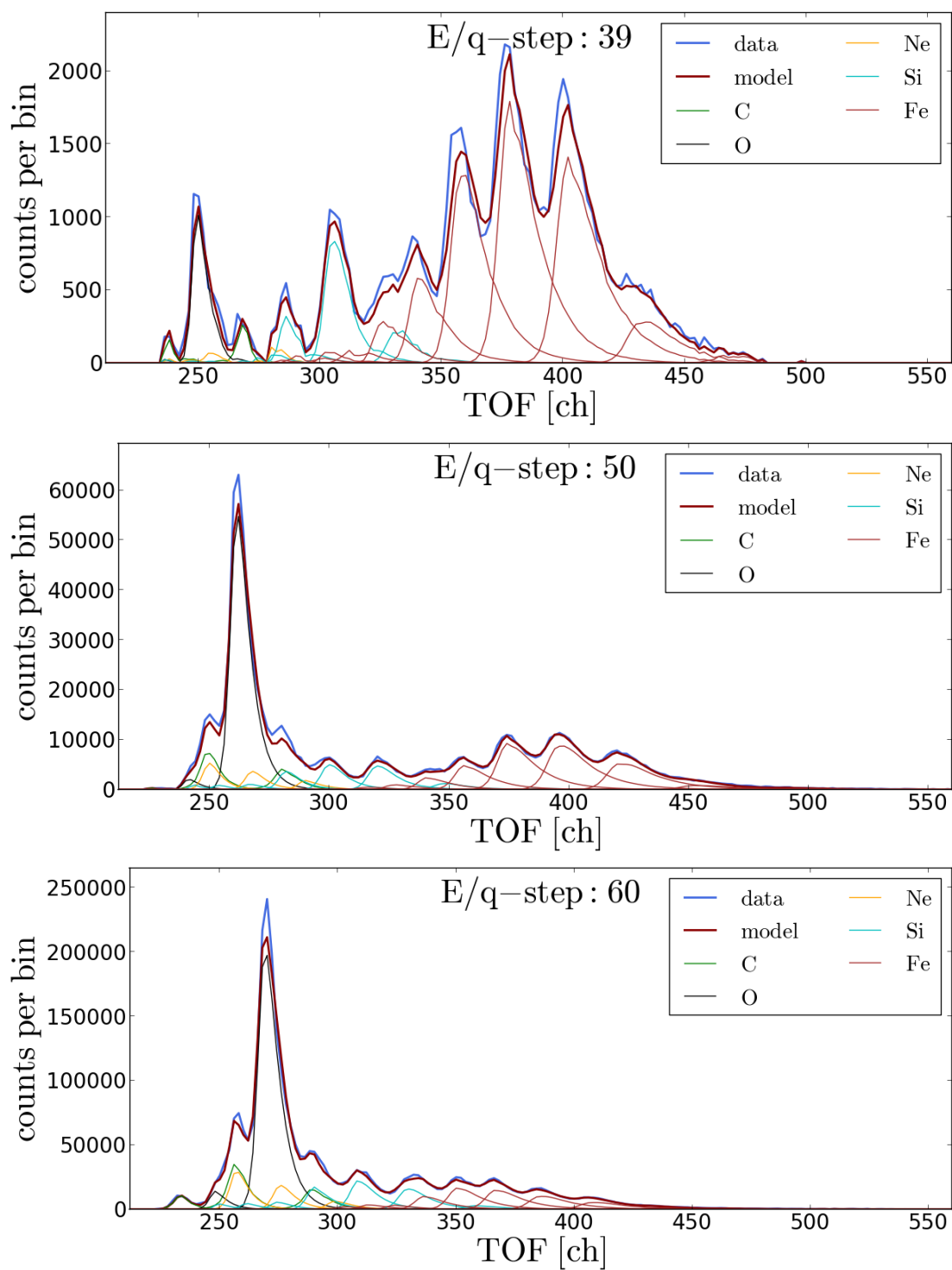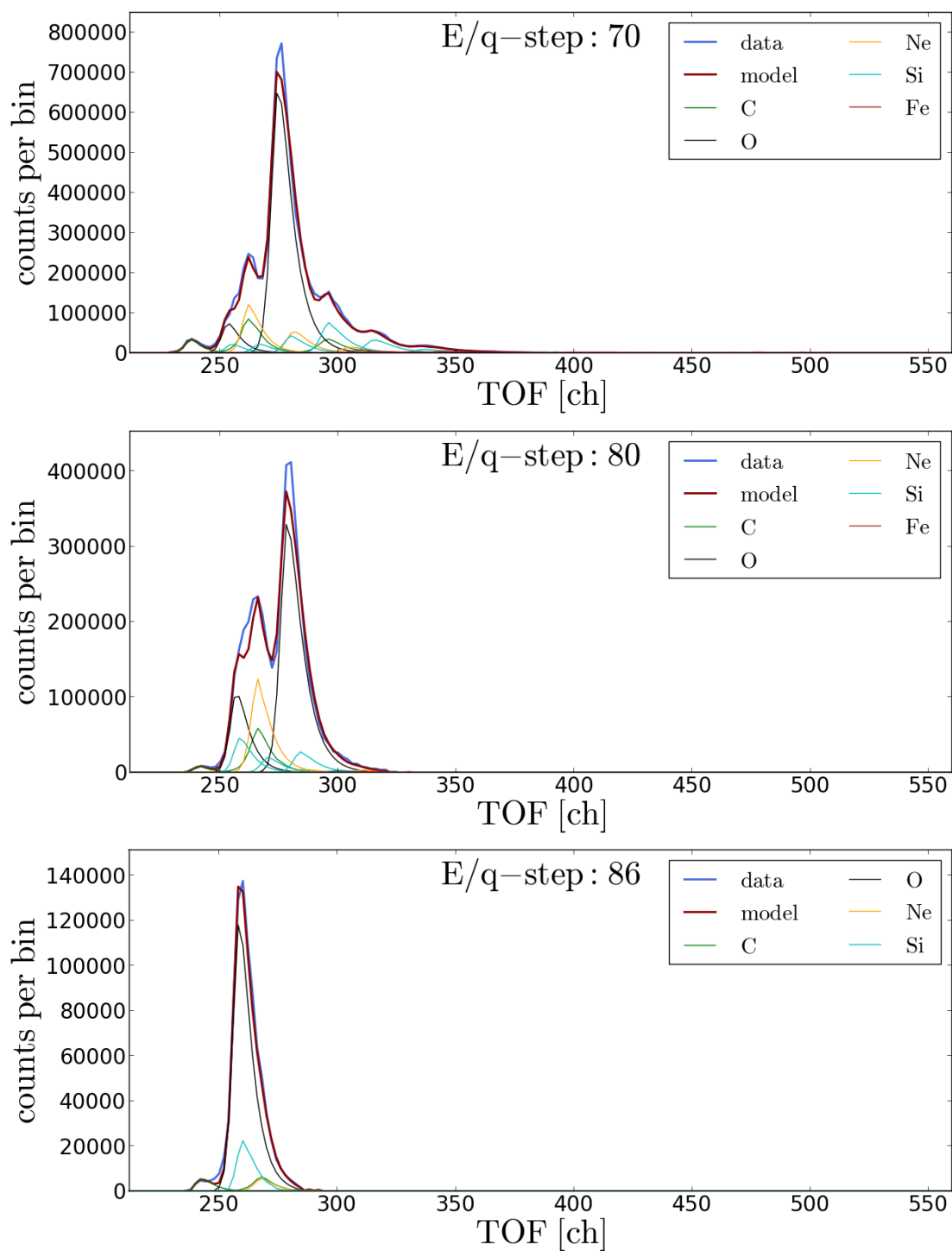
FIGURE C.43

F𝚒𝚐𝚞𝚛𝚎 C.44
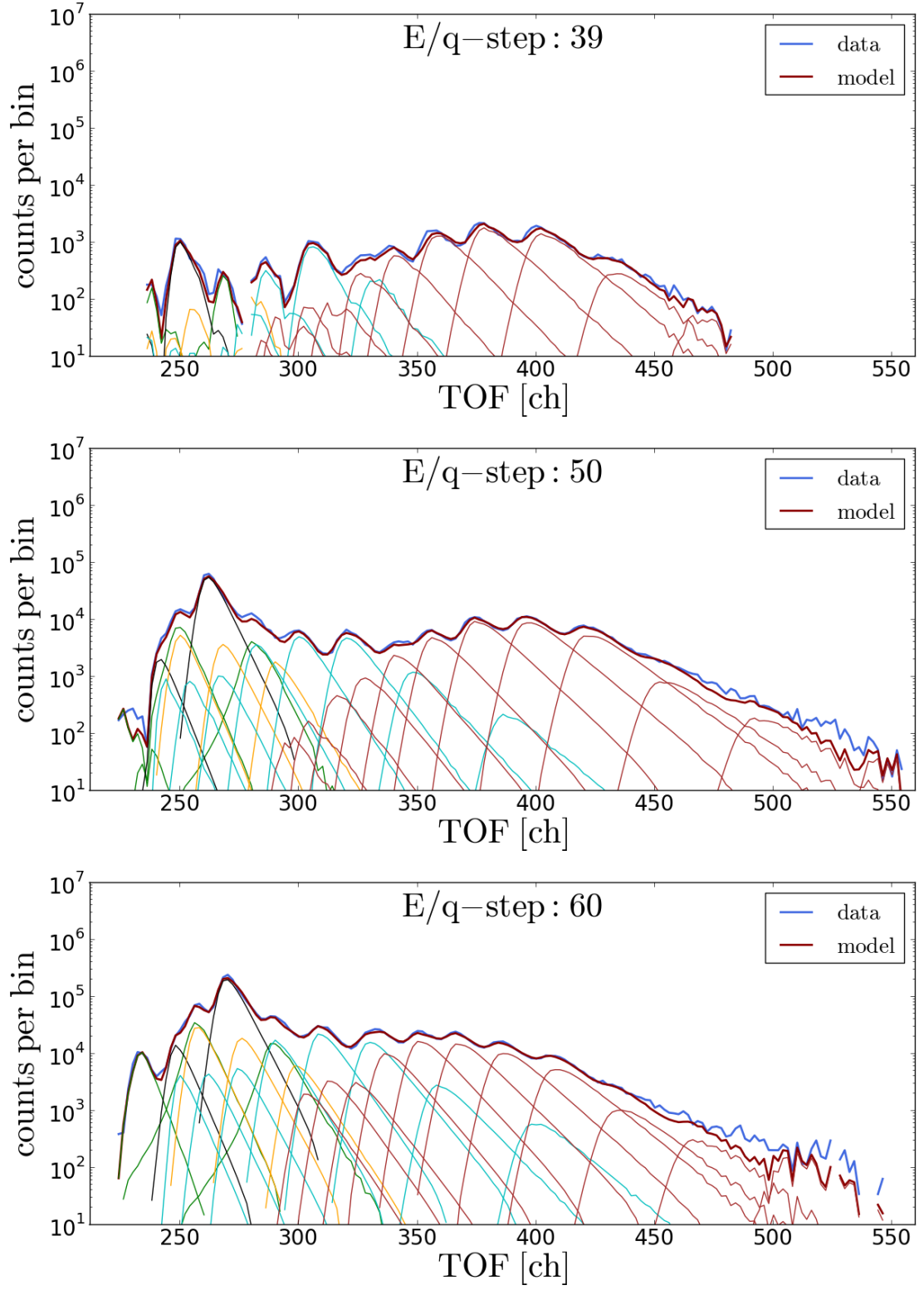
FIGURE C.45
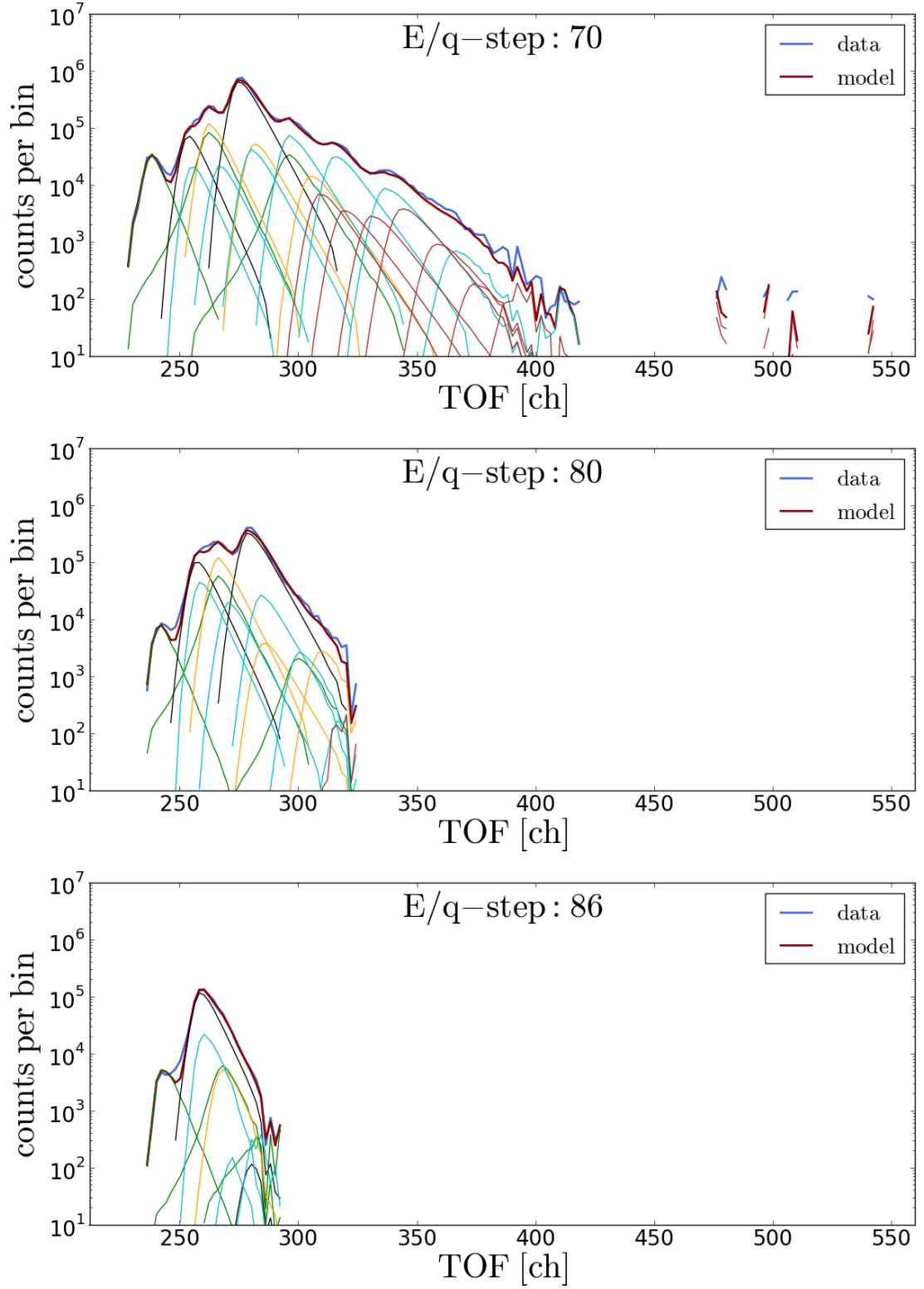
FIGURE C.46
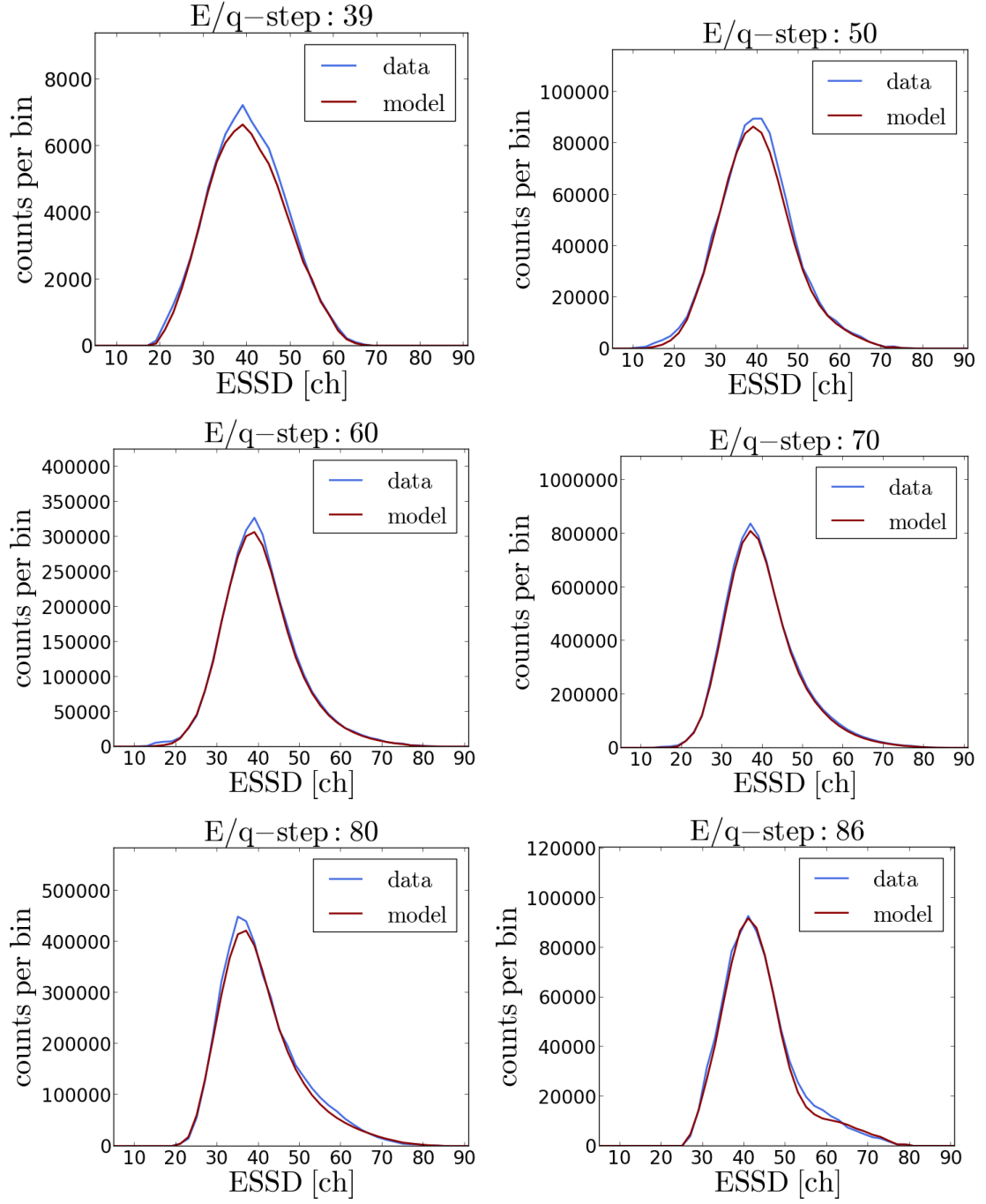
FIGURE C.47
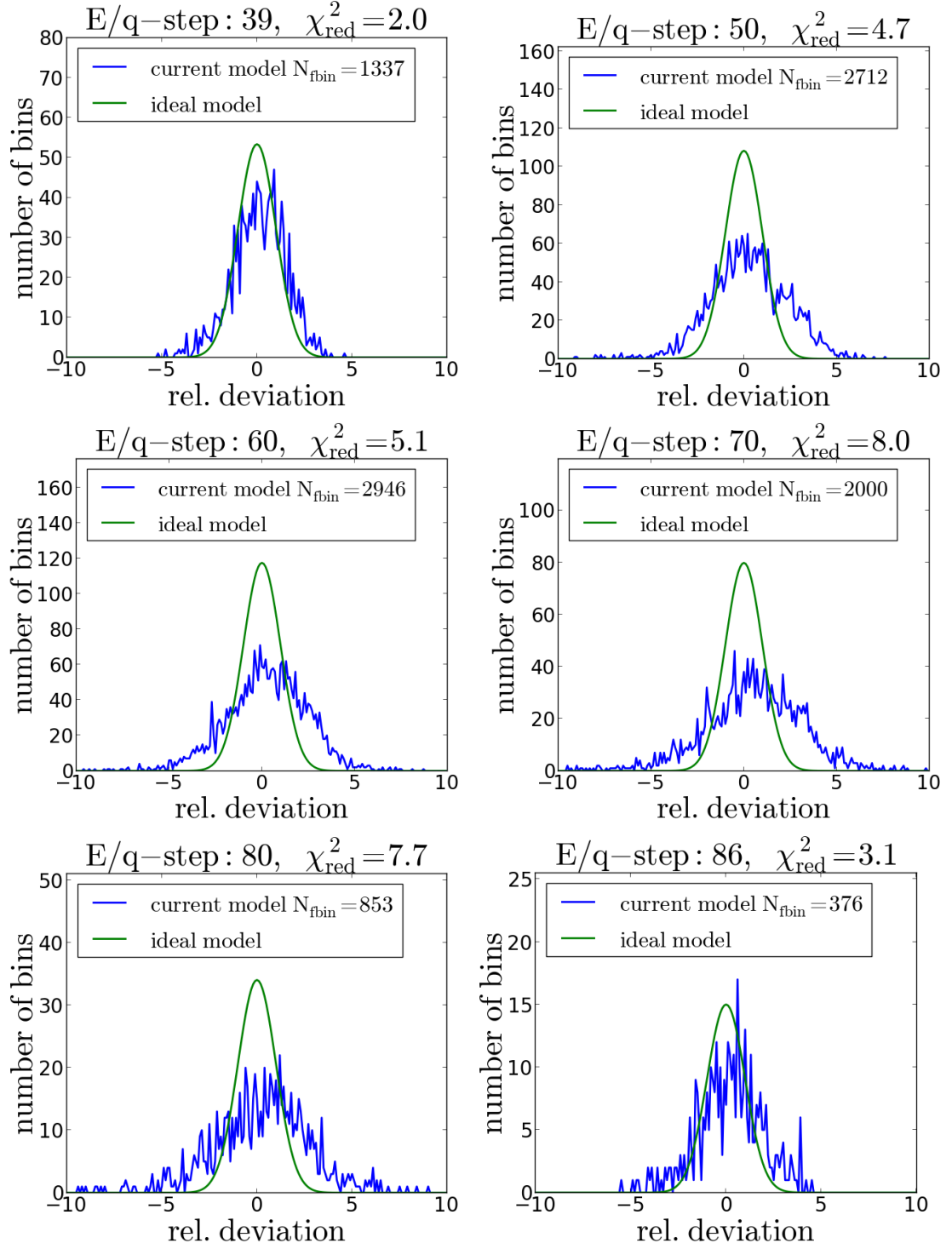
FIGURE C.48

Appendix D

Heavy Ion Long-Term Speed Spectra Measured with CELIAS/CTOF

D.1   Long-Term Slow Wind Speed Spectra Obtained from the Kappa-Moyal Full Stable Response Model

FIGURE D.1: Long-term accumulated speed mean speeds (for details see text) for the genaralized-peak-shape model (left) and the asymetric-iron model (right) for slow wind (upper) and fast wind (lower) measurement period.
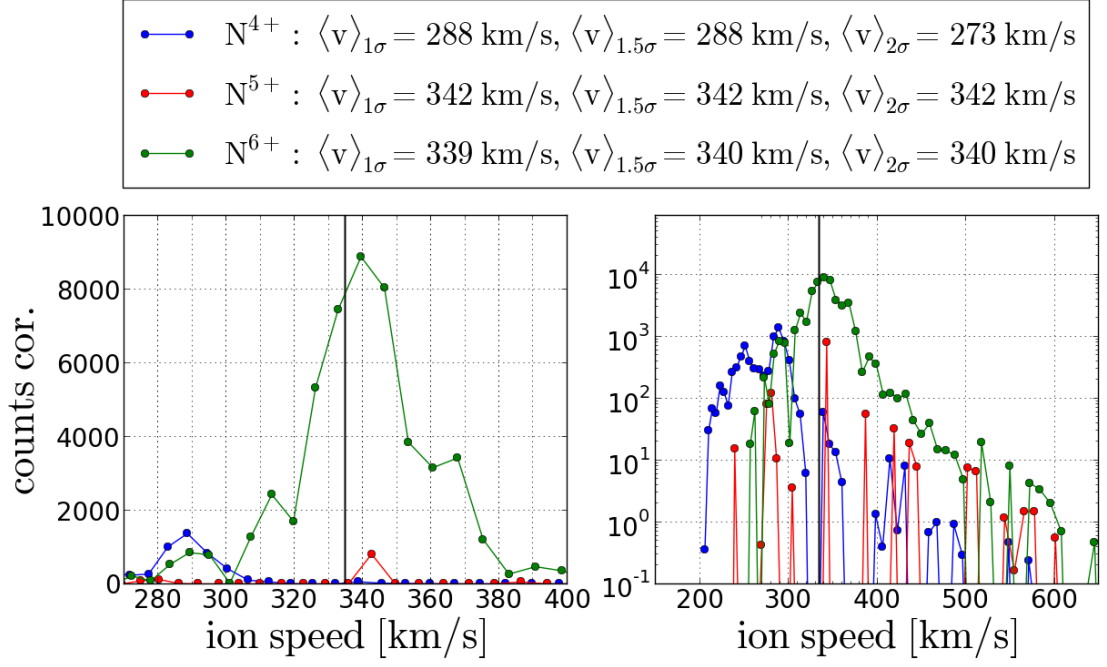
FIGURE D.2: Long-term accumulated speed mean speeds (for details see text) for the genaralized-peak-shape model (left) and the asymetric-iron model (right) for slow wind (upper) and fast wind (lower) measurement period.

FIGURE D.3: Long-term accumulated speed mean speeds (for details see text) for the genaralized-peak-shape model (left) and the asymetric-iron model (right) for slow wind (upper) and fast wind (lower) measurement period.

FIGURE D.4: Long-term accumulated speed mean speeds (for details see text) for the genaralized-peak-shape model (left) and the asymetric-iron model (right) for slow wind (upper) and fast wind (lower) measurement period.

FIGURE D.5: Long-term accumulated speed mean speeds (for details see text) for the genaralized-peak-shape model (left) and the asymetric-iron model (right) for slow wind (upper) and fast wind (lower) measurement period.
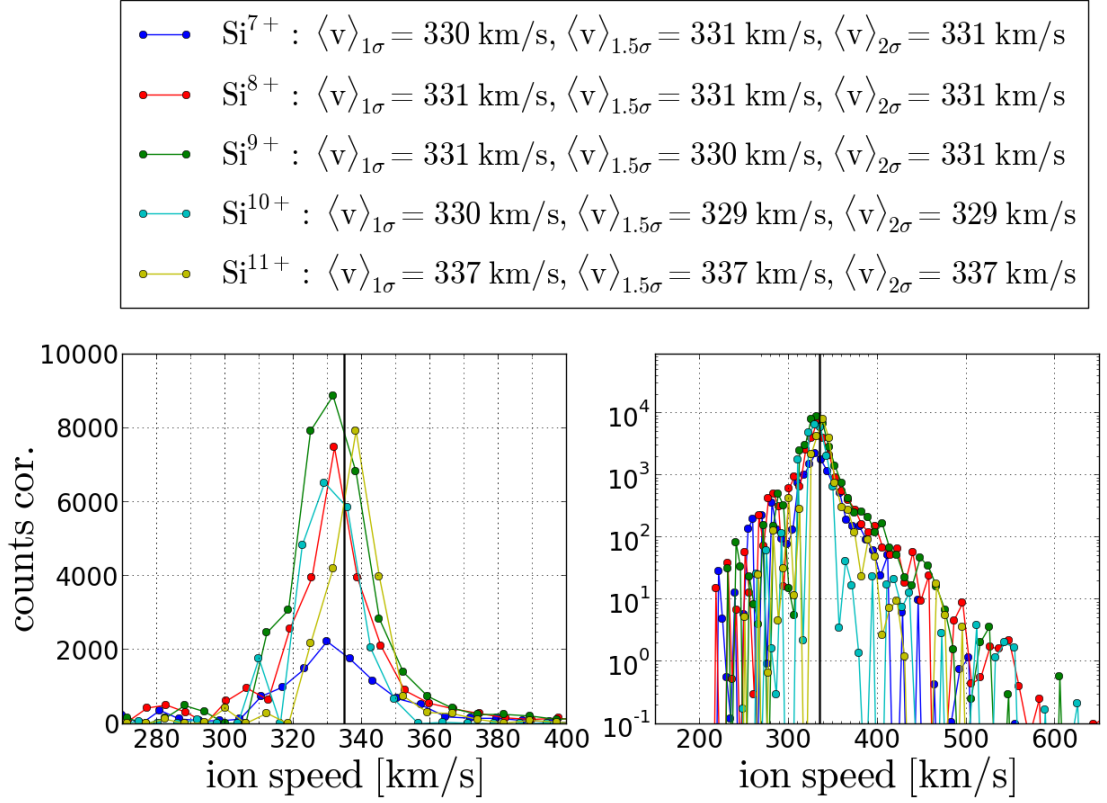
FIGURE D.6: Long-term accumulated speed mean speeds (for details see text) for the genaralized-peak-shape model (left) and the asymetric-iron model (right) for slow wind (upper) and fast wind (lower) measurement period.
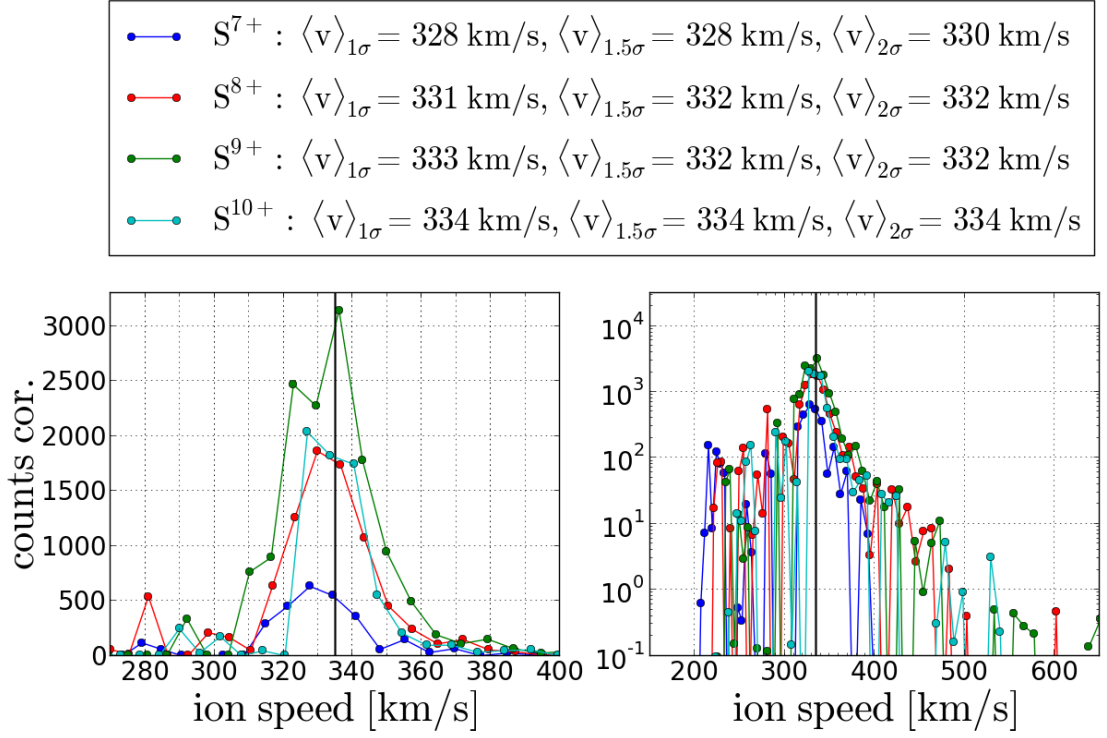
FIGURE D.7: Long-term accumulated speed mean speeds (for details see text) for the genaralized-peak-shape model (left) and the asymetric-iron model (right) for slow wind (upper) and fast wind (lower) measurement period.
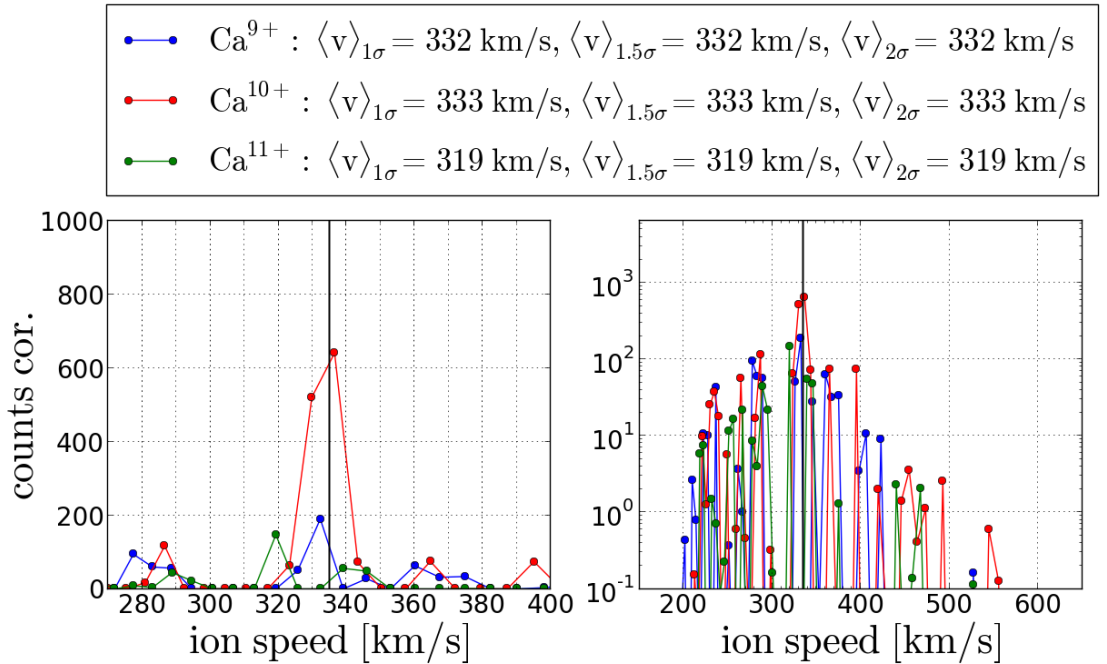
FIGURE D.8: Long-term accumulated speed mean speeds (for details see text) for the genaralized-peak-shape model (left) and the asymetric-iron model (right) for slow wind (upper) and fast wind (lower) measurement period.
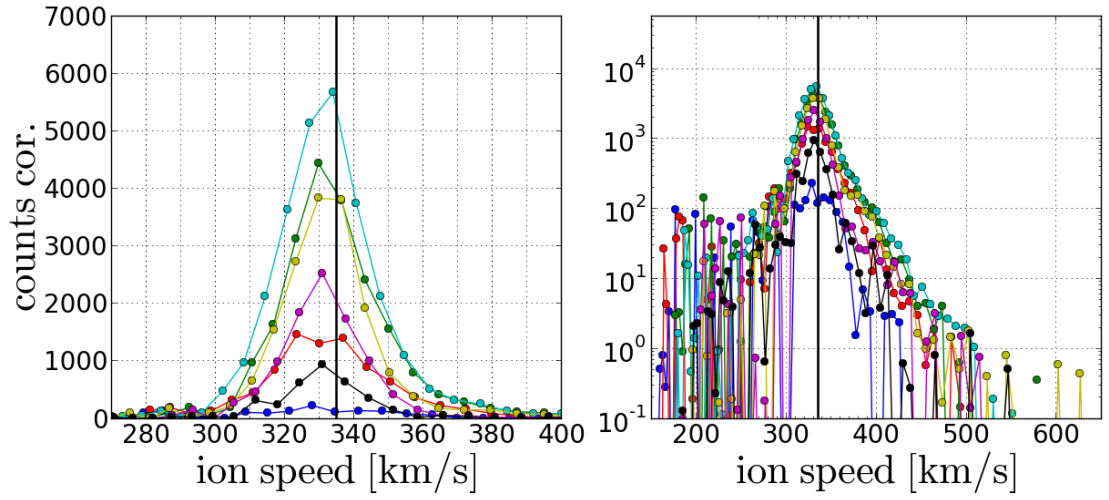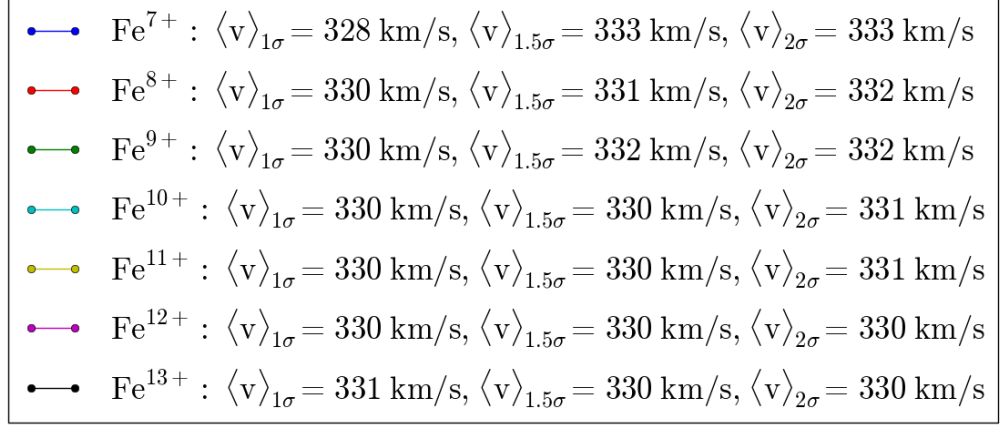
FIGURE D.9: Long-term accumulated speed mean speeds (for details see text) for the genaralized-peak-shape model (left) and the asymetric-iron model (right) for slow wind (upper) and fast wind (lower) measurement period.

Ni^{7+} : $\langle v \rangle_{1\sigma} = 288$ km/s, $\langle v \rangle_{1.5\sigma} = 293$ km/s, $\langle v \rangle_{2\sigma} = 293$ km/s

Ni^{8+} : $\langle v \rangle_{1\sigma} = 310$ km/s, $\langle v \rangle_{1.5\sigma} = 309$ km/s, $\langle v \rangle_{2\sigma} = 306$ km/s

Ni^{9+} : $\langle v \rangle_{1\sigma} = 308$ km/s, $\langle v \rangle_{1.5\sigma} = 308$ km/s, $\langle v \rangle_{2\sigma} = 313$ km/s

Ni^{10+} : $\langle v \rangle_{1\sigma} = 326$ km/s, $\langle v \rangle_{1.5\sigma} = 320$ km/s, $\langle v \rangle_{2\sigma} = 314$ km/s

Ni^{11+} : $\langle v \rangle_{1\sigma} = 334$ km/s, $\langle v \rangle_{1.5\sigma} = 334$ km/s, $\langle v \rangle_{2\sigma} = 334$ km/s

Ni^{12+} : $\langle v \rangle_{1\sigma} = 329$ km/s, $\langle v \rangle_{1.5\sigma} = 331$ km/s, $\langle v \rangle_{2\sigma} = 331$ km/s

Ni^{13+} : $\langle v \rangle_{1\sigma} = 333$ km/s, $\langle v \rangle_{1.5\sigma} = 333$ km/s, $\langle v \rangle_{2\sigma} = 333$ km/s
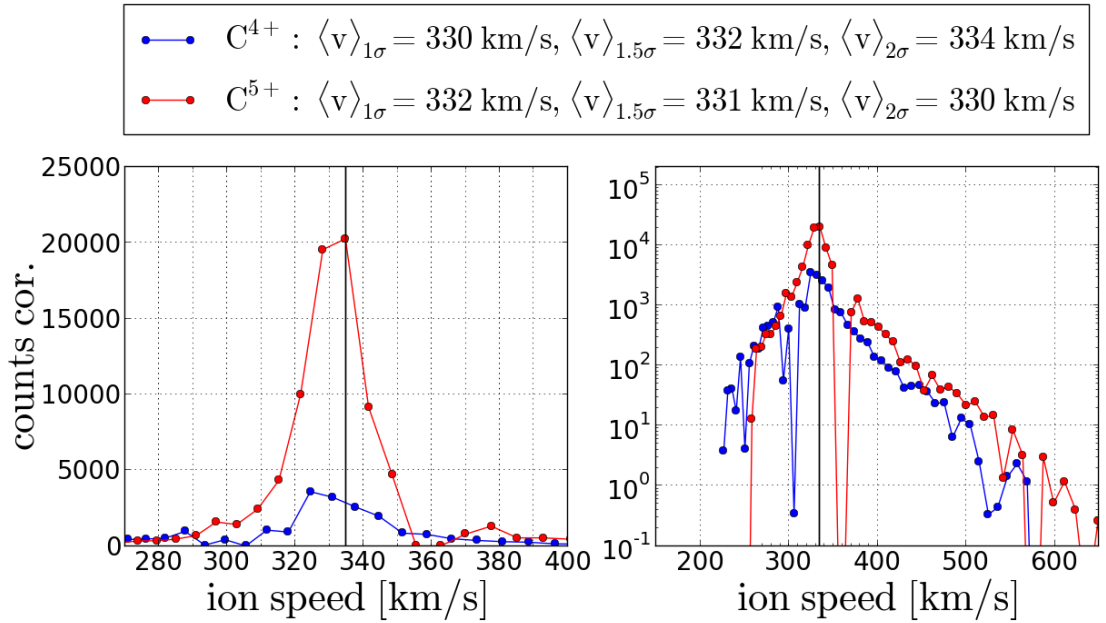
FIGURE D.10: Long-term accumulated speed mean speeds (for details see text) for the genaralized-peak-shape model (left) and the asymetric-iron model (right) for slow wind (upper) and fast wind (lower) measurement period.

D.2 Long-Term Slow Wind Speed Spectra Obtained from the Kappa-Moyal Reduced Stable Response Model

C^{5+} : $\langle v \rangle_{1\sigma} = 333$ km/s, $\langle v \rangle_{1.5\sigma} = 331$ km/s, $\langle v \rangle_{2\sigma} = 331$ km/s

O^{6+} : $\langle v \rangle_{1\sigma} = 331$ km/s, $\langle v \rangle_{1.5\sigma} = 331$ km/s, $\langle v \rangle_{2\sigma} = 331$ km/s

Ne^{8+} : $\langle v \rangle_{1\sigma} = 329$ km/s, $\langle v \rangle_{1.5\sigma} = 330$ km/s, $\langle v \rangle_{2\sigma} = 331$ km/s

Si^{8+} : $\langle v \rangle_{1\sigma} = 332$ km/s, $\langle v \rangle_{1.5\sigma} = 332$ km/s, $\langle v \rangle_{2\sigma} = 332$ km/s

Fe^{10+} : $\langle v \rangle_{1\sigma} = 330$ km/s, $\langle v \rangle_{1.5\sigma} = 331$ km/s, $\langle v \rangle_{2\sigma} = 331$ km/s

FIGURE D.11: Long-term accumulated speed mean speeds (for details see text) for the genaralized-peak-shape model (left) and the asymetric-iron model (right) for slow wind (upper) and fast wind (lower) measurement period.
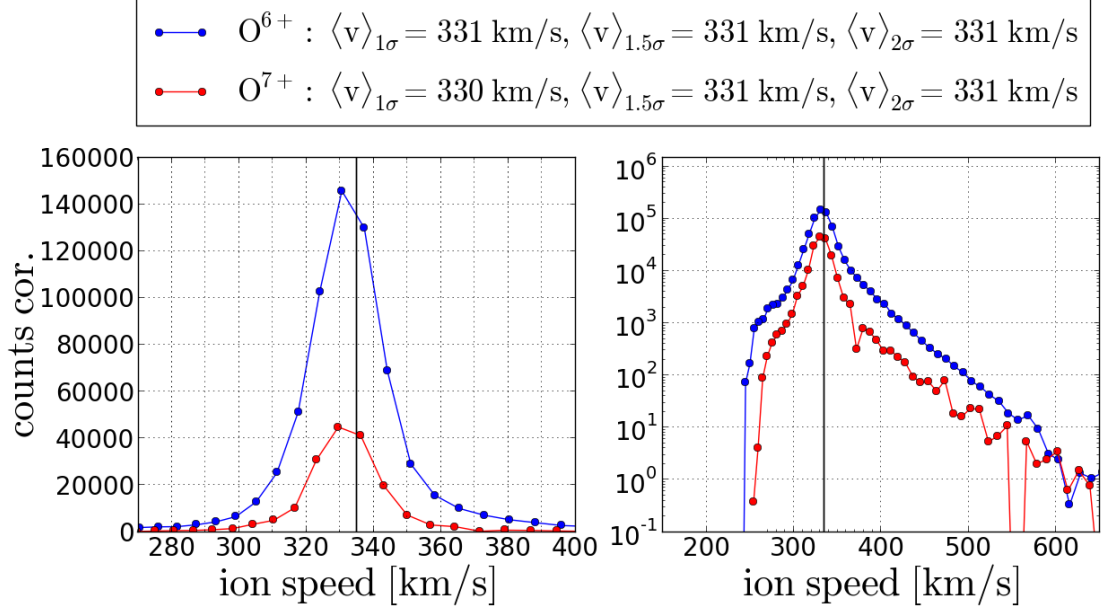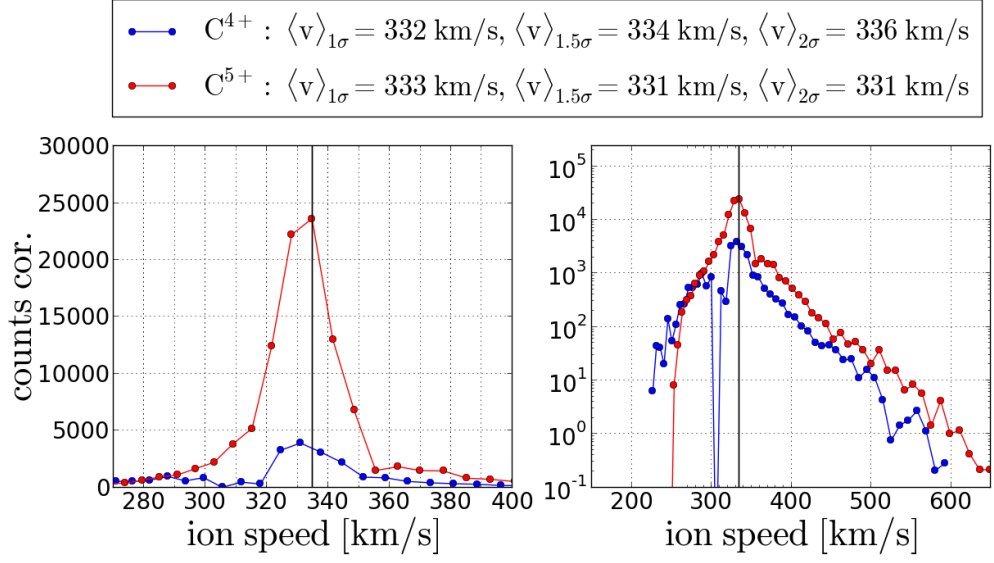
FIGURE D.12: Long-term accumulated speed mean speeds (for details see text) for the genaralized-peak-shape model (left) and the asymetric-iron model (right) for slow wind (upper) and fast wind (lower) measurement period.
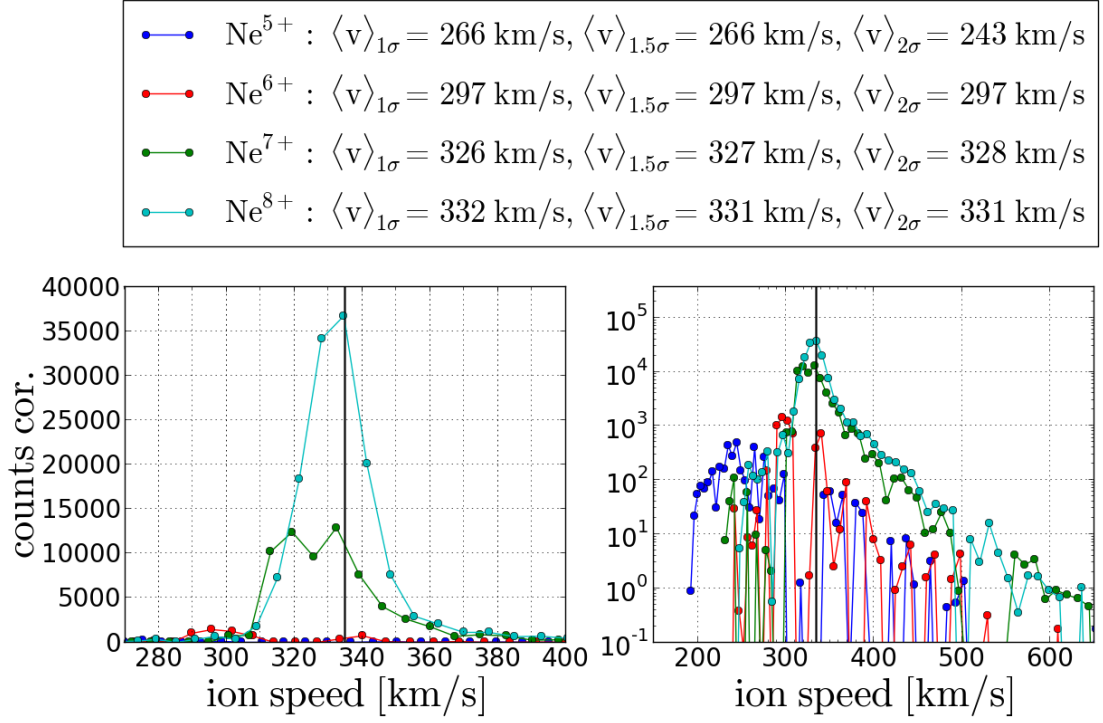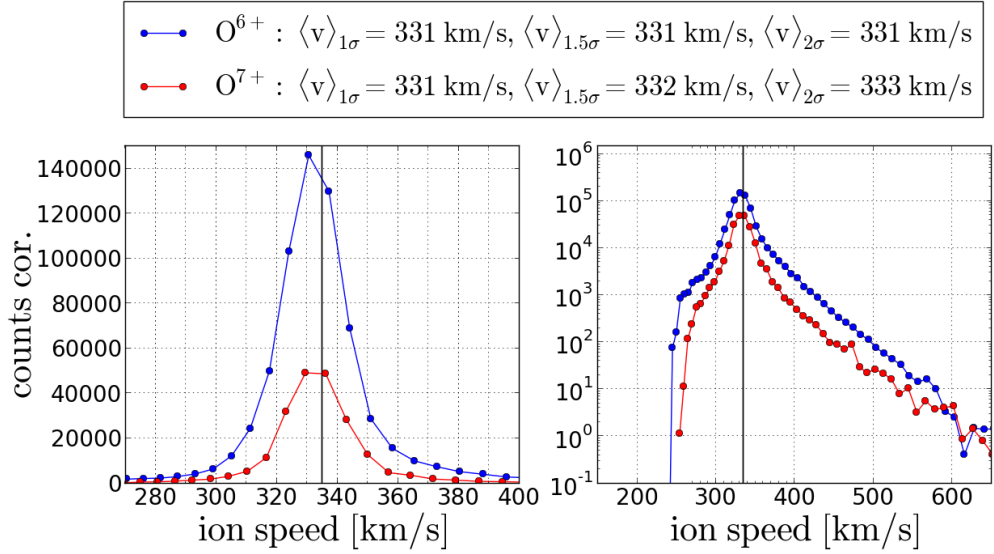

FIGURE D.13: Long-term accumulated speed mean speeds (for details see text) for the genaralized-peak-shape model (left) and the asymetric-iron model (right) for slow wind (upper) and fast wind (lower) measurement period.
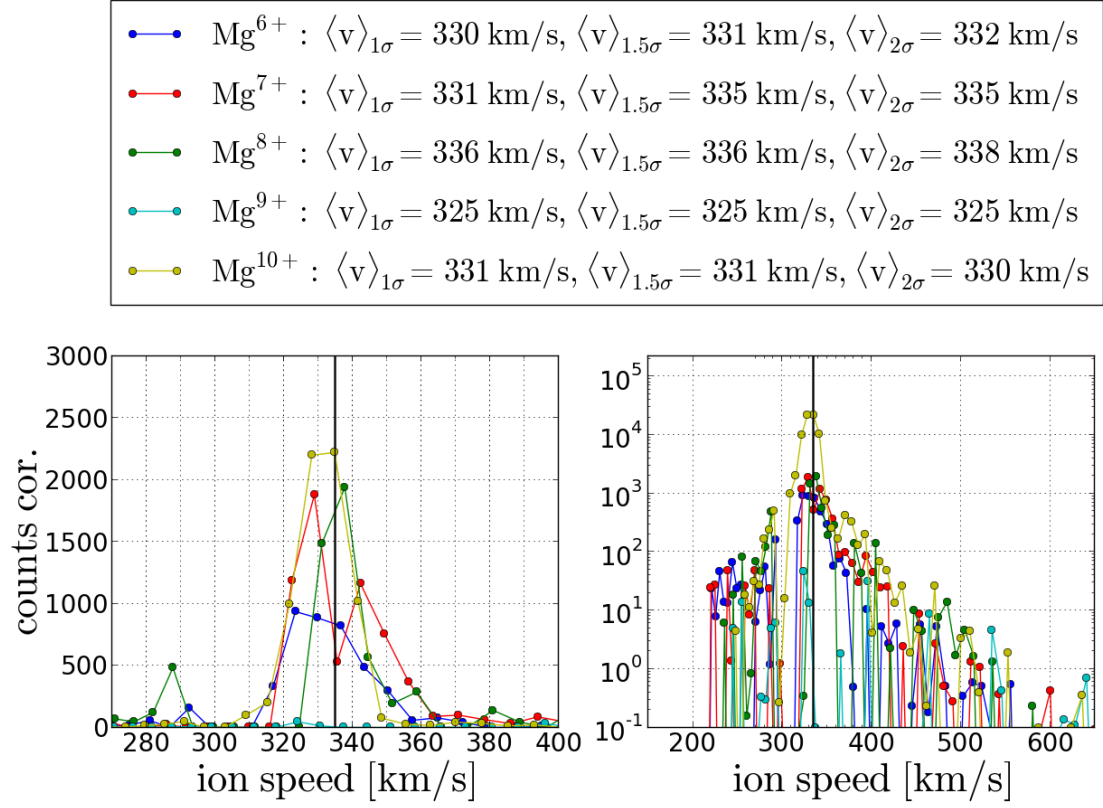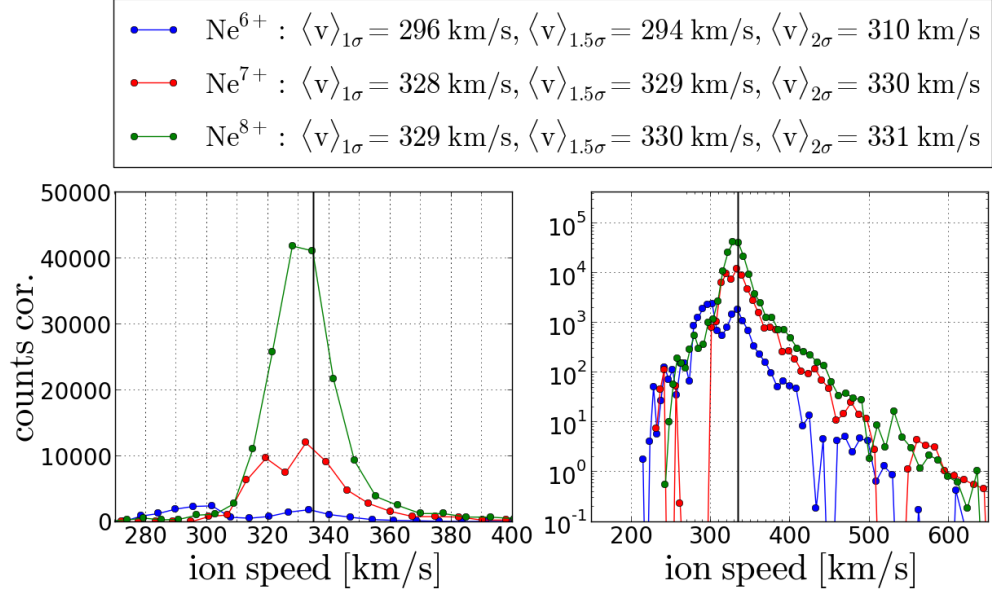
FIGURE D.14: Long-term accumulated speed mean speeds (for details see text) for the genaralized-peak-shape model (left) and the asymetric-iron model (right) for slow wind (upper) and fast wind (lower) measurement period.
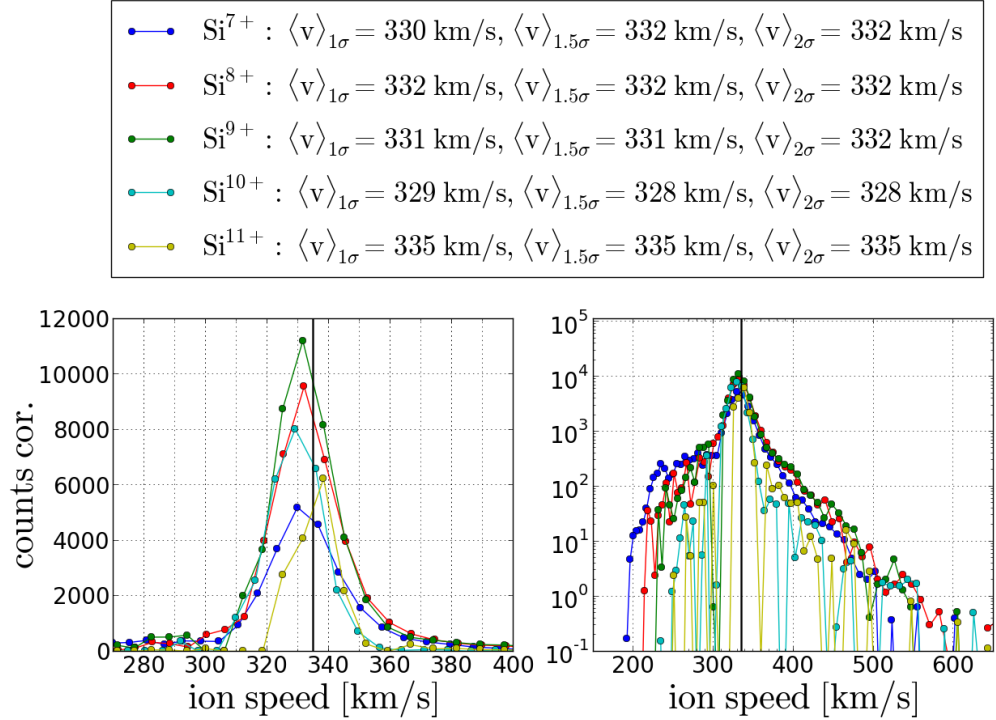
FIGURE D.15: Long-term accumulated speed mean speeds (for details see text) for the genaralized-peak-shape model (left) and the asymetric-iron model (right) for slow wind (upper) and fast wind (lower) measurement period.

$$Fe^{7+} : \langle v \rangle_{1\sigma} = 327 \text{ km/s}, \langle v \rangle_{1.5\sigma} = 310 \text{ km/s}, \langle v \rangle_{2\sigma} = 310 \text{ km/s}$$

$$Fe^{8+} : \langle v \rangle_{1\sigma} = 330 \text{ km/s}, \langle v \rangle_{1.5\sigma} = 330 \text{ km/s}, \langle v \rangle_{2\sigma} = 328 \text{ km/s}$$

$$Fe^{9+} : \langle v \rangle_{1\sigma} = 330 \text{ km/s}, \langle v \rangle_{1.5\sigma} = 332 \text{ km/s}, \langle v \rangle_{2\sigma} = 332 \text{ km/s}$$

$$Fe^{10+} : \langle v \rangle_{1\sigma} = 330 \text{ km/s}, \langle v \rangle_{1.5\sigma} = 331 \text{ km/s}, \langle v \rangle_{2\sigma} = 331 \text{ km/s}$$

$$Fe^{11+} : \langle v \rangle_{1\sigma} = 330 \text{ km/s}, \langle v \rangle_{1.5\sigma} = 331 \text{ km/s}, \langle v \rangle_{2\sigma} = 331 \text{ km/s}$$

$$Fe^{12+} : \langle v \rangle_{1\sigma} = 330 \text{ km/s}, \langle v \rangle_{1.5\sigma} = 331 \text{ km/s}, \langle v \rangle_{2\sigma} = 331 \text{ km/s}$$

$$Fe^{13+} : \langle v \rangle_{1\sigma} = 326 \text{ km/s}, \langle v \rangle_{1.5\sigma} = 326 \text{ km/s}, \langle v \rangle_{2\sigma} = 326 \text{ km/s}$$
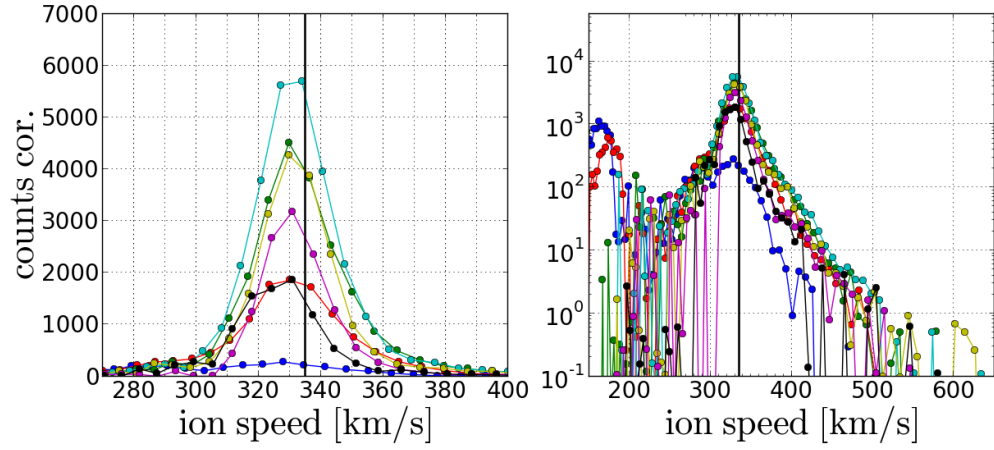
FIGURE D.16: Long-term accumulated speed mean speeds (for details see text) for the genaralized-peak-shape model (left) and the asymetric-iron model (right) for slow wind (upper) and fast wind (lower) measurement period.
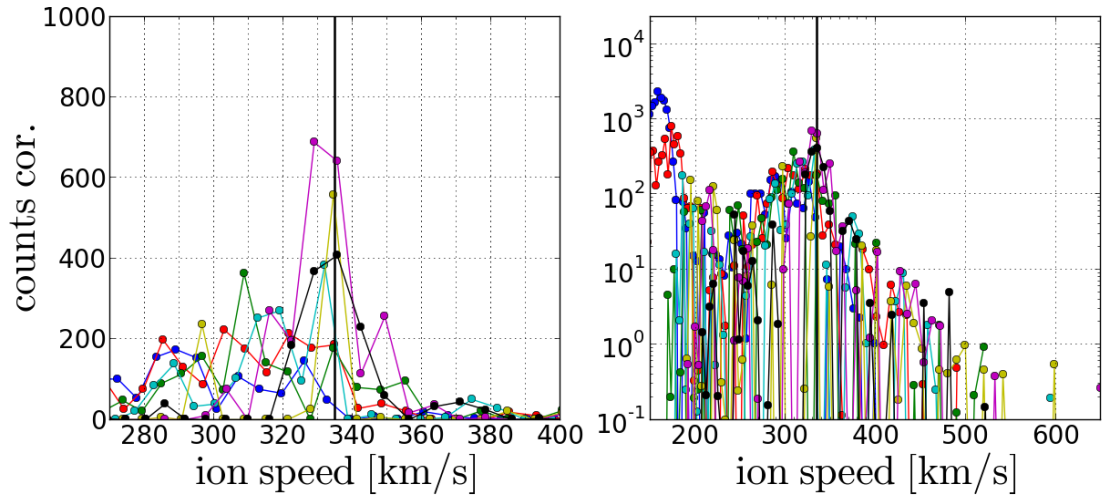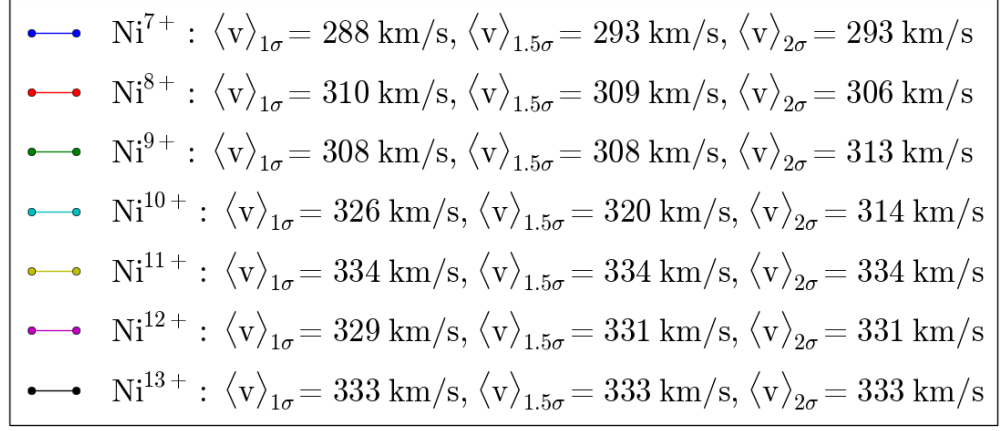
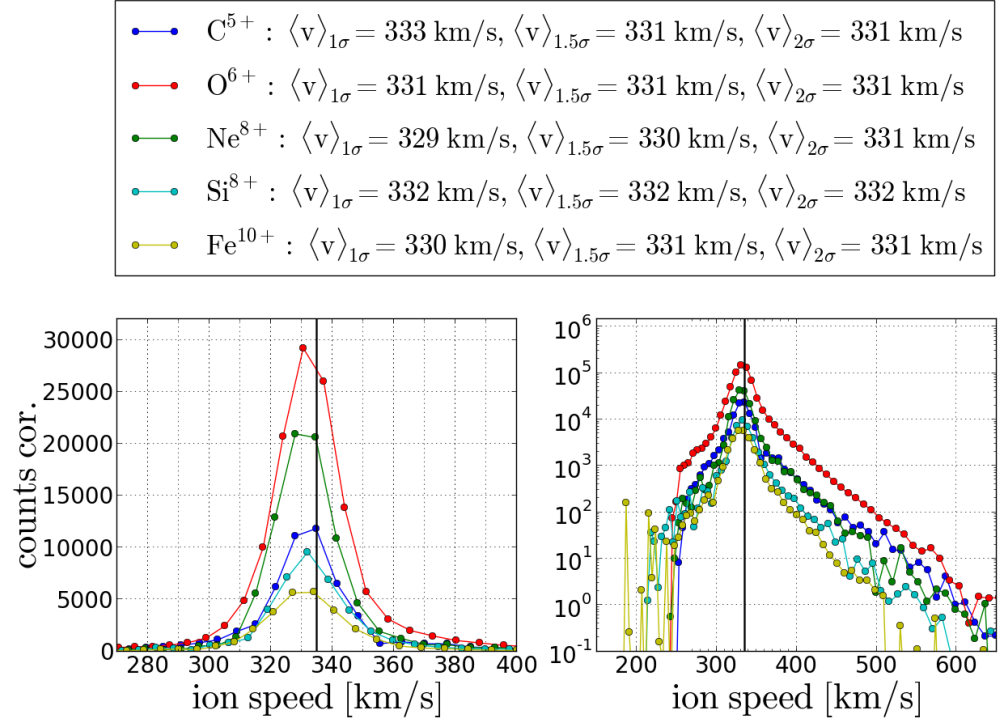## D.3 Long-Term Fast Wind Speed Spectra Obtained from the Kappa-Moyal Full Stable Response Model
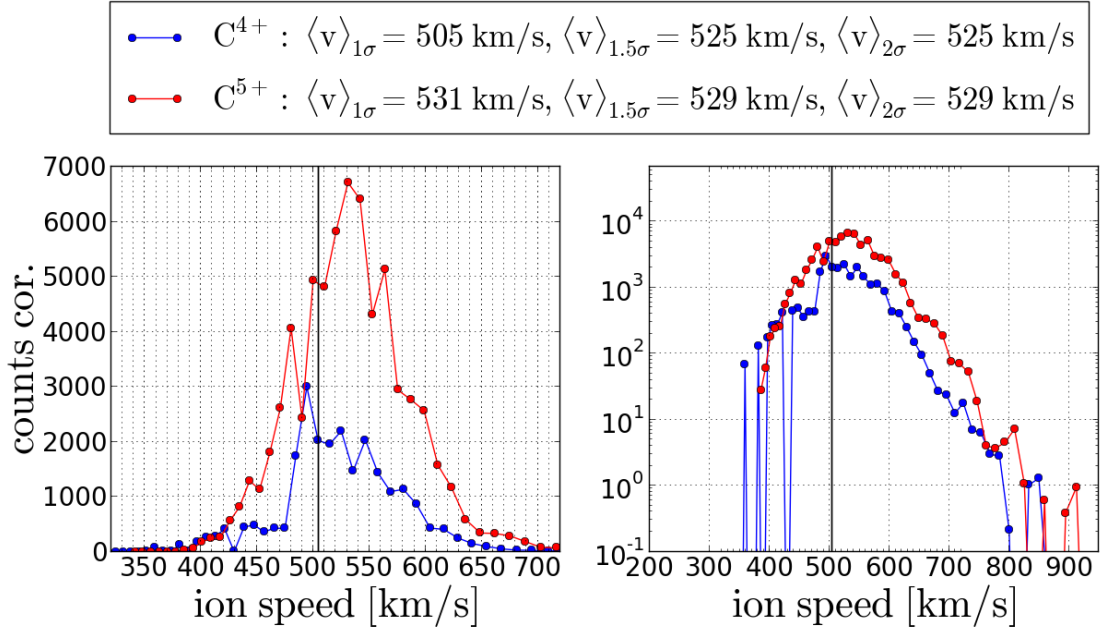
FIGURE D.17: Long-term accumulated count spectra
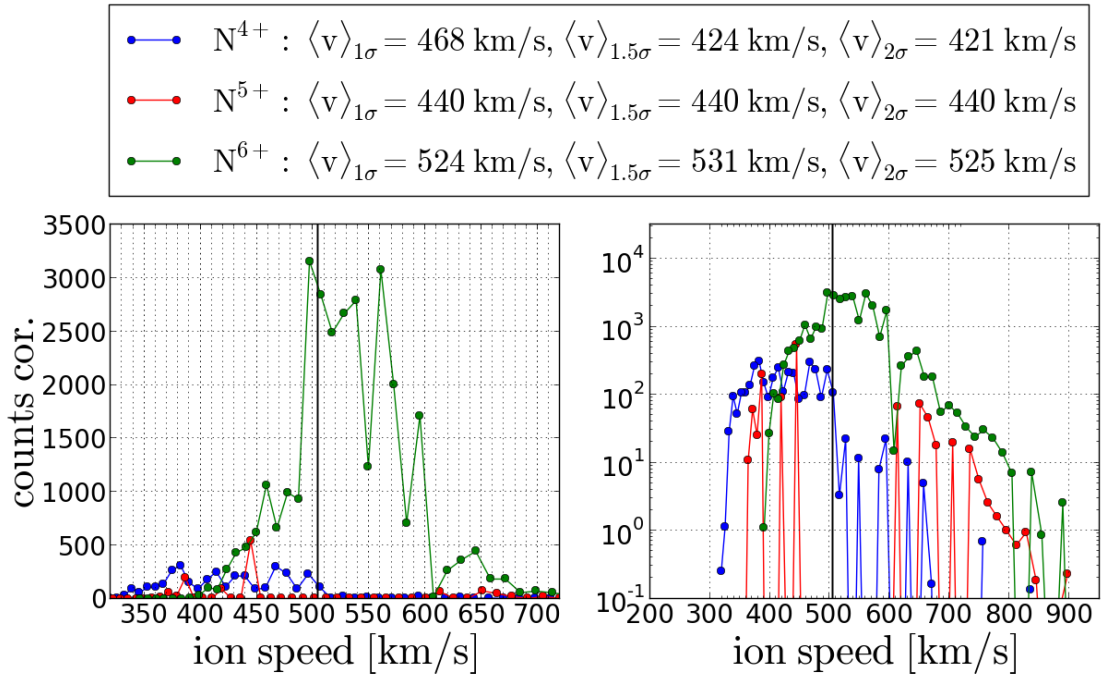
FIGURE D.18: substitute by N46!
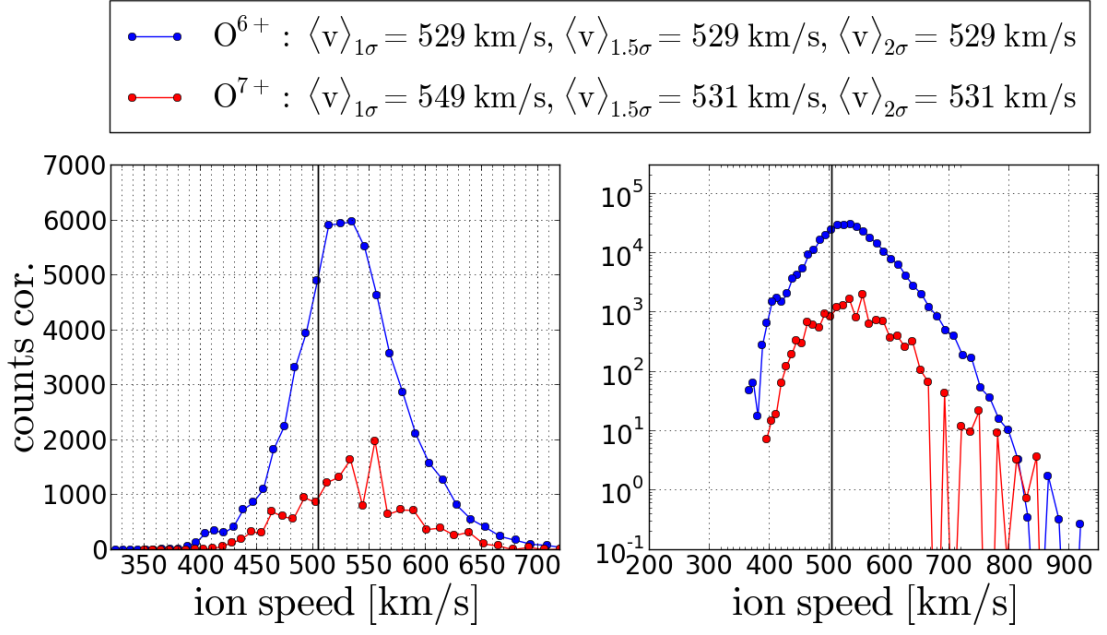
FIGURE D.19: substutute by O67 and put this in appendix!

FIGURE D.20: test1

Mg^{6+} : $\langle v \rangle_{1\sigma} = 528$ km/s, $\langle v \rangle_{1.5\sigma} = 538$ km/s, $\langle v \rangle_{2\sigma} = 532$ km/s

Mg^{7+} : $\langle v \rangle_{1\sigma} = 519$ km/s, $\langle v \rangle_{1.5\sigma} = 527$ km/s, $\langle v \rangle_{2\sigma} = 530$ km/s

Mg^{8+} : $\langle v \rangle_{1\sigma} = 545$ km/s, $\langle v \rangle_{1.5\sigma} = 512$ km/s, $\langle v \rangle_{2\sigma} = 518$ km/s

Mg^{9+} : $\langle v \rangle_{1\sigma} = 611$ km/s, $\langle v \rangle_{1.5\sigma} = 611$ km/s, $\langle v \rangle_{2\sigma} = 611$ km/s

Mg^{10+} : $\langle v \rangle_{1\sigma} = 513$ km/s, $\langle v \rangle_{1.5\sigma} = 519$ km/s, $\langle v \rangle_{2\sigma} = 531$ km/s
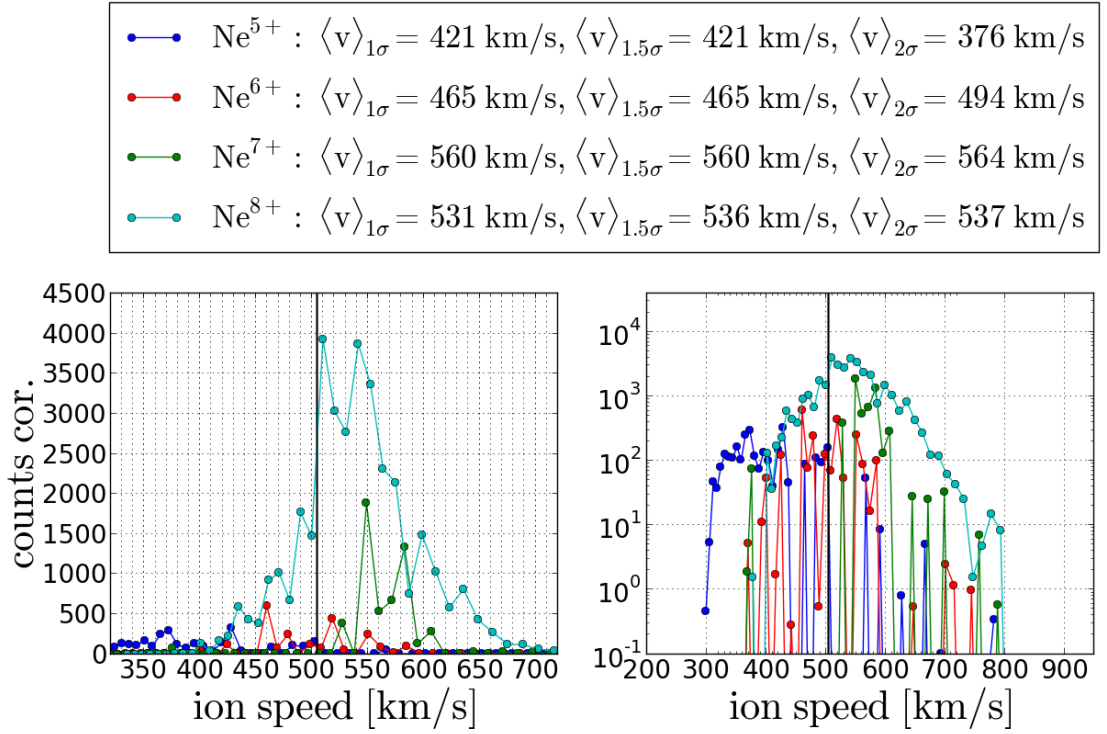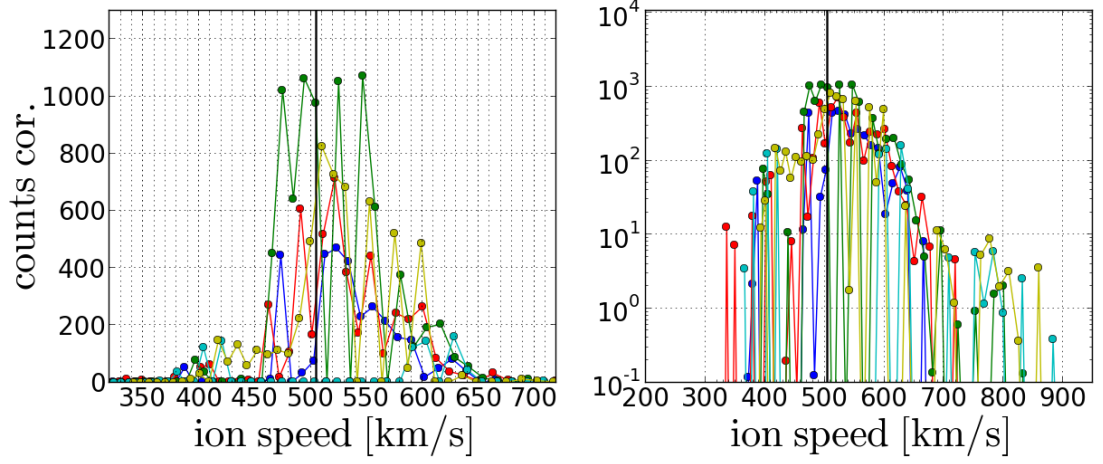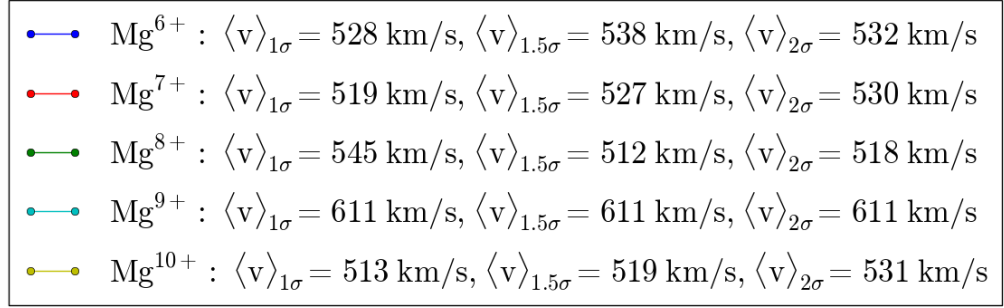
FIGURE D.21: test2
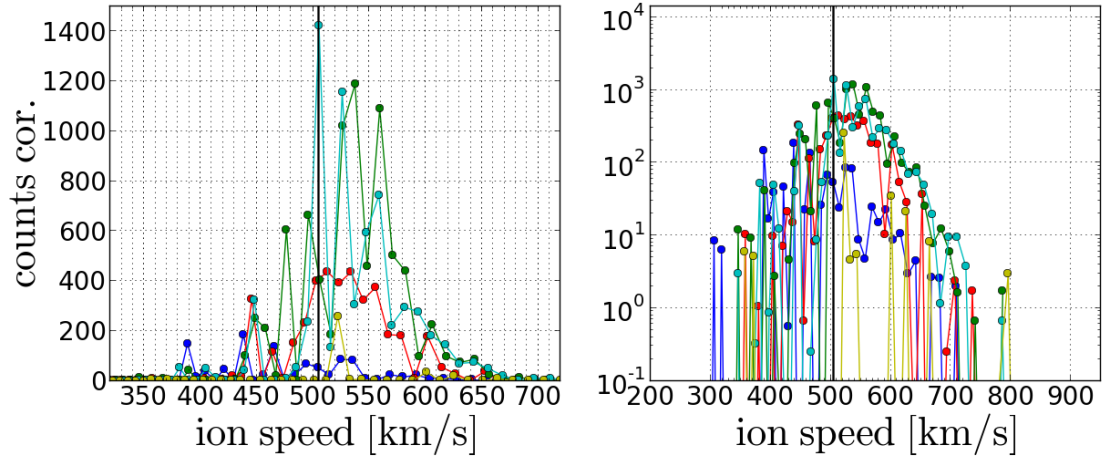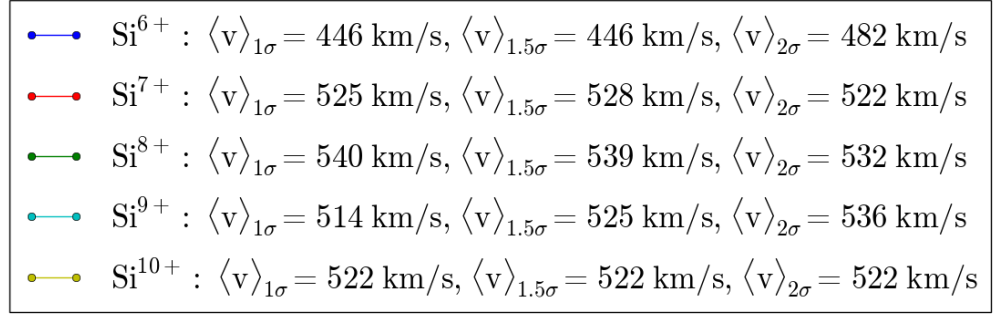
FIGURE D.22: substitut either by Si6-10 (better) or Si710.
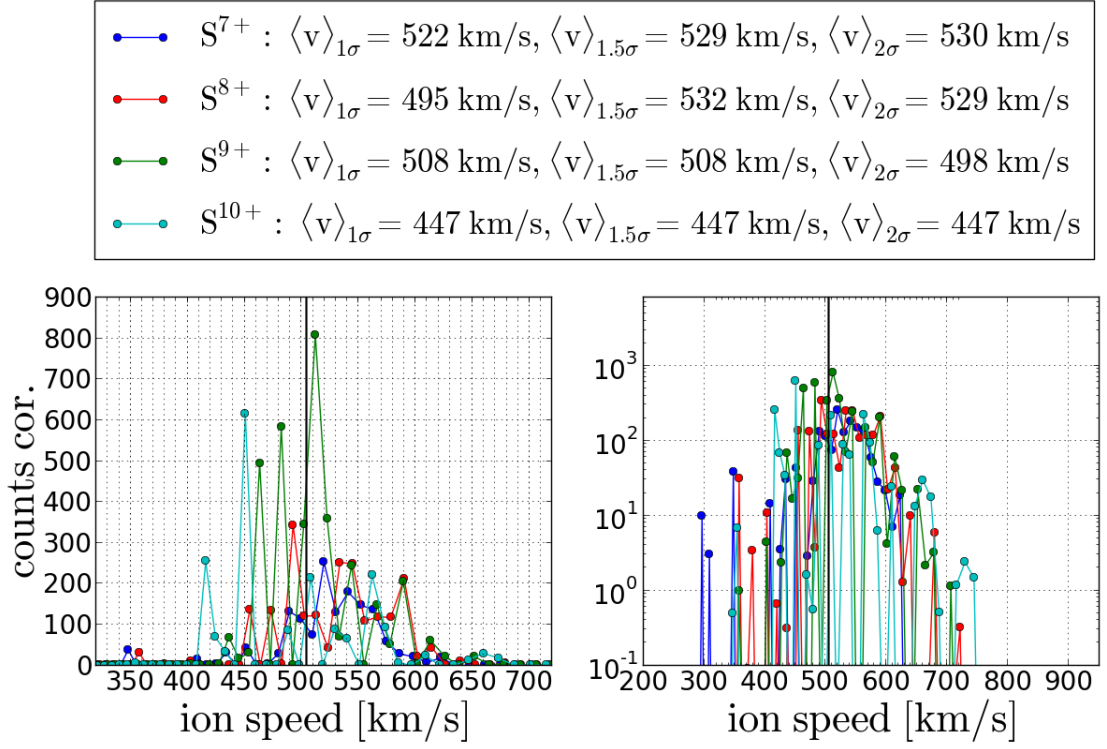
FIGURE D.23: Long-term accumulated count spectra
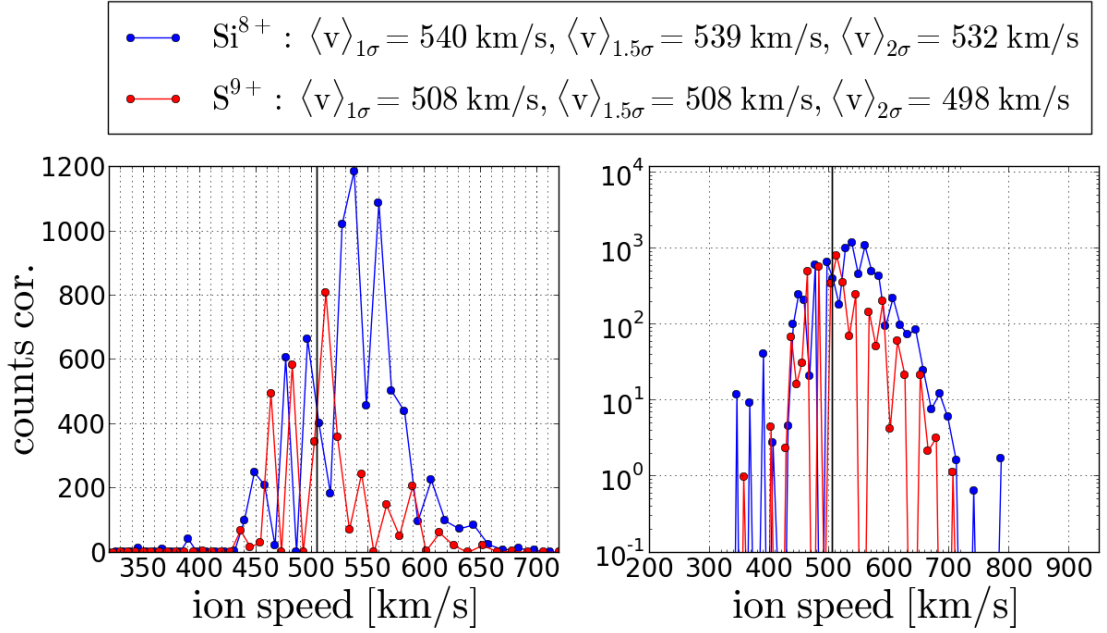
FIGURE D.24: Long-term accumulated count spectra

FIGURE D.25

Fe^{7+} : $\langle v \rangle_{1\sigma} = 516$ km/s, $\langle v \rangle_{1.5\sigma} = 516$ km/s, $\langle v \rangle_{2\sigma} = 508$ km/s

Fe^{8+} : $\langle v \rangle_{1\sigma} = 511$ km/s, $\langle v \rangle_{1.5\sigma} = 520$ km/s, $\langle v \rangle_{2\sigma} = 519$ km/s

Fe^{9+} : $\langle v \rangle_{1\sigma} = 519$ km/s, $\langle v \rangle_{1.5\sigma} = 523$ km/s, $\langle v \rangle_{2\sigma} = 524$ km/s

Fe^{10+} : $\langle v \rangle_{1\sigma} = 524$ km/s, $\langle v \rangle_{1.5\sigma} = 526$ km/s, $\langle v \rangle_{2\sigma} = 528$ km/s

Fe^{11+} : $\langle v \rangle_{1\sigma} = 533$ km/s, $\langle v \rangle_{1.5\sigma} = 530$ km/s, $\langle v \rangle_{2\sigma} = 529$ km/s

Fe^{12+} : $\langle v \rangle_{1\sigma} = 502$ km/s, $\langle v \rangle_{1.5\sigma} = 504$ km/s, $\langle v \rangle_{2\sigma} = 509$ km/s

Fe^{13+} : $\langle v \rangle_{1\sigma} = 418$ km/s, $\langle v \rangle_{1.5\sigma} = 418$ km/s, $\langle v \rangle_{2\sigma} = 433$ km/s
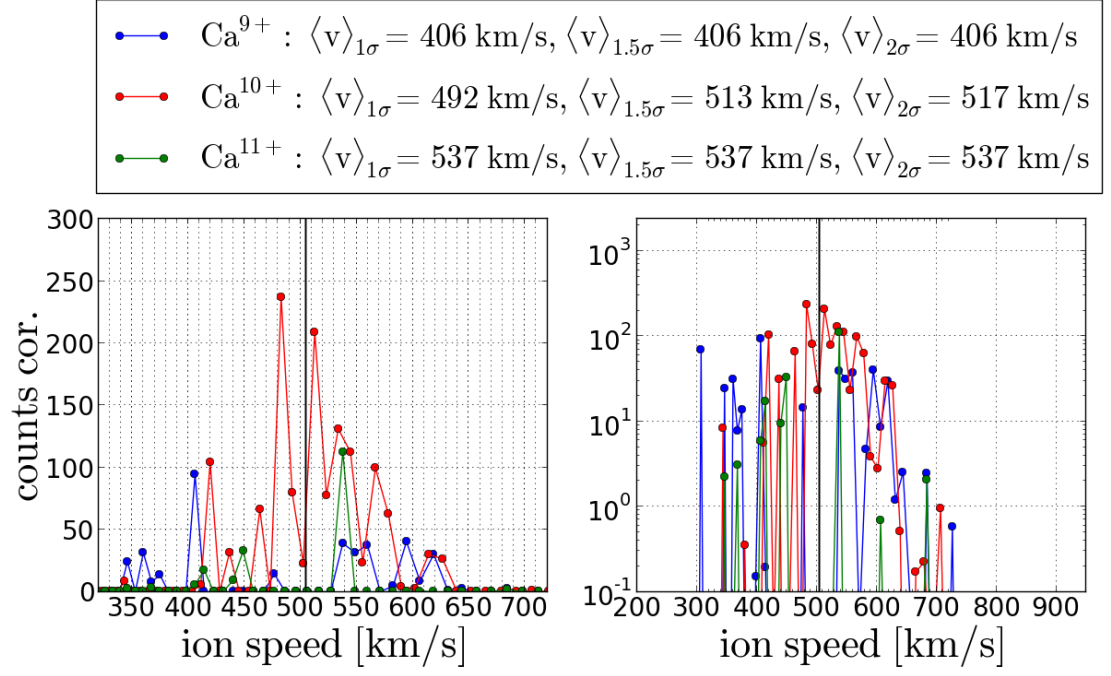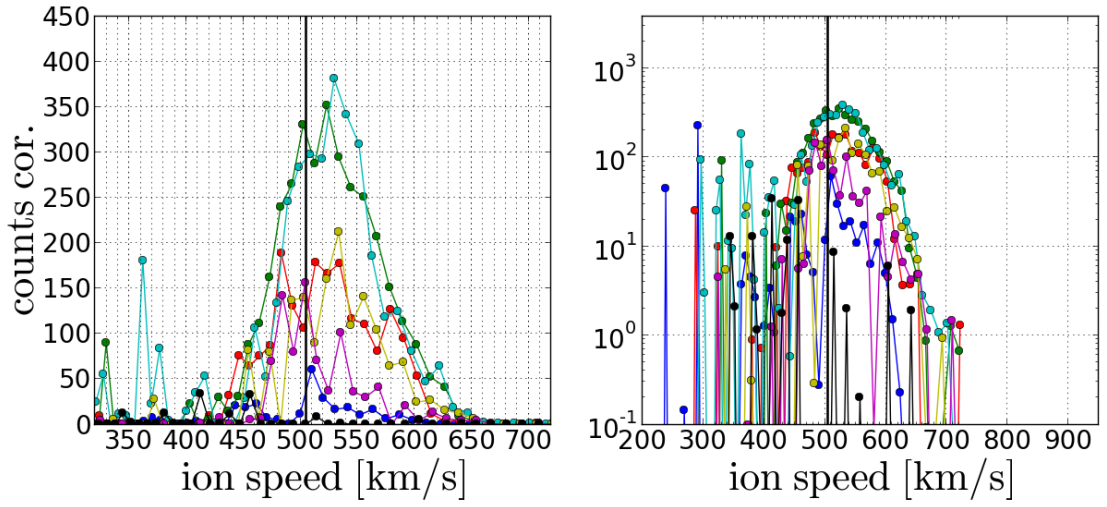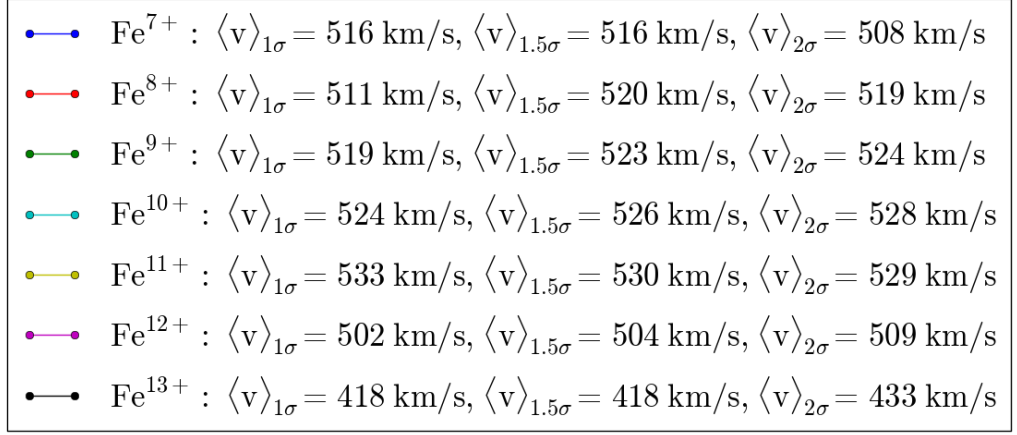
FIGURE D.26: Long-term accumulated count spectra

D.4 Long-Term Fast Wind Speed Spectra Obtained from the Kappa-Moyal Reduced Stable Response Model

Period: DOY 174-220 1996, vsw (vproton) in[500,510] km/s. Model: Kappa-Moyal Reduced Stable (28 ions included in the fit)
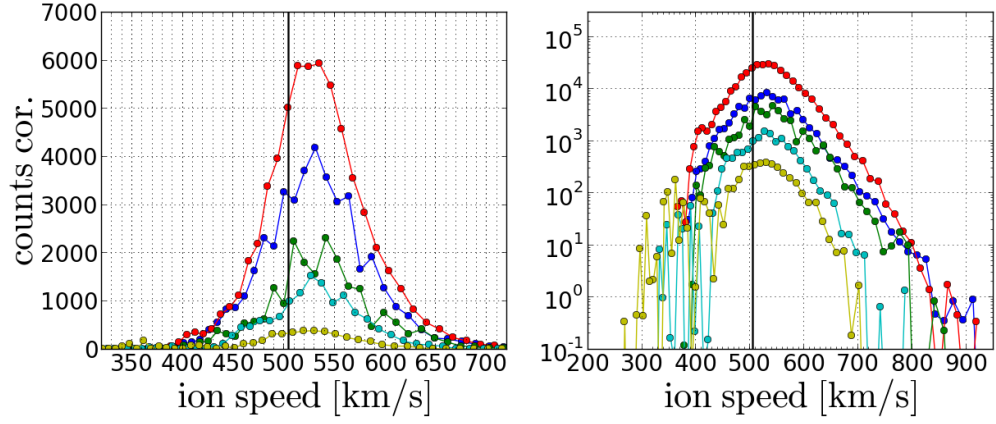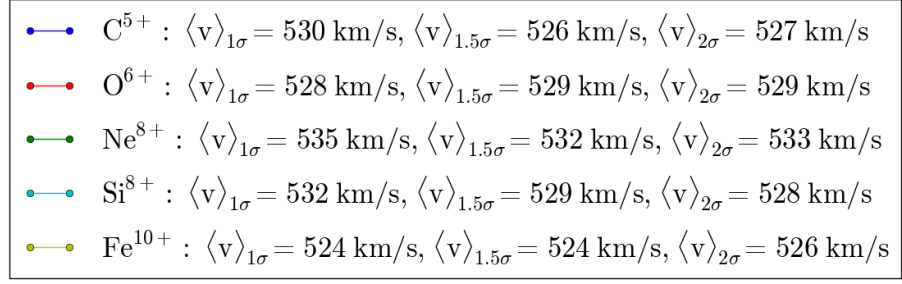
FIGURE D.27: Long-term accumulated count spectra
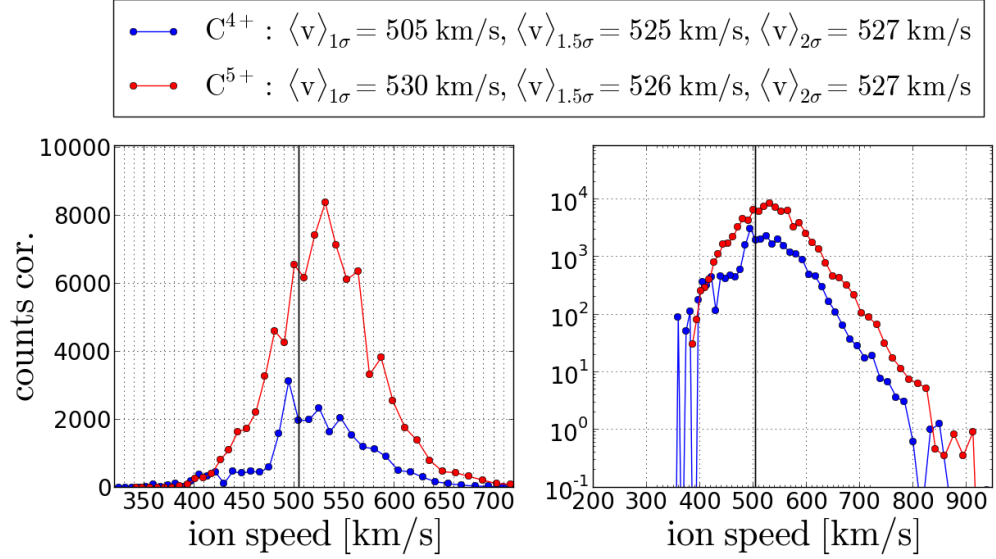
FIGURE D.28: Long-term accumulated count spectra
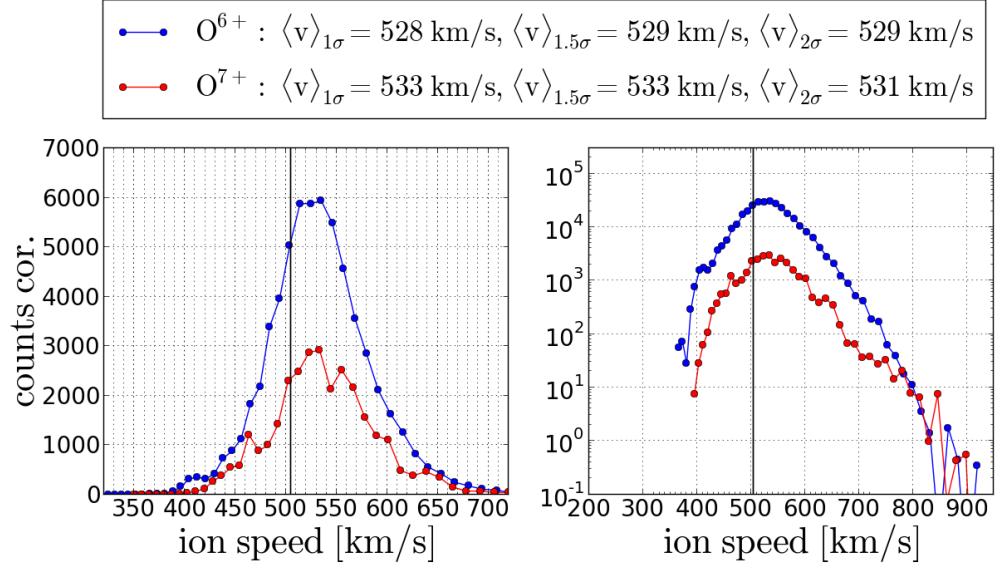
FIGURE D.29: Long-term accumulated count spectra
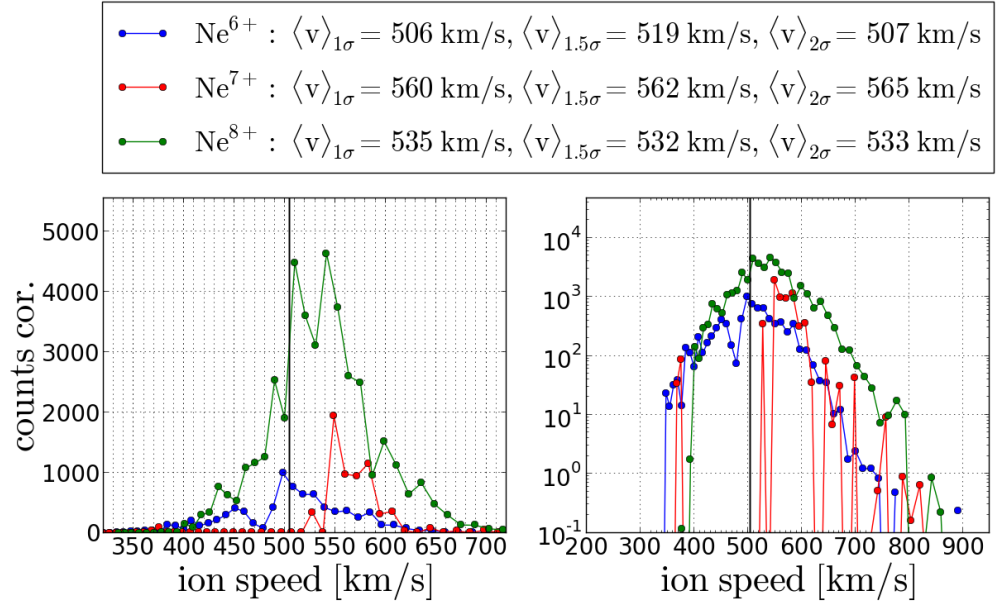
FIGURE D.30: maybe not necessary to put it here (since Ne8 is already shown), and only put this in the appendix.

Si^{6+} : $\langle v \rangle_{1\sigma} = 523$ km/s, $\langle v \rangle_{1.5\sigma} = 508$ km/s, $\langle v \rangle_{2\sigma} = 509$ km/s

Si^{7+} : $\langle v \rangle_{1\sigma} = 525$ km/s, $\langle v \rangle_{1.5\sigma} = 525$ km/s, $\langle v \rangle_{2\sigma} = 524$ km/s

Si^{8+} : $\langle v \rangle_{1\sigma} = 532$ km/s, $\langle v \rangle_{1.5\sigma} = 529$ km/s, $\langle v \rangle_{2\sigma} = 528$ km/s

Si^{9+} : $\langle v \rangle_{1\sigma} = 516$ km/s, $\langle v \rangle_{1.5\sigma} = 519$ km/s, $\langle v \rangle_{2\sigma} = 520$ km/s

Si^{10+} : $\langle v \rangle_{1\sigma} = 523$ km/s, $\langle v \rangle_{1.5\sigma} = 523$ km/s, $\langle v \rangle_{2\sigma} = 523$ km/s
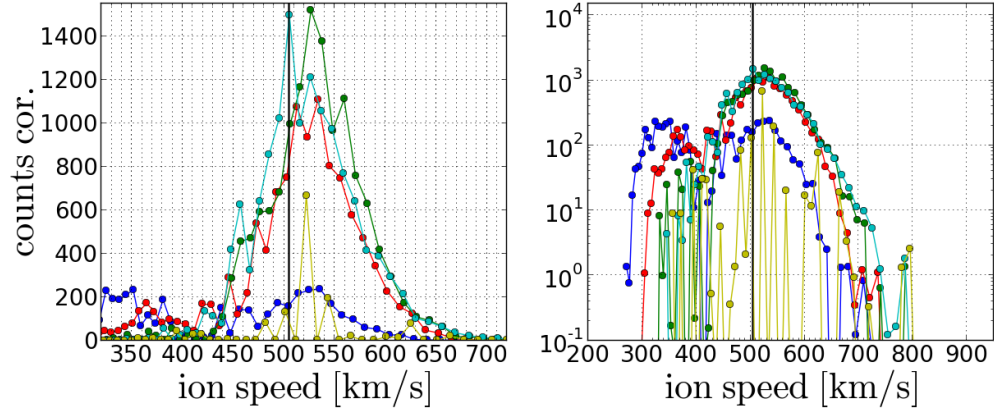
FIGURE D.31: Long-term accumulated count spectra

Fe^{7+} : $\langle v \rangle_{1\sigma} = 512$ km/s, $\langle v \rangle_{1.5\sigma} = 491$ km/s, $\langle v \rangle_{2\sigma} = 500$ km/s

Fe^{8+} : $\langle v \rangle_{1\sigma} = 523$ km/s, $\langle v \rangle_{1.5\sigma} = 520$ km/s, $\langle v \rangle_{2\sigma} = 519$ km/s

Fe^{9+} : $\langle v \rangle_{1\sigma} = 523$ km/s, $\langle v \rangle_{1.5\sigma} = 523$ km/s, $\langle v \rangle_{2\sigma} = 522$ km/s

Fe^{10+} : $\langle v \rangle_{1\sigma} = 524$ km/s, $\langle v \rangle_{1.5\sigma} = 524$ km/s, $\langle v \rangle_{2\sigma} = 526$ km/s

Fe^{11+} : $\langle v \rangle_{1\sigma} = 533$ km/s, $\langle v \rangle_{1.5\sigma} = 530$ km/s, $\langle v \rangle_{2\sigma} = 527$ km/s

Fe^{12+} : $\langle v \rangle_{1\sigma} = 513$ km/s, $\langle v \rangle_{1.5\sigma} = 520$ km/s, $\langle v \rangle_{2\sigma} = 514$ km/s

Fe^{13+} : $\langle v \rangle_{1\sigma} = 479$ km/s, $\langle v \rangle_{1.5\sigma} = 479$ km/s, $\langle v \rangle_{2\sigma} = 515$ km/s

FIGURE D.32: Long-term accumulated count spectra

D.5 Long-Term Fast Wind Spectra Utilized for the Systematic Error Estimation

Model: Kappa-Moyal Reduced Stable (28 ions included in the fit) varying tail scaling parameter $A_C \in \{0.0015, 0.0025, 0.0035, 0.0055, 0.0075\}\, \text{ch}^{-1}$ ($A_C = 0.0035$ is the optimal selected parameter.

FIGURE D.33: $A_C = 0.0015\,\text{ch}^{-1}$

$\langle v \rangle_{1\sigma}$ values (top legend):

- C^{5+} : $\langle v \rangle_{1\sigma} = 530$ km/s, $\langle v \rangle_{1.5\sigma} = 526$ km/s, $\langle v \rangle_{2\sigma} = 528$ km/s
- O^{6+} : $\langle v \rangle_{1\sigma} = 528$ km/s, $\langle v \rangle_{1.5\sigma} = 526$ km/s, $\langle v \rangle_{2\sigma} = 528$ km/s
- Ne^{8+} : $\langle v \rangle_{1\sigma} = 529$ km/s, $\langle v \rangle_{1.5\sigma} = 531$ km/s, $\langle v \rangle_{2\sigma} = 530$ km/s
- Si^{8+} : $\langle v \rangle_{1\sigma} = 532$ km/s, $\langle v \rangle_{1.5\sigma} = 525$ km/s, $\langle v \rangle_{2\sigma} = 526$ km/s
- Fe^{10+} : $\langle v \rangle_{1\sigma} = 523$ km/s, $\langle v \rangle_{1.5\sigma} = 523$ km/s, $\langle v \rangle_{2\sigma} = 524$ km/s

Second legend:

- Fe^{7+} : $\langle v \rangle_{1\sigma} = 510$ km/s, $\langle v \rangle_{1.5\sigma} = 492$ km/s, $\langle v \rangle_{2\sigma} = 492$ km/s
- Fe^{8+} : $\langle v \rangle_{1\sigma} = 514$ km/s, $\langle v \rangle_{1.5\sigma} = 515$ km/s, $\langle v \rangle_{2\sigma} = 515$ km/s
- Fe^{9+} : $\langle v \rangle_{1\sigma} = 519$ km/s, $\langle v \rangle_{1.5\sigma} = 519$ km/s, $\langle v \rangle_{2\sigma} = 519$ km/s
- Fe^{10+} : $\langle v \rangle_{1\sigma} = 523$ km/s, $\langle v \rangle_{1.5\sigma} = 523$ km/s, $\langle v \rangle_{2\sigma} = 524$ km/s
- Fe^{11+} : $\langle v \rangle_{1\sigma} = 533$ km/s, $\langle v \rangle_{1.5\sigma} = 527$ km/s, $\langle v \rangle_{2\sigma} = 524$ km/s
- Fe^{12+} : $\langle v \rangle_{1\sigma} = 510$ km/s, $\langle v \rangle_{1.5\sigma} = 516$ km/s, $\langle v \rangle_{2\sigma} = 507$ km/s
- Fe^{13+} : $\langle v \rangle_{1\sigma} = 487$ km/s, $\langle v \rangle_{1.5\sigma} = 513$ km/s, $\langle v \rangle_{2\sigma} = 518$ km/s

FIGURE D.34: $A_C = 0.0025\,\mathrm{ch}^{-1}$

C^{5+} : $\langle v \rangle_{1\sigma} = 530$ km/s, $\langle v \rangle_{1.5\sigma} = 526$ km/s, $\langle v \rangle_{2\sigma} = 527$ km/s

O^{6+} : $\langle v \rangle_{1\sigma} = 528$ km/s, $\langle v \rangle_{1.5\sigma} = 529$ km/s, $\langle v \rangle_{2\sigma} = 529$ km/s

Ne^{8+} : $\langle v \rangle_{1\sigma} = 535$ km/s, $\langle v \rangle_{1.5\sigma} = 532$ km/s, $\langle v \rangle_{2\sigma} = 533$ km/s

Si^{8+} : $\langle v \rangle_{1\sigma} = 532$ km/s, $\langle v \rangle_{1.5\sigma} = 529$ km/s, $\langle v \rangle_{2\sigma} = 528$ km/s

Fe^{10+} : $\langle v \rangle_{1\sigma} = 524$ km/s, $\langle v \rangle_{1.5\sigma} = 524$ km/s, $\langle v \rangle_{2\sigma} = 526$ km/s

Fe^{7+} : $\langle v \rangle_{1\sigma} = 512$ km/s, $\langle v \rangle_{1.5\sigma} = 491$ km/s, $\langle v \rangle_{2\sigma} = 500$ km/s

Fe^{8+} : $\langle v \rangle_{1\sigma} = 523$ km/s, $\langle v \rangle_{1.5\sigma} = 520$ km/s, $\langle v \rangle_{2\sigma} = 519$ km/s

Fe^{9+} : $\langle v \rangle_{1\sigma} = 523$ km/s, $\langle v \rangle_{1.5\sigma} = 523$ km/s, $\langle v \rangle_{2\sigma} = 522$ km/s

Fe^{10+} : $\langle v \rangle_{1\sigma} = 524$ km/s, $\langle v \rangle_{1.5\sigma} = 524$ km/s, $\langle v \rangle_{2\sigma} = 526$ km/s

Fe^{11+} : $\langle v \rangle_{1\sigma} = 533$ km/s, $\langle v \rangle_{1.5\sigma} = 530$ km/s, $\langle v \rangle_{2\sigma} = 527$ km/s

Fe^{12+} : $\langle v \rangle_{1\sigma} = 513$ km/s, $\langle v \rangle_{1.5\sigma} = 520$ km/s, $\langle v \rangle_{2\sigma} = 514$ km/s

Fe^{13+} : $\langle v \rangle_{1\sigma} = 479$ km/s, $\langle v \rangle_{1.5\sigma} = 479$ km/s, $\langle v \rangle_{2\sigma} = 515$ km/s

FIGURE D.35: $A_C = 0.0035\,\mathrm{ch}^{-1}$

288

Legend (top):

- C^{5+} : $\langle v \rangle_{1\sigma} = 532$ km/s, $\langle v \rangle_{1.5\sigma} = 530$ km/s, $\langle v \rangle_{2\sigma} = 530$ km/s
- O^{6+} : $\langle v \rangle_{1\sigma} = 531$ km/s, $\langle v \rangle_{1.5\sigma} = 534$ km/s, $\langle v \rangle_{2\sigma} = 534$ km/s
- Ne^{8+} : $\langle v \rangle_{1\sigma} = 537$ km/s, $\langle v \rangle_{1.5\sigma} = 540$ km/s, $\langle v \rangle_{2\sigma} = 538$ km/s
- Si^{8+} : $\langle v \rangle_{1\sigma} = 533$ km/s, $\langle v \rangle_{1.5\sigma} = 537$ km/s, $\langle v \rangle_{2\sigma} = 539$ km/s
- Fe^{10+} : $\langle v \rangle_{1\sigma} = 530$ km/s, $\langle v \rangle_{1.5\sigma} = 534$ km/s, $\langle v \rangle_{2\sigma} = 535$ km/s

Legend (middle):

- Fe^{7+} : $\langle v \rangle_{1\sigma} = 586$ km/s, $\langle v \rangle_{1.5\sigma} = 586$ km/s, $\langle v \rangle_{2\sigma} = 586$ km/s
- Fe^{8+} : $\langle v \rangle_{1\sigma} = 550$ km/s, $\langle v \rangle_{1.5\sigma} = 554$ km/s, $\langle v \rangle_{2\sigma} = 550$ km/s
- Fe^{9+} : $\langle v \rangle_{1\sigma} = 535$ km/s, $\langle v \rangle_{1.5\sigma} = 538$ km/s, $\langle v \rangle_{2\sigma} = 539$ km/s
- Fe^{10+} : $\langle v \rangle_{1\sigma} = 530$ km/s, $\langle v \rangle_{1.5\sigma} = 534$ km/s, $\langle v \rangle_{2\sigma} = 535$ km/s
- Fe^{11+} : $\langle v \rangle_{1\sigma} = 535$ km/s, $\langle v \rangle_{1.5\sigma} = 540$ km/s, $\langle v \rangle_{2\sigma} = 542$ km/s
- Fe^{12+} : $\langle v \rangle_{1\sigma} = 533$ km/s, $\langle v \rangle_{1.5\sigma} = 533$ km/s, $\langle v \rangle_{2\sigma} = 536$ km/s
- Fe^{13+} : $\langle v \rangle_{1\sigma} = 415$ km/s, $\langle v \rangle_{1.5\sigma} = 415$ km/s, $\langle v \rangle_{2\sigma} = 415$ km/s

FIGURE D.37: $A_C = 0.0075\,\mathrm{ch}^{-1}$

Bibliography

[1] *Machine Learning Techniques for Space Weather*. Elsevier, 2018.

[2] Aellig, M. and Grünwaldt, H. and Bochsler, P. and Wurz, Peter and Hefti, S. and Kallenbach, R. and Ipavich, F.M. and Hovenstadt, D. and Hilchenbach, M. and Team, CELIAS. Solar wind iron charge states observed with high time resolution with soho/celias/ctof. *Correlated Phenomena at the Sun, in the Heliosphere and in Geospace. 31st ESLAB Symposium held 22-25 September, 1997, at ESTEC, Noordwijk, The Netherlands. Edited by A. Wilson. European Space Agency, ESA SP-415, 1997. ISBN: 92-9092-660-0., p.27*, 404:27–31, 1997.
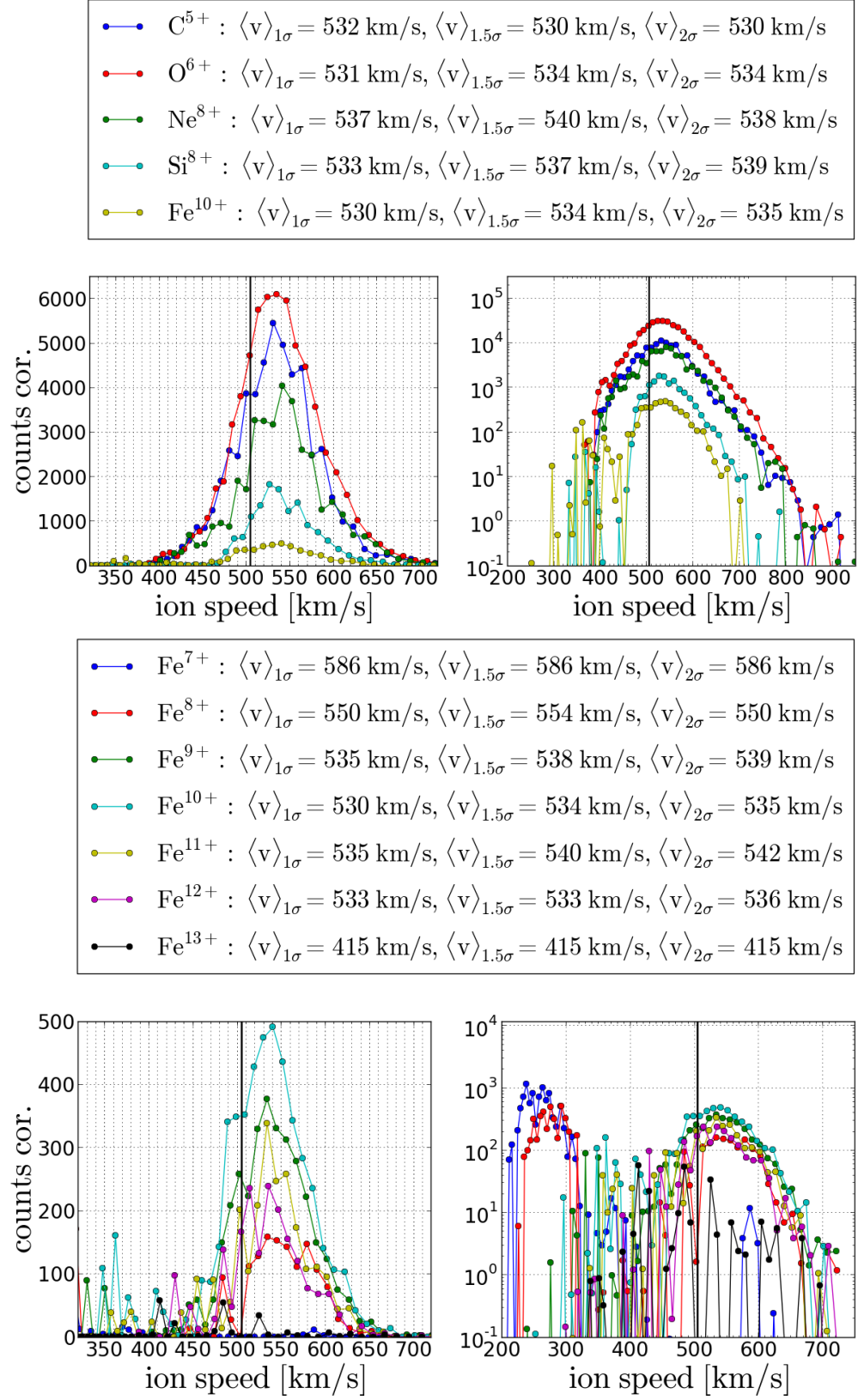
[3] S. K. Antiochos, C. R. DeVore, and J. A. Klimchuk. A model for solar coronal mass ejections. *The Astrophysical Journal*, 510(1):485–493, 1999.

[4] J. R. Asbridge, S. J. Bame, W. C. Feldman, and M. D. Montgomery. Helium and hydrogen velocity differences in the solar wind. *Journal of Geophysical Research: Space Physics*, 81(16):2719–2727, 1976.

[5] Markus J. Aschwanden. *Physics of the Solar Corona: An Introduction with Problems and Solutions*. Springer Praxis Books. Praxis Publishing Ltd Chichester UK, Berlin, Heidelberg, 2005.

[6] Axford, W.I., McKenzie, J.F. Cosmic winds and the heliosphere: The solar wind. pages 31–66, 1997.

[7] Bame, S. and Mccomas, David and Barraclough, Bruce and Phillips, J. and Sofaly, K. and Chavez, J. and Goldstein, B. and Sakurai, R. The ulysses solar wind plasma experiment. *A&AS*, 92, 1992.

[8] L. Berger, R. F. Wimmer-Schweingruber, and G. Gloeckler. Systematic measurements of ion-proton differential streaming in the solar wind. *Physical review letters*, 106(15):151103, 2011.

[9] L. Biermann. Kometenschweife und solare korpuskularstrahlung. *Zeitschrift für Astrophysik*, 29:274–286, 1951.

[10] Peter Bochsler. Minor ions in the solar wind. *The Astronomy and Astrophysics Review*, 14(1):1–40, 2007.

[11] S. Bourouaine, E. Marsch, and F. M. Neubauer. Temperature anisotropy and differential streaming of solar wind ions. correlations with transverse fluctuations. *Astronomy & Astrophysics*, 536:A39, 2011.

[12] R. Chhiber, A. V. Usmanov, W. H. Matthaeus, and M. L. Goldstein. Solar wind collisional age from a global magnetohydrodynamics simulation. *The Astrophysical Journal*, 821(1):34, 2016.

[13] S. R. Cranmer and A. A. van Ballegooijen. On the generation, propagation, and reflection of alfven waves from the solar photosphere to the distant heliosphere. *The Astrophysical Journal Supplement Series*, 156(2):265–293, 2005.

[14] Steven R. Cranmer. Coronal holes and the high-speed solar wind. *Space Science Reviews*, 101(3/4):229–294, 2002.

[15] Mausumi Dikpati and Peter A. Gilman. Global solar dynamo models: Simulations and predictions. *Journal of Astrophysics and Astronomy*, 29(1-2):29–39, 2008.

[16] U. Feldman. On the sources of fast and slow solar wind. *Journal of Geophysical Research*, 110(A7):261, 2005.

[17] W. C. Feldman, J. A. Asbridge, S. J. Bame, and M. D. Montgomery. Double ion streams in the solar wind. *Journal of Geophysical Research*, 78:2017–2027, 1973.

[18] G. Allen Gary. Plasma beta above a solar active region: Rethinking the paradigm. *Solar Physics*, 203(1):71–86, 2001.

[19] S. P. Gary. What is a plasma instability? *Eos, Transactions American Geophysical Union*, 73(49):529, 1992.

[20] S. Peter Gary, Lin Yin, Dan Winske, and Daniel B. Reisenfeld. Alpha/proton magnetosonic instability in the solar wind. *Journal of Geophysical Research: Space Physics*, 105(A9):20989–20996, 2000.

[21] J. Geiss. Solar wind composition experiment. *Apollo 16 Prel Sci Rep NASA Spec Pub*, 305(14):1–10, 1972.

[22] J. Geiss, G. Gloeckler, R. von Steiger, H. Balsiger, L. A. Fisk, A. B. Galvin, F. M. Ipavich, S. Livi, J. F. McKenzie, and K. W. Ogilvie. The southern high-speed stream: results from the swics instrument on ulysses. *Science (New York, N.Y.)*, 268(5213):1033–1036, 1995.

[23] Daniel J. Gershman, Thomas H. Zurbuchen, Lennard A. Fisk, Jason A. Gilbert, Jim M. Raines, Brian J. Anderson, Charles W. Smith, Haje Korth, and Sean C. Solomon. Solar wind alpha particles and heavy ions in the inner heliosphere observed with messenger. *Journal of Geophysical Research: Space Physics*, 117(A12):n/a–n/a, 2012.

[24] Gloeckler, G. and Geiss, J. and Balsiger, H. and Bedini, P. and Cain, J.C. and Fischer, J. and Fisk, L. A. and al. The solar wind ion composition spectrometer. *Astronomy and Astrophysiscs*, 92:267–289, 1992.

[25] L. Gomberoff and R. Elgueta. Resonant acceleration of alpha particles by ion cyclotron waves in the solar wind. *Journal of Geophysical Research: Space Physics*, 96(A6):9801, 1991.

[26] K.I. Gringauz. Results of observations of charged particles observed out to r=100,000 km with the aid of charged-particle traps on soviet space rockets. *Astronomcheskii Zhurnal*, 37:716, 1960.

[27] David H. Hathaway. The solar cycle. *Living reviews in solar physics*, 12:4, 2015.

[28] S. Hefti, H. Grünwaldt, F. M. Ipavich, P. Bochsler, D. Hovestadt, M. R. Aellig, M. Hilchenbach, R. Kallenbach, A. B. Galvin, J. Geiss, F. Gliem, G. Gloeckler, B. Klecker, E. Marsch, E. Möbius, M. Neugebauer, and P. Wurz. Kinetic properties of solar wind minor ions and protons measured with soho/celias. *Journal of Geophysical Research: Space Physics*, 103(A12):29697–29704, 1998.

[29] Verena Heidrich-Meisner and Robert F. Wimmer-Schweingruber. Solar wind classification via k -means clustering algorithm. In *Machine Learning Techniques for Space Weather*, pages 397–424. Elsevier, 2018.

[30] R. Hernandez and E. Marsch. Collisional time scales for temperature and velocity exchange between drifting maxwellians. *Journal of Geophysical Research: Space Physics*, 90(A11):11062, 1985.

[31] Joseph V. Hollweg and Philip A. Isenberg. Generation of the fast solar wind: A review with emphasis on the resonant cyclotron interaction. *Journal of Geophysical Research: Space Physics*, 107(A7):6551, 2002.

[32] Ian W. Hoppock, Benjamin D. G. Chandran, Kristopher G. Klein, Alfred Mallet, and Daniel Verscharen. Stochastic proton heating by kinetic-alfvén-wave turbulence in moderately high-beta plasmas. *Journal of plasma physics*, 84(6), 2018.

[33] D. Hovestadt, M. Hilchenbach, A. Brgi, B. Klecker, P. Laeverenz, M. Scholer, H. Grnwaldt, W. I. Axford, S. Livi, E. Marsch, B. Wilken, H. P. Winterhoff, F. M.

Ipavich, P. Bedini, M. A. Coplan, A. B. Galvin, G. Gloeckler, P. Bochsler, H. Balsiger, J. Fischer, J. Geiss, R. Kallenbach, P. Wurz, K.-U. Reiche, F. Gliem, D. L. Judge, H. S. Ogawa, K. C. Hsieh, E. Mbius, M. A. Lee, G. G. Managadze, M. I. Verigin, and M. Neugebauer. Celias - charge, element and isotope analysis system for soho. *Solar Physics*, 162(1-2):441–481, 1995.

[34] F. M. Ipavich, A. B. Galvin, G. Gloeckler, D. Hovestadt, S. J. Bame, B. Klecker, M. Scholer, L. A. Fisk, and C. Y. Fan. Solar wind fe and cno measurements in high-speed flows. *Journal of Geophysical Research: Space Physics*, 91(A4):4133, 1986.

[35] Philip A. Isenberg and Joseph V. Hollweg. On the preferential acceleration and heating of solar wind heavy ions. *Journal of Geophysical Research: Space Physics*, 88(A5):3923, 1983.

[36] Philip A. Isenberg, Martin A. Lee, and Joseph V. Hollweg. The kinetic shell model of coronal heating and acceleration by ion cyclotron waves: 1. outward propagating waves. *Journal of Geophysical Research: Space Physics*, 106(A4):5649–5660, 2001.

[37] J. C. Kasper, K. G. Klein, T. Weber, M. Maksimovic, A. Zaslavsky, S. D. Bale, B. A. Maruca, M. L. Stevens, and A. W. Case. A zone of preferential ion heating extends tens of solar radii from the sun. *The Astrophysical Journal*, 849(2):126, 2017.

[38] J. C. Kasper, A. J. Lazarus, and S. P. Gary. Hot solar-wind helium: direct evidence for local heating by alfvén-cyclotron dissipation. *Physical review letters*, 101(26):261103, 2008.

[39] C. F. Kennel and F. Engelmann. Velocity space diffusion from weak plasma turbulence in a magnetic field. *Physics of Fluids*, 9(12):2377, 1966.

[40] Xing Li and Shadia Rifai Habbal. Proton/alpha magnetosonic instability in the fast solar wind. *Journal of Geophysical Research: Space Physics*, 105(A4):7483–7489, 2000.

[41] S. Livi, E. Marsch, and H. Rosenbauer. Coulomb collisional domains in the solar wind. *Journal of Geophysical Research: Space Physics*, 91(A7):8045, 1986.

[42] E. Marsch, C. K. Goertz, and K. Richter. Wave heating and acceleration of solar wind ions by cyclotron resonance. *Journal of Geophysical Research: Space Physics*, 87(A7):5030–5044, 1982.

[43] E. Marsch, K.-H. Mühlhäuser, H. Rosenbauer, R. Schwenn, and K. U. Denskat. Pronounced proton core temperature anisotropy, ion differential speed, and simultaneous alfvén wave activity in slow solar wind at 0.3 au. *Journal of Geophysical Research: Space Physics*, 86(A11):9199, 1981.

[44] E. Marsch, K.-H. Mühlhäuser, H. Rosenbauer, R. Schwenn, and F. M. Neubauer. Solar wind helium ions: Observations of the helios solar probes between 0.3 and 1 au. *Journal of Geophysical Research: Space Physics*, 87(A1):35, 1982.

[45] E. Marsch, K.-H. Mühlhäuser, R. Schwenn, H. Rosenbauer, W. Pilipp, and F. M. Neubauer. Solar wind protons: Three-dimensional velocity distributions and derived plasma parameters measured between 0.3 and 1 au. *Journal of Geophysical Research*, 87(A1):52, 1982.

[46] Eckart Marsch. Kinetic physics of the solar corona and solar wind. *Living reviews in solar physics*, 3, 2006.

[47] B. A. Maruca, S. D. Bale, L. Sorriso-Valvo, J. C. Kasper, and M. L. Stevens. Collisional thermalization of hydrogen and helium in solar-wind plasma. *Physical review letters*, 111(24):241101, 2013.

[48] Lorenzo Matteini, Petr Hellinger, Bruce E. Goldstein, Simone Landi, Marco Velli, and Marcia Neugebauer. Signatures of kinetic instabilities in the solar wind. *Journal of Geophysical Research: Space Physics*, 118(6):2771–2782, 2013.

[49] D. J. McComas, B. L. Barraclough, H. O. Funsten, J. T. Gosling, E. Santiago-Muñoz, R. M. Skoug, B. E. Goldstein, M. Neugebauer, P. Riley, and A. Balogh. Solar wind observations over ulysses' first full polar orbit. *Journal of Geophysical Research: Space Physics*, 105(A5):10419–10433, 2000.

[50] D. J. McComas, H. A. Elliott, N. A. Schwadron, J. T. Gosling, R. M. Skoug, and B. E. Goldstein. The three-dimensional solar wind around solar maximum. *Geophysical Research Letters*, 30(10):n/a–n/a, 2003.

[51] J. F. McKenzie and E. Marsch. Resonant wave acceleration of minor ions in the solar wind. *Astrophysics and Space Science*, 81(1-2):295–314, 1982.

[52] M. Neugebauer, B. E. Goldstein, S. J. Bame, and W. C. Feldman. Ulysses near-ecliptic observations of differential flow between protons and alphas in the solar wind. *Journal of Geophysical Research: Space Physics*, 99(A2):2505, 1994.

[53] Marcia Neugebauer and Conway W. Snyder. Mariner 2 observations of the solar wind: 1. average properties. *Journal of Geophysical Research: Space Physics*, 71(19):4469–4484, 1966.

[54] E. N. Parker. Dynamics of the interplanetary gas and magnetic fields. *The Astrophysical Journal*, 128:664, 1958.

[55] Jean Carlos Perez and Benjamin D. G. Chandran. Direct numerical simulations of reflection-driven, reduced magnetohydrodynamic turbulence from the sun to the alfvén critical point. *The Astrophysical Journal*, 776(2):124, 2013.

[56] Gerd W. Prölss. *Physics of the Earth's Space Environment: An Introduction*. Springer Berlin Heidelberg, Berlin, Heidelberg, 2004.

[57] W. K. H. Schmidt, H. Rosenbauer, E. G. Shelly, and J. Geiss. On temperature and speed of he ++ and o 6+ ions in the solar wind. *Geophysical Research Letters*, 7(9):697–700, 1980.

[58] Carolus J. Schrijver and George L. Siscoe, editors. *Heliophysics: Space storms and radiation : causes and effects*. Cambridge University Press, Cambridge, 2010.

[59] M. Snyder C. W., Neugebauer. Direct observations of the solar wind particles by the marinner ii spcecraft. *Proceedings from the 8th International Cosmic Ray Conference*, 1:210–219, 1963.

[60] Snyder C. W., Neugebauer, M. Solar particles and sun-earth relations. *Proceedings from the 8th International Cosmic Ray Conference*, 1:210–219, 1951.

[61] L. Spitzer. : Physics of fully ionized gases. *New York: Interscience*, 2nd edition, 1962.

[62] Lyman Spitzer. *Physics of Fully Ionized Gases: Second Revised Edition*. Dover Books on Physics. Dover Publications, Newburyport, 2nd ed. edition, 2013.

[63] J. T. Steinberg, A. J. Lazarus, K. W. Ogilvie, R. Lepping, and J. Byrnes. Differential flow between solar wind protons and alpha particles: First wind observations. *Geophysical Research Letters*, 23(10):1183–1186, 1996.

[64] Takeru K. Suzuki and Shu-ichiro Inutsuka. Solar winds driven by nonlinear low-frequency alfvén waves from the photosphere: Parametric study for fast/slow winds and disappearance of solar winds. *Journal of Geophysical Research: Space Physics*, 111(A6):1089, 2006.

[65] Patrick J. Tracy, Justin C. Kasper, Thomas H. Zurbuchen, Jim M. Raines, Paul Shearer, and Jason Gilbert. Thermalization of heavy ions in the solar wind. *The Astrophysical Journal*, 812(2):170, 2015.

[66] Bruce T. Tsurutani and Gurbax S. Lakhina. Some basic concepts of wave-particle interactions in collisionless plasmas. *Reviews of Geophysics*, 35(4):491–501, 1997.

[67] C.-Y. TU and E. Marsch. Two-fluid model for heating of the solar corona and acceleration of the solar wind by high-frequency alfven waves. *Solar Physics*, 171(2):363–391, 1997.

[68] R. von Steiger, J. Geiss, G. Gloeckler, and A. B. Galvin. Kinetic properties of heavy ions in the solar wind from swics/ulysses. *Space Science Reviews*, 72(1-2):71–76, 1995.

[69] R. von Steiger, N. A. Schwadron, L. A. Fisk, J. Geiss, G. Gloeckler, S. Hefti, B. Wilken, R. R. Wimmer-Schweingruber, and T. H. Zurbuchen. Composition of quasi-stationary solar wind flows from ulysses/solar wind ion composition spectrometer. *Journal of Geophysical Research: Space Physics*, 105(A12):27217–27238, 2000.

[70] R. von Steiger and T. H. Zurbuchen. Kinetic properties of heavy solar wind ions from ulysses-swics. *Geophysical Research Letters*, 33(9):6360, 2006.

[71] Fei Xu and Joseph E. Borovsky. A new four-plasma categorization scheme for the solar wind. *Journal of Geophysical Research: Space Physics*, 120(1):70–100, 2015.

Acknowledgements

Erklärung gemäß Paragraph 9 Abs. 7. der Prüfungsverfahrensordnung der Christian-Albrechts-Universität zu Kiel für Studierende der Bachelor- und Master-Studiengänge

Hiermit erkläre ich, dass ich die Doktorarbeit selbstständig verfasst und keine anderen als die angegebenen Quellen und Hilfsmittel benutzt habe und die Arbeit in keinem anderen Prüfungsverfahren eingereicht habe.

Unterschrift:

Ort, Datum: